4D reconstruction of alpine deformations in the western Alps : implications on the orogenic wedge evolution

Antoine Mercier

▶ **To cite this version:**

Antoine Mercier. 4D reconstruction of alpine deformations in the western Alps : implications on the orogenic wedge evolution. Earth Sciences. Université Claude Bernard - Lyon I, 2023. English. ⟨NNT : 2023LYO10176⟩. ⟨tel-04390525v3⟩

HAL Id: tel-04390525

https://hal.science/tel-04390525v3

Submitted on 18 Sep 2024

HAL is a multi-disciplinary open access archive for the deposit and dissemination of scientific research documents, whether they are published or not. The documents may come from teaching and research institutions in France or abroad, or from public or private research centers.

L'archive ouverte pluridisciplinaire **HAL**, est destinée au dépôt et à la diffusion de documents scientifiques de niveau recherche, publiés ou non, émanant des établissements d'enseignement et de recherche français ou étrangers, des laboratoires publics ou privés.

Distributed under a Creative Commons CC BY-NC-ND 4.0 - Attribution - Non-commercial use - No Derivative Works - International License

4D Reconstruction of Alpine deformations in the Western Alps

Antoine Mercier

▶ **To cite this version:**

Antoine Mercier. 4D Reconstruction of Alpine deformations in the Western Alps: Implications on the orogenic wedge evolution. Tectonics. Univeristé Claude Bernard Lyon 1, 2023. English. NNT : 2023LYO10176 . tel-04390525

HAL Id: tel-04390525
https://hal.science/tel-04390525

Submitted on 12 Jan 2024

HAL is a multi-disciplinary open access archive for the deposit and dissemination of scientific research documents, whether they are published or not. The documents may come from teaching and research institutions in France or abroad, or from public or private research centers.

L'archive ouverte pluridisciplinaire **HAL**, est destinée au dépôt et à la diffusion de documents scientifiques de niveau recherche, publiés ou non, émanant des établissements d'enseignement et de recherche français ou étrangers, des laboratoires publics ou privés.

Distributed under a Creative Commons Attribution - NonCommercial - NoDerivatives 4.0 International License

THÈSE DE DOCTORAT DE L'UNIVERSITÉ CLAUDE BERNARD LYON 1

Ecole Doctorale N°52
Physique et Astrophysique

Domaine : Sciences de la Terre et de l'Univers

Discipline : Tectonique

Soutenue publiquement le 10/10/2023, par :

Antoine MERCIER

4D reconstruction of Alpine deformations in the Western Alps
Implications on the orogenic wedge evolution

Reconstitution 4D des déformations alpines dans les Alpes occidentales
Implications sur l'évolution du prisme orogénique

Devant le jury composé de :

ROLLAND Yann, Maître de conférence, Univ. Savoie Mont-Blanc	**Rapporteur**
VAN DER BEEK Peter, Professeur, Univ. Potsdam (Allemagne)	**Rapporteur**
SIMOES Martine, Chargée de recherche CNRS, Univ. Paris Cité	**Examinatrice**
BADER Anne-Gaëlle, Ingénieure géologue, BRGM	**Examinatrice**
GARDIEN Véronique, Professeure, Univ. Lyon 1	**Présidente**
LELOUP Philippe Hervé, Directeur de recherche CNRS, Univ. Lyon 1	**Directeur de thèse**
BODIN Thomas, Directeur de recherche CNRS, ENS de Lyon	**Co-Directeur de thèse**
MAHEO Gweltaz, Maître de conférence, Univ. Lyon 1	**Invité**
MONIÉ Patrick, Directeur de recherche CNRS, Univ. de Montpellier	**Invité**

Il était une fois, en bordure du ciel, un grand dôme de neige qui recouvrait les sommets et dominait la vallée. C'était le plus haut de tous; avant même que les savants l'aient mesuré, on le savait: il était le premier à être habité par les rayons du soleil et, le soir, c'est encore sur ses pentes qu'ils s'attardaient après avoir abandonné toutes les autres cîmes.

Un peu plus tard, la nuit venant, il soutenait le ciel, et parfois une étoile, lourde d'être seule, toujours suspendue, venait se poser sur ces crêtes et veiller avec lui; les neiges éternelles sont faites de poussières d'étoiles...

Puis le jour venait: en maître et seigneur, le grand dôme de glace, un peu distant comme il convient, régnait sur les vallées; il avait peu de rapport avec elles; il distribuait les eaux, et là-haut il ne traitait qu'avec les vents, les astres et les tempêtes.

Gaston Rébuffat

"L'attrait du mystère", *Mont-Blanc, Jardin Féérique*, éditions Guérin, 1998.

The Ph.D. thesis has been prepared in the:

Laboratoire de Géologie de Lyon : Terre, Planète, Environnement

UMR CNRS 5276 (CNRS, ENS, Université Lyon1, UJM)

Université Claude Bernard, Lyon1

Campus de la Doua, bâtiment Géode

2, rue Raphaël Dubois

69622 Villeurbanne Cedex

The Ph.D. thesis grant was funded by the French Ministry of Research, Higher Education and Innovation through the University Claude Bernard of Lyon 1 and the doctoral school n°52 PhAst. Research work has been partly funded by the French National Center for Scientific Research (CNRS) through the National Earth Sciences Institute (INSU) and the Laboratoire de Géologie de Lyon.

This work was also possible thanks to the successful collaboration with qualified researchers from different laboratories:

Abstract

Although the Western Alps have been widely studied in the last decades, the geometry and chronology of the deformation are still controversial. This Ph.D. aims is to examine the Cenozoic evolution of the Mont-Blanc and Aiguilles Rouges mountains, two of the external crystalline massifs (ECM), through a multidisciplinary approach that provides constraints on both the structure 3D geometry and deformation kinematics. To unravel the 3D geometry, we performed a structural analysis based on new field data, microtectonics, and 3D geological modelling together. We used GeoModeller software to build a 3D geological model of 60 x 65 km comprising the Mont-Blanc massif, the Aiguilles Rouges, the Helvetic nappes, and the subalpines chains. To efficiently process and store structural data, we designed a database (*DataGeol*) that contains 3955 structural measurements in 3053 localizations. Our results show a large thrusting of the Mesozoic sedimentary cover above the Aiguilles Rouges and Mont-Blanc basement toward the WNW, corresponding to a décollement level localized above the Triassic unconformity, which locally also affects the basement. The shortening accommodated by this thrust has been estimated from previously published cross-sections to be between 13 and 32 km. To quantify the exhumation history, we performed 13 new thermochronological ages (AHE, AFT, ZHE, ZFT) that together with the existing data set are input into the numerical simulation of the Pecube algorithm. We applied a method based on the inverse method coupled with Bayesian inference to quantify the simulation parameters and the associated uncertainties. Independently, timing constraints were obtained using *in situ* $^{40}Ar/^{39}Ar$ data on six mylonites. The results of the two methods are consistent, allowing to better constrain the timing of thrust propagation in relation to the exhumation: (i) the Helvetic nappe system started immediately after the end of the Penninic nappe system at about 32 Ma. (ii) The development of western Mont-Blanc shear zone (MBsz) is correlated with the exhumation of the Mont-Blanc from 22 Ma to 14 Ma. Thermobarometric deformation conditions were estimated by petrogeochemical quantification and lattice preferred orientation of quartz crystals and suggest that the deformation occurred below 500°C and between 0.47 and 0.74 GPa. During this period, the deformation of the Helvetic nappes is coeval with that of the western MBsz, the Mont-Blanc being a duplex thrust; (iii) the Aiguilles Rouges began to exhume after 12 Ma, before a phase of acceleration after 6 Ma; (iv) after 14 Ma, the MBsz becomes a breach thrust that cross-cut the Helvetic nappes; (v) the two massifs experienced a common recent phase of high exhumation at 1 Ma, coeval with relief building and most likely related to glacial valley incision. Globally, the Mont-Blanc massif was exhumed about 7 km more than the Aiguilles Rouges. This new tectonic model implies that three major thrust systems have propagated in sequence from the internal part to the external one and have shaped the external Western Alps: the Penninic, Helvetic, and Alpine Sole thrust systems. The period between 22 and 14 Ma was a transition of the main thrust system between the Helvetic Nappes rooting above the ECM to the Alpine Sole

thrust rooting below the External External Massifs. The late exhumation of the external ranges of the Western Alps was mostly controlled by steep reverse faults, including back thrust. At that time, thick-skin deformation in the more internal part of the belt was coeval with thin-skin deformation in the external part.

Keywords: Orogen, Western Alps, 3D Geological Modeling, *in situ* $^{40}Ar/^{39}Ar$ dating, Exhumation, Bayesian Inference, Thermochronolgy, Tectonics

Résumé

Bien que les Alpes occidentales aient été largement étudiées au cours des dernières décennies, la géométrie et la chronologie des déformations dans le prisme orogénique alpin sont encore largement débattues. L'objectif de cette thèse de doctorat est d'examiner l'évolution au Cénozoïque du Mont-Blanc et des Aiguilles Rouges, deux massifs cristallins externes (MCE), à travers une approche multidisciplinaire permettant de contraindre à la fois sur la structure, la géométrie 3D et la cinématique des déformations. Pour reconstruire la géométrie 3D, nous avons réalisé une analyse structurale basée sur de nouvelles données de terrain, de la microtectonique et de la modélisation géologique 3D. Pour cela, nous avons utilisé le logiciel GeoModeller pour construire un modèle géologique 3D de 60 x 65 km comprenant le massif du Mont-Blanc, des Aiguilles Rouges, des nappes Helvétiques et des chaînes subalpines. Pour traiter et stocker efficacement les données de terrain, nous avons conçu une base de données (*DataGeol*) qui contient 3955 mesures structurales situées dans 3053 localisations. Nos résultats montrent un chevauchement important vers l'WNW de la couverture sédimentaire Mesozoïque au-dessus du socle des Aiguilles Rouges et du Mont-Blanc correspondant à un niveau de décollement localisé au-dessus de la discordance Triasique, mais qui affecte localement le socle. Le raccourcissement accommodé par ce chevauchement est estimé d'après des coupes géologiques publiées et se situe entre 13 et 32 km. Pour quantifier l'histoire d'exhumation, nous avons réalisé 13 nouveaux âges thermochronologiques (AHE, AFT, ZHE, ZFT) qui, une fois combinés à l'ensemble des données existantes, sont introduits dans le logiciel de simulation numérique Pecube. Pour quantifier les paramètres de simulation et les incertitudes associées, nous avons appliqué une nouvelle méthode basée sur des méthodes inverses couplées à de l'inférence Bayésienne. Indépendamment, des contraintes sur la chronologie ont été obtenues en utilisant la datation *in situ* $^{40}Ar/^{39}Ar$ sur six mylonites. Les résultats des deux méthodes sont cohérents et permettent de mieux contraindre la chronologie de la propagation de la déformation dans le prisme orogénique alpin en association avec l'exhumation : (i) le système de chevauchement des nappes Helvétiques a débuté immédiatement après la fin du chevauchement Pennique, vers 32 Ma ; (ii) Le fonctionnement de la zone de cisaillement du Mont-Blanc (MBsz) est corrélé avec l'exhumation du Mont-Blanc entre 22 Ma et 14 Ma. Les conditions thermobarométriques de la déformation ont été estimées par quantification pétrogéochimique et sur l'orientation préférentielle des cristaux de quartz et suggèrent que la déformation s'est produite en dessous de 500°C et entre 0,47 et 0,74 GPa. Pendant cette période, la déformation des nappes helvétiques est synchrone avec celle de la MBsz, le Mont-Blanc formant un duplex entre ces structures ; (iii) les Aiguilles Rouges commencent à s'exhumer après 12 Ma, avant une phase d'accélération après 5 Ma ; (iv) après 14 Ma, la MBsz devient un chevauchement qui recoupe les nappes helvétiques ; (v) les deux massifs connaissent une phase récente commune de forte exhumation à 1 Ma, contemporaine avec la formation du relief et probablement liée l'incision glaciaire Qua-

ternaire. Globalement, le massif du Mont-Blanc a été exhumé d'environ 7 km de plus que les Aiguilles Rouges. Ce nouveau modèle tectonique implique que trois grands systèmes de chevauchement se sont propagés en séquence de la partie interne à la partie externe du prisme : le système de chevauchement Pennique, Helvétique et le chevauchement basal alpin. La période comprise entre 22 et 14 Ma a été marquée par une transition entre les nappes helvétiques qui s'enracinent au-dessus des ECM et le chevauchement basal alpin qui s'enracine au-dessous des ECM. L'exhumation tardive des ECM des Alpes occidentales a été principalement contrôlée par des failles inverses raides et des rétro-chevauchements. À cette époque, la déformation en *thick-skin* dans la partie interne de la chaine coïncidait avec la déformation en *thin-skin* dans la partie externe.

Mots clés : Orogénèse, Alpes occidentales, Modélisation géologique 3D, datations *in situ* $^{40}Ar/^{39}Ar$, Exhumation, Inférence Bayesienne, Thermochronologie, Tectonique

Remerciements

Une thèse de doctorat est avant tout une aventure humaine, un travail d'équipe, en collaboration. Dans ces quelques lignes, je tiens à remercier toutes les personnes qui ont contribué à la bonne réalisation de cette aventure.

Je tiens tout d'abord à remercier les rapporteurs et examinatrices du jury : Peter Van Der Beek, Yann Rolland, Anne-Gaëlle Bader, Véronique Gardien et Martine Simoes, pour avoir accepté de lire et d'évaluer ce travail.

Ensuite, mes remerciements vont naturellement à mon directeur de thèse : Hervé Leloup. Merci de m'avoir donné ce beau projet avec confiance, d'avoir cru en mes capacités et de m'avoir accompagné dans son aboutissement. Merci de m'avoir transmis ta passion et ta rigueur pour les roches qui se déforment. Je garderai un souvenir inoubliable de cette histoire, de ces journées de terrain dans toutes les conditions : sous un soleil radieux le plus souvent, mais aussi sous la pluie, l'orage et la neige ; et aussi dans des lieux incroyables : à 2900 m au bout d'une corde au sommet des Aiguilles Rouges ; et dans des hébergements parfois atypiques : de la ferme du berger Suisse à cette cabane perdue sous les Grandes Jorasses qu'est le refuge de Boccalatte.

Je remercie mes deux autres encadrants pour leur accompagnement dans ce travail : merci à Thomas Bodin pour sa disponibilité et sa pédagogie (expliquer l'inférence Bayésienne à un géologue n'est pas de tout repos !) et merci à Gweltaz Maheo pour son accompagnement, la transmission de son expérience et nos discussions enrichissantes.

Je tiens également à remercier les membres extérieurs de mon comité de suivi de thèse, en commençant par Thierry Dumont : merci pour son retour sur mes travaux et pour nos discussions pertinentes qui ont contribué à l'amélioration et à la précision de ce travail. Merci également à Jean Philippe Perillat et Cécile Lasserre pour leur accompagnement, leur écoute, et leur disponibilité.

À présent, je remercie les organismes financeurs de cette thèse de doctorat, en premier lieu le ministère de l'enseignement supérieur, de la recherche et de l'innovation pour le financement de ma bourse de thèse. Ensuite je remercie l'INSU et l'Observatoire de Lyon, qui ont financé une partie de ces travaux de recherches. Et enfin, je remercie le laboratoire de Géologie de Lyon (LGL), qui m'a accueilli dans ses locaux et qui a financé nos missions de terrain.

Ce travail n'aurait pas été possible sans la fructueuse collaboration de nombreuses personnes, chercheurs, ingénieurs et techniciens. Tout d'abord, je remercie Patrick Monié, directeur de recherche CNRS et Arthur Iemmolo, technicien, tout deux du laboratoire Géosciences Montpellier pour leur accompagnement dans les datations argon et pour avoir effectué les datations U/He sur zircon. Merci spécialement à Patrick pour nos discussions enrichissantes et ses

retours sur l'interprétation des données, cela a grandement contribué à la qualité de ce travail. Merci à Jocelyn Barbarand, professeur à l'Université Paris-sud pour avoir effectué les datations en traces de fission sur apatites, base essentielle de notre étude de l'exhumation. Merci à Valérie Magnin, ingénieure au laboratoire ISTerre pour m'avoir formé avec pédagogie et patience à l'utilisation de la microsonde électronique. Merci à Cyril Langois, Maître de Conférence, et Thierry Douillard, ingénieur de recherche CNRS, tout deux du laboratoire Mateis de l'INSA Lyon pour leur disponibilité, et leur accompagnement dans la réalisation des mesures EBSD sur quartz. Leurs compétences et leur savoir-faire ont permis d'acquérir des données de qualités, nécessaires à la discussion des résultats. Merci à Clémentine Fellah, ingénieure de recherche CNRS au LGL pour m'avoir formé à l'utilisation du microscope électronique, pour son expérience, sa pédagogie et son aide dans le traitement des données. Merci à Christoph Glotzbach, chercheur à l'Université de Tubingen en Allemagne, pour notre collaboration et sa confiance. Merci à Xavier Robert, chargé de recherche IRD, pour ses précieux conseils, l'apport de son expérience en modélisation thermocinématique et pour la relecture du chapitre 6 du manuscrit. Je remercie Pierre Valla pour ses réponses à mes questions sur Pecube ainsi que pour sa transmission d'expérience lors de l'école d'été thermonet. Merci à Gabriel Courrioux, Séverine Caritg, Anne-Gaëlle Bader et Simon Lopez, ingénieurs au BRGM, pour m'avoir formé à l'utilisation de GeoModeller avec passion et pédagogie, pour avoir cru en ce projet et pour l'avoir soutenu.

Je remercie chaleureusement Philippe Grandjean, ingénieur de recherche au LGL pour avoir accepté de grimper au sommet des Aiguilles Rouges avec un drone sur le dos, grâce à ses compétences et son expérience, nous avons obtenu des images magnifiques de ce sommet si particulier. Merci à Sophie Passot, ingénieure d'étude au LGL, pour avoir traité efficacement les données issues de l'imagerie du drone. Son expérience a permis d'acquérir un modèle photogrammétrique de grande qualité, essentiel à notre étude structurale de ce sommet. Merci également pour son aide dans les recherches bibliographiques dans les archives de la bibliothèque (la biblio sur les Alpes est longue !). Merci à Emmanuel Robert, Ingénieur de recherche aux collections de paléontologie du LGL, pour son accompagnement et ses conseils dans l'élaboration de DataGeol. Merci également à Grégory Salvignol, Ingénieur informatique au CNRS pour son aide dans le développement de DataGeol et son déploiement sur les serveurs de l'Observatoire de Lyon. Merci à Andreas Christensen ingénieur en développement web pour avoir conçu l'interface web de DataGeol. Merci également à Thomas Courrier, pour son aide dans l'élaboration initiale de DataGeol. Enfin, merci à Colette Guilbaud, technicienne de recherche au LGL, pour avoir préparé les lames minces et épaisses qui ont servi à l'étude microtectonique. Son savoir-faire et son application ont permis d'obtenir des lames minces de qualité, facilitant l'analyse des roches.

Un grand merci à Michel Cara, Professeur émérite de l'Université de Strasbourg (et Chamoniard aguerri) pour son accueil chaleureux, son repérage d'affleurement dans la vallée de Chamonix, pour nous avoir fait découvrir les travaux de L. Collet et E. Paréjas dans les Aiguilles Rouges et pour m'avoir invité à présenter mes travaux devant le grand public dans le cadre des conférences de l'association des réserves naturelles des Aiguilles Rouges. Merci également à Michel Delamette, Géologue indépendant, docteur en sciences de la Terre de l'Université de Genève et docteur en Paléontologie de l'Université de Lyon, pour nos échanges et nos divergences de points de vues qui ont fait avancer ce travail, et pour nous avoir accompagnés sur le terrain au col de la Croix du Bonhomme. Merci à Robert Fleming, géologue, pour avoir relu et corrigé ce manuscrit.

Je remercie le Conservatoire des Espaces Naturels (CEN) de Haute-Savoie pour nous avoir donné l'autorisation de travailler et d'échantillonner dans les réserves naturelles des Aiguilles Rouges. Merci spécialement à Laurent Delomez, garde au CEN pour nous avoir accompagné sur le terrain.

Merci maintenant à mes collègues du LGL qui n'ont pas directement participé à ce travail mais qui y ont contribué au quotidien par leur soutien et leur bienveillance pendant ces trois années de thèse : merci spécialement à Jean-Emmanuel Martelat, Vincent Grossi, Antoine Triantafyllou, Véronique Gardien, Pascal Allemand et Marianne Metois.

Je remercie aussi la relève, Maureen et les autres étudiants que j'ai eu la chance de rencontrer, de suivre en stage ou d'avoir en cours. Je crois que j'ai autant appris d'eux, qu'ils ont appris de moi.

À présent, je tiens à remercier Isabelle Manighetti, sans qui, indirectement, ce travail n'aurait peut-être pas vu le jour. Merci d'avoir cru en mes compétences, de m'avoir soutenu dans mes projets et de m'avoir transmis, avec bienveillance, ta passion pour les failles et ta rigueur de travail.

Merci à Elena pour ton soutien et ton amitié depuis notre première année d'étude ensemble, la réalisation de mes projets en a dépendu. Merci Raphaël pour les moments que nous avons partagés ensemble, nos discussions, nos débats et ces journées de terrain au milieu des fentes de quartz ! Merci à Laetitia, Niels, Cheng-Long pour la bonne humeur dans le bureau 601 et pour les moments que nous avons partagés ensemble. Merci Alexandre et Manon pour nos escapades Jurassiennes à vélo ou à pied ! Enfin, merci à mes amis proches, parfois non-géologues (oui, j'en ai aussi) qui m'accompagnent dans la vie depuis si longtemps : Elke, Camille, Gaëtan, Laura et Ismaël.

Je dédie cette thèse de doctorat à mes deux grands-mères, qui ont, dans des styles très différents, toujours été d'un soutien inconditionnel pendant toutes les étapes de ma vie. Elles sont source d'inspiration et de courage et se sont elles m'ont transmis leur amour pour la nature et la beauté. Je remercie chaleureusement, ma mère, mon père, ma sœur, et ma famille, qui n'ont pas toujours compris ce que je gratouillais dans les Alpes (je ne sais pas vous comprendrez mieux après la lecture de ce pavé) mais qui m'ont toujours soutenu et encouragés dans ma passion.

Enfin, merci à Sandrine et Jean-Yves, qui m'ont soutenus dans ce projet et même parfois accompagnés sur le terrain le week-end ! Merci à Faustine, pour avoir été d'un soutien sans faille pendant ces trois années. Merci de m'avoir aidé sur le terrain et d'avoir porté quelques-uns de mes échantillons !

Contents

GENERAL INTRODUCTION **31**

The general questions to be addressed in this work 31

The general "ingredients" for understanding the evolution of the mountain belts 32

Manuscript organization 33

I SCIENTIFIC BACKGROUND **37**

1 Dynamics of orogenic wedges **39**

1.1 Introduction 42

1.2 The orogenic wedge model 42

1.3 Style of deformation 45

1.4 Different orogenic wedge around the Earth 45

1.4.1 Taiwan 46

1.4.2 The Himalayas 47

1.4.3 The Alps 50

1.5 Contribution of mechanical models to the comprehension of Alpine wedge dynamics 51

1.5.1 Analogous models 51

1.5.2 Numerical simulations 54

2 Tectonic structure of the Western Alps **59**

2.1 Introduction 61

2.2 Deep structure of the Western Alps 61

2.3 Tectonic units 64

2.3.1 The External domain 64

2.3.2 Helvetic Nappe system 67

2.4 Dynamic evolution of the collision 69

2.4.1 Inherited structures 69

2.4.1.1 Post-Variscan extension . . . 69
2.4.1.2 Saalian compression phase . . . 69
2.4.1.3 Mesozoic extension . . . 70
2.4.1.4 Eocene - Oligocene extension . . . 72
2.4.2 Compression . . . 75
2.4.2.1 Hypotheses of the compression sequence in the Western Alps 75
2.4.2.2 Mont-Blanc deformation hypothesis . . . 83
2.4.2.3 Subalpine chain deformation models . . . 86
2.5 Strike-Slip motion in the Western Alps . . . 89
2.6 Amount of shortening in the Western Alps . . . 89
2.7 Amount and timing of exhumation . . . 93

II 3D STRUCTURAL GEOLOGY 97

3 Development of a relational database for organizing field geological data: *DataGeol* 99
3.1 Objective . . . 102
3.2 Experimental design, material, and methods . . . 102
3.2.1 The design of a relational database . . . 102
3.3 Data description . . . 105
3.3.1 Acquisition . . . 105
3.3.2 Field missions . . . 107
3.3.3 Locations . . . 107
3.3.4 Lithology description . . . 109
3.3.5 Plane and line measurements . . . 109
3.3.6 Samples . . . 111
3.3.7 Samples sections . . . 112
3.4 Display in a GIS . . . 112
3.5 Data availability . . . 114

4 Building a 3D geological model of a structurally complex Alpine region 117
4.1 The move to the third dimension in structural geology . . . 120
4.1.1 Geostatistical and historical background . . . 121
4.1.2 3D geological modeling . . . 121
4.1.3 Geographical extent . . . 122
4.2 Data and methods . . . 122
4.2.1 Stratigraphic pile . . . 126
4.2.1.1 Pseudo-series . . . 127

4.2.2 Workflow . . . 128
4.2.3 Model resolution and complexity . . . 129
4.2.4 Quantification of errors in the data . . . 129
4.3 Large thrusting and late faulting shape the Aiguilles Rouges crystalline massif . 132
4.3.1 Introduction . . . 132
4.3.2 Geological Setting . . . 133
4.3.3 Data and Methods . . . 137
4.3.3.1 Structural Analysis . . . 137
4.3.3.2 3D Geological Modeling . . . 137
4.3.4 Structures and cover/basement relationships in the Aiguilles Rouges . . 138
4.3.4.1 Geological background . . . 138
4.3.4.2 Thrusting evidence in the Aiguilles Rouges . . . 142
4.3.4.3 Reverse faulting in the Aiguilles Rouges range and the Chamonix Synclinorium . . . 153
4.3.5 Relative timing of the main structures . . . 159
4.4 3D geological model of the Mont-Blanc, Aiguilles Rouges and Subalpine chains 161
4.4.1 Thrusting along the Eastern margin of the Mont-Blanc massif . . . 161
4.4.1.1 Back thrusting on the Eastern side of the Mont-Blanc massif 170
4.4.1.2 Preliminary synthesis on the cover / basement interface on the Eastern side of the Mont-Blanc massif . . . 170
4.4.2 Western side of the Aiguilles Rouges: thrusting of the cover . . . 172
4.4.2.1 Preliminary synthesis on the cover / basement interface on the Western side of the Aiguilles Rouges . . . 189
4.5 Structure of the subalpine chains . . . 189
4.5.1 Désert de Platé . . . 189
4.5.2 The mysterious origin of the "wildflysch" formation . . . 189
4.5.3 Cross section through the Arve Valley . . . 191
4.5.4 Bornes - Aravis . . . 193
4.6 Strike-slip faulting and active tectonics . . . 197
4.7 Synthesis of 3D structure and cover / basement relationship in the Mont-Blanc, Aiguilles Rouges and subalpine chains . . . 199
4.8 Data Availability, Model output, and visualization . . . 201
4.8.1 Data availability . . . 201
4.8.2 Instructions to visualize the 3D GeoModel . . . 201

III KINEMATICS AND THERMAL EVOLUTION 203

5 Timing and conditions of the deformation 205

5.1 Introduction . . . 208
5.2 Synthesis on the Alpine structures chronology and conditions of the deformation 208
5.2.1 Penninic Nappe System . . . 208
5.2.2 The Helvetic nappe system . . . 210
5.2.3 Mont-Blanc shear zones and back-thrusts . . . 211
5.2.4 Vallorcine - Miéville shear zone . . . 212
5.3 Analytical techniques . . . 213
5.3.1 Quantitative Electron Microprobe analysis . . . 213
5.3.2 Lattice Preferred Orientation (LPO) of quartz grains . . . 213
5.3.2.1 Origin of Lattice-Preferred Orientation . . . 214
5.3.2.2 Electron backscatter diffraction (EBSD) . . . 215
5.4 *In situ* $^{40}Ar/^{39}Ar$ Dating of synkinematic white micas . . . 216
5.4.1 The Mont-Blanc shear zone . . . 216
5.4.2 The Helvetic Nappe system . . . 226
5.4.2.1 The Roselette klippe . . . 227
5.4.2.2 The Petit Col Ferret . . . 229
5.4.3 Vallorcine-Miéville shear zone . . . 232
5.5 Significance of the age data . . . 236
5.6 Implications for the deformation sequence in the Western Alps . . . 240
5.7 Data availability . . . 244

6 Exhumation history of Mont-Blanc and Aiguilles Rouges 247
6.1 Introduction . . . 250
6.2 Geological setting and exhumation of the Western Alps . . . 251
6.3 Quantification of denudation and relief histories . . . 253
6.4 Thermochronology data . . . 255
6.4.1 (U-Th)/He data . . . 257
6.4.1.1 Apatite (U-Th)/He (AHE) . . . 258
6.4.1.2 Zircon (U-Th)/He (ZHE) . . . 258
6.4.2 Fission-track data . . . 259
6.4.2.1 Apatite fission tracks (AFT) . . . 259
6.4.2.2 Zircon fission tracks (ZFT) . . . 260
6.4.3 Qualitative interpretation . . . 264
6.4.3.1 Age-Elevation relationship . . . 264
6.4.3.2 Pseudoelevation plot . . . 264
6.5 Methodology . . . 266
6.5.1 Quantitative thermochronology through thermo-kinematic numerical simulation: *Pecube* . . . 266

6.5.1.1 Fault parameters . . . 267
6.5.1.2 Thermal parameters . . . 268
6.5.2 Bayesian Inference: defining a posterior solution . . . 270
6.5.2.1 The likelihood function . . . 270
6.5.2.2 The prior . . . 271
6.5.3 Approximating the posterior probability distribution . . . 271
6.5.3.1 Exploring the parameter space with the Neighborhood Algorithm . . . 271
6.5.3.2 Sampling the posterior distribution . . . 272
6.5.3.3 Choosing a level of complexity . . . 272
6.5.4 Inversion of synthetic data: what can *Pecube* infer? . . . 273
6.5.4.1 The design of a fictional scenario . . . 273
6.5.4.2 Results on the inversion of synthetic data . . . 273
6.6 Inversion of thermochronological data . . . 278
6.6.1 Inversion results on the Aiguilles Rouges . . . 278
6.6.2 Inversion results on the Mont-Blanc and Aiguilles Rouges . . . 278
6.7 Discussion . . . 286
6.8 Conclusion . . . 287
6.9 Data availability . . . 290

IV DISCUSSION, IMPLICATIONS AND CONCLUSIONS 293

7 Discussion and implications 295
7.1 Implications in the structural evolution of Mont-Blanc and Aiguilles Rouges . . 296
7.1.1 Amount of Cenozoic Exhumation . . . 296
7.1.2 Constraints on the amount of absolute timing of Cenozoic deformations 299
7.1.2.1 Aiguilles Rouges backthrusts . . . 299
7.1.2.2 Pormenaz - Merlet shear zone . . . 299
7.1.2.3 Mont-Blanc shear zone . . . 300
7.1.2.4 Helvetic Thrusts . . . 302
7.2 Implications of the structural evolution of the Alps . . . 304
7.2.1 Shortening of the Helvetic nappes and lateral extent of the Helvetic thrusts . . . 304
7.2.2 Late reverse faults at the boundary of the external ranges . . . 305
7.2.3 A conceptual model for Alpine External Crystalline Massifs deformation 306
7.3 Implications on the Alpine orogenic wedge . . . 308

CONCLUSIONS AND PERSPECTIVES 312

APPENDICES **365**

A SYNTHÈSE EN FRANÇAIS **365**
A.1 Objectif . . . 365
A.2 Méthodologie . . . 365
A.3 Cadre géologique (Chapitre 1 et 2) . . . 367
A.4 Développement d'une base de donnée relationnelle : *DataGeol* (Chapitre 3) . . . 369
A.5 Construction d'un modèle géologique 3D (Chapitre 4) . . . 370
A.6 Chronologie de la déformation (Chaptitre 5) . . . 371
A.7 Histoire d'exhumation du Mont-Blanc et des Aiguilles Rouges (Chapitre 6) . . . 373
A.8 Conclusions et implications . . . 374
A.8.1 Implications à l'échelle du Mont-Blanc et des Aiguilles Rouges . . . 374
A.8.2 Quelle est la séquence de déformation dans les Alpes externes . . . 375
A.8.3 Implication à l'échelle des Alpes occidentales . . . 375
A.8.4 Implications à l'échelle du Prisme orogénique . . . 376

B Supporting information for chapter 4 **377**

C Supporting information for chapter 5 **383**
C.1 Basis of $^{40}Ar/^{39}Ar$ dating method . . . 384
C.1.1 Extraction procedure and analysis . . . 386
C.2 Treatment of EBSD data with MTex . . . 389
C.3 EBSD results . . . 394
C.4 *In situ* laser ablation maps . . . 399
C.5 EBSD measurement details . . . 405
C.6 In-situ $^{40}Ar/^{39}Ar$ raw data on white mica . . . 406

D Supporting information for chapter 6 **413**
D.1 1D posterior probability functions . . . 417
D.2 Protocols . . . 421

E Sciences communications **435**

F Tectonophysics **441**

List of Figures

1.1 Nomenclature of a collisional orogen. 42
1.2 Schematic illustration of the orogenic Coulomb-wedge model (modified after Dielforder (2017) and Dahlen (1984)). 43
1.3 Schematic summary of processes at convergent plate margins (compiled from Dielforder et al. (2020) and Dielforder and Hampel (2021). 44
1.4 Thin-skin and thick-skin tectonics along a thrust fault from Pfiffner (2014). . . 45
1.5 Worldwide digital elevation model showing the distribution of relief on the Earth's surface. 46
1.6 Geodynamical context and simplified geological map and cross sections of Taiwan from Simoes et al. (2012). 47
1.7 Cross section through the orogenic wedge of Taïwan (Malavieille, 2010). . . . 48
1.8 Himalayas structural map and simplified cross-section, from Leloup et al. (2010). 49
1.9 Interpreted cross-section of the Alps from the ECORS-CROP seismic experiment (Guellec et al., 1990). 50
1.10 Alpine orogenic wedge analog model evolution from time increment t_0 to t_{38}. From Bonnet et al. (2007). 52
1.11 Trajectories (measured relative to a fixed reference) of three points located in the converging plate, from Bonnet et al. (2008). 53
1.12 Thermal evolution of an orogenic wedge. From Simoes et al. (2012). 54
1.13 Structural evolution of viscoelastoplastic deformation model with an intermediate décollement weaker than the basal one and erosion (Model–M5). From (Dal Zilio et al., 2020). 55
1.14 Simulations of series of thermomechanical models from Bauville and Schmalholz (2015). 57

2.1 Crustal structure of the northern Western Alps as imaged by the ECORS-CROP project. 62
2.2 Depth sections along the CIFALPS2 profile across the northern Western Alps. From (Paul et al., 2022). 63

2.3 Tectonic map of the Alps, from (Pfiffner, 2014). 65
2.4 Metamorphic structure of the Western Alps. Modified from (Bousquet et al., 2012). 66
2.5 Structural map of the External Crystalline Massifs (ECM) of the Western Alps. 67
2.6 Geological cross-section through the Helvetic nappes system (Pfiffner, 2014). . 68
2.7 Schematic overview of the Mesozoic sedimentary sequence of the Helvetic / Dauphinois in the Western Alps (Pfiffner, 2014) 71
2.8 Geodynamic chart of Iberia and Adria against Europe tectonic plates. Modified from Angrand and Mouthereau (2021). 72
2.9 Geodynamic reconstruction of the Tethys–Atlantic area shown in orthographic projection. Modified from Angrand and Mouthereau (2021). 73
2.10 Balanced and restored cross-section of the underfilled portion of the Alpine foreland basin. Colorized from Sinclair (1997). 74
2.11 Structural evolution of the external Alps alps along an NW-SE section across the Aiguilles Rouges and Mont Blanc massifs from Leloup et al. (2005). 76
2.12 Paleogene evolution of the Alpine foreland in the southern part of the Western Alps after Dumont et al. (2012). 78
2.13 Shortening sequence of the European proximal margin during the collisional Alpine phase (Boutoux et al., 2016) 80
2.14 Tertiary tectonic phases in the subalpine chains (Vercors, Chartreuse, Bauges and Bornes) from Kalifi et al. (2020). 82
2.15 Proposed hypotheses for Mont-Blanc kinematic evolution. 86
2.16 Schematic representation of four deformation models in the Western Alps. . . . 88
2.17 Compilation of Ar–Ar on phengite and U–Pb on allanite / epidote / monazite ages along the Western External Alps from Rolland et al. (2022). 90
2.18 Paleogeographic reconstruction of the Helvetic Nappe System in the central and Western Alps from Pfiffner (2011), redrawn after Kempf and Pfiffner (2004). 91
2.19 Restored displacement field of the Jura and subalpine chains above the external crystalline massifs from Affolter (2003). 92
2.20 Cross section through the north-Western Alps from Bellahsen et al. (2014). . . 93
2.21 Thermal path for the external crystalline massifs as proposed by Girault et al. (2022). 94

3.1 Workflow of DataGeol databse. 103
3.2 Entity Relationship Diagram (ERD) of *DataGeol*. 106
3.3 General map with outcrops locations within DataGeol database 108
3.4 Diagram describing the measurement conventions characterizing the orientation of a plane and a line in space. Redrawn from Allmendinger et al. (2011). . 110

3.5 SVG symbols used for data display in a GIS, adapted from Federal Geographic Data Committee (2006). . . . 113
3.6 Example of plane measurements orientation display in QGIS in the Emosson area. . . . 113

4.1 GeoModel extent . . . 123
4.2 Karst system of the Folly massif . . . 125
4.3 Geological pile for the 3D geological model of the Mont-Blanc and Aiguilles Rouges massifs . . . 128
4.4 Workflow followed to build the 3D geological model . . . 130
4.5 Overview of the 3D geological model. . . . 131
4.6 Structural frame of the western Alps . . . 134
4.7 Contrasting models for Alpine deformation of the external crystalline massifs and their cover, as exemplified in the Aiguilles Rouges and Mont-Blanc massifs. 135
4.8 Structure of the Chamonix Synclinorium. . . . 137
4.9 View of the 3D Argentière GeoModel. . . . 139
4.10 Undeformed Triassic sandstones resting unconformably on top of variscan basement. . . . 141
4.11 Cover/basement relationships at the col de Barberine (Aiguilles Rouges massif). 144
4.12 Cover/basement relationships in the western side of Aiguilles Rouges (Site HGT2). . . . 145
4.13 Supplementary field data at site HGT2 . . . 146
4.14 Supplementary field data at site HGT3 . . . 146
4.15 Folding of the Mesozoic cover on the western flank of the Aiguilles Rouges. . . 147
4.16 Supplementary field data at site HGT5 (Sixt window). . . . 148
4.17 Cover/basement relationships at the Aiguille du Belvédère (Aiguilles Rouges massif). . . . 149
4.18 Field observations at site HGT6 (Aiguille du Belvedère). . . . 150
4.19 Cover/basement relationships near Pormenaz (Aiguilles Rouges massif) 151
4.20 Cover/basement relationships in the north of the Chamonix Synclinorium . . . 153
4.21 Views of 3D Posettes GeoModel . . . 154
4.22 Steep thrust affects the limestones, and initial foliation is cross-cut by steep faults (station AR453). b) Flat reverse fault associated with the Pormenaz-Merlet shear zone with a striation trending N120, indicating top to the northwest 155
4.23 Thin section of sample ARe096, (station AR0370b) from the Gietroz fault. . . . 156
4.24 Finhaut back thrust . . . 157
4.25 Le Tour back thrust . . . 158
4.26 Cross-sections of the Argentiere 3D GeoModel . . . 160

4.27 Structural map output from the 3D Geological model. 161
4.28 Field observations and interpretation of the Bonhomme area. 164
4.29 Section of the Grande Écaille and field observations 165
4.30 Field observations from the Grande ÉEcaille area. 166
4.31 Cover/basement contact on the eastern side of the Mont-Blanc massif. 168
4.32 Cover / Basement contact on the road to the col des Planches, north of Sembrancher. 169
4.33 Mont-Blanc back thrust field observations. 171
4.34 Cross sections through the 3D geological model in the Haut-Giffre - Dents Blanches massif. 172
4.35 Evidence of thrusting at the bottom of the Morcles nappe. 174
4.36 Field observations and output cross-section of Morcles nappe from the 3D GeoModel. 175
4.37 Panorama and field observations from Dents Blanches. 176
4.38 Interpreted panorama and field pictures from the col d'Emaney. 178
4.39 Panorama to the Pointes d'Aboillon and the col de Barberine, from the col d'Emaney. 179
4.40 Field observation in the Cirque des Fonds. 179
4.41 Structural frame of the Bostan - Criou massif. 180
4.42 Field observation from the Vallon de Bostan. 181
4.43 Panorama and field observations in the Vallon des Chambres (Haut-Giffre). . . 184
4.44 Panorama and field observations from the Col d'Anterne area (western Aiguilles Rouges). 186
4.45 Field observations of the deformations affecting the Carboniferous in the Pormenaz - Anterne area. 187
4.46 Interpreted panoramas of the Pointe de Sales and the Fiz. 188
4.47 Panorama and field observation in the Platé massif. 190
4.48 Wildflysh ("Flysch à bloc"). 192
4.49 Field observations and natural cross-section from the Arve Valley. 194
4.50 Cross sections through the 3D geological model in the subalpine chains. 195
4.51 Panorama and field observation in the Bornes massif. 196
4.52 Field observations of strike-slip faulting in the Mont-Blanc, Aiguilles Rouges and subalpine chains. 198
4.53 Synthesis cross sections through the study area. 200

5.1 Structural framework of the Mont-Blanc and Aiguilles Rouges and the sampling sites for $^{40}Ar/^{39}Ar$ absolute dating. 209
5.2 Quartz slip systems versus temperature, updated after Toy et al. (2008). 215

5.3 Quartz slip systems, modified after Passchier and Trouw (2005). 215
5.4 Photomicrographs of studied mylonites. 218
5.5 Dated samples from the western Mont-Blanc shear zone. 220
5.6 White micas composition plots. 221
5.7 Chemical maps of the Si (pfu) (top) and XMg ($XMg = \frac{Mg}{Fe+Mg}$) (bottom) content of the studied mylonites. 222
5.8 Pressure temperature isopleths computed for phengite from Si contents (Massonne and Schreyer, 1987). 223
5.9 Phase diagram equilibria performed on sample ARe001 using the bulk composition from the EPMA chemical mapping. 223
5.10 Cumulative probability plot of *in-situ* $^{40}Ar/^{39}Ar$ ages. 225
5.11 Inverse isochron plots of in situ $^{40}Ar/^{39}Ar$ ages. 226
5.12 Quartz recrystallization microstructures from studied mylonites. 227
5.13 Field observations at the Roselette klippe. 228
5.14 Cross section of the Italian side of the Petit Col Ferret 231
5.15 Field observations in the Vallorcine-Miéville shear zone. 232
5.16 Lattice Preferred orientation of quartz ribbons with dated mylonitic rocks. . . . 234
5.17 Pressure / temperature plot with the compilation of the published thermobarometric estimations for the Mont-Blanc massif 237
5.18 Recalculated variations of the closure temperature with cooling rate according to estimated Arrhenius parameters. 238
5.19 Compilation of the timing constraints on the main alpine deformations within the western Alps and Jura fold and thrust belt 243

6.1 Simplified geological settings of the Mont-Blanc and Aiguilles Rouges basement massifs and associated thermochronological data. 252
6.2 Balance of processes acting in the exhumation according to the terms defined by England and Molnar (1990). 254
6.3 Surface processes acting in a collision orogen. Simplified and redrawn from Wolf et al. (2022). 255
6.4 Schematic diagram illustrating the basis of the thermochronology method inferring exhumation histories. 256
6.5 Effective closure temperatures for various commonly used thermochronometers from Chew and Spikings (2015). 260
6.6 Location of the sampling regions. 263
6.7 Age-elevation and pseudo-elevation plot for the Aiguilles Rouges and Mont-Blanc thermochronological data 265
6.8 Crustal Thermal Pecube numerical simulation 268

6.9 Modeling Workflow . . . 270
6.10 Workflow designed to generate synthetic data. . . . 274
6.11 Inversion results of synthetic noised thermochronological data from the Aiguilles Rouges. . . . 275
6.12 Inversion results of synthetic noised thermochronological data from the Mont-Blanc and Aiguilles Rouges with a regional exhumation . . . 276
6.13 Inversion results of synthetic noised thermochronological data from the Mont-Blanc and Aiguilles Rouges with differential exhumation. . . . 277
6.14 Result of the inversion of thermochronological data from the Aiguilles Rouges . 280
6.15 Comparison of observed and predicted thermochronological data from Aiguilles Rouges median solution of posterior distribution. . . . 281
6.16 Results of the inversion of thermochronological data from the Mont-Blanc and Aiguilles Rouges **without** differential exhumation in between the two massifs . 283
6.17 Results of the inversion of thermochronological data from the Mont-Blanc and Aiguilles Rouges **with** differential exhumation in between the two massifs . . . 284
6.18 Comparison of observed and predicted thermochronological data for the parameter combination output from the median values of the posterior probability distribution functions. . . . 285
6.19 Overall exhumation history and topography evolution of Mont-Blanc and Aiguilles Rouges, computed from the parameterization MB006. . . . 289

7.1 Sections highlighting the Triassic unconformity in order to estimate the amount of exhumation between the Aiguilles Rouges and Mont-Blanc massifs. . . . 298
7.2 Time-Deformation constraints on the Cenozoic evolution of The Mont-Blanc and Aiguilles Rouges . . . 303
7.3 A conceptual model for western Alps External Crystalline massifs deformation 310
7.4 Cross section through the Alps along the ECORS-CROP transect (Guellec et al., 1990) and the northern CIFALP transect (Paul et al., 2022; Malusà et al., 2021). . . . 311

B.1 Data used for calculating the mean plane and mean lineation in the stereo plots used in Figure 3a. . . . 381

C.1 Chart of isotopes decay of Chlorine, Argon, Potassium, and Calcium. . . . 385
C.2 Illustration of isochrones plots (left) and inverse isochrone plot (right). . . . 386
C.3 Operating diagram of the extraction line for $^{40}Ar/^{39}Ar$ dating at *Geosciences Montpellier laboratory*. . . . 387
C.4 Quartz slip systems, modified after Passchier and Trouw (2005). . . . 388
C.5 EBSD analysis reference frame . . . 389

C.6 c-axis orientation map 390
C.7 c-axis orientation map with reconstructed grains 392
C.8 Pole figure of the c-axis and a-axis orientation 392
C.9 Equivalent radius of the grain size distribution 393
C.10 Mapped zones with EBSD within the thin section. 395
C.11 EBSD results of sample ME119. 396
C.12 EBSD results of sample C4. 397
C.13 EBSD results of sample ARe309. 398
C.14 *In situ* laser ablation map with spot numbers for sample ARe001. 399
C.15 *In situ* laser ablation map with spot numbers for sample C4. 400
C.16 *In situ* laser ablation map with spot numbers for sample ME147. 401
C.17 *In situ* laser ablation map with spot numbers for sample ME119. 402
C.18 *In situ* laser ablation map with spot numbers for sample ARe309. 403
C.19 *In situ* laser ablation map with spot numbers for sample ARe293. 404

D.1 Posterior probability functions from parameterization MB002. 417
D.2 Posterior probability functions from parameterization MB003. 417
D.3 Posterior probability functions from parameterization MB004. 418
D.4 Posterior probability functions from parameterization MB005. 419
D.5 Posterior probability functions from parameterization MB006. 420
D.6 Radial plots from AFT analysis. 432
D.7 Radial plots from AFT analysis. 433

List of Tables

3.1 Lexicon and vocabularies source description. 104
3.2 Organization of the folders into the data repository. 105
3.3 Description of the fields from the Mission table 107
3.4 Description of the fields from the Mission table 108
3.5 Description of the fields from the lithology description table. 109
3.6 Description of the fields from the planes table 110
3.7 Description of the fields from the lines table 111
3.8 Description of samples table 111
3.9 Description of sample sections table 112

4.1 Summary of the data incorporated to the 3D geological model 126

5.1 Identification, location, and description of the samples used for $^{40}Ar/^{39}Ar$ dating. 212
5.2 Bulk composition used to reconstruct the phase diagram. 217
5.3 Representative mineral composition for analyzed samples from EPMA chemincal mapping. 224
5.4 Summary of ages and thermo-barometric estimated conditions. 235

6.1 Apatite Fission Track Results From the Aiguilles Rouges and Mont-Blanc massifs, Western Alps 261
6.2 (U-Th)/He Results From the Aiguilles Rouges and Mont-Blanc massifs, Western Alps 262
6.3 Thermal and crustal parameters sets within the Pecube numerical simulation. . 269
6.4 Input parameters for program Neighborhood Algorithm in the Bayesian stage . 272
6.5 Thermal-kinematic (Pecube) inversion results of the Aiguilles Rouges models. . 279
6.6 Thermal-kinematic (Pecube) inversion results of the Mont-Blanc and Aiguilles Rouges models. 282

B.1 Locations of outcrops used in section 4.3. 378
B.2 Measures plotted in the stereographic diagrams in Figure 4.8. 379

B.3 Summarizing measurement conditions, details of used instruments, and sample preparation during Electron BackScattered Diffraction (EBSD) analysis. 379
B.4 Details on datations samples from figure 7.2. 380

C.1 Summarizing measurement conditions, details of used instruments, and sample preparation during Electron BackScattered Diffraction (EBSD) analysis. 405
C.2 In-situ $^{40}Ar/^{39}Ar$ data on white mica from sample **ARe001**. 407
C.3 In-situ $^{40}Ar/^{39}Ar$ data on white mica from sample **ME147**. 408
C.4 In-situ $^{40}Ar/^{39}Ar$ data on white mica from sample **C4**. 409
C.5 Infrared laser in-situ $^{40}Ar/^{39}Ar$ data on white mica from sample **ME119**. . . . 410
C.6 Infrared laser in-situ $^{40}Ar/^{39}Ar$ data on white mica from sample **ARe309**. . . . 411
C.7 Infrared laser in-situ $^{40}Ar/^{39}Ar$ data on white mica from sample **ARe293**. . . . 412

D.1 Thermal-kinematic (Pecube) inversion results of the synthetic Aiguilles Rouges models. 414
D.2 Thermal-kinematic (Pecube) inversion results of the synthetic models from SY008 to SY0012, using a normally distributed noise in the data centered on 0 with a standard deviation of 0.4. 415
D.3 Thermal-kinematic (Pecube) inversion results of the synthetic models from SY002 to SY006, using a normally distributed noise in the data centered on 0 with a standard deviation of 0.8. 416
D.4 Apatite fission track data for sample **ARe024** 423
D.5 Apatite fission track data for sample **ARe025** 424
D.6 Apatite fission track data for sample **ARe026** 425
D.7 Apatite fission track data for sample **ARe031** 426
D.8 Apatite fission track data for sample **ARe086** 427
D.9 Apatite fission track data for sample **ARe152** 428
D.10 Apatite fission track data for sample **ARe165** 429
D.11 Apatite fission track data for sample **ARe184** 430
D.12 Apatite fission track data for sample **ME130** 431

GENERAL INTRODUCTION

The general questions to be addressed in this work

Continent-to-continent collisions are an important expression of plate tectonics, giving rise to mountain belts (Dewey et al., 1973). Mountain building results from the crustal thickening associated with the various stages of the lithosphere convergence, from subduction to collision. Collisions play a crucial role in plate tectonics (Wilson, 1966; Le Pichon, 1968) as a localized strain zone along the plate interface (Tapponnier et al., 1986) that has significant implications in seismic hazards (Angelier et al., 2000; Mugnier et al., 2013), climate evolution (Raymo and Ruddiman, 1992; Raymo et al., 1988), and even in the global carbon cycle (Chamberlin, 1899; Hilton and West, 2020; Gaillardet et al., 1999).

From the convergence of continental lithospheres to the resulting thickening, the mechanical behavior of the crust, especially the mechanisms of crustal stacking, has been widely discussed (Boyer and Elliott, 1982; Pfiffner et al., 2000; Mattauer, 1975). What is the importance of vertical versus horizontal displacements in crustal thickening of mountain belts, what is the geometry of the deformation, where and how does the deformation propagate and evolve over time, what is the importance of inherited structures in strain localization, what is the importance of climatic forcing on orogen evolution ? Answering these questions is crucial to understand the mechanics of continental lithosphere, as the thickening modes during the collision are controlled by litosphere rheology (strength) (Mouthereau et al., 2013; Burov and Diament, 1995).

The Ph.D. aims to examine the Cenozoic evolution of the orogenic wedge in the Western Alps through a particularly complex, iconic, and controversial site: the Mont-Blanc massif. This area has been extensively studied since the pioneering work of De Saussure (1796) and the first conceptualization of rock deformation related to geological processes. Over the decades, the tectonic concepts of deformation and faulting have progressed, and new field observations remain essential for formulating and evaluating major conceptual models. Moreover, the same field observation may be assessed differently over the years with the evolution of concepts. In addition, since the 1990s, the contribution of large geophysics projects to infer the large-

scale structure of the Alps has shed new light on the evolution of the collision (Guellec et al., 1990; Malusà et al., 2021; Pfiffner et al., 1997). At the same time, advances in computational performance allow us to now build more complex numerical models to simulate natural processes. The combined use of these skills enables the construction of a conceptual geometrical and kinematic model of the evolution of a mountain belt based on observations.

The general "ingredients" for understanding mountain belt evolution

To address these questions, we present an integrative approach that provides constraints on both the 3D geometry of the structures and the kinematics of the deformations.

Tectonics is mainly a **geometrical problem**: A good understanding of the precise **3D** geometry of the structure is the key. Too often geologists are restricted to 2D space through maps and cross sections, mainly because the work materials are in 2D (notebook, paper sheet, computer screen); therefore, it seems convenient to simplify the problem in 2D. This approach may be sufficient when geology is quite geometrically simple, cylindrical and the shortening direction is constant over time and when data are acquired regularly along sections. However, geological data is often sparse and irregularly distributed within the study area and simple interpolation of surface data into sections is not sufficient.

Therefore, we need to build a 3D geological model based on field measurements to assess this complex geometry. Since the 1990s, the advancement of numerical computation with geostatistics has revolutionized structural geology by introducing 3D modeling techniques that provide a more accurate and detailed representation of geological features (Mallet, 1992; Lajaunie et al., 1997; Calcagno et al., 2008). We use GeoModeller software that simulates the subsurface with successive strata belonging to the same unit. Significant and coherent 3D models have been constructed using a geostatistical method using both interface locations and structural orientation data.

In structural geology, it is often very difficult to retrieve the original data used for the interpretation of geological maps or cross sections after their publication, making it impossible to assess how well constrained the model is, or for other authors to increment the dataset or even propose other models based on the same data. To address this issue, we need first to build a database template for structural geologists to share their data with the scientific community and secondly to provide a structural measurement dataset to efficiently process and store the data, facilitating their process for 3D geological modeling.

Tectonics is also a **problem of motion**: because mountain belts evolve over time, it is

necessary to combine the 3D geometry with a kinematic reconstruction to address the whole **4D** solution (3D geometry + 1D time). To address the 4D problem, numerous data are needed: field observation that allows to constrain structures and contact geometry and estimate their kinematics. On the regional scale, the structural study is based mainly on published geological maps, which we complete and update with abundant field observation, measurements and mapping; on the outcrop scale we characterize the style, intensity, and geometry of the deformation by qualitative observation and precise measurements of the orientation of the structural features (stratigraphy, cleavage, shear planes, lineations, etc.). We meticulously select oriented samples and produce oriented thin sections to characterize the deformation at a microscopic scale. The main shear criteria used are the relationship between the shear and cleavage planes (Berthé et al., 1979), the asymmetrical boudinage (Lacassin, 1988), the delta and sigma porphyroclasts (Hanmer and Passchier, 1991), and lattice preferred orientation in quartz (Gapais and Barbarin, 1986; Passchier and Trouw, 2005). Absolute timing constraints are obtained first using the relative chronology of cross-cutting structures and second with absolute dating. In addition, thermobarometric conditions are estimated by petrogeochemical quantification.

To quantify the amount and timing of exhumation of the massifs, we use thermochronological data that record the cooling of rocks. However, the relation between rock cooling and exhumation is not straightforward and is related to the complex interaction between erosion and tectonic. To quantify the role of each driving force, we can numerically simulate the exhumation process with algorithms specifically designed (e.g., Gallagher et al., 1998; Braun, 2003; Braun et al., 2012). The input of the simulation are observed thermochronological ages, and the output are estimated thermochronological ages that depend on the parameters used for the simulation. The estimated data can be compared to the observed data, and using the inverse method, the simulation parameters are adjusted to reduce the difference between the two. However, the complexity of the problem leads to a non-unicity of convergence. Therefore, we use a two-stage method: After a first stage of parameter exploration by inversion (neighborhood algorithm) (Sambridge, 1999a), we resample the results obtained with a Bayesian method to obtain a probability density distribution that describes the simulation parameters and uncertainties (Sambridge, 1999b). In addition, inversions of synthetic data generated by direct models (which we know are the input parameters) are used, to assess the ability of the inversion and the data to quantify each simulation parameter.

Manuscript organization

This Ph.D. work involves many methods that could not be grouped into the classical chapter of "materials and methods". Consequently, the methodology applied in each part will be detailed in the corresponding chapter. The chapters that detail the results correspond to

published or submitted research articles, and in consequences adaptations were made for consistency.

Chapter 1: Dynamics of orogenic wedges: Reviews the general aspects of the dynamics of orogenic wedges. Three natural examples of orogenic wedges are briefly presented to evaluate the parameters that control their evolution, and a discussion on the contribution of modeling (analogous or numerical) to understanding the evolution of orogenic wedges is proposed.

Chapter 2: Tectonic structure of the Western Alps: Detail structure of the Alpine orogenic wedge, starting from the deep structure inferred by geophysical experiments. We present the different tectonic units, the evolution of the belt, and the different deformation sequences proposed in the Western Alps and more locally in the Mont-Blanc massif. This part aims to present the state of the art on the evolution of the Western Alps.

Chapter 3: Development of a relational database for organizing field geological data: *DataGeol*: Presentation of the design of a database that was developed for the management and process of structural data. This part also acts as a Ph.D. data management plan that gives the data organization and repositories that store all the data from this work.

Chapter 4: Building a 3D geological model of a structurally complex Alpine region field descriptions of the structure and cover / basement relationship in the Mont-Blanc, Aiguilles Rouges, and Subalpine ranges. We detail the construction of three 3D geological models. Part of this chapter has been published in the *Tectonophysics* journal and is available in appendix F p. 441. To avoid duplication, part of the introduction of the publication has been moved to Chapter 2 and the discussion and implications have been moved to Chapter 8 of the Ph.D. manuscript.

Chapter 5: Timing and conditions of the deformation Absolute dating of synkinematic minerals using *in situ* $^{40}Ar/^{39}Ar$ dating technique applied to six shear zones within the Mont-Blanc massif. This chapter discusses the chronology of the deformation in the area and sets in motion the 3D structures described in Chapters 4 and 5. This chapter was written in preparation for submission to the *Tectonics* journal.

Chapter 6: Exhumation history of Mont-Blanc and Aiguilles Rouges Detailed investigation of the inversion of thermochronological data to infer the exhumation history of the Mont-Blanc and Aiguilles Rouges massif. This work also uses synthetic data to evaluate the ability of the numerical simulation to retrieve the exhumation history and quantify the uncertainties on

the simulation parameters. This chapter was written in preparation for submission to the *JGR Solid Earth* journal.

Chapter 7: Discussion and implications Discussion on the implications of the results in the Mont-Blanc and Aiguilles Rouges, the Alps and more broadly in orogenic wedges. Perspectives are open for future investigations.

Part I

SCIENTIFIC BACKGROUND

Chapter 1

Dynamics of orogenic wedges

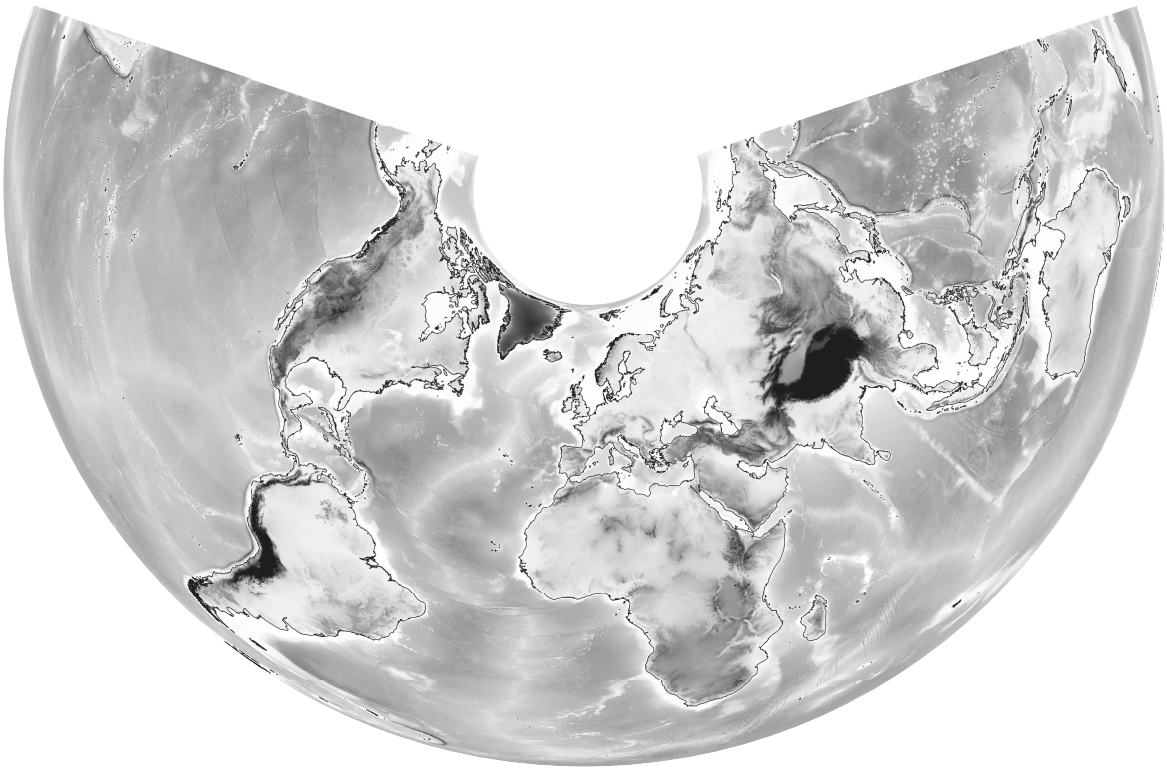

Worldwide digital elevation model showing the distribution of relief on the Earth's surface. Topographic data from https://www.gebco.net/

Abstract

Continental mountain belts are the result of the accretion of two colliding continents. In this chapter, we review the general aspects of the dynamics of orogenic wedges on Earth. The Coulomb-wedge model has been proposed to explain the tectonic evolution of various mountain belts. This model is based on the triangular shape of the orogen in the cross-section and on the fact that the convergence is accommodated by a megathrust that constitutes the plate interface. During the collision, the deformation migrates in sequence towards the outer part of the belt. This mechanical model allows one to calculate the orientation of the maximum principal stress and predicts the stress conditions under which a wedge is mechanically stable or unstable. Through the investigation of three natural examples of orogenic wedges (Taïwan, Himalaya, Alps), and although orogens are different and have specificities, we identified a common scenario of deformation during the collision: continental subduction, antiformal stack, and exhumation of the inner part, propagation of the deformation in the foreland. Analogous and numerical models simulate the propagation of deformation in an orogenic wedge. These models highlighted the influence of erosion/sedimentation, crust rheology, localized décollements and inherited prestructuration on orogen evolution.

Résumé

Les chaines de montagnes continentales sont le résultat de l'accrétion de deux continents en collision. Dans ce chapitre, nous passons en revue les aspects généraux de la dynamique des prismes orogéniques. Le modèle de Coulomb a été proposé pour expliquer l'évolution tectonique de chaines de montagnes. Ce modèle est basé sur la forme triangulaire de la collision en coupe et sur le fait que la convergence est accommodée par un mega-chevauchement à l'interface des plaques. Lors de la collision, la déformation migre progressivement en séquence vers la partie externe de la chaine. Ce modèle mécanique permet de calculer l'orientation des contraintes principales maximales et de prédire les conditions de contrainte sous lesquelles le prisme est mécaniquement stable ou instable. Grâce à l'étude de trois exemples naturels de prismes orogéniques (Taïwan, Himalaya, Alpes), et bien que les orogènes soient différents et présentent des spécificités, nous avons identifié un scénario commun de déformation pendant la collision : subduction continentale, empilement crustal et exhumation de la partie interne, puis propagation de la déformation dans l'avant-pays. Les modèles analogues et numériques simulent la propagation de la déformation dans un prisme orogénique. Ces modèles ont mis en évidence l'influence de l'érosion/sédimentation, de la rhéologie de la croûte, de la localisation des décollements et de la préstructuration héritée sur l'évolution du prisme orogénique.

1.1 Introduction

In the context of plate tectonics, continental mountain belts are the result of the accretion of two colliding continents. In the last decades, understanding the dynamics of collision orogens has been a major topic of research (e.g., Chamberlin, 1925; Platt, 1986; Malavieille, 2010; Konstantinovskaya and Malavieille, 2005; Bonnet et al., 2008; Dal Zilio et al., 2020; Mattauer, 1975). The following diagram shows the three main domains of an orogenic belt (Fig. 1.1). The internal zone (*hinterland*) constitutes the most internal zone of the belt, where the metamorphism is the most intense. In the *foreland*, there is the fold and thrust belt part, which implies the sedimentary cover that is deformed by the propagation of thrusts from the basement. The cover is often detached from the basement and displaced in nappes. Globally, the deformation intensity decreases towards the outer part of the belt.

In this chapter, we first expose the orogenic wedge theory and briefly set the mechanical aspect of this model. Later, we describe the evolution of collisional orogen through the non-exhaustive analysis of three examples of mountain belts. These descriptions will be compared with the analogous and numerical modeling of orogenic wedges, allowing one to define the main parameters that control the dynamics of orogenic wedges.

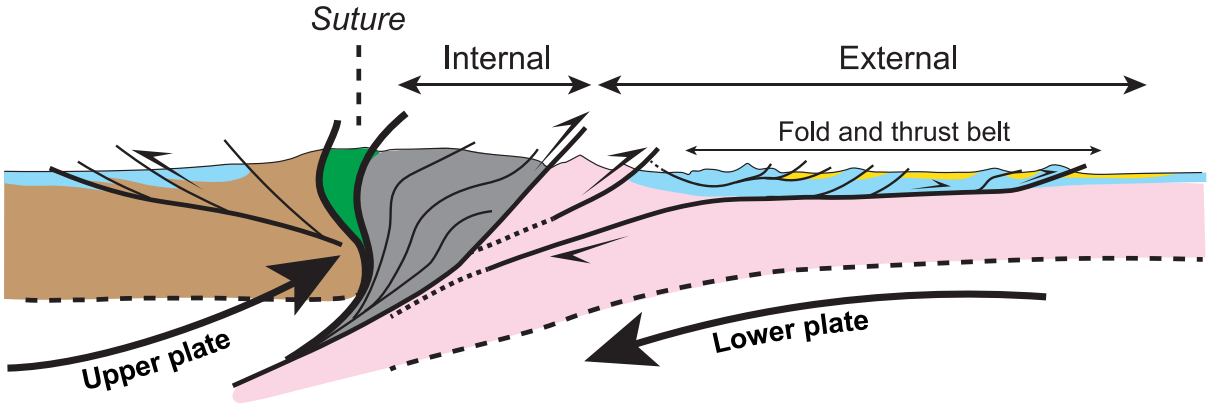

Figure 1.1. Nomenclature of a collisional orogen.

1.2 The orogenic wedge model

The convergence of two colliding continents leads to the closure of the oceanic domain by subduction of the lower plate below the upper plate. The upper plate acts as a rigid stopper that scratches the lower plate and stacks the sedimentary cover, building a sedimentary accretion wedge. At some point, when the oceanic domain has been totally subducted, the continental part of the lower plates starts to subduct as well, leading to continental subduction and the beginning of collision. The orogenic Coulomb-wedge model has been proposed to explain the tectonic evolution of various mountain belts, including the Alps (e.g., Platt, 1986), Taiwan

(e.g., Malavieille et al., 2002), and the Himalayas (e.g., Avouac, 2003). According to this model, the geometry of the belt has a triangular shape and the convergence is accommodated by a megathrust (a major shear zone) that constitutes the plate interface (Fig. 1.2). During the collision, there is a sequential migration of the deformation front towards the outer part of the belt. The orogenic wedge model allows us to calculate the orientation of the maximum principal stress and predicts the stress conditions under which a wedge is mechanically stable or unstable and the dip angle of the ruptures. The stability of the orogenic wedge is based on the equilibrium between the tectonic accretion, driven by horizontal tectonic forces that lead to thickening of the wedge (with faulting and folding), the internal friction coefficient, the megathrust dip angle, and megathrust effective basal friction. The evolution of these physical parameters is controlled by the fight between tectonic accretion (faulting) that thickens the wedge and surface processes such as erosion and sedimentation that flatten it (Fig. 1.3) (e.g., Dielforder et al., 2020; Dal Zilio et al., 2020; Bonnet et al., 2007; Avouac and Burov, 1996).

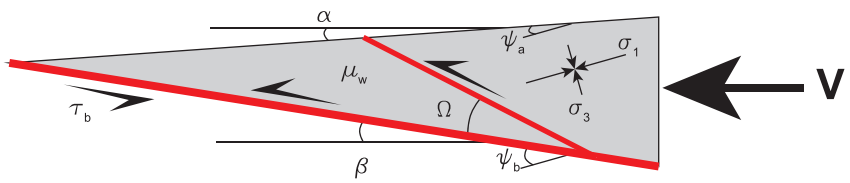

Figure 1.2. Schematic illustration of the orogenic Coulomb-wedge model (modified after Dielforder (2017) and Dahlen (1984)). The angles α, β, and Ω describe the geometry of the wedge. The parameters are μ describes the effective internal friction, τ the basal friction of the megathrust, and σ the principal stress components. The relationship between those physical parameters determines the stability of the wedge. In the geometry depicted, the wedge is stronger than the basal fault slip. To overcome this difference, another thrust breaks through the wedge with an angle $\Omega > 0$ to the basal fault. This configuration is close to out-of-sequence thrusting, which is a classically observed behavior of fold and thrust mountain belts.

Applying this physical model to a mountain belt, the driving forces may be summarized as follows:

- **Tectonic forces**: Related to the velocity field of the convergence and its evolution through time. They control the total amount of shortening, the direction and velocity of convergence.
- **Rheology**: The strength and mechanical behavior of the lithosphere determine how it responds to collision and the amount of localization of the deformation. The main shortening is accommodated on the megathrust at the base of the orogenic wedge. Décollements will concentrate the deformation in roughly flat and weak layers, such as cover / basement interface, whereas crustal ramps are steeper and root deeper in the basement.
- **Erosion and sedimentation**: The interplay between erosion and sedimentation processes influences the shape, topography, and exhumation of the wedge. Erosion removes ma-

terial from the top of the wedge, reduces the load enhancing uplift, and allows crustal exhumation; while sedimentation adds weight to the foreland basins. As a consequence, the mass moves during the collision and can modify the distribution of the deformation within the orogenic wedge.

- **Structural inheritance**: faults and deformations inherited from previous orogens or extensions can localize or influence the response of the crust to the collision.

Investigating the dynamic of orogenic wedges was carried out with experimental modeling that represents the brittle-frictional deformation behavior of rocks with physical materials (Graveleau et al., 2012, for a review.). Experimental modelling is an essential tool for examining tectonics and relief dynamics, as it has the advantage of enabling the formation and growth of instabilities, as is the case in natural settings. However, the parameters that control the rheology and mechanics of the orogenic wedge are approximated by the experiment, and limitations arise: for example, the flexural response to tectonic loading, the increase in temperature with depth, or the presence of fluid overpressure cannot be reproduced. Later, numerical simulations mathematically described the dynamic evolution of the orogenic wedge (e.g., Spitz et al., 2020; Bauville and Schmalholz, 2015; Dal Zilio et al., 2020). These new kinds of experiments help to better quantify the physical forces acting and could consider temperature and establish the foundation for understanding the mechanics of orogenic wedges. However, these experiments also have limitations, such as the way of localizing the deformation and initiating faults.

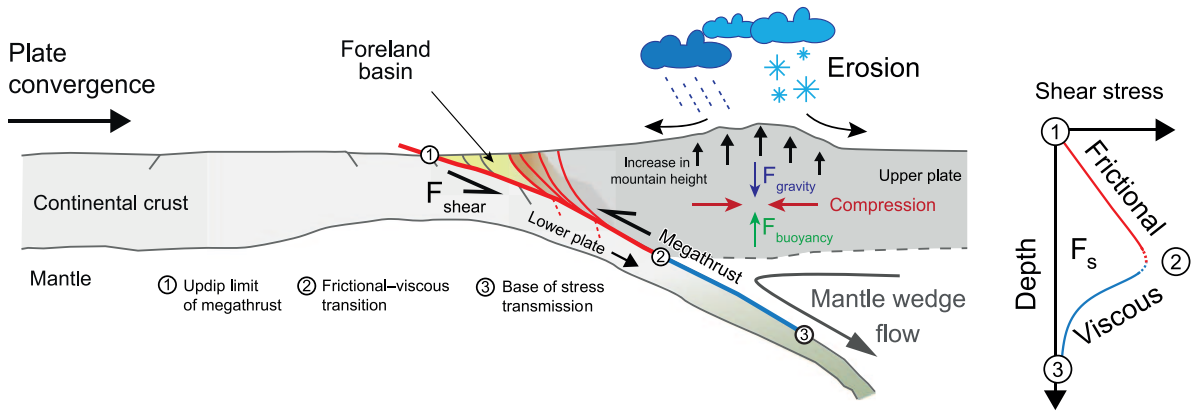

Figure 1.3. Schematic summary of processes at convergent plate margins (compiled from Dielforder et al. (2020) and Dielforder and Hampel (2021). Plate convergence is accommodated by forcing one plate beneath the other. The megathrust constitutes the plate interface and is segmented into a frictional, and a viscous segment where temperatures are large enough for viscous shear to occur at low shear stresses. The downdip termination of the viscous segment is related to mantle wedge flow. Erosion modulates the surface topography and removes mass from the mountain range. If the shear force of the megathrust is greater than the effect of gravity, then the vertical stress is greater than the horizontal stress and the mountain height must increase, which may be driven by accretion or tectonic shortening.

1.3 Style of deformation

During the collision, the shortening is accommodated by deformation, but the tectonic "style" varies depending on the configuration (Pfiffner, 2017, for a review.). Around the Earth we observe that deformation propagates differently according to the geometry of the belt. When the propagation of the deformation is mainly horizontal, with the development of flat faults propagating into weaker layers, known as thrusts or "décollements", the tectonic style is described as *Thin-skin* because only a thin part of the crust is involved in the deformation. When the deformation originates deeper in the crust and involves the basement and a steep fault, the tectonic style is described as **Thick-Skin** because a thick part of the crust is involved in the deformation. These two styles of deformation can be coeval along the same thrust system (Fig. 1.4). The displacement of a steep thrust (thick skin) can be transferred to the interface between the cover / basement and propagate as a décollement thrust in the thin-skin style (Fig. 1.4). Understanding when and where an orogenic wedge has experienced a thin-skin or thick-skin deformation is crucial for evaluating the behavior of crustal deformation, the localization of deformation, and also fundamental for the process of restoring cross-sections.

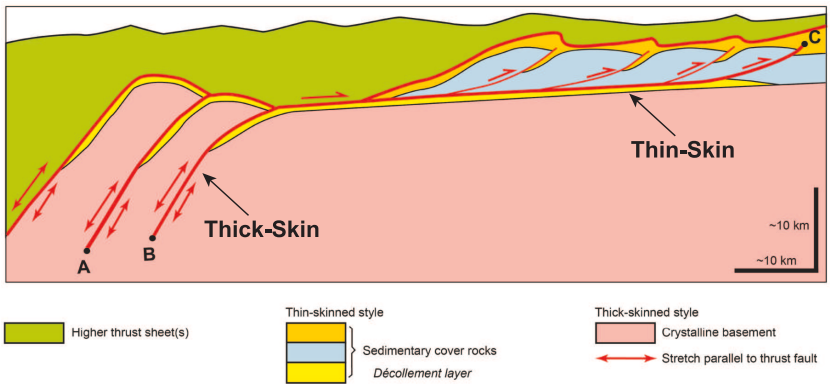

Figure 1.4. Thin-skin and thick-skin tectonics along a thrust fault from Pfiffner (2014). The displacement of a steep thrust (thick skin) can be transferred to the interface between the cover/basement and propagate in as a décollement thrust in thin-skin style.

1.4 Different orogenic wedge around the Earth

The Earth has several intra-continental mountain belts on its surface (Fig. 1.5). The "Alpine" orogenic belts, runs from the Alps to the Himalayas and is a major collision zone resulting from the convergence of several southern plates toward the huge northern Eurasian plate. In the following, we will give a quick overview of three structurally different orogens: Taïwan, the Himalayas, and the Alps, to highlight the commonalities and differences between the orogenic wedge structure and evolution and to identify the key parameters that control their dynamic evolution.

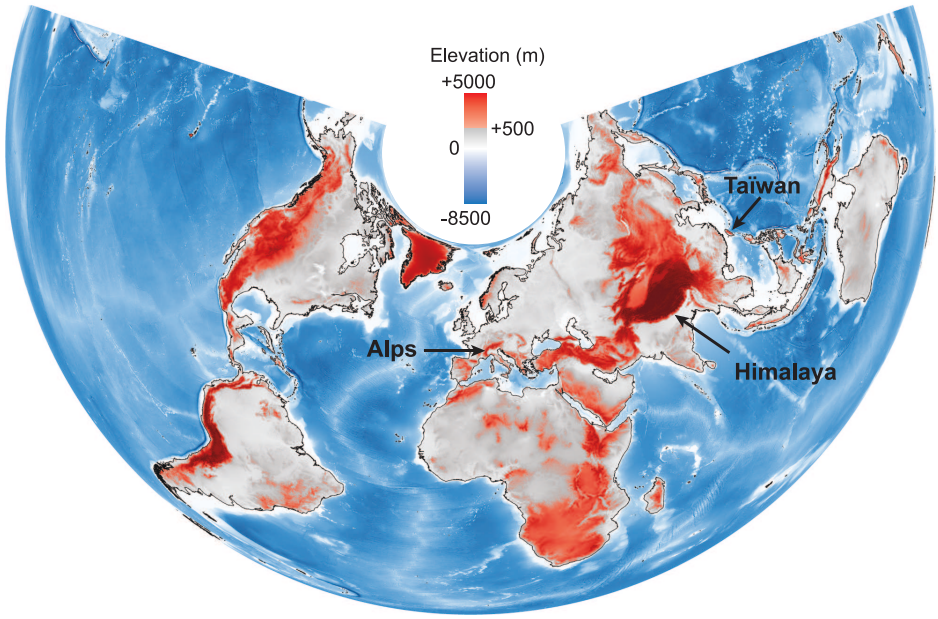

Figure 1.5. Worldwide digital elevation model showing the distribution of relief on the Earth's surface. Bathymetry is shown in variations of blue, topography below 500m is in light gray, and relief above 500 in variations of red. The "Alpine" orogenic belt resulting from the closure of the Thethys Ocean is well visible, running from the Alps until the Himalayas. Topographic data from https://www.gebco.net/. Projection is Albers equal-area conic projection (IAU-2015:39900)

1.4.1 Taiwan

Taiwan Island, located in the Philippine Sea, east of China, is a west-verging arc-collision wedge. The collision results from the collision between the Chinese passive margin (Eurasian plate in the west) and the Luzon volcanic arc (in the east) (Fig. 1.6). The collision is considered young, as it started about 6.5 Ma ago (e.g., Chi, 1981; Lin et al., 2003; Sibuet and Hsu, 2004; Byrne et al., 2011) and the present-day earthquake activity suggests that the orogen is still active (e.g., Carena et al., 2002; Shyu et al., 2005). The thrusting sequence of the collision is commonly described by three stages of deformation (Mouthereau et al., 2001): the first stage of submarine accretion started at 6.5 Ma and lasted up to 2 Ma. The second stage occurred during the late Pliocene Early Pleistocene and is responsible for the exhumation and denudation of the central range, and the last deformation started in the middle Pleistocene and is and is a fold and thrust belt propagation and is still ongoing. According to Malavieille (2010), the shortening is mainly accommodated by frontal accretion thrust on the Western foreland side of the wedge, against the Eurasia plate (Fig. 1.7). The internal part grows and is exhumed by stacking of tectonic units at depths associated with strong erosion (Simoes et al., 2007; Simoes et al., 2012). The antiformal stack deforms and folds a previous décollement (Fig. 1.7). The deformation is therefore thin-skinned in the foreland, favored by flat thrusts involved in the basement located on the Eurasia plate. In the hinterland, the deformation is thick-skinned and

is responsible for the ongoing crustal thickening.

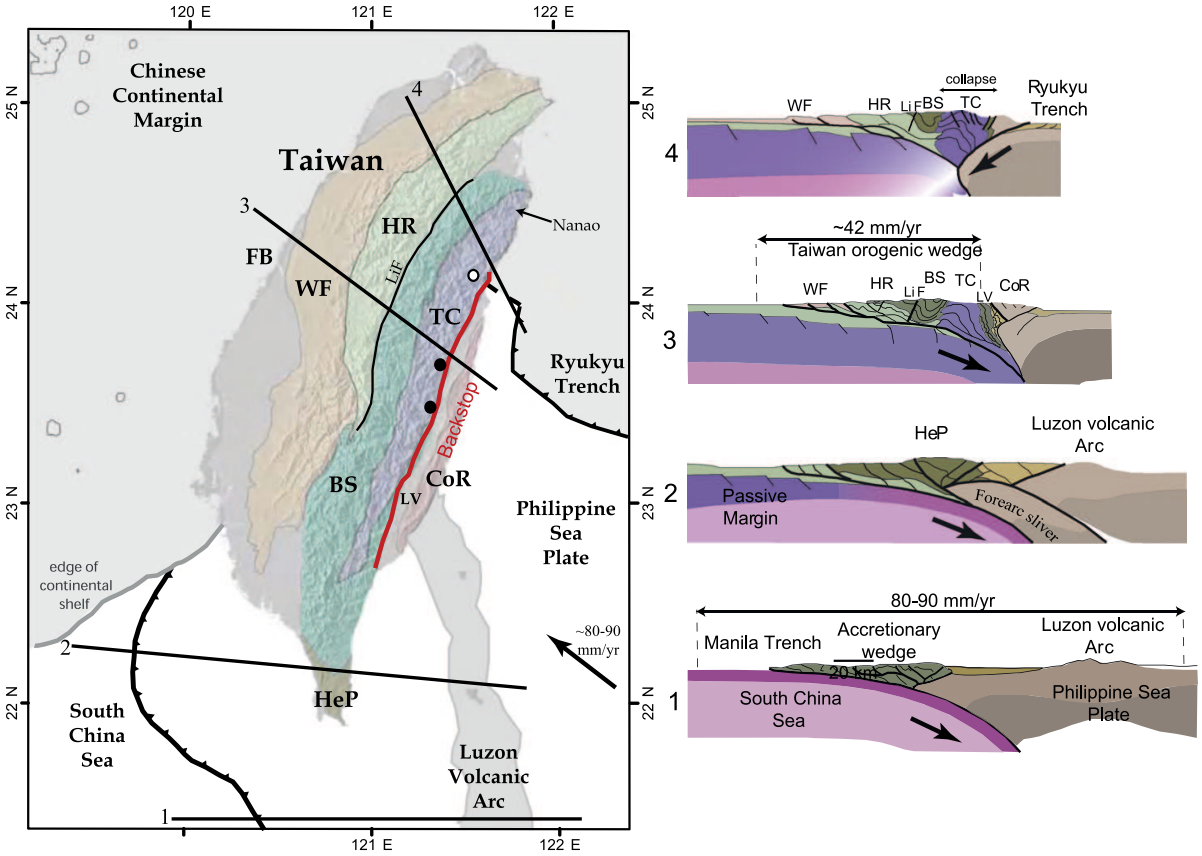

Figure 1.6. Geodynamical context and simplified geological map and cross sections of Taiwan from Simoes et al. (2012). Left: The Taiwan orogenic wedge refers to the accreted sequences of the passive margin, west of the LV. The main tectonostratigraphic units are the Foreland Basin (FB), the Western Foothills (WF), the Hsueshan Range (HR), the Backbone Slates (BS), the Tananao Complex (TC), the Hengchun Peninsula (HeP) and the Coastal Range (CoR). The Lishan fault (LiF) is also reported. Right: Cross-sections across the Taiwan collision zone from Molli and Malavieille (2010), showing the northward evolution from an oceanic subduction (1) to an arc–continent collision (2) and a mature orogenic wedge (3), as well as the final collapse of this wedge related to the reversal of the subduction polarity (4).

1.4.2 The Himalayas

The Himalayas result from the continental collision between India and Asia after the closure of the Tethys Ocean at about 55 Ma (e.g., DeCelles et al., 2004; Allégre et al., 1984). First, the thickening started at about 45 Ma, associated with the underplating of the Indian plate under the Asiatic plate until 30 Ma (Fig. 1.8). This burial phase is associated with the eo-Himalayan metamorphism (e.g., Cottle et al., 2009; Godin, 2003). From the south, the phyllites and quartzites of the Lesser Himalaya (LH) are underplated below the Himalayan Crystalline Slab (HCS) which is a sliver of gneiss and granites, with the Main Central Thrust (MCT). This underplating exhumed the HCS between 25 and 10 Ma and is associated with

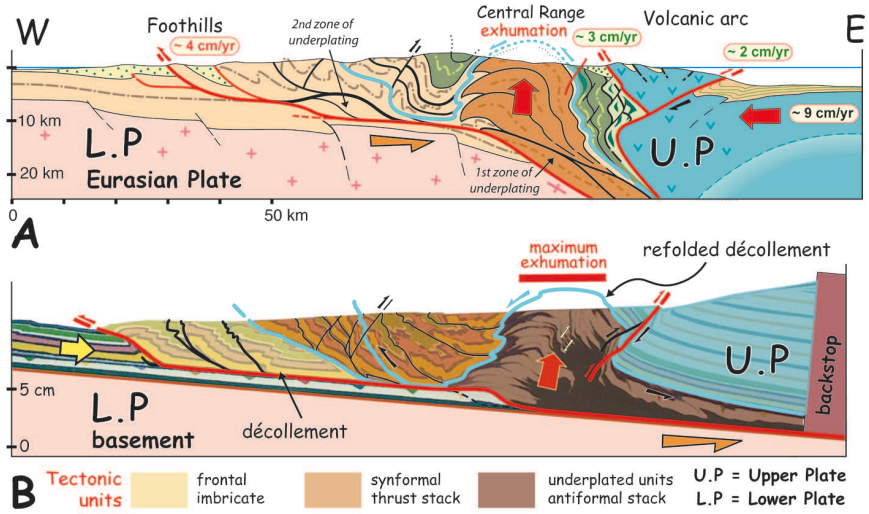

Figure 1.7. Cross section through the orogenic wedge of Taïwan (Malavieille, 2010). (A) Interpretive geological section of Taiwan orogenic wedge inspired by (B) experiment with décollement and erosion. Medium-term shortening rates on main active faults are indicated.

the neo-Himalayan metamorphism. In the north, the HCS is separated from the weakly metamorphosed Tethyan sedimentary series (TSS) by the South Tibetan Detachment (STD). The South Tibetan Detachment (STD) system corresponds to a series of north-dipping structures that accommodate the normal motion of the Tethyan sedimentary series (TSS) with respect to the underlying High Himalayan Crystalline series (Leloup et al., 2010). This structure has attracted the attention of many scientists, as this fault runs for more than 1500 km along the Himalayan range and shows normal faulting in a direction parallel to the thrust direction (Fig. 1.8) (Burg, 1983; Burchfiel et al., 1992). Driven by various hypotheses of deformation models, the origin and mechanics of the STD have been debated for decades. Leloup et al. (2010) proposed a brief review of the proposed models for the initiation and evolution of the STD: Early models assumed that the STD's were merging at depth with the Main Central Thrust (MCT), isolating a crustal wedge expulsed upward (e.g., Burg et al., 1984; Burchfiel and Royden, 1985; England and Molnar, 1993; Hodges et al., 1996; Grujic et al., 1996; Grasemann et al., 1999). For others, STD's never merges to the surface, but defines, respectively, the top and bottom of a channel flow of low-viscosity lower crust expulsed from beneath the Tibetan plateau (e.g., Beaumont et al., 2001). This mechanism is often considered to be enhanced by localized erosion on the southern Himalayan slopes. Others consider that STD and MCT accommodate the southward intrusion of high-crystalline series (Price, 1986, "tectonic wedging" of). The main difference from that of the crustal wedge models is that the STD and the MCT merge southward and that the STD emerges northward as the Greater Counter Thrust (Yin, 2006; Webb et al., 2007).

Later, the deformation migrated to the south along the Main Basal Thrust (MBT) and is related to the deposition of the Siwaliks in the foreland. Then the external part of the range deforms as a fold and thrust belt that developed above the Main Frontal Thrust (MFT). MCT,

MBT, and MFT connect at depth with the main Himalayan thrust (MHT), which is a large décollement below the crystalline crustal basement that has accommodated at least 200 km (DeCelles et al., 2002). However, little is known about the location of that décollement layer. The MHT is structured with flat ramps that extend below the Lesser Himalayas and are responsible for the exhumation of the Lesser Himalaya (Bollinger et al., 2004) (Fig. 1.8). Above the ramp, the underplating process creates a duplex structure that is responsible for the exhumation of the Lesser Himalayan sequence. The thrust sequence propagated southward (toward the outer part of the belt), with the main frontal thrust (MFT) being the last in this sequence and still seismogenic (Katmandu earthquake 2010) (Mugnier et al., 2013).

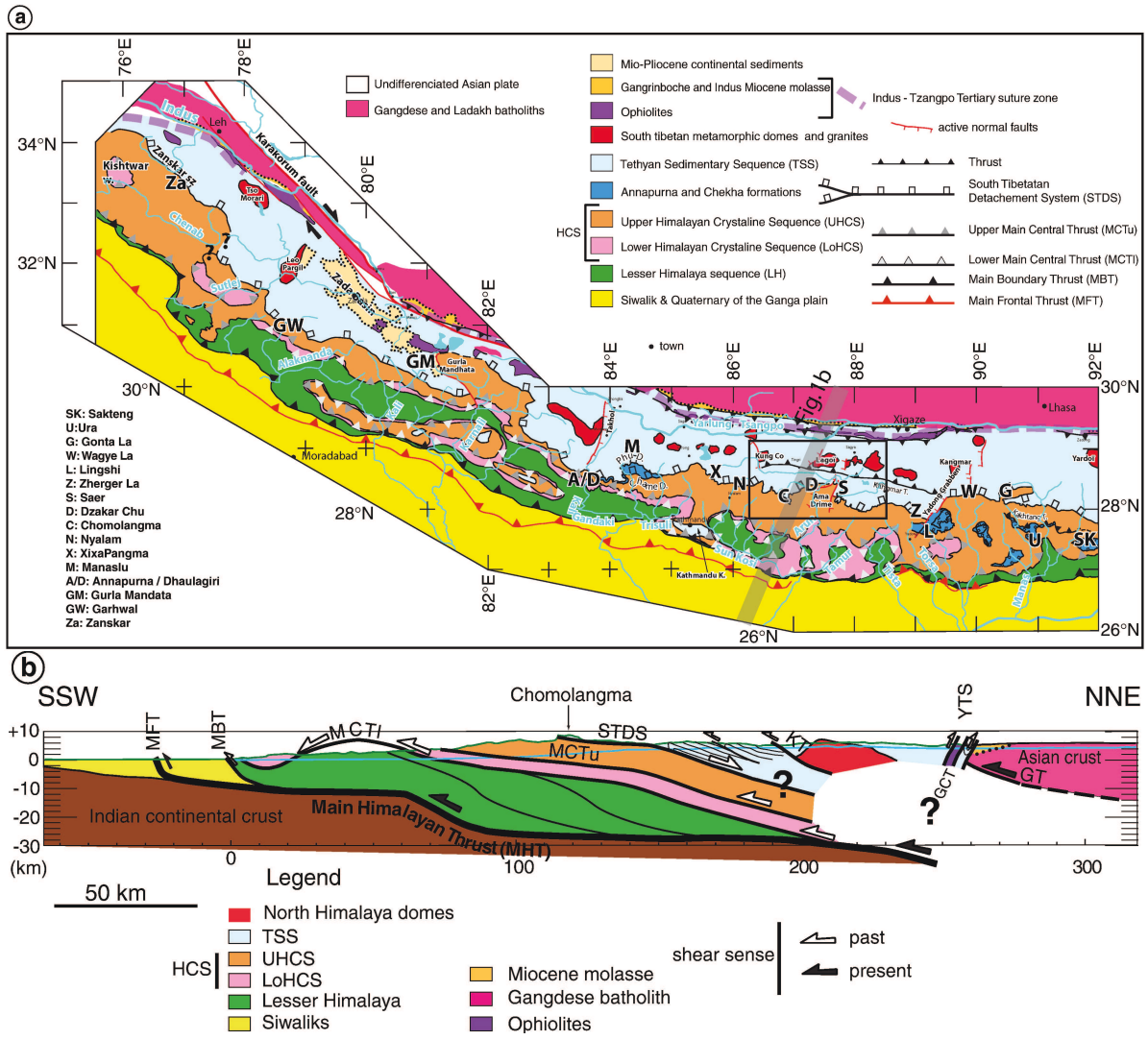

Figure 1.8. Himalayas structural map and simplified cross-section. The major units as well as the main contacts are depicted. From Leloup et al. (2010).

1.4.3 The Alps

The Alps are the result of the continental collision between Europe and Apulia after the closure of the Tethys Ocean during the Cretaceous. The continental collision started from the Upper Cretaceous / Paleocene (Nicolas et al., 1990; Pfiffner et al., 1997) along the suture zone in Sesia. During the late Eocene, the closure of the Briançonnais sub-domain along the Penninic thrust led to the underthrusting of the external domain. Crustal thickening occurred during the Miocene with the stacking of crustal ramps in the External Crystalline Massifs (Guellec et al., 1990; Mugnier et al., 2013; Nicolas et al., 1990) and was associated with their exhumation (Leloup et al., 2005; Glotzbach et al., 2008; Glotzbach et al., 2011; Van der Beek et al., 2010). Several authors have suggested that Mesozoic inherited structures have played a significant role in the structuration of the Western Alps (e.g., Escher et al., 1988; Ramsay, 1981; Burkhard and Sommaruga, 1998; Bellahsen et al., 2012; Boutoux et al., 2014). From the seismic experiment, ECORS-CROP Guellec et al. (1990) have published their interpretation of the Alps: the deformation is controlled by crustal flakes that stack above a crustal thrust. The deformation is transferred from the crust to the cover through a décollement at the bottom of the sedimentary cover (Subalpine and Jura fold and thrust belt). In this interpretation, the deformation is therefore of thick-skin skin style in the External Crystalline Massifs leading to their exhumation and thin-skin in the external and foreland domains, propagating the deformation far away from the belt.

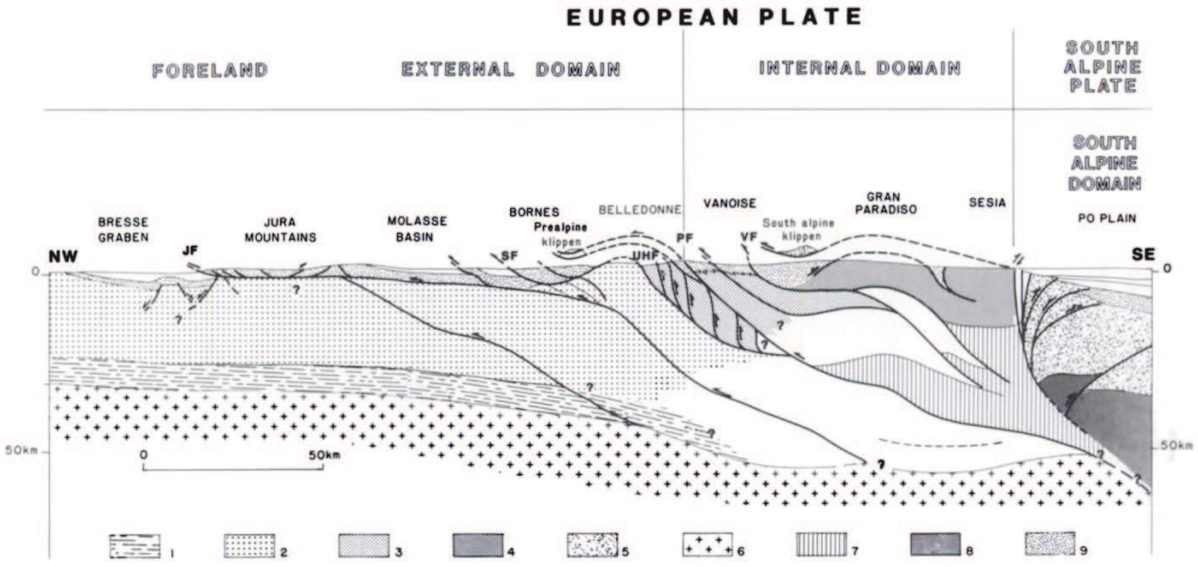

Figure 1.9. Interpreted cross-section of the Alps from the ECORS-CROP seismic experiment (Guellec et al., 1990). In this interpretation, the basement of the external crystalline massifs is connected to deep crustal ramps, leading to a thick-skin tectonic style while in the foreland the deformation is thin-skin above a large decollement. J.F: Jura Front; S.F: Subalpine Front; U.H.F: Ultra-Helvetic Front; P.F: Penninic Front; V.F: Vanoise Front; 1: Lower

1.5 Contribution of mechanical models to the comprehension of Alpine wedge dynamics

In the following section, we focus on the Alpine collision and compare the description of the belts with analogous and numerical modeling of the evolution of orogenic wedges.

In tectonics, interpretations of field observations are associated with conceptual models that aim to explain the observations. These models can be conceptual, mechanical, or kinematic based on numerical and experimental simulations. The models are simplified representations of natural processes to simulate their dynamic evolution and quantify the acting forces. In a few decades, several experimental and later numerical model simulations investigated the evolution of orogenic wedges during a collision. Experimental models use granular materials, such as sand, that are progressively pushed against an immobile wall (Graveleau et al., 2012; Konstantinovskaya and Malavieille, 2005; Bonnet et al., 2007). From the first seismic experiments investigating the deep structure of the Alps (e.g., Nicolas et al., 1990; Guellec et al., 1990; Burkhard and Sommaruga, 1998), analogous models have tried to reproduce the Alpine evolution (e.g., Bonnet et al., 2007).

1.5.1 Analogous models

Analog modeling approaches have been used to simulate the propagation of deformation in an orogenic wedge and analyze the effects of décollements and erosion on the deformation style (e.g., Konstantinovskaya and Malavieille, 2005; Konstantinovskaya and Malavieille, 2011; Malavieille, 2010). In a case study of the Alps, Bonnet et al. (2007) built a series of experimental models using the interpreted cross-section of the Alps proposed by Burkhard and Sommaruga (1998). They established a prestructured lower plate, underthrusted by an upper plate (Fig. 1.10). During the first stages of the collision (t_0 to t_{16}), the lower plate is underthrusted below the upper plate. The reference points are rapidly buried to a depth of about 4 km (Figs. 1.10 and 1.11). This is the **burial phase**, below the nappes. From t_{16} to t_{29}, the thrust stacking from the lower plate induces the reference points to rise. This rise is associated with erosion that removes the material from above that accumulates in the foreland basin open at the front. As the points approach the surface, this is the **exhumation phase**. Note that the exhumation rate is much slower than the burial rate (Fig. 1.11). From this point on, the previous nappe becomes progressively inactive. From t_{29} to the end, the anticlinal stacking of the lower plate slows and the deformation migrates out of the orogen, towards the front of the orogen (Figs. 1.10 and 1.11). From the beginning, the deformation propagates in sequence (from the inner part of the belt to the outer part). The main thrusts have a vergence (direction of thrust) opposed to the motion of the lower plate, and locally there is the development of back thrust in the antiformal stacking in the lower plate (Fig. 1.10).

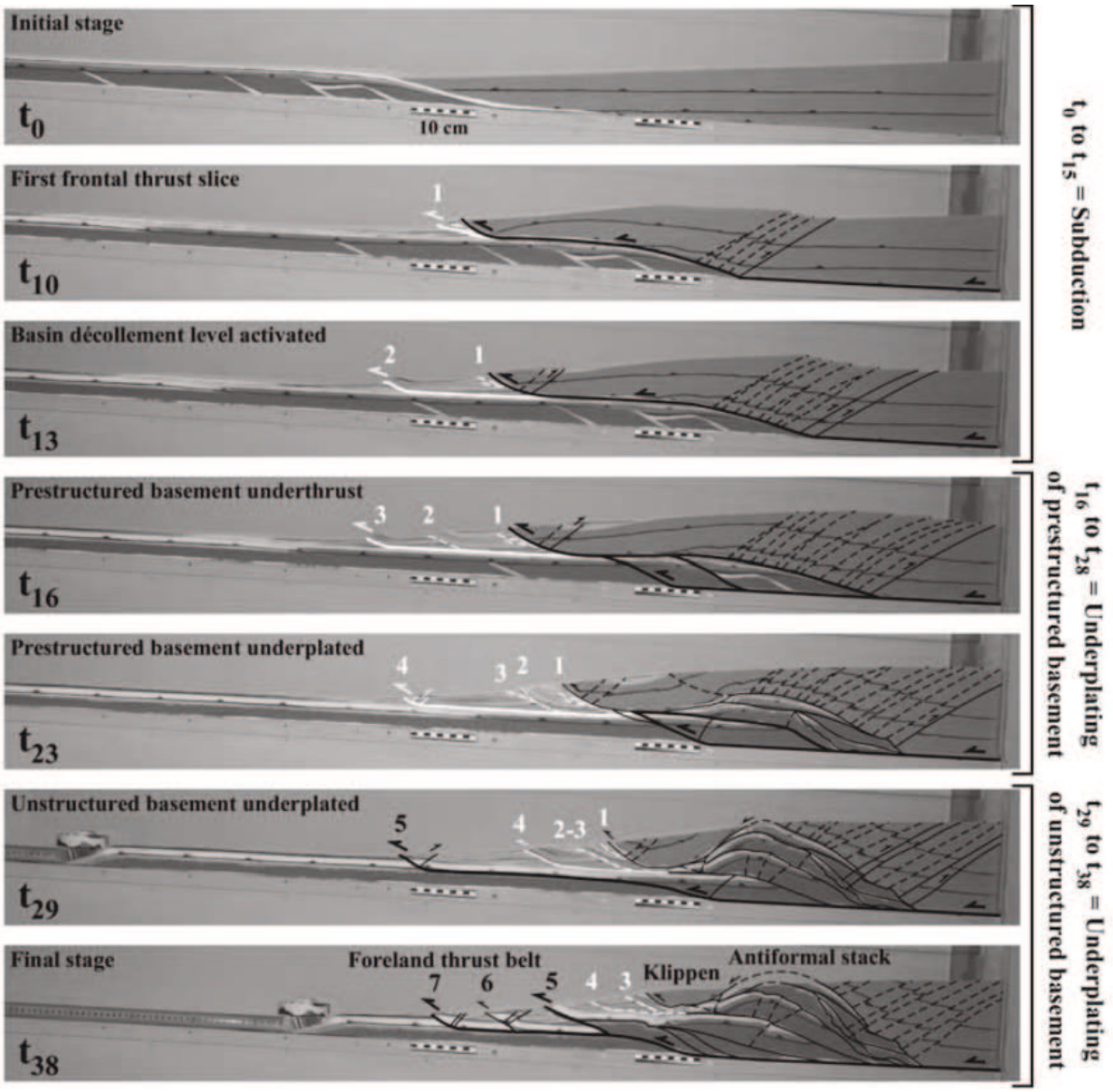

Figure 1.10. Alpine orogenic wedge analog model evolution from time increment t_0 to t_{38}. From Bonnet et al. (2007).

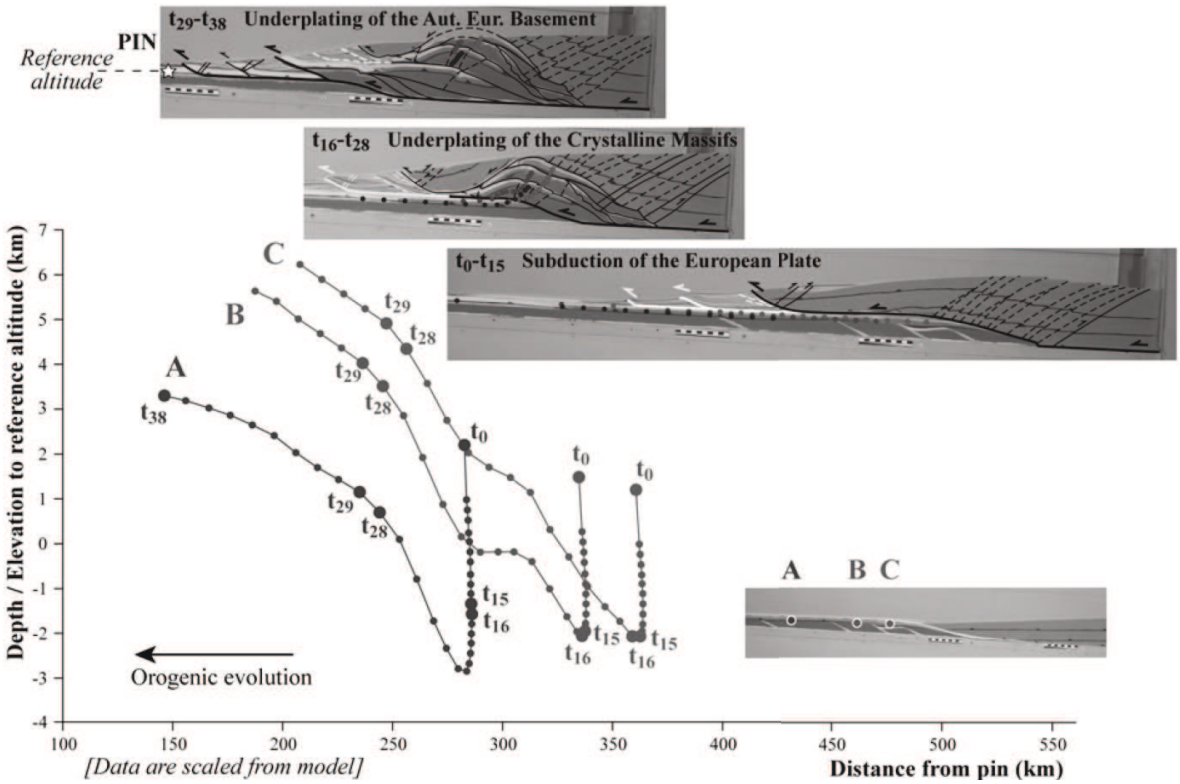

Figure 1.11. Trajectories (measured relative to a fixed reference) of three points located in the converging plate. The studied points are named in reference to the Alpine setting (picture): A = top of "Infra-Rouges" massif and B = top of "Aiguilles Rouges" massif are both situated at the top of the basement units and C = Top of "Helvetic" nappes is inside the cover. The horizontal component of the movement is measured relative to a pin located in the undeformed part of the lower plate (white star) and the vertical component to the reference altitude of the pin at the end of the experiment (dashes). Three stages of evolution appear, each one governed by a major tectonic mechanism: subduction of the lower plate, underplating of the basement units, and underplating of the homogeneous and most external part of the basement. From Bonnet et al. (2008).

From this modeling, Bonnet et al. (2007) and Bonnet et al. (2008) have shown that the evolution of the orogenic wedge is strongly related to (i) the rheology of the materials, (ii) the rate of erosion and sedimentation, and (iii) the boundary conditions of the collision. In the case of the orogenic wedge of the Alps, of the various models performed, the one that seems to have the most similarities with the Alpine orogen has a low erosion and sedimentation rate. However, a critical review may arise in the 2D configuration of the model: the orientation of the inherited faults that localize the deformation in the lower plate is ideal for inversion because the extension and shortening directions are the same.

As seen in analogous modeling, during the first steps of the collision, the material from the subducted plate is pushed down deeply, increasing the metamorphic conditions (i.e., pressure and temperature) and reaching at some point the "peak temperature" (i.e., the maximum temperature reached by the rocks). Later, with the evolution of the collision, the orogenic wedge is accreted and thickens. The erosion processes that continue at the surface remove material and exhume the crust. For this reason, rocks exposed by erosion through the upper nappe may provide information about the path that they experienced during burial and exhumation. Metamorphic petrology, combined with thermochronology, can be applied to decipher this history (Fig. 1.12, Simoes et al. (2012)). By employing different thermochronological methods with varying closure temperatures, we can gain insight into the thermal record of burial and exhumation and quantify the kinematics over time.

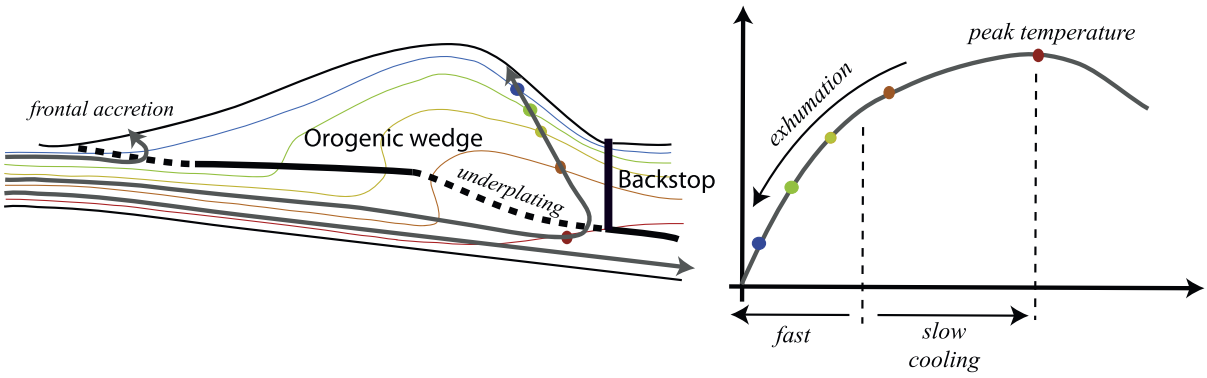

Figure 1.12. Thermal evolution of an orogenic wedge, with typical temperature–time history of exhumation in the interior of the wedge from Simoes et al. (2012). Rocks from the downgoing plate may be accreted to the wedge by frontal accretion or underplating before being exhumed.

1.5.2 Numerical simulations

According to Dal Zilio et al. (2020), numerical experiments can reproduce the evolution described in analog experiments and can be used to quantify the conditions needed to obtain a structural evolution observed in orogenic belts. They additionally allow one to explore in more detail how the mechanical properties of basal décollements and erosion may favor the

episodic migration of thrust ramps and the formation of a duplex structure. Dal Zilio et al. (2020) modeled 2D orogenic wedge (50x250km) with non-temperature-dependent viscoelasto-plastic deformation equations. There is no prestructuration of the wedge with normal faults, but weaker layers are introduced in the wedge to localize the deformation. The initial geometry of the prism is fairly simple: with a sedimentary cover resting on a rigid basement. Several parameterizations are tested, for example, with one level of décollement without erosion and two levels of décollement with erosion. The parameterization that looks more like the Alps is the one with two levels of décollement and erosion (Fig. 1.13).

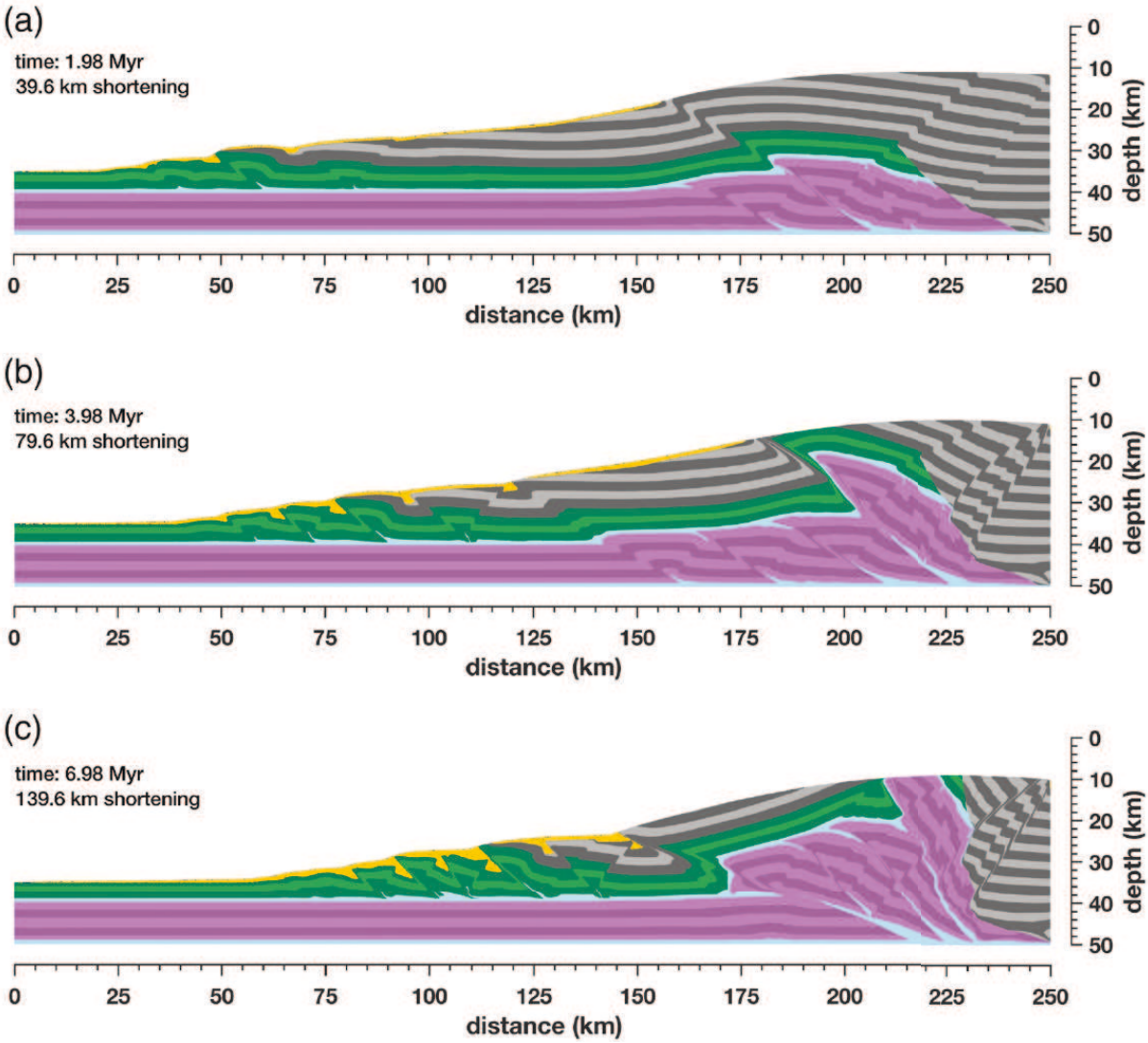

Figure 1.13. Structural evolution of viscoelastoplastic deformation model with an intermediate décollement weaker than the basal one and erosion (Model–M5). The model shows the development of midcrustal ramps, a duplex structure, and out-of-sequence thrusting (Dal Zilio et al., 2020)

The results of Dal Zilio et al. (2020) suggest that it is conceivable that large levels of décollements will propagate throughout the orogenic wedge and that they are necessary for crustal thrusts to connect to them. These may be thermally activated shear zones (Mercier et al.,

2017) or levels of décollements at the contact between the crystalline basement and sedimentary cover. Similarly to Bonnet et al. (2007), the results of Dal Zilio et al. (2020) suggest that taking erosion into account in the simulation strongly influences the evolution of the wedge: erosion removes material from the inner part of the wedge, allowing the duplex accretion to thicken and also exhume the weaker later in the inner part of the prism. This duplex structure forms but does not grow in simulations without erosion. Therefore, to understand the geometry of the orogenic wedge and its evolution (and to model it), it is fundamental to know the position, number, and geometry of the weaker layers.

Numerical experiments can include the effect of heat and viscoplastic shear heating in the propagation of the deformation. Bauville and Schmalholz (2015) and Spitz et al. (2020) evaluated the mechanical parameters that control thin-skin vs. thick-skin tectonics style in nappe formation (that is, folding vs. thrusting) (Fig. 1.14). They computed simulations using (i) linear viscous, (ii) power-law viscous, and (iii) viscoelastoplastic and temperature-dependent viscosities. The simulations test different parameterizations: viscosity contrasts between cover and basement, thermal control, etc. Their overall results suggest that, in the absence of any softening mechanism, strain localization occurs along weak layers and is thus mainly controlled by the viscosity contrast between the basement (high viscosity) and the cover (low viscosity) and the initial geometry of that boundary. Flat low viscosity layers (e.g. evaporite layer or temperature softened layers) promote the transport of a large horizontal thrust nappe, while steep boundaries (that is, inherited normal fault) promote the folding of the basement and sediments (Spitz et al., 2020; Bauville and Schmalholz, 2015; Kiss et al., 2020). These models suggest that for a basement with high viscosity ($\geq$1023 Pa.s) and in the absence of any localization mechanism, shortening of a previous graben can produce basement folding and squeeze out sediments with a geometry comparable to the basement fold nappe proposed for the Morcles Nappe by Escher et al. (1988), while in the absence of graben thrust nappe with large horizontal transport such as the Wildhorn and Glarus nappes develop.

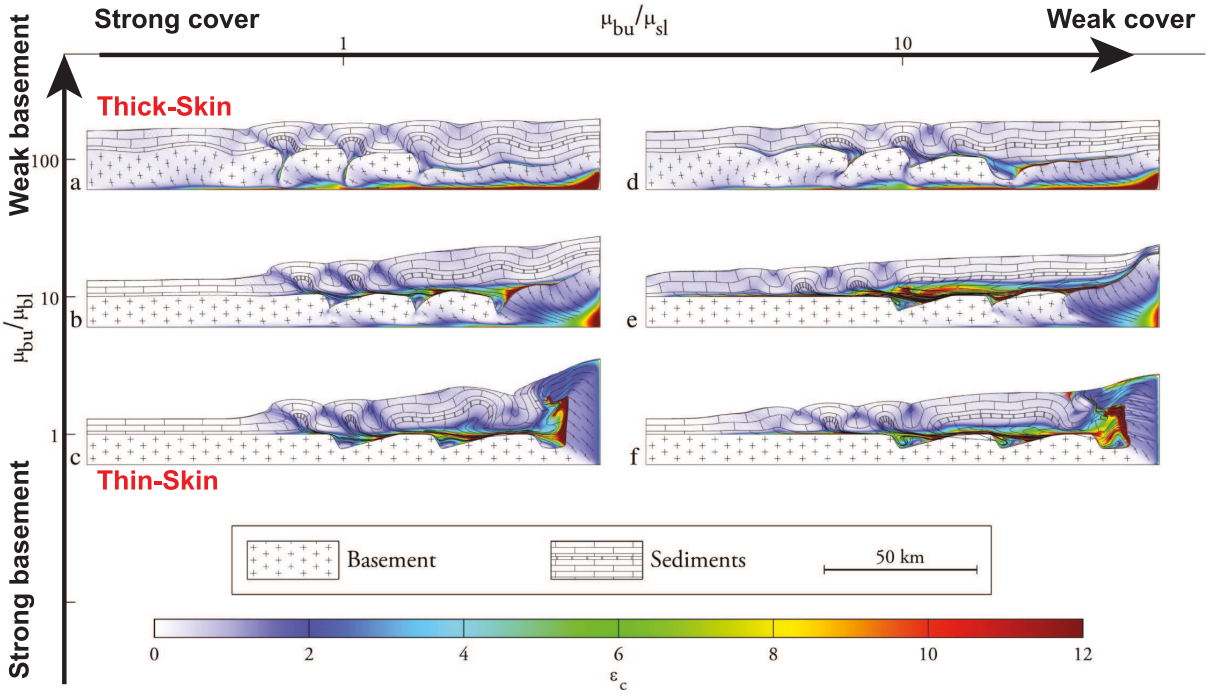

Figure 1.14. Simulations of series of thermomechanical models from Bauville and Schmalholz (2015). Simulations consider power-law viscoelastoplastic rheology and temperature-dependent viscosities including shear heating. Simulations are shown at 30% shortening

Chapter's key points

- Continental mountain belts are the result of the accretion of two colliding continents, and the mechanical Coulomb-wedge model has been proposed to explain the tectonic evolution of mountain belts.
- The propagation of the deformation can be categorized in the **thin-skin** style when the deformation is along a flat thrust, often localized in weak layers called "Décollements", and in the **thick-skin** style when the deformation is characterized by steep thrusts, often rooted in the basement. Note that flat thrusts may root in steep crustal thrusts and that thick-skin and thin-skin may be simultaneous.
- The stability of the orogenic wedge is controlled by the equilibrium between the tectonic forces and the strength of the thrust and the orogenic wedge. The evolution of these parameters is controlled by tectonic accretion and surface processes such as erosion and sedimentation.
- Analogous and numerical simulations of orogenic wedges highlighted the influence of erosion and crust prestructuration on orogen evolution.

Chapter 2

Tectonic structure of the Western Alps

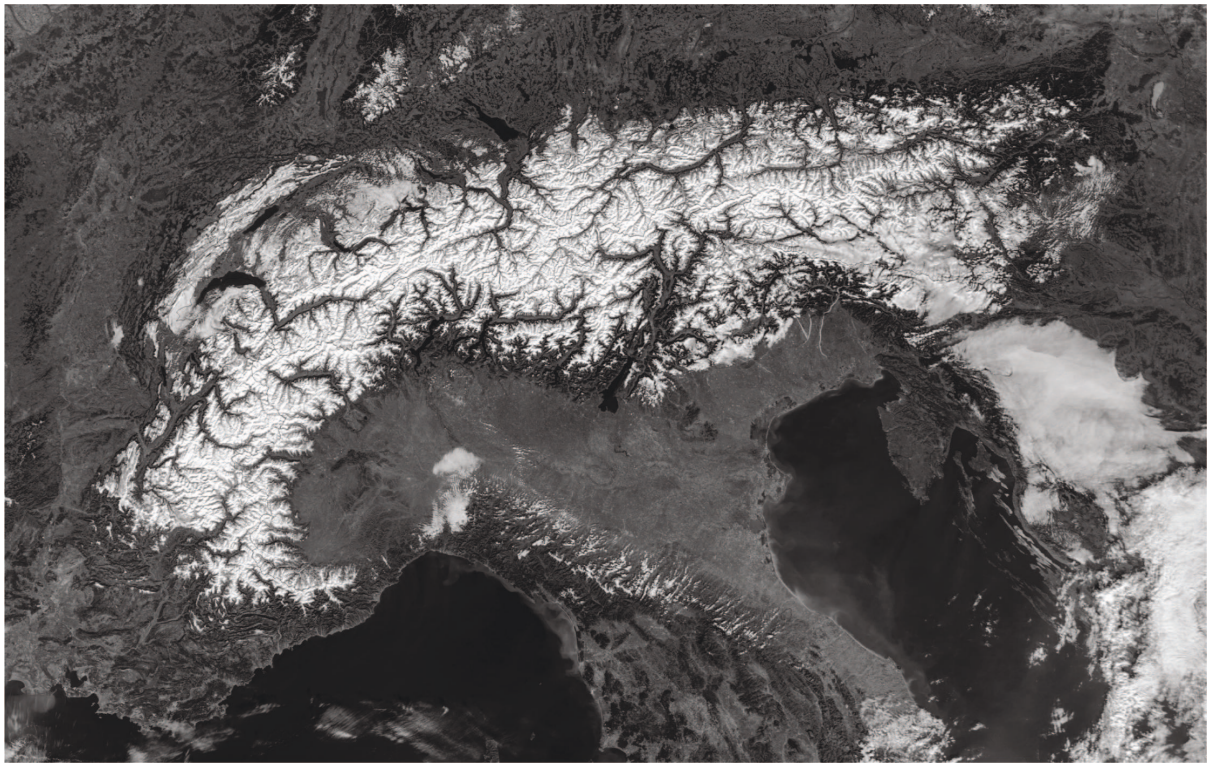

The Alpine arc, acquired from the MODIS satellite on March 4, 2002.

Abstract

The Western Alps are an accretionary wedge resulting from the Cenozoic convergence between Europe and the continental margins of Apulia. The wedge is split into two parts: the internal domain, containing rocks that have been deformed at high temperature and/or deeply subducted during the Alpine orogeny, and the external domain, where the Alpine metamorphism is limited to greenschist facies. Before the Alpine collision, the European margin inherited structure from (i) the post-Variscan extension, (ii) the Saalian compression, (iii) the Mesozoic extension, and (iv) the Eocene - Oligocene extension. Different models have been hypothesized for the Alpine collision; in the external domain, they propose that the collision began in the Eocene with the Penninic thrust system, which thrusts the internal part on top of the external one. Later, the deformation migrated towards the East in the External Crystalline Massifs. In the case of the Mont-Blanc massif, numerous deformation models have been proposed, based on different interpretations of field observation and data, and the sequence, timing, style, and amount of deformation in this massif remains unclear.

Résumé

Les Alpes occidentales sont considérées comme un prisme orogénique résultant de la convergence entre l'Europe et la marge continentales Apulienne au Cénozoïque. Le prisme est divisé en deux parties : d'un côté le domaine interne, incluant des roches déformées à haute température profondément enfouies pendant l'orogenèse alpine, et de l'autre le domaine externe, où le métamorphisme alpin est resté limité au faciès schistes verts. Avant la collision alpine, la marge européenne a hérité de la préstructuration: (i) de l'extension post-varisque, (ii) de la compression saalienne, (iii) de l'extension mésozoïque et (iv) de l'extension éocène-oligocène. À partir de là, différents modèles ont été proposés pour expliquer la séquence de déformation pendant la collision alpine ; dans le domaine externe, la collision aurait commencé à l'Éocène avec le chevauchement Pennique, qui a chevauché la partie interne du prisme sur la partie externe. Ensuite, la déformation a migré vers le nord-est dans les massifs cristallins externes et les nappes subalpines et Helvetiques. Dans le cas du massif du Mont-Blanc, de nombreux modèles de déformation ont été proposés, basés sur différentes interprétations des observations et des données de terrain. Finalement, la séquence, la chronologie, le style et l'ampleur de la déformation dans ce massif restent mal compris.

2.1 Introduction

For two centuries, the European Alps have been a natural laboratory for studying the deformation of the continental lithosphere during mountain building. Since the early studies, a constant question has been to evaluate the importance of vertical versus horizontal displacements in the construction of reliefs. Although the occurrence of large thrust sheets, as initially proposed from field observations (e.g., Bertrand, 1881; Argan, 1916), is now well explained in the context of plate tectonics, controversies still arise regarding the precise geometry, amount, and timing of major thrust during the orogeny.

2.2 Deep structure of the Western Alps

Starting from a broad perspective, during the 1980s, huge geophysical projects have been conducted to reveal the deep structure of the Western Alps (e.g., Mugnier et al., 1990; Nicolas et al., 1990; Paul et al., 2022; Malusà et al., 2021). Using the interpretation of the tomographic profile from Paul et al. (2022) and Malusà et al. (2021) and including the previous work of the past seismic profiles of the ECORS-CROP experiment (e.g., Mugnier et al., 1990; Nicolas et al., 1990), the deep structure of the Western Alps can be inferred: The vertical seismic reflection profile of ECORS-CROP (Fig. 2.1) successfully observed the lower SE-dipping European crust, the frontal Pennine thrust, the upper Adriatic mantle under the gravity anomaly of Ivrea and the Po Basin fill (Fig. 2.1). However, the European Moho was not constrained under the Alpine subduction wedge.

The recent work of Paul et al. (2022) and Malusà et al. (2021) on the CIFALPS experiment explores the structures and physical properties of the crust. The upper 20-25 km of the European lower plate consists mainly of granitic crust and associated sedimentary cover. Below the Jura fold and the thrust belt, the Moho discontinuity is located at about 25-35 km. Further east, below the external crystalline massif, a "Moho step" is imaged, with a depth that abruptly reaches 40-45 km below the Gran Paradiso massif (Fig. 2.2, Paul et al. (2022)). The interpretation of such a "Moho step" remains unclear. The authors suggest that it could correspond to a Variscan inheritance because it is parallel to the eastern Variscan shear zone (EVSZ), which is recognized as a major lithospheric fault, active between 320 and 250 Ma (Guillot et al., 2009). Further east, on the Adriatic plate, the Moho is dipping eastward and is located much shallower, even close to the Earth's surface near Ivrea. In the Bouguer anomaly profile (Zahorec et al., 2021), the higher density of mantle rocks near the surface, together with amphibolites of the Sesia-Lanzo unit and the lower crustal block of the Ivrea-Verbano zone (Scarponi et al., 2020), induces a strong and narrow Bouguer anomaly known as the "Ivrea Gravity Anomaly" (IGA) (Fig. 2.2, Paul et al. (2022). Geophysical investigation of the deep structure of the Alps also

emphasizes geometric variations from north to south in the geometry of continental subduction (Paul et al., 2022): The Moho is shallower in the north and dips quickly with an abrupt step, whereas in the south the Moho dips more regularly. As a consequence, the dip angle of the subduction differs from north to south, and the subduction wedge is thicker in the Southern Alps than in the Northern Alps.

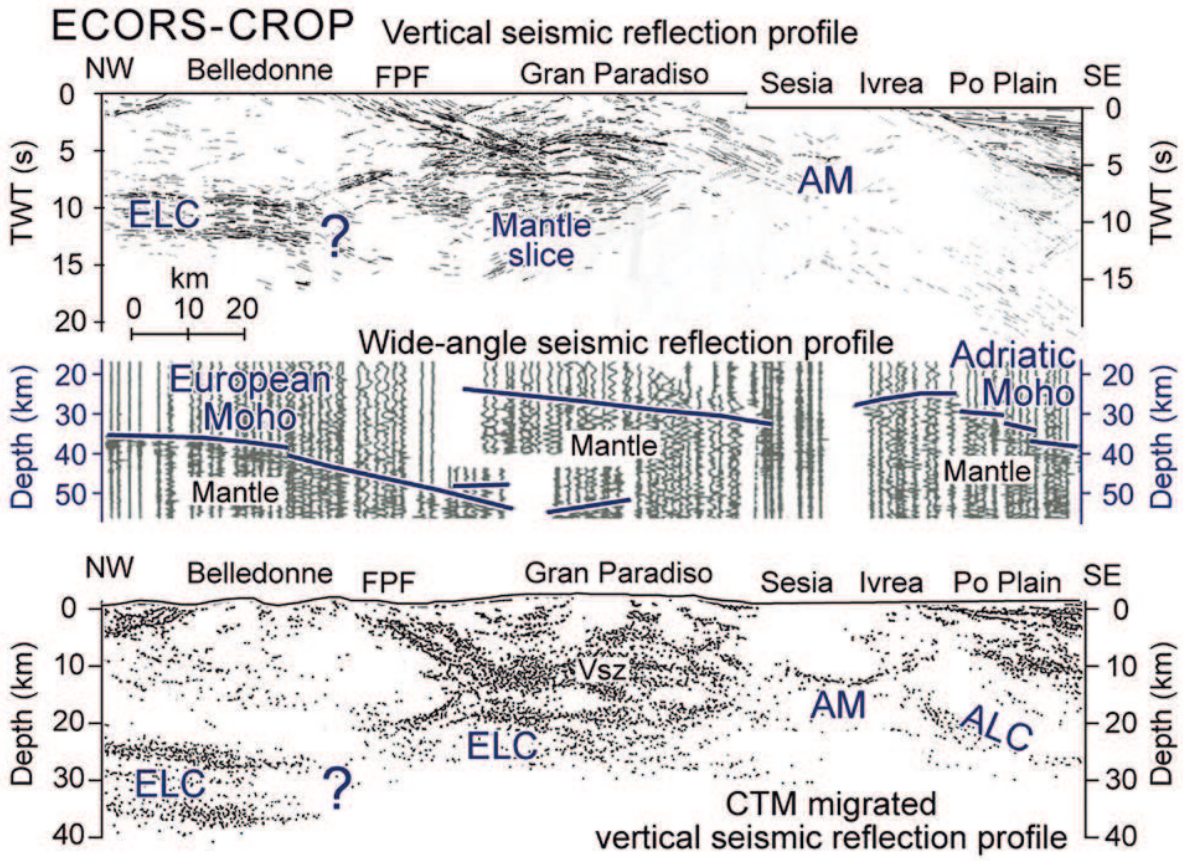

Figure 2.1. Crustal structure of the northern Western Alps as imaged by the the ECORS-CROP project. Compilation of and legend from Malusà et al. (2021). a) Line drawing of the ECORS-CROP vertical seismic reflection profile (TWT = two-way travel time). The European lower crust (ELC) beneath the European foreland and the top of the Adriatic mantle (AM) beneath the Ivrea zone are clearly imaged, as well as the SE-dipping Frontal Pennine Fault (FPF) and the Po Plain basin fill. To the east of the FPF, no European Moho is imaged beneath the Alpine subduction wedge. b) ECORS-CROP wide-angle reflection seismic profile (same location as profile in "a") and inferred Moho-like reflectors (thick blue lines, after Thouvenot et al. (1990). Note the reflector with Moho characteristics imaged beneath the Gran Paradiso at about 25–35 km depth, and the European Moho imaged farther west beneath the frontal part of the Alpine metamorphic wedge. c) Migrated ECORS-CROP seismic reflection profile based on the common tangent method (CTM, after Thouvenot et al. (1996)) as reinterpreted by Schmid and Kissling (2000): the reflectors at about 25–35 km depth beneath the Gran Paradiso dome would not mark the top of a mantle slice, as proposed by Nicolas et al. (1990), but the interface between upper and lower European crust; the reflectors located at 10–15 km depth beneath the Gran Paradiso would mark the Valais suture zone (Vsz). ALC = top of the Adriatic lower crust beneath the Po Plain.

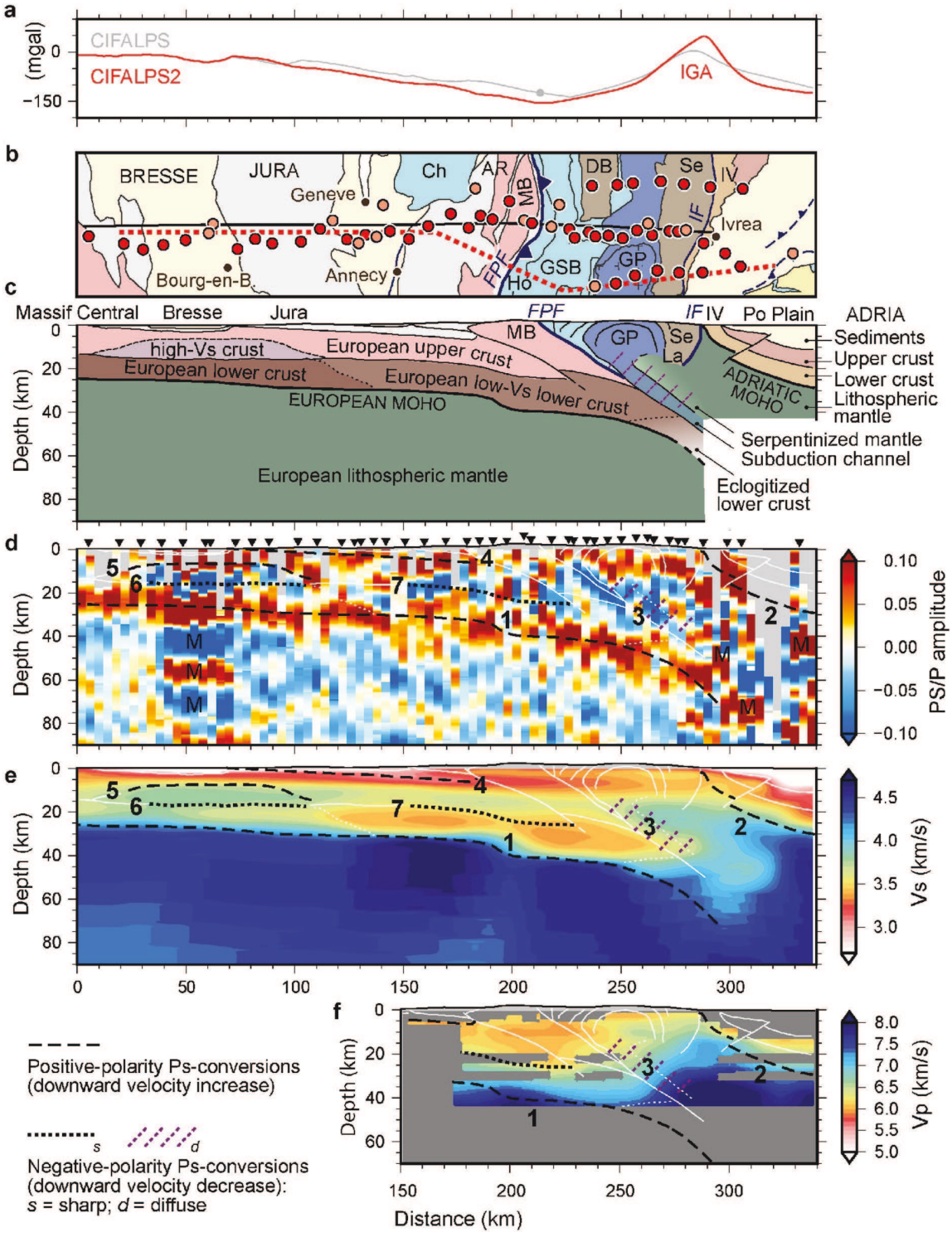

Figure 2.2. Depth sections along the CIFALPS2 profile across the northern Western Alps. a. Bouguer anomaly from the gravity database of Zahorec et al. (2021) (in red); IGA: Ivrea gravity anomaly. The Bouguer anomaly along the CIFALPS profile is shown for comparison; b. Geological map around the main profile; c. Interpretive geologic cross-section; d. CCP stacked section for teleseismic earthquakes of 0-100 back-azimuth; e: Vs section from Nouibat et al. (2021) used for time-to-depth migration of the CCP stack (Vp/Vs = 1.8); f. Vp section from the local earthquake tomography of Solarino et al. (2018). Note the consistency between interfaces identified by independent methods in (d) and (e). Figure and legend from Paul et al. (2022).

2.3 Tectonic units

The Western Alps are described as an accretion wedge resulting from the Cenozoic convergence between Europe and the continental margin of Apulia. The anterior subduction of the ocean started during the mid-Cretaceous and led to the collision in the Paleogene. The collision wedge is divided into units that have historically been defined from different paleogeographic domains of sedimentation, mostly based on the Mesozoic series. From these reconstructions, we can first define, from east to west: the sedimentary cover deposited on the continental Adriatic margin, defined as the *Austroalpine* or *South-alpine* cover, and the sediments deposited in the marine basin between the continental European and Adriatic margins, described as the *Penninic* cover (equivalent to the *Briançonnais* in France) (Fig. 2.3). These two domains constitute the internal part of the Alpine belt. The corresponding basement of the internal domain contains ophiolites inherited from the suture and rocks that have been deformed at high temperature and/or deeply subducted during the Alpine orogeny (e.g., Chopin et al., 1987) (Fig. 2.4). The continental European margin starts west of the Penninic thrust and defines the external part of the belt, constituted by the sedimentary cover belonging to the European margin, and refers to the Helvetic cover (equivalent to the *Dauphinois* in France). In the basement of the external domain, the Alpine metamorphism is limited to green-schist facies (e.g., Bousquet et al., 2004; Bousquet et al., 2012) (Fig. 2.4).

2.3.1 The External domain

The external domain exposes the basement ridges, the External Crystalline Massifs (ECM), and their folded sedimentary cover (Fig. 2.3). The basement consists of Variscan (>300 Ma) metamorphic gneisses, granites, and sedimentary rocks from the Carboniferous / Permian. The overlying sedimentary cover spans in age from the Triassic to the Miocene. The external crystalline massifs straddle for 330 km along the belt. From north to south, they have the geographical denomination of Aar, Mont-Blanc, Aiguilles Rouges, Grand-Châtelard, Belledonne, Ecrins, and Argentera (Fig. 2.5). The structure of the External Crystalline massifs is often described as paleo-horst, with their present-day geometry controlled by large Mesozoic normal faults, parallel to the thrusts, and that have been inverted in the Cenozoic during alpine deformations (e.g., Lemoine and Tricart, 1986; Bellahsen et al., 2012; Bellahsen et al., 2014; Boutoux et al., 2014). This hypothesis is mainly based on field observations in the Oisans - Ecrins massif, where the inherited normal faults are well preserved. Previous researchers proposed that external crystalline massif deformation is mainly thick-skinned, building anticline cores that expel Mesozoic cover from grabens (e.g., Ramsay, 1981; Escher et al., 1993). This hypothesis is mainly based on the Morcles nappe and the Mont-Blanc massif. From the results of the seismic profiles, others have suggested that the external crystalline massifs are crustal

culminations above thrust ramps (e.g., Lacassin et al., 1990; Menard and Thouvenot, 1987; Pfiffner et al., 1997). The sedimentary cover is folded and locally forms the Helvetic nappes, whose extent, geometry, and timing are still discussed.

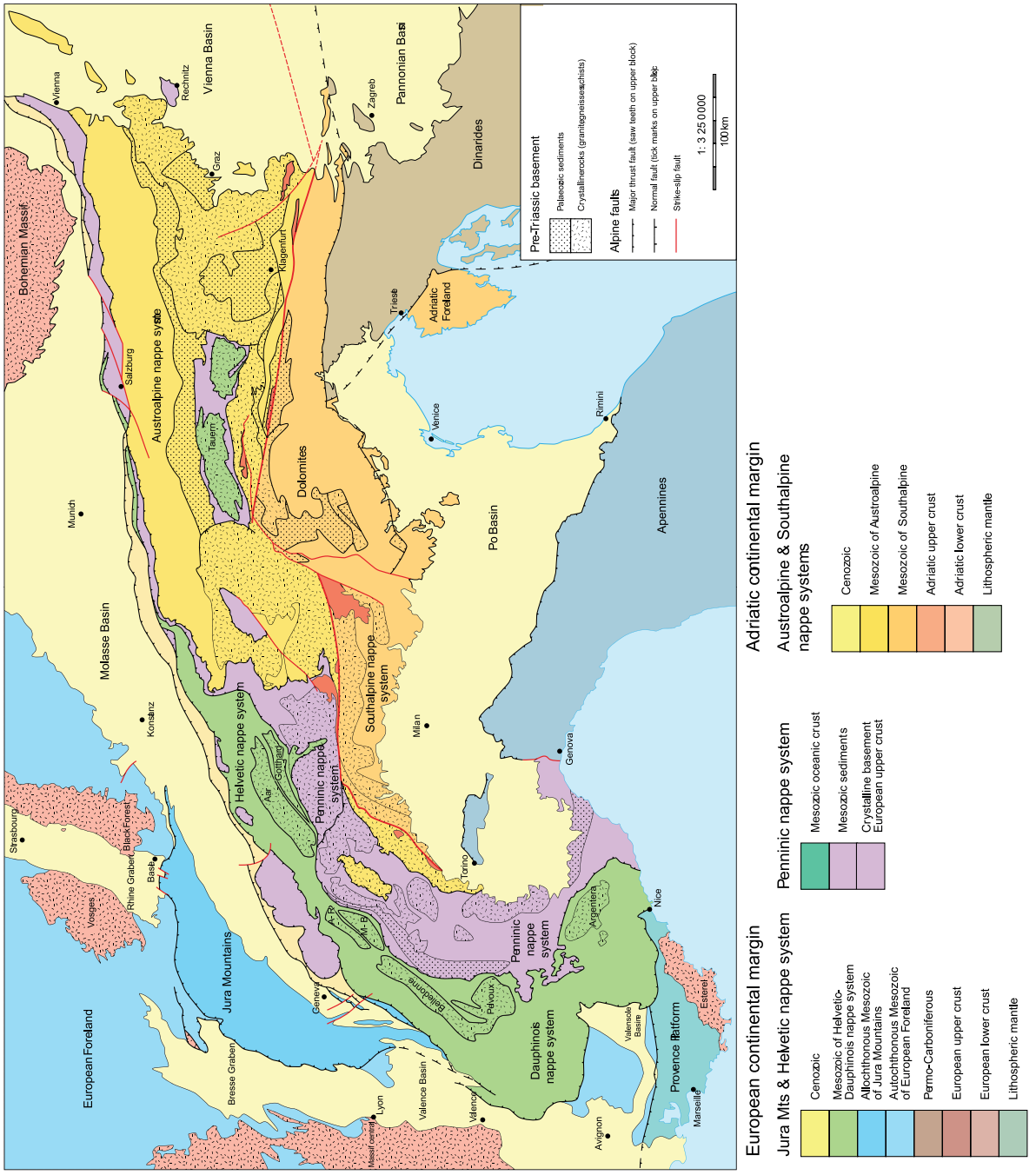

Figure 2.3. Tectonic map of the Alps. The Jura Mountains and Dauphinois–Helvetic nappe systems are part of the European continental margin, and the Austroalpine and Southalpine nappe systems represent the Adriatic margin. The Penninic nappe system in between is derived from the Valais basin, the Briançon microcontinent, and the Penninic Ocean. From Pfiffner (2014).

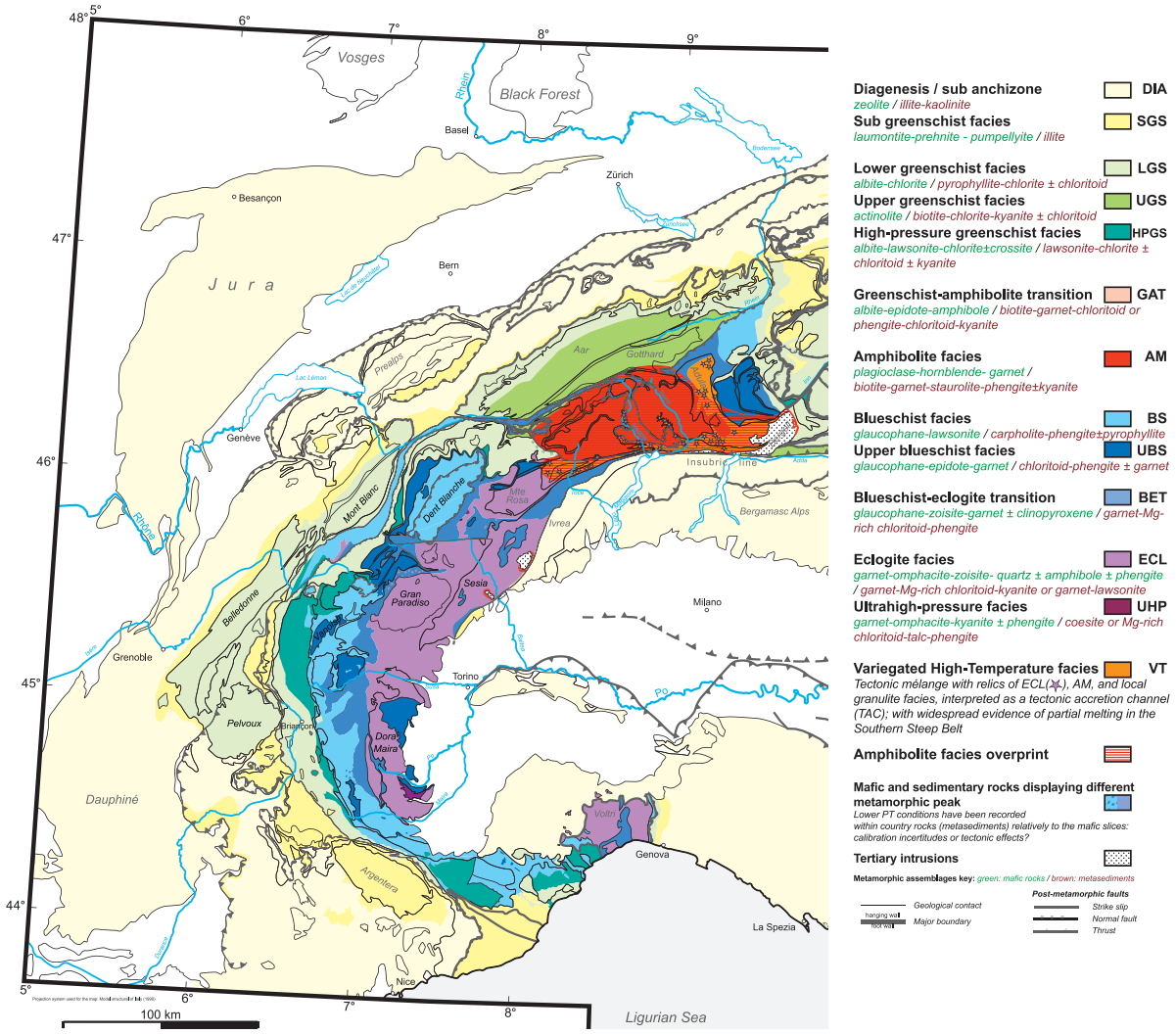

Figure 2.4. Metamorphic structure of the Western Alps. Modified from (Bousquet et al., 2012).

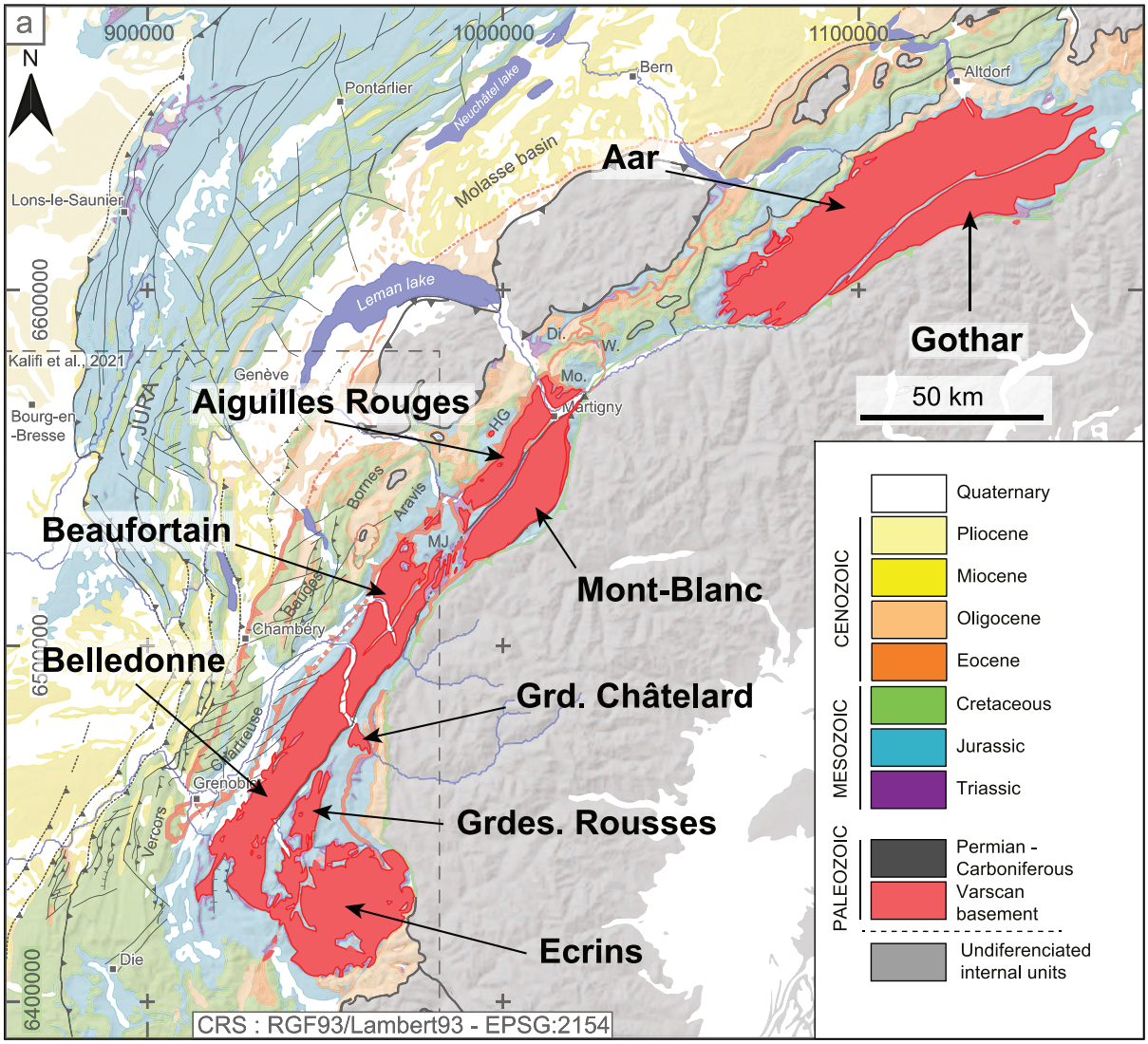

Figure 2.5. Structural map of the External Crystalline massifs (ECM) of the Western Alps. ECMs are highlighted in red: from north to south: the Aar and Gotthard massifs, the Mont-Blanc and Aiguilles Rouges, the Beaufortain massif, The Belledonne, Grandes Rousses and Grand Châtelard massif, and finally the Ecrins massif.

2.3.2 Helvetic Nappe system

The sediments deposited on the European margin during the Mesozoic are referred to as belonging to the Helvetic domain (or the Dauphinois domain). During the continental collision, this domain was affected by numerous nappe thrusts. Some authors consider these nappes to be the result of the inversion of inherited half-grabens (e.g., Escher et al., 1993; Ramsay, 1981). The deformation style of these nappes is debated: Some authors argue for a ductile folded basement that has deformed the cover in a thick-skin tectonic style (Ramsay, 1981; Escher et al., 1993; Epard, 1990; Burkhard and Sommaruga, 1998). However, others argue that the emplacement of the Helvetic nappe is dominated by thin-skin tectonics, with a significant motion of the sedimentary cover above its basement and with a maximum displacement greater

than 20 km (Pfiffner, 2014; Collet and Paréjas, 1920; Egli and Mancktelow, 2013; Leloup et al., 2005) (Fig. 2.6). The Helvetic nappes cover the external Alps extensively, and several sub-sedimentation domains have been defined according to the Mesozoic stratigraphic series. In the Mont-Blanc area, the uppermost Helvetic nappe is the Wildhorn Nappe, which could be equivalent to the Subalpine Nappe in France (Pfiffner et al., 2011) (see Chapter 4). With the Diablerets Nappe below, these two nappes are considered to root under the Penninic thrust, on the eastern side of the External Crystalline Massifs (Fig. 2.3). Below, the well-known Morlces nappe is suggested to root on the Western side of Mont-Blanc, in the Angle fault and the Chamonix synclinorium (Ramsay, 1981; Escher et al., 1993; Epard, 1990; Epard, 1986).

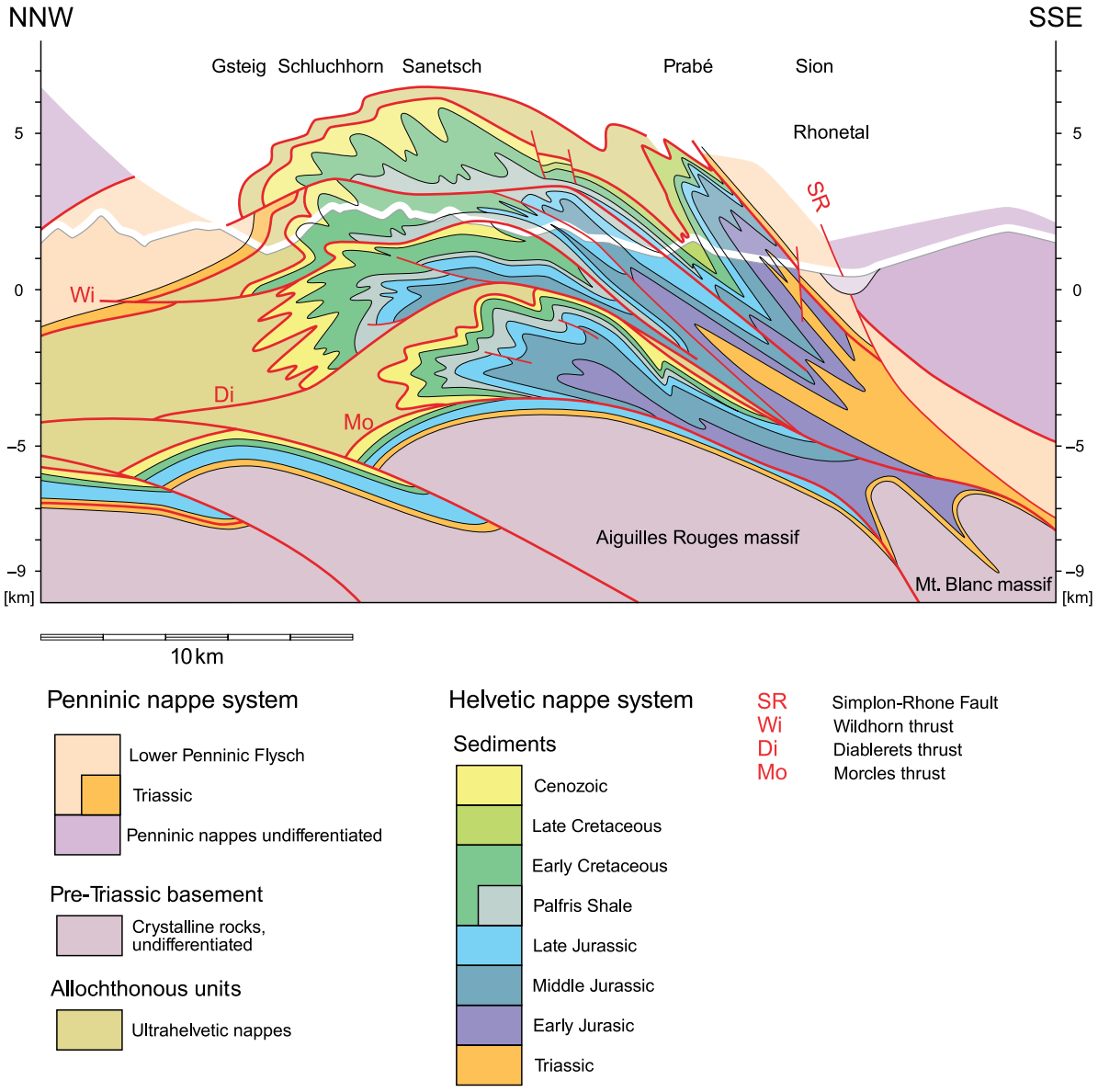

Figure 2.6. Geological cross-section through the Helvetic nappes system. The structure is characterized by the stacking of nappes, limited by thrusts at their base and large recumbent folds (Pfiffner, 2014)

2.4 Dynamic evolution of the collision

In this section, we will review the evolution of the Alps from the prestructuration of the European lithosphere due to anterior orogens and extensions to the alpine collision.

2.4.1 Inherited structures

As stated in Chapter 1, inherited structures can play a major role in the localization of deformation and the structure of the belt. In this part, we list the anterior deformation phases that have structured the European lithosphere.

2.4.1.1 Post-Variscan extension

After the Variscan orogeny, two phases of extension affected the European crust. The first started during the early Carboniferous and is characterized by a NW-SE stretching direction in the French Massif Central (e.g., Faure, 1995). The second extension phase occurred during the late Carboniferous-Early Permian with an opening direction of NNE-SSW and is believed to be related to post-orogenic collapse reflecting the over-thickened crust (e.g., Malavieille et al., 1990; Gardien et al., 2022). These extensions are associated with large transpressional systems (e.g., Rolland et al., 2009; Trap et al., 2016; Vanardois et al., 2022). These extensions are well preserved in Europe and the Western Alps, with Carboniferous / Permian basins (e.g., Alès, Saint-Etienne, Salvan Dorénaz). It is estimated that the opening started at 308 ± 3 Ma (Moscovian, Carboniferous) with coarse detrital deposits and lasted until at least 295 ± 3 Ma (Asselian, Permian) (Capuzzo and Bussy, 2000; Capuzzo et al., 2003; Capuzzo and Wetzel, 2004). Further west in the European plate, the Saint-Etienne leucogranite emplacement, on the footwall of the Pilat extensional shear zone, has been dated at 303 ± 2 Ma (zircon U–Pb) (Gardien et al., 2022), and the end of the extension is estimated to end at 298.5 ± 1.5 Ma ($^{40}Ar/^{39}Ar$ on mica) (Gardien et al., 2022).

2.4.1.2 Saalian compression phase

Introduced by Stille (1940) in North America and later documented in France by Pruvost (1956), this phase was located between the Cisuralian and Guadalupian during the Permian. In France, the Saalian orogen is documented as a stratigraphic unconformity of the Permian on top of the Carboniferous Pruvost (1956). In the Alps, Pilloud (1991) observed deformations in the Salvan-Dorénaz Carboniferous basin (Switzerland, Valais) that he attributed to a deformation phase anterior to the Alpine collision. He related these deformations to the Saalian (Permian) deformation phase. Later Pairis et al. (1992), attributed the deformation of the Carboniferous sediments in the Pormenaz area (Aiguilles Rouges) to this Saalian phase. Except for these

works, Saalian deformations are barely documented in France and the Alps and may have played an important role in the structure of the Alps.

2.4.1.3 Mesozoic extension

From the late Permian to the early Triassic period, the reliefs flattened during a peneplanation and constituted the platform where Mesozoic sedimentation would occur. During the Mesozoic, the opening of the Tethys Ocean began, in relation to the breakup of Pangea (e.g., Dumont et al., 2008; Schettino and Turco, 2009). From the Triassic period, the European continent was submerged by a shallow lagoon, depositing the so-called Buntsandstein facies. This deposition is characterized by shallow subaquatic marine sandstones, alternated with emergence phases, pointing to a micro-tidal environment (Stingl, 1989). In the Aiguilles Rouges massif, this formation shows ripple marks and reptilian tracks (Demathieu and Weidmann, 1982; Avanzini and Cavin, 2009) attributed to the Lower to Middle Triassic. Above, the series comprises white dolostones, cargneules, and evaporites. Starting from the Triassic, the extension is NW-SE to N-S directed (Dumont et al., 2008) (Fig. 2.8). The rifting progressively intensifies during the Lower Jurassic (Le Breton et al., 2017) (Figs. 2.8 and 2.9) leading to the formation of the Helvetic / Dauphinois basin and the deposition of an alternance of marls and limestones(Lemoine and Tricart, 1986). During this period, the sedimentation rate is very high due to the strong subsidence of the passive margin (Fig. 2.7). Later, the sedimentation is enriched in carbonate, with the development of massive Tithonian limestones in the Upper Jurassic. The Lower Cretaceous is mainly composed of marls and dark sandy limestone and is followed by the so-called Urgonian limestones, which are made of shallow-water reef limestones. This homogeneous unit often marks the highest peaks and crests of the Subalpine Chains. The Upper Cretaceous is made of limestone and marls (Fig. 2.7).

Sediment thickness variations related to activation of normal faults have been described in the Cévènnes-Ardèche basins (Elmi, 1984). In the Alps, the deformations associated with Mesozoic rifting are mainly described in the Oisans and Ecrins massifs and are characterized by a network of normal faults that bound tilted blocks (e.g., Graciansky et al., 1989; Lemoine and Tricart, 1986; Lemoine and Trumpy, 1987; Dumont, 1988). Excluding the so-called Ornon fault in the Oisans massif, although the Jurassic extension may seem well documented in the Western Alps, *in situ* tectonic characterization and measurements of such normal faults are quite rare. From micro-tectonic measurements in the Bourg d'Oisans area, Grand (1988) estimated a change in the extension direction from N-S in the late Triassic to WNW-ESE during the Lower Jurassic. Others suggested that the main direction of extension varies from N-S to NE-SW (Lemoine and Trumpy, 1987; Dumont et al., 1984; Dumont et al., 2008). Age constraints on these faults are only based on sedimentological evidence; there is no absolute dating of such inherited normal faults in the Western Alps. In the other External Crystalline Massifs, evidence

of normal faults is less abundant; in the Chamonix valley, Boutoux et al. (2016) refers to a "Chamonix Mesozoic normal fault" bounding the west side of the Chamonix Syncline, but such a normal fault has never been characterized by tectonic field evidence.

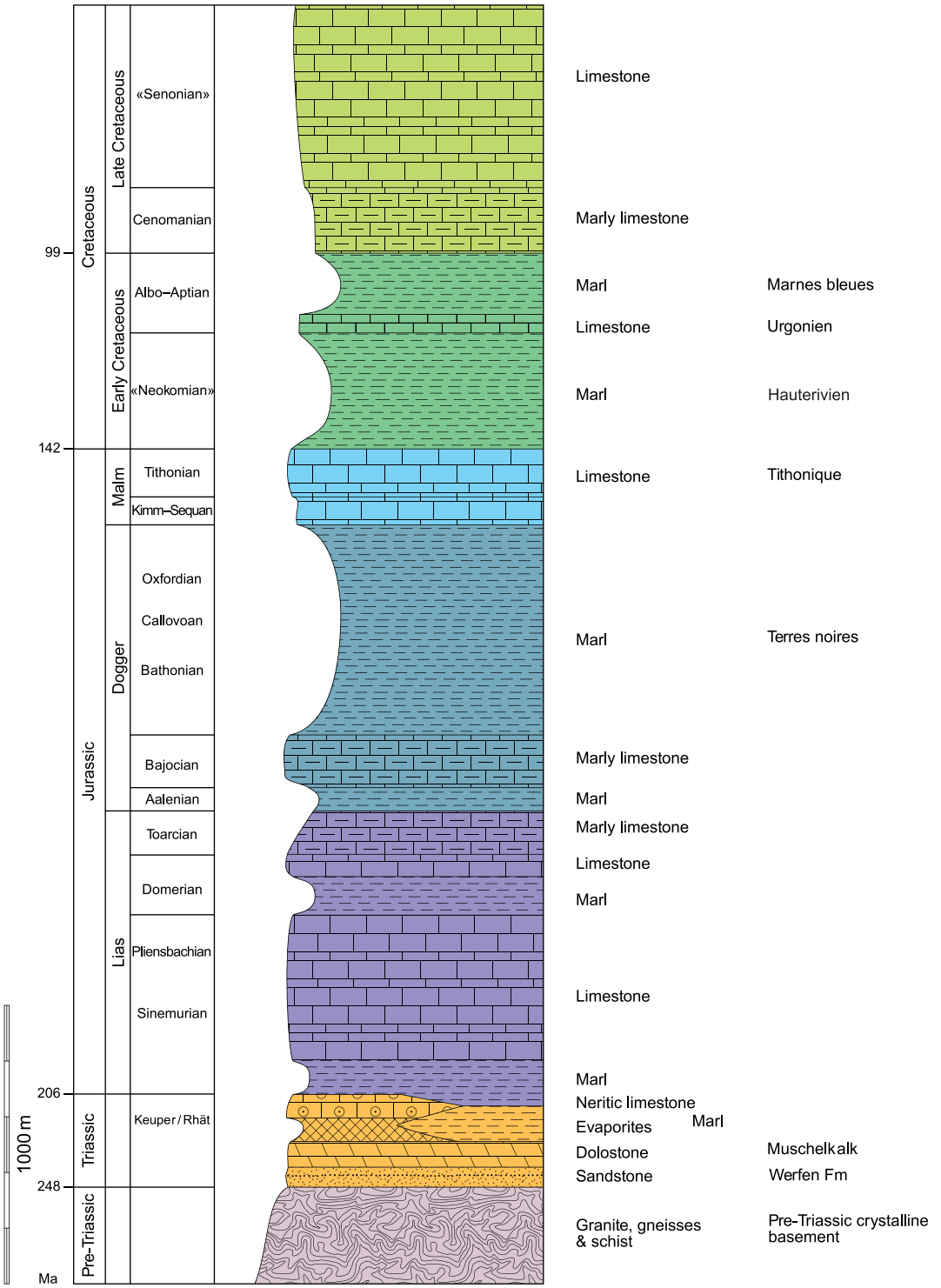

Figure 2.7. Schematic overview of the Mesozoic sedimentary sequence of the Helvetic / Dauphinois in the Western Alps (Pfiffner, 2014)

2.4.1.4 Eocene - Oligocene extension

During the Eocene to Oligocene period, an extension phase is probably related to the opening of the West European Rift and propagated southward (Dèzes et al., 2004), contemporaneously with compression in the Western Alps (Figs. 2.8 and 2.9). The first phase of extension from 35 to 23 Ma is well documented in the Provence (Merle and Michon, 2001) and corresponds to an E-W oriented extension. From 23 Ma, the second phase of the extension induced the opening of the Gulf of Lion and Liguro - Provencal basin, associated with the rotation of the Sardinia - Corsica block rotation (Ferrandini et al., 2003; Gattacceca et al., 2007). This late extension, controlled by asthenospheric flow, is suggested to account for volcanism in the Massif Central. During the Oligocene, sedimentation is dominated by lacustrine and fluviatile deposits in the basins. Before this opening phase in Western Europe, the onset of convergence of the European plate in the north and the Adriatic plate in the south began in the Cretaceous, leading to the continental collision from the Eocene (Fig. 2.8).

In the Western Alps, the syntectonic deposits are mainly composed of white nummulitic limestones whose deposition is controlled by extensive normal syndepositional faulting (Pairis and Pairis, 1975). Some of these faults are inferred to have extended perpendicular to the thrust front (trending NW-SE) (Villars et al., 1988), while other faults were parallel to the thrust front. The stratigraphic thickness of the nummulitic limestones is variable but can be up to 130 m, as documented in the Platé massif (Pairis et al., 1992).

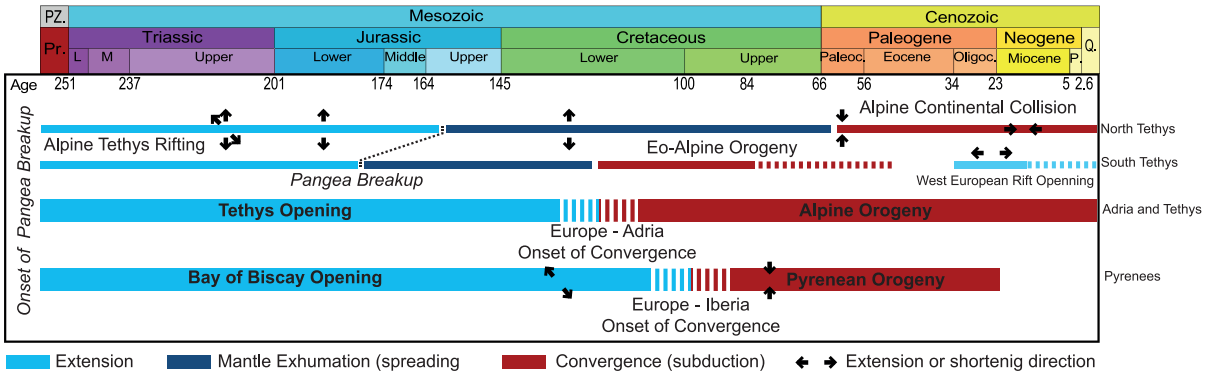

Figure 2.8. Geodynamic chart of Iberia and Adria against Europe tectonic plates. Modified from Angrand and Mouthereau (2021).

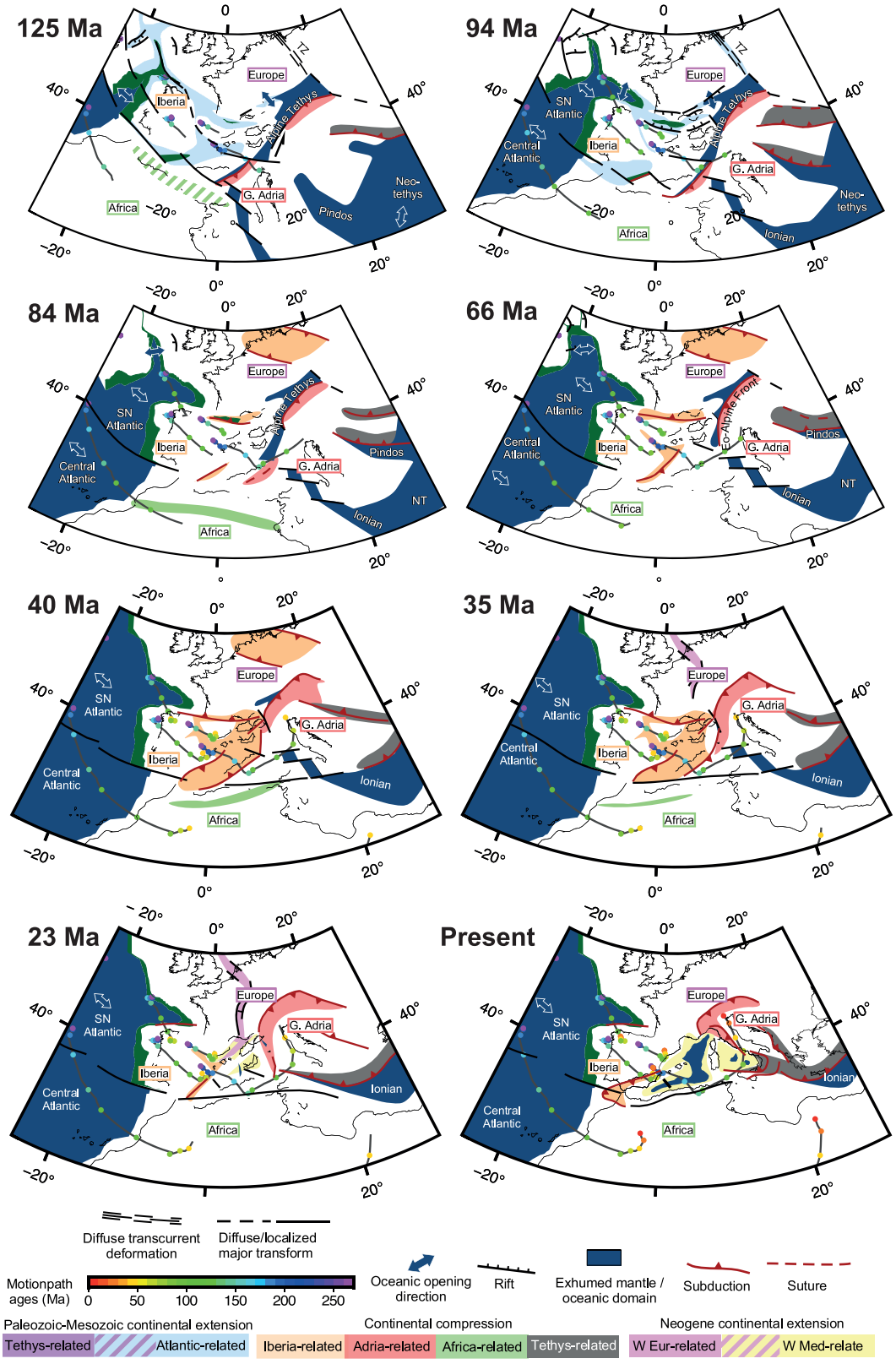

Figure 2.9. Geodynamic reconstruction of the Tethys–Atlantic area shown in orthographic projection. Modified from Angrand and Mouthereau (2021).

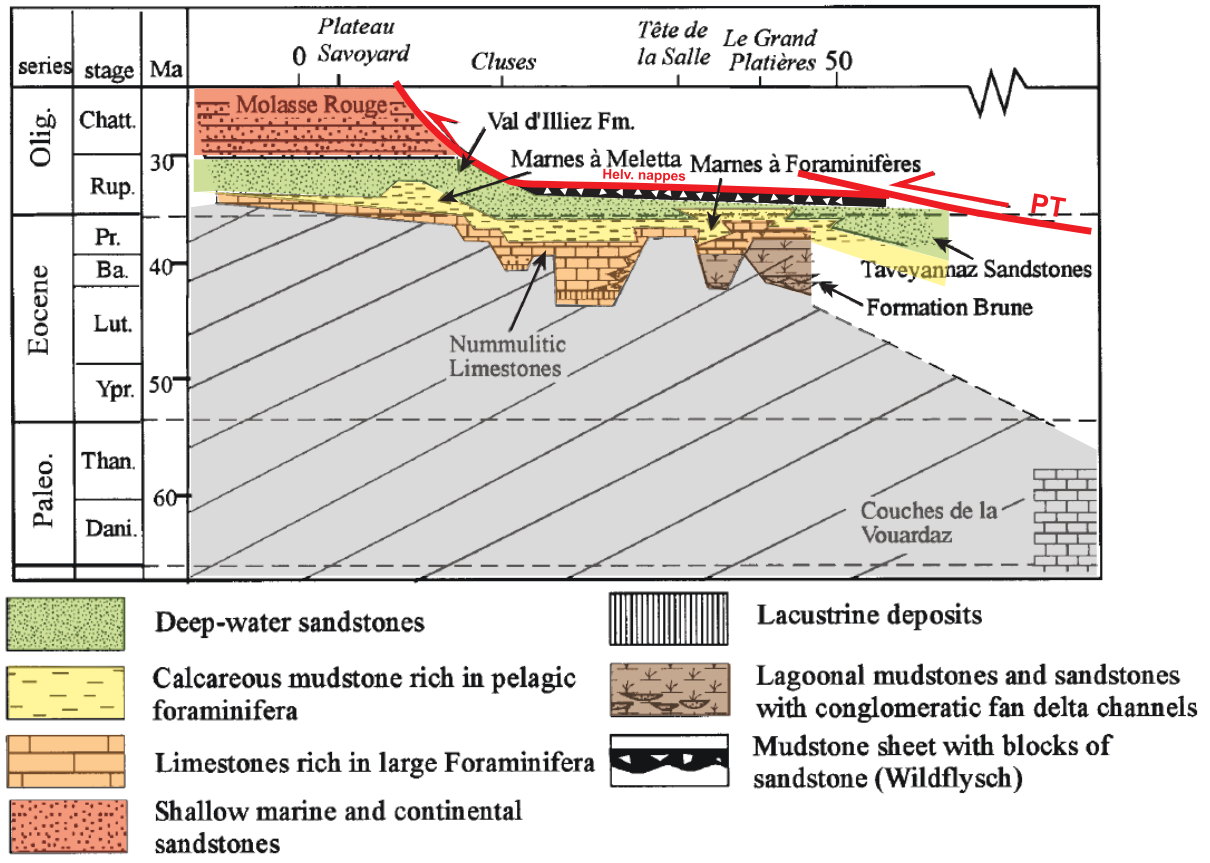

Figure 2.10. Balanced and restored cross-section of the underfilled portion of the Alpine foreland basin. Colorized from Sinclair (1997). The lower unit, which is composed of white nummulitic limestones has been deposited during the Eocene extension and normal faulting. The upper unit is composed of flyschs deposits that have been sedimented during in the flexural basin at the front of the Penninic and Helvetic thrusts systems.

2.4.2 Compression

2.4.2.1 Hypotheses of the compression sequence in the Western Alps

Several authors have proposed different evolutions of the Western Alps and External Crystalline Massifs. We will present three hypotheses from Leloup et al. (2005), Dumont et al. (2012), and Bellahsen et al. (2014), ordered by publication year.

Leloup et al. (2005) proposed a chronological reconstruction of the Miocene deformation of the Western Alps, based on structural fieldwork, thermochronology and geochronology (Fig. 2.11).

1. During the Mesozoic and until the early Eocene, the Mont-Blanc and Aiguilles Rouges were buried below the Helvetic sedimentary series.
2. From the Upper Eocene, the Valaisan series were thrust to the north along the Penninic thrust Nappes.
3. From 30 Ma to 15 Ma, thrusting took place along an Helvetic Basal Décollement (HBD), bringing the Helvetic nappes on top of the actual External Crystalline massifs. During this time, Mont-Blanc was buried under the nappes and reached its thermal peak at 400 °C and 14 to 20 km depth, while the upper part of the Aiguilles Rouges was at 9 km depth and 300 °C.
4. After 22 Ma, the initiation of the Alpine Sole thrust induced uplift and exhumation of the External Crystalline massifs.
5. From 12 Ma, the activation of the Mont-Blanc shear zone (Western side) induces relative vertical motion between the Mont-Blanc and the Aiguilles Rouges.
6. From 5 Ma, motion along the Mont-Blanc shear zone coincides with back-thrusting of the Mont-Blanc massif.
7. Before 4 Ma, the motion along the Mont-Blanc shear zone stopped.

In summary, the tectonic scenario of Leloup et al. (2005) suggests that the Helvetic nappes are emplaced above a basal thrust (Helvetic Basal Décollement) after 22 Ma later offset by a major shear zone in the Western side of the massif at 9 Ma and a back thrust after 5 Ma.

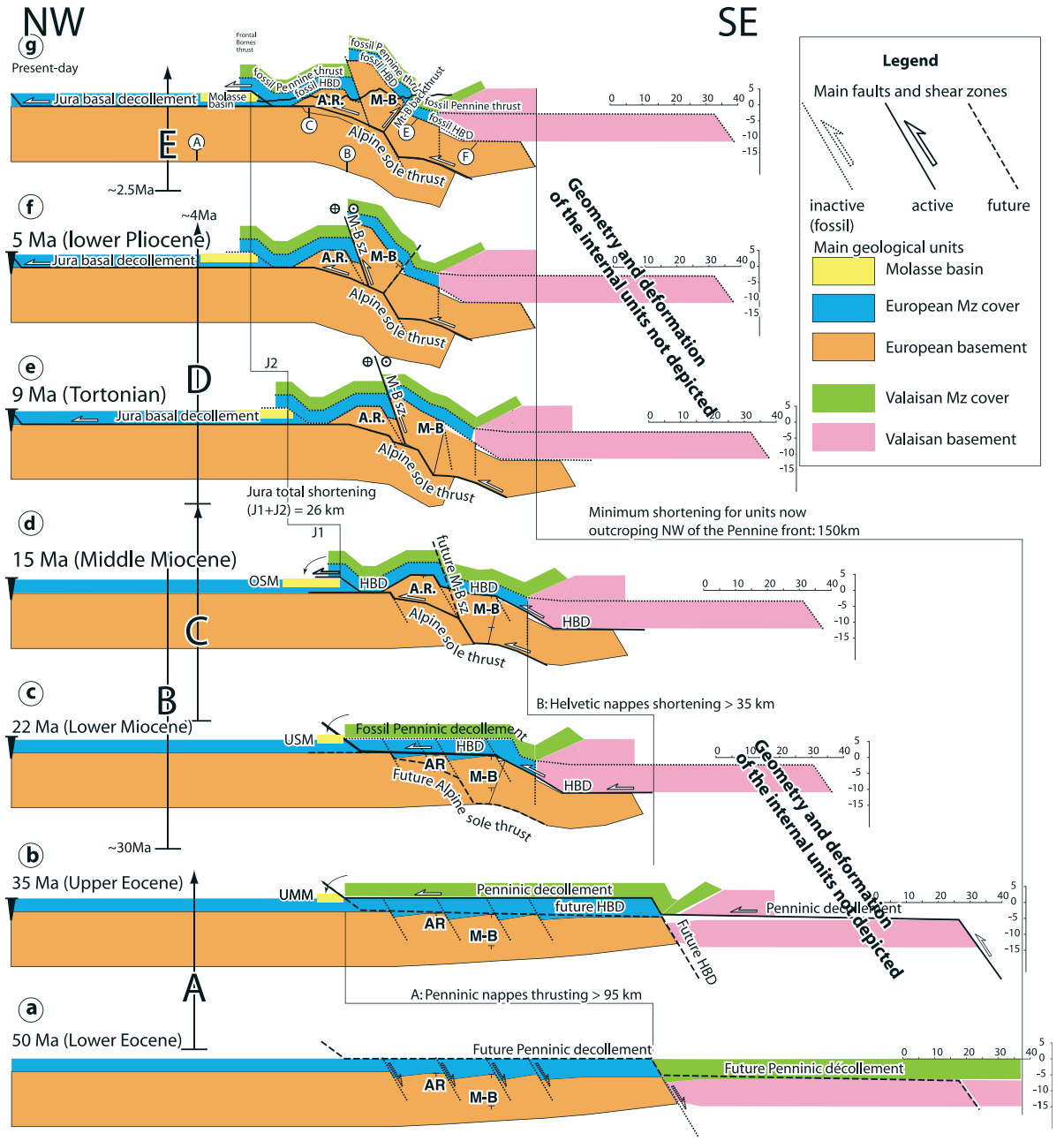

Figure 2.11. Structural evolution of the external Alps alps along an NW-SE section across the Aiguilles Rouges and Mont Blanc massifs. The structural evolution of the internal Alps, mostly occurring before 32 Ma, is not depicted. Shortening estimates in the Jura and Helvetic nappes from Affolter (2003). A to D refers to the main deformation phases in the Aiguilles Rouges and Mont Blanc massifs. The bottom line of the section does not correspond to the Moho but rather to a passive marker at the top of the layered lower crust. From Leloup et al. (2005).

This evolution has been contested by Rolland et al. (2007): the authors argue that there is no evidence for a two-phase thrust / backthrust evolution and that the Mont-Blanc deformation is not restricted to two main shear zones on each side of the massif, but also accommodated by numerous anastomosed shear zones within the massif (Gourlay, 1986; Choukroune and Gapais, 1983). Furthermore, Rolland et al. (2007) suggested that the Mont-Blanc back thrust is a complex network of southeast verging shear zones as described by (Guermani and Pennacchioni, 1998) and have dated synkinematic white micas using the $^{40}Ar/^{39}Ar$ dating technique. Their result suggests that the shear zones were active at about 16 Ma.

Rolland et al. (2007) proposed another scenario for Mont-Blanc evolution: based on the similarity of the metamorphic assemblages and age conditions to the east and west of Mont-Blanc, they suggest that the deformation was most likely synchronous on the two sides of the massif and related to a transpressive pop-up structure connected to the Rhône dextral fault system (see section 2.5) that transfers dextral motion to west verging thrusting (Hubbard and Mancktelow, 1992). From about 16 Ma, motion on the southeast verging shear zones of the Mont-Blanc began. **In summary, they suggest that the tectonic scenario of figure 2.11g should be set since 16 Ma.**

Dumont et al. (2008), Dumont et al. (2011), and Dumont et al. (2012) proposed subdivision of the Alpine collision from sedimentological and structural studies of the Écrins massif from the Priabonian to the Oligocene. They identified three major shortening episodes:

1. D1: a pre-Priabonian (34 Ma) shortening oriented north - south, supposedly linked with the Pyrenean - Provence orogeny. This event is recorded by high-angle basement thrust sealed by Priabonian sediments in the south and southwest of the Écrins massif. These pre-Priabonian compressional structures are tilted by the younger east-west shortening event.
2. D2: During the late Eocene, north-to-west convergence was recorded in the Pelvoux.
3. D3: From the early Oligocene, top-to-west intense shear occurred at the eastern edge of the Pelvoux massif and underthrusted the external domain.

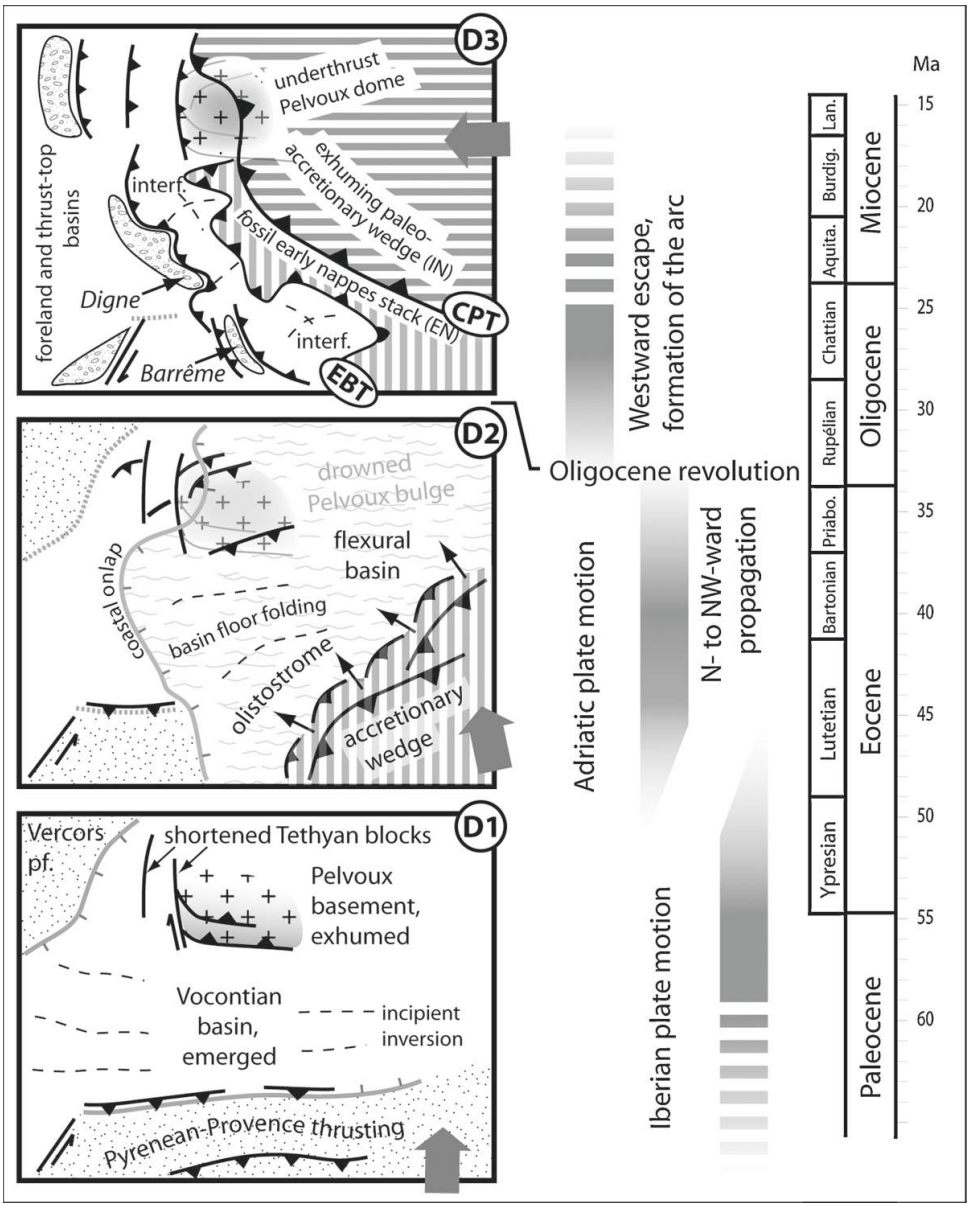

Figure 2.12. Paleogene evolution of the Alpine foreland in the southern part of the Western Alps after Dumont et al. (2012). The D1 structures and basement exhumation are sealed by Priabonian sediments to the south of the Pelvoux massif but are not dated. The required N-S shortening component is assigned to the Eocene motion of the Iberian plate whose effects are known in the Pyrenean and Provence realms. The D2 deformation is expected to occur diachronously in the foreland of the propagating accretionary wedge (vertical hatching) and follows shortly the NNW to NW ward propagation of the flexural basin. It corresponds to the continental subduction stage, and it reached the Pelvoux area around the Eocene-Oligocene boundary. The D3 collision stage overprinted completely the previous orogenic wedge, which was indented westwards by the Internal metamorphic nappes stack (horizontal hatching), giving birth to the Western Alpine arc. This overprint is shown by interference structures, deformation, and uplift of the previously emplaced, low metamorphic grade nappes (EN, vertical hatching), whose erosion fed the molasse basins together with metamorphic rocks issued from the exhuming paleo-accretionary wedge (IN).

Bellahsen et al. (2014) and Boutoux et al. (2016) proposed a reconstruction of the Miocene Western Alps evolution (Figs. 2.20 and 2.13):

1. During Mesozoic times, opening of the Chamonix basin, bounded on its Western side by a normal fault.
2. From 35 Ma, continental subduction and exhumation of the internal units.
3. From 30 Ma, the innermost Helvetic nappes (Diablerets and Wildhorn) were detached from their basement and stacked on the Mont-Blanc cover.
4. At 23 Ma, inversion of the Chamonix basin and expulsion of the sedimentary cover from the basin by a basement folding and activation of the Mont-Blanc shear zone.
5. Later, at 17 Ma, the shortening of the Aiguilles Rouges massif is associated with the deformation of subalpine chains.
6. From 11 Ma, the Jura décollement started and roots below the Aiguilles Rouges.

In summary, the tectonic scenario proposed by Boutoux et al. (2016) and Bellahsen et al. (2014) suggests that the Upper Helvetic Nappes (Wildhorn and Diablerets) are emplaced above thrusts and right after the Penninic Nappes at about 30 Ma. However, later, the Morcles nappe deformation is of a rather different style and is controlled by the Chamonix graben and the activation of the Mont-Blanc shear zone at 17 Ma.

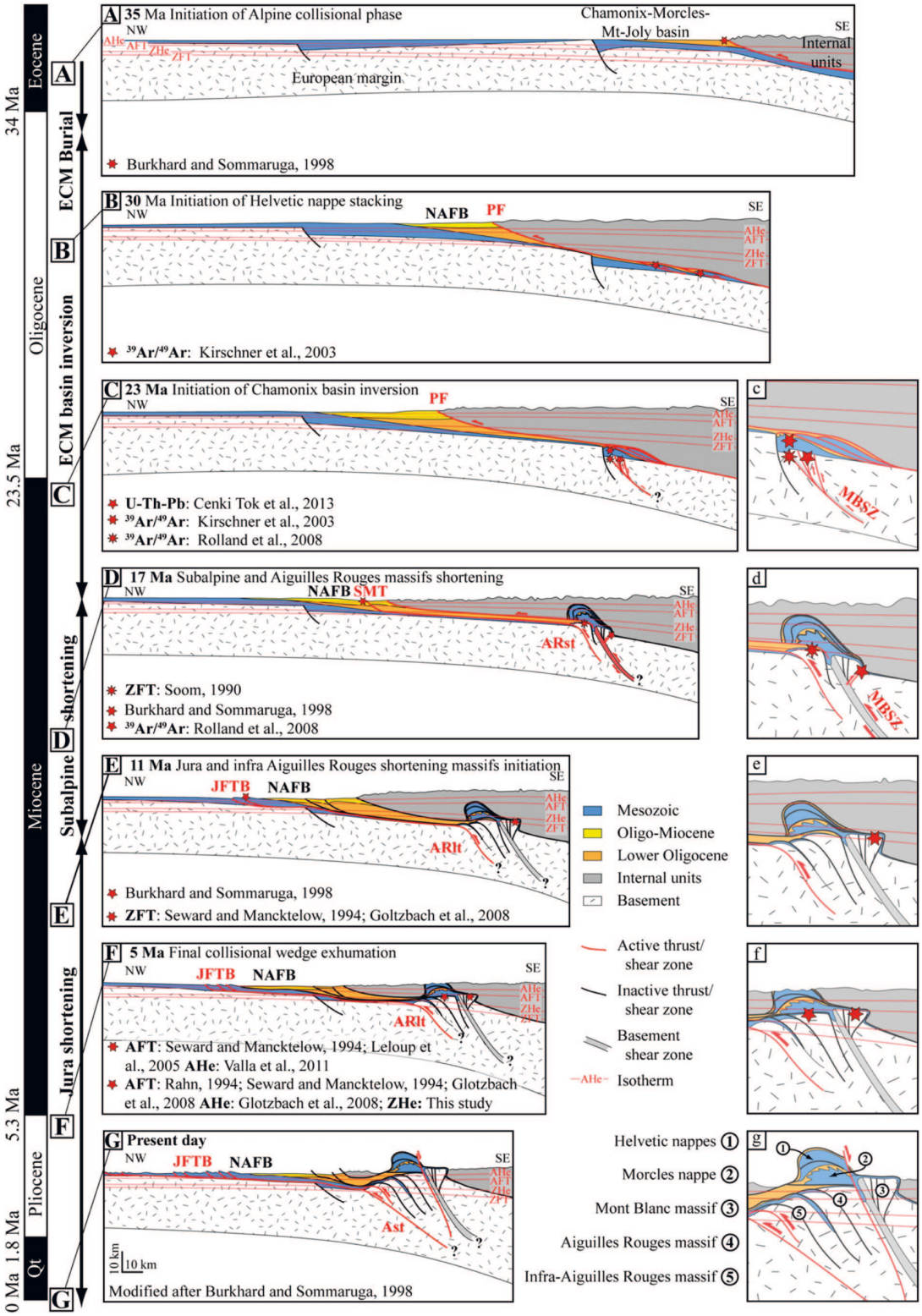

Figure 2.13. Shortening sequence of the European proximal margin during the collisional Alpine phase (Boutoux et al., 2016)

Kalifi et al. (2020) proposed an evolution of the deformation sequence in the subalpine chains (including Vercors, Chartreuse, Bauges, and Bornes), based on tectono-stratigraphic analysis of the distribution of Miocene deposits in relation with fault zones. Their results suggest the following scenario (Fig. 2.14):

1. **E-W extension from Upper Eocene (?) to the Oligocene**: North-South trending fault on the eastern side of the Massif Central, contemporaneous with the filling of the Valence basin.
2. **Compression ESE-WNW from Upper Rupelian (?) to the lower Miocene (31 (?) to 18 Ma**: Fault zone 1 (ZF1) was active for a long period between approximately 28 and 18 Ma. The allochthonous unit transported by ZF1 is particularly affected by NE-SW dextral detachments in the Chartreuse region.
3. **Compression E-ESE/W-WNW from Upper Burdigalian to Serravalien ((?) – 18 – 12(?)) Ma**: Westward propagation of the deformation front (in sequence activation of the faults: SAL, ZF2 to ZF5). ZF2 corresponds to the emergence of the basal Belledonne thrust fault. Thus, the base of the S2a sequence, which dates the activation of the SAL fault, indirectly also dates the activation of the Belledonne thrust.
4. **Activation of the Jura front from Tortonian or post-Tortonian (post 10.8 Ma):** The terminal depositional sequences record the birth of the Jura front, with overlap of the Mesozoic series into the Miocene.

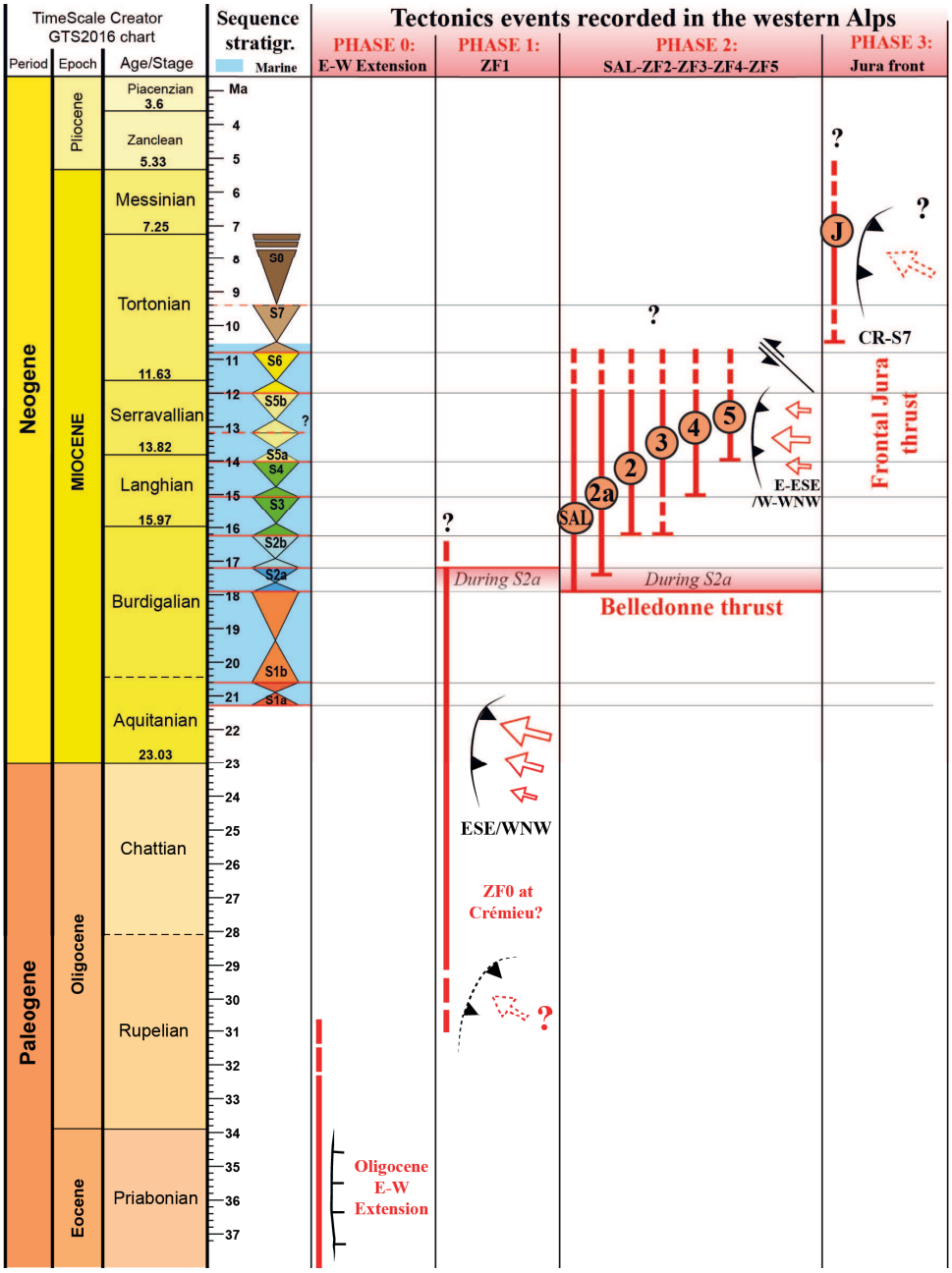

Figure 2.14. Tertiary tectonic phases in the subalpine chains (Vercors, Chartreuse, Bauges and Bornes) from Kalifi et al. (2020). Simplified structural diagrams. Red arrows indicate the directions of shortening. The size of the arrow depends on the intensity of deformation.

2.4.2.2 Mont-Blanc deformation hypothesis

This Ph.D. work focuses on the Mont-Blanc and Aiguilles Rouges massifs and the surroundings. Since the investigation of early workers on the tectonic deformation of the Mont-Blanc and Aiguilles Rouges massifs, tens of hypotheses have been proposed for the Western Alps deformation. We will review some of them below, however, our point is not to evaluate the relevance of each interpretation, but to identify how the conception of deformation evolved over time and how it impacted the interpretations.

Collet and Paréjas (1920), proposed a two-stage deformation model, in which the sedimentary cover is deformed above a basal thrust and later offset by steeper thrusts (Fig. 2.15a). In this model, the majority of the shortening is accommodated in the Chamonix Valley and the subalpine chains are allochthonous. Gourlay and Ricou (1983), proposed a coeval deformation of both the basement and the cover, proposing a duplexing of the Mont-Blanc and Aiguilles Rouges massifs (Fig. 2.15b). Following a similar idea, Butler (1985) suggested a complex duplex structure of the Mont-Blanc deformation, with multiple imbricated slices of the basement (Fig. 2.15 c). Gillcrist et al. (1987) argue that the Mont-Blanc massif and the Morcles Nappe resulted from the closure of a Jurassic inherited basin bounded by a normal fault (Fig. 2.15d). Mont-Blanc is structured by a major thrust at its base, affecting the sedimentary cover and cutting off the basement corner above the normal fault.

Ramsay (1981), Escher et al. (1988), and Escher et al. (1993) proposed a very different model, where the deformation is very distributed and not localized in shear zones or faults. The Mont-Blanc basement acts as a recumbent fold, expelling the Mesozoic cover from an inherited Mesozoic basin and forming the internal folds of the Morcles nappe. In this model, the deformation occurs in one single phase of both basement and cover deformation, therefore the cover remains autochthonous (or para-autochthonous) (Fig. 2.15e). This interpretation is widely used in the science community and is even used as a reference to compare the results of numerical modeling (e.g., Spitz et al., 2020).

Leloup et al. (2005) argue for a deformation model much closer to that of Collet and Paréjas (1920). Here, the deformation of the cover occurs above a basal décollement thrust that is later offset by steep thrusts (Fig. 2.15f). The Mont-Blanc deformation is controlled by a major shear zone between the Angle and Lavancher faults that runs along the Chamonix Valley. This model suggests a large displacement of the cover above the basement and roots all the nappes eastward of the Mont-Blanc massif. Rolland et al. (2008) and Cenki-Tok et al. (2013) focused on the internal deformation of the Mont-Blanc basement. They suggest that the main thrust occurred along the NW side of the Mont-Blanc massif and that, at the same time, a strike-slip movement occurred on the SE side, forming a positive flower structure (Fig. 2.15g). This model invokes a more distributed deformation of the Mont-Blanc basement along several

shear zones inside the massif. Egli and Mancktelow (2013) suggested a model similar to the one of Leloup et al. (2005), with a basal décollement of the Mesozoic cover above the basement and rooted east of the Mont-Blanc massif. However, the deformation along the Mont-Blanc shear zone is mainly in the strike-slip deformation, which belongs to the Simplon - Rhône fault system (Seward and Mancktelow, 1994).

Finally, Boutoux et al. (2016) brought back the idea of an inherited basin bounded by a normal fault in the Chamonix Valley. Their interpretation considers that the sedimentary cover is not significantly detached from the basement and that the main deformation occurs along the Mont-Blanc shear zone, west of the Mont-Blanc massif.

In summary, from these various interpretations, a key issue regarding the deformations in the external Alps is the **relation between the cover and the basement**.

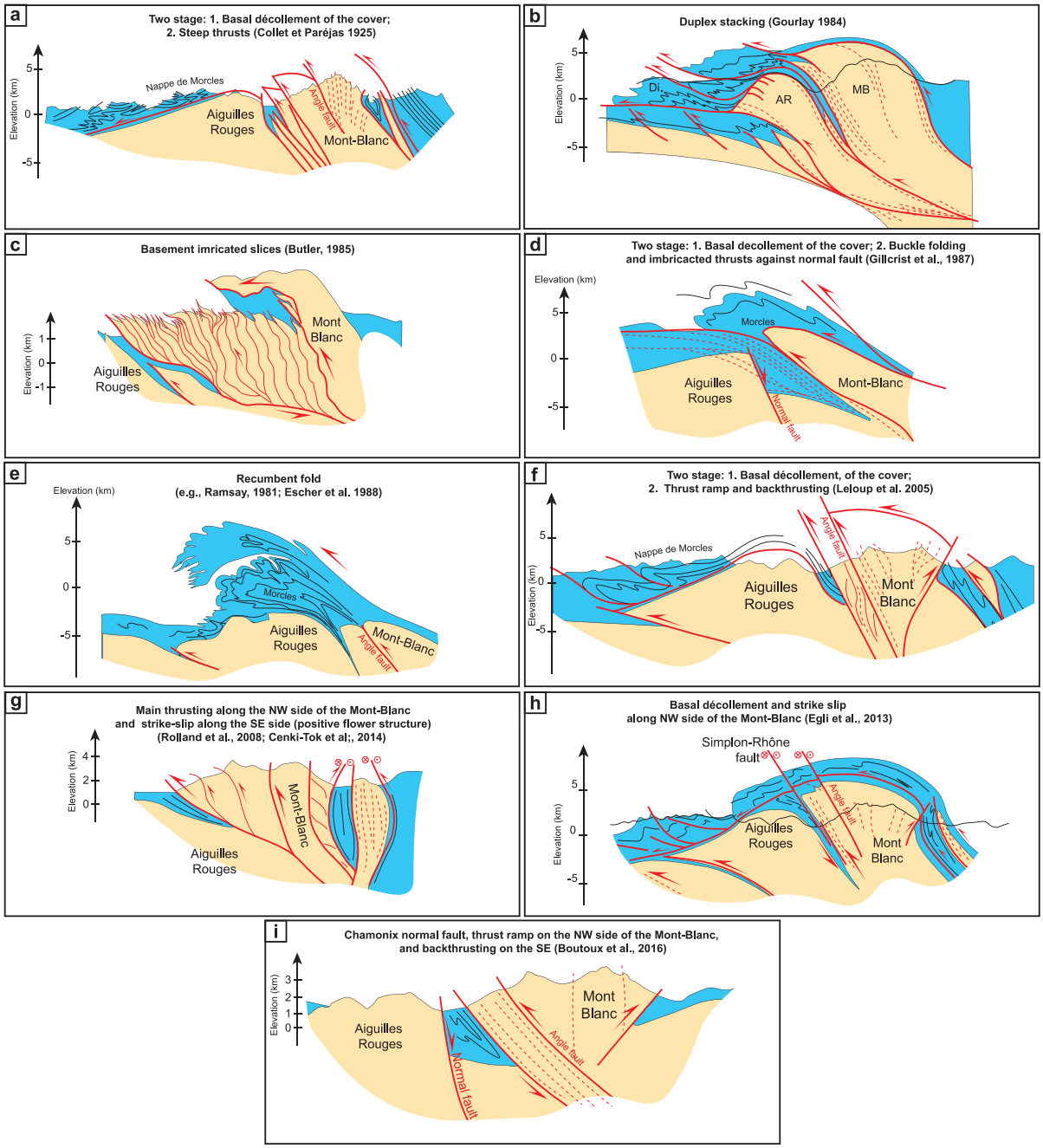

(Figure caption on next page)

Figure 2.15. Proposed hypotheses Mont-Blanc kinematic evolution. a) Collet and Paréjas (1920) have proposed a 2-step scenario with a décollement of the sedimentary cover, followed by steep thrusts; b) Gourlay and Ricou (1983) argue for a duplex stacking; c) Butler (1985) suggested a similar idea with the complex imbrications of basement slices; d) Gillcrist et al. (1987) suggested a basal décollement of the sedimentary cover, followed by imbricated thrusts against a normal fault; e) Ramsay (1981) and Escher et al. (1988) have proposed that the Mont-Blanc is the fold core of the recumbent Morcles nappe; f) Leloup et al. (2005), proposed a 2-step model where the cover is detached from the basement and root east of the Mont-Blanc, later the basal décollement is cross-cut by steep thrust ramp from the northWestern side of the Mont-Blanc and a back thrust on the southeastern side; g) Rolland et al. (2008), pursue that idea of "pop-up" structure but with a significant strike-slip motion along the back-thrust, suggesting a positive flower structure; h) Egli and Mancktelow (2013) present a 2-step model similar to Leloup et al. (2005), where the sedimentary cover is significantly detached from the basement, and later offset by steep fault. However, the major motion along that thrust is in strike-slip mode; i) Boutoux et al. (2016) argue for a normal fault bounding a "Chamonix basin" and a sedimentary cover not significantly detached from the basement.

2.4.2.3 Subalpine chain deformation models

The Mont-Blanc cover, either the Helvetic domain or the Subalpine chains, has also been a matter of debate for decades. A very complete compilation of models has been proposed by Affolter et al. (2008), Affolter (2003), and Faure et al. (1999). Based on the work of these authors, we propose a compilation of the various interpretations:

The gravity sliding model proposes that the deformation of the Jura and subalpine chain is linked and related to the exhumation of the External Crystalline Massif (Fig. 2.16a). This explanation has been first proposed by Reyer (1892) and later re-used by Laubscher (1961) but appeared quickly to be a weak explanation because such gravitational sliding of the cover on top of the External Crystalline Massif requires a large extension in the cover that does not root in the basement, which has never been documented.

The allochthonous model (Subalpine chain rooting model of Affolter et al. (2008) has been first suggested by Laubscher (1973) and proposes that the Jura deformation results from the propagation of the deformation from the Helvetic Nappes and the Subalpine chain, invoking that the deformation of the subalpine chain and the Jura deformations were combined and largely displaced over the external crystalline basement. In a second stage of deformation, the increase in external crystalline uplift would be related to out-of-sequence thrusts.

The Crustal Ramp model (External Basement massif rooting model of Affolter et al. (2008)) argues for a thrust system that deforms the Subalpine chain and is responsible for the deposition of Miocene molasse (Kalifi et al., 2020). This model has been popularized by Boyer and Elliott (1982). Leloup et al. (2005), Boutoux et al. (2016), Glotzbach et al. (2008), and Glotzbach et al. (2011) argue that the exhumation of the Mont-Blanc massif occurred from about 20 Ma,

coevally with the Jura deformation, suggesting a rooting of the Jura basal thrust below the External Crystalline Massifs and that the thrusts responsible for the exhumation of the external crystalline massifs are also rooted on the basal thrust. This argument is in line with the interpretation of the ECORS seismic experiment that suggests that the External Crystalline Massifs are culminations above large crustal ramps (e.g., Mugnier et al., 1990; Lacassin et al., 1990).

The Duplex model suggests that the deformation of the Subapline chains and the Helvetic Nappes partly roots in the basement thrust ramps in the External Crystalline Massifs. This model implies a coeval deformation of the external Crystalline Massifs and the Helvetic Nappes and subalpine chains.

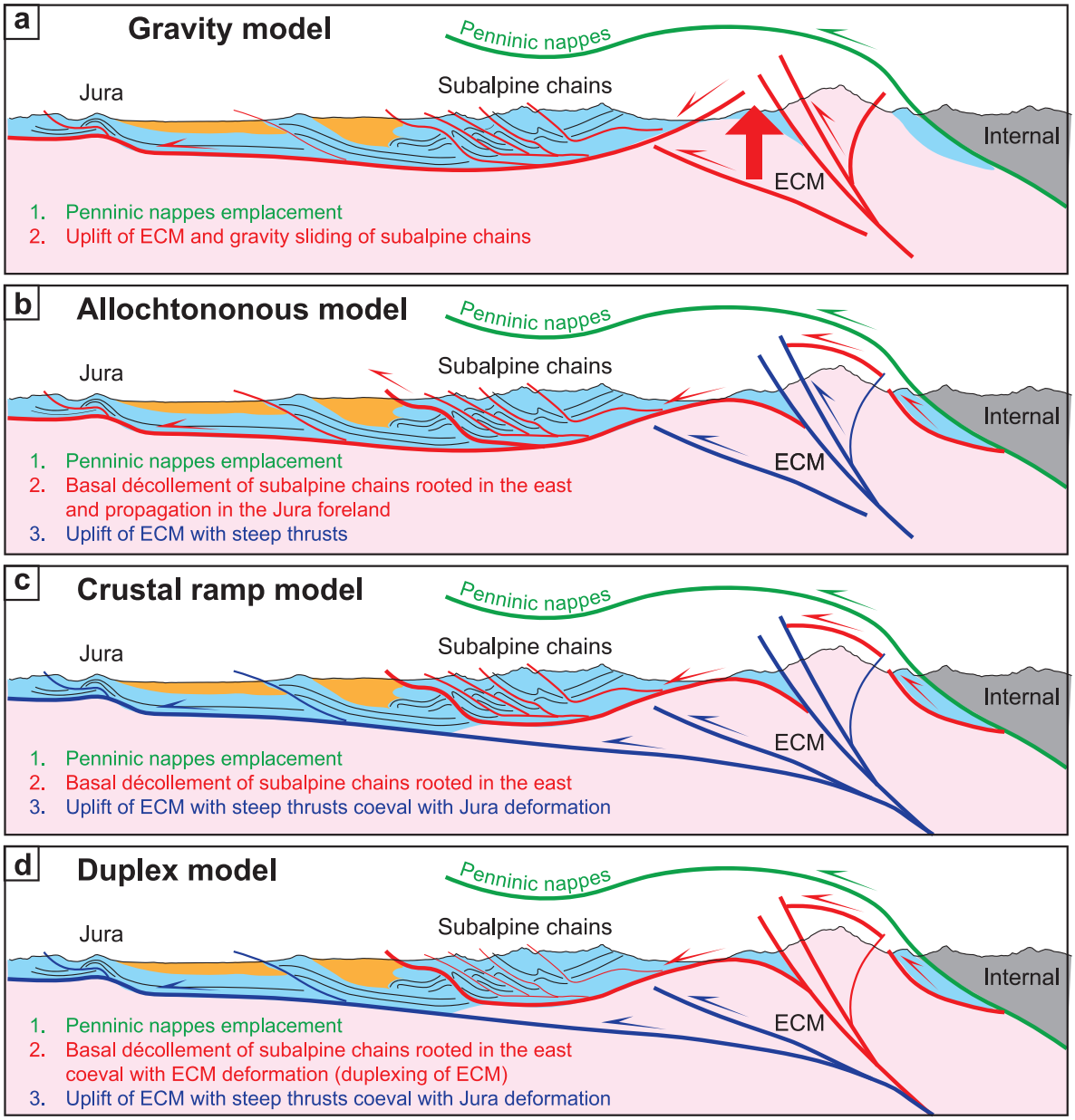

Figure 2.16. Schematic representation of four deformation models in the Western Alps. The cross-section is across the Jura chain, Bornes and Aravis subalpine chains, and the Aiguilles Rouges and Mont-Blanc external crystalline massifs (ECM). a. Gravity model: Gravitational sliding of the subalpine chains and Jura coevally with the uplift of the ECM; b. Allochthonous model: all Subalpine Chains and Jura are rooted east of the ECM and deform altogether, later offset by steeper thrust during the exhumation of ECM; c. Crustal Ramp model: basal décollement of the Subalpine Chains rooted east of the ECM, Jura deformation rooted west of ECM on crustal ramps. d. Basal décollement of the subalpine chains rooted east of the ECM, coeval with ECM deformation in a duplex, later offset by steep thrust during the exhumation of ECM.

2.5 Strike-Slip motion in the Western Alps

Although the main deformation in the Western Alps is clearly the result of northwest-directed thrust tectonics, several NE-SW oriented strike-slip faults are present in the external crystalline massifs, and some of them are still seismogenic (Fréchet et al., 2010; Guéguen et al., 2021; Billant et al., 2015; Cara et al., 2017; Minetto et al., 2022; Thouvenot et al., 2003). Their implication in the evolution of the Alps is debated, and the timing, conditions, and beginning of the strike-slip activity remains unclear. Some authors consider that these strike-slip faults are connected in a major dextral strike-slip system that runs from the Simplon normal fault to the Argentera massif (Hubbard and Mancktelow, 1992; Cenki-Tok et al., 2013; Rolland et al., 2008; Bergemann et al., 2019). The southwest-directed Simplon normal fault directed to the southwest has been documented to be active since 20 Ma (Campani et al., 2010). This timing coincides with the activation of shear zones in the External Crystalline massifs of the Western Alps (Fig. 2.17). In the case of the Mont-Blanc massif, Cenki-Tok et al. (2013), Rolland et al. (2003), and Rossi et al. (2005) have described shear zones that trend from N$40°$ to N$60°$ and have subvertical stretching lineations with a minor dextral component. On a large scale, these thrust / strike-slip distributed zones may reflect a general dextral strike-slip deformation through the Alps: in the Rhône Valley in Switzerland, between Mont-Blanc and Aiguilles Rouges, and through the Belledonne massif (Fig. 2.17) (Rolland et al., 2022). The correlation of the normal motion of the Simplon fault and the thrusting / dextral strike-slip in the external crystalline massif is mainly based on the timing of deformation and poorly constrained with tectonic field evidence. The overall strike-slip motion is compatible with the counterclockwise rotation of the Apulian plate (e.g., Collombet et al., 2002).

2.6 Amount of shortening in the Western Alps

To properly assess the boundary conditions during the Alpine collision in the Western Alps, the estimation of finite shortening seems a prerequisite. The calculated amount of shortening depends on the structural decision made regarding how the shortening is accommodated. These values are approximate as they result from the hypothesis of a planar strain along a single uniform direction. In front of the Mont-Blanc massif, Bellahsen et al. (2014) estimated a NW-SE shortening of 17 km within the Bornes, while Affolter (2003) estimates a total shortening of 30 to 36.5 km for subalpine nappes at the same location. This difference arises from the fact that Bellahsen et al. (2014) attributed only a part of the shortening of the Bornes massif to basement thrusts and did not consider the shortening of the Helvetic nappes (in red in Fig. 2.20). From the Bornes and Aravis massifs, Pfiffner (2011) and Pfiffner (2014) calculated a shortening of about 50 km, which is much higher than the value obtained by Affolter (2003) and Bellahsen et al. (2014). Further south, Kalifi et al. (2021) propose an interpretation for

the northern part of Vercors and the eastern part of Chartreuse where these massifs are klippes above a thrust they call Fault Zone 1 (FZ1), with shortening estimates between 14.1 and 5.8 km in the north and south of Chartreuse, respectively.

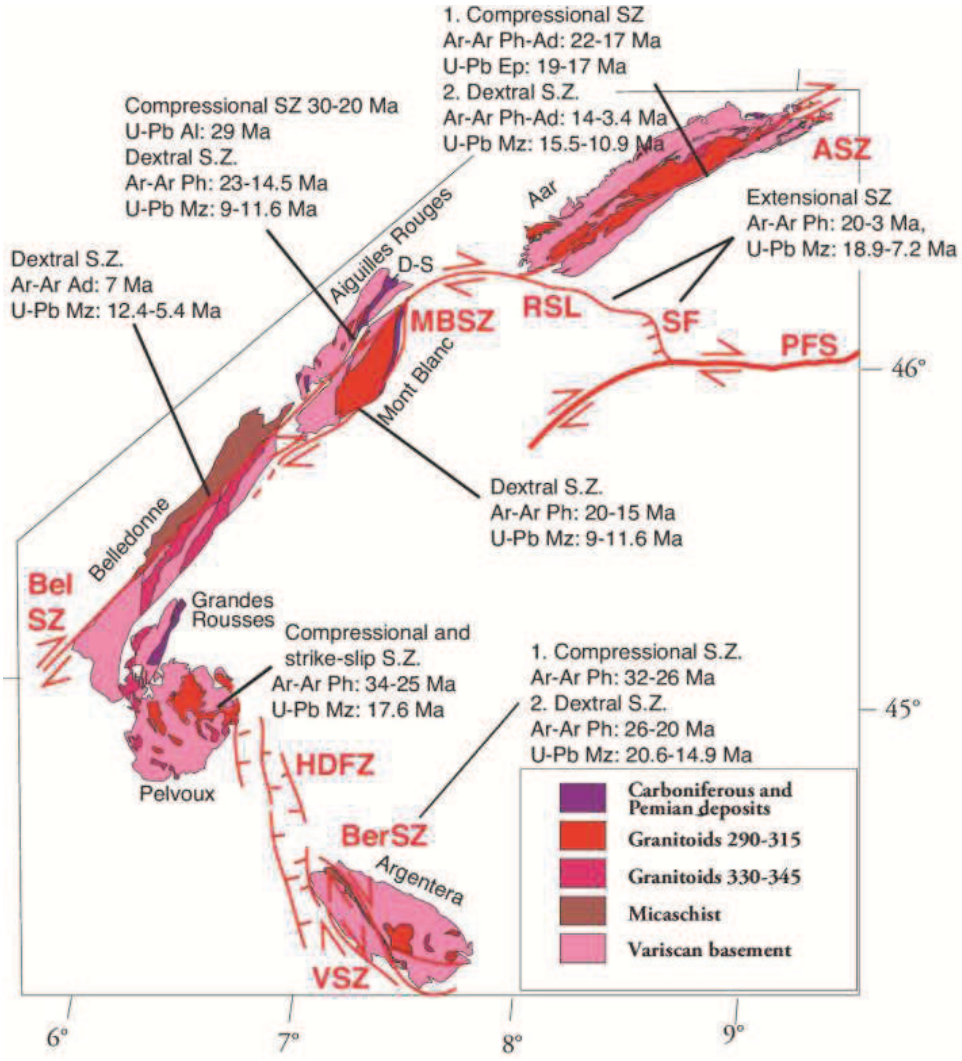

Figure 2.17. Compilation of Ar–Ar on phengite and U–Pb on allanite / epidote / monazite ages along the Western External Alps from Rolland et al. (2022). ASZ: Aar Shear zone (Ar–Ar on phengite (Ph) from Challandes et al. (2008) and Rolland et al. (2009), U–Pb on epidote (Ep) by Peverelli et al. (2021) and on monazite (Mz) by Ricchi et al. (2019)); BelSZ: Belledonne Shear Zone (U–Pb on Monazite by Gasquet et al. (2010) and Janots et al. (2019), Ar–Ar on adularia (Ad) by Gasquet et al. (2010)), BerSZ: Bercesio Shear Zone (Ar–Ar on phengite by Sanchez et al. (2011), and U–Pb on monazite by Ricchi et al. (2019)), HDFZ: High Durance Fault System (Ar–Ar on phengite by Simon-Labric et al. (2009) and Bellanger et al. (2015), U–Pb on Monazite by Gasquet et al. (2010), MBSZ: Mont Blanc Shear Zone (U–Pb on allanite (Al) by Cenki-Tok et al. (2013) and on Monazite by Bergemann et al. (2019), Ar–Ar on Phengite by Rolland et al. (2008)); PFS: Periadriadic Fault System, RSL: Rhone Simplon Line and SF: Simplon Fault (Ar–Ar on phengite by Campani et al. (2010); U–Pb on monazite by Gnos et al. (2021); VSZ: Valetta Shear Zone (same refs as for BerSZ)

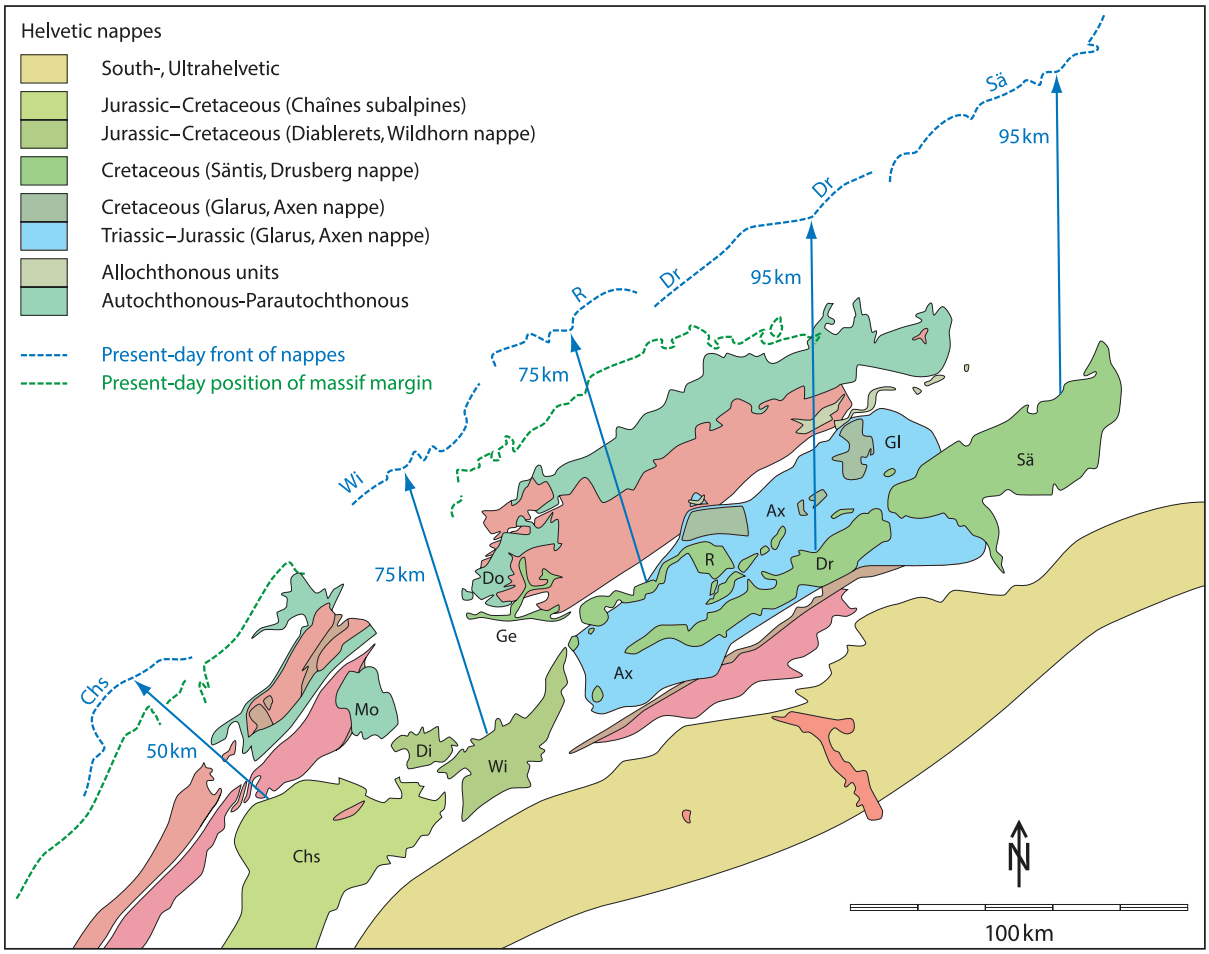

Figure 2.18. Paleogeographic reconstruction of the Helvetic Nappe System in the central and Western Alps. In this reconstruction, the displacement of the Helvetic Nappes above the Crystalline External Massifs is increasing from south to north. From the south, the subalpine chains have been displaced about 50 km above the Mont-Blanc and Aiguilles Rouges, while further north the Wildhorn Nappe has been displaced about 75 km, and the Drusberg Nappe has been displaced about 95 km above the Aar massif. Figure from Pfiffner (2011), redrawn after Kempf and Pfiffner (2004).

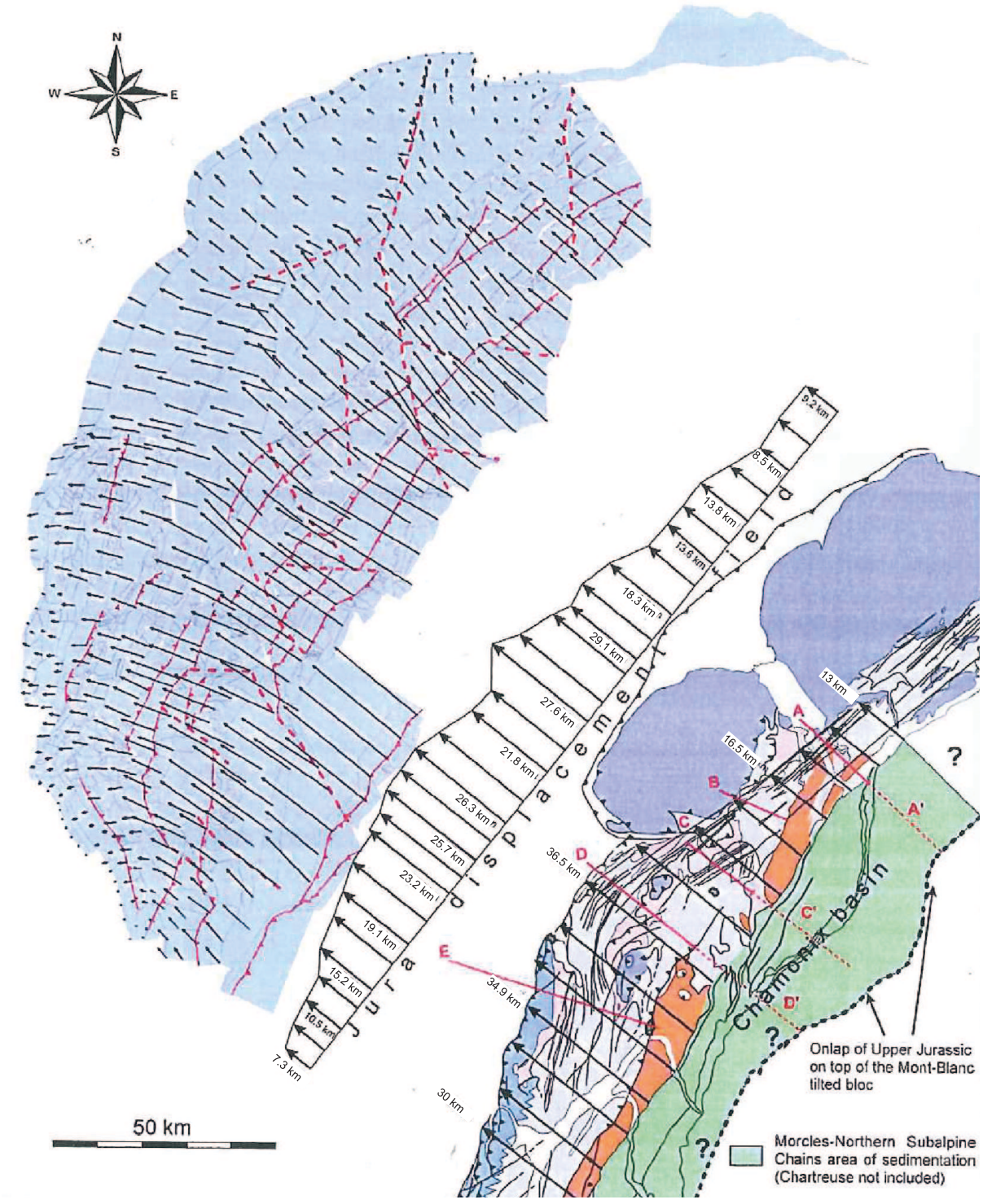

Figure 2.19. Restored displacement field of the Jura and subalpine chains above the external crystalline massifs. In this reconstruction, the Subalpine chains and Helvetic Nappes above the Mont-Blanc and Aiguilles Rouges have been displaced about 30 to 36.5 km from south to north Affolter (2003).

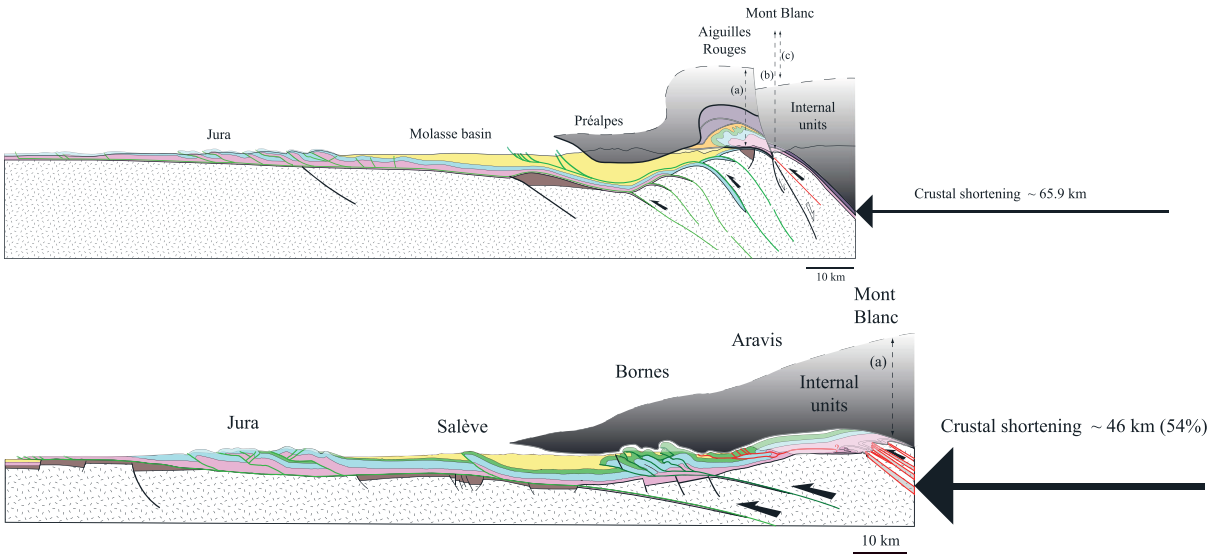

Figure 2.20. Cross section through the north-Western Alps from Bellahsen et al. (2014): the Prealpes-Mont Blanc cross-section (Burkhard and Sommaruga, 1998), the subalpine (Bornes) and Jura parts are redrawn from (Affolter et al., 2008). The Jura and Molasse basins were constrained by seismic data. A total amount of shortening of about 65.9 km is recorded for the entire external zone: 10.6 km for the ECM during early Miocene times characterized by large basement Alpine shear zones in the Mont Blanc massif.

2.7 Amount and timing of exhumation

The thermal history of the External Crystalline massif has been extensively studied in the last decades (Valla et al., 2012; Valla et al., 2011; Van der Beek et al., 2010; Girault et al., 2022; Leloup et al., 2005; Glotzbach et al., 2008; Glotzbach et al., 2011; Seward and Mancktelow, 1994; Boutoux et al., 2016). In the Mont-Blanc massif, Glotzbach et al. (2011) and Glotzbach et al. (2008) simulated the Mont-Blanc exhumation using the Pecube algorithm (Braun, 2002; Braun et al., 2012). Their results suggested a step-by-step exhumation, initiating at about 22 Ma, followed by a decrease in exhumation at about 6 Ma, possibly lithologically controlled (crystalline rocks emerging through sedimentary cover), and a final increase in exhumation at 1 Ma, most likely controlled by the glacial valley incision during the Quaternary. Using forward numerical simulation in the Northern Aiguilles Rouges massif, Valla et al. (2012) suggested a late Miocene exhumation (8-10 Ma) followed by a moderate (0.3-0.5 $\mathrm{km\,Ma^{-1}}$) exhumation rate. They found a late increase in exhumation at about 1 Ma, related to the carving of the Rhône valley. Using inverse and forward thermal history modeling (HeFTy) in the Aiguilles Rouges and Mont-Blanc massif, Boutoux et al. (2016) proposed that the Mont-Blanc and the Aiguilles Rouges massifs experienced continuous exhumation since 18 Ma. Girault et al. (2022) applied the same methodology as Boutoux et al. (2016) in the Belledonne and Grandes Rousses massifs and suggested a continuous exhumation of Belledonne since about 18 to 20 Ma in the northern part of the massif and about 25 to 27 Ma in the southern part of the Belle-

donne and Grandes Rousses massifs. Applying the inversion of the thermochronological data in the Ecrins massifs, Van der Beek et al. (2010) highlighted a decrease in exhumation between 6 and 5 Ma, at a time similar to that of Mont-Blanc (Glotzbach et al., 2011; Glotzbach et al., 2008). Girault et al. (2022) noticed a diachronism in the exhumation of the External Crystalline Massifs: approximately 18 Ma in Aar, Mont-Blanc, Aiguilles Rouges and about 25 to 27 Ma in Belledonne, Grande Rousses and Pelevoux, interpreted to be related to the timing of activation of the frontal ramps.

In summary, according to the available thermochronological data and the modeled thermal paths, it is unclear if the External Crystalline Massifs have experienced a continuous or step-by-step exhumation. Exhumation has probably started at about 20 Ma in the north ECM and earlier at about 25 to 27 Ma in the southern ECM.

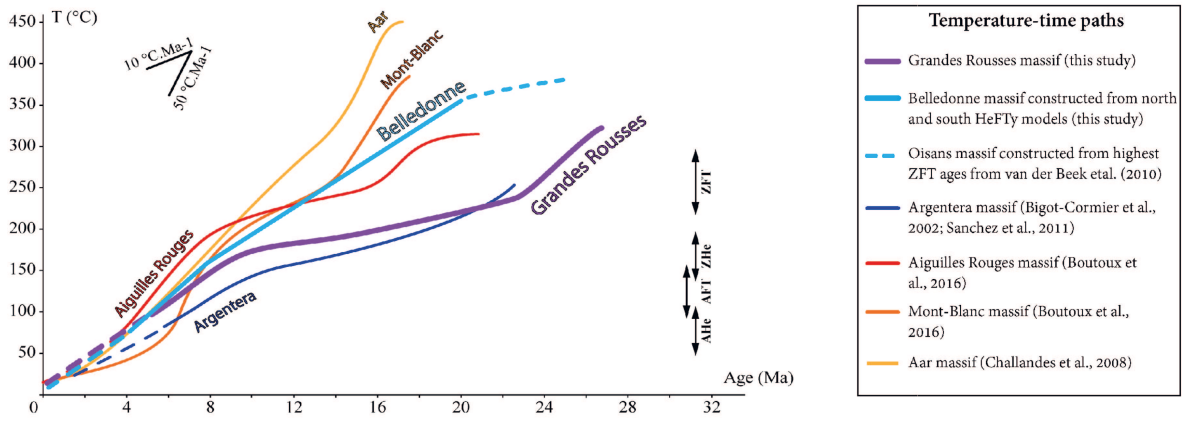

Figure 2.21. Thermal path for the external crystalline massifs as proposed by Girault et al. (2022).

Chapter's key points

- The Western Alps are an accretionary wedge resulting from the Cenozoic convergence between Europe and the continental margins of Apulia.
- The orogenic wedge is split into two parts: the internal domain, which contains rocks that have been deformed at high temperature and deeply subducted during the Alpine orogeny, and the external domain, where the Alpine metamorphism is limited to green schist facies.
- Prior to the alpine collision, the European margin inherits structure from
  1. The post-Variscan extension.
  2. The Saalian compression.
  3. The Mesozoic extension.
  4. The Eocene - Oligocene extension
- Deformation models have proposed that the collision began in the Eocene with the Penninc thrust system and later, the deformation migrated towards the east in the external crystalline massifs. I
- In the Mont-Blanc massif, the debate in the deformation models arise from:
  - The tectonic relationship between the basement and the cover.
  - The style of deformation (thrust nappes vs. fold nappes).
  - The root of the thrusts.
  - The sequence of deformation.

Part II

3D STRUCTURAL GEOLOGY

Chapter 3

Development of a relational database for organizing field geological data: *DataGeol*

Microfolding from the Montagne des Posettes along with a professional Freiberger geological compass. Photo: Antoine Mercier (2018).

Abstract

We designed a relational database specifically built for the storage and processing of structural geology data: *DataGeol*. The relational database efficiently organizes the data into different tables, guarantees the unicity of the data with primary keys (PK), and guarantees the integrity of the among tables with foreign keys (FK). Tables are standardized with vocabularies and standards that guarantee interoperability in the geoscience community. The database is coded in structured query language (SQL) using the open-source PostgreSQL system. Practically, on returning from a field mission, the user enters the information he has recorded in his field notebook in various dedicated tables (locations, measurements, observations, samples, etc.). Tables are organized, linked, and merged to output tables named "views", allowing data to be exported in different formats for processing and display in a GIS or 3D geological models. This database was built for the storage and organization of 3D structural geology data from the western Alps and was used in the building of a 65 x 63 km 3D geological model based on potential field interpolation. The dataset includes outcrop locations, lithological descriptions, geological features measurements, samples, and analyses. Data were acquired in situ in the field during field missions. Locations are georeferenced using a hand-GPS device, and measurements of planar and linear geological features were measured using high-precision geological compasses. The data set compiles data from other published data sets in the same area. This database is also intended to serve as a template for the storage and diffusion of structural data in the international scientific community.

Résumé

Nous avons conçu une base de données relationnelle spécifiquement destinée au stockage et au traitement des données issues de géologie structurale: *DataGeol*. La base de données organise efficacement les données dans différentes tables, garantit l'unicité des données avec des clés primaires (PK) et l'intégrité des tables entre elles avec des clés étrangères (FK). Les tables sont standardisées à l'aide de vocabulaires et de normes qui garantissent l'interopérabilité au sein de la communauté géoscientifique. La base de données est codée en *standard query language* (SQL) à l'aide du système open source PostgreSQL. En pratique, au retour d'une mission de terrain, l'utilisateur saisit les informations qu'il a renseigné dans son carnet de terrain dans les différentes tables dédiées (affleurements, mesures, observations, échantillons, etc.). Les tables sont organisées, reliées et fusionnées en tables de sortie appelés "vues", ce qui permet d'exporter les données dans différents formats pour les traiter et les afficher dans un SIG ou les implémenter dans des modèles géologiques 3D. Cette base de données a été créée pour le stockage et l'organisation des données structurales 3D provenant des alpes occidentales. Ces données ont permit la construction d'un modèle géologique 3D de 65 x 63 km basé sur l'interpolation de champs de potentiels. L'ensemble des données inclue les localisations des affleurements, les descriptions lithologiques, les mesures des structures géologiques, les échantillons et les analyses. Les données proviennent de différentes missions de terrain effectuées dans la zone d'étude. Les affleurements ont été géoréférencés à l'aide d'un GPS de randonnée et les mesures des géologiques ont été effectuées à l'aide de boussoles géologiques professionnelles. Ce jeu de données compile également des données publiées dans la même zone par d'autres auteurs. Cette base de données à également pour but de servir d'exemple pour le stockage et l'archivage de données structurales dans la communauté scientifique internationale.

3.1 Objective

Structural geology studies, including maps, are models built from data. Most often, these are field observations and measurements of geological features: orientations of planes such as bedding, cleavage, shear planes, faults, etc., or lines such as lineations or slickenlines on faults. Unfortunately, it is often very difficult to retrieve the original data used for the interpretation of geological maps or cross sections after their publication, making it impossible to assess how well-constrained the model is, or for other authors to increment the data set or even propose other models based on the same data.

The geological structure and evolution of the western Alps have been widely studied in recent decades (e.g., Leloup et al., 2005; Bellahsen et al., 2014, and references therein.), however, the use of a database to organize the data acquired in the field is very rare. The first objective of this study is to propose a database template for structural geologists to share their data with the scientific community using internationally approved standards and vocabularies. The second objective of this study is to provide an example by providing a dataset of structural geological data from the Western Alps: lithological descriptions of outcrops, structural measurements, and sample locations.

To reach the objectives, the database template needs to fulfill specifications:

1. An organization that allows to enter the maximum of information efficiently.
2. Wide accessibility and interoperability
   (a) Use of open access software and data formats.
   (b) Standardization of terms used with internationally approved vocabularies.
3. Flexibility according to users' practices and the evolution of concepts.
4. A process and application of the data efficiently.

3.2 Experimental design, material, and methods

3.2.1 The design of a relational database

DataGeol is a relational database that has been specifically designed for the storage and processing of structural geology data. The database efficiently organizes the data into different tables. The tables are checked by constraints specified in the database design. Primary keys guarantee the unicity of each data record within a table, and foreign keys guarantee the integrity of the relations between tables (Fig. 3.2). Tables are also standardized with vocabulary and standards, which guarantee interoperability in the geoscience community. To do so, we used

the standards of DarminCore (Wieczorek et al., 2012) and GeoSciML 4.1 (Simons et al., 2006; Sen and Duffy, 2005; Raymond et al., 2012) (Table 3.1).

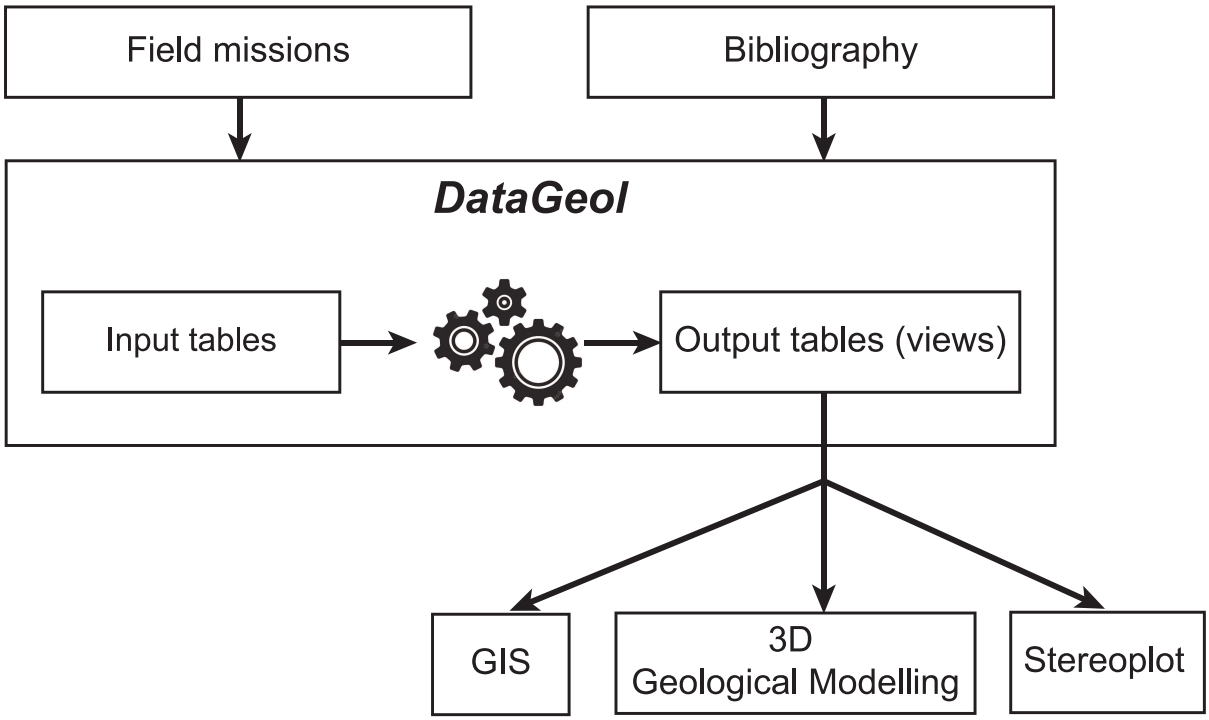

Figure 3.1. Workflow of DataGeol databse. When returning from a field mission, the user can enter the data recorded during the survey in input tables. The data are processed and output in tables named 'views' that are made for visualization. From these tables, the data may be used in GIS, 3D GeoModeling software or stereoplots.

Table 3.1. Lexicon and vocabularies source description.

Lexicon	Source
Alteration facies	OGC Geoscience Markup Language v4.1 (GeoSciML)
Contact type	OGC Geoscience Markup Language v4.1 (GeoSciML)
Reference Projection System	EPSG Geodetic Parameter Dataset v10.076
Fault movement sens	OGC Geoscience Markup Language v4.1 (GeoSciML)
Fault sens criterion	This database
Fossils	
Chronostratigraphy chart	International Commission on Stratigraphy
Line type	OGC Geoscience Markup Language v4.1 (GeoSciML)
Plane type	OGC Geoscience Markup Language v4.1 (GeoSciML)
Metamorphic facies	OGC Geoscience Markup Language v4.1 (GeoSciML)
Observation site type	
Particle shape	OGC Geoscience Markup Language v4.1 (GeoSciML)
Particle type	OGC Geoscience Markup Language v4.1 (GeoSciML)
Planar polarity	OGC Geoscience Markup Language v4.1 (GeoSciML)
Sample aim	This database
Sample section type	
Sample type	This database
Simple lithology	OGC Geoscience Markup Language v4.1 (GeoSciML)
Time zones	

Technically, the database is coded with the Structured Query Language (SQL) through the open-source PostgreSQL 13.0 system with the graphical interface Pgadmin 6.2.1. The tables are organized around the *location* table that localizes all the other information (in red in Fig. 3.2). Four satellite tables are related to the locations (in green in Fig. 3.2): the *lithology description* table that stores the data relative to petrologocial observations within a location, the *measurements* table that stores the orientations of planes and lines, and the table *samples* that stores the data related to samples collected in the field. The *samples* table is connected to the *lihtology description* table and the *measurements* table because a sample is associated with a petrological description and eventually an orientation. The contact between two distinct geological formations is stored in the *contacts* table, connected to the lithology description and the *measurements* table. Another group of tables refers to the analysis performed on the samples (in yellow in Fig. 3.2): the cut of thin sections, geochronological or thermochronological analysis. Other tables are auxiliary tables that store metadata (in blue in Fig. 3.2): the names of the geologists who performed the observations or measurements in the *geologists* table, the details of the field missions in the *field mission* tables and compasses used for the measurements in the *instruments* table. All the other tables (in gray in Fig. 3.2) are vocabularies that standardize the terms used in the database.

From the connection between tables, the data are organized, concatenated, processed (geographic system transformation, universal time to local time, strik-dip-quadrant to dip-dir

convention, etc.) and displayed in tables called "views". These tables are the output tables of the database.

3.3 Data description

Structural data are provided in seven tables formatted in commas separated values (.csv) (Table 3.2). The data are displayable in text format using any text editor, as a table format (e.g., Open Office calc or Excel), or in a Geographical Information System interface (GIS) (e.g., QGIS, ArcMap). The stylings for display in a GIS are provided in .qml format with symbols provided as .svg symbols.

Table 3.2. Organization of the folders into the data repository.

Folder Name	Description
vocabularies	Lexicons used in the databse in .csv
fct	Functions computed to convert data in .sql
input	**Input** tables of the databse .csv
kmz	**Outupt** views in .kmz for GoogleEarth
shp	**Outupt** views in .shp for QGIS
views	**Outupt** views in .csv
tar	**Database** source code compressed in .tar
svg	SVG symbols for the display in a GIS.

3.3.1 Acquisition

Field measurements were made by the authors during 30 field missions in the western Alps over 27 years (of which 10 during this Ph.D.). Positioning has been carried out mainly with hand GPS (Garmin Montana 680 and Garmin eTrex 32), or exceptionally with Samsung Touch Pad with the FieldMoveTM app. Dip measurements have been made using professional geological compasses (Universal Topochaix 1002A compass and Freiberger 64 compass). The measured values of planar and linear orientations were noted on-site in a field book, using the following notation: Strike azimuth (0-180°), dipping angle (0-90°), and quadrant direction of dip (N,NE,E,SE,S,SW,W,NW). The spatial precision of the GPS device measurements ranged from $\sim$ 3 m to several tens of meters depending on the satellite's visibility at the time and location of the point saving. The angle precision of the professional compass is close to 1°, however, the actual error associated with the measurement is probably higher as the measured surfaces are not perfectly planar, the actual error on the measurement is estimated to be of the order of 1° in dip and azimuth.

When returning from a field mission, the correctness of the outcrops locations was checked on a GIS with orthophotos (10 to 20 cm of spatial resolution) and the associated metadata of

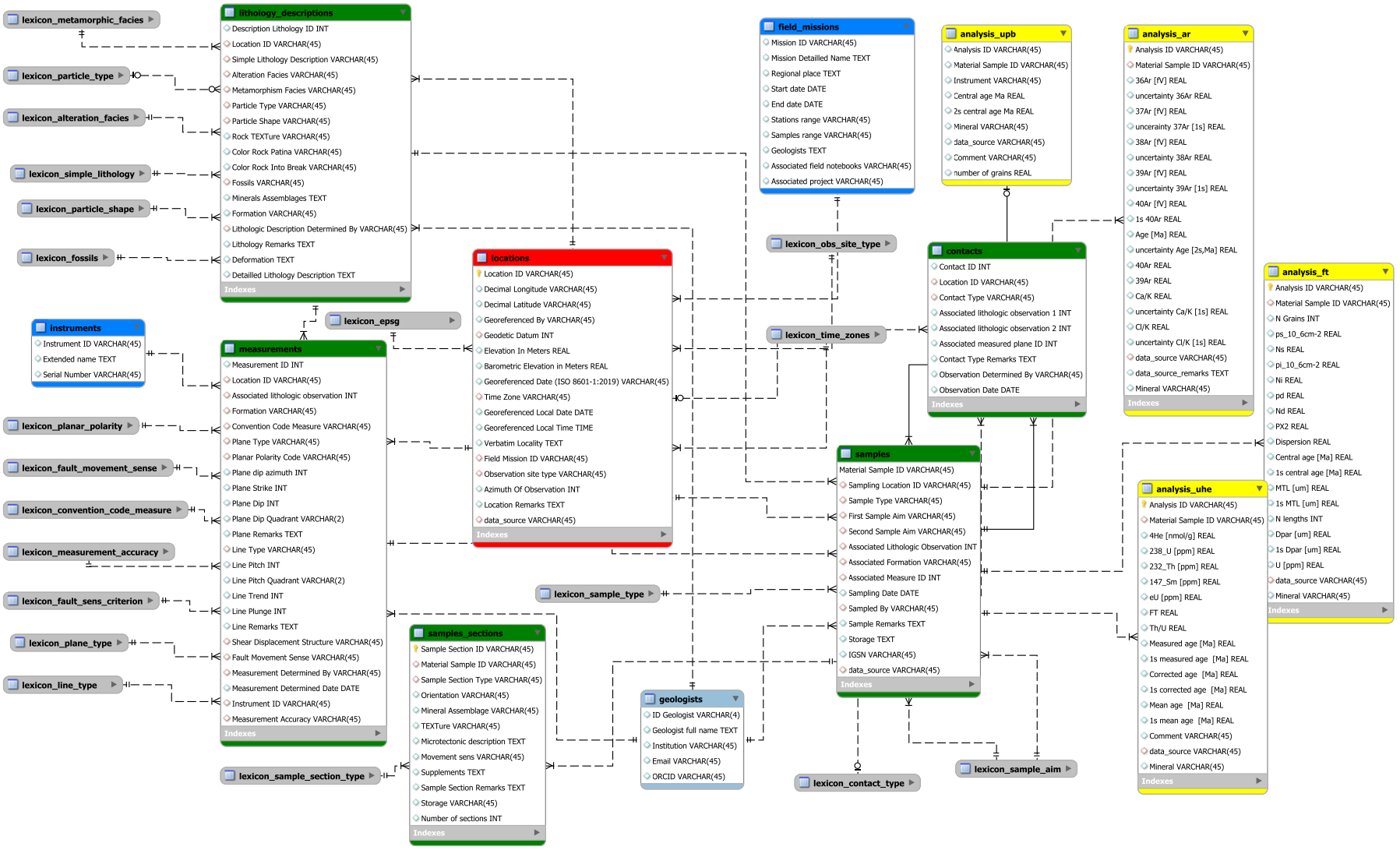

Figure 3.2. Entity Relationship Diagram (ERD) of *DataGeol*. Each box represents a table, and the extended tables show the column names and data types. Gray boxes are lexicons related to the main (colored) tables.

each location was entered manually in PostgreSQL through the Pgadmin graphical interface. Structural data were read from the field notebook to the standardized table. A link has been established between the PostgreSQL database and QGIS with the PostGIS module.

3.3.2 Field missions

An observational field mission is a time of consecutive days in a defined area where the observations were made. The mission is uniquely recorded with an identifier composed of the year and month, and the first five letters of the general location (e.g., 2022-08-ARAVI). See the table field description in table 3.3

Table 3.3. Description of the fields from the Mission table

Field Name	Description
Mission ID	Unique identifier of the field mission [Primary Key].
Regional Place	The general name of the area (e.g., mountain massif name).
Start Date	First day of the field mission in the format [yyy-mm-dd].
End Date	Last day of the field mission in the format [yyy-mm-dd].
Locations Range	Range of the location identifiers recorded during the survey.
Samples Range	Range of the Sample identifiers recorded during the survey.
Participants	Geologists who worked during the field mission project.
Field Notebooks	Identifiers of the field notebooks used by the scientists during the field survey.
Associated Project	Project in which the field survey is included.

3.3.3 Locations

Although observation is a process that may be extended in time and space, locations refer to discrete points in space and time where observation has been carried out. The position corresponds to a relatively small area of observation (less than 10 m). The chosen date and time correspond to the first moment when the position has been saved with a GPS device. The nature of the location is variable (in situ natural outcrops, roadside, quarry, etc.; see observation site lexicon).

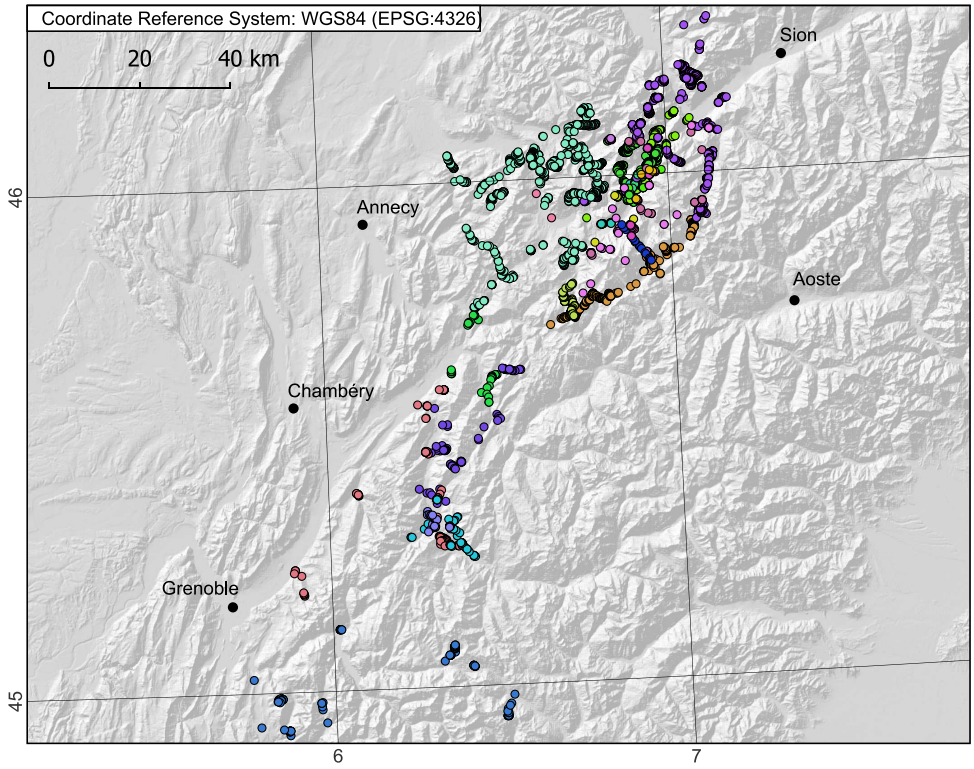

Figure 3.3. General map with outcrops locations within DataGeol database

Table 3.4. Description of the fields from the Mission table

Field Name	Description
Location ID	Unique identifier of the station [Primary Key].
Decimal Longitude	The longitude in decimal degrees (WGS84/EPSG:4326).
Decimal Latitude	The Latitude in decimal degrees (WGS84/EPSG:4326).
Elevation In Meters	Elevation in meters above sea level.
Geodetic Datum1	Projected reference system used to project coordinates.
Easting in Meters	Projected easting (x) coordinate in meters.
Northing in Meters	Projected northing (y) coordinate in meters.
Georeferenced By	Method or instrument (e.g., GPS device) used for localization.
Verbatim Locality	Extended description of the general position of the location.
Georeferenced Date	Date of the outcrop localization in the format [yyyy-mm-dd].
Georeferenced Time	Time of the outcrop localization in the format [hh:mm:ss].
Time zone1	Time zone where the outcrop is localized.
Mission Detailed Name2	Full name of the associated field mission.
Observation site type1	Description of the outcrop type, associated with a lexicon.
Location Remarks	Any other metadata or comment that cannot fit in the other fields.

3.3.4 Lithology description

The lithology description table aims to characterize the petrological facies at a location. This table is quite general and refers to a simple description lexicon. It is appropriate to describe any type of rocks and facies: magmatic, metamorphic or sedimentary. The lithologic description will be related to a sample or a measurement. Note that there can be several lithological description per location ID.

Table 3.5. Description of the fields from the lithology description table.

Field Name	Description
Description Lithology ID	Unique identifier of the measurement.
...	...
Simple Lithology Description	Description of the outcrop facies.
Alteration Facies	Description of the alteration facies.
Metamorphism Facies	Description of the matamorphic facies.
Particle Type	Description of the sedimentary type of clast.
Particle Shape	Description of the sedimentary type of clast.
Rock Texture	Description of the rock texture.
Color Rock Patina	Description of the rock patina color.
Color Rock Into Break	Description of the rock color into break.
Fossils	Identification of fossils in a sedimentary rock.
Deformation	Brief description of the deformation.
Minerals Assemblages	Identification of the mineral assemblage.
Formation	Associated geological formation.
Lithologic Description Determined By	Geologist who performed the description.
Lithology Remarks	Supplementary remarks regarding the lithology.

3.3.5 Plane and line measurements

Measurement refers to the numerical quantification of a natural feature or phenomenon. In structural geology, measurements characterize geological structures such as planes or lines in space. The data describe the orientation of a plane by using the dip-direction convention [dip/azimuth of dip] which is internationally adopted: the dip is the maximum angle between the measured plane and the horizontal (Fig. 3.4), the dip azimuth is the clockwise angle from the geographical north to the dipping direction of the measured plane (Fig. 3.4). The orientation of a line is given using the trend and plunge conventions. The plunge of a line is the angle from the horizontal plane to the line. Trend is the clockwise angle from the geographical north to the direction of the line plunge.

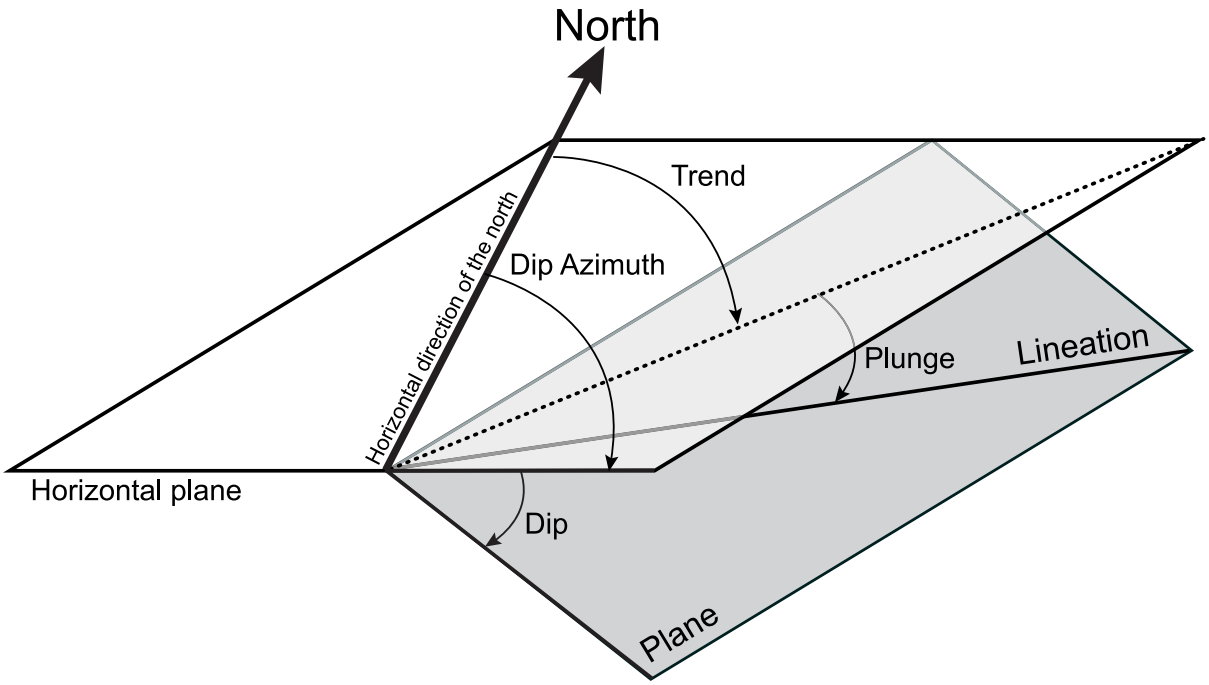

Figure 3.4. Diagram describing the measurement conventions characterizing the orientation of a plane and a line in space: the Dip describes the maximum angle between the measured plane and the horizontal surface. The Dip Azimuth describes the angle between the north and the dipping direction of the measured plane. The plunge of a line describes the angle between the line and the horizontal. The trend describes the angle between the north and the plunge direction of the line. Note that in the drawn situation, the line is on the plane, however, lines can exist without planes (e.g., fold axis) and can be characterized without a plane measurement. Redrawn from Allmendinger et al. (2011).

Table 3.6. Description of the fields from the planes table

Field Name	Description
Measurement ID	Unique identifier of the measurement (Primary Key).
...	...
Measurement Determined By2	Geologist who performed the measurement.
Instrument ID2	Identifier of the instrument that made the measurement.
Formation2	Geological formation associated with the measurement.
Plane type1	Geological plane measured (e.g., cleavage, bedding, etc.)
Polarity1	Bedding upright, overturned, or vertical.
Plane dip	Maximum dip angle of the plane $[0° \leq 90°]$.
Azimuth	Azimuth direction of the dip in angle degrees, clockwise, from the north $[0° \leq 360°]$.

Table 3.7. Description of the fields from the lines table

Column	Description
Measurement ID	Unique identifier of the measurement (Primary Key).
...	...
Measurement Determined By2	Geologist who performed the measurement.
Instrument ID2	Identifier of the instrument that made the measurement.
Formation2	Geological formation associated with the measurement.
Trend	Azimuth direction of the dip in angle degrees clockwise, from the north [$0° \leq 90°$].
Plunge	The dip angle of the line [$0° \leq 360°$]
Fault movement sens	Motion associated with a shear criterion
Instrument	The instrument that performed the measure.

3.3.6 Samples

The description table of sample includes the unique identifier that is required for properly identify the sample. The sample is associated with a lithological description, a location and eventually a measurement. After filling this table with sample, analyzes or sections tables may refer to this table.

Table 3.8. Description of samples table

Field Name	Description
Material Sample ID	Unique identifier of the sample.
Location ID	Identifier of the associated location.
...	...
Sampling Date	Date of which the sample has been collected.
Sampling Determined By	Geologist who performed the sampling.
Sample type	Description of the type of sample.
First Sample Aim	First intended use for the sample.
Second Sample Aim	Second intended use for the sample.
Lithology Description	Description of the sample's facies.
Alteration Facies	Description of the sample's alteration.
Metamorphism Facies	Description of the sample's metamorphic facies.
Formation	Associated geological formation.
Plane type	Oriented plane of the sample.
Plane Orientation	Orientation of the plane use for orienting the sample.
Line type	Oriented line on the sample.
Line Orientation	Orientation of the line on the sample.
Sample Remarks	"Free field" for any supplementary comment.
Current storage	Location of the current storage of the sample.
Location on GIS	Code for GIS location.

3.3.7 Samples sections

The samples sections are the first step in the analyze of microstructural features. In this table, the type of section (thin, thick, etc.) is entered and refers to a sample. The section may oriented on the sample, this orientation is reported from the sample table. If the analyzes are performed on the section from the analyze table, they can be related the section.

Table 3.9. Description of sample sections table

Field Name	Description
Sample Section ID	Unique identifier of the sample section.
Location ID	Identifier of the associated location.
...	...
Sampling Date	Local date of the sampling.
Simple Lithology Description	Simple description of the sample's facies.
Detailed Lithology Description	Extended description of the sample.
Thin Section Orientation	Spatial orientation of the section.
Plane type	Plane used for orienting the sample.
Plane Orientation	Orientation of the plane.
Line Type	Type of line visible on the sample.
Line orientation	Orientation of the line on the sample.
Number of sections	Number of available sample section
Position on GIS	Code for display in GIS.

3.4 Display in a GIS

In structural geology, the change in scale is crucial, and geographical information systems (GIS) are powerful tools to display georeferenced data on various scales. In this work, we used the QGIS software (QGIS Development Team, 2023) to display geological data. The symbology was designed for the display of numerous structural data: To do so, we adapted the internationally approved symbology for geological maps, from Federal Geographic Data Committee (2006) (Fig. 3.5). The force of GIS is to allow the superimposition of data from different types (vectorized or rasterized), allowing one to display punctual structural data with a background map or orthophotos. GIS can also adapt the symbology according to the field values, making it possible to show the orientation of strike and dip measurements on a map. The symbology and syles used in QGIS during this work are provided in the data repository (see below).

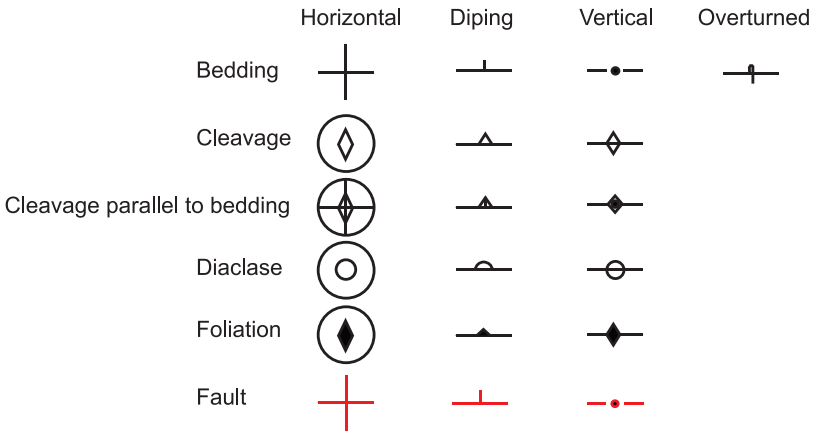

Figure 3.5. SVG symbols used for data display in a GIS, adapted from Federal Geographic Data Committee (2006).

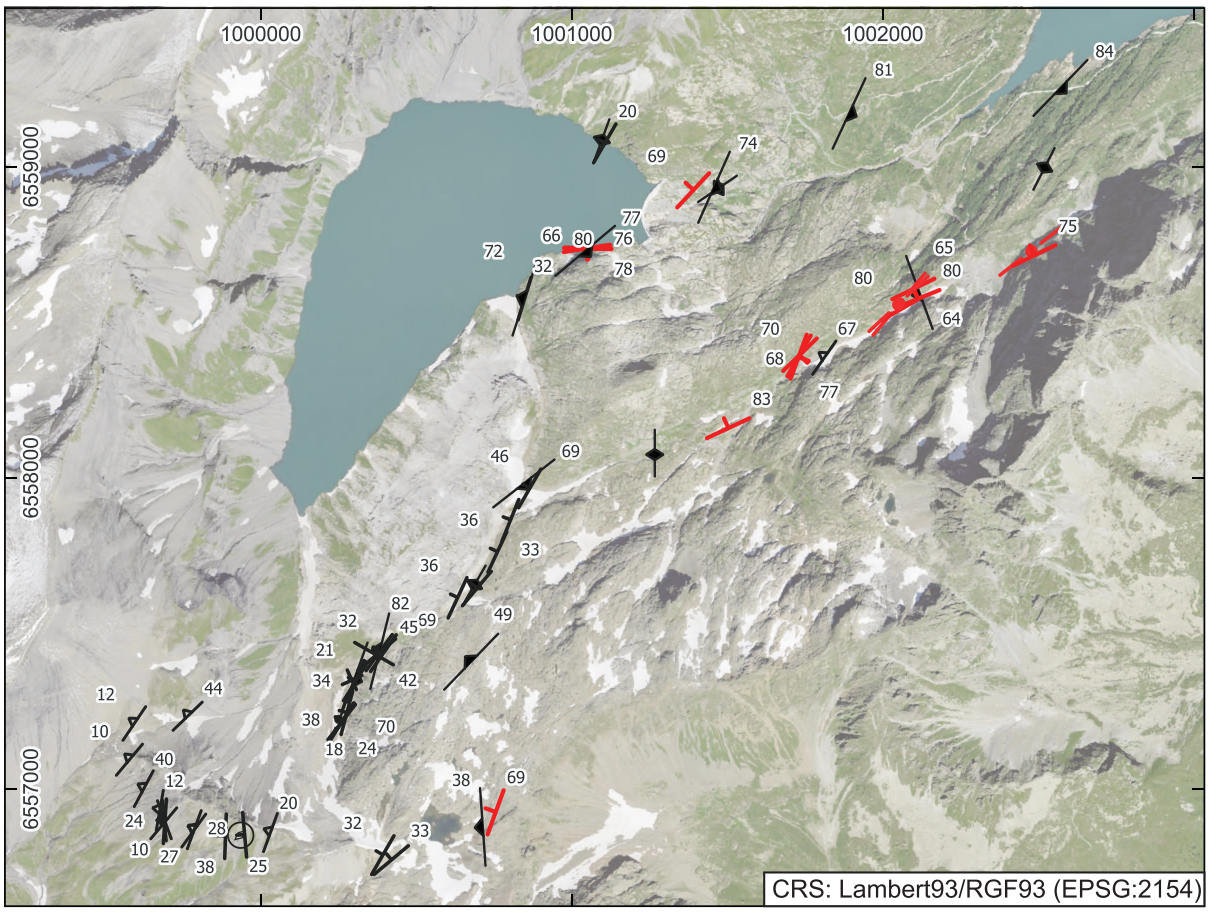

Figure 3.6. Example of plane measurements orientation display in QGIS in the Emosson area.

3.5 Data availability

Launch by the European Union in 2020, the FAIR principles describe how research data should be organized, so that it can be more easily accessed, understood, exchanged and reused by the scientific community. In line with this purpose and because this work has been fully funded by public research grants, all the data produced during this Ph.D. work are made available through trusted directories. We selected the Mendeley data repository because it is a free and secure cloud-based communal repository.

- Chapt. 4 (from 4.3 to 4.3.5): `https://data.mendeley.com/datasets/snx9zkrvts/1`
- Chapt. 4 (from 4.4): `https://data.mendeley.com/datasets/grjx9y4mwj/1`
- Chapt. 5: `https://data.mendeley.com/datasets/b9xh763rsh/1`
- Chapt. 6: `https://data.mendeley.com/datasets/4dn8v2r2fc/1`

Acknowledgments

This work was supported by the CNRS INSU. It forms part of the PhD project of Antoine Mercier at Université Claude Bernard Lyon 1, supported by the French Ministry of Research and Higher Education. The authors thank Emmanuel Robert for the discussion that greatly helped the design of DataGeol and the implementation of the international standards. We also thanks Grégory Salvignol for his help with the development of DataGeol on the OSUL servers and Andreas Christensen who developed the web interface of *DataGeol*.

Chapter's key points

- We designed a relational database for the storage and processing of structural geology data named *DataGeol*.
- Tables are standardized with vocabularies and standards that guarantee interoperability in the geoscience community.
- The database allows to organized the data to ease their export in different formats for display in a GIS or 3D geological models.
- *DataGeol* was used to organize geological data from the western Alps and was used in the building of a 65 x 63 km 3D geological model.
- The data set compiles data from other published data sets in the same area.
- *DataGeol* aims to serve as a template for the storage and diffusion of structural data in the geoscience community.

Chapter 4

Building a 3D geological model of a structurally complex Alpine region

Southern side of the Aiguille du Belvédère, the highest peak of the Aiguilles Rouges (2 965 m). Photogrammetric mosaic from drone surveying. Photo: Philippe Granjean, Antoine Mercier, and Philippe Hervé Leloup (2021).

Part of this chapter has been published in the *Tectonophysics* journal and is available in appendix F p. 441 with the following co-authors and reference:

Mercier, A., Leloup, P. H., Courrioux, G., Caritg, S., Lopez, S., Grandjean, P., Passot, S., and Kalifi, A. (2023). Large thrusting and late faulting shape the Aiguilles Rouges crystalline massif (Western Alps), structural implications. *Tectonophysics*, 847, 229691 doi:10.1016/j.tecto.2022.229691.

To avoid duplication, part of the introduction of the publication has been moved to Chapter 2 and the discussion and implications have been moved to Chapter 7 of the Ph.D. manuscript.

Abstract

We used 3D geological modeling in Mont-Blanc, Aiguilles Rouges, subalpine chains and helvetic nappes, to quantify their tectonic evolution and structural relationship. The 3D geological model was built using GeoModeller software which interpolates orientation and contact data with the cokrigeage algorithm. The model is 65 x 63 km, and includes 1500 measured structural data, 2 seismic profiles, 3 drill holes, 4 underground pipes, and even speleology data. The results of the structural analysis and 3D mapping highlight a thrusting of the mesozoic cover abvove the Mont-Blanc and Aiguilles Rouges crystalline massifs with a large thrust, often localized at the cover / basement interface (décollement), but that locally mylonitizes the basement. We highlight a change in the deformation style from the Morcles nappe to the subalpine nappe: the Morcles nappe is a large recumbend fold intensively sheared at its base, while in the south the deformation in the subalpine nappe is essentially in the cover / basement interface with a very efficient décollement. Later, the Helvetic nappes are deformed by the exhumation of the Mont-Blanc and the Aiguilles Rouges. In the Mont-Blanc, there is a large shear zone on the west side of the massif that seems to concentrate most of the deformation, whereas on the eastern side the deformation is more distributed along anastomosed shear zones. The Aiguilles Rouges are structured by a series of back thrusts.

Résumé

Nous appliquons une étude structurale avec de la modélisation géologique 3D au Mont-Blanc, Aiguilles Rouges, chaînes subalpines et nappes helvétiques, pour quantifier leur évolution tectonique et leurs relations structurales. Le modèle géologique 3D a été construit à l'aide du logiciel GeoModeller qui interpole les données d'orientation et de contact à l'aide de l'algorithme de cokrigeage. Le modèle mesure 65 x 63 km et comprend 1500 données structurales mesurées, 2 profils sismiques, 3 forages, 4 conduites souterraines et même des données spéléologiques. Les résultats de l'analyse structurale et de la cartographie 3D mettent en évidence un chevauchement de la couverture sédimentaire mésozoïque au-dessus des massifs cristallins du Mont-Blanc et des Aiguilles Rouges avec une localisation de la déformation à l'interface couverture / socle (décollement), mais qui, localement mylonitise localement le socle. Ces résultats suggèrent un changement dans le style de déformation entre la nappe de Morcles et la nappe subalpine : la nappe de Morcles correspondant un grand pli couché et intensément cisaillé à sa base, alors qu'au sud la déformation dans la nappe subalpine est essentiellement localisée à l'interface couverture / socle avec un niveau décollement plus efficace. Plus tardivement, les nappes helvétiques sont déformées par l'exhumation du Mont-Blanc et des Aiguilles Rouges. Dans le Mont-Blanc, c'est la zone de cisaillement ouest du massif qui semble concentrer la majeure partie de la déformation, alors qu'a l'est, la déformation est plus distribuée le long de zones de cisaillement anastomosées. De leur côté, les Aiguilles Rouges sont structurées par une série de rétro-chevauchements.

4.1 The move to the third dimension in structural geology

The main challenge in structural geology is related to the fact that the subsurface is not accessible by direct observation and surface observations are often local; however, geologists want to unravel the geology at all locations. Usually, surface data are "manually" interpolated into cross sections from field orientation measurements. Similarly, a drill hole allows the retrieval of rocks at a depth of one dimension, and a seismic profile allows the recognition of geological features in 2D. This approach may be sufficient when geology is simple and cylindrical and when data are acquired regularly along sections. However, geological data are often sparse and irregularly distributed within the study area and simple interpolation of surface data into sections is not sufficient.

To address this problem, since the 1990s, the advancement of numerical computation with geostatistics has revolutionized structural geology by introducing 3D modeling techniques that provide a more accurate and detailed representation of geological features (e.g., Mallet, 1992; Lajaunie et al., 1997; Calcagno et al., 2008). The stratigraphical approach used in GeoModeller simulates the subsurface with successive strata belonging to the same unit. Significant and coherent 3D models have been constructed using a geostatistical method using both interface locations and structural orientation data. Since then, the usefulness of 3D geometric models to better understand geology has become well established (e.g., Strzerzynski et al., 2005; Marquer et al., 2006; Campani et al., 2014; Marconato et al., 2021; Thornton et al., 2018).

In very complex structural areas such as the western Alps, the use of 3D geological modeling is seldom (Thornton et al., 2018), while it seems to be a requirement to properly visualize the 3D variations of the structures in space. This work examines the 3D geological geometry of a structurally complex and debated alpine region: the Mont-Blanc and Aiguilles Rouges massifs.

Here, we present a detailed 3D structural study of the cover / basement relationships in the Aiguilles Rouges and Mont-Blanc external crystalline massifs of the western Alps. We will also describe the deformation in the Helvetic nappe and subalpines chains of Morcles, Haut-Giffre, Aravis, and bornes. This work is based on novel field observations and measurements used in a 3D geological model, allowing one to investigate the 3D evolution of the structures.

Organization of the chapter During this Ph.D. work, three 3D GeoModels encompassing different zones were performed in the area: the largest encompasses the whole Mont-Blanc massif, Aiguilles Rouges, Morcles, Haut-Giffre, Platé, Bornes and Aravis. The following sections will detail this methodology, the conceptualization of the model, and the data used in this model. The two smaller models are concentrated in the Chamonix synclinorium, in the tight zone of Mesozoic sediments between the Mont-Blanc and Aiguilles Rouges. The two smaller

models and structural studies have been published in the *Tectonophysics* journal and will be presented in section 4.3 p. 132. The published manuscript is available in the appendix F, p. 441.

4.1.1 Geostatistical and historical background

The birth of 3D geological modeling began with Mallet (1992), they designed the first software able to interpolate geological surfaces in 3D: GOCAD. From there, the development of 3D geological modeling is mainly based on the same philosophy: the interpolation of surfaces from known positions and orientations of the geological surfaces. From this statement, several interpolation methods have been designed. The variety of methods used in 3D Geo-Modeling comes from the choice in the interpolation function. Basically, there are two main methods that are often used: the geostatistical method and the radial base method. **The radial base method** performs the interpolation using a radial base function (e.g., Carr et al., 2001), which interpolates the surfaces by computing a field defined with algebraic distances. The advantage of this method is that they are optimized for algorithms and are economical in computing resources. For example, this is the interpolation function used in Leapfrog software (Cowan et al., 2002). The geostatistical method was initially developed by Lajaunie et al. (1997), and is based on cokrigeage interpolation (Matheron, 1963) using covariance functions. This is the method used in GeoModeller (Calcagno et al., 2008) or GemPy (Varga et al., 2019). The innovation of this method is the distinct consideration of the points that define the surface location and orientation data during interpolation. The mathematics is of high complexity, so to still assess the method, the interpolation we can be summarized as follows: F the scalar field interpolated, n is the number of data, t is the position of the data, λ_i a weight and p the point of the scalar field.

$$F(p) = \sum_{i}^{n} \lambda_i \, Cov(t_n, p) \tag{4.1}$$

4.1.2 3D geological modeling

Classically, the geometry of the geological structure deduced from observations at the surface and at depth is depicted through surface mapping and vertical cross-sections. When numerous cross-sections are performed, a relatively precise idea of the 3D geometry can be given. However, the cross-sections are only 2D projected representations of the surrounding data, and the original 3D data position, orientation, and uncertainty are lost. The 3D geomodeling does not interpolate the interpreted cross sections, but consider each point of observation and measurement independently in the 3D space. Furthermore, the model is not only geometric, but interpolates the data onto 3D surfaces considering the geological rules:

- **Superposition**: The layers of rocks on top are younger than those deposited below.
- **Horizontality**: Layer beds are deposited subhorizontally and maybe later deformed.
- **Continuity**: Layer beds are continuous laterally and may be broken or displaced by faults.
- **Cross-cutting**: Older features are cut across by younger features.
- **Actualism (Uniformitarianism)**: This hypothesis assumes that the physical principles and natural processes that operate today operated in the same way as they did in the past.

Building a geological model from these rules implies that (i) the stratigraphic sequence is known, (ii) folds that could overturn the pile are known and characterized, and (iii) accidents (faults) are known and mapped. These geological rules and concepts are always implicitly taken into account when building a geological model, however, in a structurally complex area it is challenging to interpolate properly the structures laterally and at depth. Moreover, the presentation of results is also not easy when it involves several stratigraphic formations and faults. Numerical geological modeling has been developed from this statement.

4.1.3 Geographical extent

Three distinct geological models have been performed in the area:

Mont-Blanc 3D GeoModel the model largest encompasses a geographical extent of 63 x 65 km comprising the Mont-Blanc massif, Aiguilles Rouges, Morcles, Haut-Giffre, Dents Blanches, Platé, Bornes, Aravis and north of Beaufortain (Figs. 4.1 and 4.5).

Argentière 3D GeoModel a smaller 3D geological model is focused in the Chamonic Synclinorium between the Aiguilles Rouges and the Mont-Blanc massif, this model encompasses a 14.3 x 20.3 km zone. This model will be detailed in the section 4.3.3.2.

Posettes 3D GeoModel To better characterize the precise geometry of the synclinorium in its central part, we performed a smaller geomodel that allows a more detailed visualization of the synclinorium. This model will be detailed in the section 4.3.3.2.

4.2 Data and methods

As discussed before, the geostatistical method considers separately the **contacts** that define the position of a surface and the **orientations** that characterize the direction of the dip and

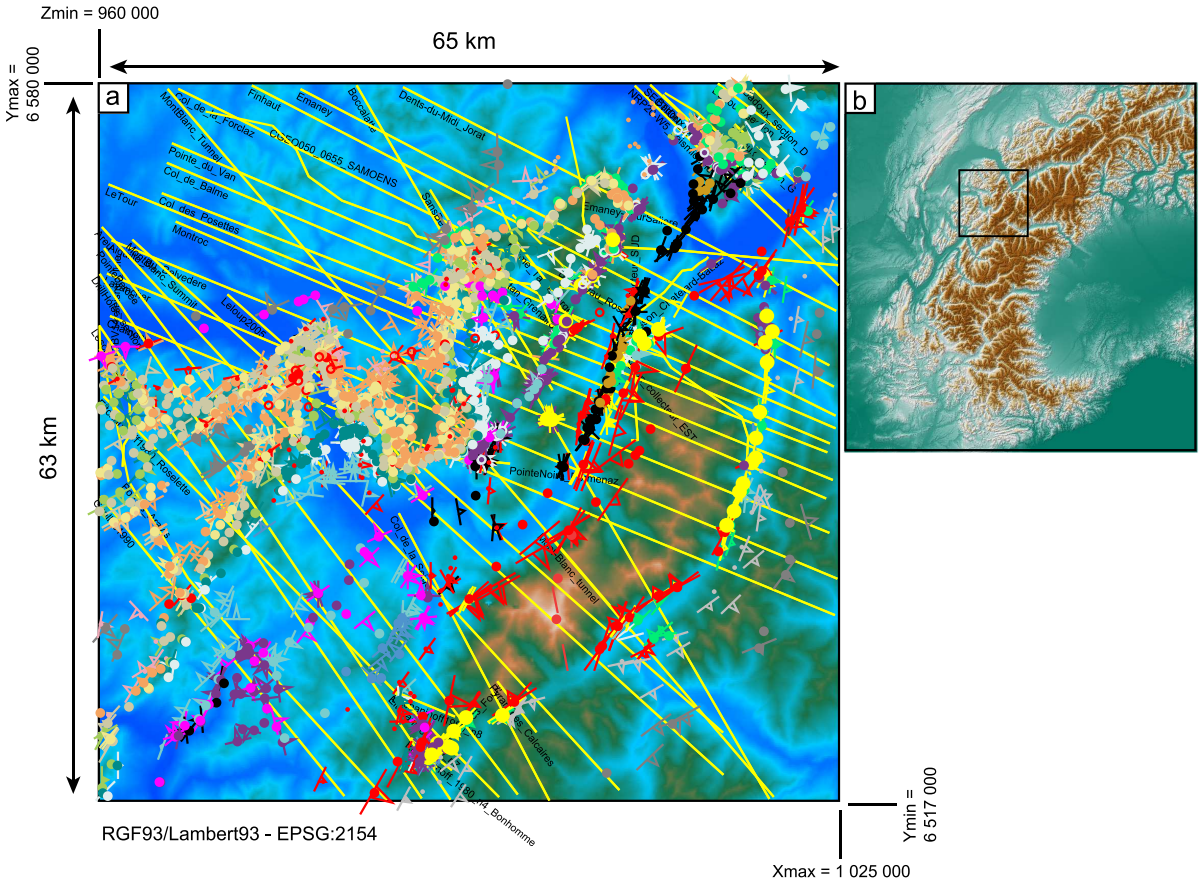

Figure 4.1. GeoModel extent in geographic coordinates (in meters) in the RGF93 reference ellipsoid and Lambert93 projection system (EPSG:2154).

the polarity of the surface.

Structural data From field observations, it is possible to define the location of the base (or top) of a defined geological unit. For instance, the bottom of the Triassic unconformity can be followed continuously and characterized with a discrete surface. An outcrop where the two units are normally joint is said to be a **contact**. The orientations of the surfaces are given by the dip measurement and the polarity: overturned or normal. A total of 20 field missions have been performed in the area, from 1996 to 2022, (of which 10 during this Ph.D.), and dip measurements have been made using professional geological compasses. A database was specifically designed for the storage and processing of structural geology data: *DataGeol*. The structural data are manually inserted by the user and are exported for GIS or GeoModeller (see Chapter 3 for details). The structural data were not imported all at once into the model, but one by one to check the relevance of each data. 1 569 orientation data were used from field observation in the GeoModel.

Published geological maps and cross sections The Mont-Blanc area is widely covered by geological maps and studies (Table 4.1), although these maps yield a model resulting from the interpolation of observed data, extracting data from these maps is not straightforward. First, in some maps, the dip measurements performed on the field are reported on the map, which allows us to use the measurements directly as inputs in the model. Second, the indication of the contact between two geological formations can be used as contact data in the model.

Seismic profiles Two seismic profiles run through the Mont-Blanc area, in the North, the NRP-20 profile goes through the Rhône valley. In the South, along the Bornes-Aravis massifs, runs the ECORS-Crop seismic line is located.

Bore holes In the 1980s, oil companies drilled the Subalpine chains with bore holes. Three are within the study area: LBL-1, FAY-1, and BZN-1. The BZN-1, drilled by the EURAFRED company near the village of Brizon, is the deepest, reaching the Triassic sandstones at a depth of -3075 mTVD (below the reference ellipsoid), giving constraint for the Triassic unconformity at depth. The particularity of this well bore is that it encountered the Tithonian limestones three times and they are limited by faults, indicating the thrusting of this unit. Esso-Rep drilled the FAY-1 well-bore through the Prealpine klippe, near the village of Faucigny. Again, drilling reached the Triassic sandstones at a depth of -3814 mTVD. The third well (LBL-1), performed by EURAFREP in the Arve Valley, goes no further than the Tithonian limestones at a depth of -1389 mTVD.

Speleology Speleologists have explored and monitored the extensive tunnel network in the Haut-Giffre massif. The Geologist from the Vulcain group of speleology (Xavier Robert) kindly provided us the contacts points between stratigraphical formations within the tunnels, giving us the opportunity to have constraints in the 3D GeoModel at depth (Fig. 4.2).

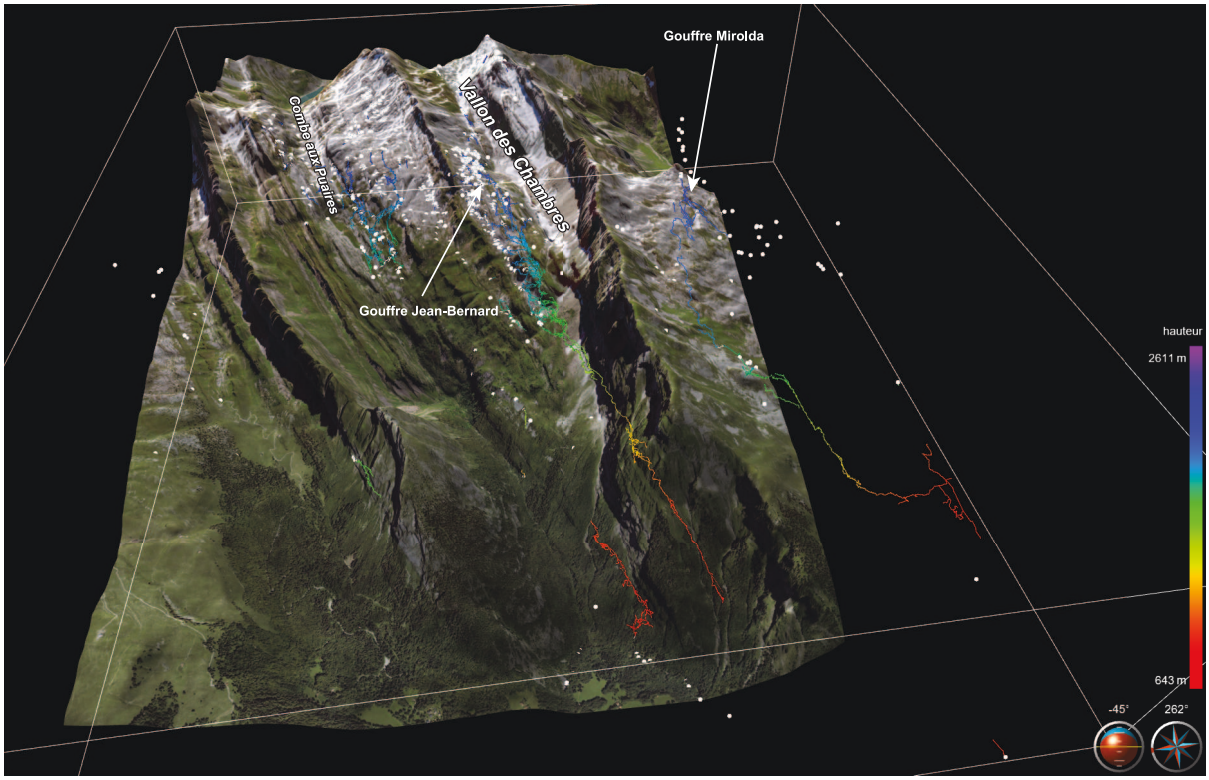

Figure 4.2. Karst system of the Folly massif. 3D view available in this link. From Xavier ROBERT, G.S. Vulcain, ©Creative Commons.

Underground pipes The water flowing from the Mont-Blanc glaciers is used to produce electricity. The EDF and Emosson-SA companies are exploiting together this resource and have kindly accepted to give us access to the geological survey along the penstock galleries running through the massif. See figure 4.27 for the locations of the pipes. All three pipes arrive at or exit the hydroelectric power plant in Le Châtelard, near the France-Switzerland border. The first pipe (*Collecteur sud*) runs from the Argentière glacier, where it collects water, to the south until the Châtelard station and climbs to the Emosson dam. This pipe crosses the Mont-Blanc shear zone, the Col de Balme, Les osettes, and Permo-Carboniferous syncline. The second tube runs from Chatleard station to Foully village in Switzerland on the eastern side of Mont-Blanc (*Collecteur est*). This pipe goes through the Permo-Carboniferous syncline, Les Posettes, the Mont-Blanc shear zone, and the Mont-Blanc granites. Finally, the third pipe runs from Châtelard station to La Bâtiaz in the Rhône valley (*Collecteur nord*), crossing along-strike the Permo-Carboniferous syncline.

Table 4.1. Summary of the data incorporated to the 3D geological model

Data type	Source
Geological maps	Finhaut (n°24) Collet et al. (1952)
	Mont-Blanc (n°704)Antoine et al. (1979)
	Cluses (n°679)Pairis et al. (1992)
	Saint-Gervais (n°703) Mennessier et al. (1977)
	Haute-Savoie Pfiffner et al. (2011)
	Annecy - Ugine (n°702) Doudoux et al. (1992)
	Chamonix (n°680) Ayrton et al. (1987)
	Sembrancher (n°77) Burri et al. (1983)
	Samoëns (n°655) Plancherel et al. (1998)
	Dent de Morcles (n°58) Badoux et al. (1971)
	Amberger (1959)
Seismic profiles	NRP20: Pfiffner (1993)
	ECORS: Guellec et al. (1990)
Drill-holes	LBL-1
	BRZ-1
	FAY-1
Underground pipes	Châtelard - Bâtiaz (10 900 m)
	Châtelard - La Fouly (18 000m)
	Châtelard - Argentière glacier (10 200m)

4.2.1 Stratigraphic pile

A relative chronology must be defined for the formations within the series to satisfy the geological concept of superposition. Furthermore, a relationship between the series that are not parallel to each other must be defined: *erode* if the series cross-cuts the oldest ones and **onlap** if it does not. These rules can be summarized as follows (Calcagno et al., 2008):

- The interfaces of geological formations having sub-parallel behaviors are grouped together into series.
- A chronology defines the time order of series within the model.
- A relationship is defined for each series to drive its behavior with respect to the chronologically older ones:
  - *Erod* allows a series to truncate older series.
  - *Onlap* enables the series to be present on top of older series, without changing the geometry of older series.

4.2.1.1 Pseudo-series

We stated that the interpolation of surfaces follows the principles of horizontality and continuity. Now, the superposition and cross-cutting principles must be parametrized to build the model properly. The timing of deposition of the geological units is defined by the **stratigraphic pile**, composed of **formations** and **series**. A formation is a geological unit that can be clearly distinguished in the field. When formations are nearly parallel, they can be grouped together into a **series**, and one scalar field is used to model a series. Practically, this means that the thickness is globally constant within the formations in the series. If the formations are not parallel, it is necessary to use a different scalar field for each formation and therefore split them into different series.

Because our model is in a very complex structural area, the usual schema using formation and series is difficult to achieve. Indeed, the formations that are supposed to be parallel and grouped together in a series have, in reality, strong thickness variations due to the intense deformation that affected them. At first sight, a nappe could be considered as a fault plane, but in geological modeling, a fault is defined as a discrete plane that offsets formations and requires data constraints from both sides of the fault. In the case of thrust nappes, this requirement is complicated to achieve, mainly because the root of the nappes could be outside the model box or because the wall of the nappe is another nappe itself. To overcome this issue, nappes are defined by different series. For example, we determined the Upper Jurassic from the Morcles Nappe and separately the Upper Jurassic from the Subalpine nappe. For consistency, all formations corresponding to the same stratigraphic age are colored the same according to their official age for display. However, their potential fields are separated and computed differently depending on the nappe series to which they belong. Since the deformation propagates westward, the youngest nappe is therefore the lowest and the older the highest. Within a nappe thrust, the formations are deformed and subject to strong thickness variations but still roughly parallel: for example, the orientation of the Urgonian limestones in the Morcles nappe follows roughly the orientation of the Hauterivian limestones from the same nappe. To keep this information in the modeling, we applied external constraints, using the orientations of the other formations belonging to the same nappe. In summary, a pseudo-series is built when each formation is modeled with its own potential field, but also taking into account the constraints from the neighborhood formations. Consequently, all series must have orientation and contacts from each partition defined by faults, which increase considerably the complexity of the model and the number of data required.

Description of the stratigraphic pile of the model The pre-Triassic basement of the massif is composed of polymetamorphic gneiss and migmatites that are not differentiated in the model. The crystalline basement is overlaid by the carboniferous unconformity and above the Permian

sediments. The post-Varsican granites are intrusive into the polymetamorphic basement. The Mesozoic sequence starts with the Triassic unconformity, which is materialized by the famous sandstones with reptile footprints in the Vieux Emosson area. On the eastern side of Mont-Blanc (e.g., Bonhomme area, Dalle de l'Amone, Champex) the Triassic is topped by the Liassic "grès singuliers". These two formations that start the Mesozoic are the only autochthonous formations of the model.

Figure 4.3. Geological pile for the 3D geological model of the Mont-Blanc and Aiguilles Rouges massifs. From bottom to top: the pre-Triassic basement is composed of polymetamorphic variscan rocks, Carboniferous/Permian sediments, and intrusive granites. The autochthonous cover is composed of Triassic and Liassic sediments. The overlying sediments are all allochthonous and are part of three main nappes (Basal, Morcles, Subalpine): the Helvetic Nappe System. These nappes are themself topped by the Ultra-Helvetic Nappes system and the Penninic Nappes system.

4.2.2 Workflow

Observations and data are acquired in the field, a conceptual structural model is developed based on assumptions and geological knowledge of the area, the model is parameterized (stratigraphic pile, faults, model extent, etc.) according to the initial conceptual model. Af-

ter the computation and the interpolation of surfaces, the geometrical model can be visualized and evaluated in comparison with the conceptual structural model. As a consequence, the parameterization may change or new data may be acquired to reduce the difference between the conceptual model and the geometrical model and then approximate the reality. It may be noted that the conceptual model can also evolve after the computation of the geometrical model.

This process is not limited to a simple representation of reality, but works back and forth during the building of a geometrical model: the starting assumptions may evolve, for example, the stratigraphic pile defined can change according to new considerations of geological formations or the attribution of a measurement. The geological principles enumerated above must be respected and may affect the concepts stated initially. Similarly, the data acquisition strategy can be driven by geological modeling to fill gaps in data coverage. Finally, 3D geological modeling differs from classical mapping and cross sections: The output result has to be seen as a step in the geological understanding process of a region.

4.2.3 Model resolution and complexity

Regarding the geological complexity of an area, simplification of the reality is necessary. This simplification is driven by the choices the geologist makes in the model design or in the stratigraphic pile definition. For example, one can merge stratigraphic units in the pile even if they are distinguishable in the field but too thin to be modeled adequately or irrelevant for the model's interpretation. Similarly, faults, which are often complex damage zones in reality, are simplified into a discrete plane in modelling. From the data itself, the dip measurements are necessarily chosen according to the complexity of the model. For example, folded bedding with a kilometer-scale bend radius may have smaller-scale microfolds, and a dip measurement from one of these microfolds can dip in the opposite direction from the regional fold and then is irrelevant for the modelling, These choices of data and stratigraphic pile depend on the *geological resolution* of the modelling and are at the discretion of the modeller.

4.2.4 Quantification of errors in the data

Erros may come from different sources. **Measurement errors** depends on the tool used to perform the measurement: with a professional geological compass (e.g., Freiberger, Topochaix, etc.), such as the one used to perform our measurement, the measurement error is close to 1° when measuring on a perfectly flat surface. However, when using a pad or a smartphone, the related measurement error can vary considerably and thus is more difficult to estimate. The second type of error is related to the attribution of an observation in the field to a specific formation defined in the model. This error is related to the interpretation of the geologist and is very hard to evaluate. To attenuate the effects of such errors and make a smoother

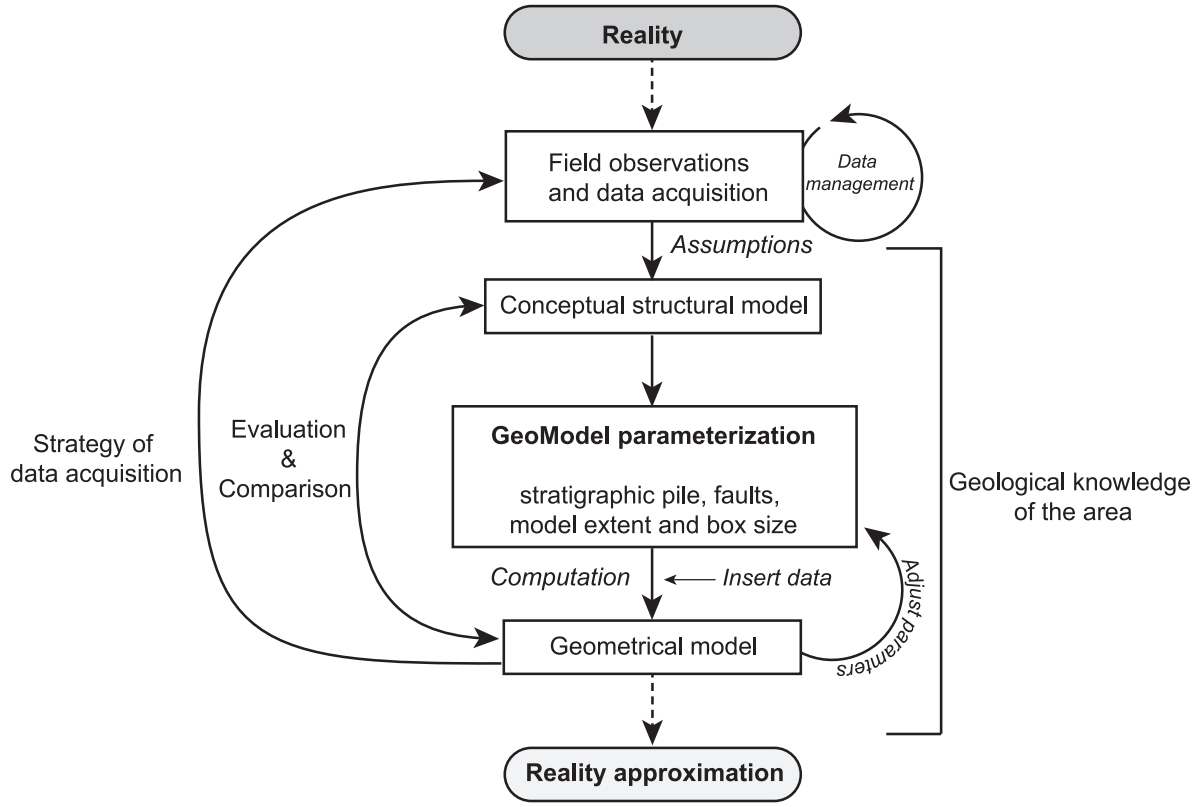

Figure 4.4. Workflow followed to build the 3D geological model. The objective is to describe and characterize reality. To do so, field observation and data are acquired in the field, a conceptual structural model is developed based on assumptions and geological knowledge of the area. The model can be parameterized (stratigraphic pile, faults, model extent, etc.) according to the initial conceptual model. After the computation and the interpolation of surfaces, the geometrical model can be visualized and evaluated in comparison with the conceptual structural model. In consequence, the parameterization may change, or new data may be acquired to reduce the difference between the conceptual model and the geometrical model and then approximate the reality. It may be noted that the conceptual model can evolve as well after the computation of the geometrical model. Adapted from Wellmann and Caumon (2018).

model,Lajaunie et al. (1997) included an attenuation parameter in the interpolation: known as the **nugget effect** (*effect pépite*).

The presented model has very tight overturned folds, especially within the Morcles Nappe. Therefore, we attenuated the nugget effect in Morcles Nappe and Subalpine series from 10^{-2} to 10^{-3} for the orientation data; and from 10^{-6} to 10^{-7} for the geology contacts. This change reduces the flexibility of the interpolation and force the surfaces to follow the constraints data more sharply. On the other hand, interpolation requires more constraints to properly build the surfaces and increase the complexity.

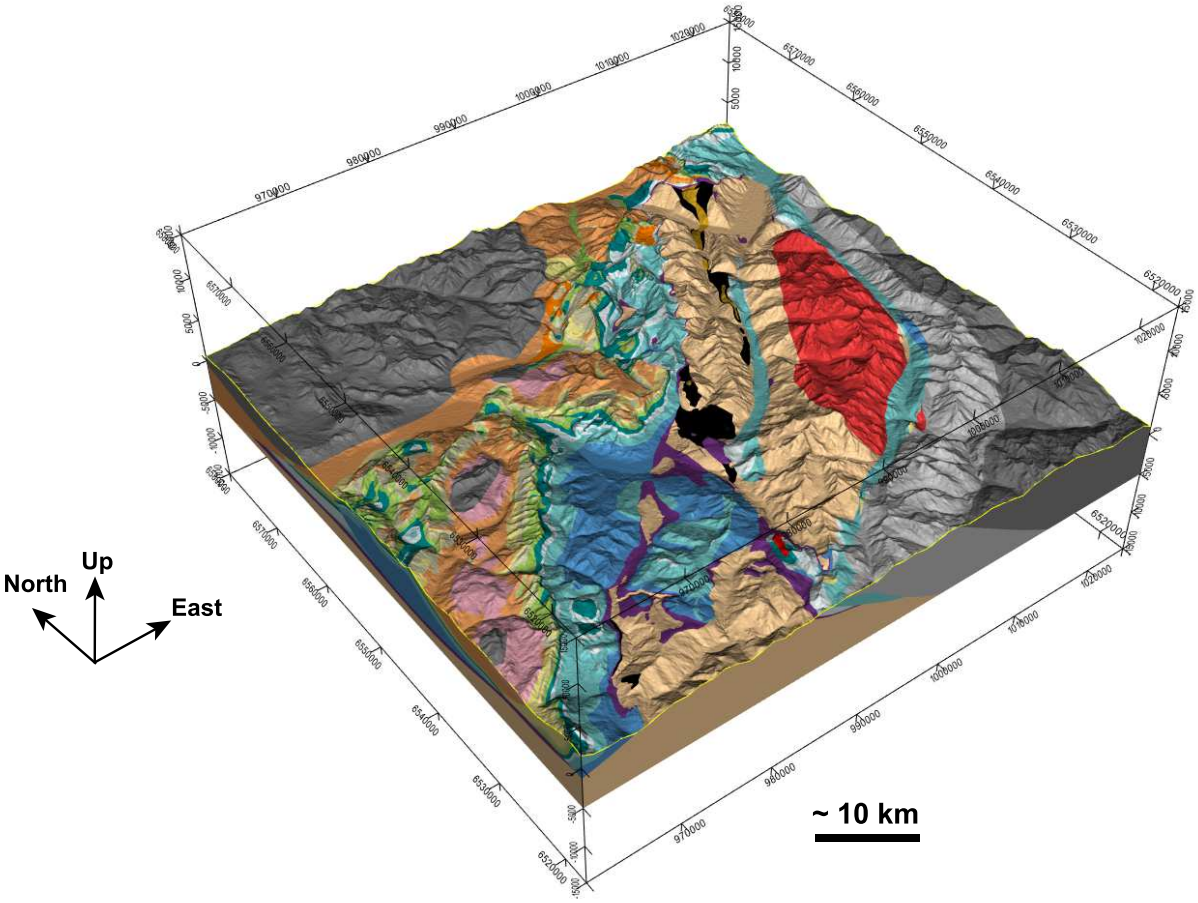

Figure 4.5. Overview of the 3D geological model. The model encompasses a geographical extent of 63 x 65 km, comprising the Mont-Blanc, the Aiguilles Rouges, the Morcles, the Haut-Giffre, Platé, Bornes, and Aravis massifs.

4.3 Large thrusting and late faulting shape the Aiguilles Rouges crystalline massif

In this section, we will describe the issues related to the Chamonix synclinorium between the Mont-Blanc and Aiguilles Rouges massifs. The results presented here have been published in the *Tectonophysics* journal with the following coauthors and referencing:

Mercier, A., Leloup, P. H., Courrioux, G., Caritg, S., Lopez, S., Grandjean, P., Passot, S., and Kalifi, A. (2023). Large thrusting and late faulting shape the Aiguilles Rouges crystalline massif (Western Alps), structural implications. *Tectonophysics*, 847, 229691, doi: 10.1016/j.tecto.2022.229691.

For clarity, the manuscript of the original publication has been partly truncated: part of the introduction has been moved in Chapter 2 and the implications regarding the evolution of Mont-Blanc and Aiguilles Rouges have been moved in the synthesis and discussion in Chapter 7. The original manuscript is available in the appendix F, p. 441.

4.3.1 Introduction

Two completely different views are proposed in the external domain of the Western Alps. For most authors, the current geometry is the result of the intense folding of the Mesozoic sedimentary cover, originally deposited in half grabens, together with the basement in a ductile basement fold nappe (e.g., Escher et al., 1993). In this case, the geometry of the half grabens guides later deformation(s), and the cover is considered para-autochthonous because horizontal displacements are moderate (e.g., Escher et al., 1993; Burkhard and Sommaruga, 1998; Bellahsen et al., 2014). Alternatively, it is proposed that the Mesozoic cover is significantly displaced to the west above a thrust: the Helvetic Basal Thrust (HBT) (e.g., Leloup et al., 2005; Pfiffner, 2014).

The existence and kinematics of such a thrust are important not only for the understanding of the regional geology but also have implications on a) the estimate of total shortening in the external Alps; b) the timing and mechanism of uplift of the external ranges; c) the timing and mechanism of folding within the Subalpine chains; d) the way shortening is absorbed in a layered media with contrasting rheology (sedimentary cover vs. basement); e) the influence of the initial geometry (paleo-topography: horst and grabens) on the deformation style. Here, we present a detailed 3D structural study of the cover/basement relationships in the Chamonix synclinorium between the Mont-Blanc and Aiguilles Rouges ranges. These field observations are the key to characterizing the deformation within the orogenic wedge and thus discussing the

outcome of the rheological models (e.g., Spitz et al., 2020; Bauville and Schmalholz, 2015).

4.3.2 Geological Setting

The Western Alps are an accretionary wedge resulting from the Cenozoic convergence between Europe and the continental margins of Apulia. The anterior subduction of the ocean started during the mid-Cretaceous and led to the collision in the Paleogene. The wedge is split into two parts: the internal domain containing ophiolites and rocks that have been deformed at high temperature and/or deeply subducted during the Alpine orogeny, and the external domain where the Alpine metamorphism is limited to green-schist facies (e.g., Bousquet et al., 2004). The internal domain is thrust above the external one along the west-verging Penninic thrust, with the Prealps being interpreted as a klippe of the internal domain (e.g., Mosar, 1989) (Fig. 4.6). This interpretation implies at least 95 km of thrust to the NW above the Penninic thrust, which has later been folded upward to expose a window of the external domain in the Mont-Blanc/Aiguilles Rouges area (Fig. 4.6). Motion in the Penninic thrust was associated with sedimentation of flysch deposits in a flexural basin during the Upper Eocene/Lower Oligocene (e.g., Homewood, 1983; Ruffini et al., 1997) and ended at ≈30 Ma (e.g., Pfiffner et al., 2002).

The external domain exposes both basement ridges, the external crystalline massifs, and their folded sedimentary cover (Fig. 1). The basement consists of Variscan (> 300Ma) metamorphic gneisses, granites, and Carboniferous/Permian sedimentary rocks. The overlying sedimentary cover spans in age from the Triassic to the Miocene. The external crystalline massifs straddle for 330 km along the belt from the Aar to the Ecrins and form slivers separated by sedimentary rocks (Fig. 4.6) that have been interpreted as paleohorsts inherited from Mesozoic rifting (e.g., Lemoine and Tricart, 1986), crustal culminations above thrust ramps (e.g., Lacassin et al., 1990; Menard and Thouvenot, 1987; Pfiffner et al., 1997), anticline cores (e.g., Escher et al., 1993), or a combination of those. The sedimentary cover is folded and locally forms the Helvetic Nappes whose extent, geometry, and timing are still discussed.

The Mont-Blanc and Aiguilles Rouges ranges are two NE-SW trending external crystalline massifs separated by a narrow structure filled with Mesozoic sediments: the so-called Chamonix synclinorium, trending N030° (Fig. 4.6). From the early 1920s, it has been suggested that the Chamonix synclinorium corresponds to the root of the Morcles Nappe, the lowest of the Helvetic nappes (Collet and Paréjas, 1920; Paréjas, 1922; Eltchaninoff, 1982; Butler, 1985). However, thrusting at the bottom of the Morcles Nappe has been minimized or even denied. For example, Ayrton (1980) proposes that the synclinorium is the contact zone between the autochthonous sedimentary cover of the Mont-Blanc and that of the Aiguilles Rouges. Several authors propose that the Morcles Nappe is para-autochthonous, being the reverse limb of a buckle anticline, whose core consists of the folded basement (the so-called

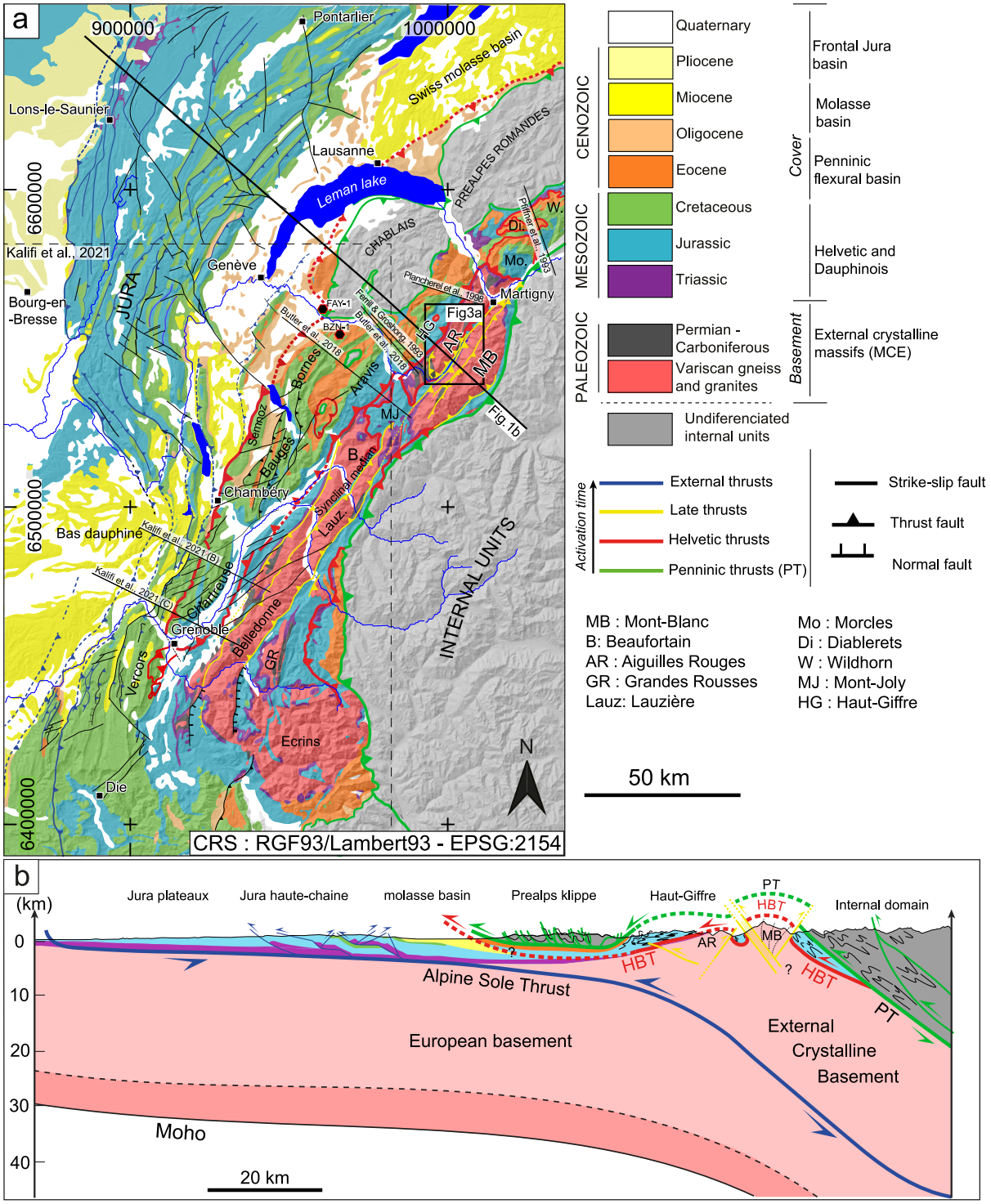

Figure 4.6. Structural frame of the western Alps. a) Structural map with the main thrust systems: Penninic thrust, Helvetic thrust, Basal Sole Thrust, and late thrusts. The black frame corresponds to the location of Fig. 3a. Location of cross-sections that are discussed in the text is indicated with the reference therein (Plancherel et al., 1998; Butler et al., 2018; Kalifi et al., 2021). b) Synthetic cross-section of the Western Alps. The crustal structure is from Lacassin et al. (1990) and Pfiffner et al. (1997), the Jura deformation from Affolter (2004) and Affolter et al. (2008), the structure of the Prealps klippe is from Mosar (1989), the structure of the Aiguilles Rouges and Mont-Blanc area is from this study, and Leloup et al. (2005); the structure in the internal domain is from Ceriani et al. (2001). The cros-section trace is shown in the map (a).

external Mont-Blanc) and the periphery of cover rocks expulsed from a Mesozoic Half-graben (Ramsay, 1981; Epard, 1986; Escher et al., 1993; Burkhard and Sommaruga, 1998; Egli and Mancktelow, 2013; Bellahsen et al., 2014) (Fig. 4.7a).

Alternatively, a two-phase scenario has been proposed, with the first thrust toward the NW of most of the cover and part of the basement; and second exhumation of Mont-Blanc along the steep reverse Mont-Blanc shear zone and doming of the Aiguilles Rouges above a deeper thrust (Leloup et al., 2005) (Fig. 4.7b).

However, others consider that the linear shape of the Chamonix Synclinorium and of the Mont-Blanc range is partly due to the right-lateral strike-slip faulting along the Simplon Rhône fault system (Gourlay and Ricou, 1983; Hubbard and Mancktelow, 1992; Seward and Mancktelow, 1994) connected to the Simplon low-angle detachment fault that was active between ≈8.5 and 4 Ma (Campani et al., 2010).

In the Northwestern Alps, instrumental earthquakes are best explained by a strike-slip stress state with σ_1 trending WNW-ESE (Fréchet et al., 2010). The most significant instrumental earthquake in the Aiguilles Rouges area was the Mw 4.5 Vallorcine earthquake (8 September 2005) that activated the N060° trending right-lateral Gros-Nol fault (Fréchet et al., 2010) (Fig. 4.8 a). This fault is oblique to the Chamonix synclinorium that trends ≈N030°.

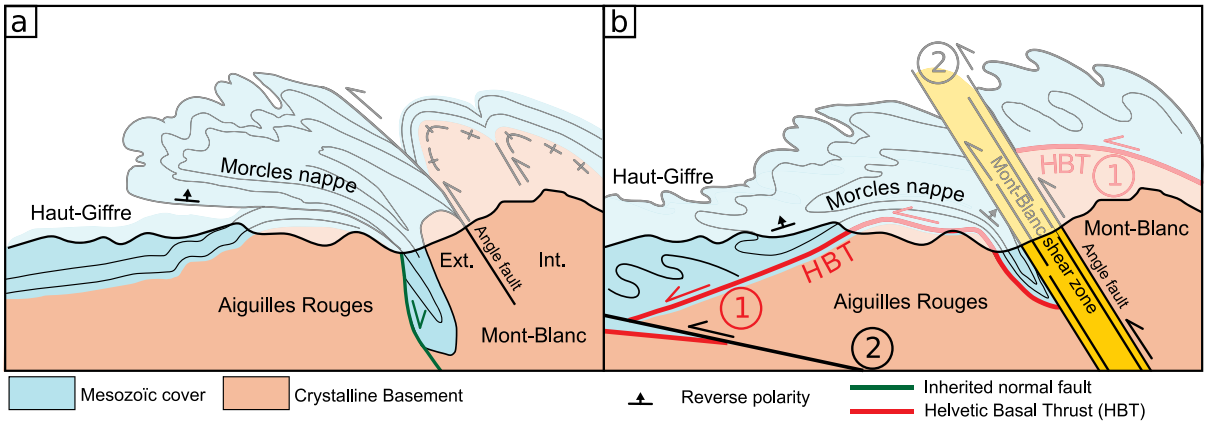

Figure 4.7. Contrasting models for Alpine deformation of the external crystalline massifs and their cover, as exemplified in the Aiguilles Rouges and Mont-Blanc massifs. a) One-stage folding of a thick sedimentary series located within half grabens, resulting in parautochthonous folds (basement fold nappe). The external Mont-Blanc basement (Ext.) is tightly folded and the normal limb of the cover roots in the Angle Fault (e.g., Escher et al., 1988; Escher et al., 1993). b) Two stages of deformation model. 1st stage: Thrusting (mostly décollement of the cover with respect to the basement) toward the west. 2nd stage: offset of the thrust level by a reverse shear zone (Mont-Blanc shear zone) and updoming of the Aiguilles Rouges (e.g., Leloup et al., 2005).

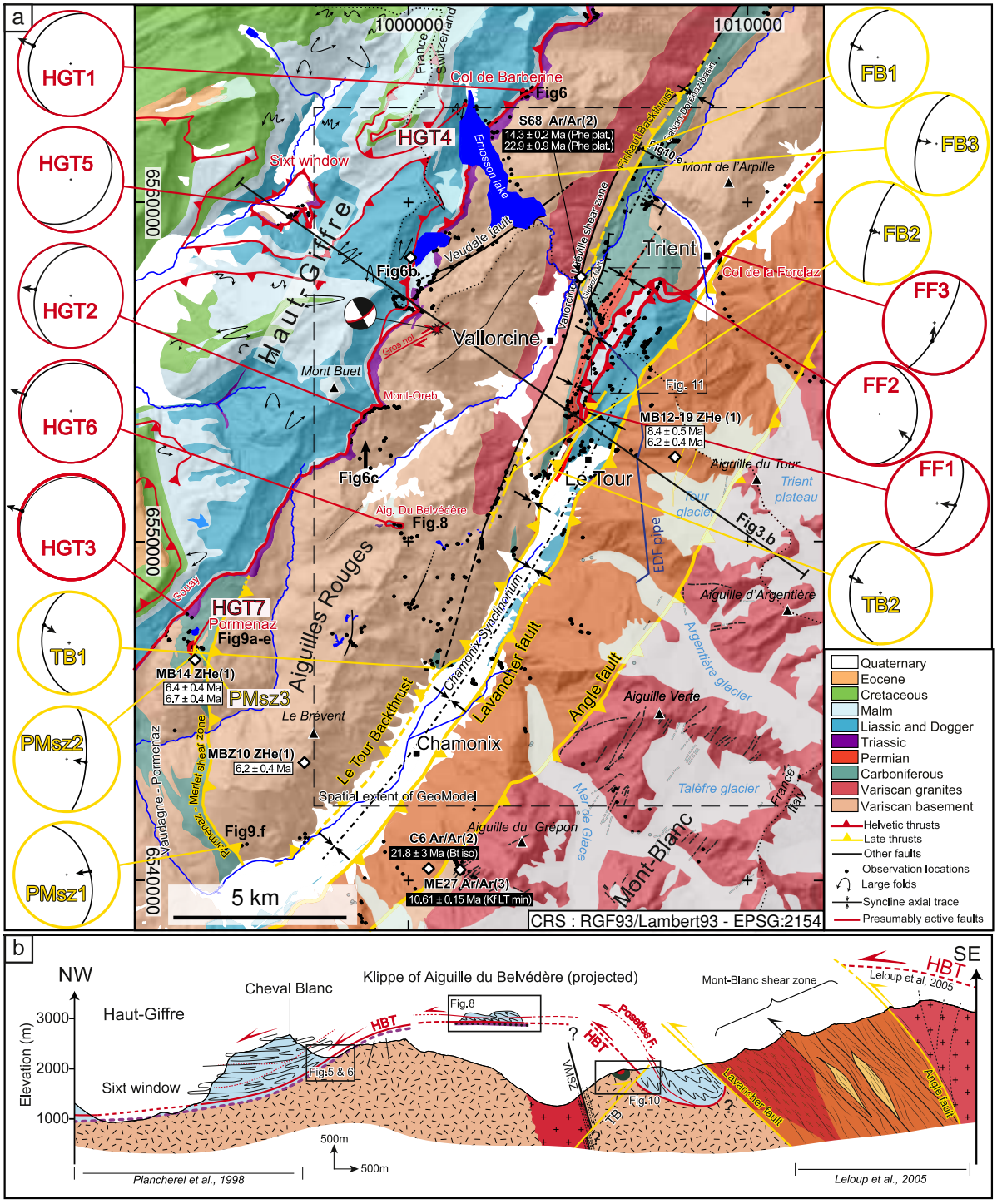

(Figure caption on next page)

Figure 4.8. Structure of the Chamonix Synclinorium. a) Structural map. Location in Fig. 1a. The structure of the Haut-Giffre cover is from Pfiffner et al. (2011). HGTx, TBx, PMszx, FFx, FBx are acronyms for sites corresponding to several locations (HBT: Haut-Giffre Décollement, TB: Le Tour back thrust, PMsz: Pormenaz-Merlet shear zone, FF: Forclaz fault, FB: Finhaut back thrust). Samples and datations references are (1: Boutoux et al. (2016); 2: Rolland et al. (2008) and 3: Leloup et al. (2005). ZHe is for thermochronology ages with the U/Th/He technique on Zircons, Ar/Ar is for geochronology ages with the $^{40}Ar/^{39}Ar$ method. Bt.: Biotite; Kf.: Potassium-rich feldspar; Phe.: Phengite; Min.: Minimum age; Plat.: Plateau age; Iso.: Inverse isochrone age. The map without stereo plots and surcharge is available as Fig. S1. Stereo plots show mean fault or shear plane kinematics in each site (Lower hemisphere equal-area projection, arrows showing Upper block motion). Precise locations and sites are given in Table S1. Mean shear or fault plane measures reported in the stereo-plots are available in Table B.2. Stereoplots with all data from each site are available in Fig. B.1. Dashed black frames correspond to the spatial extent of the GeoModel (Fig. 4.9) and the zoom in the Posettes area (Fig. 4.21) Cross-section. Location and legend on (a). All structural data, locations, sites, samples, and 3D GeoModels are provided in a repository, see the Data Availability statement.

4.3.3 Data and Methods

4.3.3.1 Structural Analysis

At the regional scale, the structural study is based mainly on published geological maps at the 1:50 0000 scale in France (Corbin and Oulianoff, 1928; Ayrton et al., 1987; Pairis et al., 1992) and 1:25 000 in Switzerland (Collet et al., 1952), which we completed and updated with field observations, measurements and mapping. At the outcrop scale, we characterize the style, intensity, and geometry of the deformation by qualitative observation and precise measurements of the orientation of the structural features (stratigraphy, cleavage, shear planes, lineations, etc.). We meticulously select oriented samples and produce oriented thin sections to characterize the deformation at a microscopic scale. The main shear criteria used are the relationship between cleavage and shear planes (Berthé et al., 1979), asymmetrical boudinage (Lacassin, 1988), delta and sigma porphyroclasts (Hanmer and Passchier, 1991), and lattice preferred orientation in quartz (Gapais and Barbarin, 1986; Passchier and Trouw, 2005).

4.3.3.2 3D Geological Modeling

Classically, the geometry of the geological structure deduced from observations at the surface and at depth is depicted through surface mapping and vertical cross-sections. When numerous cross-sections are performed, a relatively precise idea of the 3D geometry can be given. However, the cross-sections are only 2D projected representations of the surrounding data, and the original 3D data position, orientation, and uncertainty are lost. The 3D geological approach of GeoModeller implements numerically geological concepts to build an implicit 3D model based on geological rules (Calcagno et al., 2008). The interface between two geological formations corresponds to an isopotential surface described by a potential field. This potential field is interpolated from the measured orientation data (stratification, cleavage, or foliation)

using the geostatistical method developed by Lajaunie et al. (1997). The method uses the structural orientation data, that locally defines the gradient of the potential field. The interface is the isopotential surface passing through the contact points observed in the field. Formations with interfaces that are sub-parallel to each other and thus share the same potential field are grouped into a series. Defining a series interface requires at least one structural measurement (orientation) within the series and one contact point (location). This is well adapted to model sedimentary series, but can also be used in magmatic and metamorphic rocks when their internal structures are parallel to their interface (Calcagno et al., 2008). A relative chronology must be defined for the formations within the series to satisfy the geological concept of superposition. In addition, a relationship between series that are not parallel to each other must be defined: erode if the series crosscuts the oldest ones and onlap if it does not (Calcagno et al., 2008). Faults are discontinuities that offset potential fields; their relative timing must be defined to respect the cross-cutting relationships

The 3D geological model encompasses a 14.3 x 20.3 km zone (Figs. 4.8 and 4.9) and is based on new structural measurements at 432 locations on the surface. Some structural measurements are taken from published geological maps (Corbin and Oulianoff, 1928; Amberger, 1959; Ayrton et al., 1987; Pairis et al., 1992). Other subsurface observations are taken along water penstock pipes provided by the Emosson SA company (Fig. 4.8a). The resulting model has been built by distinguishing eight geological formations (Fig. 4.9) with their structural relationships defined according to the geology observed in the field and described in the bibliography. The model views are shown in Figs. 4.9, 4.21, and 4.26. To better characterize the precise geometry of the synclinorium in its central part, we performed a smaller geomodel that allows a more detailed visualization of the synclinorium, distinguishing four formations within the Mesozoic series (Figs. 4.9a, 4.21 and 4.24). The 3D GeoModels and their associated data are provided in the repository.

4.3.4 Structures and cover/basement relationships in the Aiguilles Rouges

4.3.4.1 Geological background

Basement of the Aiguilles Rouges and Mont-Blanc ranges Within the Aiguilles Rouges, the basement corresponds to gneiss and granites with a polymetamorphic Variscan history and overlain by Carboniferous/Permian sediments (e.g., Von Raumer and Bussy, 2004). During the Variscan history, the Aiguilles Rouges followed a clockwise P-T path with the formation of eclogites under maximum metamorphic conditions of $\geq$ 60 km depth and 700 ± 75 °C (Vanardois et al., 2022) possibly at $\approx$ 395 Ma. High-K calc-alkaline granite emplacement occurred at 332 ± 2 Ma in the south of the massif (Bussy et al., 2000), with a maximum temperature likely reached at 327 ± 2 Ma (Bussy et al., 2000) during crustal thickening. Migmatization

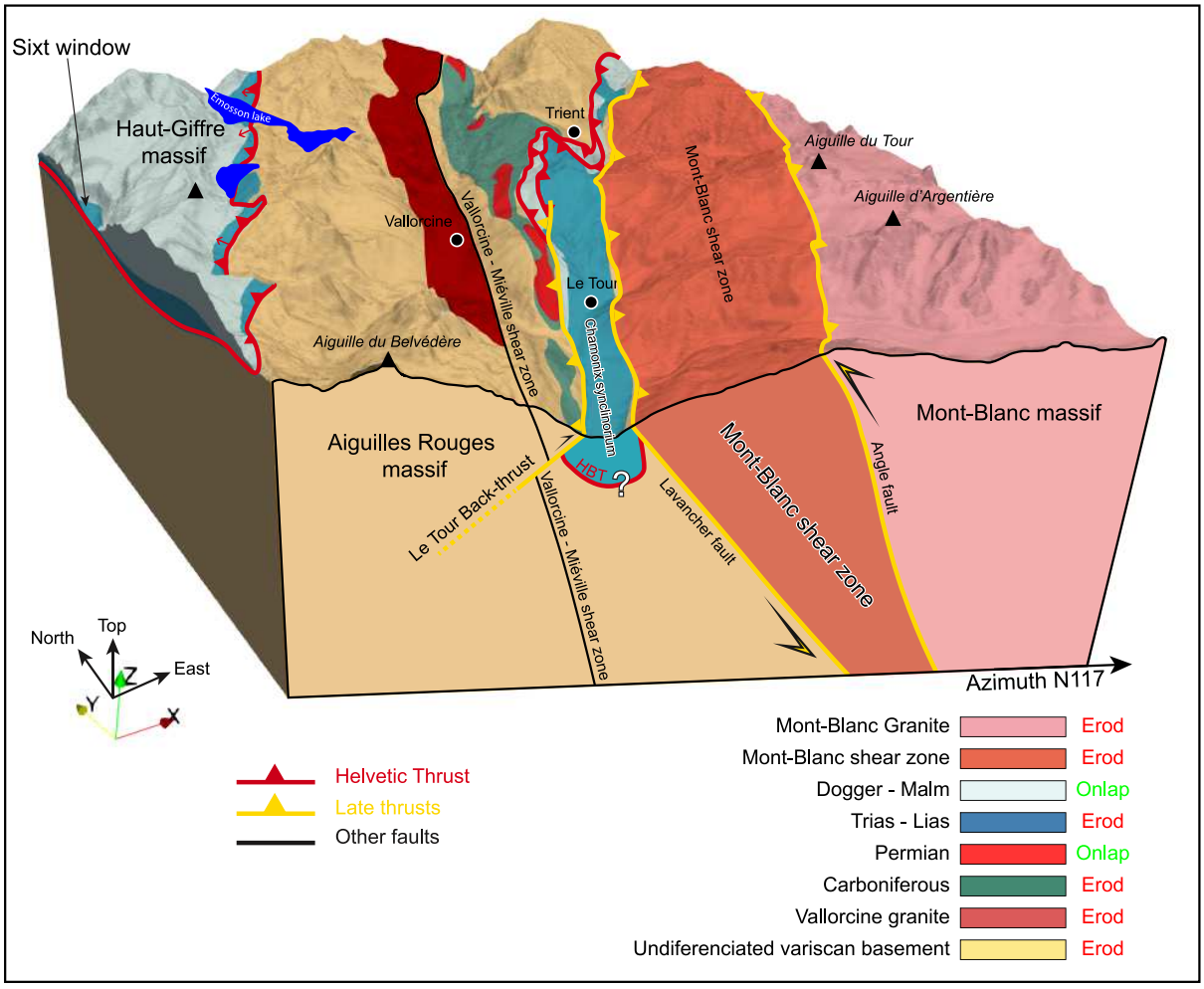

Figure 4.9. View of the 3D GeoModel. The model is cross-cut perpendicularly to the structures across the Chamonix Synclinorium south of Le Tour village. See the associated stratigraphic pile and their relation that were used in the modeling.

occurred at 320 ± 1 Ma during decompression, in part within the transpressive NE-SW right-lateral Berard-Emosson shear zone (Bussy et al., 2000; Genier et al., 2008; Simonetti et al., 2020). The long and narrow Vallorcine granite intruded that shear zone at 306.5 ± 1.5 Ma (Bussy et al., 2000). Its emplacement is interpreted to take place during NE-SW dextral strike-slip deformation (Brändlein et al., 1994). The granite is bounded in the south-east by the Vallorcine-Mieville shear zone (Fig. 4.8a) that is interpreted to be a late Variscan strike-slip shear zone (Reinhard and Preiswerk, 1927; Steck and Vocat, 1973) partly reactivated during the Alpine orogeny under low-grade metamorphic conditions (Kerrich et al., 1980; Steyrer and Sturm, 2002; Rolland et al., 2008). The precise history of that fault is most likely polyphase and is still being discussed. Post-Variscan cooling and exhumation were very fast, and the sedimentation in the Salvan-Dorénaz basin started at 308 ± 3 Ma (Moscovian, Carboniferous) by coarse detrital deposits and lasted until at least 295 ± 3 Ma (Asselian, Permian) (Capuzzo and Bussy, 2000; Capuzzo et al., 2003; Capuzzo and Wetzel, 2004). Variscan gneiss and granites are unconformably overlain by Triassic sandstones. Within the Aiguilles Rouges Alpine metamorphism and deformation are milder than in the Mont-Blanc massif with a maximum temperature of 320 $^{\circ}$C in the Carboniferous rocks (Boutoux et al., 2016), and mostly brittle deformation (e.g., Von Raumer and Bussy, 2004).

Within the Mont-Blanc massif, the basement is very similar to the Aiguilles Rouges. The massif is mainly composed of a calc-alkaline granite intruding Variscan metamorphic gneiss. The granite has been dated by U/Pb on zircons at 304 ± 3 Ma (Bussy and Raumer, 1993).

Cover of the Aiguilles Rouges and Mont-Blanc ranges On the western margin of the Aiguilles Rouges massif, the base of the Mesozoic sedimentary cover corresponds to a sandstone layer dipping 15° to 35° to the northwest that can be continuously followed for approximately 25 km (e.g., Amberger, 1959; Ayrton et al., 1987; Pairis et al., 1992) (Fig. 4.8a and b). The layer marks a clear stratigraphic and angular unconformity as it rests on Variscan gneiss with steep foliation (average N12°, 70°E) (Fig. 4.10). The sandstone level is conformably overlain by red and green siltites, dolostones, and cargneule attributed to the Triassic (Collet et al., 1952; Ayrton et al., 1987; Pairis et al., 1992). The same succession is found at several localities along the unconformity and defines the Triassic autochthonous cover of the Aiguilles Rouges. Locally, white limestone is found above this series (Fig. 4.8a) and is attributed to the Upper Jurassic (Collet et al., 1952; Ayrton, 1972) or the Cretaceous (Ayrton et al., 1987; Pairis et al., 1973; Pairis et al., 1992). At other locations, the succession is topped by black Aalenian slates (Ayrton et al., 1987; Collet et al., 1952; Pairis et al., 1992). This Mesozoic series has been interpreted as an incomplete stratigraphic succession resulting from condensed sedimentation on top of a Mesozoic horst (e.g., Corbin and Oulianoff, 1928; Ayrton et al., 1987).

The autochthonous / allochthonous nature of the cover above the Aiguilles Rouges base-

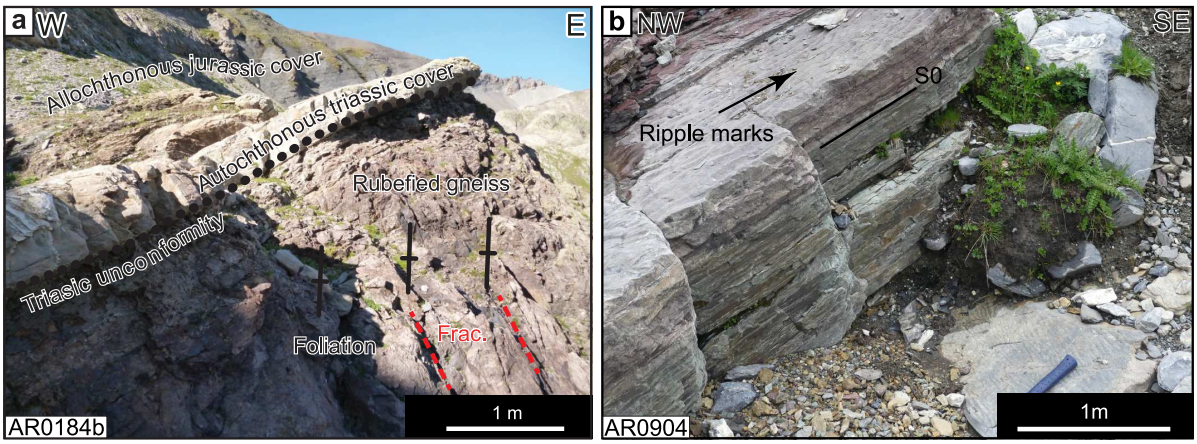

Figure 4.10. Undeformed Triassic sandstones resting unconformably on top of variscan basement: a) Basal Triassic unconformity with stratigraphic and angular unconformity above Variscan gneiss that show a steep foliation (bottom of the Haut-Giffre); b) red and green siltites showing ripple marks (Barberine pass area).

ment has been debated for decades. On the western flank of the Aiguilles Rouges, the Mesozoic series above the Triassic has been considered as the para-autochthonous cover of Mont-Blanc, belonging to the Morcles fold-nappe with insignificant thrust with respect to the underlying basement (e.g., Escher et al., 1988; Bellahsen et al., 2014). In the highest peak of the Aiguilles Rouges, Aiguille du Belvédère (Fig. 4.8a), Collet and Paréjas (1920) proposed that the Aalenian is thrust atop the Triassic, but the associated folds were later interpreted as local structures of minor importance (e.g., Corbin and Oulianoff, 1928; Ayrton et al., 1987). Similarly, white limestones in Pormenaz (Fig. 4.8a) have been considered allochthonous (Duparc et al., 1966; Dobmeier and Von Raumer, 1995) or autochthonous (Pairis et al., 1992).

The complex geometry of the Chamonix synclinorium has led to several interpretations. Some consider that the western boundary of the Chamonix synclinorium corresponds to the Triassic basal unconformity atop the Variscan gneiss (Ayrton, 1980; Ayrton et al., 1987). In the paraautochthonous hypothesis, this boundary is a Mesozoic normal fault bounding a half-graben filled by a thick series of syn-rift sediments, while the top of the horst presents an incomplete stratigraphic succession (e.g., Bellahsen et al., 2014; Boutoux et al., 2016). However, such a normal fault has never been characterized with direct evidence. Further north, in the Morcles massif, Héli (1972) suggests that the Chamonix synclinorium corresponds to a deep Priabonian basin with detrital deposits sourced from the Aiguilles Rouges cover. Some argue that Mesozoic sediments are not autochthonous but are thrust above the basement (Leloup et al., 2005; Pfiffner et al., 2011). Others consider that a major thrust within the Chamonix synclinorium separates the autochthonous covers of Mont-Blanc and Aiguilles Rouges (Ayrton, 1980; Ayrton et al., 1987).

For most authors, the Chamonix synclinorium corresponds to the root of the Morcles

Nappe, but the interpretation varies depending on the style of deformation and amount of motion at the base of the nappe. For some, the Morcles Nappe is a large anticline affecting both the basement and the cover (ductile basement fold nappe), the eastern boundary of the Chamonix synclinorium corresponding to the reverse limb of the fold, the external Mont-Blanc being the core of the fold and the normal limb rooting in the Angle fault (e.g., Epard, 1986; Escher et al., 1988; Escher et al., 1993) (Fig. 4.7a). However, no clear evidence of the folding of the Mont-Blanc basement has ever been published. Others propose that the external Mont-Blanc is not folded, but corresponds to an Alpine reverse shear zone that brings the basement on top of the synclinorium (e.g., Bellière, 1956; Eltchaninoff, 1982; Butler, 1985; Leloup et al., 2005) (Fig. 4.7b). This $\approx$ 3 km wide deformation zone is characterized by a south-east dipping greenschist foliation that trended from N000° to N066° (N034°; 53°E on average). Previously interpreted as the result of three distinct Variscan deformation events (Belliere, 1988), this deformation is rather interpreted as a network of Alpine shear zones affecting Variscan mylonites, gneisses, and granites (Leloup et al., 2005). The shear criteria in the Alpine mylonites indicate a thrust from the top to the northwest thrust (Leloup et al., 2005). As the mineral and stretching lineation have pitches between $90°$ and $60°$ E (average azimuth N$100°$), this corresponds to a thrust with a minor dextral component. The Upper part of the Mont-Blanc shear zone corresponds to the Angle fault (Corbin and Oulianoff, 1928), and the Lower one to the Lavancher fault (Fig. 4.8). The Mont-Blanc shear zone dies-out southwest and northeast of Mont-Blanc with a maximum offset between Chamonix and l'Argentière (Leloup et al., 2005). In this interpretation, the overturned stratigraphic sequence along the eastern boundary of the Chamonix synclinorium is a drag fold below the reverse fault. A variation of the basement fold nappe model is that the Mont-Blanc massif is part of a large anticline with the Mont-Blanc shear zone that makes up the western reverse limb of that fold (e.g., Egli et al., 2017). However, others consider that the linear shape of the Chamonix Synclinorium, and of the Mont-Blanc range is partly due to the right-lateral strike-slip faulting along the Simplon Rhône - Belledonne fault system (Gourlay and Ricou, 1983; Hubbard and Mancktelow, 1992; Seward and Mancktelow, 1994).

4.3.4.2 Thrusting evidence in the Aiguilles Rouges

Thrusting along the western margin of the Aiguilles Rouges To the north of the Aiguilles Rouges, next to the Col de Barberine (site HGT1, Fig. 4.8a), the autochthonous Triassic is folded, brecciated and overlain by a sliver of Variscan migmatitic gneiss itself overlain by Triassic quartzite (Fig. 4.11a). While the gneiss sliver does not appear to have been deformed at low temperatures, the Upper part of the Triassic level is strongly deformed, affected by recumbent folds (Fig. 4.11b), and strongly brecciated at the contact (Fig. 4.11a). The Triassic is overlain by a slice of limestone attributed to the Eocene, directly overlain by limestones

attributed to the Upper Jurassic (Collet et al., 1952) (Fig. 4.11a). The stratigraphic series is isoclinally folded and foliated with S/C relationships suggesting a top to N285° shearing (Fig. 4.11c). These observations imply both the duplication of the Triassic/basement contact and intense top-to-the-northwest shearing of a reverse stratigraphic series.

Further south, in the Mont-Oreb area (site HGT2, Fig. 4.8a), above the Triassic, white limestones attributed to the Upper Jurassic are strongly deformed. The limestones are metamorphosed into marbles, and a strong west-dipping schistosity affects both the limestone and the calcite veins (Fig. 4.12a). The cleavage bears a stretching lineation trending N280° (Fig. 4.13a) and asymmetry of the folds suggests a top-to-west shear sense. intensively sheared within a major décollement (Fig. 4.12c). At nearby location AR0184 (Fig. 4.12c), the underlying Triassic sandstones are also strongly deformed, affected by an isoclinal fold with the axial plane and axis parallel to the cleavage and stretching lineation, respectively (Fig. 4.13). The limestones are overlain by strongly foliated and folded black slates attributed to the Aalenian, implying decoupling between the two units and thus another fault at the top of the limestones (Fig. 4.12c). The same fault is visible atop the white limestones at several locations, for example, near the Vieux Emosson lake (Fig. 4.8, Fig. 4.12b). Further south along the Souay River (site HGT3, Fig. 4.8 a), above the carboniferous sediments of the Pormenaz basin, Triassic brecciated cargneules are overlain by white limestones that are metamorphosed into marbles and mylonitized (Fig. 4.14a). The marbles bear a well-visible stretching lineation, trending N288° and are also asymmetrically folded with an axis trending N032° (Fig. S5b). The lineation, shear plane, and asymmetry of the fold suggest a direction of shear towards the WNW.

Above the white limestone, the Aalenian black slates are affected by numerous spectacular isoclinal folds. The folds do not show systematic vergence (Fig. 4.15a and b) and are even sometimes closed (Fig. 4.15d). Given the steepness of the topographic slopes, few measurements of these folds have been performed, but north of the Emosson lake (Site HGT4, Fig. 4.8a) stratification and cleavage measurements indicate two families of fold axis trending N209° and N280° and sharing an almost horizontal axial plane (Fig. 4.15c). Such folds are widespread in the Haut-Giffre Mesozoic cover (Fig. 4.8a).

We interpret all these field observations as reflecting a major $\approx$ 500 m thick shear zone that affects the Mesozoic cover above the Aiguilles Rouges basement. We call the base of that shear zone the Haut-Giffre Thrust (HGT). The direction of shearing is given by the orientation of the stretching lineation and the shear sense is top to the WNW motion (Fig. 4.8a). Within the shear zone, several folds are sheath folds that have highly curvilinear axes, with some axis parallel to the direction of transport. Such folds occur in shear zones with a high simple shear strain ($\gamma \geq$10) (Cobbold and Quinquis, 1980; Quinquis et al., 1978; Lacassin and Mattauer, 1985).

The present-day dip of the HGT with its top to the WNW motion would correspond to a normal fault configuration (Fig. 4.12c). But local basement duplication implies that the fault is an additive, as it duplicates formations and is thus more likely a tilted thrust. Slices of relatively young formations (Upper Jurassic in the south, Eocene in the north) near the base of the shear zone suggest that it is a sheared reverse limb, equivalent to the reverse limb of the Morcles nappe outcropping less than 15 km to the northeast (Escher et al., 1993).

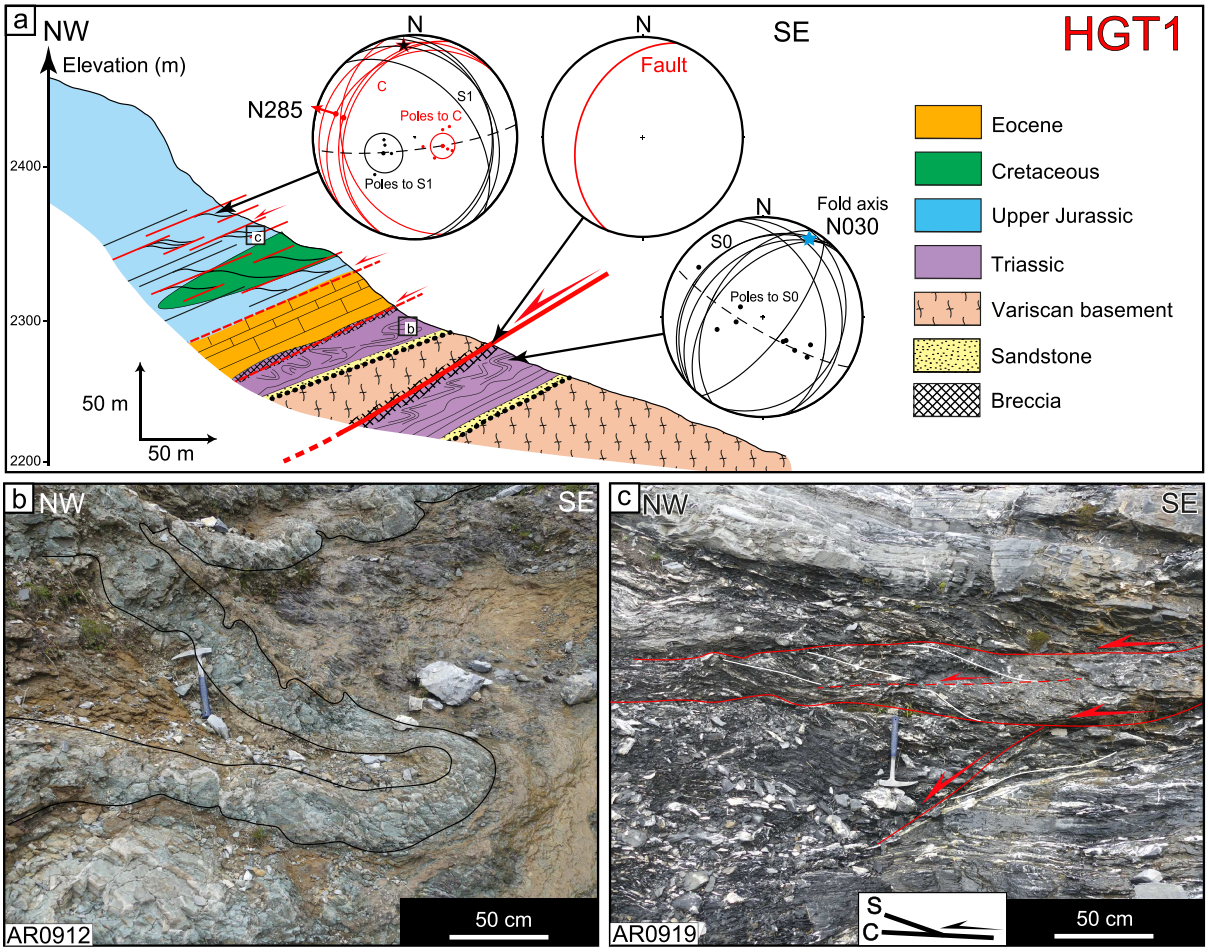

Figure 4.11. Cover/basement relationships at the col de Barberine (Aiguilles Rouges, site HGT1). a) Field cross-section along a talweg 300 m west of the Barberine pass. Stratigraphic ages from Collet et al. (1952). Stereo plots (equal-area, Lower hemisphere projection) show the geometry of structures in b and c. b) Recumbent fold in red and green Triassic siltites at location AR0912. The fold axis trends N30°; b) Strongly sheared black shales at location AR0919. S/C relationships indicate top to the N285° shearing.

West of the Aiguilles Rouges, the Giffre River has dug a deep valley in the Mesozoic sediments. In this valley, 4 km northeast of Sixt-Fer-a-Cheval village, there is a small outcrop of the basement (Site HGT5, Fig. 4.8a). There, the Variscan basement corresponds to chlorite-bearing schist with a nearly horizontal foliation and is unconformably topped by Triassic sandstones (Fig. 4.16). Above, the Triassic succession (sandstone, dolostone, green, and red siltites) is nearly horizontal, itself overlain by intensively folded and sheared black slates

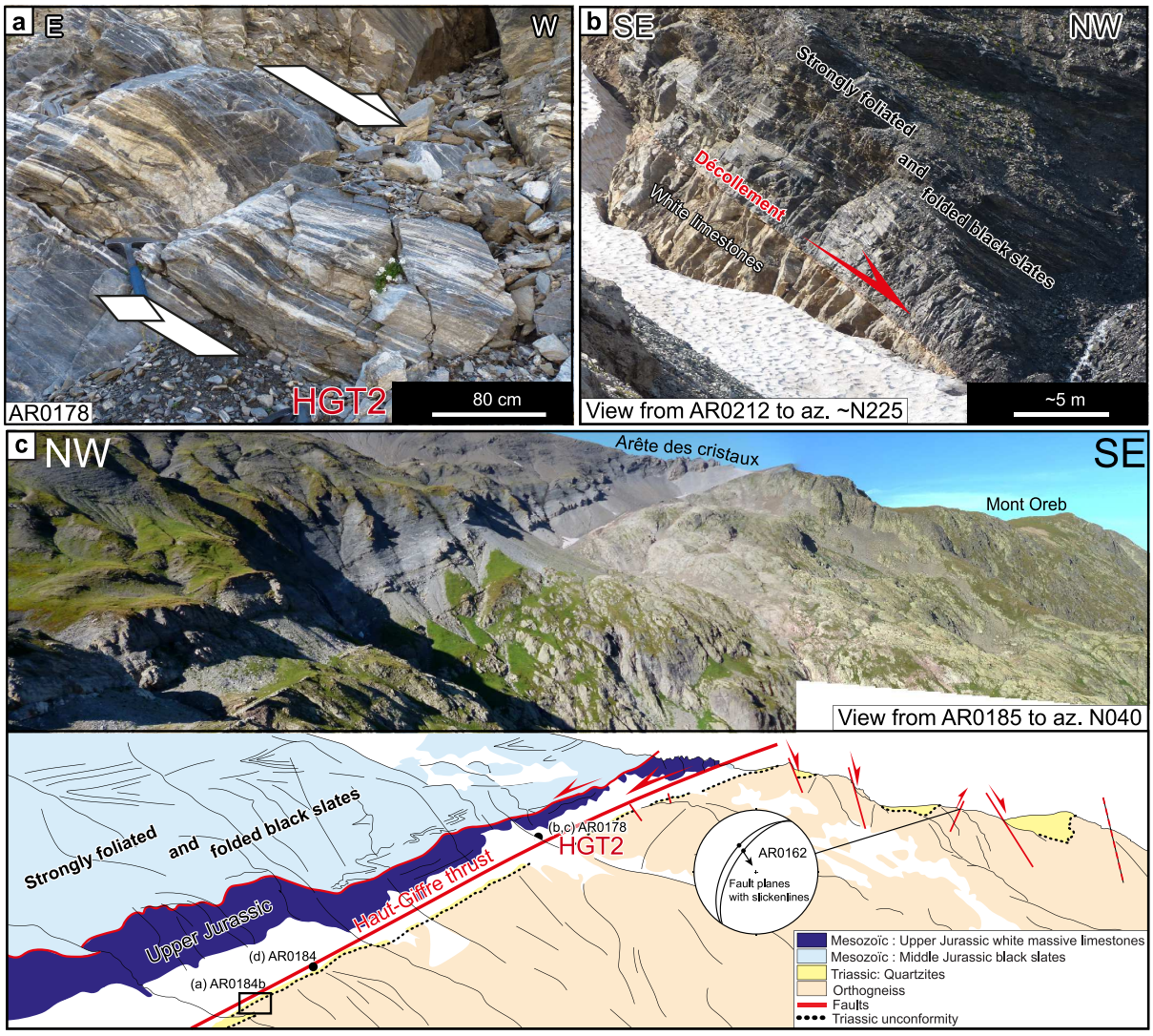

Figure 4.12. Cover/basement relationships in the western side of Aiguilles Rouges. a) Shear zone at the base of the Mesozoic sedimentary cover, above the Triassic unconformity at site HGT2; b) Localized décollement above white limestones. The décollement is associated with a shear zone in the Aalenian slates; c) Picture at the top and interpreted panoramic view at the bottom of the Haut-Giffre thrust (view from location AR0185, towards $\approx$ N40°). The Upper Jurassic white limestones are visible as well as intense folding within the Lower Mesozoic slates above.

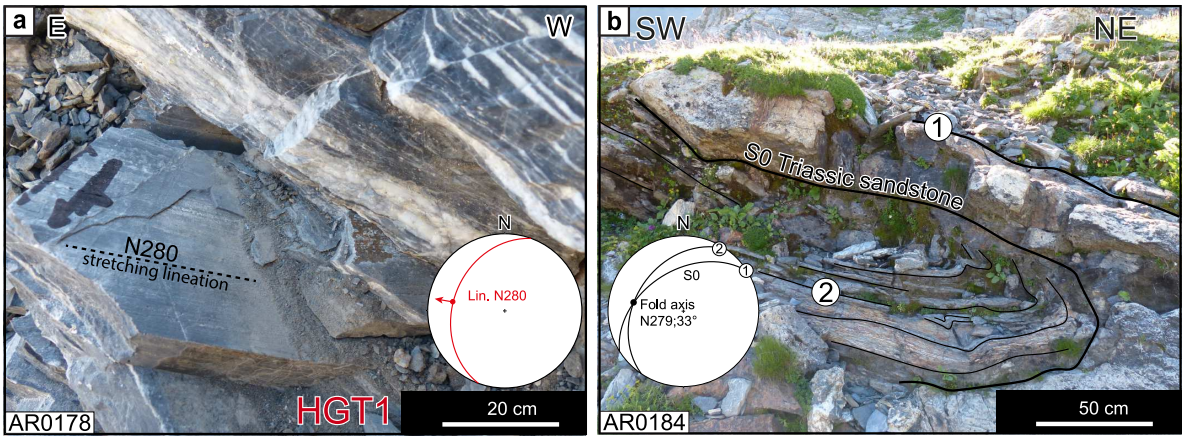

Figure 4.13. Supplementary field data at site HGT2. a) Stretching lineation trending N280°, compatible with a displacement towards the WNW inside the shear zone at the bottom of the Mesozoic sedimentary serie. (b) Triassic sandstone layer affected by an isoclinal fold with the fold axis trending N279°. This fold is a sheath fold that has highly curvilinear axes, with the axis parallel to the direction of transport. Such folds occur in shear zones with a high simple shear rate ($\gamma \geq 10$) (Cobbold and Quinquis, 1980; Quinquis et al., 1978; Lacassin and Mattauer, 1985).

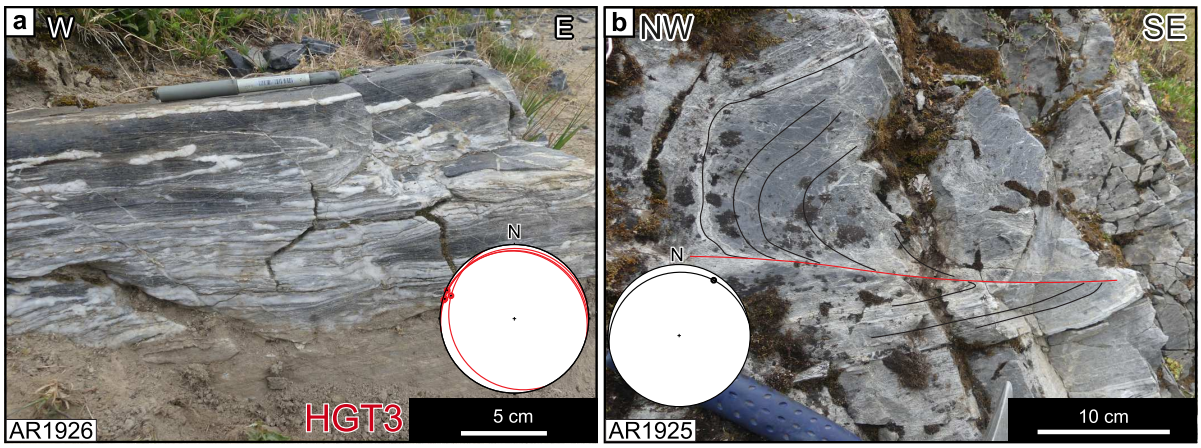

Figure 4.14. Site HGT3 (Souay area): a) white limestones that are mylonitized and metamorphosed into marbles. They bear a well-visible stretching lineation, trending N288°. The limestones are also asymmetrically folded with axis trending N32° and shear planes cross cutting the axial plane. The lineation, shear plane, and asymmetry of the fold suggest a direction of shear towards the WNW.

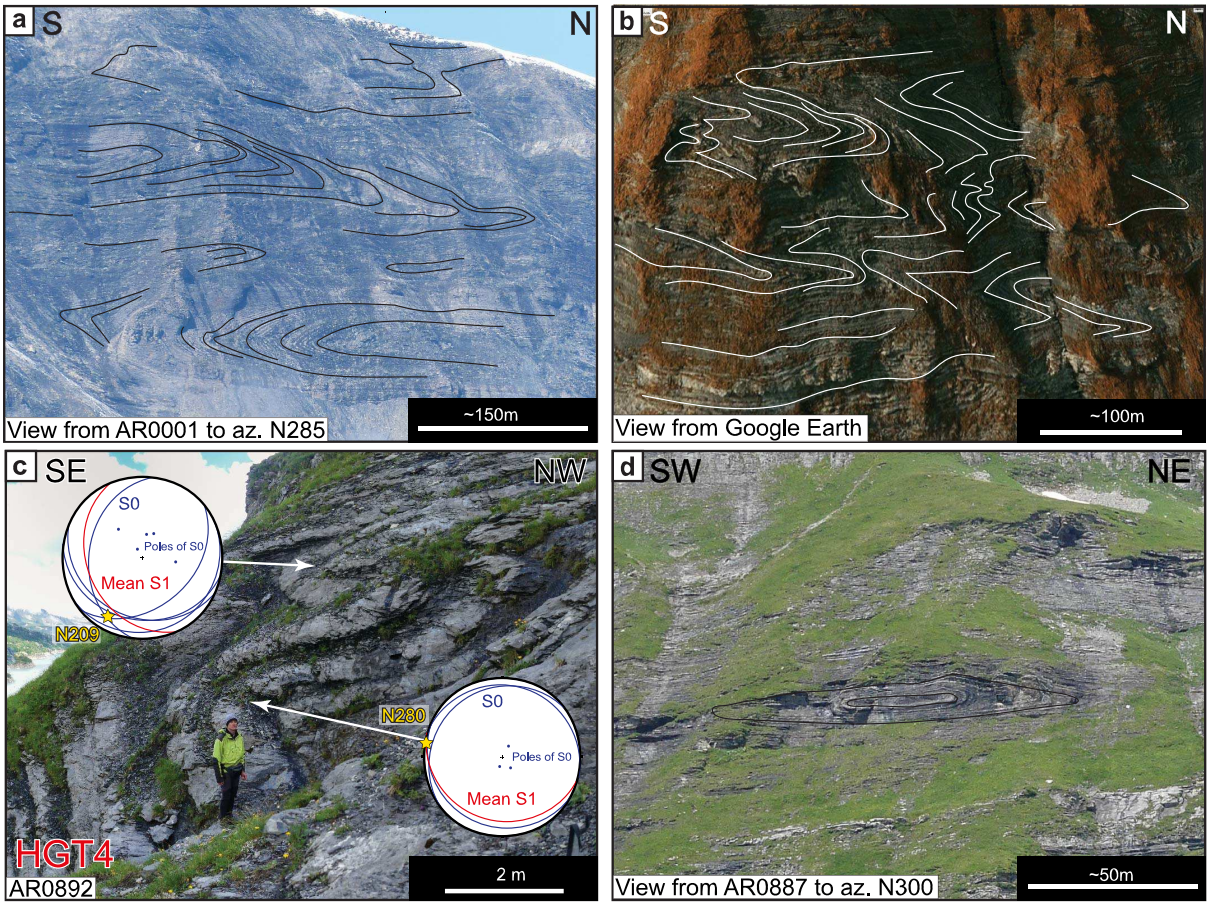

Figure 4.15. Folding of the Mesozoic cover on the western flank of the Aiguilles Rouges. Locations in Fig. 4.8a. a) Large isoclinal folds on the Haut-Giffre massif seen from the Montagne des Posettes. Some stratifications are highlighted in black. b) Google EarthTM view of the slope above the Emosson lake. Some stratifications are highlighted in white; c) Two different types of folds affecting the Mesozoic cover above the Emosson lake (site HGT4): stereo plots (equal-area, Lower hemisphere projection) show the bedding and cleavage of the folds: one with N280° trending axis, and the other with N209 trending axis; d) Entirely closed sheath fold above Emosson Lake (view from location AR0887, towards azimuth $\approx$ N300°).

with shear planes trending N038°; 32 SE (Fig. 4.16). This outcrop is therefore a window through the HHaut-Giffre thrust. This window is an important constraint for the geometry of the 3D GeoModel (Fig. 4.8b and 4.9).

Thrusting atop the Aiguilles Rouges Atop the Aiguilles Rouges (Aiguille du Belvédère, site HGT6), Mesozoic sediments are interpreted as a buttress of an autochthonous incomplete series deposited atop a Mesozoic horst (e.g., Corbin and Oulianoff, 1928; Ayrton et al., 1987). However, if the basal part of the series is the autochthonous level of Triassic sandstone described above, the overlying dolostone layers are affected by intense northwest verging folds with N32° trending axis and south-east dipping axial planes (Fig. 4.17a, b, and c), while the Upper part of the summit is composed of flat-lying (sub-horizontal) black slates, with a stretching lineation striking N285° (Fig. 4.18). Our interpretation is thus rather that the Mesozoic cover at this location is affected by two main top-to-the-NW flat faults (Fig. 4.17a), with transport direction towards ≈ N310° (Fig. 4.18b) for the bottom fault and ≈ N285° for the top fault (Fig. 4.18 a). These faults probably connect with the Haut-Giffre thrust located less than 2.5 km away (Fig. 4.8). Because the peak is in a high mountain area, access is quite challenging. Therefore, we acquired high-resolution drone images to build a 3D photogrammetric digital elevation model (DEM). Fig. 4.17 a is a screenshot of the model. See Data availability for more information and links to visualize and download the model.

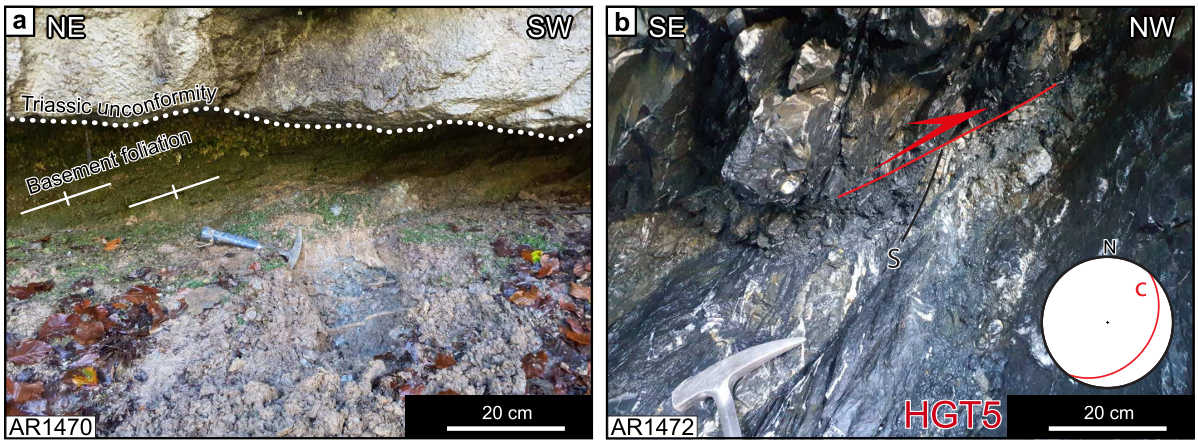

Figure 4.16. Site HGT5 (Sixt window): a) Horizontal basal Triassic unconformity above chlorite-bearing schist basement; b) Thrust fault into the Jurassic limestones above the Triassic series. The shear sense is towards the NW.

Seven kilometers southwest of the Aiguille du Belvédère, another buttress of limestones atop the basement is described at the Crête Blanche de Pormenaz (site HGT7, Fig. 4.8a). At this location, the Triassic sandstones rest on dark Carboniferous series and are overlain by white limestones (Fig. 4.19a). Triassic sandstones are affected by cataclastic foliation (Fig. 4.19b). The bottom of the limestone is also deformed and marmorized, with indications of

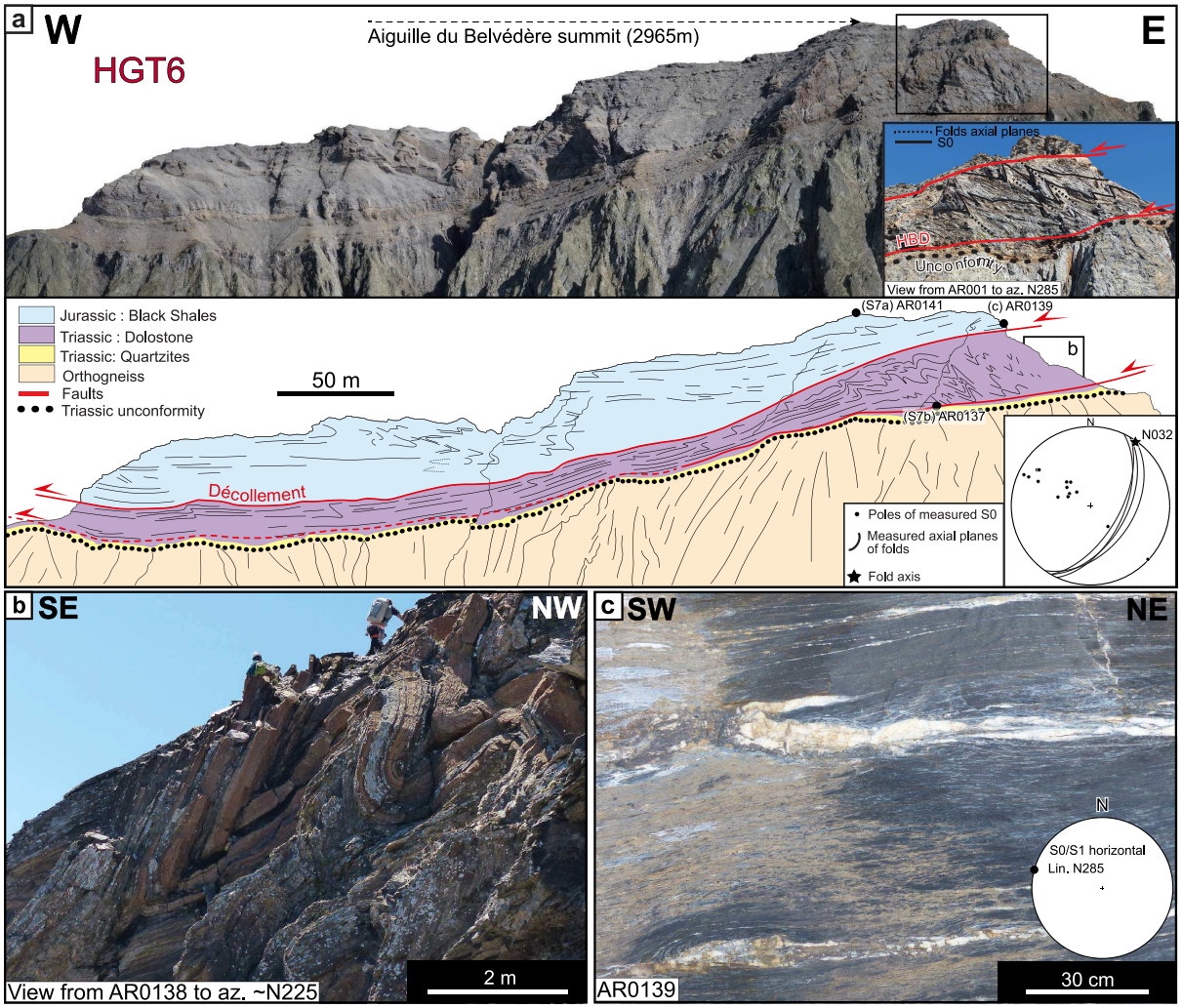

Figure 4.17. Cover/basement relationships at the Aiguille du Belvédère. a) Panorama of the summit view from the south. Top: a screenshot of the 3D photogrammetric model. Bottom: geological interpretation. Insets: picture and stereo-plot (equal area, Lower hemisphere projection) of northwest verging folds within the Triassic dolostones. The folds have an axis trending N32° b) Tight northwest verging folds within the Triassic sedimentary cover (view from location AR0138, towards azimuth N225°). The folded dolostones bears a stretching lineation striking N130° (see Fig. 4.18b); c) Highly deformed mesozoic black slates with calcite isoclinal folding and boudinage (location AR0139) bearing a stretching lineation striking N285° (Fig. 4.18a).

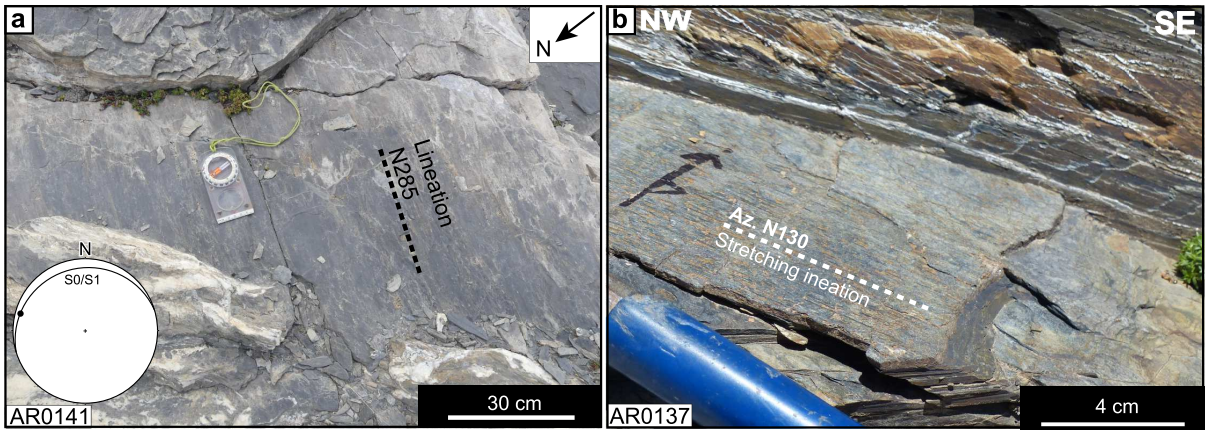

Figure 4.18. Field observations at site HGT6 (Aiguille du Belvedère). a) Stretching lineation trending N285°, affecting the black slates atop the summit; b) Sheared and stretched dolomites above the Triassic unconformity. The stretching lineation trends N130°.

foliation boudinage (Fig. 4.19c), suggesting that the basal contact of the limestones and the Triassic is tectonic rather than stratigraphic. This implies that the Mesozoic forms a small klippe. Therefore, we interpret the basal contact as part of the Haut-Giffre décollement rather than an undeformed stratigraphic contact.

Thrusting of the cover on the eastern side of the Aiguilles Rouges: the Forclaz Fault

In the northwest of the Chamonix synclinorium, the Mesozoic sediments rest on top of the Aiguilles Rouges basement along an east-dipping contact: the Forclaz fault (Fig. 4.8, and Fig. 4.20a). At site FF1 the Mesozoic rocks rest on top of Carboniferous sandstones and are strongly deformed with a cleavage steeply dipping to the east and a downdip lineation. A few kilometers further north at the foot of the Croix de Fer summit (site FF2, Fig. 4.8a), the contact cannot be observed directly, but the overlying Upper limestones appear much less steep and bear a well-printed stretching lineation trending N130° (Fig. 4.20a). The basal contact is well exposed at location AR0190 (site FF3, Fig. 4.8a, 4.20b, and 4.20c) along the road to the Forclaz pass, where Mesozoic sediments are separated from gneiss by a 50 cm thick quartz level (Fig. 4.20b). This quartz level was previously interpreted as the basal Triassic sandstone layer resting unconformably atop the Variscan gneiss (Ayrton, 1980; Ayrton et al., 1987). A thin section of the sample Are042, from that quartz layer, has been cut perpendicular to the fault contact and parallel to the lineation. On the microscale, the quartz grains are angular with a size below 100 µm. This suggests that the layer more likely corresponds to a deformed level that separates the sedimentary rocks from the basement (Fig. 4.20d). Crystallographic Preferred Orientation (CPO) analysis of quartz using Electron back-scattered diffraction (EBSD) of sample ARe042 thin section has been performed (Fig. 4.20c) (technical information about the analysis is provided in Table B.3). Data were processed with the MTex algorithm (Hielscher and Schaeben, 2008), 5788 grains were identified on 343 007 pixels, using a misorientation threshold of 15°

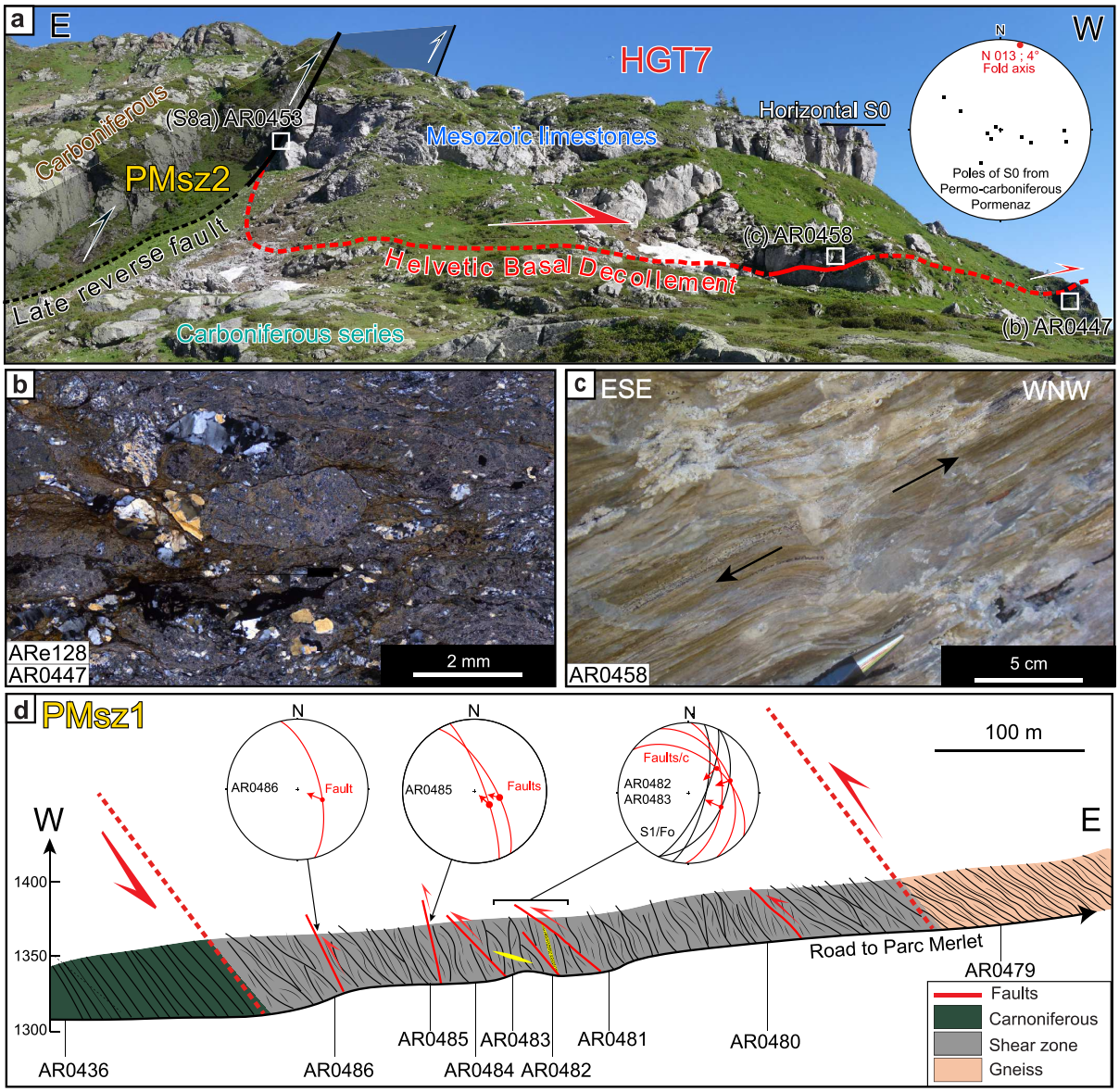

Figure 4.19. Cover/basement relationships near Pormenaz (Aiguilles Rouges massif). a to c) The Crête Blanche klippe. a) General view of the klippe, the limestones are thrusted westward above a basal thurst, before being offset by a late steep thrust. Stereo-plot (Lower hemisphere, equal area) on the right shows poles of bedding planes of the Carboniferous sediments in the Pormenaz zone: average folds axis dips $\approx 4°$ to N13°; b) Foliation and metamorphosed quartzite (location AR0447); c) Marmorized limestones showing foliation boudinage, indicating ESE-WNW-oriented stretching (location AR0458); d) Cross-section of the Merlet-Pormenaz shear zone along the road to the Merlet parc. Stereo plots (Lower hemisphere, equal area) show fault planes and shear planes along the section.

and a minimal grain size of 5 pixels. The presented stereographic plot (equal area, Lower hemisphere) shows the orientations of the crystallographic axis ($< a >$ and $< c >$), with color according to the density of points (one point per grain identified). The CPO suggests the activation of the quartz crystallographic basal plane, at about 350 to 400 $^{\circ}$C (Passchier and Trouw, 2005), with a top-to-west reverse shearing along the $< a_1 >$ axis trending N122° (Fig. 4.21c and d).

We interpret the Forclaz fault as a west verging thrust because (i) site FF3 shows a top to the northwest thrusting of the Mesozoic sediments above the Aiguilles Rouges basement (Fig. 4.20b and c) (ii) As already pointed out by Ayrton (1980), folds within the overlying Mesozoic have an NW vergence.

Thrusting within the Chamonix synclinorium: the Posettes fault Within the Mesozoic synclinorium, the Posettes fault dips to the southeast, runs subparallel to the Forclaz Fault, and brings middle Jurassic black slates on top of strongly folded Upper Jurassic limestones (Fig. 4.20a, 4.8a and b). This geometry is well constrained in the 3D models, particularly in the Montagne des Posettes zoom-in model (Fig. 4.21). The black slates are also strongly folded, describing a large fold with a steep axis (trend 70° / plunge 68°) and with a core of middle Jurassic limestones that constitute the Croix de Fer summit (Ayrton, 1980). Further east, the Mesozoic series dip to the southeast and are cut by the Mont-Blanc shear zone that rises the Mont-Blanc basement (Leloup et al., 2005) (Fig. 4.20a).

The steep axis folds have been interpreted as reflecting the strike-slip motion along the Rhône valley, being part of the Simplon-Rhône dextral fault (Hubbard and Mancktelow, 1992). As Ayrton (1980) we rather interpret them as large sheath folds, like those observed in the Haut-Giffre, some of them with an axis nearly parallel to that of the shearing direction within the cover décollement zone. In this interpretation, the base of the Mesozoic cover of the Chamonix synclinorium corresponds to the same Haut-Giffre thrust.

Synthesis on the thrusting above the Aiguilles Rouges To sum up, the faults and shear zones found on the western limb (Haut-Giffre thrust - HGT), on top (Pormenaz and Belvédère klippes), and on the eastern limb (Forclaz fault) are segments of the same thrust at the base of the helvetic nappes: the basal Helvetic thrust (HBT) (Fig. 4.8b). Motion on the HBT is everywhere top to the WNW and its antiformal shape results from the later updoming of the Aiguilles Rouges. The HBT is nearly parallel to the cover/basement interface and is the base of a strongly sheared reverse limb of a recumbent fold. It corresponds to the base of the Morcles Nappe. It affects the Jurassic and Triassic series and even locally the basement.

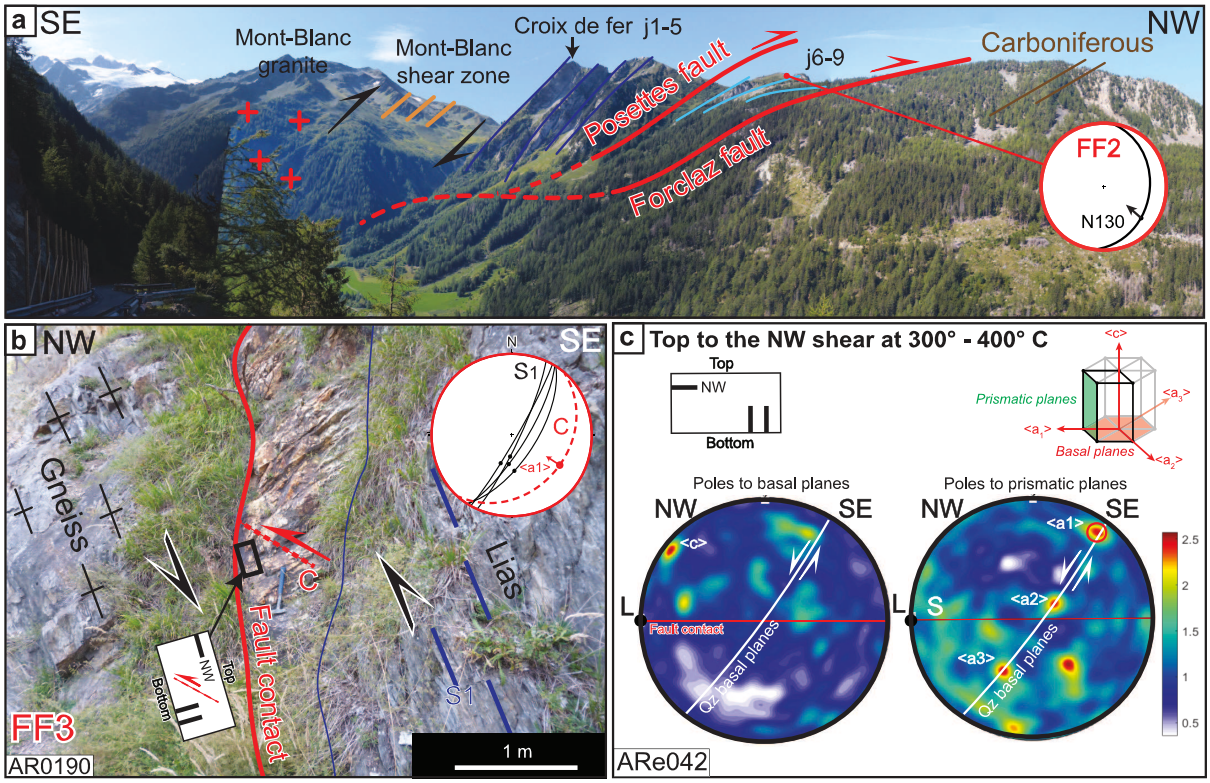

Figure 4.20. Cover/basement relationships in the north of the Chamonix Synclinorium. a) The Mont-Blanc shear zone, Posettes, and Forclaz fault viewed from the north. b) Forclaz Fault quartz layer at site FF3 (location AR0190). Plotted S1 refers to the cleavage in the Liassic slates, dashed red line corresponds to the shear plane inferred from CPO analysis, plotted lineation refers to the $< a_1 >$ direction; c) Crystallographic preferred orientations (CPO) of $< c >$ and $< a >$ axis of quartz sample ARe042 measured with EDSD technique. Equal area projection, Lower hemisphere, color as a function of the measurement density, fault contact is plotted as horizontal (red line) and the lineation is in the NW-SE direction (black circle). The pattern suggests an activation of the crystallographic basal plane along the $< a_1 >$ direction, compatible with a top to the northwest sense of shear.

4.3.4.3 Reverse faulting in the Aiguilles Rouges range and the Chamonix Synclinorium

Pormenaz-Merlet shear zone The southwest side of the Aiguilles Rouges is characterized by the contact zone between gneiss and Carboniferous sediments (Site PMsz1, Fig. 4.8a). The contact corresponds to a 350 m wide shear zone with foliation north-south striking and steeply dipping ($\approx 70°$) to the west (Fig. 4.19d). The shalLower shear planes trend from N156° to N182° and bear lineations trending N50° to N130°, indicating a top to west thrusting (Fig. 4.19d).

Returning to the Pormenaz Crête-Blanche (Site PMsz2, Fig. 4.8a), the white limestones described in section 4.3.4.2 abut against the Carboniferous series. This contact corresponds to a steep reverse fault trending N3° ; 70° SE that brings the Carboniferous on top of the Mesozoic limestones (Figs. 4.19a and 4.22a). A few decameters to the east the same shear zone brings the Variscan gneiss of the Aiguilles Rouges on top of the Carboniferous (site PMsz3 Fig. 4.8a).

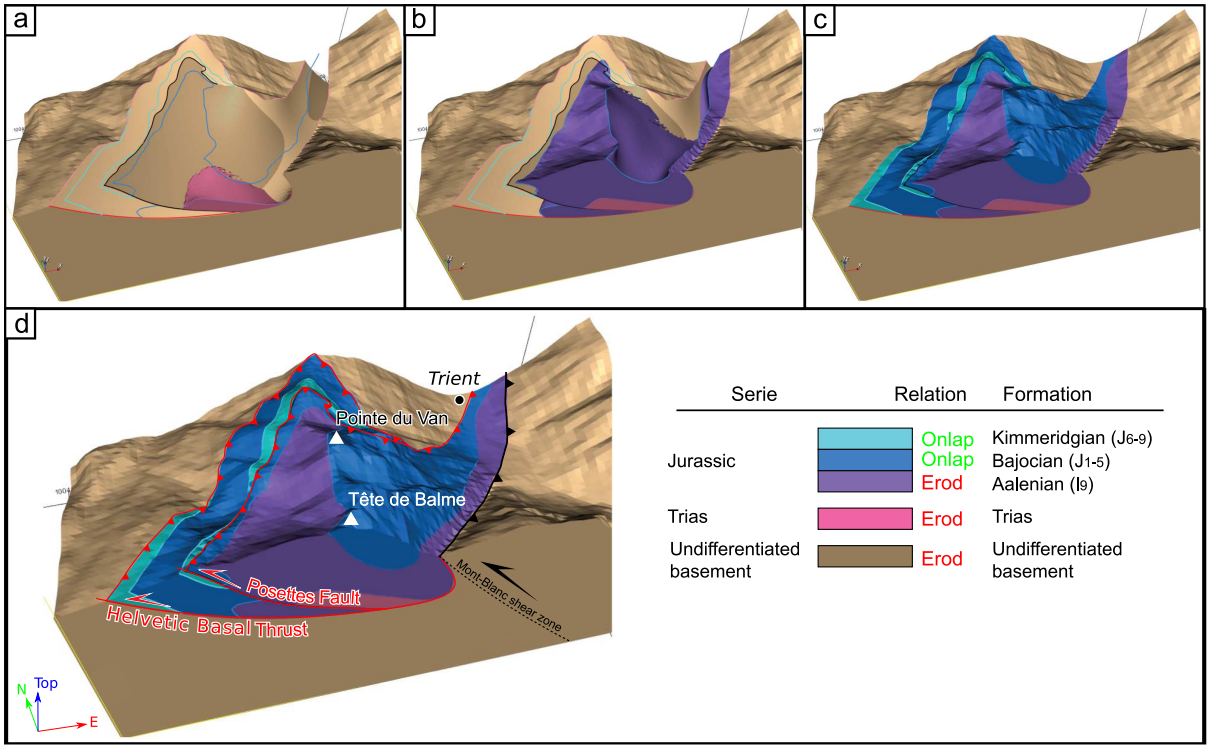

Figure 4.21. Views of 3D GeoModel, from the central part of the synclinorium: the Montagne des Posettes. a) to d), views of the GeoModel with the different layers removed. The basal decollement and the Posettes thrust are highlighted in red. The Mont-Blanc shear zone is not modeled here, however, its position is shown in the figure. The stratigraphic pile of the model as well as the relationship between them is shown in d

There, flat reverse faults with striation trending N130° affect the carboniferous, showing top-to-the-northwest shear (Fig. 4.22b).

These observations lead to the interpretation of the eastern boundary of the Carboniferous sediments as a continuous reverse shear zone, as already suggested by Pairis et al. (1992) and Dobmeier and Von Raumer (1995). The fact that the shear zone bounds the Crête-Blanche klippe implies that it is younger than the Haut-Giffre thrust. Carboniferous sediments below the shear zone are affected by folds with an axis striking N13° (Fig. 4.19a), suggesting an ≈E-W direction of compression, compatible with the measurements of the faults above.

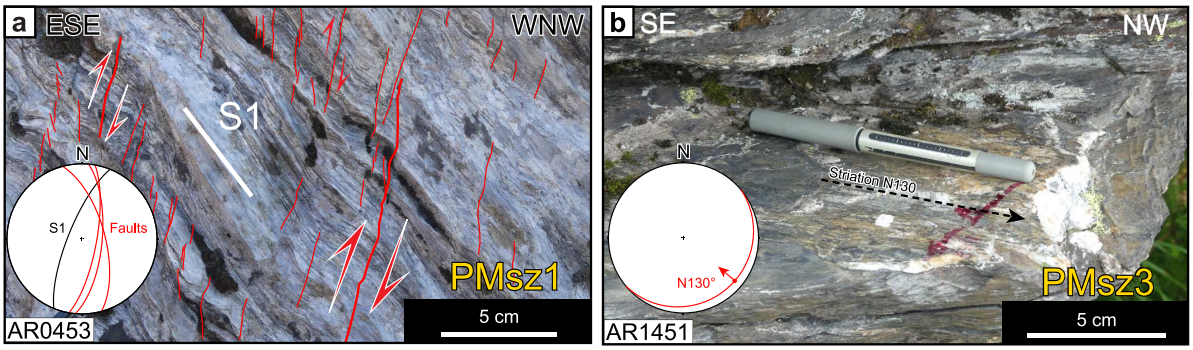

Figure 4.22. Steep thrust affects the limestones, and initial foliation is cross-cut by steep faults (station AR453). b) Flat reverse fault associated with the Pormenaz-Merlet shear zone with a striation trending N120, indicating top to the northwest

Back Thrusting on the eastern side of the Aiguilles Rouges North of the Aiguilles Rouges, at the limit between the Salvan-Dorenaz Carboniferous - Permian basin and the basement of the Aiguilles Rouges (Site FB1, Fig. 4.8a) the Permian sediments show an ≈ N32° sub-vertical schistosity and west-dipping reverse shear planes trending N12° on average (Fig. 4.24a and b). These observations indicate that at this location the Variscan basement is thrust toward the east over the Salvan-Dorenaz basin, along a previously unreported thrust fault, which we call Finhaut back thrust. According to the published geological map (Collet et al., 1952), the Finhaut back thrust probably extends 5 km to the south (Fig. 4.8a). Within the basin, the sediments are strongly folded with a fold axis trending ≈ N30° and steep axial plane schistosity trending N20° on average (Fig. 4.24c). Similar folds are found in the Carboniferous/Permian sediments of the Posettes area on the other side of the valley. A previously unreported ≈ N20° trending normal fault, the Gietroz fault, offsets the basin (Fig.4.242c). A thin section of the ARe096 sample (Fig. 4.23) indicates a normal shear sense in the fault. Both the Finhaut back thrust and the folds affecting the Salvan-Dorenaz basin could have formed coevally during an ≈ N110° compression phase, while the Gietroz fault is probably younger.

West-dipping reverse faults and shear zones trending ≈ N20°, although never described in the literature, are relatively common in the eastern part of the Aiguilles Rouges. Another

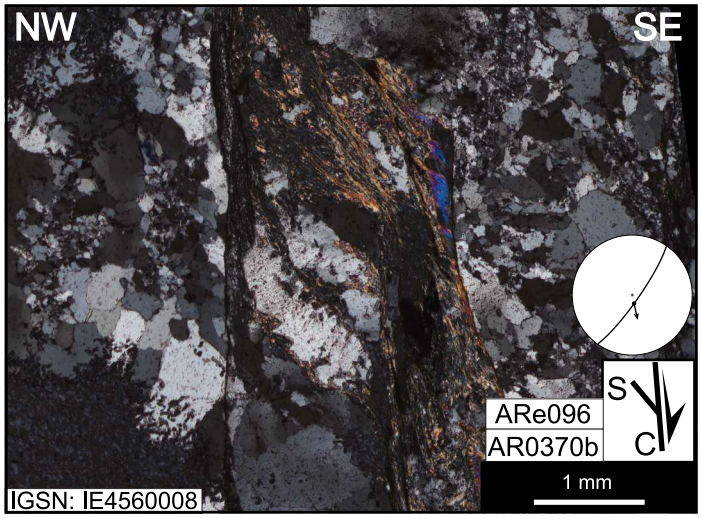

Figure 4.23. Thin section of sample ARe096, (station AR0370b) from the Gietroz fault. The sample is a pseudotachylite with quartz and micas, the C/S relation is interpreted as normal sense of shear (southeast down).

example can be found further south (site FB2, Fig. 4.8a), where reverse faults trend N17° ; 77° W with clear evidence of thrusting towards the southeast. Numerous such faults are also visible on the eastern shore of Emosson Lake (site FB3, Fig. 4.8a) striking on average N15° ; 59° W with striations azimuth trending ≈ N105°. Such a fault trending ≈ N33° ; 60° W with a striation with a pitch of 75° N is also visible at site HGT1 (location AR0162) in between possibly earlier normal faults (Fig. 4.12c).

The brittle regime of these faults suggests that they occur under low-pressure / low-temperature conditions and could be related to recent deformations. These observations suggest that the back thrust in the Aiguilles Rouges has been overlooked and may play an important role in the structuration and exhumation of the massif.

Further south in the Chamonix valley, most of the western border of the synclinorium is hidden by Quaternary deposits. However, a large outcrop of limestones attributed to the Jurassic (Ayrton et al., 1987) is visible at site TB1 (Fig. 4.8a). These limestones are affected by a schistosity that trends N72° ; 40° N and are overlain by the basement of Aiguilles Rouges composed of Variscan gneiss and a Permo-Carboniferous tight syncline (Fig. 4.25a). Just above the contact, the Permian green siltites are foliated (N2° ; 44° E) and a bear mineral lineation (N126°). The thin section cut parallel to the lineation shows a clear thrust top to the southeast with S/C criteria (sample ARe033, Fig. 4.25c). At this location, the Aiguilles Rouges basement is therefore thrust above the cover.

Six kilometers further north near le Tour village (site TB2, Fig. 4.8a) Mesozoic sediments are also found below the Aiguilles Rouges basement. The Permian green siltites are foliated, with S / C criteria that indicate a top to the southeast reverse shear (Fig. 4.25b and d). This

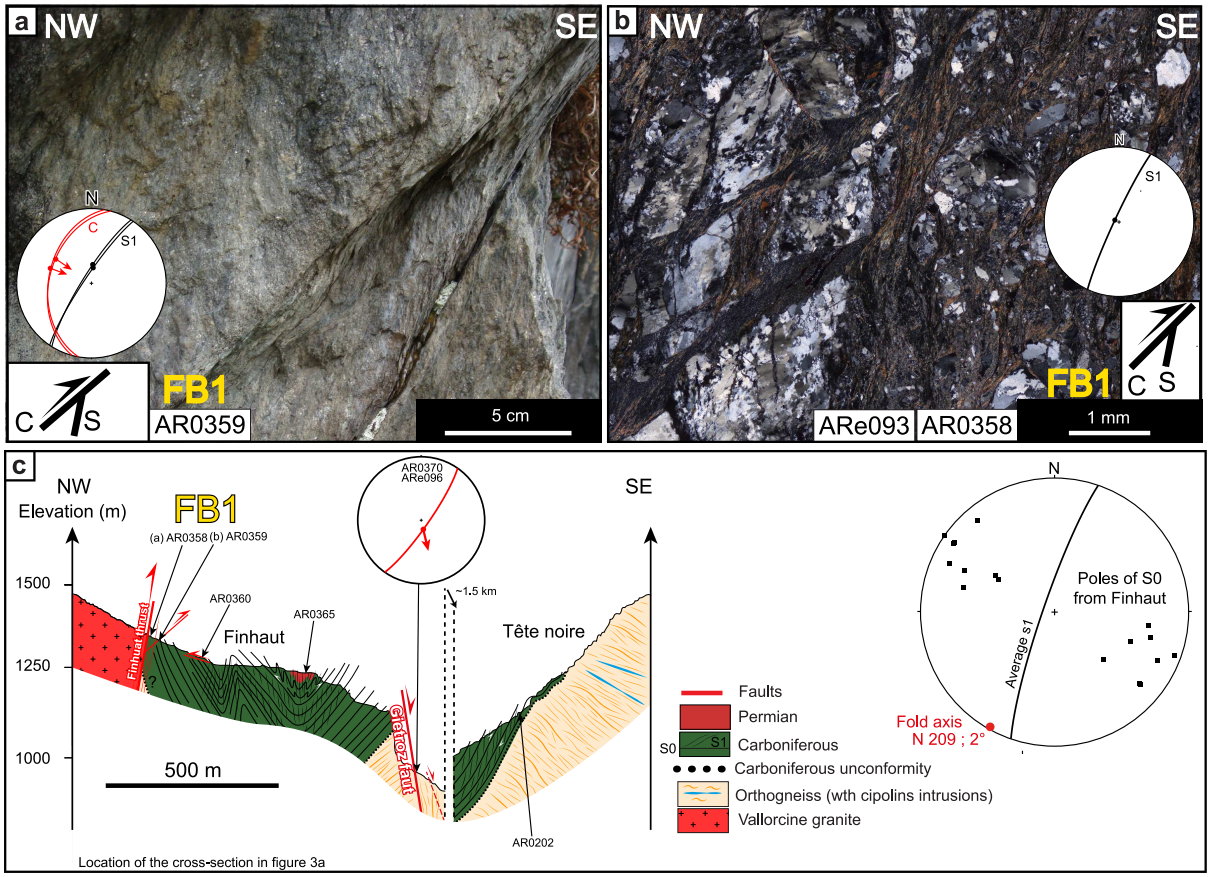

Figure 4.24. The Finhaut back thrust. a) Thin section of sample ARe093 of the Finhaut thrust (site FB1, Fig. 4.8a). Greenschist foliation strike N25° ; 85° W and S/C relationships imply a reverse motion. b) Shear planes within Carboniferous sediments in the footwall of the Finhaut back-thrust at location AR0359. Shear planes (C) strike N10° ; 42° W, C/S relation implies a top to the south-east sense of shear. c) Cross-section across the Salvan-Dorénaz basin, see Fig. 4.8a for location. Stereo plots (equal area, Lower hemisphere projection) in the Finhaut area the average folds axis dips 2° to N209°.

contact continues ≈ 2 km toward the northeast (Fig. 4.8a). The two faults at sites TB1 and TB2 have the same direction and the same kinematics and are interpreted as a back-thrust fault of the Aiguille Rouges above the Chamonix synclinorium that we call the Le Tour Back thrust (Fig. 4.8a).

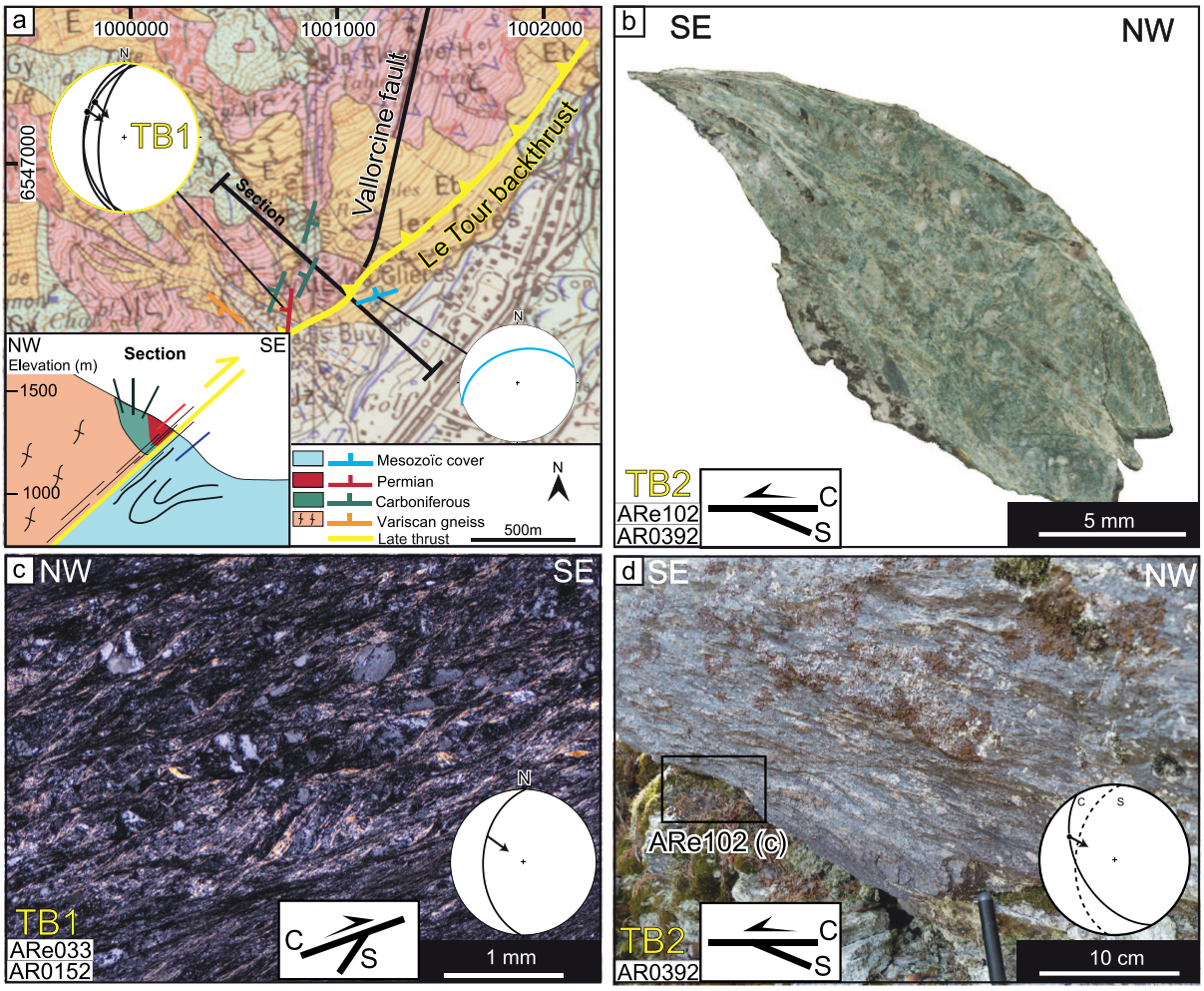

Figure 4.25. Le Tour back thrust. a) Structural map and cross-section (inset). The background is the 1:50.000 geological map (Ayrton et al., 1987). Stereo plots (Lower hemisphere, equal-area projection) show the orientations of the foliation in the Mesozoic sediments in the over-thrusting Permian schists. b) Thin section of the sample ARe102, S/C relationship suggests top to the south-east reverse sense of shear; c) Thin section of sample ARe033 cut parallel to lineation. S/C relationship suggests top to the southeast reverse sense of shear. d) Location of sample ARe102 from location AR0392, S/C relationships indicates top to the south-east sense of shear.

Further south there is no outcrop of Mesozoic sediments and the Tour back-thrust cannot be mapped. We infer that this fault is hidden by the Quaternary deposits (Fig. 4.8a). Cartographically, the Tour back thrust is parallel to the Finhaut back thrust, thus they have possibly been activated at the same time. Le Tour back thrust is seen in the GeoModel, bringing the Posettes Permo-Carboniferous syncline atop the Chamonix Synclinorium (Fig. 4.9 and fig. 4.26a, b, and c).

4.3.5 Relative timing of the main structures

After the deposition of Mesozoic and Cenozoic sediments, the first widespread shortening tectonic phase in the area involved thrusting of the Mesozoic / Cenozoic cover toward the west along a relatively flat structure that we term the Helvetic basal thrust (HBT) (HBD of Leloup et al. (2005)). This structure was later cut and offset by steeper thrusts on both sides of the Chamonix synclinorium: the Mont-Blanc shear zone on the western edge of the Mont-Blanc (Eltchaninoff, 1982; Butler, 1985; Leloup et al., 2005; Egli and Mancktelow, 2013) and the Le Tour and Finhaut back thrusts along the eastern edge of the Aiguilles Rouges.

The relative chronology of the Pormenaz-Merlet shear zone is difficult to establish. Toward the south, the shear zone appears to be cut by the Le Tour back thrust and/or the Mont-Blanc shear zone as it is not seen on the southern side of the Chamonix valley, but the precise field relationships are obscured by Quaternary deposits (Fig. 4.8). The shear zone cuts and offsets the Crête Blanche klippe that we interpret as part of the HBT (Fig. 4.19 a), but further north the shear zone does not significantly offset the HBT (Fig. 4.8). We interpret this apparent inconsistency as due to a decrease of the Merlet-Pormenaz shear-zone offset toward the north, whilst this point still requires further field investigations. Therefore, we infer that the Merlet-Pormenaz shear zone is younger than the HBT and older than the Mont-Blanc shear zone. Thus, it is an Alpine structure that has never been described as such.

The Vallorcine fault has a polyphase history and corresponds in fact to several structures active both before and during the Cenozoic, but it appears to not significantly offset the Le Tour back-thrust.

The Gietroz normal fault has a limited extent and offsets (Fig. 4.24c) which renders its relative timing difficult to determine. The main extension phases in the area (early Jurassic and Eocene-Oligocene) are antecedent to the Alpine shortening phases, but the fault seems to offset the folds associated with the Finhaut back thrust (Fig. 4.24c).

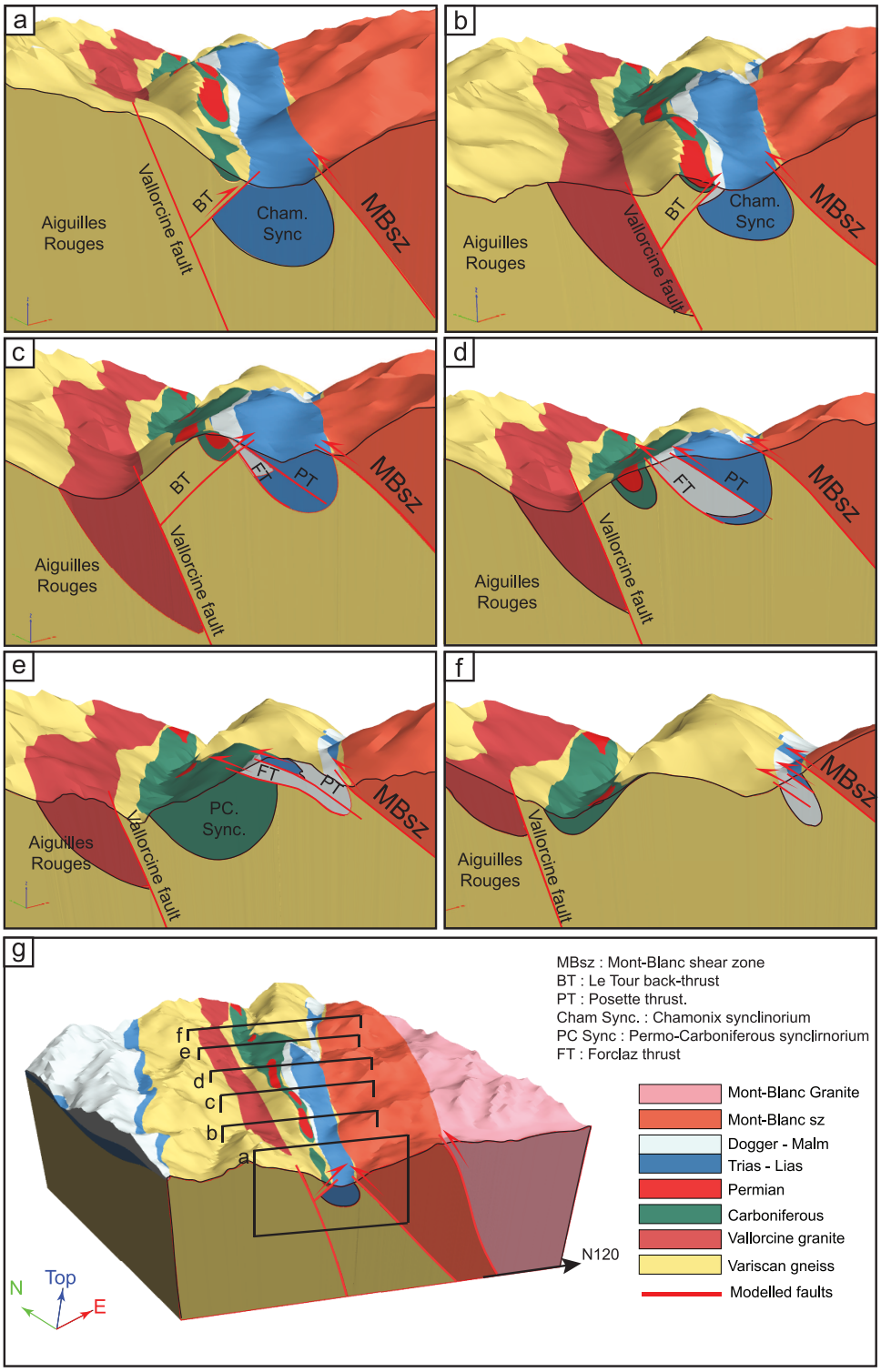

Figure 4.26. Cross-sections of the Argentiere 3D GeoModel highlighting the structural continuity of the Chamonix synclinorium. a to f: successive cross-sections from south to north. Note that Finhaut thrust has not been included in this model, and that the precise shape of the Chamonix synclinorium is not constrained at depth

4.4 3D geological model of the Mont-Blanc, Aiguilles Rouges and Subalpine chains

In the following section, we present a detailed structural study based on the 3D GeoModel of the entire Mont-Blanc massif and surrounding areas. The structural description is based on field observations, microtectonic characterization, and published structural data.

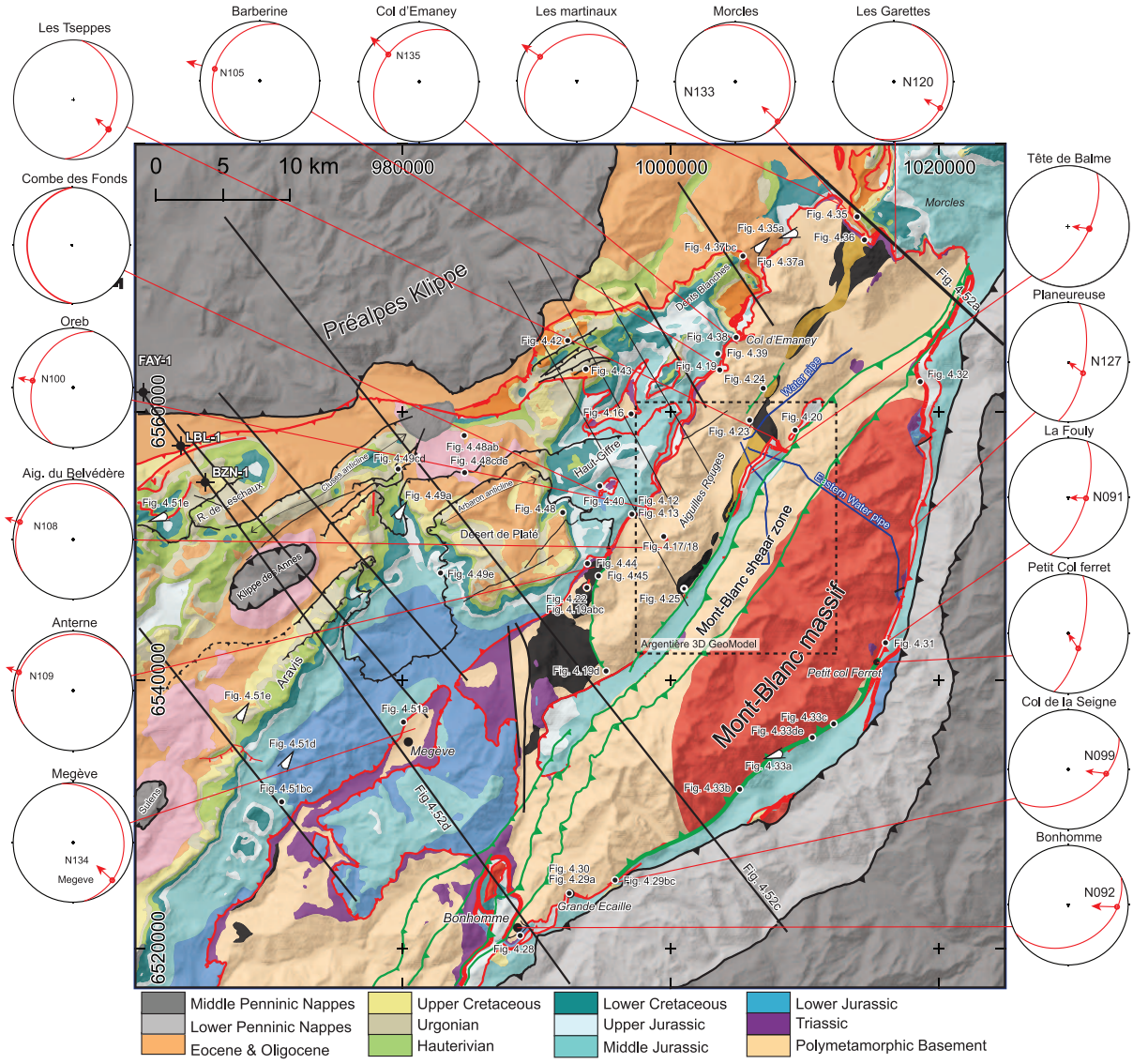

Figure 4.27. Structural map output from the 3D Geological model. Stereoplot are in Lower hemisphere, equal area and show foliation or shear planes kinematics in the studied areas with stretching lineation or slickenline directions, the arrow indicates the motion the Upper block motion.

4.4.1 Thrusting along the Eastern margin of the Mont-Blanc massif

Bonhomme In the southeastern tip of the Mont-Blanc massif, the well-known "Grès Singuliers" formation consists of Lower Jurassic clastic sandstones reflecting the emergence of the

massif at that time (e.g., Antoine et al., 1975; Eltchaninoff, 1982; Ribes et al., 2020). Their distribution is restricted to the western side of the Mont-Blanc massif, where they can be observed in the Bonhomme region, where they overlie the Triassic deposits (Fig. 4.28).

The bottom of the sedimentary series corresponds to a sandstone layer dipping in the southeast (Emosson formation) (Mennessier et al., 1977). This layer marks a sedimentary unconformity above the Mont-Blanc basement. The Triassic series continues with dolostones that do not appear to have been affected by any deformation, although they appear to be brecciated at some locations (Leloup, 2023; Dall'Asta et al., 2022). The Lower Jurassic is characterized by sandstones attributed to the Sinemurian / Pliensbachia and named the "Grès Singuliers" formation (Landry, 1976; Epard, 1990; Ribes et al., 2020; Eltchaninoff-Lancelot et al., 1980). These sandstones, up to 50 m thick, have been interpreted as the result of a local uplift of the Mont-Blanc basement associated with a normal fault (Epard, 1990) or a large extensional detachment fault (Ribes et al., 2020; Dall'Asta et al., 2022). The top of the overlying "Grès Singuliers" formation bears a stretching lineation trending N93° (Fig. 4.28b and c), suggesting that the above cover has been transported in that direction, stretching the sandstone surface. Above, in the Nant des Lotharets (Figs. 4.28a and d), the Middle Jurassic corresponds to Aalenian southeast dipping slates that are strongly foliated with an S/C relationship indicating a top-to-the-west shearing (Figs. 4.28a and d). Further up in the series, the Upper Jurassic limestones are strongly foliated and metamorphosed to marble with asymetric boudinaged calcite veins and have a lineation trending N95° (Fig. 4.28e). These observations imply a thrusting of the middle and Upper Jurassic cover above the autochthonous Triassic and Lower Jurassic "Grès Singuliers" formations. South of the Rocher du Bonhomme, the basement and autochthonous series are affected by a fault, oriented N40°, dipping to the northwest of 30° and bearing a slickenline trending N270° (Fig. 4.28f) and g). Ribes et al. (2020) and Dall'Asta et al. (2022) described this fault as part of a major detachment that emphasizes a necking of the European crust, inherited from the Tethys rifting (Dall'Asta et al., 2022). From unclear field evidence, the authors suggest a detachment of the Jurassic cover above the basement, southward, which is not in agreement with our field observation. In fact, the foliation of the fault gouge is nearly horizontal (Fig. 4.28f) and the fault plane dips westward, implying a normal sense of motion of the Upper compartment in the west direction according to the slickenline (Fig. 4.28g). The idea of a large detachment fault suggested by Ribes et al. (2020) and Dall'Asta et al. (2022) has also been contested in detail by Leloup (2023). However, this normal fault affects the basement, the Triassic, and the Lower Jurassic; in fact, its timing could be related to the Jurassic rifting of the Tethys event or related to the Eocene opening of the European Western Rift.

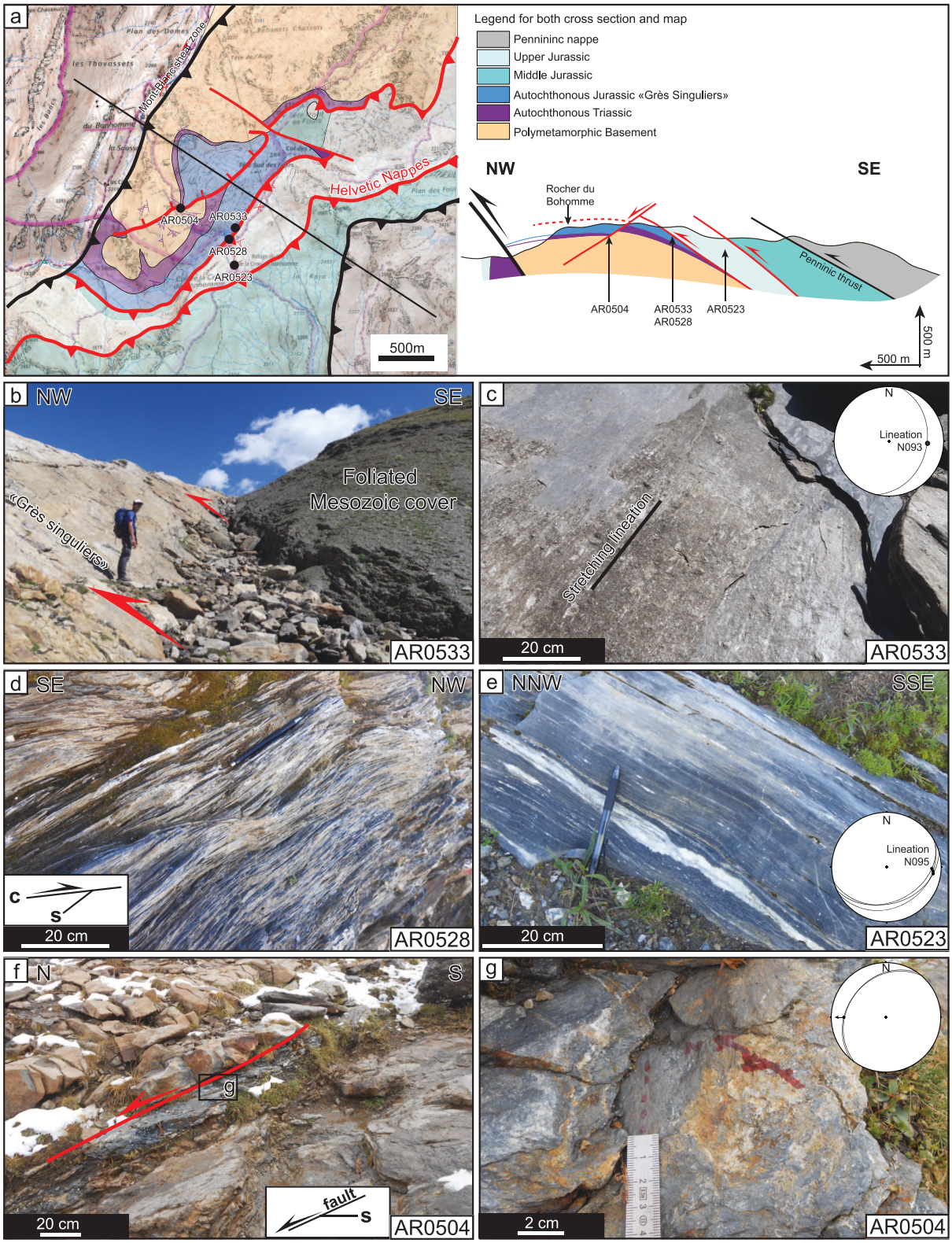

(Figure caption on next page)

Figure 4.28. Field observations and interpretation of the Bonhomme area. a) Map and cross section outputted from the 3D GeoModel, the middle and Upper Jurassic cover is trusted above the autochthonous Triassic and Lower Jurassic cover; b) Nant des Lotharets, contact between the foliated Aalenian black slates and the Lower Jurassic "Grès Singuliers"; c) Stretching lineation at the top of the "Grès Singuliers" formation, below the basal thrust of the nappes; d) S/C relationship indicating a top-to-the-west sense of shear within the Aalenian foliated black slates; e) Upper Jurassic metamorphized to marble above the Aalenian black slates, the stretching lineation oriented N$95°$ indicate a stretching direction E-W; f) Normal fault affecting the basement and the autochthonous Triassic sandstones, the fault plane is dipping westward and the associated foliation within the core of the deformation zone is nearly horizontal, indicating an apparent top-to-the-west sense of motion of the roof; g) Slickenline on top of the fault plane in oriented azimuth N$100°$.

The Grande Ecaille Further north along the eastern side of the Mont-Blanc massif, the Grande Écaille is an impressive summit, clearly visible from the path between the Refuge du Col de la Croix du Bonhomme and the Refuge Robert Blanc. Viewed from the south, the sedimentary cover's foliation is clearly visible, dipping about $50°$ towards the southeast (Fig. 4.29). Below (westwards) the basement is composed of Variscan gneiss and shows a planar preferential orientation, parallel to the cover's orientation and to the contact. Below the cover / basement contact, the basement shows a SE-dipping foliation of N$58°$; $35°$ S (Figs. 4.30a and b), subparallel to the overlying limestones that have a foliation oriented N$45°$; $55°$ SE and a lineation oriented N073 (Fig.4.30c). Near the col de la Seigne (Fig. 4.29 a), the basement also shows a strong foliation, oriented N$52°$ to N$67°$ with a lineation striking N$80°$ (Fig. 4.29b). A thin section has been made, cut perpendicularly to the foliation and along the lineation (Fig. 4.29c). Microstructural interpretations indicate a mylonitization of the basement, highlighted by quartz grains (≈ 0.5 mm diameter), and the S/C relationship shows a clear top-to-the-northwest sense of shear along with the tiny white micas that have crystallized most likely during deformation. This sample ARe176 is a good candidate for $^{40}Ar/^{39}Ar$ *in situ* dating.

In the Grande Ecaille region, above the mylonitized basement, the limestones are strongly foliated, with an asymmetric boudinage of calcite veins showing a top-to-west sense of shear (Fig.4.30d). This section has been already described in detail by Antoine et al. (1975), their description highlights the presence of mylonitized basement slices inside the deformed limestones (Fig. 4.30a). However, their interpretation is that the contact between the Jurassic cover and the basement is stratigraphic (autochthonous cover). On the contrary, from field observations we argue that both the cover and the basement are affected by strong top-to-west deformation and that the cover is thus allochtonous. These observations are in agreement with those in the Nants des Lotharets area, where it has been observed that the Jurassic cover is thrust toward the west. This interpretation is in agreement with that of (Egli and Mancktelow, 2013)

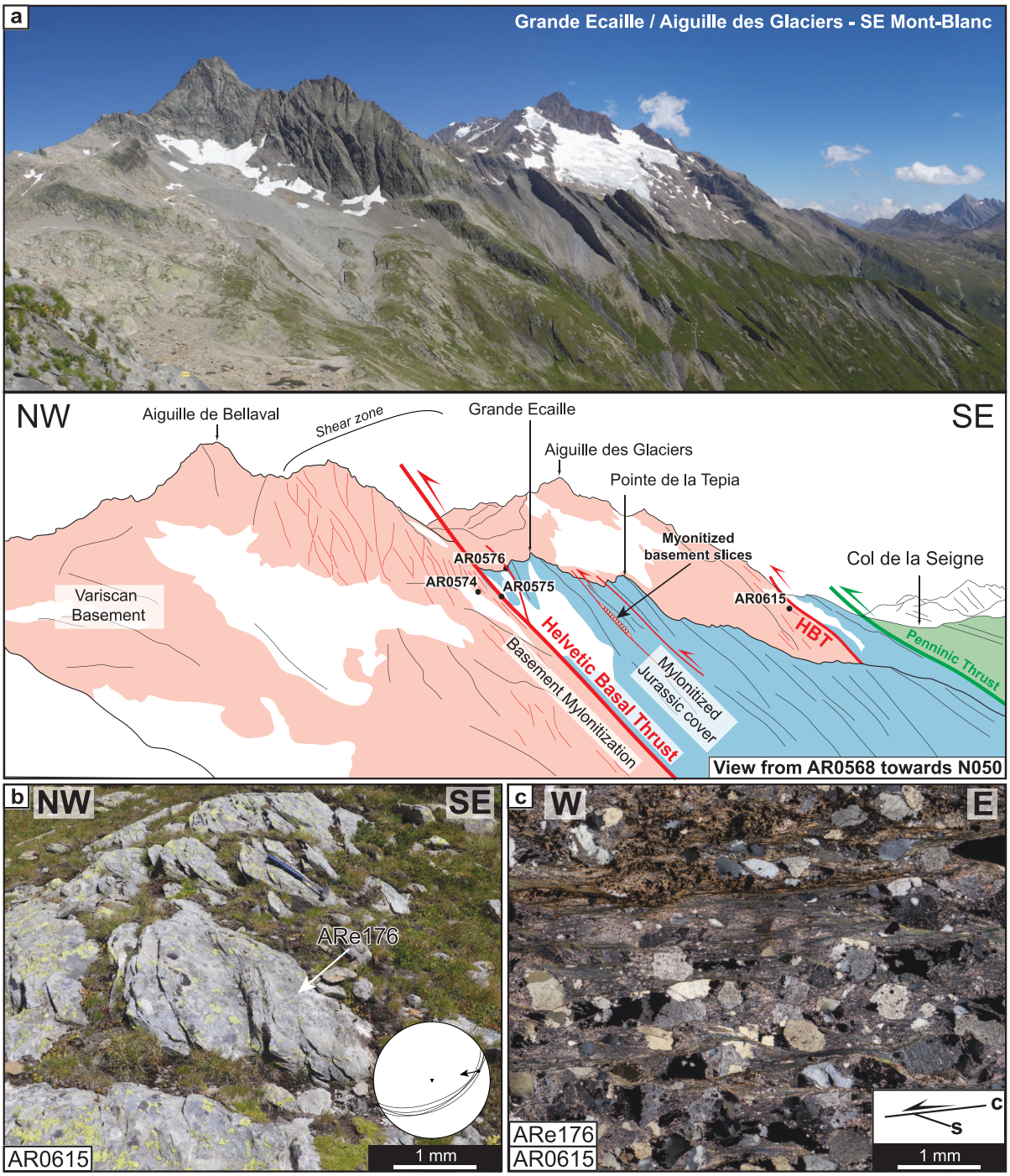

Figure 4.29. Section of the Grande Écaille and field observations. a) Panorama from the location AR0568 towards the azimuth N50°; b) Foliated basement dipping east parallel to the overlying nappes and bearing a E-W lineation; c) Optical microscopic image of a thin section cut perpendicularly of the foliation and parallel to the lineation from sample ARe176 (see b). The microstructural observations shear bands cross-cutting the foliation indicate a clear top-to-the-west sense of shear.

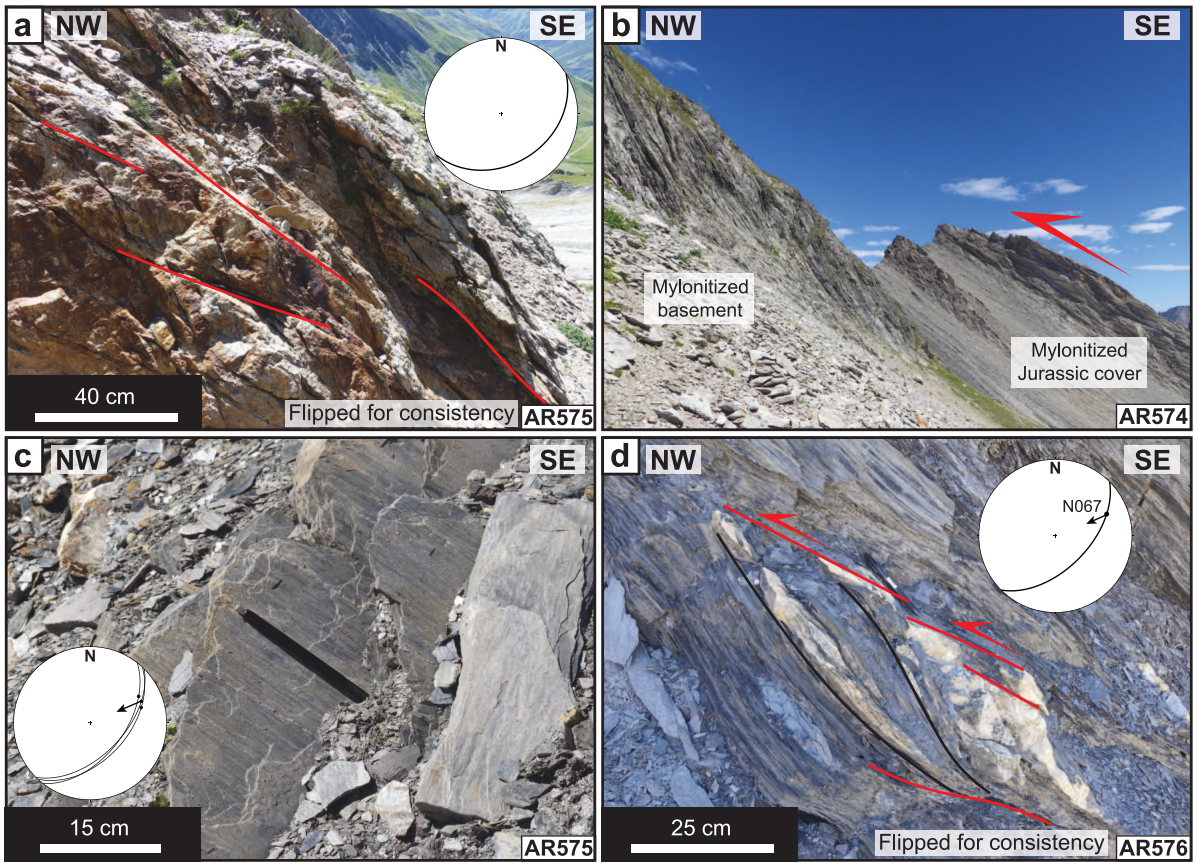

Figure 4.30. Field observations from the Grande ÉEcaille area. a) Foliated basement below the basal contact of the nappe; b) Mylonitized basement and cover at the contact of the nappe; c) Strongly foliated limestones bearing a stretching lineation trending N73°; d) Asymetric boudinage of calcite with a stretching lineation trending N67°.

Petit Col Ferret - La Fouly Further north (Fig. 4.27), on the southern side of the Petit Col Ferret (Italy), the basement is affected by a series of small backthrusts that slightly offset the Mesozoic cover on its top (Fig. 4.31f), and thus the Mont-Blanc back thrust seems to die out further north. In the Combe des fonds, on the northern side of the Petit Col Ferret (Switzerland), the sedimentary cover is on top of the basement and the contact is nearly north-south oriented and dipping eastwards. There, the regular stratigraphic succession described in the Bonhomme area (autochthonous Triassic, Lower Jurassic, etc.) is not respected, and the Upper Jurassic is directly in contact with the basement. There, the Upper Jurassic limestones are strongly foliated and marmorized, with rolling structures (Fig. 4.31a) and asymmetric boudinage (Fig. 4.31b) clearly indicating a top-to-west sense of shearing. Very few estimates of the temperature deformation of ductile marble are available; however, some authors suggest that ductile deformation of limestone can occur between 200 and 250 °C (Molli et al., 2011). Strongly foliated levels of crystalline rocks are embedded within the marbles and asymmetrically boudinaged (Fig. 4.31c and d). Similar intercalations of basement slices have also been documented in the north-Belledonne massif by Landry (1978) and Eltchaninoff-Lancelot et al. (1980) and in the Aiguilles Rouges at the col de Barberine (Fig. 4.11). The origin of these crystalline "slices" embedded in the sedimentary cover is still unclear, and some authors have suggested that they are olistostromes that have fallen from the footwall of a normal fault during the opening of a basin. Although olistotromes have been documented in the Eocene flysch below the Morcles nappe, there is no mention of such blocks within the Upper Jurassic. We suggest that these blocks come from the basement and have been stretched during nappe transport. Further north, at Petit Col Ferret, the basement of Mont-Blanc is mylonitized and affected by deformations related to the Helvetic nappes transport (See Fig. 5.14 from Chap. 5 at p. 231).

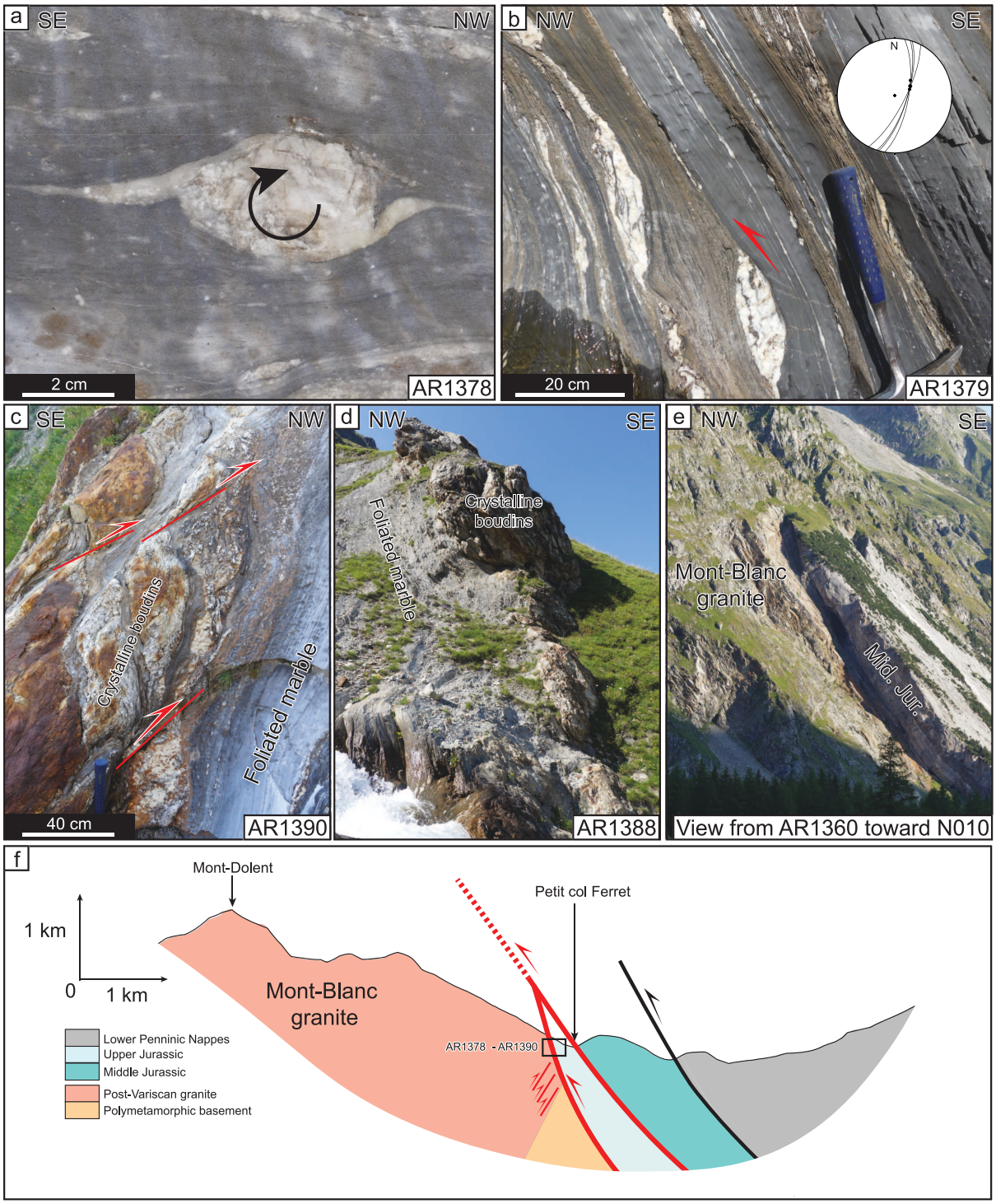

Figure 4.31. Cover/basement contact on the eastern side of the Mont-Blanc massif, from the northern side of the Petit Col Ferret (Switzerland). a) Rolling in the Upper Jurassic limestones, indicating a top-to-the-west sense of shearing; b) Asymmetrically boudinaged calcite veins within the Upper Jurassic limestones, suggesting a top-to-the-west sense of shear; c and d) Asymmetrically boudinaged basement blocks within the Upper Jurassic limestones; e) Dalle de l'Amone, made of Triassic sandstone and Lower Jurassic sandstones.

Sembrancher North of Sembrancher village, on the road to the Col des Planches, the basal contact of the Helvetic Nappes on the basement can be described. From the east, the Upper Jurassic limestones are strongly foliated and maramorized with rolling porphyroclasts of calcite (Fig. 4.32a) indicating a top-to-northwest sense of shear and a stretching lineation oriented N140. Near the same location, the limestones are also boudinaged and shear, the stretching lineation indicates a direction of motion from N120° to N126° (Fig. 4.32b). The basal contact of the Triassic is characterized by a clastic microconglomerate of quartz, blocks of dolostones, limestones, and Cargneules (Fig. 4.32c). The basement below the contact is affected by a reverse fault oriented N10° ; 57° E (Fig. 4.32d). Both the crystalline basement and the Triassic are affected by the same fracture cleavage, suggesting that the unconformity was locally used as a décollement.

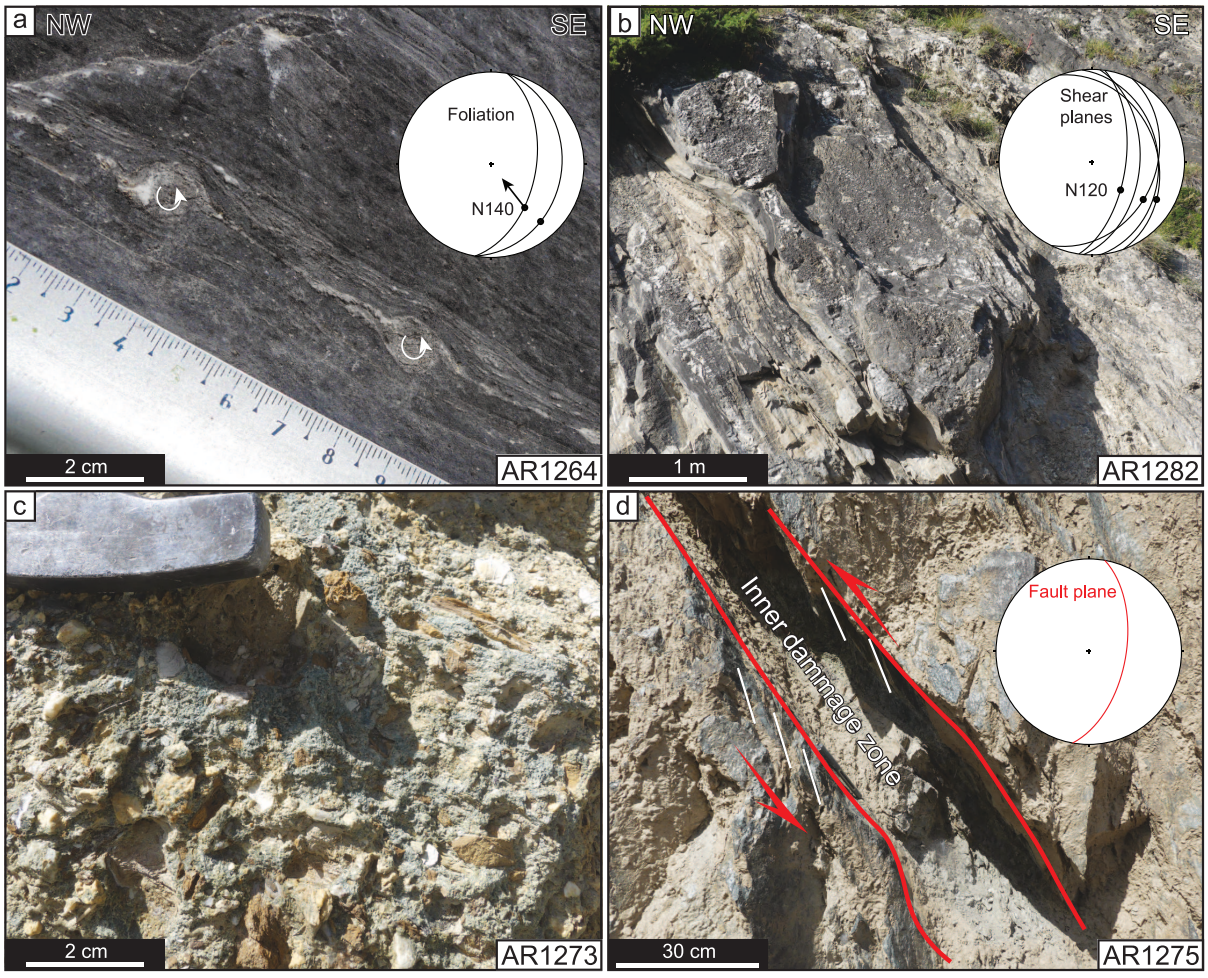

Figure 4.32. Cover / Basement contact on the road to the col des Planches, north of Sembrancher. a) The Upper Jurassic limestones are strongly foliated and marmorized with rolling prophyroclasts of clacite; b) Boudinaged limestones; c) Clastic breccia; d) Reverse fault in the crystalline basement below the Triassic unconformiry.

4.4.1.1 Back thrusting on the Eastern side of the Mont-Blanc massif

The eastern contact of the cover / basement in the Mont-Blanc massif is dipping westward from the Col de la Seigne in the south to the Petit Col Ferret further north. This contact has been suggested to be a back thrust fault (Leloup et al., 2005), a back thrust / fold of the Mont-Blanc (Egli and Mancktelow, 2013), or a tilted normal fault, reactivated during alpine orogeny (Ribes et al., 2020). From Mont-Fréty, the contact is visible and oriented about N$40°$ to N$70°$, with the Mont-Blanc granites standing above the overturned Jurassic limestones (Fig. 4.33a and b). Near the Italian exit of the Mont-Blanc tunnel in the Brenva Valley, the granites are crosscut by a fault, associated with a gouge. The fault plane is oriented N$40°$, dipping to the northwest, with a down-dip slickenline and bears in some part pseudotachylite patches. The foliation within the fault gouge is nearly vertical (Fig. 4.33b), suggesting a reverse top to the southeast sense of motion. Further north, on the way to the Boccalate hut, the granite is mylonitized and is oriented toward about N$60°$, with a clear S/C relationship indicating a top-to-southeast sense of shearing (Fig. 4.33c). About a kilometer further north, the same contact is oriented N$45°$ and covered by calcite step-crystallization, with a nearly horizontal slickenline, suggesting a strike-slip reactivation. The microstructural criteria could indicate a dextral strike-slip motion based on the step-crystallization of calcite. A thin section in the granite against the contact has been made (Fig. 4.33e) and reveals a cataclastic deformation, with broken quartz grains embedded in a fine quartz and white mica matrix. These field observations are in agreement with a back thrust of the Mont-Blanc massif towards the southeast as documented by Leloup et al. (2005), Rolland et al. (2008) and Egli and Mancktelow (2013). The timing of activity of this structure remains debated, and Leloup et al. (2005) have suggested a recent (< 5 Ma) activity along this structure due to the brittle deformation associated with it. Furthermore, Rolland et al. (2008) have dated synkinematic white micas using $^{40}Ar/^{39}Ar$ from shear zones within the Mont-Blanc massif with a top-to-the-southeast sense of shear. Their results suggest a narrow age range of 15.8 to 16.0 Ma of activity in these shear zones. Finally, the dated northwest dipping shear zones are more internal within the Mont-Blanc granite and could have been initiated before and at a higher temperature than the back thrust fault described here. In any case, the deformation was active from about 16 Ma, under ductile conditions of deformations, continued in a fragile regime, and later the contact could have been reactivated in strike-slip (dextral) mode in brittle conditions.

4.4.1.2 Preliminary synthesis on the cover / basement interface on the Eastern side of the Mont-Blanc massif

From the observations from the eastern side of the Mont-Blanc, we highlighted that the Jurassic sedimentary cover is thrusted above the Mont-Blanc. The autochthonous cover consists of the Triassic sandstones and locally to the Lower Jurassic "grès singuliers" sandstones.

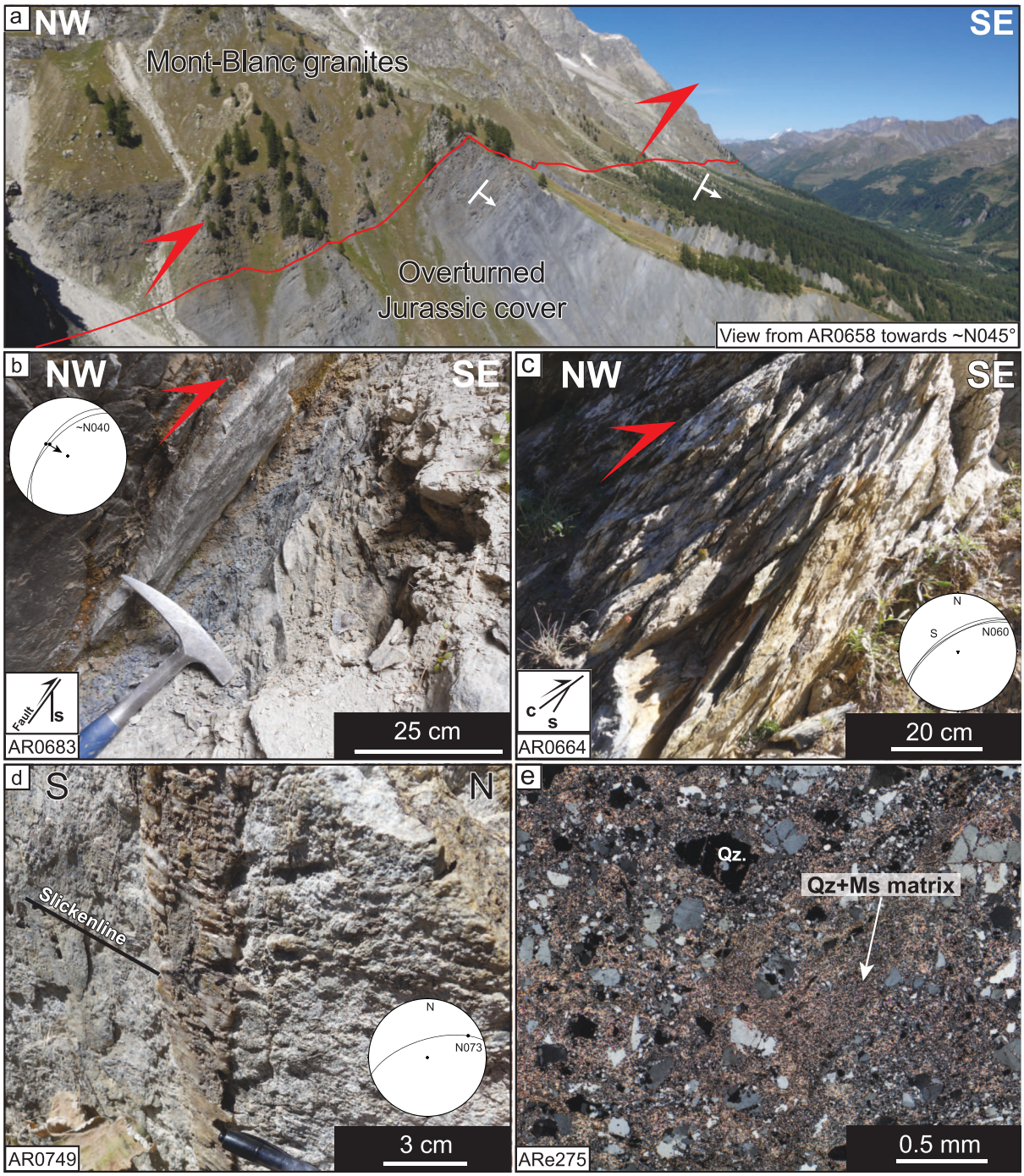

Figure 4.33. Mont-Blanc back thrust field observations. a) Panorama from the Mont Fréty to the northeast. The northwest dipping contact of the cover/basement is well visible; b) In the Brenva Vallon (near the Italian exit of the Mont-Blanc tunnel), the granite is cross-cut by a fault N40°, northwest dipping fault, bearing a down-dip lineation. The foliation in the fault gouge is nearly vertical, suggesting a top-to-the-southeast sense of motion; c) Mylonitized basement above the cover/basement interface in the path to the Boccalate hut. The S/C relationship indicates a top-to-the-southeast sense of shear; d) Cover/basement contact oriented N43° and dipping northwest is covered by calcite step-crystallization and bearing a nearly horizontal slickenline; d) Thin section of the contact in (c), showing a cataclastic deformation with broken quartz grains embedded in a fine quartz and white micas matrix

However, in the Grande Ecaille and the Petit Col Ferret, the basal thrust affects the basement in mylonites. The Mont-Blanc is limited by a backthrust that overturns the sedimentary cover towards the southeast.

4.4.2 Western side of the Aiguilles Rouges: thrusting of the cover

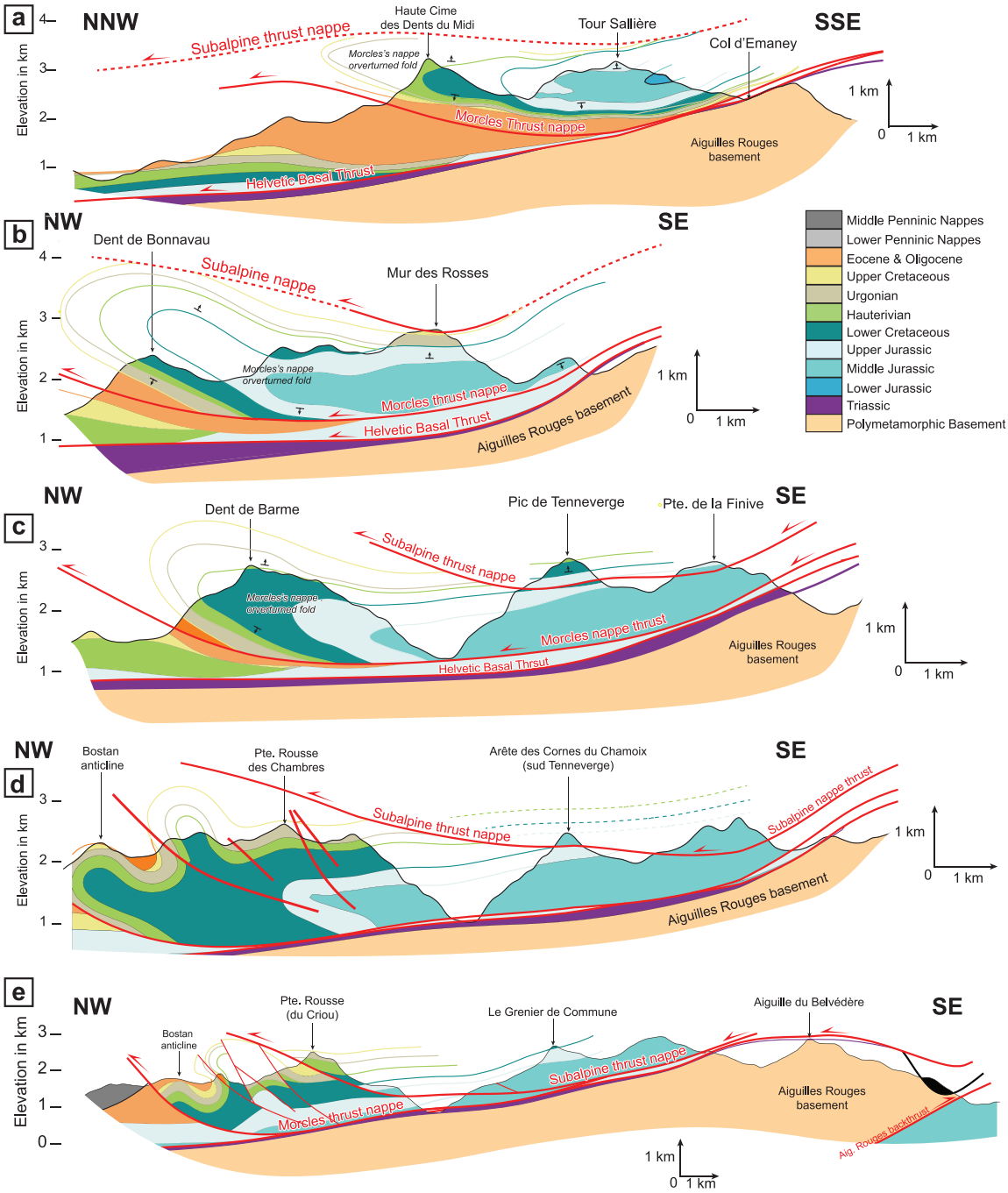

Figure 4.34. Cross sections through the 3D geological model in the Haut-Giffre - Dents Blanches massif.

Dent de Morcles On the northern bank of the Rhône valley, the Morcles massif is structurally above the Aiguilles Rouges (Fig. 4.27). Several authors have described the so-called Dent de Morcles as a recumbent fold consisting of Jurassic and Cretaceous limestones (e.g., Héli, 1972; Epard, 1990; Escher et al., 1988; Ramsay, 1981; Pfiffner, 1993). This unit is considered the lowest of the Helvetic Nappe system. Seen from the south bank of the Rhône Valley, the Grandes and Petite Dents de Morcles are well visible: The Upper part consists of Hauterivian and Urgonian limestones, while the Lower part consists of Upper Cretaceous and Eocene flysch deposits (Fig. 4.35a). Flysch deposits above the Morcles nappe thrust are strongly folded (Figs. 4.35b and c) with folds cross-cut by an axial plane cleavage (Fig. 4.35c). Blocks of sandstones or crystalline rocks are embedded and boudinaged within the flysch, as it is a clastic sedimentary deposit (Figs. 4.35d and e).

The Mesozoic and Cenozoic cover below the Morcles nappe has often been described as para-autochthonous to say that it has been inverted in the limb of a large fold, but has not been significantly translated with respect to the underlying basement (e.g., Escher et al., 1993; Ramsay, 1981), however, our observations are clearly different. In the Jurassic, near l'Au d'Arbignon (Fig. 4.36a), the cover is cut by a nearly horizontal fault with a lineation trending from N118° to N115° (Fig. 4.36a and b). The S/C relationship associated with the deformation leads to a top-to-west sense of shearing of that fault, indicating that the cover is significantly detached from the basement, although it is rather difficult to quantify the associated displacement. Above the Morcle's basal thrust, the Urgonian limestones are strongly marmorized and elongated, giving them a "glassy" aspect (Fig. 4.36c). The lineation is clearly visible, indicating a strong simple shear component in the deformation. The limestones are strongly foliated and boudinaged (Fig. 4.36d).

From these observations, we confirmed that the Morcles massif corresponds to a reverse stratigraphy series from a large recumbent fold, limited at its base by two thrust sheets with an increase in the localization of the strain towards the thrust. The Upper thrust is located within the Eocene flysch, inducing a strong simple shear deformation in the flysch and the Urgoninan limestones, and the Lower thrust is located above the Triassic, in the Upper Jurassic limestones. These observations are in line with the description and quantification Austin et al. (2008) and Ebert et al. (2007) in the Morlces nappe.

Dents Blanches Looking at the southern side of the Rhône Valley from the Dent de Morcles, the panorama on the Dents Blanches massif also shows the reverse limb of the Morcles nappe (Fig. 4.37a). Below the Cime de l'Est, a recumbent fold is visible, most likely equivalent to the one visible in the Dent de Morcles summit. The bottom of the inverted sequence and the basal thrust are not easy to access, and we could reach them at very few points. There, according to the geological map of Collet et al. (1952) the basal thrust is punctuated with thin slices of

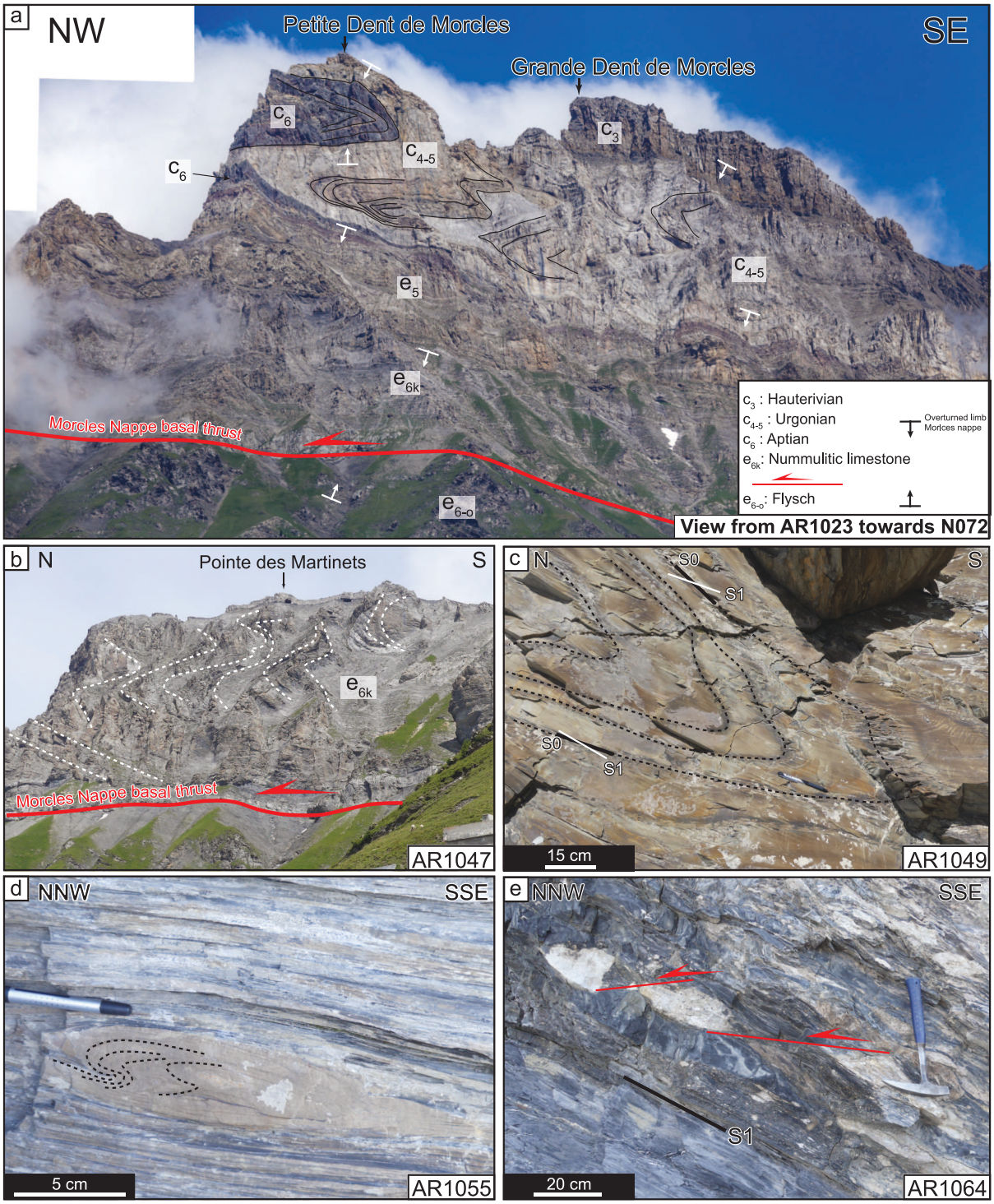

Figure 4.35. Evidence of thrusting at the bottom of the Morcles nappe. a) Panorama of the Dent de Morcles reverse limb seen from Mex; b) Intense folding in the Eocene flysch above the thrust; c) fold in the Eocene flysch cross-cut by axial plane cleavage; d) intensely sheared flysch above the décollement; e) sheared boudins of granite in the Eocene flysch.

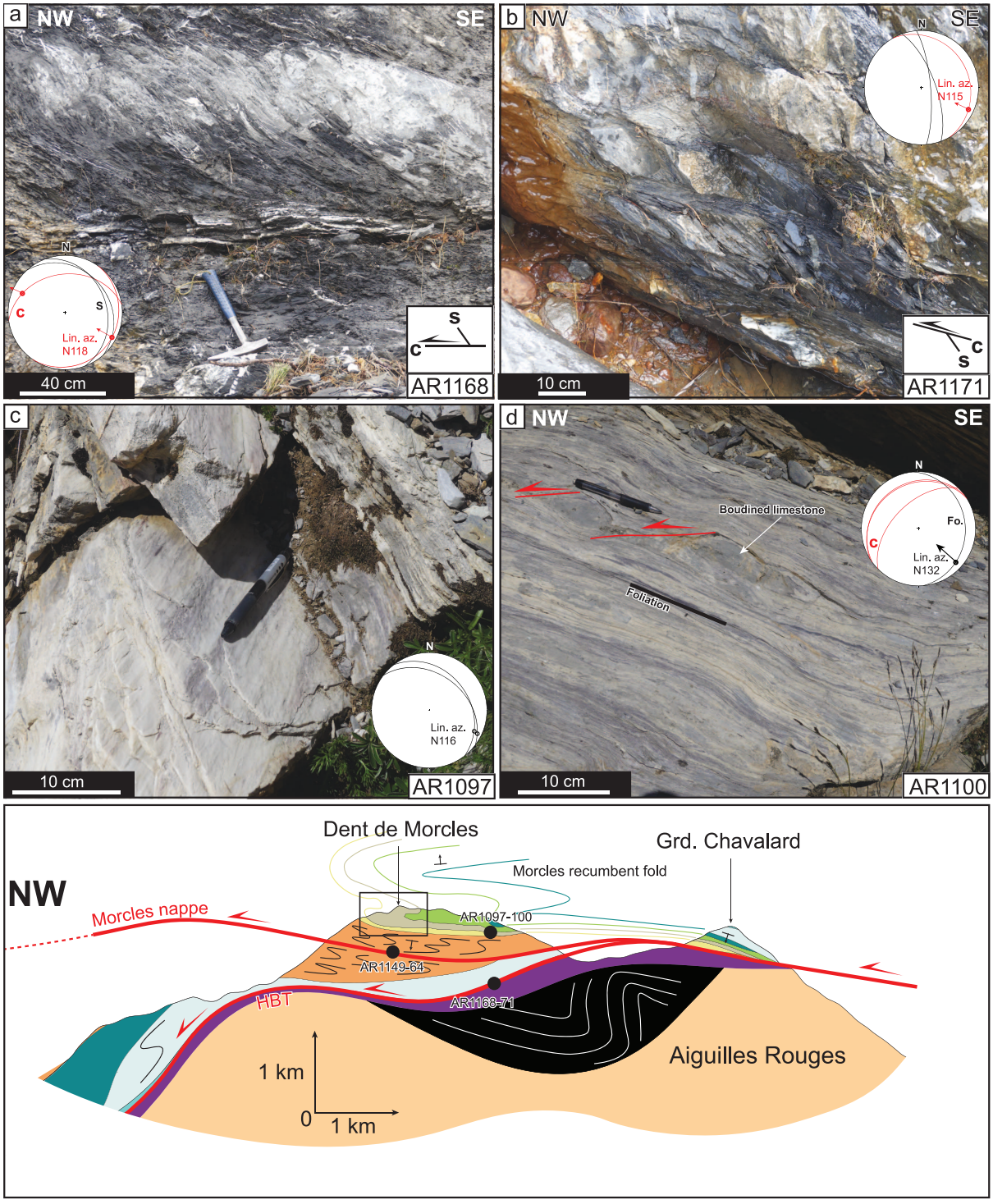

Figure 4.36. Field observations and output cross-section of Morcles nappe from the 3D GeoModel. a and b) Intensively shared Jurassic cover above the Triassic (Helvetic Basal Thrust), s/c relationship and lineations indicate clear top-tot-the-northwest sense of shearing; c) Marmorized Urgonian limestones, with a clear stretching lineation striking N116. The limestones are highly deformed and thinned, with a glassy texture; d) Sheared and boudinaged Urgoninan limestones in the Morcles nappe. e) Cross section through the Morcles nappe output from the 3D GeoModel, the location of the field observations are localized in the section.

mylonitized basement and Triassic dolostones. Our observation suggests that the dolostones are sheared towards the west (Fig. 4.37b). Below, the Eocene flysch is folded with isoclinal folds (Fig. 4.37c).

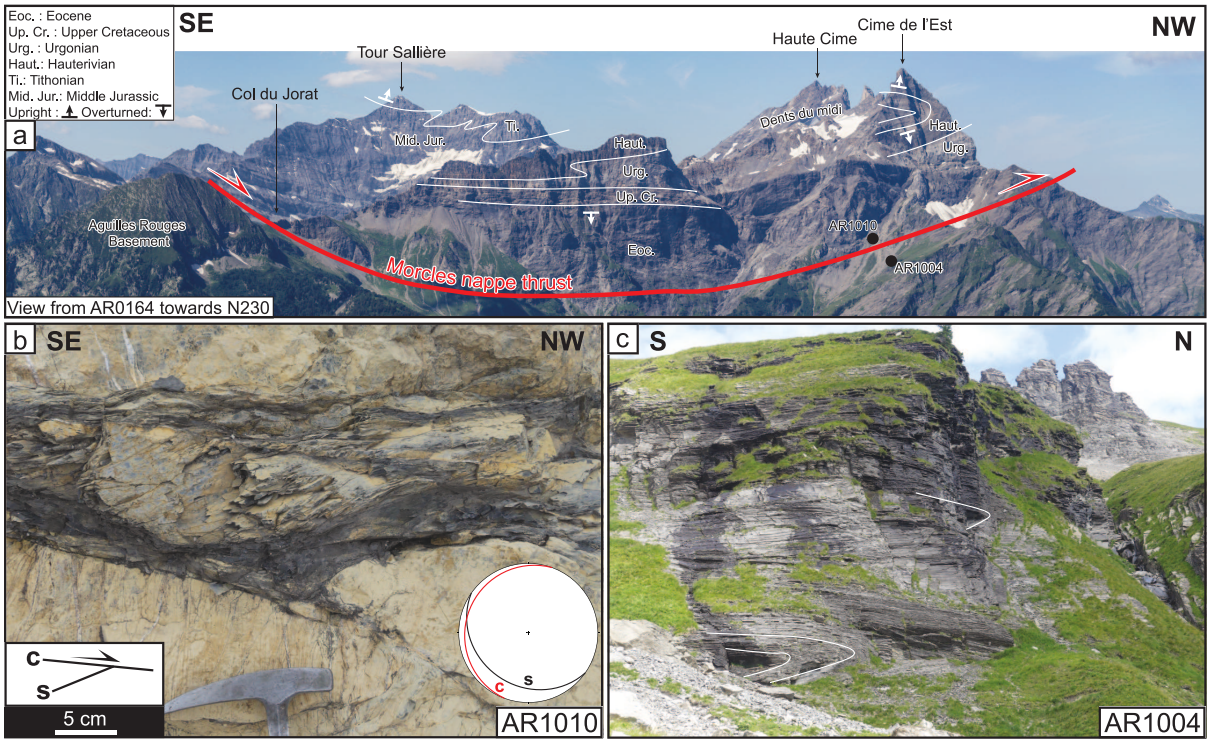

Figure 4.37. Panorama and field observations from Dents Blanches. a) Panorama on the Dents Blanches and the Tour Salière. The sheared reverse limb of the Morcle's nappe is visible with the recumbent fold of the Cime de l'Est, equivalent to the one in the Dent de Morcles; b) Sheared dolostones at the bottom of the Morcle's nappe basal thrust, S/C relationship indicate top-to-the-west sense of shearing; c) Isoclinal and sheath folds within the Eocene flysch below the Morcle's nappe thrust, suggesting an intense shearing of the nappe.

The Col d'Emaney In the northwest of the Aiguilles Rouges massif, at the Col d'Emaney, the typical stratigraphic succession of the Helvetic / Dauphinois cover is not fully respected. From bottom to top, the autochthonous Triassic is characterized by the regular basal layer of sandstone (Emosson formation). Still, in the Upper part of the Triassic series, there is a layer of brecciated Cargneules (Figs. 4.38a and e). Above the Triassic, white limestones have been characterized as belonging to the Upper Jurassic, like in the Souay area further south. These limestones are strongly folded with isoclinal and sheath folds, suggesting an intense simple shear deformation (Fig. 4.38d). Above the Upper Jurassic limestones lies the Eocene flysch, also strongly foliated, with a clear stretching lineation trending N290° (Fig. 4.38c). Above the Eocene, white limestones are found again, attributed to the Urgonian facies in the Cretaceous (Collet et al., 1952). These limestones are strongly foliated and metamorphized into marble with a clear stretching lineation trending N310° (Fig. 4.38b). This section is described in the 3DGeoModel in Fig. 4.34a. Looking southwest from the Col d'Emaney (Fig. 4.39), the

Urgonian limestones seem very thin and even truncated before the Col de Barberine. Above, the dark limestones attributed to the Hauterivian and the massive white limestones attributed to the Upper Jurassic show a clear fold. The black slates above, attributed to the middle Jurassic, show an impressive sheath fold that is more than a few hundred meters long, suggesting a significant shearing.

From these observations, we suggest that the autochthonous cover in the Col d'Emaney is limited to the Triassic, and a first décollement zone may be identified within the brecciated Cargneules. The overlying strongly foliated limestones are most likely from the same formation as those of the Souay (see also Fig. 4.44b) and constitute the "soft layer" localizing the deformation at the bottom of the Morcles nappe. Above the series is overturned, starting with the Eocene flysch at the bottom; the Urgonian limestones seem thinned or truncated by the deformation. The overlying middle Jurassic limestones are strongly folded with sheath folds similar to those observed in the Mont-Buet (see also Fig. 4.15). The cover/basement contact has also been documented in the Col de barberine (see also Fig. 4.11).

Cirque des Fonds In the Cirque des fonds in the Triassic outcrop in the northern Talweg of the Cirque. At location AR2040 and AR2041 (Figs. 4.40a and b) the Triassic formation is made of a tick Cargneules. The river was not deep enough to reach the basal sandstone and the basement. The Cargneules are clastic and affected by deformation (Fig. 4.40a). Above, the overlying middle Jurassic limestones are strongly deformed and cross-cut by a flat fault dipping to the southwest (Fig. 4.40c). 400 meters to the southeast, the limestones are foliated and bear a lineation trending N300 suggesting that the basal part of the middle Jurassic and the Cargneules of the Triassic are used as a Décollement layer.

Bostan The Vallon de Bostan is limited on its southern flank by the massive cliff of the Dents d'Oddaz (Fig. 4.27 and 4.41). This cliff is composed of the overturned stratigraphic succession of the Hauterivian and Urgonian limestones (Fig. 4.42a). This cliff is limited at its base by a thrust that overturns the Upper Cretaceous and Eocene series. The northern tip of the Dents d'Oddaz corresponds to the Corne au Taureau Blanches. Here, the overturned succession can be seen: The Upper Cretaceous is strongly folded (Fig. 4.42b). Within the Dents d'Oddaz clif, several normal faults affect the Urgonian and Hauterivian series. These normal faults are limited by the thrust, suggesting that they are anterior to the folding and have been overturned with the Urgonian and Hauterivian without being reactivated or inverted (Fig. 4.42a). On the northern side of the Vallon, the Bostan fold is conform to the morphology and shapes the Tête de Bostan summit. This fold is most likely limited by a thrust above the Ultra-Helvetic formation.

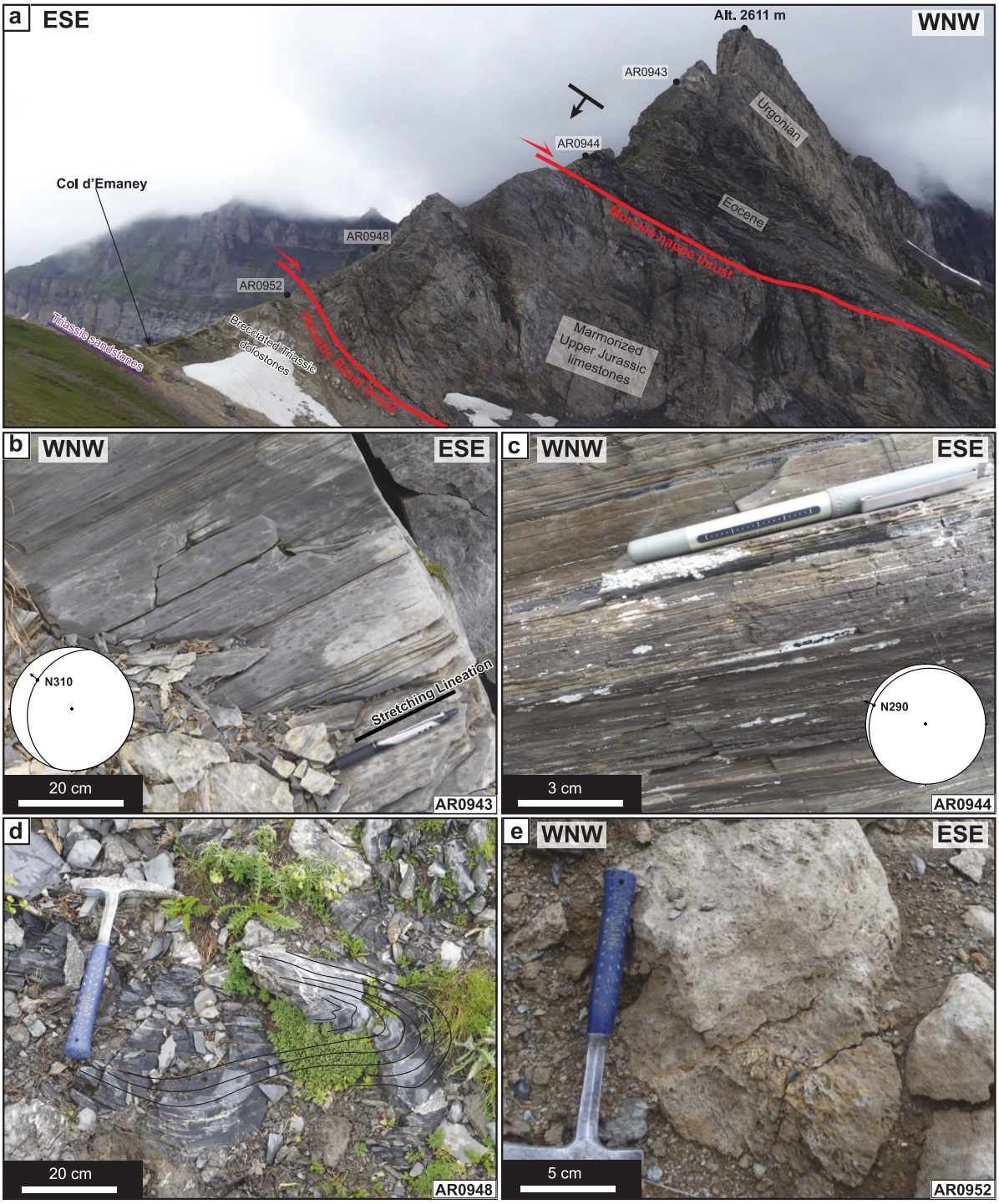

Figure 4.38. Interpreted panorama and field pictures from the col d'Emaney. a. Interpreted panorama of the Col d'Emaney: the Upper part is the Morcles nappe overturned sequence, composed of marmorized Urgnonian limestones overlying the Eocene sediments. The underthrusted series is composed of marmorized Upper Jurassic limestones. The basal thrust is over thrusting the Triassic sediments; b. Marmorized Urgonian limestone, with a stretching lineation trending N310; c. Foliated Eocene flysch with a stretching lineation trending N290; d. Isoclinal fold within the Upper Jurassic below the Morcles Nappe thrust; e. Brecciated cargneule in the Upper part of the Triassic series, below the Helvetic Basal thrust.

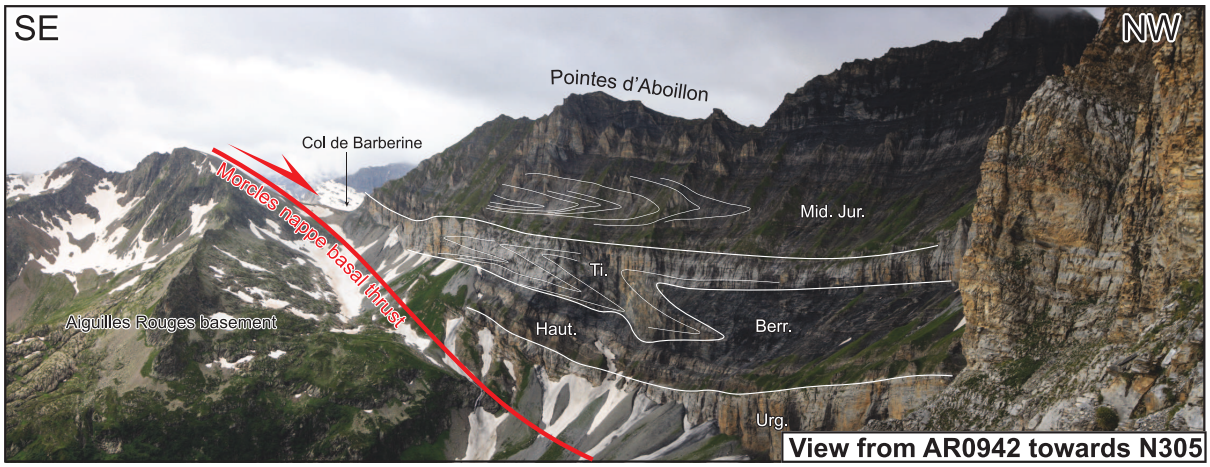

Figure 4.39. Panorama to the Pointes d'Aboillon and the col de Barberine, from the col d'Emaney.

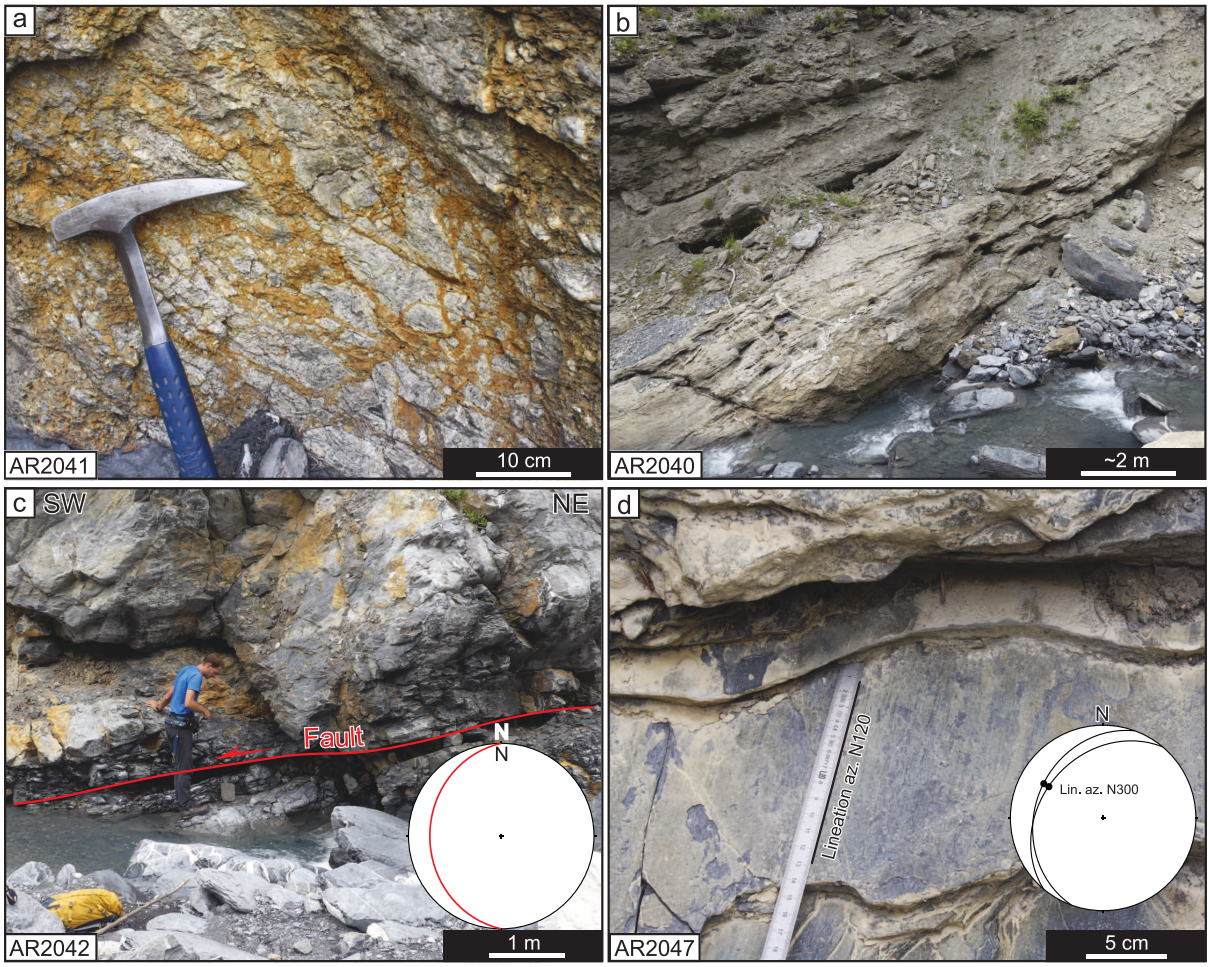

Figure 4.40. Field observation in the Cirque des Fonds. a) Brecciated Cargneules within the Trissic series; b) foliated and brecciated Cargneules; c) Sub-horizontal fault plane within the Triassic dolostone; d) Foliated Jurassic limestones, bearing a lineation oriented azimuth N120°; e) Subvertical strike-slip fault striking N120° bearing an horizontal slickenline. The movement sense could not be inferred; f) Strike-slip fault oriented N75° ; 72° bearing a slickenline with a pitch of 10 W. The sense could not be inferred.

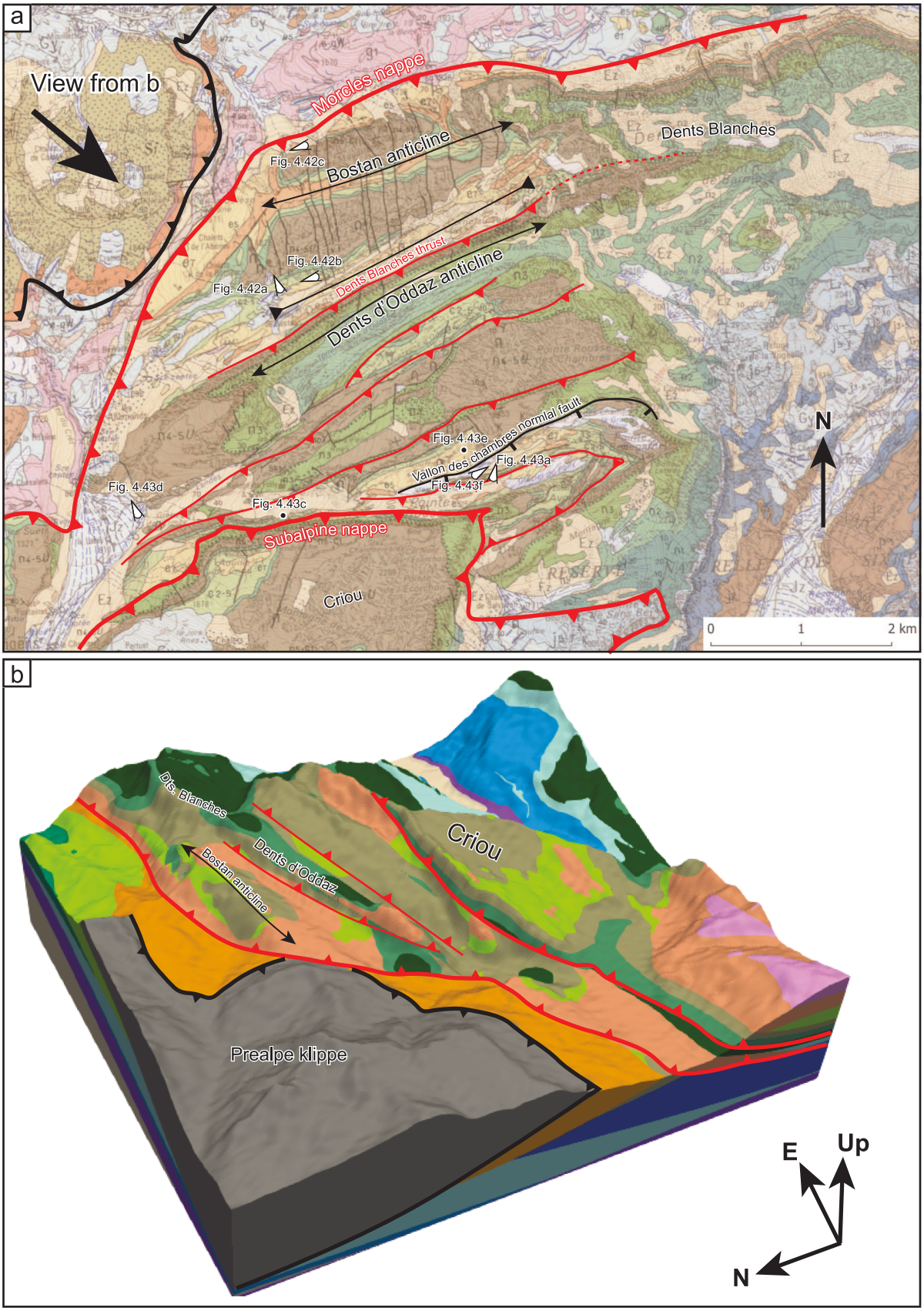

Figure 4.41. Structural frame of the Bostan - Criou massif. a) Background: 1:50 000 geological map of Samoëns (Plancherel et al., 1998).

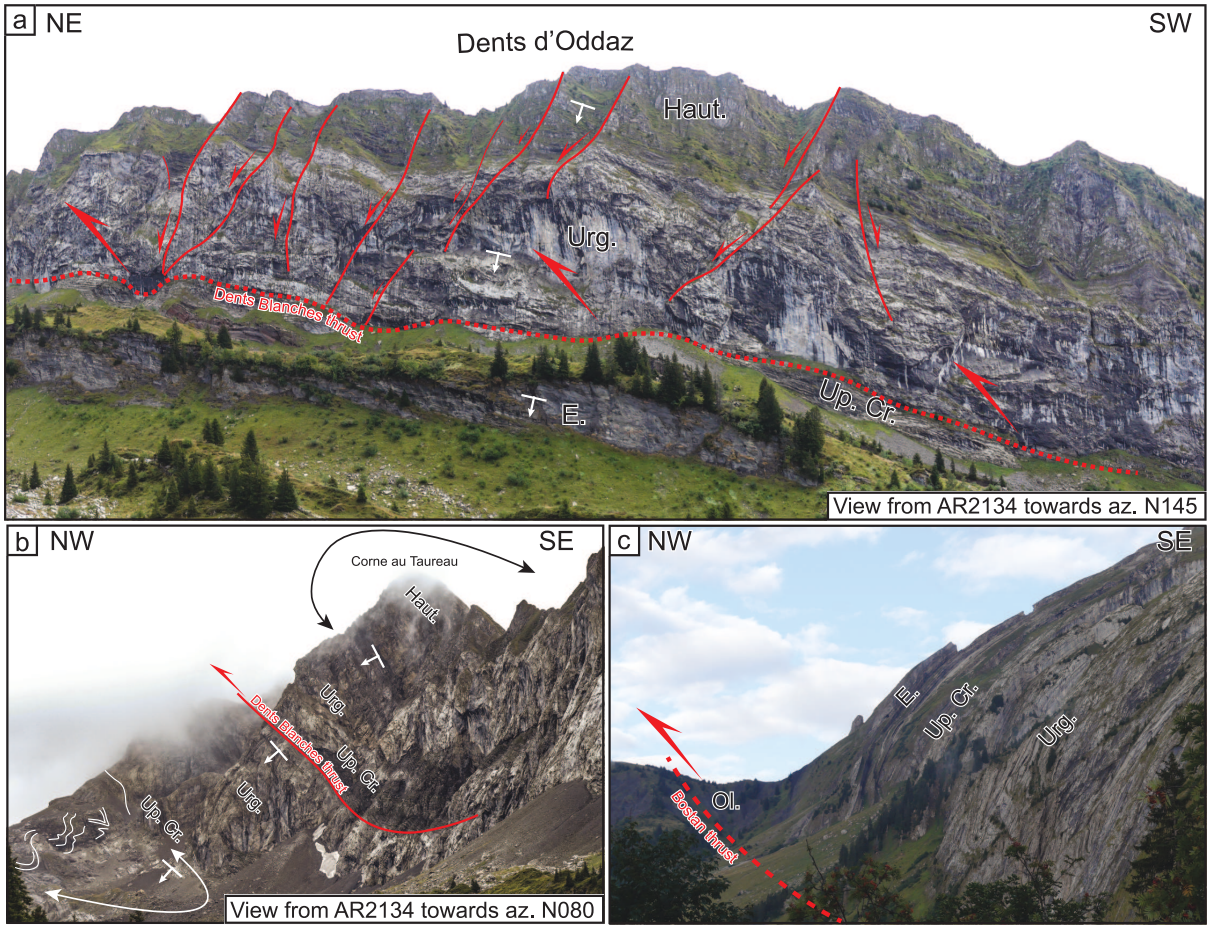

Figure 4.42. Field observation from the Vallon de Bostan. a) Northwestern side of the Bostan fold and the supposed emergence of the Morcles nappe thrust; b) Panorama on the overturned Cretaceous series above the Dents Blanches thrust; c) Panorama on the Dents d'Oddaz, the Cretaceous series is overturned and several normal faults cross-cut the Urgonian and Hauterivian limestones. These normal faults does not seem to propagate below the Dents Blanches thrust, and have been overturned without being reactivated.

Vallon des Chambres In the Vallon des Chambres, on the northern side of the Criou massif (Fig. 4.27), the Cretaceous succession (Hauterivian, Urgonian, Upper Cretaceous) overthrusts and overturns the Eocene with the Criou thrust (Fig. 4.43a). The brown Hauterivian is deformed and folded right above the thrust (Figs. 4.43b and c). From the northern face of the Criou, the Criou thrust duplicated the Urgonian formation by thrusting the Urgonian and Hauterivian on top of the Upper Cretaceous (Fig. 4.43e). The Criou thrust is composed of a Lower branch localized in the Eocene. From the Lac des Chambres, this thrust is highlighted by a clearly visible flat fault at the bottom of a large recumbent fold in the nummulitic limestones (Fig. 4.43e and f). The Lac des Chambres depression is bounded by a normal fault on its northern side, parallel to the nummulitic bedding.

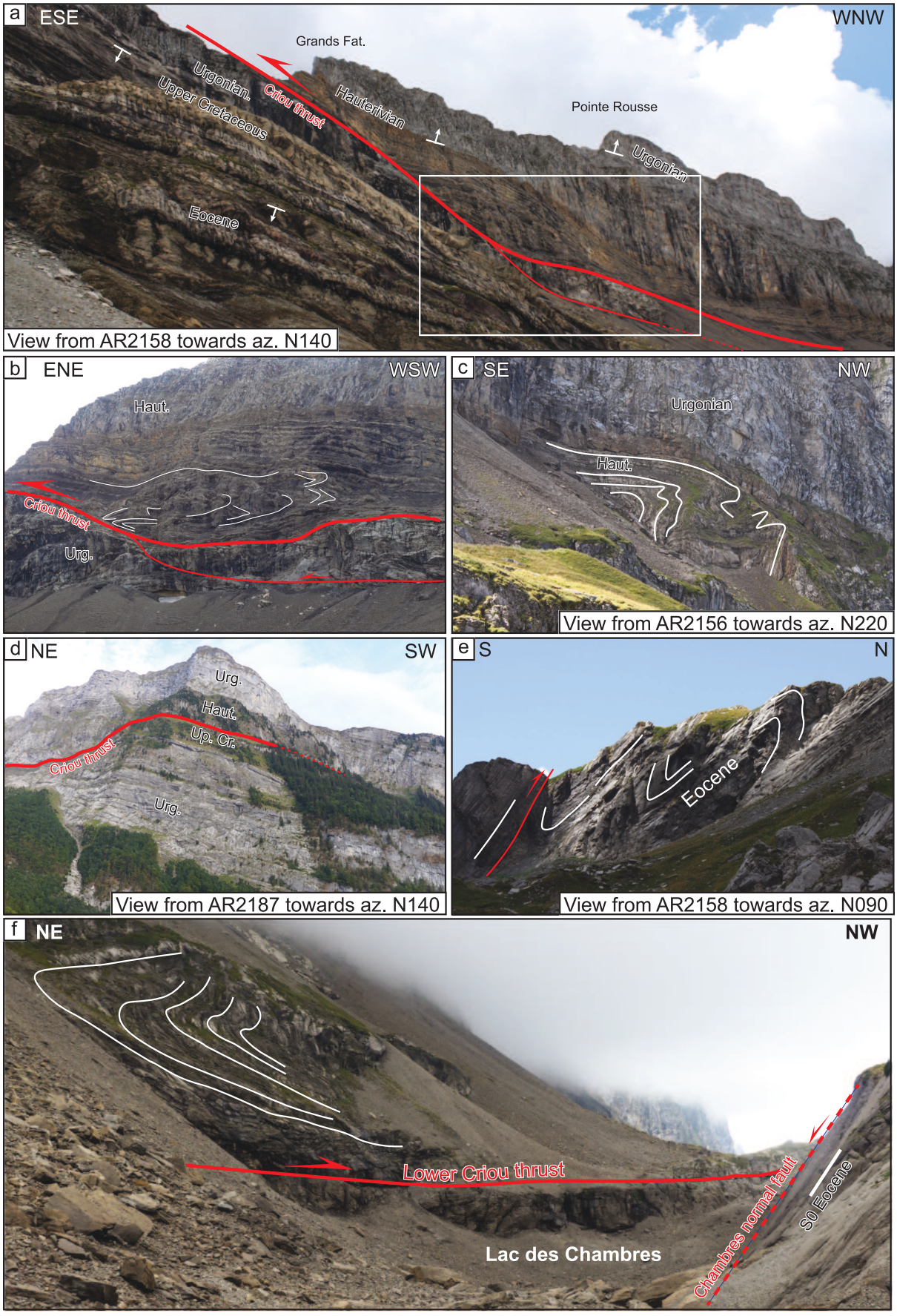
a
ESE
WNW
Grands Fat.
Urgonian.
Upper Cretaceous
Criou thrust
Hauterivian
Pointe Rousse
Urgonian
Eocene
View from AR2158 towards az. N140
b
ENE
WSW
Haut.
Criou thrust
Urg.
c
SE
NW
Urgonian
Haut.
View from AR2156 towards az. N220
d
NE
SW
Urg.
Haut.
Up. Cr.
Criou thrust
Urg.
View from AR2187 towards az. N140
e
S
N
Eocene
View from AR2158 towards az. N090
f
NE
NW
Lower Criou thrust
Chambres normal fault
S0 Eocene
Lac des Chambres

Figure 4.43. Panorama and field observations in the Vallon des Chambres (Haut-Giffre). a) Panorama on the southern face of Pointe Rousse from the Vallon des Chambres, the normal series of the Hauterivian and urgonian thrust and overturns the Eocene series with the Criou thrust; b) Zoomed view of the Criou thrust and the associated deformations in the Hauterivian formation; c) Criou thrust in the southern face of the Criou. The Hauterivian and Uronian formations are thrust above the Upper Cretaceous; d) fold in the Hauterivian above the Criou thrust; e) tight asymmetric folds and a reverse fault affecting the Eocene formation, below the Criou thrust; f) large fold above the Lower branch of the Criou thrust within the Lac des Chambres.

Anterne From the col d'Anterne, the massive Fiz cliff does not appear deformed or sheared, and the stratigraphic series looks continuous and upright from the Tithonian to the Eocene and is affected by few normal faults with limited offset (Fig. 4.44a). The summit of the cliff (Tête à l'Âne) is folded and truncated by the ultra-Helvetic nappe thrust (Fig. 4.44a). However, the cross section through the Lower to middle Jurassic from the Refuge d'Anterne to the Col d'Anterne shows an intense deformation. The brecciated cargneules that are atop Triassic sandstones appear to have been deformed at low temperatures. Above, the white limestones are attributed to the Upper Jurassic (Pairis et al., 1973; Amberger, 1959). These authors consider that the Upper Jurassic is in stratigraphic contact on top of the Triassic, suggesting reduced sedimentation above the Aiguilles Rouges. These limestones may be the result of condensed sedimentation but are strongly foliated and mylonitized and appear to significantly absorb deformation (Fig. 4.44 b). Above, dark slates are attributed to the Toarcian-Bajocian (Pairis et al., 1992) and are also strongly foliated and mylonitized, with relicts of boudinaged stratification beds (Fig. 4.44c). The slates are injected with calcite veins that are truncated by shear planes and boudinaged with asymmetry that indicates a top toward the northwest shear (Figs. 4.44d and d). Shear planes have a stretching lineation trending from N100° to N106°. These observations indicate that, like the col d'Emaney, the autochthonous cover above the Aiguilles Rouges is limited to the Triassic sandstones, the brecciated cargneules may reflect the Lower bound of the deformation zone, but most of the deformation is located within the Upper Jurassic and the Lower to middle Jurassic. The overlying cover (from Tithonian to Upper Cretaceous) does not appear deformed or intensively sheared, unlike the Urgonian in the Morcles nappe.

In the same area, the Pormenaz - Merlet shear zone described above (see section 4.3.4.3, p. 153) overturns the Carboniferous sandstones and shales (Figs. 4.45a and b). The continuity of this shear zone in the subapline nappe is unclear: the shear zone does not seem to exent and offset the subalpine nappe. Furthermore, autochthonous Triassic sandstones are deposited in stratigraphic unconformity above the folded carboniferous sandstones and shales, indicating a deformation in the Carboniferous prior to the Triassic deposition (Fig. 4.45 c). However, as described before, the Crête Blanche klippe, limited at its base by the Helvetic basal thrust is cross-cut by a steep fault few meters below and running parallel to the Pormenaz - Merlet shear zone, indicating that this fault was active during the alpine orogeny.

We hypotetize that deformations occured in the Pormenaz Carboniferous sediments prior than the Triassic deposition, most likely during the Saalian deformation phase (see section 2.4.1.2, p. 69). Later, during the Alpine orogeny, the Pormenaz - Merlet shear zone was active and overturned the Carboniferous sediments and offset the Crête Blanc klippe.

Pointe de Sales On the northern side of the Fiz cliff, the Pointe de Sales delimits the tip of an impressive clif showing the regular Mesozoic stratigraphic sucession from the Tithonian to the Eocene. Several steep reverse faults with limited offset affect the series (Fig. 4.46a). A steep normal fault with roughly the same dip as the reverse faults is also visible and seems to be reused in the reverse fault (Fig. 4.46a). Below, the series is limited by a large thrust that duplicates and overturns the underlying Tithonian limestone (Figs. 4.46b and c). This thrust is locally named the Salvagny thrust. In the above series, the Hauterivian is affected by a well-marked cleavage,suggesting that the bedding may be reused as shear planes. The Pointe de Sales is also affected by a normal fault that can be seen from the northern and eastern faces of the summit. This fault affects the formation from the Hauterivian to the Upper Cretaceous, indicating that its timing of motion is most likely post-Eocene.

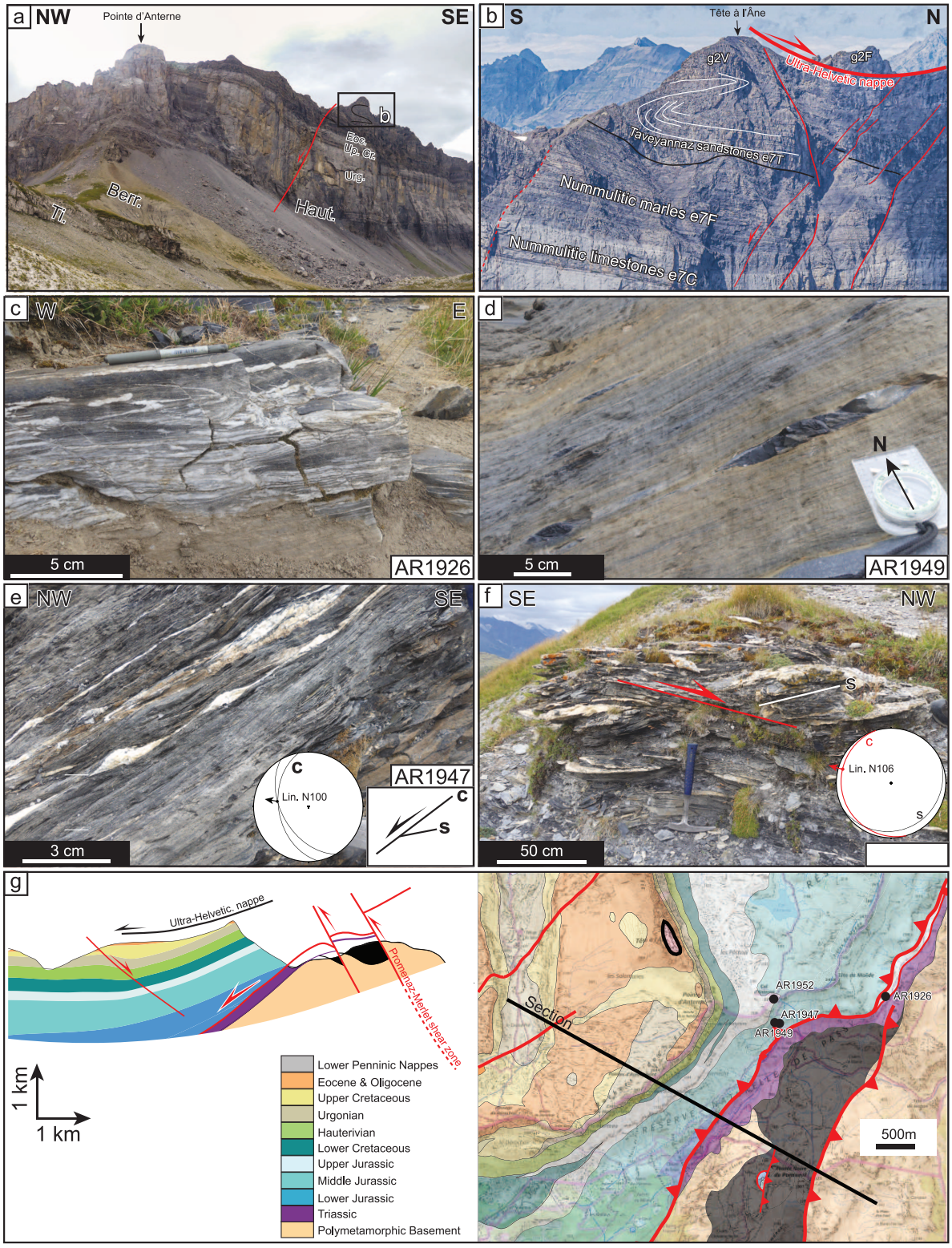

Figure 4.44. Panorama and field observations from the Col d'Anterne area (western Aiguilles Rouges). a) Panorama from the Col d'Anterne to the massive Fiz cliff. Atop the Tête à l'Âne, there is a klippe of the ultra-Helvetic thrust, folding the Eocene cover below; b) Stronly marmorized and foliated limestones from the Souay; c) boudinaged middle Jurassic; d) Asymmetric boudinage from the middle Jurassic in the path to the col d'Anterne; e) Asymmetric boudinage of the middle Jurassic at the col d'Anterne; f) Cross section and map output from the 3D geological model.

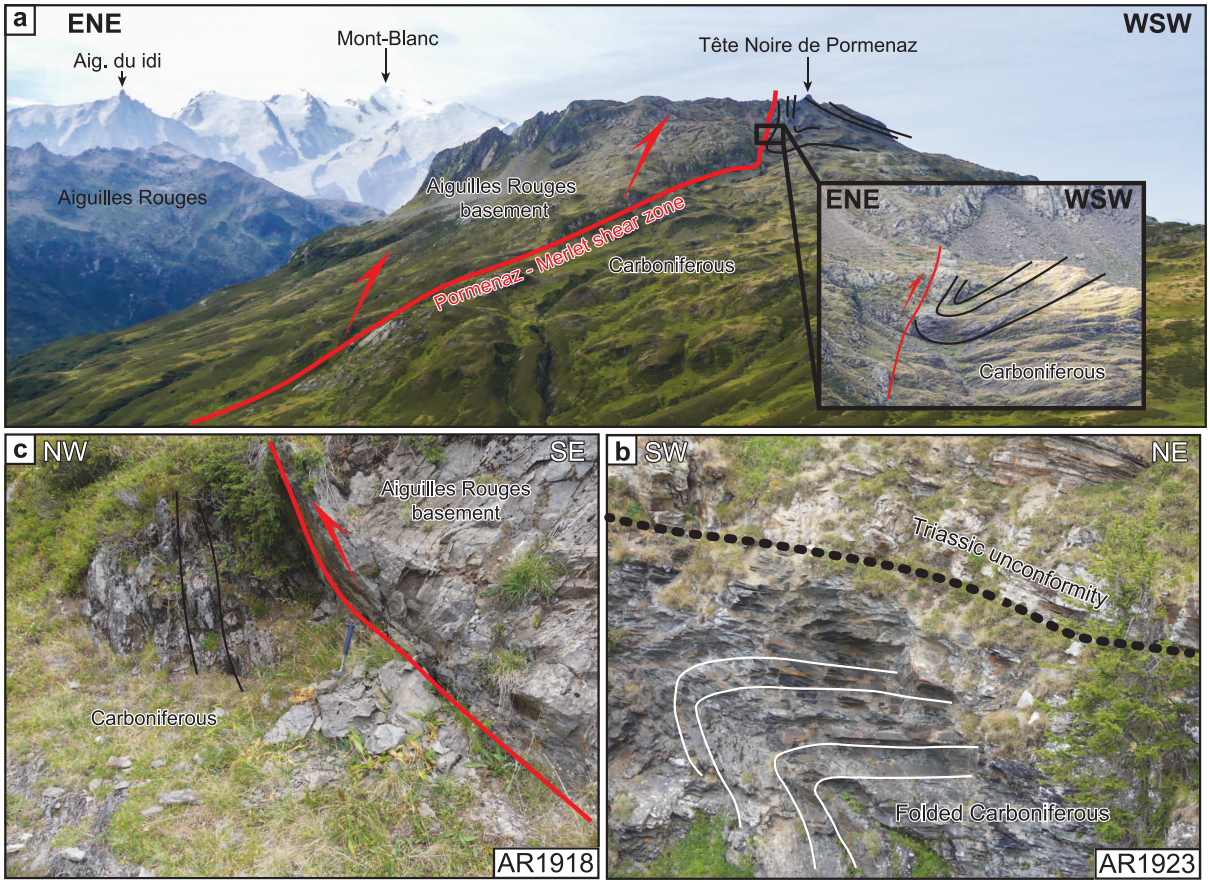

Figure 4.45. Field observations of the deformations affecting the Carboniferous in the Pormenaz - Anterne area. a) Pormenaz - Merlet shear zone that thrust the basement above the Carboniferous sandstones and shales and overturns them; b) Zoom in the Pormenaz - Merlet shear zone contact with the Carboniferous and the basement; c) The Triassic unconformity deposited above the folds in the Carboniferous, indicating a deformation in the Carboniferous prior than the Triassic deposition.

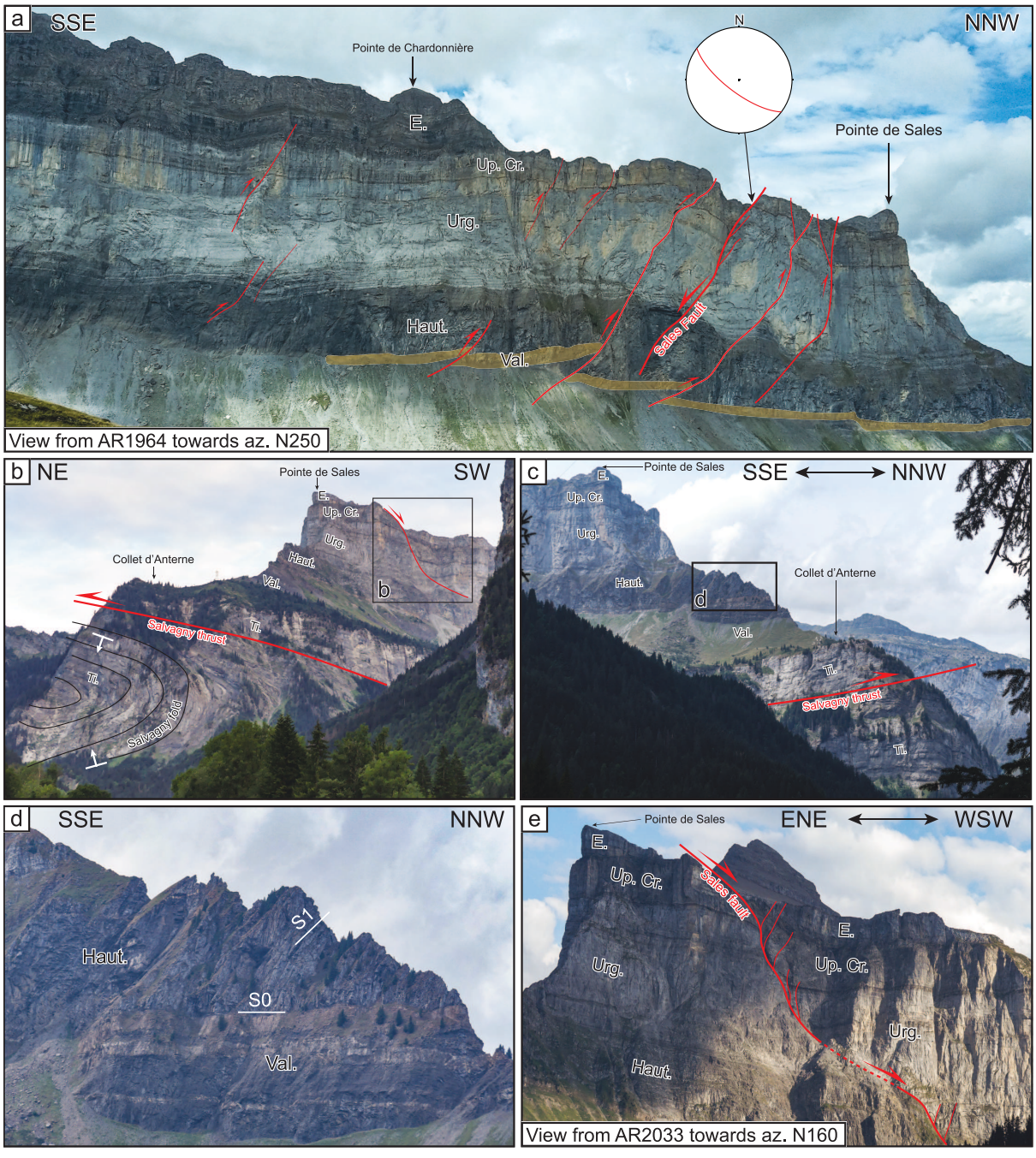

Figure 4.46. Interpreted panoramas of the Pointe de Sales and the Fiz. a) Pointe de Sales and the overturned Salvagny fold below the Salvagny thrust seen from the northwest; b) Sales normal fault seen from the NNW; c) Pointe de Sales seen from the ENE; d) Fracture cleavage effecting the Hauterivian limestones; e) Barre des Fiz seen from the ENE.

4.4.2.1 Preliminary synthesis on the cover / basement interface on the Western side of the Aiguilles Rouges

From the observations from the Dent the Morcles in the north to the Pointe de Sales in the south (Fig. 4.27) and observations on the western margin of the Aiguilles Rouges (Section 4.3.4.2, p. 142), we evidenced two thrusts that significantly affected the cover of the Aiguilles Rouges and, locally, the basement. The most basal one follows approximately the basement / cover interface and can be characterized as a décollement layer localized in the Upper Jurassic limestones and the Triassic dolostones and cargneules this thrust refers to the Helvetic Basal Thrust. The second is located below the Morcles nappe and emerges in front of the Bostan fold in the north. This thrust brings the Morcles nappe on top of the Eocene flysch. Above the thrust, the Morcles nappe is a large recumbent fold, considerably sheared at its base, and that significantly stretches the sedimentary series. Above, a third thrust delimits the base of the subalpine nappe. This thrust emerges in the Vallon des Chambres in the Criou massif where the thrust is located in the Hauterivian formation. These three thrusts systems seem to merge in the Col d'Anterne area.

4.5 Structure of the subalpine chains

In this section we will describe the structure of the Subalpine nappe, that is structurally above the helvetic basal thrust, and the Morcles nappe previously described. First, we will describe the natural cross-section of the Arve Valley from southeast to northwest, then the Bornes and Aravais massifs and finally the nature of the cover / basement relationship of these massifs.

4.5.1 Désert de Platé

The so-called "Désert de Platé" delimits a large karstic plateau of nummulitic white limestones that does not seem to have been intensively deformed but affected by a large-wavelength bending (Figs. 4.47a and b). The massif is affected by large normal faults that cross the plateau oriented approximately N80° (Fig. 4.47b).

4.5.2 The mysterious origin of the "wildflysch" formation

According to Pfiffner (2014), the structural description of a "Wildflysch" is a melange that formed during the emplacement of a nappe, at its front, where the basal thrust emerges at the surface. The sedimentary description consists of a chaotic mixture of blocks from various lithologies (limestones, sandstones, conglomerates, crystalline rocks), embedded in a dark shale matrix. The wildflysh formation is found in the Helvetic series in the Platé and Giffre

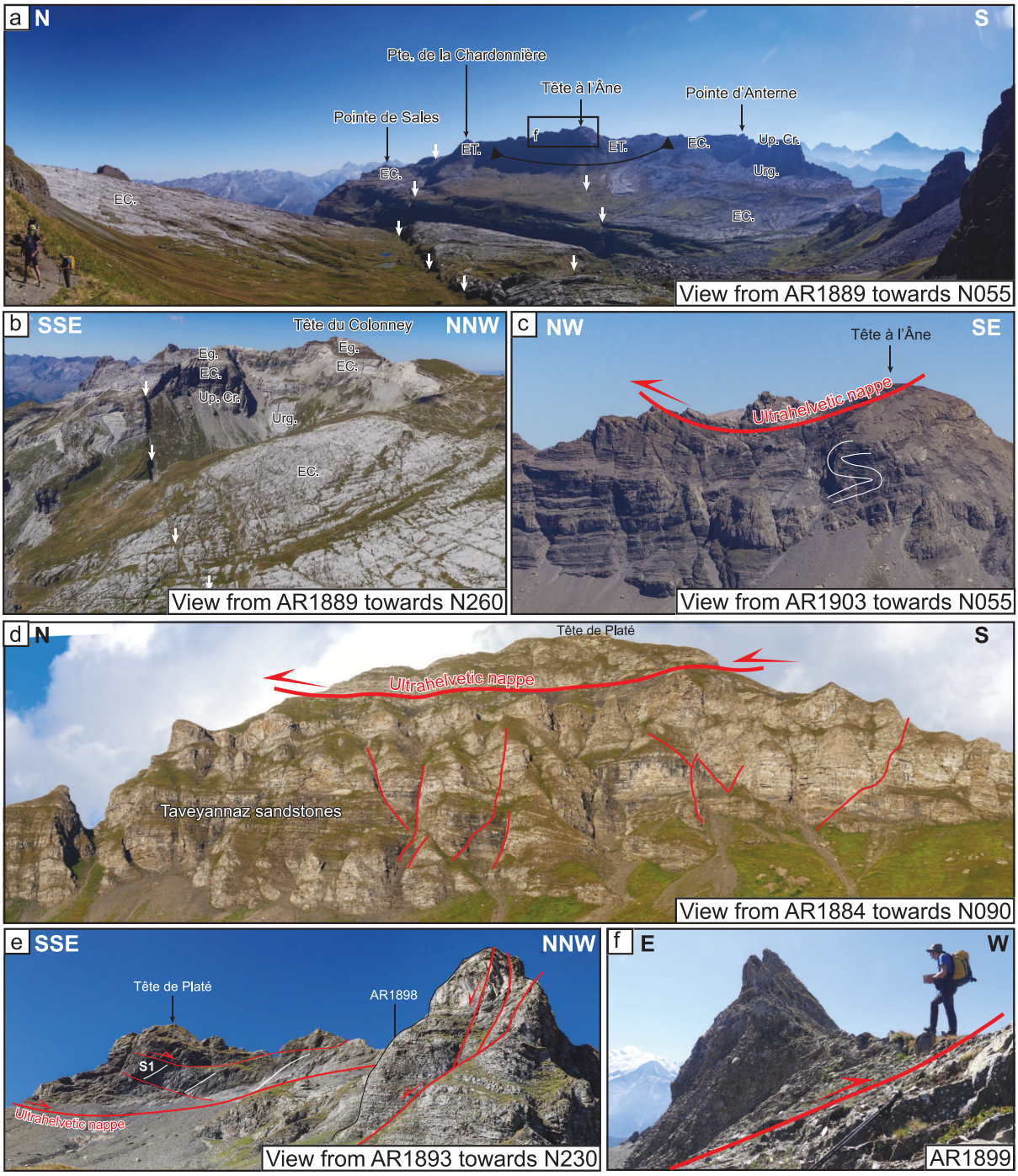

Figure 4.47. Panorama and field observation in the Platé massif. a) Panorama on the Vallon de Sales and the Tête à l'Âne; b) Panorama on the Tête du Colonney; b) Zoomed view of the Tête à l'Âne and the Ultra-helvetic kilippe on top; d) Panorama on western side of the Pointe de Platé and the Ultra-Helvetic klippe on top; e) Panorama from the eastern side of the Pointe de Platé; f) Basal contact of the ultra-helvetic nappe. Abbreviations are: EC.: Eocene Limestones, ET.: Taveyannaz sandstones, Eg.: Eocene Conglomerate, Urg.: Urgonian, Up. Cr.: Upper Cretaceous.

massifs (Tête de Platé, Tête à l'Âne, Pointe de la Cupoire, and the northern slopes of Morillon ski resort). In the subalpine chains, the origin of this formation is a matter of debate: For some authors (Moret, 1922; Lillie, 1937; Martini, 1966), the "wildflysch" formation is a thrust nappe below and associated with the internal prealps. For others (DE LEPINAY, 1981; Kindler, 1988), this formation is purely of sedimentary origin and made of olistosromes of various lithologies and terminates the Helvetic series.

We investigated this question in the massif. In the Pointe the Platé the Upper part of the summit is limited by a deformation zone above the Taveyannaz sandstones (Fig. 4.47d). The formation is made of black shale and clastic conglomerate that seem to be affected by flat faults and oblique cleavage planes (Fig. 4.47d and e). On the other side of the vallon de Sales, on top of the Tête à l'Âne, the Taveyannaz sandstones are overturned indicating a clear charriage of a nappe (Fig. 4.44a) and that has been later bent (Fig. 4.47f). The same fold is clearly visible from the other side (Fig. 4.44b). From the northern slopes of the Morillon ski resort, several blocks of various lithologies outcrop in a shale matrix (Fig. 4.48a and b). At the bottom of a large block of limestones, the shale is sheared with S/C criteria indicating a top to north sense of shear. On top of the Pointe de la Cupoire (Fig. 4.27), the same shales outcrops above the Grès de Taveyannaz formation. They are strongly deformed with S/C criteria (Fig. 4.48c), asymmetric boudinage of clasts (Fig. 4.48d) and lineations trending N120 to N160° indicating a top-to-north sense of shear. Further northeast, in the Ruisseau de la Joux de Lévy, within the same shale formation, S/C criteria indicate the top-to-west sens of shear without a clear lineation. On top of the Pointe de Platé, this formation is also visible (Figs. 4.47a and b).

From these observations, we argue that the "wildflysch" formation is affected by an strong internal deformation and limited at its base by a thrust. This thrust nappe delimits klippes atop the Pointe de Platé and the Tête à l'Âne and has been later folded and thrusted, suggesting that its emplacement was before the subalpine chain deformation. In summary, we suggest that the "wildflysch" formation is made of clastic sediments deposited in the flexural basin below the Penninic thrust nappes that was later thrusted west to northwest before the deformation of the subalpine chains.

4.5.3 Cross section through the Arve Valley

The natural cross section through the Arve valley provides a good geological section through the subalpine chains. On the southern side of the valley, the Urgonian unit is offset by normal faults (Fig. 4.49a). To the south, the Pointe d'Areu is a klippe of the Hauterivian laid on the Upper Cretaceous. The underlying Eocene is folded below and straightened vertically (Fig. 4.49a). On the southern side, the Magland anticline is limited at its base by a thrust fautl that seems to reuse an older normal fault (Fig. 4.49b). Further north, in the Balme area, the

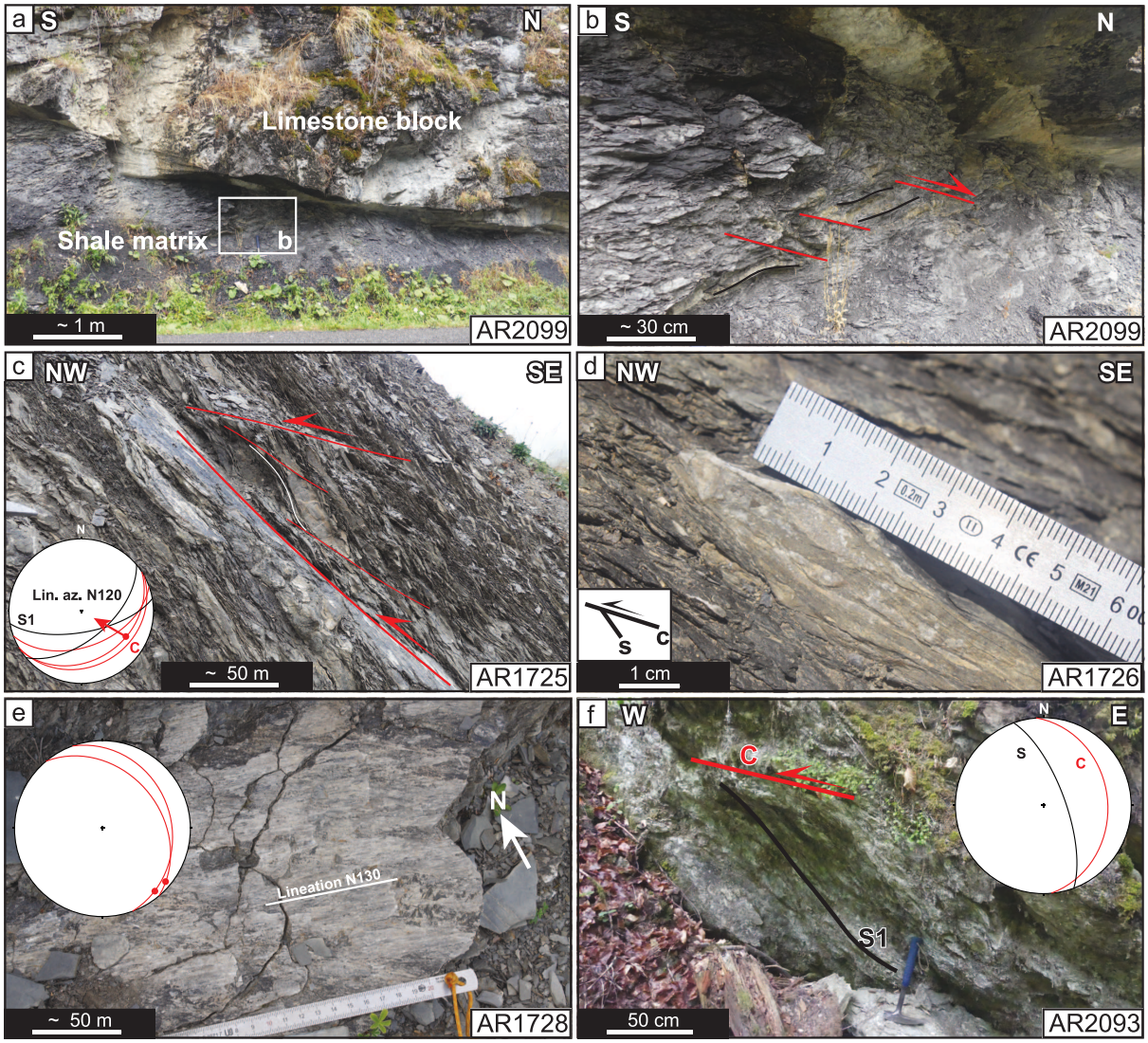

Figure 4.48. Wildflysh ("Flysch à bloc"). a) Huge block of the "Flysch à bloc" in the Ultra-Helvetic nappe; b) Shearing at the bottom of the block indicating a top-to-north sense of shear; c) Flysch on top of the Pointe de la Cupoire, S/C relationship and lineation indicate top-to-northwest sense of shear; d) Asymmetric boudinage of clast in the flysch in the Pointe de la Cupoire; e) Stretching lineation in the flysch; f) S/C relationship indicate top-to-west sense of shear.

Urgonian unit seems cut by three small normal faults that do not continue deeper in the unit (Fig. 4.49b). Faure et al. (1999) have suggested that these normal faults are, in fact, part of the same inherited normal fault, that has been offset by bedding sliding. Others have suggested that this thrust is a ramp that reuses an inherited normal fault (Pairis et al., 1992). The northern part of the section is limited by the Balme complex thrust system (Fig. 4.49b and c), which has been described in detail in Faure et al. (1999). The underlying Eocene unit is intensely stretched and affected by low-angle normal faults, interpreted as large-scale C' shear planes resulting from simple shear deformation and suggesting a significant displacement along the Balme thrust. Further north, the Cluses anticline delimits the front of the subalpine chains and the emergence of the thrust in the foreland (Fig. 4.50a). Further south, the Urgonian unit is overturned again, with a $35°$ dipping overturned limb and limited by the Vange thrust. Below that thrust, the so-called Arpenaz folds describe a recumbent fold with the Tithonian limestone unit, indicating a thrust direction toward the NNW (Fig. 4.49e).

4.5.4 Bornes - Aravis

The Bornes and Aravis massifs gather the massifs in the south of the Arves Valley (Fig. 4.27 and 4.50). A cross-section through the massifs can be achieved along the Col des Aravis road from Flumet in the southeast to Saint-Pierre-en-Faucigny in the northwest. In the Foron Talweg, west of Megève town, the basal contact of the Triassic sandstones above the crystalline basement can be seen: the basement seems to be affected by deformation as well as the Triassic formation. Above, the Jurassic cover is deformed to slates and asymmetrically boudinaged calcite veins are visible (Fig. 4.51a). The shear planes bear a stretching lineation oriented $N308°$, indicating a nappe transport in that direction. From this location, the cover / basement contact of the subalpine bornes and Aravis is characterized by a thrust.

Further south, in Flumet (Fig. 4.27), the Triassic unconformity rests on the mica schists and does not seem to have been deformed. However, the overlying Jurassic cover is strongly foliated and affected by asymmetric boudinage. The stratification is strongly microfolded and cross-cut by the foliation (Fig. 4.51c). Along the road to the Col des Aravis, at la Giettaz, the Jurassic sedimentary cover is folded and overturned at a larger scale, indicating a transport to the NNW (Fig. 4.51d).

To the northwest, the Leschaux thrust duplicates the Urgonian massive limestones and locally overturns the beddings (Fig. 4.51e). This thrust is also connected with a back thrust that has a limited offset. Finally, above the Col des Aravis, the Merdassier shows large normal inherited normal faults that offset the Eocene sediments and that have been tilted during the subalpine chain deformation (Fig. 4.51f).

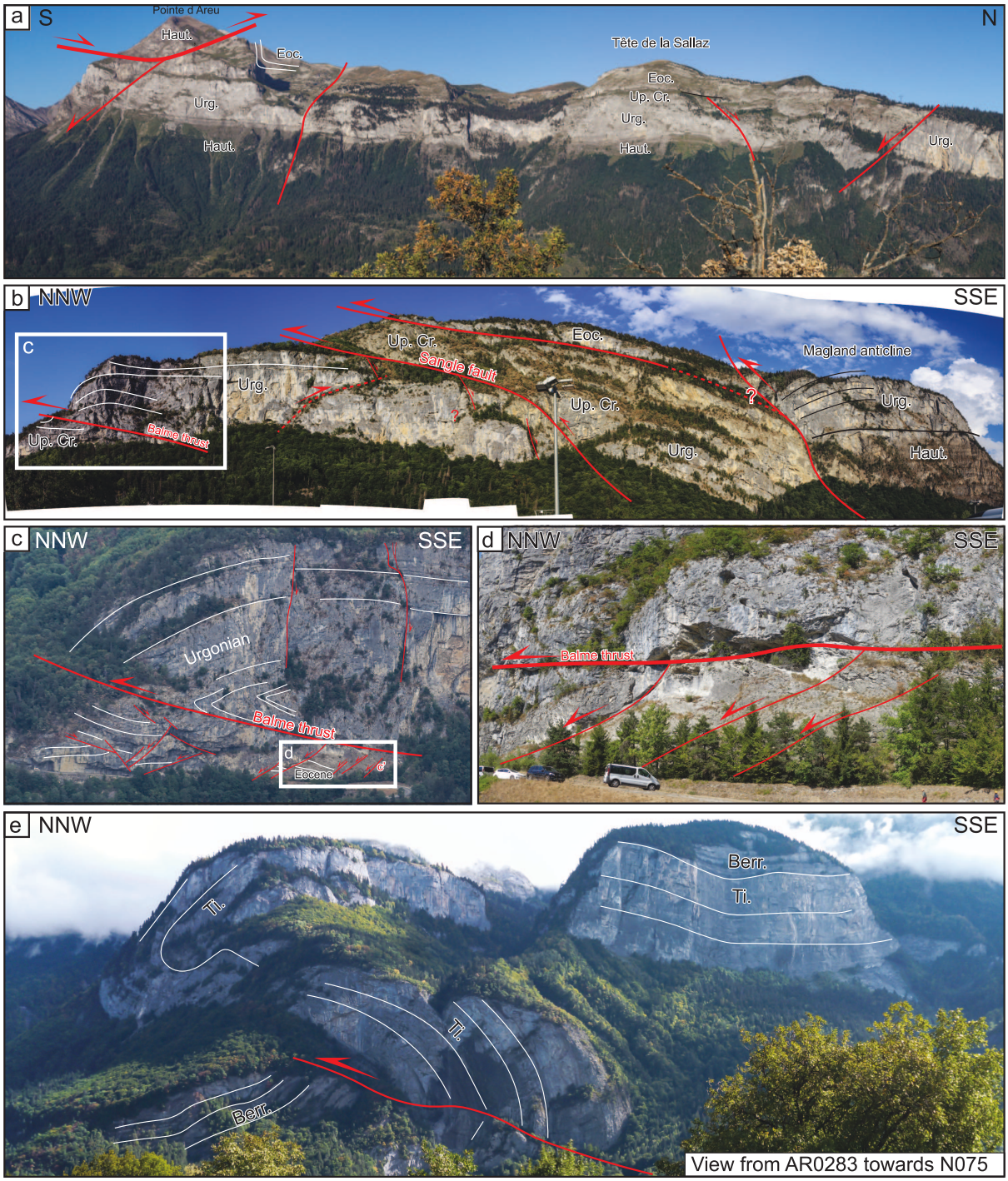

Figure 4.49. Field observations and natural cross-section from the Arve Valley. a) Panorama of the western flank of the Arve Valley and the Poitne d'Areu; b) Panorama of the eastern flank of the Arve Valley and the Balme thrusts; c) Zoom within the fold and the Balme thrust; d) Shear thrust planes below the Balme thrust; e) Arpenaz recumbent fold. Abbreviations are: Eoc.: Eoce; Up. Cr.: Upper Cretaceous; Urg.: Urgonian; Haut.: Hauterivian.

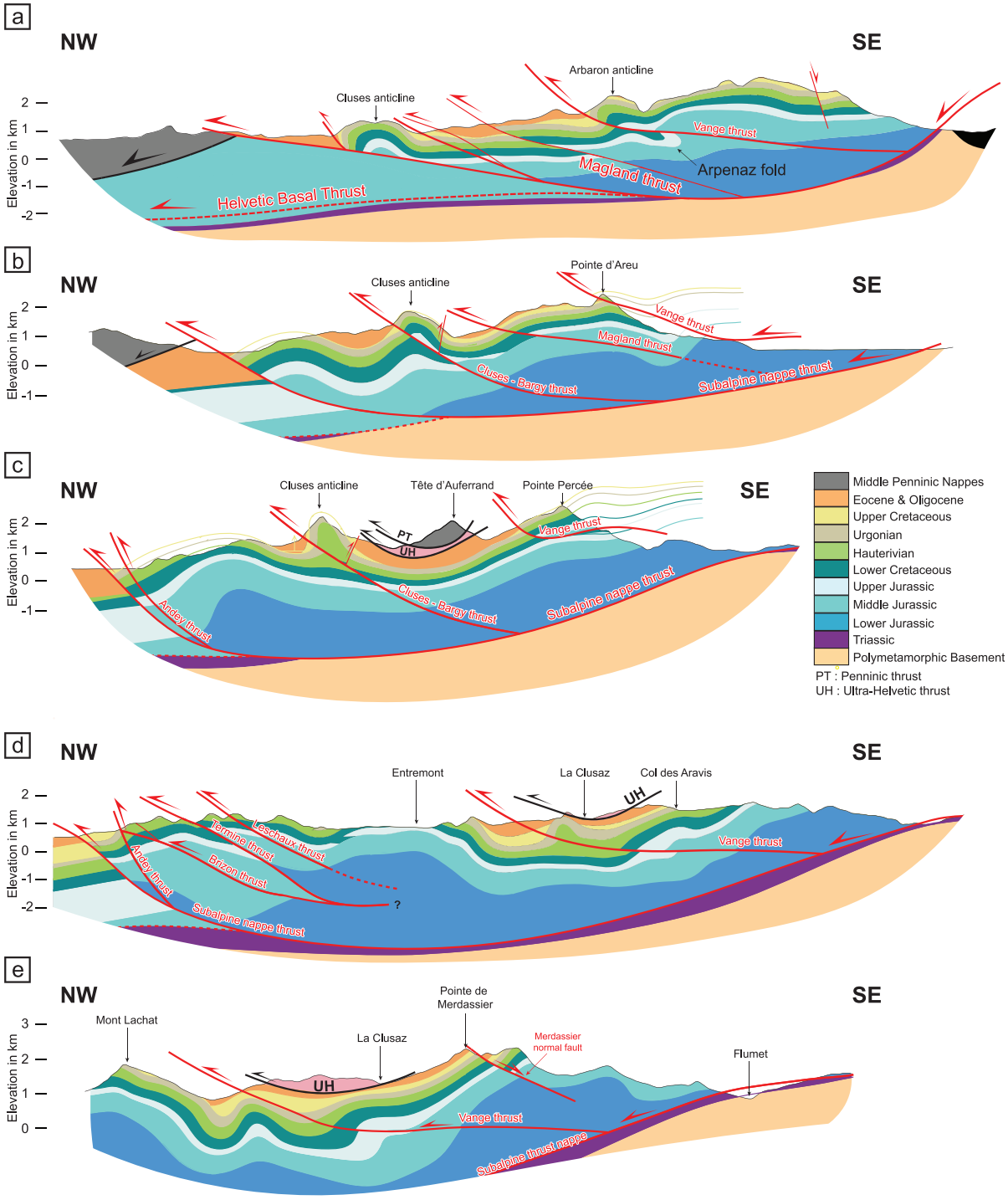

Figure 4.50. Cross sections through the 3D geological model in the subalpine chains.

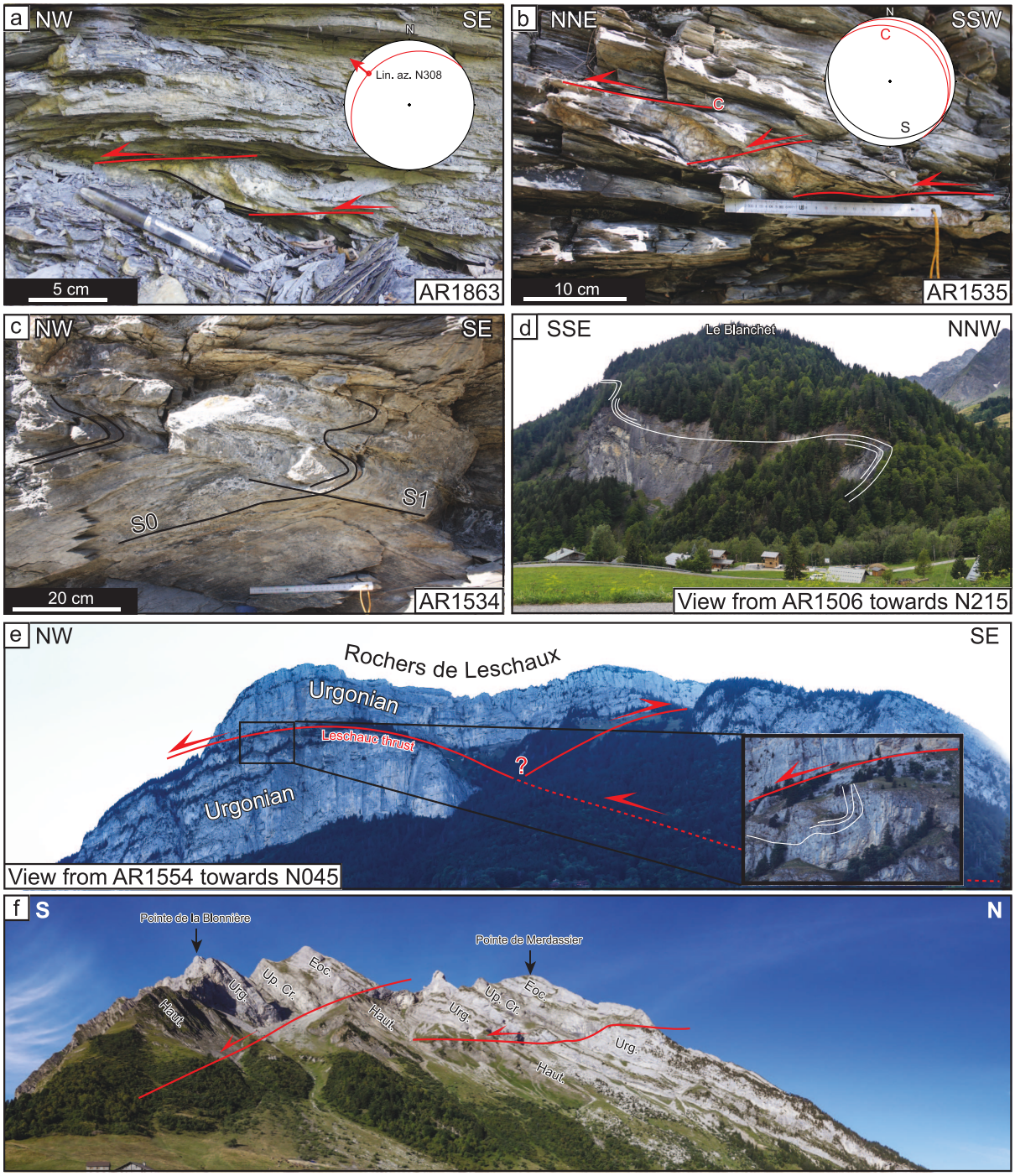

Figure 4.51. Panorama and field observation in the Bornes massif. a) Boudinaged calcite vein in the Foron Talweg, west of Megève town. The asymmetric boudinage and lineation indicate top-to-west (N308) sense of shear; b) the asymmetric boudinage affecting a calcite vein at the bottom of the Jurassic cover, above the Triassic unconformity; c) Microfolded S0 cross-cut by the foliation S1; d) Recumbent fold in the Jurassic cover; e) Rocher de Leschaux thrust and back thrust, the Urgonian limestones are duplicated; f) Tilted normal faults in the Merdassier.

4.6 Strike-slip faulting and active tectonics

We compiled our measurements of strike-slip fault in the study area (Fig. 4.52): three groups of faults have been identified. The first group trends N40° on average and is mainly dextral, the second group trends N124° on average and is mainly left-lateral. If these two groups are conjugated, they are compatible with either a E - W compression or a N - S extension. This state of stress is compatible with the recent seismic activity observed in the Mont-Blanc and Aiguilles Rouges (see paragraph below). A third group of W-E oriented strike-slip faults has been measured without a clear determination of the strike-slip motion. If these fault are dextral, their orientation are compatible with a NW - SE compression, most likely related to the Mont-Blanc shear zones. These faults have been observed all over the area, in the basement and the cover. The characteristic of the deformation is brittle, with slickenlines and quartz or calcite crystallization, suggesting late activation of these faults. These observations necessarily requires more investigation to retrieve a clear interpretation.

In the Mont-Blanc and Aiguilles Rouges, the most significant instrumental earthquake is the Mw 4.5 Vallorcine earthquake (8^{th} September 2005). That earthquake activated a N60° trending dextral strike-slip fault, The Gros-Nol Fault (Fig. 4.8) (Fréchet et al., 2010). That fault is close to, and parallel with, the Veudale Fault (Fig. 4.8 and 4.52). Whilst the main aftershocks cluster lie along the Gros Nol fault, a second cluster is located on the Veudale fault (Fréchet et al., 2010) where that fault dextrally offset the Triassic unconformity by approximatelly 180 m (Collet et al., 1952; Ayrton et al., 1987) (Fig. 4.8). The largest historical earthquake is the Chamonix earthquake (April 29^{th} 1905) whose moment magnitude is estimated at Mw 5.3 ± 0.3 (Cara et al., 2017). The Remuaz normal fault (Fig. 4.8), which has a clear morphological trace, is the most likely source of the earthquake (Cara et al., 2017). This fault trends N14° and dips 70° E with slickenlines with a pitch of 70° N. This is markedly different from the Gros-Nol and Veudale faults, but all these faults are compatible with various states of stress that can either be WNW-ESE compression or NNE-SSW extensions. Comparison with other instrumental earthquakes in the external part of the Alps favor an WNW-ESE compression (Fréchet et al., 2010).

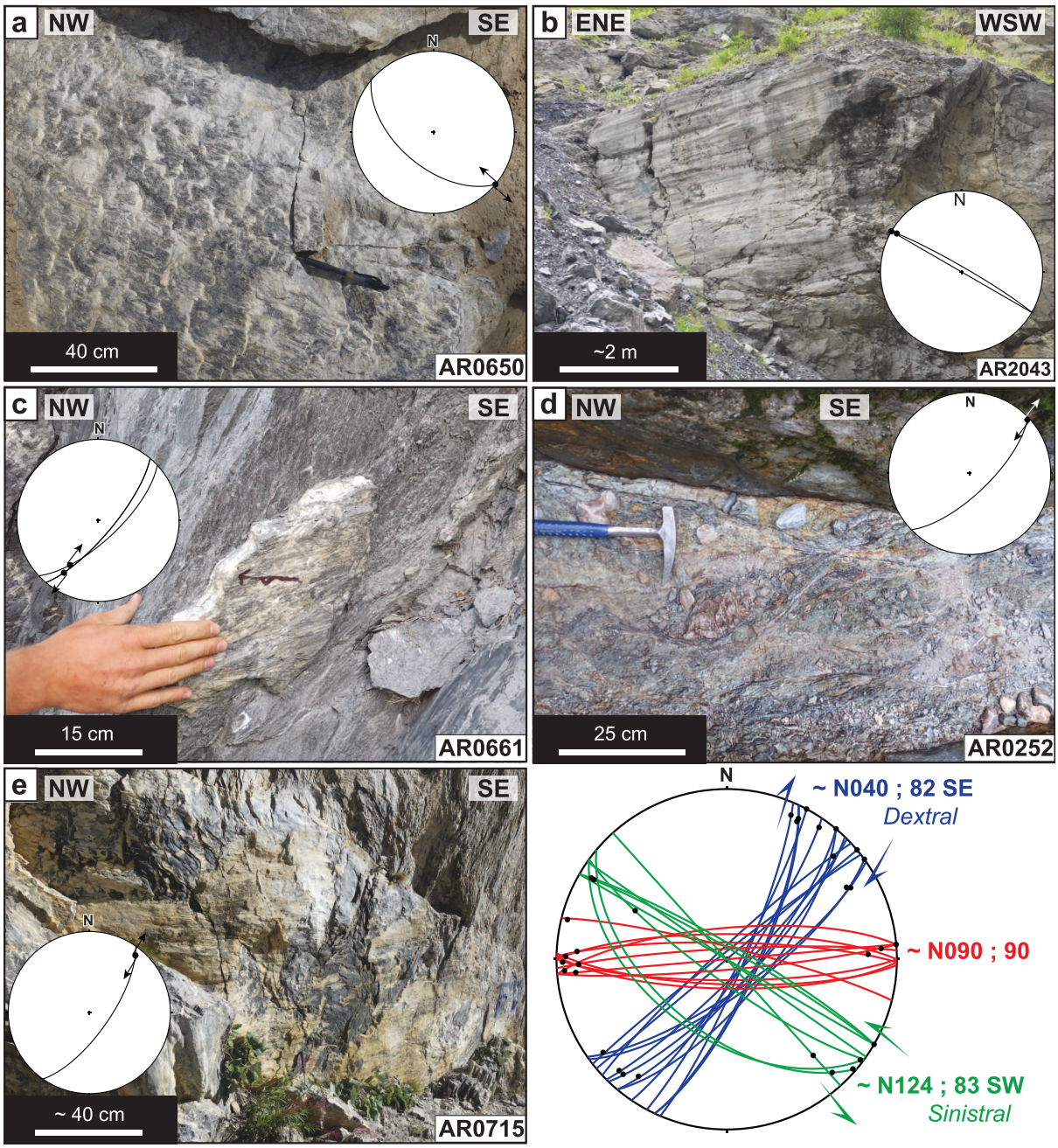

Figure 4.52. Field observations of strike-slip faulting in the Mont-Blanc, Aiguilles Rouges and subalpine chains. a) Sinistral strike slip fault in the easter side of the Mont-Blanc massif with calcite step cristallisation; b) Strike slip fault ('miroir') in the Cirque des Fonds in the Haut-Giffre massif; c) Dextral strike-slip fault on the helvetic nappes on the eastern side of the Mont-Blanc massif; d) Veudale dextral strike-slip fault in the Aiguille Rouges, the gouge is about 75 cm wide and show S/C relationship; e) Dextral strike-slip fault south of the Petit Col Ferret; f) Stereoplot (Lower hemisphere, equal area), compiling the measured strike slip faults in the Mont-Blanc, Aiguilles Rouges and the subalpine chains: three group of faults have been identified.

4.7 Synthesis of 3D structure and cover / basement relationship in the Mont-Blanc, Aiguilles Rouges and subalpine chains

In summary, the shear zones described on the eastern side of the Mont-Blanc (Grande Ecaille, Petit Col Ferret, la Fouly and Sembrancher), on the western side of the Mont-Blanc (Posettes and Forclaz), on top of the Aiguilles Rouges (Pormenaz, Belvédère, Morcles) and on the western side of the Aiguilles Rouges (Col de Barberine, Col d'Emaney, Cirque des Fonds, and Col d'Anterne/Souay) are parts of the same thrust system at the bottom of the helvetic nappes: the Helvetic Basal Thrust (Fig. 4.27). The nappe transport on this thrust system is mainly from WNW to NW. The thrust is nearly following the cover / basement interface and can be described as a décollement. But locally mylonitize the basement (e.g., Col Ferret). Actually, this thrust system is composed of a basal thrust that is righ above the basement and an Upper thrust that corresponds to the bottom of the Morcles nappe. These two thrusts merge above the Aiguilles Rouges, near the Col d'Anterne.

Above, the Criou thrust is part of a larger thrust system attributed to the subalpine chains nappe. This thrust connects with the Helvetic Basal thrust near the col d'Anterne. The faults described above. Further south, the deformation seems to be mainly localized at the bottom of the sedimentary series, and the deformation is more distributed above, with folds and thrusts. The Haut-Giffre massif seems to be the site of an abrupt change in the deformation style, from a "fold nappe" to a "thrust nappe".

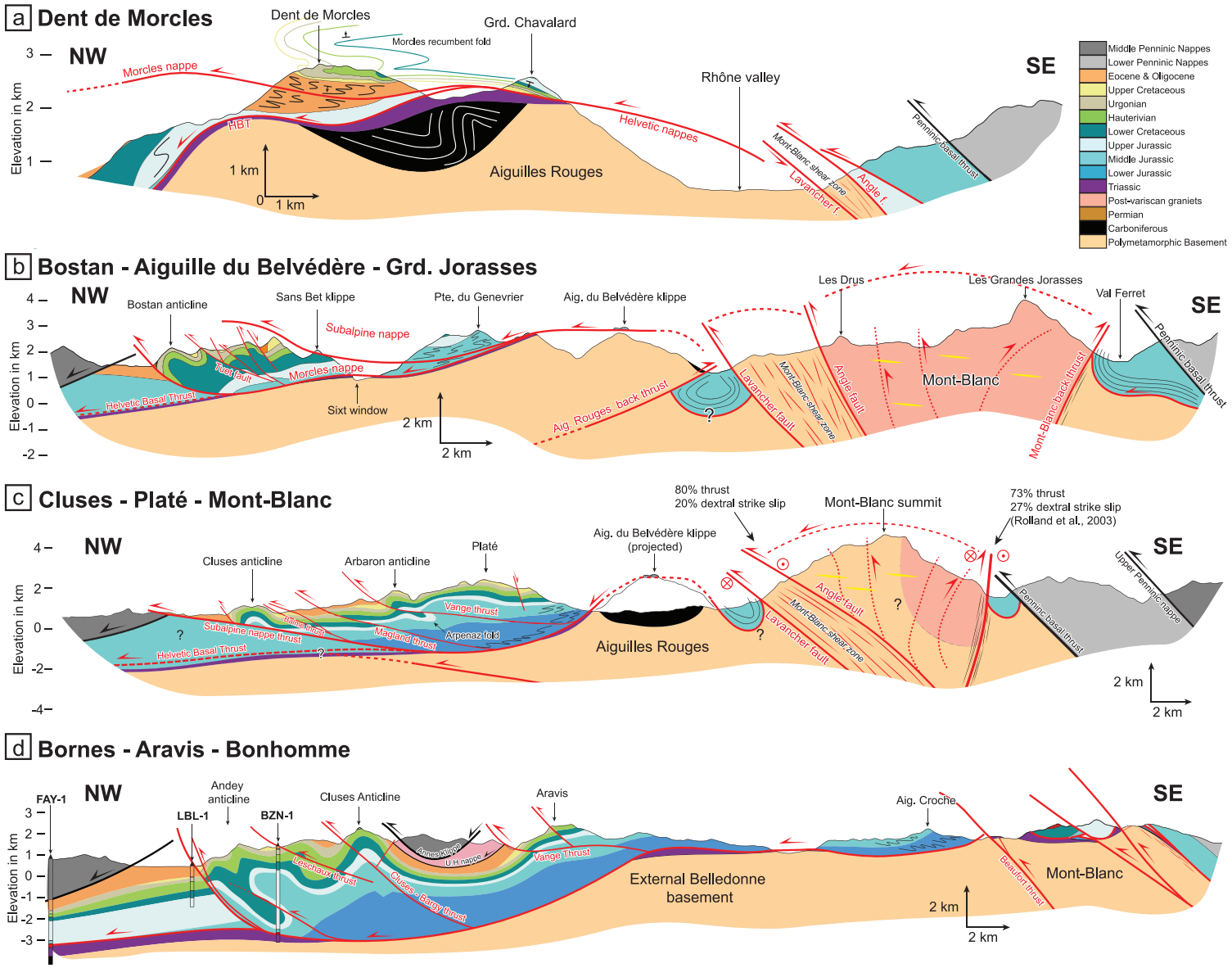

Figure 4.53. Synthesis cross sections through the study area (see location of the section in fig. 4.27.)

4.8 Data Availability, Model output, and visualization

4.8.1 Data availability

All the data used in this chapter: location of the observed measurement, measurements and constraints used in modeling are stored in a repository with the following `https://data.mendeley.com/datasets/grjx9y4mwj/1`. Stereographic plots were performed using Stereonet v.11 programs of Allmendinger et al. (2011) and Cardozo and Allmendinger (2013), freely available on Rick Allmendinger `https://www.rickallmendinger.net/stereonet`.

4.8.2 Instructions to visualize the 3D GeoModel

To visualize the surfaces in paraview

1. Download and open Paraview open source software (`https://www.paraview.org/download/`)
2. Under *File* select *Load state*
3. Navigate to *Mercier 3DGeoModel MontBlanc.pvsm*
4. Under *Load State Data File Options* select *Search File Names Under a Specified Directory* and ensure the directory path is correct.
5. $\rightarrow$ OK ... and wait. The model is quite heavy, and the display can take several seconds to a minute.
6. Individual layers can be set hiden by clicking the "eye" symbol on the left pannel
7. Cross sections can be performed doing:
   (a) Select all the layers and apply the filter "group dataset"
   (b) To the grouped dataset, make applying a filter "clip"

To visualize and compute with GeoModller

1. Launch GeoModeller
2. Load the .xml file provided in the repository.

Chapter's key points

- We built a 3D geological model of 65 x 63 km in the Mont-Blanc, Aiguilles Rouges, subalpine chains, and helvetic nappes. The model interpolates structural data with a statistical method to build the surfaces.
- The model has been built using 1500 measured orientation data, 2 seismic profiles, 3 drill holes, 4 underground pipes and speleology data.
- The result of the structural analysis and 3D mapping highlights a thrusting of the mesozoic cover above the Mont-Blanc and Aiguilles Rouges with a large thrust, often localized at the cover / basement interface (décollement).
- There is a change in the deformation style of the Helvetic nappes from north to south: in the north, the Morcles nappe is a large recumbent fold insensively sheared at its base, while in the south, the deformation in the subalpine nappe is essentially in the cover / basement interface and the décollement is very efficient, leading to a softer deformation of the overlying cover.
- The helvetic nappes are offset by steep thrusts.
  - In the Mont-Blanc, there is a large shear zone on the west side and more distributed shear zones on the eastern side, leading to a pop-up structure. The western Mont-Blanc shear zone strikes N030 to N040 on average, with an N110 direction of thrust on average.
  - In the Aiguilles Rouges, there is a series of back thrusts that tend N020 to N030.

Part III

KINEMATICS AND THERMAL EVOLUTION

Chapter 5

Timing and conditions of the deformation

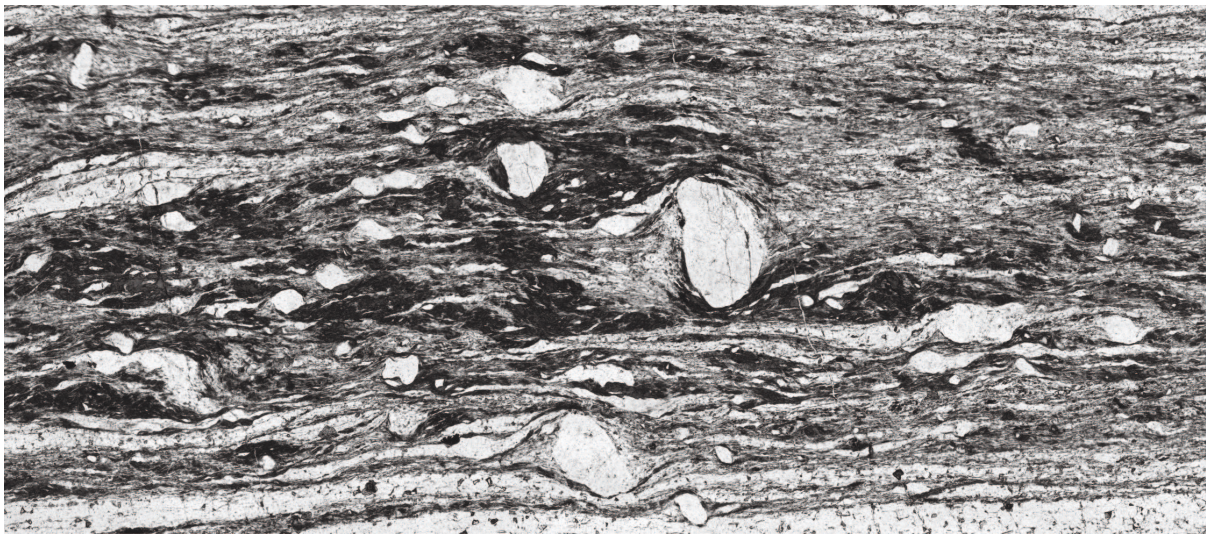

Ultramylonite from the Mont-Blanc shear zone, viewed through an optical microscope (Sample P-A from the Plan de l'Aiguille). Sampling: Philippe Hervé Leloup (2014); Photo: Antoine Mercier (2022).

Abstract

Constraining the alpine deformation sequence of the Western Alps is the key to understanding the mechanics of the crustal wedge. This work proposes to investigate the timing of thrust propagation through a detailed analysis of six mylonitic rocks from the Mont-Blanc massif from four distinct structures (Mont-Blanc shear zones, Helvetic nappes on both sides of the Mont-Blanc and the Vallorcine-Miéville shear zone). Synkinematic white micas were dated using *in situ* $^{40}Ar/^{39}Ar$ dating method. The three samples from the Mont-Blanc shear zone ranges from 14.9 to 17.3 Ma. The sample from the Helvetic nappes on top of the Mont-Blanc (eastern side) yield an age of 13.7 Ma and the sample from the Roselette klippe (south of Mont-Blanc) attributed to the Helvetic nappes, yielded an age of 16.3 Ma. Thermobarometric conditions of the deformation were estimated by petrogeochemical quantification and lattice preferred orientation of quartz crystals and suggest that the deformation occurred below 500°C and between 0.47 and 0.74 GPa. The similarity in the ages from the western shear zone of the Mont-Blanc and the Helvetic nappes on top, leads to the conclusion that the Helvetic Nappe system was working simultaneously with the Mont-Blanc shear zone in a duplex-like system. These new data are combined with previously published absolute dating of the deformation and enable unraveling the thrusting sequence of the Western Alps: The (i) the Helvetic nappe system started immediately after the end of the Penninic nappe system at about 32 Ma. (ii) The Mont-Blanc shear zone develop from 22 Ma to 14 Ma synchronously with the Helvetic nappes in a duplex system. As suggested by previous authors, the northwest Mont-Blanc shear zone and the SE-directed shear zones back thrusting on the southeastern side of the massif are working simultaneously and these opposite movements give rise to an overall pop-up structure of the Mont Blanc massif. (iii) After about 14 Ma, the Mont-Blanc shear zone becomes a breach thrust that intersects the Helvetic nappes. This tectonic evolution implies that three major thrust systems have propagated in sequence from the internal part to the external one: the Penninic, Helvetic, and Alpine Sole thrust systems.

Résumé

L'étude de la séquence de déformation alpine des Alpes occidentales est essentielle pour comprendre la mécanique du prisme orogénique. Dans ce chapitre, nous proposons d'étudier la séquence de propagation des chevauchement au travers d'une analyse détaillée de mylonites du massif du Mont-Blanc provenant de quatre structures majeures (la zone de cisaillement du Mont-Blanc, les nappes helvétiques sur les deux versants du Mont-Blanc et la zone de cisaillement de Vallorcine-Miéville). Nous avons daté les micas blancs synkinématiques avec la méthode *in situ* $^{40}Ar/^{39}Ar$. Les trois échantillons de la zone de cisaillement du Mont-Blanc ont fourni des âges allant de 14.9 à 17.3 Ma. L'échantillon provenant des nappes helvétiques au dos du Mont-Blanc (Est) donne un âge de 13.7 Ma et l'échantillon de la klippe de Roselette (au sud du Mont-Blanc) et attribué aux nappes helvétiques, donne un âge de 16.3 Ma. Les conditions thermobarométriques de la déformation ont été estimées par quantification pétrogéochimique et par l'orientation préférentielle des cristaux de quartz. Les résultats suggèrent que la déformation s'est produite en dessous de 500°C et entre 0,47 et 0,74 GPa. La similitude des âges de la zone de cisaillement du Mont-Blanc et des nappes helvétiques au dessus conduisent à la conclusion que les nappes helvétiques fonctionnait simultanément avec la zone de cisaillement du Mont-Blanc dans un système de type duplex. Ces nouvelles données sont combinées avec les datations absolues de la déformation publiées et permettent de proposer un scénario sur la séquence de chevauchement des Alpes occidentales: (i) Les nappes Helvétiques ont commencé à chevaucher le domaine externe immédiatement après la fin de la mise en place des nappes penniques, vers 32 Ma. (ii) La zone de cisaillement du Mont-Blanc se développe de 22 Ma à 14 Ma de manière synchrone avec les nappes Helvétiques dans un système en duplex. Comme proposé par des auteurs précédents, la zone de cisaillement nord-ouest du Mont-Blanc et les zones de cisaillement rétrochevauchantes dirigées vers le sud-est du massif fonctionnent conjointement et ces mouvements opposés donnent lieu à une structure pop-up générale du massif du Mont-Blanc. (iii) Après environ 14 Ma, la zone de cisaillement du Mont-Blanc devient un chevauchement plus raide qui recoupe les nappes Helvétiques. Cette évolution tectonique implique que trois grands systèmes de chevauchement se sont propagés en séquence depuis la partie interne vers la partie externe : le chevauchement penninique, helvétique et le chevauchement basal alpin.

5.1 Introduction

To constrain the deformation timing, this work proposes a detailed investigation of six mylonitic rocks from the Mont-Blanc massif from four distinct structures (Helvetic Nappes on both sides of the Mont-Blanc, Mont-Blanc shear zone, Vallorcine-Miéville shear zone). Pressure-temperature conditions of deformation are estimated in each sample through combined microstructural and microchemical studies. The microstructural study is based on the micro-structure description and lattice-preferred orientation of quartz obtained from Electron Backscattered Diffraction (EBSD). The microchemical study is based on electronic microprobe punctual analyses and maps. The age data are obtained using the *in situ*, laser ablation $^{40}Ar/^{39}Ar$ dating method. The significance of the age data with respect to that of deformation is discussed in light of the petro-structural study.

The age constraints are then used to discuss the timing of propagation of thin-skin tectonics toward the west through a duplex in the Mont-Blanc massif, and later transition to thick-skin tectonics. These results suggest a new tectonic model for the evolution of the Alpine orogenic wedge.

5.2 Synthesis on the Alpine structures chronology and conditions of the deformation

5.2.1 Penninic Nappe System

The Penninic Nappe system is a complex system of nappes consisting of Mesozoic and Paleozoic sediments and crystalline rocks under which the Western Alps are underthrusted (Ceriani et al., 2001; Simon-Labric et al., 2009). The basal contact of the Lower Penninic Nappe is called the Penninic thrust. The Eocene flyshes are interpreted to have been deposited in the foreland basin of that thrust during the Eocene (Ruffini et al., 1997). Flysch sedimentation lasted after 32.5 ± 0.2 Ma because it mobilizes volcanic clasts that have been dated (Ruffini et al., 1997). Despite being one of the main alpine structures, its timing is constrained only by a few absolute ages: In the southern Alps (Pelvoux) synkinematic phengites of three strike-slip and one thrust located immediately below the Penninic thrust yield $^{40}Ar/^{39}Ar$ ages between 31 and 33 Ma, interpreted to reflect motion on the thrust (Simon-Labric et al., 2009). East of the Mont-Blanc massif, white micas from a mylonite located 500 m above the Penninic thrust near the Col de la Seigne yield a $^{40}Ar/^{39}Ar$ spectrum with an age ranging from 27.92 to 35.2 Ma with a mini plateau at 30 Ma interpreted to reflect motion on the main thrust (Egli et al., 2017) (Fig. 5.1b). Cenki-Tok et al. (2013) have used U/Pb dating on allanite from a shear zone within the Mont Blanc massif and found an age of 29.4 ± 0.9 Ma that has been interpreted as related

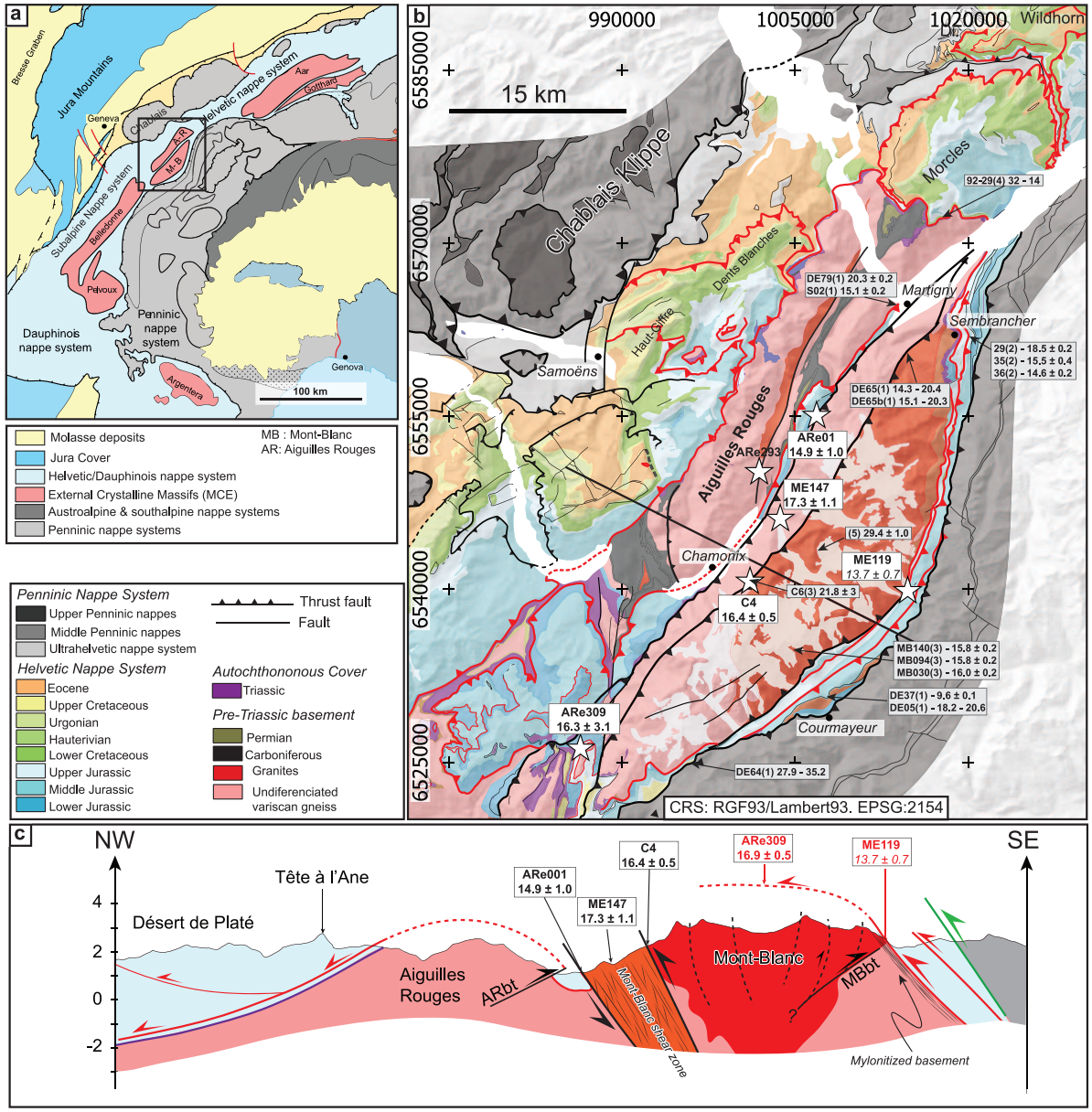

Figure 5.1. Structural framework of the Mont-Blanc and Aiguilles Rouges and the sampling sites for $^{40}Ar/^{39}Ar$ absolute dating. a. Tectonic map of the Western Alps modified from Pfiffner (2014); b. Detailed structural map of the Mont-Blanc and Aiguilles Rouges, modified after Pfiffner et al. (2011). The white stars locate the dated samples in this work. Grayish framed boxes locate the other geochronological constraints obtained from previous studies with the sample name and the reference (1: Egli et al. (2017), 2: Crespo-Blanc et al. (1995), 3: Rolland et al. (2008), 4: Kirschner et al. (1996) and Kirschner et al. (2003) and 5: Cenki-Tok et al. (2013)); c. Geological cross-section through the Mont-Blanc massif with the age results obtained.

to the underthrusting of the massif below the Penninic nappe system (Fig. 5.1b) because of the similarities of fluids with those from the Penninic thrust (Rossi et al., 2005; Cenki-Tok et al., 2013). In summary, the Penninic thrust was active during the Eocene - Oligocene, taking place after about 32.5 Ma (Ruffini et al., 1997). Direct geochronological constraints suggest that its

motion occurs between 32.5 and 29 Ma (Cenki-Tok et al., 2013; Egli et al., 2017; Simon-Labric et al., 2009).

5.2.2 The Helvetic nappe system

The Helvetic Nappe system is a complex imbrication of cover thrust nappes detached from the underlying basement and transported to the West (Leloup et al., 2005; Ramsay, 1981; Egli and Mancktelow, 2013; Egli et al., 2017; Escher et al., 1988)). Four main thrust nappes have been distinguished from top to bottom: the Wildhorn Nappe, the Diablerets Nappe, the Morcles Nappe, and the Hevetic Basal thrust Nappe (Mercier et al., 2023, (Chapt. 4)). From the eastern side of the Mont-Blanc, Crespo-Blanc et al. (1995) used $^{40}Ar/^{39}Ar$ dating on synkinematic white micas, attributed to the emplacement of the Diablerets nappe, and found ages of about $\approx$ 15 Ma along the thrust. This age has been interpreted as a deformation age because the white detrital micas embedded within the limestones far from the thrust have yielded significantly older ages of about $\approx$ 27 Ma, probably corresponding to a cooling age. Fine-grained synkinematic white micas (2 to 6 μm) from ductile mylonites at the base of the Morcles nappes (Fig. 5.1b) yield an age spectrum $^{40}Ar/^{39}Ar$ with apparent ages between 32 and 14 Ma (Kirschner et al., 1996). This was interpreted as crystallization ages during nappe emplacement. From the Diableret Nappe, Kirschner et al. (2003) using the Rb/Sr dating method have obtained ages around 18 Ma, interpreted as the end of mica growth in the deformation. Using $^{40}Ar/^{39}Ar$ on synkinematic white micas within the thrust nappe, the same authors obtained total gas ages between 14.5 and 18.5 Ma. Although their results are equivocal, the ages obtained are in good agreement with the ages at la Batiaz obtained by Egli et al. (2017), on the eastern side of the Aiguilles Rouges massif (western side of Mont-Blanc). There, synkinematic white mica on a northwest thrusting fault yields a plateau age of 20.3 ± 0.2 Ma interpreted as related to the motion of the Mont-Blanc shear zone (Egli et al., 2017), but that Mercier et al. (2023, Chapt. 4) instead assign to the Helvetic nappe emplacement. In the external part of the belt, in the subalpine domain, some interpret that the Helvetic nappe system bounded molasse deposits during the Miocene (Kalifi et al., 2020). The dating of these foreland sediments by comparison of the $^{86}Sr/^{87}Sr$ in shells with that of the global ocean yields ages between 21 and 8 Ma, suggesting that the Helvetic nappe system stated to be active before 21 Ma (Kalifi et al., 2021). U/Pb calcite dating of the faults in the front in of the Moucherotte klippe at $\approx$15 Ma (Bilau et al., 2023), can be interpreted as evidence that the thrust lasted until at least that time.

From the available geochronology data, the Helvetic Nappe system appears to have been active for a long time interval, initiating soon after the end of the Penninic thrust (or synchronously?) at about 32 Ma and lasting until 15 Ma. However, few clear ages can univocally be associated with that thrusting event.

5.2.3 Mont-Blanc shear zones and back-thrusts

The Mont-Blanc deformation is characterized by a network of anastomosed, reverse / right lateral shear zones directed towards the northwest on its western side and directed to the southeast on its eastern side, forming a fan-shaped geometry structure (Bertini et al., 1985; Leloup et al., 2005; Rolland et al., 2008; Rossi and Rolland, 2014). On the western side, there is a 4 km thick deformation zone, striking about N$34°$ (Leloup et al., 2005), with a partly oblique dextral strike-slip sense of shear and a mean thrust direction N$280°$ (Leloup et al., 2005; Rolland et al., 2008). The Mont-Blanc granite above is affected by numerous anastomosed green-schist shear zones that bear muscovite + biotite + albite + chlorite (Rolland et al., 2003; Rossi et al., 2005; Rossi and Rolland, 2014).

On the western side of the massif, $^{40}Ar/^{39}Ar$ dating has been applied to synkinematic white micas from the upper part of the Mont-Blanc shear zone and yield ages of 21.8 $\pm$ 3 Ma (inverse isochron) (Rolland et al., 2008). Two duplicates of white micas located further north along the same fault yield a complicated age spectrum in the range of 14.3 - 20.41 Ma, with a mini plateau at $\approx$ 18 Ma (Egli et al., 2017).

$^{40}Ar/^{39}Ar$ phengite ages from three locations on the southeastern side of the Mont-Blanc massif are close to 16 Ma, interpreted as a deformation age corresponding to the end of motion along shear zones related to the Mont-Blanc back thrust (Rolland et al., 2008). On the other hand, Leloup et al. (2005) suggested that the Mont-Blanc back thrust fault, overturning the Mesozoic cover, was active more recently due to its brittle deformation characteristics. However, this structure has no *in situ* geochronological dating.

Low-temperature thermochronology data from both sides of the Chamonix Valley at a similar elevation (1010-1350 m) yield similar zircon fission-track ages similar between 3.4 Ma on the Mont-Blanc side and 4.5 Ma on the Aiguilles Rouges side, suggesting that no significant movement occurred in the shear zones since then (Leloup et al., 2005; Glotzbach et al., 2008; Boutoux et al., 2016). Themo-kinematic simulations (Glotzbach et al., 2008; Glotzbach et al., 2011)) suggest an episodic exhumation of the Mont-Blanc range with initiation at 22 ± 2 Ma, with a rate of 0.50 ± 0.15 km Ma^{-1}, which could be associated with the movement along the Mont-Blanc shear zone, followed by a decrease to values of 0.15 ± 0.65 km Ma^{-1} at 6 ± 2 Ma that could correspond to the end of the motion along the shear zone.

In brief, the shear zones on the western side of the Mont-Blanc massif most likely started about 22 Ma at $\approx$ 400 °C and lasted until 6 Ma at $\approx$ 200 °C. On the eastern part, reverse / right-lateral deformation started after 16 Ma (Rolland et al., 2008), but could have lasted until more recent time as suggested by Leloup et al. (2005).

5.2.4 Vallorcine - Miéville shear zone

The Vallorcine granite is a high-K calc-alkaline granite that crystallized at 332 ± 2 Ma (Bussy et al., 2000). It is bounded on its south-eastern side by the Vallorcine-Miéville shear zone, which has been interpreted as a late Variscan right-lateral shear zone (Steck and Vocat, 1973). Migmatisation occurred at 320 ± 1 Ma during decompression, in part within the right-lateral Berard-Emosson transpressive shear zone in the NE-SW direction (Bussy et al., 2000; Genier et al., 2008; Simonetti et al., 2020), contemporaneously with the opening of the Salvan-Dorénaz basin as a pull-apart (Capuzzo et al., 2003). Some authors interpret the shear zone as a left-lateral fault (Steyrer and Sturm, 2002), while others consider it a Cenozoic reverse fault (Kerrich et al., 1980). Near the France-Switzerland border, mylonites from the Vallorcine-Miéville shear zone have been dated with the $^{40}Ar/^{39}Ar$ method and produce two pseudoplateau deformation ages of 14.3 ± 0.2 Ma and 22.9 ± 0.9 (Rolland et al., 2008). These ages have been interpreted as being related to reverse faulting coeval with that along the Mont-Blanc shear zone. (Rolland et al., 2008). The precise kinematics of the Vallorcine-Mieville shear zone remain to be deciphered.

Six samples have been collected along three major structures within the Mont-Blanc massif: three from the Mont-Blanc shear zone, two from the Helvetic nappe system, and one from the Vallorcine-Miéville shear zone (Table 5.1).

Table 5.1. Identification, location, and description of the samples used for $^{40}Ar/^{39}Ar$ dating.

Sample	Lat.[1] d.dd	Lon.[1] d.dd	Structure	Measure Str. Dip. Quad. in degrees	Verbatim Locality
ARe001	46.02572	6.97210	MBsz	N010;30SE Lin. az. N109	Col de Balme
ME147	45.94587	6.94587	MBsz	N015;67SE Lin. az. N073	Bottom of Argentière glacier
C4	45.89951	6.88742	MBsz	N028;43SE Lin. az. N140	Plan de l'Aiguilles
ME119	45.89813	7.06471	HBT	N045;75SE Lin. az. N120	Petit Col Ferret
ARe309	45.76310	6.68611	HBT	N013;18SE Lin. az. N094	Aiguille de Roselette
ARe293	6.904615	45.9816	VMsz	1N003;62E Lin. az. N062	Les Chésérys (Aiguilles Rouges)

[1]Latitude and longitude expressed in decimal degrees
in the WGS84 geodetic datum (EPSG:4326).
MBzs: Mont-Blanc shear zone ; HBT: Helvetic Basal Thrust.
Ros. Klippe: Roselette Klippe ; VMsz: Vallorcine-Miéville shear zone.

5.3 Analytical techniques

In this part we will describe the techniques used to infer the deformation conditions of the mylonites.

5.3.1 Quantitative Electron Microprobe analysis

To unravel the deformation conditions and depict the eventual zoning in the compositions of the white micas, we performed a quantitative electron microprobe analysis (EPMA) and high-resolution elementary mapping. High-resolution chemical analyzes and mineral mapping were acquired with an electron probe micro-analyzer (EPMA) JEOL JXA-8230 at the Institut des Sciences de la Terre (ISTerre) of the University of Grenoble Alpes. The mineral maps have been calibrated using punctual analyzes and have been acquired using a 5 keV accelerating voltage and a beam current of 12 nA with a beam size of about 1 $\mu\mathrm{m}$. X-ray maps were also acquired to evaluate the composition variability of mylonitized samples. Natural standards were used to correct for instrumental drift.

The mapping and quantitative data were processed using XMapTools 4.1 (Lanari et al., 2014; Lanari et al., 2019; Lanari et al., 2023). Data processing has been done using the standard workflow recommended by the XMapTools user guide. Semi-quantitative maps are calibrated based on punctual quantitative measurements (about 10 to 20 points per mineral species) to yield quantitative maps. Supervised classification is used for mineral discrimination within the map. The user draws several Regions of Interest (ROI) for each mineral to "teach" the classification for discrimination. A probability value is obtained for each pixel that has been classified. We later applied a quality filter that removes all pixels below the threshold of 1.0 according to the standard value used in XMapTools. Finally, all the pixels kept are more likely to belong to the mineral species defined and significantly improve the data quality.

The structural formula in fraction units (pfu) is obtained by normalizing with the number of oxygen within the structural formula of the mineral (11 oxygens are used to calculate the structural formula of white micas). From the normalized map, ROIs are selected, representing the overall chemical composition of the mineral species considered. The chemical analyses of minerals are reported in table 5.3.

5.3.2 Lattice Preferred Orientation (LPO) of quartz grains

In many deformed rocks, the orientations of the crystals are not randomly distributed but are preferentially oriented in a specific pattern according to the deformation conditions (Passchier and Trouw, 2005). This orientation pattern is known as lattice preferred orientation (LPO). Using an Electron Microscope it is possible to quantitatively map with high resolution

the orientation of grains, which provides information about the origin of the LPO and unravels the deformation conditions.

During processes of deformation, the internal crystals develop dislocations to reduce their internal stress energy (which is at a minimum when there are no dislocations). These dislocations are vacancies or interstitial defaults in the crystalline network and are induced by differential stress. When dislocations are grouped into a planar network, they form sub-grain boundaries that separate newly formed grains. The new grains are slightly misoriented with respect to their neighborhoods and lead to a "chessboard" pattern, which is called a Lattice Preferred Orientation (LPO) of the subgrains. Trépied et al. (1980) had shown that subgrain disorientation depends on the dislocation slip system operating during deformations. Other studies (e.g., Lister and Price, 1978) have shown that the slip system that operates during quartz deformation depends on deformation mechanisms such as temperature and strain rate. Therefore, the study of dislocations and subgrain formation in a quartz-rich rock fault can provide important information about the conditions of deformation.

5.3.2.1 Origin of Lattice-Preferred Orientation

The type of LPO pattern that developed in a deformed rock depends on many parameters and is variable depending on the mineral type studied; we present here the predominant mechanisms in quartz LPO:

- **The deformation**
  - *The slip system operating*: basal c-axis, prismatic-c or prismatic-a. This parameter is temperature-dependent (Fig. 5.2 and 5.3).
  - *The ratio of stretching rate*: plane strain, flattening or constrictional, determining the direction of rotation of the crystal.
  - The ratio of stretching rate: The LPO increases in strength with increasing strain.
  - *The kinematic vorticity*: simple shear (non-coaxial) deformation leads to LPO patterns with 2^{nd} degree symmetry while pure shear (coaxial) deformation leads to 4^{th} degree symmetry.
- **The thermo-barometric conditions:**
  - *The activity of dynamic recrystallization* : bulging and grain boundary migration.
  - *Growth of grains*.
- **Preexisting lattice preferred orientation**

Therefore, the characterization of such preferred orientation is useful to quantify the deformation type and conditions that affected a rock sample.

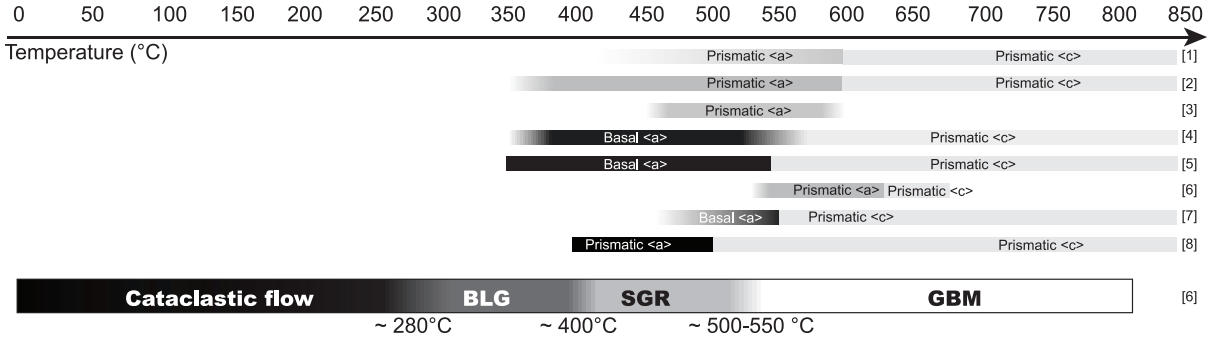

Figure 5.2. Quartz slip systems versus temperature, updated after Toy et al. (2008). References are: [1]: Lister and Dornsiepen (1982); [2]: Mainprice et al. (1986); [3]: Schmid and Casey (1986); [4]: Okudaira et al. (1995); [5]: Takeshita (1996); [6]: Mancktelow and Pennacchioni (2004); [7] Stipp et al. (2002); [8]: Pennacchioni et al. (2010). Abbreviations: BLG: Bulging; SGR: Subgrain rotation; GBM: Grain boundary migration.

	Basal plane slip in <a> direction	Rhomboedric plane slip in <a> direction	Prismatic plane slip in <a> direction	Prismatic plane slip in [c] direction
Slip plane	(0,0,0,1) (m)	(0,-1,1,1) (1,0,-1,1) {r} (-1,1,0,1)	(0,-1,1,0) (1,0,-1,0) {m} (-1,1,0,0)	(0,-1,1,0) (1,0,-1,0) {m} (-1,1,0,0)
Slip direction	[2,-1,-1,0] [a_1] [-1,2,-1,0] [a_2] [-1,-1,2,0] [a_3]	[2,-1,-1,0] [a_1] [-1,2,-1,0] [a_2] [-1,-1,2,0] [a_3]	[2,-1,-1,0] [a_1] [-1,2,-1,0] [a_2] [-1,-1,2,0] [a_3]	[0,0,0,1] [c]

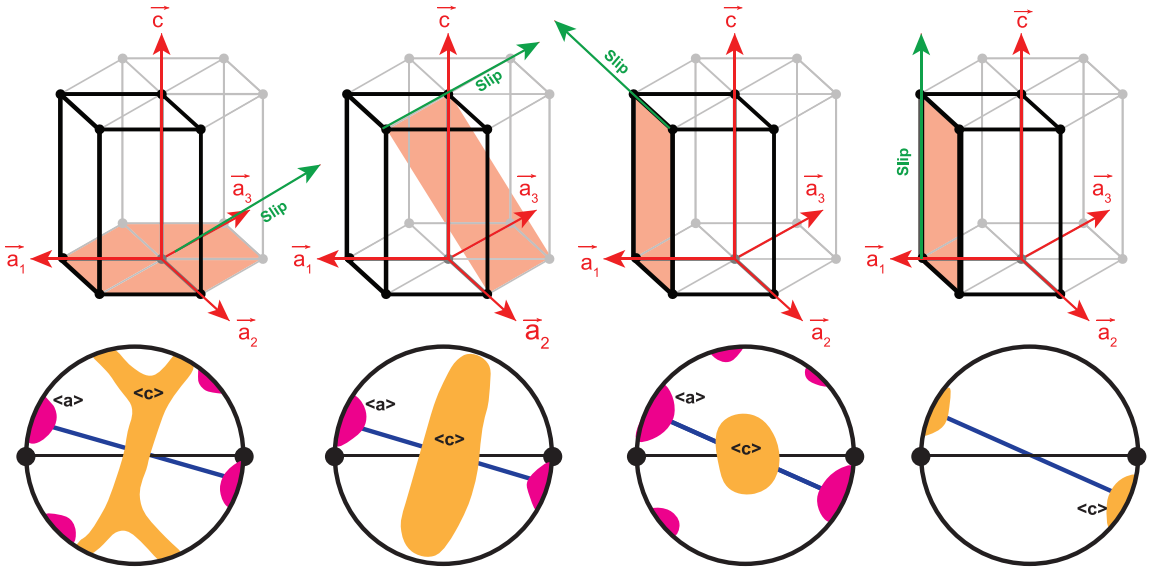

Figure 5.3. Quartz slip systems, modified after Passchier and Trouw (2005).

5.3.2.2 Electron backscatter diffraction (EBSD)

To do so, EBSD analysis was acquired in the MATEIS laboratory of INSA Lyon, using an Oxford Instruments NordlysF EBSD camera, mounted on a Zeiss Supra (Table C.1). EBSD

pattern acquisition and automatic indexing were performed using Aztec software from Oxford Instruments. The analysis was performed without carbon coating on the thin sections to increase the indexing rate. Raw orientation data have been processed using the Matlab MTex toolbox (Hielscher and Schaeben, 2008; Bachmann et al., 2010), grain reconstruction has been calculated with the Voronoi decomposition method (Bachmann et al., 2011). Grains are defined as regions of similar orientation, with a 10° misorientation threshold. Grains constrained by less than 2x2 pixels have been filtered and removed from the data, as they most likely result from misindexing.

5.4 *In situ* $^{40}Ar/^{39}Ar$ Dating of synkinematic white micas

Introduced by Maluski and Monié (1988) and Kelley et al. (1994), the *in-situ* $^{40}Ar/^{39}Ar$ dating method allows targeting specific minerals in their genuine structural position, allowing discussion on the relationship between apparent age and that position. This can help discriminate between inherited minerals and those that (re)crystallize during deformation (e.g., Ge et al., 2023; Di Vincenzo et al., 2016; Abd Elmola et al., 2022).

The sample preparation was processed by the Thin Section Lab Company (France), where thick sections were cut through the sample's chip. Sections have been double-polished with a $\approx$ 500 μm thick polishing cloth. $^{40}Ar/^{39}Ar$ analyses were undertaken at the Geosciences Montpellier laboratory (University of Montpellier, France) using *in situ* laser extraction techniques. The samples were wrapped in aluminum foil and irradiated for 20 h in the core of the TRIGA reactor at the University of Pavia (Italy) together with standard Fish Canyon sanidine (FC). *In situ* laser experiments were carried out with an Nd:YAG $\approx$ 2.5 mJ and 9 Hz infrared laser that produces pits of about 20 μm in diameter and 10 μm in depth. For each dating, more than 200 laser shots were fired on a surface of about 100 μm^2. Details of the dating procedure are given in appendix C.1.1 (p. 386).

5.4.1 The Mont-Blanc shear zone

Sample ARe001 was collected at the base of the Mont-Blanc shear zone, in the Col de Balme area, a few meters above the contact, called the *Lavancher fault*, with the underthrust Mesozoic series (Fig. 5.1c). On the macroscopic scale, the sample is a coarse-grained mylonite with foliation striking N10° ; 30° E and bearing a mineral lineation striking N109° (Fig. 5.5a). Typical S/C structures indicate a top-to-northwest sense of shear. On the microscopic scale, the sample is characterized by large porphyroclasts ($\approx$ 1 mm) of quartz and feldspar, embedded in a mylonitic foliation, bearing small quartz (10-50 μm) and white mica (Fig. 5.4 a). Quartz shows the typical recrystallization fabric with relicts of large quartz grains with undulose extinction

and new grains formed by bulging (Fig. 5.12a). White micas have crystallized in interstitial beds of foliation and mainly along the crystallization tail of the porphyroclast.

White micas show a major chemical population within the phengites series, close to the pure muscovite pole (Si = 3.3 pfu and XMg = 0.5) with an aluminum content of approximately 2.3 pfu) (Fig. 5.6 and table 5.3). Few micas have a higher Si content up to 3.7 pfu, being closer to the Celadonite pole. Applying the Massonne and Schreyer (1987) thermobarometer based on the Si content in phengite suggests that the main population corresponds to lower P-T conditions than the other white micas (Fig. 5.8). We performed an analysis of mineral equilibrium using PERPLEX software (Connolly, 1990; Connolly and Petrini, 2002). Phase diagram equilibria were performed in the system $Na_2O\ CaO\ K_2O\ FeO\ MgO\ MnO\ Al_2O_3$ $SiO_2\ TiO_2\ H_2O$, with quartz and H2O in excess, using the bulk composition of the chemical mapping (Table 5.2). The computed section corresponding to the mineral assemblage of the sample yields a pressure temperature range of 0.66 - 0.45 GPa / 510-45°C compatible both with the paragenesis (Table 5.1) and with the Si isopleth (Fig. 5.8).

Table 5.2. Bulk composition used to reconstruct the phase diagram. Expressed in oxide wt%.

SiO_2	TiO_2	Al_2O_3	FeO	MnO	MgO	CaO	Na_2O	K_2O	$Cr2$	Total
56.63	0.91	19.94	4.75	0.092	2.36	1.25	2.50	8.077	0.055	96.58

25 apparent ages have been acquired on white mica along the S and C planes of the ARe001 sample (Fig. in appendix C.14), 2 of these ages have been excluded due to a low proportion of ^{39}Ar (< 2 %) or too large atmospheric argon contamination (Table in appendix C.2). The cumulative probability plot of the 23 remaining ages shows a major peak corresponding to 16 ages, from 13.9 ± 0.2 to 16.0 ± 0.3 Ma with a mean of 14.9 ± 0.3 Ma (Fig. 5.10). An outsider is younger than 12.5 ± 0.5 Ma and five are older than 18 Ma. A well-constrained inverse isochron plot ($R^2 = 0.93$) built from all data, but the youngest and the four oldest yield an age of 15.0 ± 1.0 Ma with an intercept $^{40}Ar/^{36}Ar$ of 346.0 ± 11.4 that corresponds to a small amount of excess argon (Table in appendix C.2). For this sample, we retain an age of 14.9 ± 1.0 Ma (inverse isochrone age) for ARE001 white micas. A faint inheritance at 25 Ma may be present, represented by the spots n°11 and 20.

Sample ME147 was collected above the Argentière village, within the Mont-Blanc shear zone, (Fig. 5.1c). The sample is similar to ARe001 on the macroscopic scale: the mylonitic foliation trends N15°;67°E bearing a mineral lineation striking N73°. A similar petrographic structure is observed at the microscopic scale, with finer foliation beds and typical S/C structures, indicating a top-to-SW sense of shear. Quartz recrystallization with relicts of large quartz grains with undulose extinction and new grains formed by bulging (Fig. 5.12b). White micas are crystallized along the shear planes (c-fabric), attesting to their crystallization during the de-

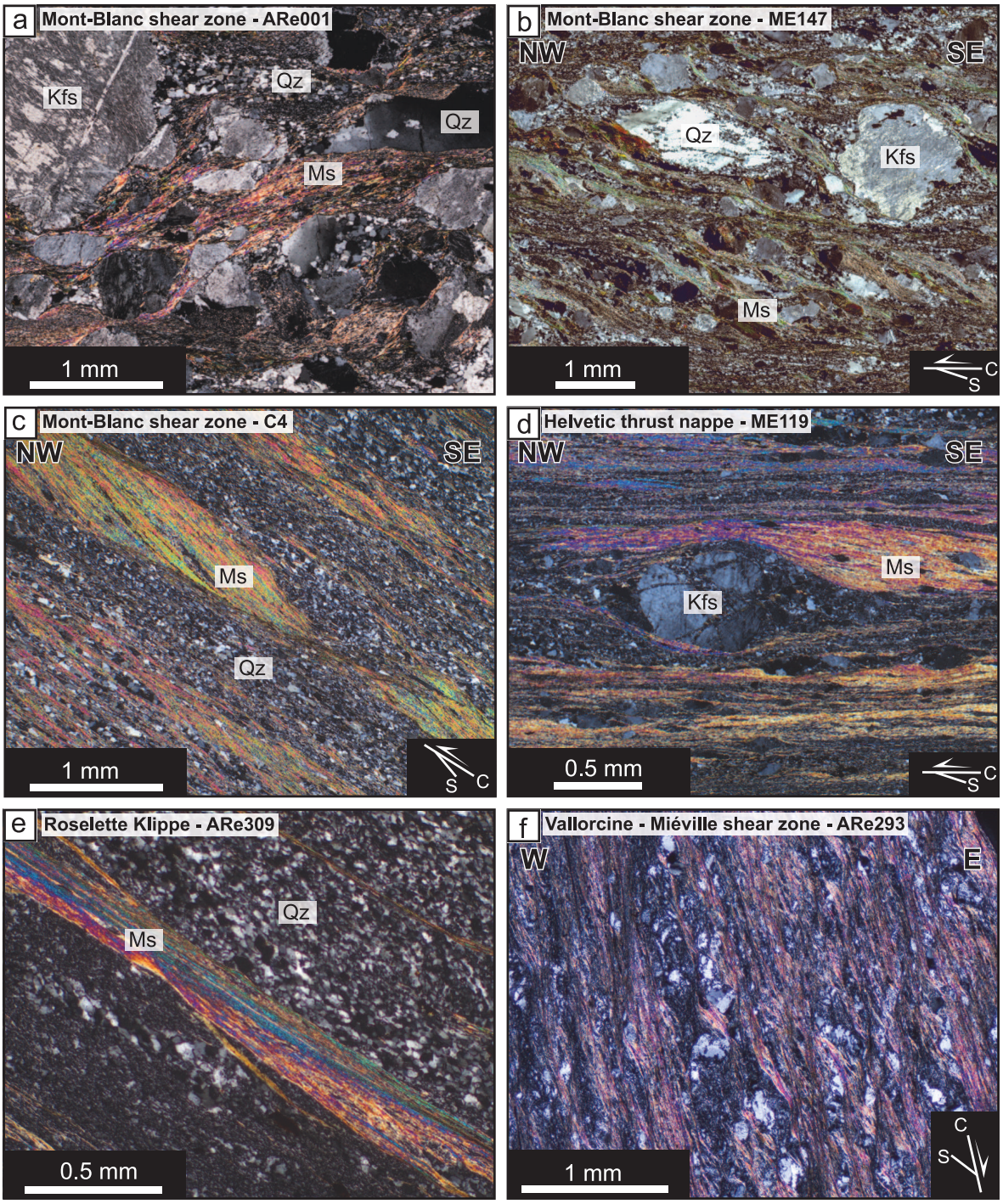

Figure 5.4. Photomicrographs of studied mylonites.

formation process. Composition analysis highlights a single white mica population very similar to the main one of ARe001 with slightly more dispersion in the Si content (Figs. 5.7 and 5.6). The Si content of that population corresponds to a slightly higher pressure (+ $\approx$ 0.4 GPa) than that for ARe001 at a given temperature (Fig. 5.8).

The ME147 sample yielded 24 apparent ages, two of which have been excluded (Table

C.3). The remaining spots show a large apparent age interval with two main populations (Fig. 5.10). The first corresponds to a broad peak with 14 spots, ranging in age from 15.3 ± 0.2 Ma to 23.6 ± 1.0 Ma with an average of 16.3 ± 3.0 Ma (Fig. 5.10). The second population corresponds to 7 spots with ages ranging from 27.3 ± 0.9 Ma to 31.7 ± 0.8 Ma with an average of 29.3 ± 1.5 (Fig. 5.10). When plotted on the inverse isochron plot, these two populations yield an age of 17.0 ± 1.1 Ma ($R^2 = 0.75$; $^{40}Ar/^{36}Ar = 361.6 \pm 10.9$) for the first and 25.8 ± 4.9 Ma ($R^2 = 0.86$; $^{40}Ar/^{36}Ar = 414.5 \pm 33.4$) Ma for the second (Fig. 5.11).

In sample ME147 we consider that the main population of white mica gives an age of 17.0 ± 1.1 Ma with a $^{40}Ar/^{36}Ar$ initial of 361.6 ± 10.9 close to that of ARe001. A significant fraction of the micas give an older age of 25.8 ± 4.9 Ma, which also corresponds to $^{40}Ar/^{36}Ar$ initial ratio of 414.5 ± 33.4 higher than the present day air (295.5).

Sample C4 was collected in the upper part of the shear zone, within the so-called *Angle fault* (Fig. 5.1b and c) (Paul and Nicolas, 1926; Corbin and Oulianoff, 1928; Butler, 1985; Belliere, 1988). On the macroscopic scale, this sample consists of a fine-grained leucocratic ultramylonite with foliation striking N2°;43° E with a well-visible mineral lineation with azimuth N140° (Fig. 5.5b). On the microscopic scale, petrography is characterized by a very fine quartz-supported matrix, with large foliation beds containing white mica fish, indicating a top-to-northwest sense of shear (Fig. 5.4). Larger biotites and feldspar are found within the matrix, possibly former relicts of the protolith inherited from the Variscan metamorphism. Due to the smaller size of the grains and the homogeneity in the structure, we suggest that the deformation of this sample is greater than in ARe001 and ME147.

Chemically, the white micas from sample C4 are aligned along the phengite composition series, with a more concentrated patch close to the muscovite-rich pole similar to ARe001 and ME147, but with a larger component closer to the celadonite pole (Figs. 5.6 and 5.7c). These more celadonite (higher Si content) rich phases corresponding to higher P-T conditions (Fig. 5.8c) are located at the interface of muscovites and other minerals (Fig. 5.7).

The preferred orientation analysis of the quartz lattice was performed at two sites within two quartz ribbons (Fig. 5.16). In the two cases, the maximums of the [c]-axis are found along two crossed girdles with four maxima for site 1 and a single maximum for site 2. This pattern is generally interpreted as the result of the activation of the basal plane as shear planes along the $< a >$ directions (Passchier and Trouw, 2005), suggesting nearly pure shear at site 1 and a top to the NW simple shear component at site 2. The pattern of the $< a >$ and {m}-axes is compatible with this interpretation (Fig. 5.16) d). This suggests that the involved slip system in quartz is mostly basal in the $< a >$ direction, indicating a relatively low deformation temperature (below 400°C), with a slip direction toward N141° to N150° (Fig. 5.16c).

Sample C4 shows a narrow apparent age range, with 18 spots ranging from 15.6 ± 0.4 to 20.8 ± 0.3 Ma (Fig. 5.10). This plot suggests in fact two age populations with 16 ages with a mean at 16.4 ± 0.5 Ma and two spots $\approx$ 20 Ma old (Fig. 5.10). Most spots show a very homogeneous argon isotopic ratio, precluding the drawing of an inverse isochron array. Therefore, in sample C4, the retained age is the mean apparent age of 16.4 ± 0.5 Ma.

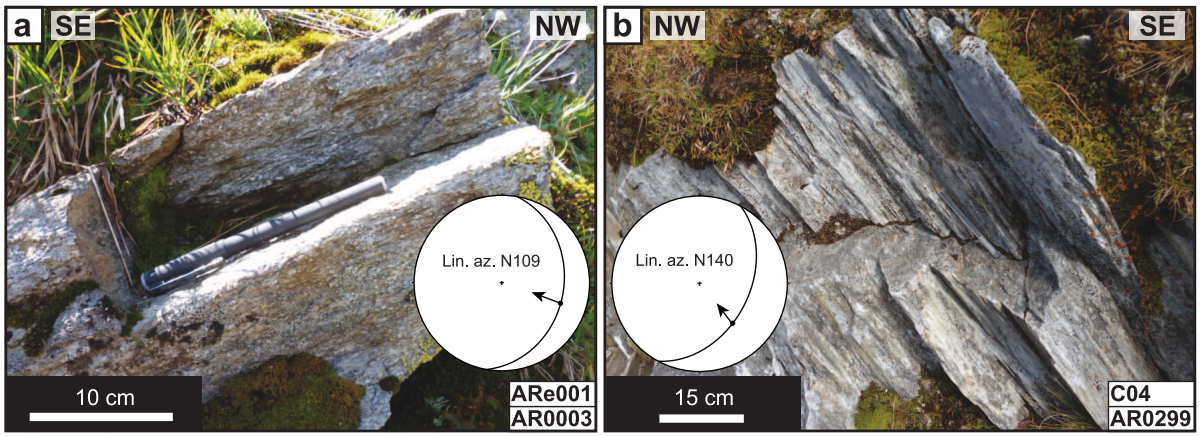

Figure 5.5. Dated samples from the western Mont-Blanc shear zone. a) Mylonite (sample ARe001) with porphyroclasts embedded in a quartz and mica-rich matrix from the bottom part of the shear zone (*Lavancher fault*); b) Ultramylonite (sample C4) from the upper part of the shear zone (Angle fault).

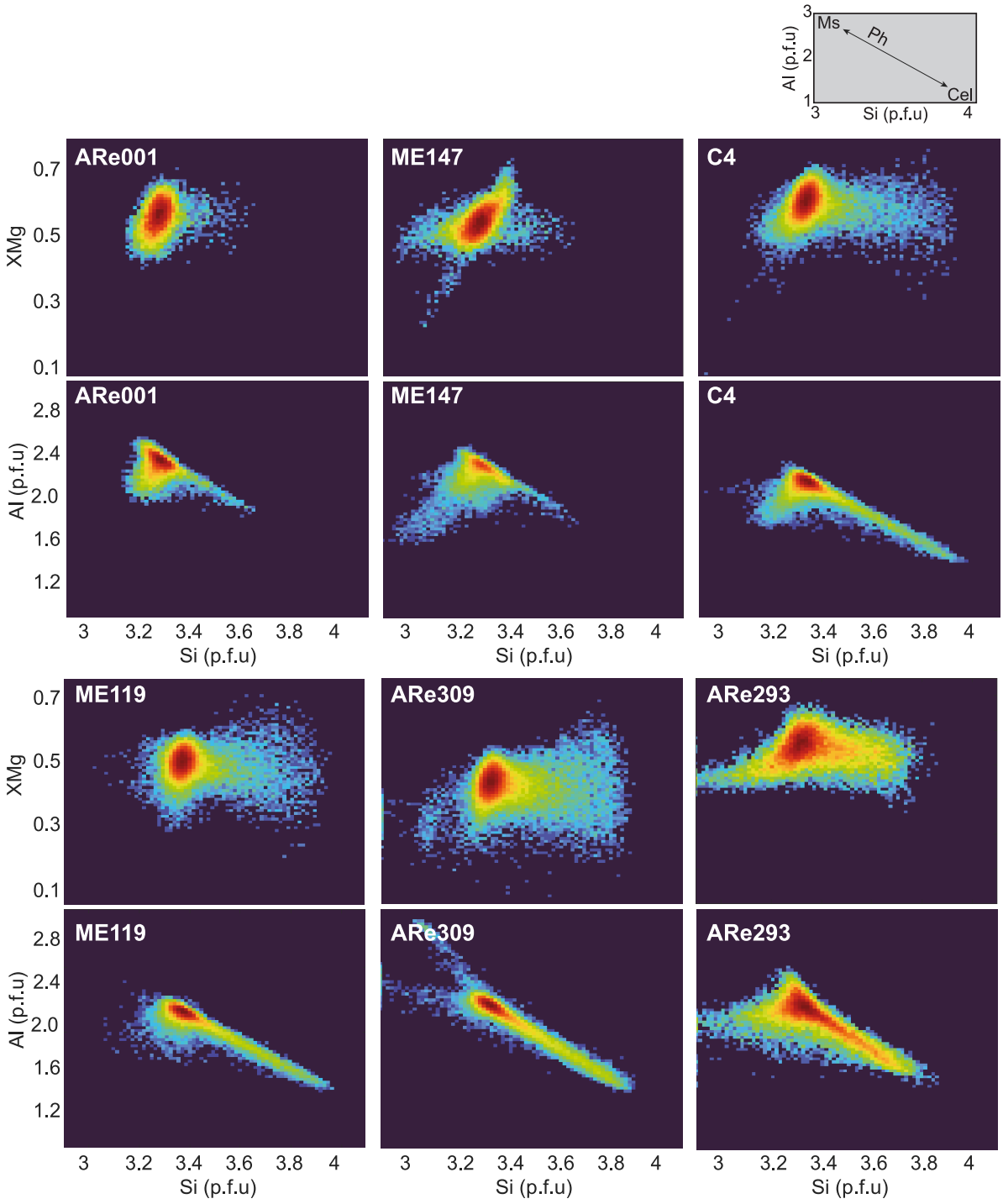

Figure 5.6. White micas composition plots. X_{Mg} (top) and Al (pfu) (bottom) as a function of Si (pfu). The phengite series is a solid solution ranging from celadonite (Al-rich) to muscovite pole (Si-rich).

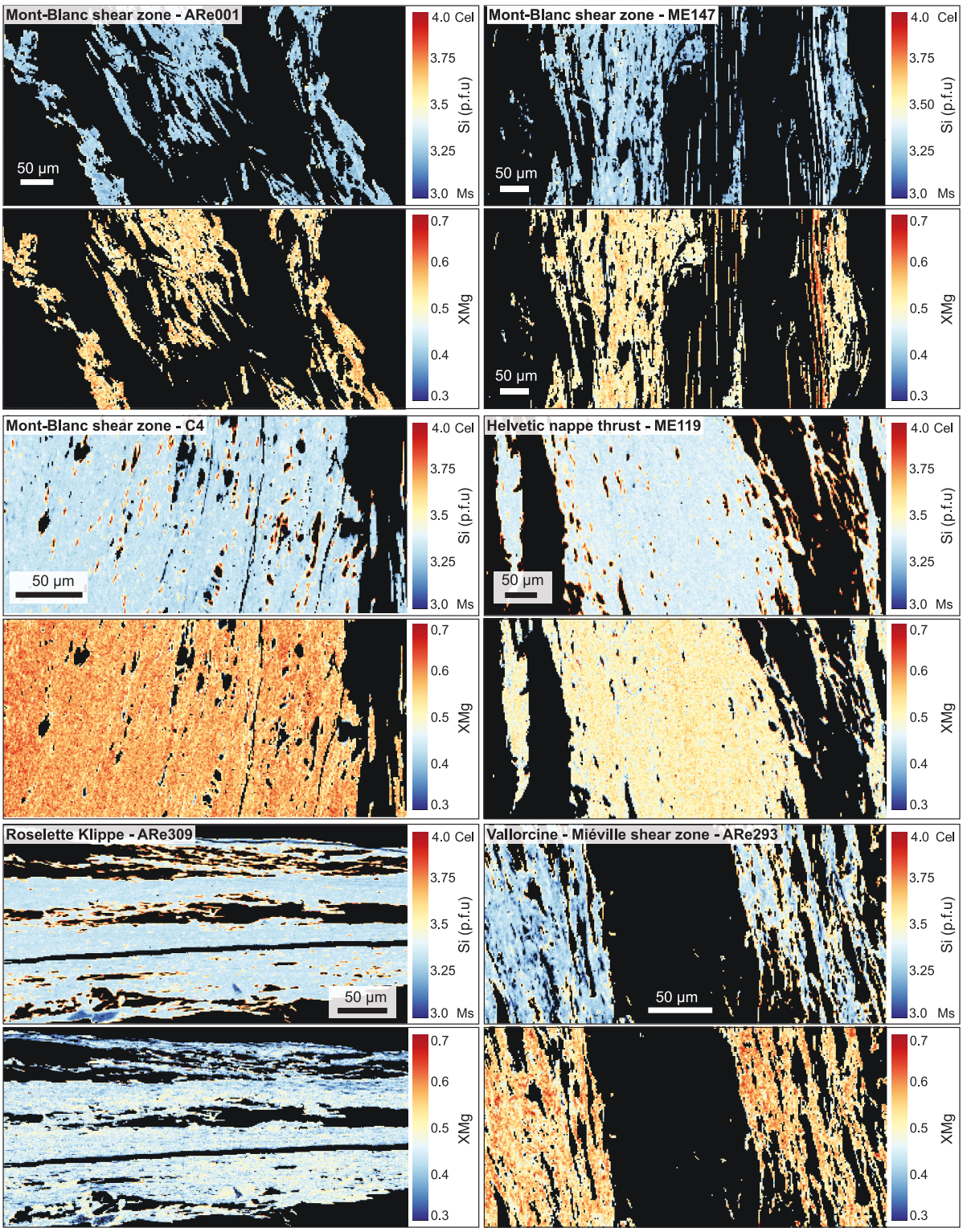

Figure 5.7. Chemical maps of the Si (pfu) (top) and XMg ($XMg = \frac{Mg}{Fe+Mg}$) (bottom) content of the studied mylonites.

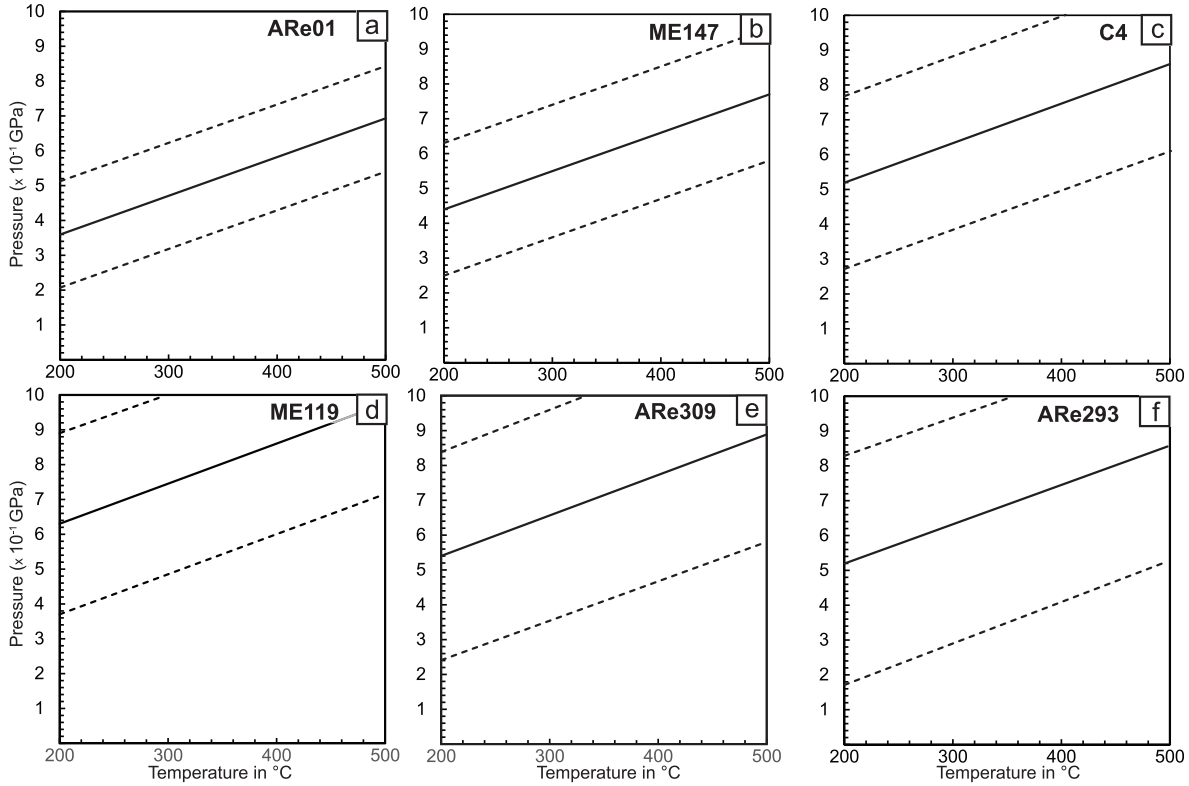

Figure 5.8. Pressure temperature isopleths computed for phengite from Si contents (Massonne and Schreyer, 1987).

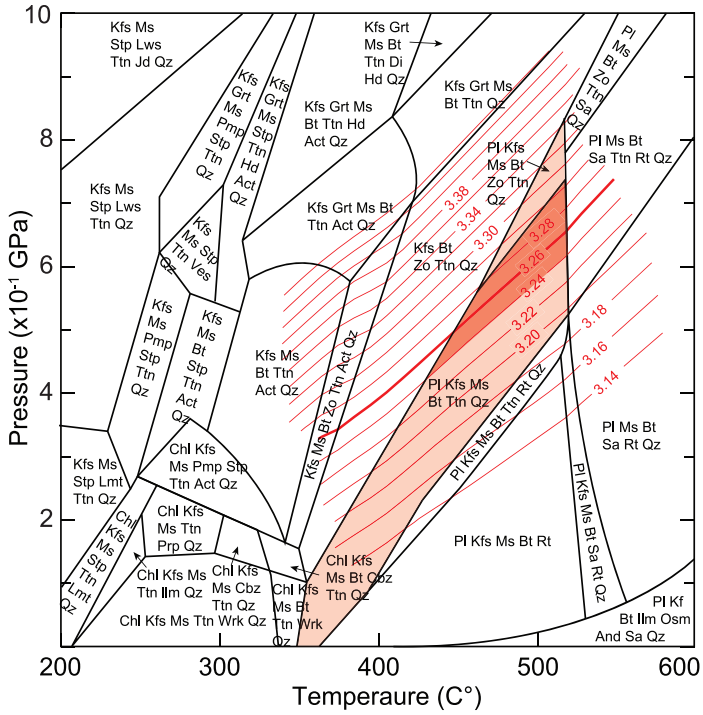

Figure 5.9. Phase diagram equilibria performed on sample ARe001 using the bulk composition from the EPMA chemical mapping. The pseudosection has been computed using the PerpleX software package (Connolly, 1990; Connolly and Petrini, 2002).

Table 5.3. Representative mineral composition for analyzed samples from EPMA chemincal mapping. Mineral abbreviations are from Whitney and Evans, 2009. $XMg = \frac{Mg}{Fe+Mg}$

Sample	ARe01-1			ME147			C4			ME119	ARe309	ARe293	
Mineral	Bt Rim	Bt Core	Ms	Bt Rim	Bt Core	Ms	Bt Rim	Bt Core	Ms	Ms	Ms	Chl	Ms
SiO_2	37.35	37.78	47.47	36.21	36.60	48.45	38.37	37.76	49.61	50.43	48.91	26.83	48.65
TiO_2	0.77	1.91	0.17	1.25	3.85	0.75	0.95	1.22	0.05	0.54	0.19	0.11	0.87
Al_2O_3	17.11	16.86	27.95	16.47	16.14	28.07	16.14	15.90	26.87	27.18	27.37	20.93	27.09
FeO	20.95	20.11	4.57	19.84	20.17	4.30	19.41	19.74	3.97	4.36	4.81	26.52	5.52
MnO	0.36	0.39	0.06	0.39	0.39	0.05	0.74	0.72	0.05	0.17	0.06	0.39	0.05
MgO	9.26	8.92	2.77	10.09	8.85	2.51	10.55	10.43	3.04	2.54	2.17	12.23	3.48
CaO	0.03	1.27	0.05	0.70	2.13	0.54	0.01	0.00	0.08	0.04	0.00	0.00	0.00
Na_2O	0.06	0.01	0.24	0.07	0.05	0.19	0.07	0.02	0.32	0.14	0.31	0.19	0.35
K_2O	9.50	9.34	10.93	9.41	9.17	10.63	9.32	9.43	11.73	10.51	10.64	0.13	9.31
Cr_2O_3	0.02	0.20	0.08	0.01	0.01	0.03	0.00	0.00	0.00	0.00	0.00	0.03	0.01
Total	95.42	96.79	94.31	94.44	97.37	95.52	95.56	95.22	95.74	95.90	94.46	87.37	95.33
Si	2.855	2.842	3.263	2.800	2.756	3.277	2.905	2.881	3.356	3.378	3.344	2.846	3.288
Ti	0.044	0.107	0.009	0.073	0.216	0.038	0.054	0.070	0.003	0.027	0.010	0.009	0.044
Al	1.542	1.495	2.264	1.501	1.434	2.238	1.440	1.430	2.143	2.146	2.206	2.619	2.159
Fe	1.339	1.266	0.264	1.283	1.272	0.244	1.229	1.259	0.225	0.244	0.275	2.357	0.316
Mn	0.024	0.025	0.004	0.025	0.025	0.003	0.047	0.047	0.003	0.010	0.004	0.035	0.003
Mg	1.055	1.001	0.285	1.163	0.995	0.253	1.191	1.186	0.307	0.254	0.221	1.938	0.354
Ca	0.002	0.101	0.004	0.059	0.167	0.039	0.001	0.000	0.006	0.003	0.000	0.000	0.000
Na	0.009	0.002	0.032	0.010	0.008	0.025	0.010	0.003	0.041	0.017	0.041	0.037	0.044
K	0.926	0.896	0.959	0.928	0.882	0.917	0.900	0.918	1.014	0.899	0.928	0.018	0.803
Cr	0.001	0.012	0.005	0.001	0.001	0.001	7.776	7.794	0.000	0.000	0.000	0.002	0.001
Oxygens	11	11	11	11	11	11	11	11	11	11	11	14	11
Sum	7.797	7.747	7.089	7.845	7.755	7.036	0.492	0.485	7.097	6.979	7.028	9.862	7.011
XMg	0.441	0.442	0.527	0.476	0.438	0.510	0.001	0.000	0.579	0.511	0.446	0.451	0.540

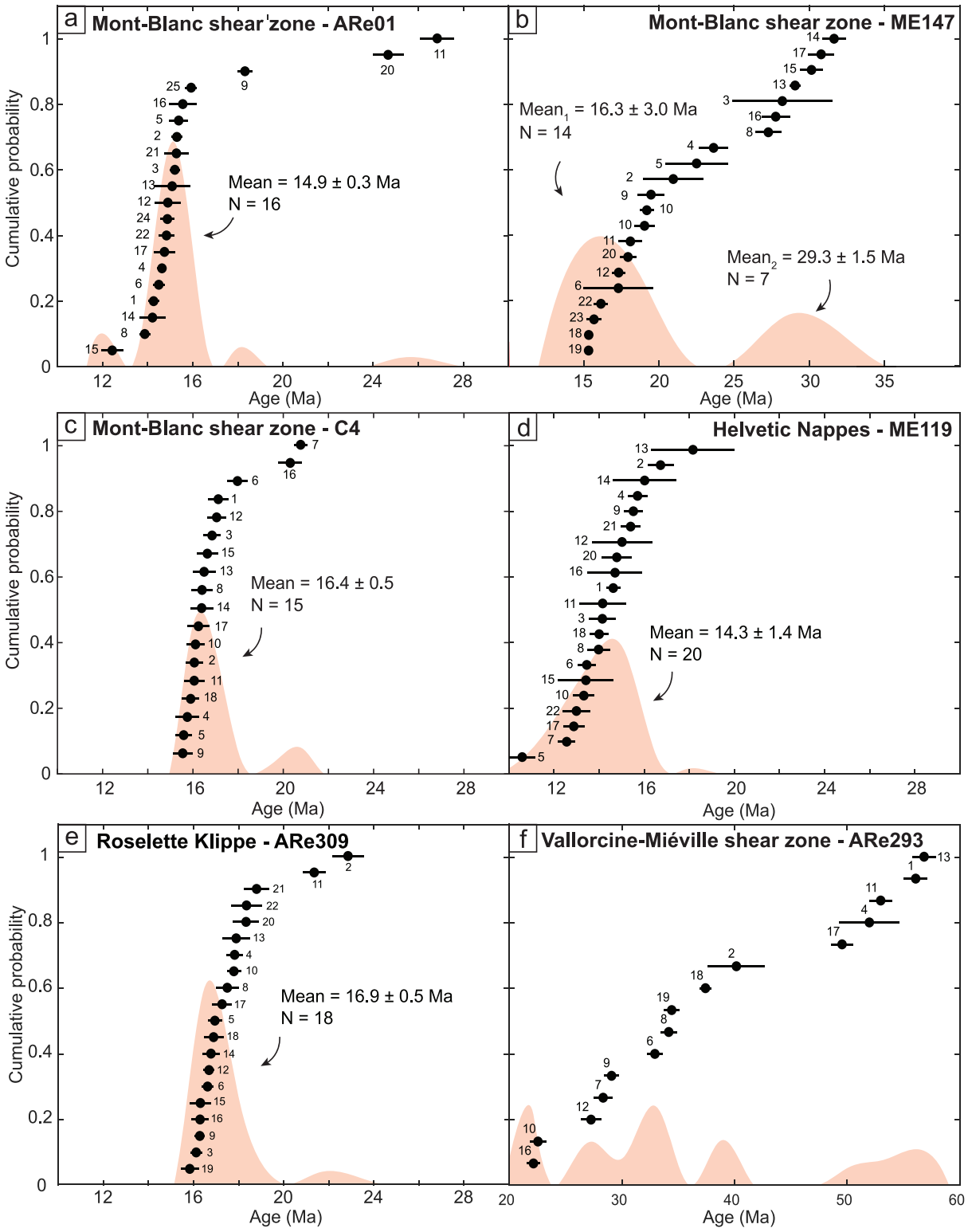

Figure 5.10. Cumulative probability plot of *in-situ* $^{40}Ar/^{39}Ar$ ages. The red-filled curve is the age distribution weighted with uncertainties and fitted by a spline function.

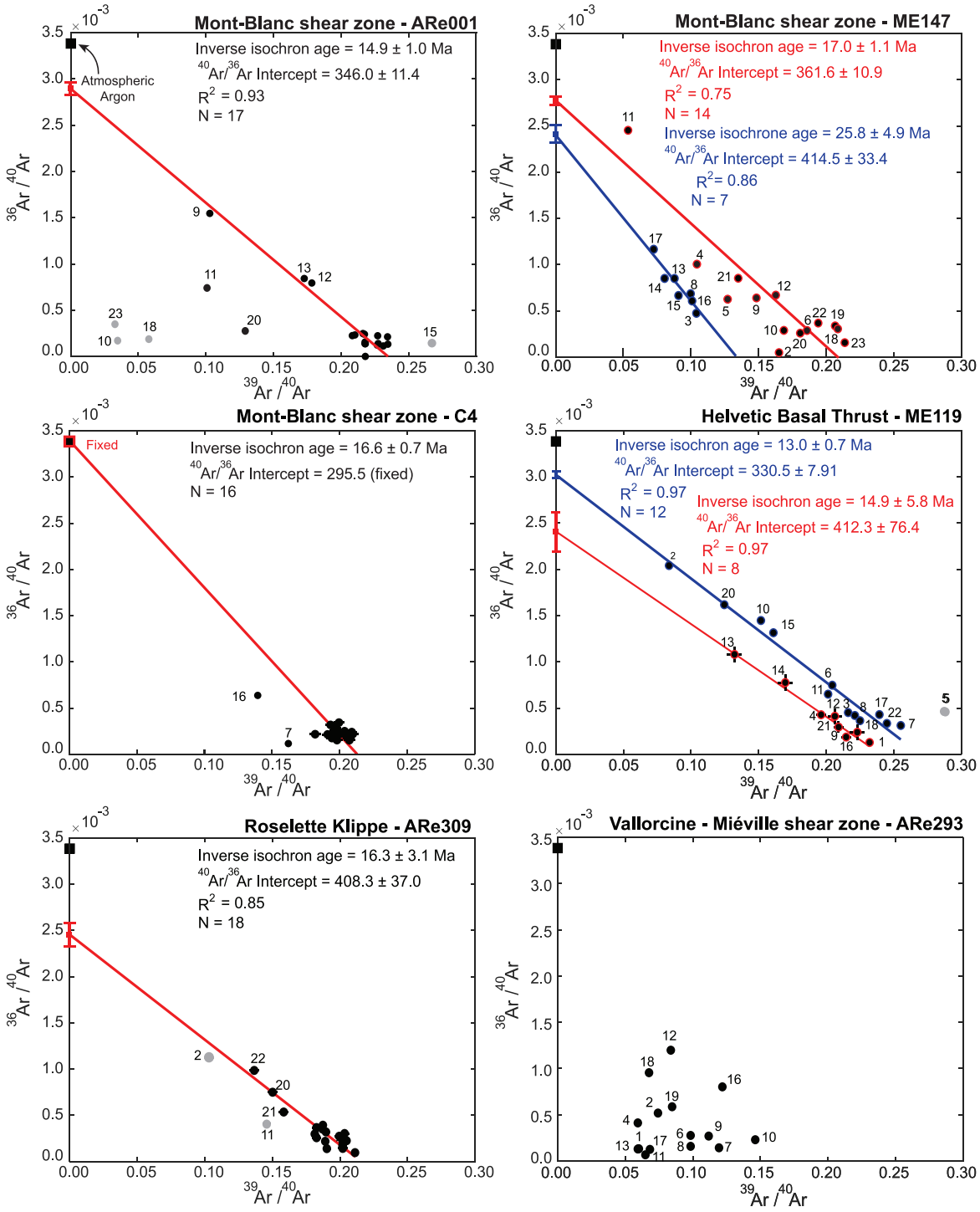

Figure 5.11. Inverse isochron plots of in situ $^{40}Ar/^{39}Ar$ ages.

5.4.2 The Helvetic Nappe system

Two samples have been collected from different parts of the Helvetic Nappes. The most basal thrust of the nappe system (HBT of Leloup et al. (2005) and Mercier et al. (2023)) has been sampled on the eastern side of the Mont-Blanc, in the Petit Col Ferret location, at the

border between Switzerland and Italy (Fig. 5.1). Another sample was collected at the base of the Roselette klippe on the southwest side of the Mont-Blanc massif (Fig. 5.1).

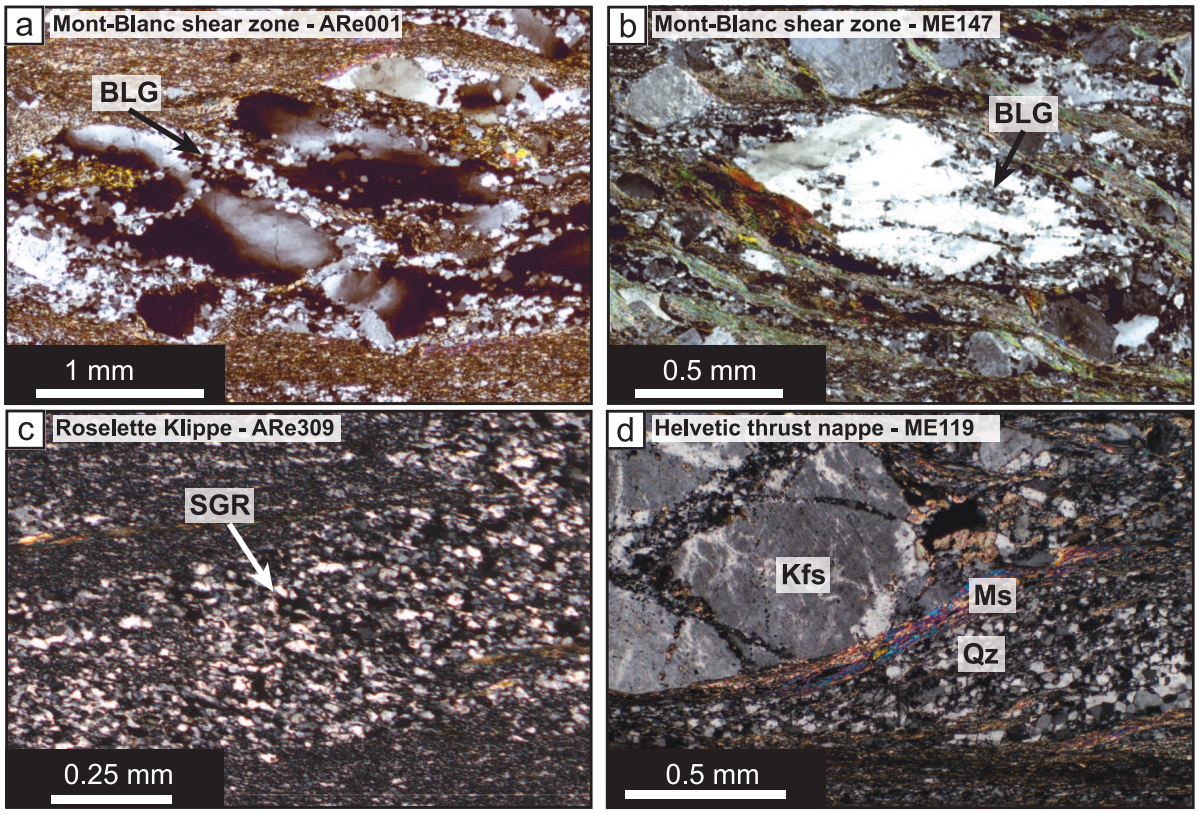

Figure 5.12. Quartz recrystallization microstructures from studied mylonites. a) Sample ARe001 shows the typical fabric of recrystallization with relicts of large quartz grain with undulose extinction and new grains formed by bulging; b) Sample ME147, relicts of large quartz grain with undulose extinction and new grains formed by bulging; c) Sample ARe309 shows crystallized quartz formed by subgrain rotation (SGR), grains have a preferred orientation that defines a continuous foliation; d) Sample ME119 shows a brittle deformation of K-feldspar and a ductile recrystallization of quartz, suggesting a temperature comprising between 300 to 350 °C.

5.4.2.1 The Roselette klippe

The Roselette klippe (approximately 3.5 km long and 200 m high) is located on the south-western tip of the Mont-Blanc massif (Fig. 5.1). This klippe consists of basement rocks thrusted above Cretaceous and Upper Jurassic limestones (Fig. 5.13a). Mesozoic sediments are locally strongly deformed with asymmetric recumbent folds that attest to top-to-WNW shear (Fig. 5.13c). The most basal part of the Helvetic Nappes is punctuated by slices of mylonitized basement (e.g., Mongiroud, North East Mont-Blanc, Switzerland) Eltchaninoff-Lancelot et al. (1980) attributed the Roselette klippe as one of the largest of them, suggesting a proximal provenance of the basement. However, the klippe does not appear to have been deformed at low temperatures far from contact, only the most basal part is mylonitized (Fig. 5.13b), and the origin of this basement klippe remains unclear.

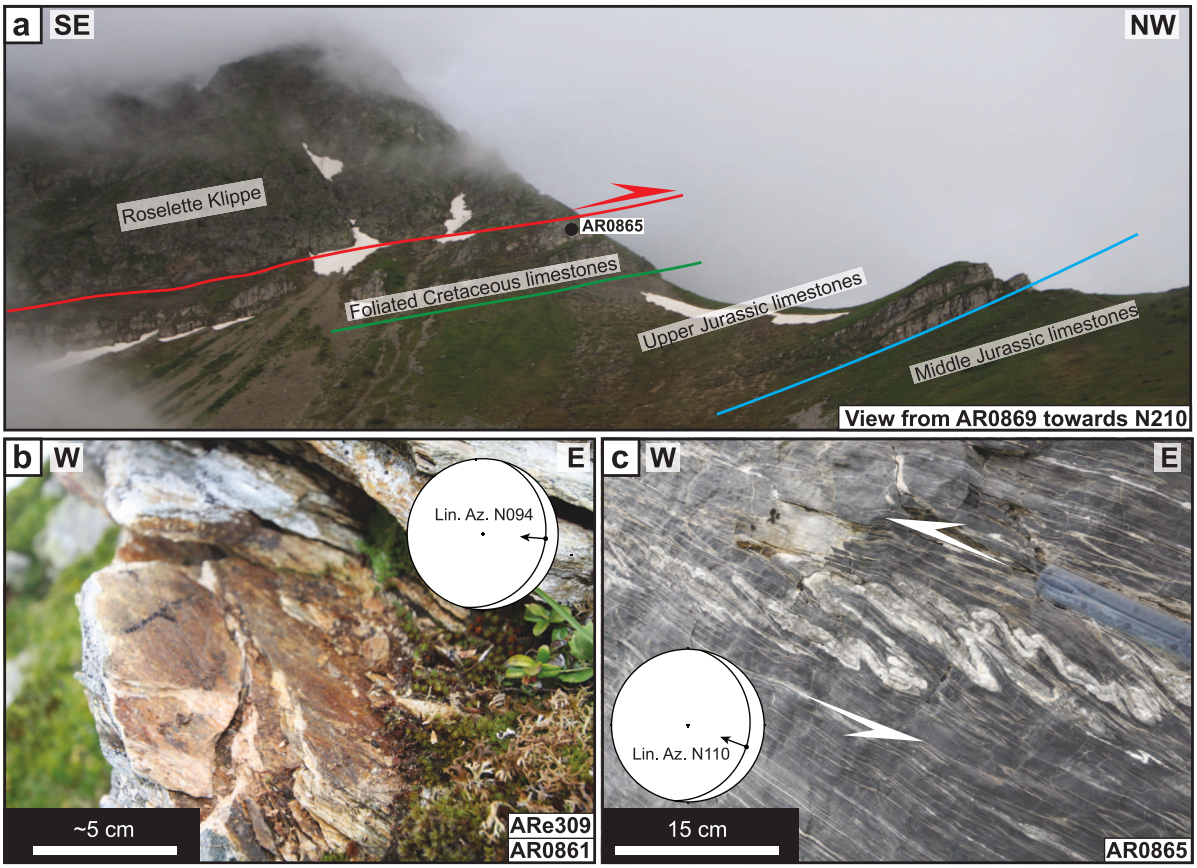

Figure 5.13. Field observations at the Roselette klippe. a. Panorama of the Roselette klippe viewed from the north, the basement overthrust and overturn the Mesozoic sedimentary cover. b. Ultrmylonitized bottom of the klippe, sample ARe309; c. Foliated and folded Cretaceous limestones below the thrust.

The ARe309 sample has been collected on the western side of the klippe, a few meters above the basal contact, where the deformation appeared to be the most intense. On the macroscopic scale, the sample consists of a fine-grained leucocratic ultramylonite with a well-marked foliation oriented N13° ; 18° SE bearing a hill-defined mineral lineation striking N140°. On the microscopic scale, the mylonite foliation shows a very fine-grained quartz matrix ($\approx$ 1 µm) interspersed between wide mica beds (Fig. 5.4). The microstructure of the quartz fabric shows crystallized quartz formed by subgrain rotation (SGR), suggesting a deformation temperature of about 400 to 500 °C. Two sites in two quartz ribbons have been analyzed with EBSD: Site 2 shows an [c]-axis maxima compatible with the activation of the basal plane along the a1 direction during a top-to-the-NW shear (Fig. 5.16). At site 2, the orientation of the [c]-axis is more complex to interpret, but the main maxima remain compatible with the one at site 2, thus suggesting a top to the NW shear (Fig. 5.16). The chemical composition of white mica is comparable to that of sample C4 with a main population with Si = 3.36 pfu Al = 2.14 pfu and XMg = 0.58 (Fig. 5.6). The corresponding P-T estimate is very close to that of C4 (Fig. 5.8).

After the exclusion of two $^{40}Ar/^{39}Ar$ data, the apparent ages range between 15.9 ± 0.4

Ma and 22.9 ± 0.7 Ma (Table C.6), The cumulative probability plot reveals a large population with 18 spots giving an average of 16.9 ± 0.5 Ma and two older ages around 23 Ma (Fig. 5.10). In the ARe309 sample, the retained age is the inverse isochrone age of 16.3 ± 3.1 Ma, which corresponds to an initial $^{40}Ar/^{36}Ar$ ration of 408.3 ± 37.0 slightly higher than for ARe001 and ME147.

5.4.2.2 The Petit Col Ferret

From west to east: the crystalline basement of the Mont-Blanc massif is affected by an east-dipping foliation oriented N045; 75 E and bearing a mineral lineation oriented N$120°$ (Fig. 5.14a and b). The overlying limestones are foliated, marmorized, and microfolded (Fig. 5.14 c). The foliation is oriented N10-30 ; 80-85 E bearing a stretching lineation oriented about N$140°$. The asymmetric boudinage of the calcite veins indicates a top-to-west sense of shear (Fig. 5.14c). To date the deformation associated with this thrusting system, we sampled a mylonitized basement sample (Fig. 5.14).

Sample ME119 is a fine-grained mylonitic rock with an asymmetric quartz boudinage that indicates a top to northwest sense of shear (Fig. 5.4d). The sample shows a well-visible foliation on the microscopic scale trending N$45°$;$75°$E bearing a mineral lineation striking N$120°$, highlighted by white micas and quartz layers. Some porphyroclasts ($> \ 0.5$ mm) of brittle feldspar are wrapped in the foliation, with asymmetric tails (Fig. 5.4). Quartz recrystallization under an optical microscope suggests a bulging type of recrystallization. The recrystallization microstructure suggests a brittle deformation of K-feldspar coeval with a ductile deformation of quartz, suggesting a temperature range that spanned between 300 and 350$°$C (e.g., Gapais, 1989). Lattice-preferred orientation analysis has been performed at three different sites of the same thin section (Fig. 5.16). At sites 3 and 2, the interpretation is similar to the one for C4 and ARe309 with a more simple shear expression of the deformation. The quartz LPO are typical of the activation of the basal plane in the $< a >$ direction during a simple shear deformation top to northwest (Fig. 5.16a). However, at site 1 the LPO of the quartz crystals is compatible with the activation of the prismatic plane in the [c] direction during a simple shear deformation top to northwest (Fig. 5.16a). Both prismatic-[c] of site 1 and basal-$< a >$ slip of sites 2 and 3 and compatible in the same deformation field with a similar direction of motion towards N$98°$ to N$120°$, appear to correspond to very different temperature conditions. Indeed, such an LPO of quartz is very unusual (even never observed?) in the external Alps. Prismatic-[c] is typical of high temperature deformation (above 550 $°$C) (Pennacchioni et al., 2010; Mancktelow and Pennacchioni, 2004), while the basal ($< a >$ sliding is typical of low temperature below 300 $°$C (Takeshita, 1996; Stipp et al., 2002) (Fig. 5.2). The deformation may have started at high temperature, with prismatic-[c], and continued with basal-a and prismatic-[c] during progressive

cooling.

The chemical composition of the white micas is comparable to that of ARe309 (Fig. 5.7), with composition in Si vs. Al close to the muscovite pole and an XMg ratio of about 0.5. The Si content on the map shows a slight enrichment in the Si content along the sides of muscovite grains.

Concerning $^{40}Ar/^{39}Ar$ dating, only two of the 23 data are excluded (Table C.5) and the remaining ages range from 10.6 ± 0.6 Ma and 18.7 ± 1.8 Ma (Fig. 5.10), corresponding to a single age population of 14.3 ± 1.4 Ma (Fig. 5.10), in good agreement with the well-constrained inverse isochron that yields an age of 13.7 ± 0.7 Ma ($R^2 = 0.87$; $^{40}Ar/^{36}Ar = 323.4 \pm 7.4$) (Fig. 5.11). We consider that the age of the main white mica population is 13.7 ± 0.7 Ma with an initial $^{40}Ar/^{36}Ar$ ratio of 331.3 ± 7.6 similar to ARe001 and ME147.

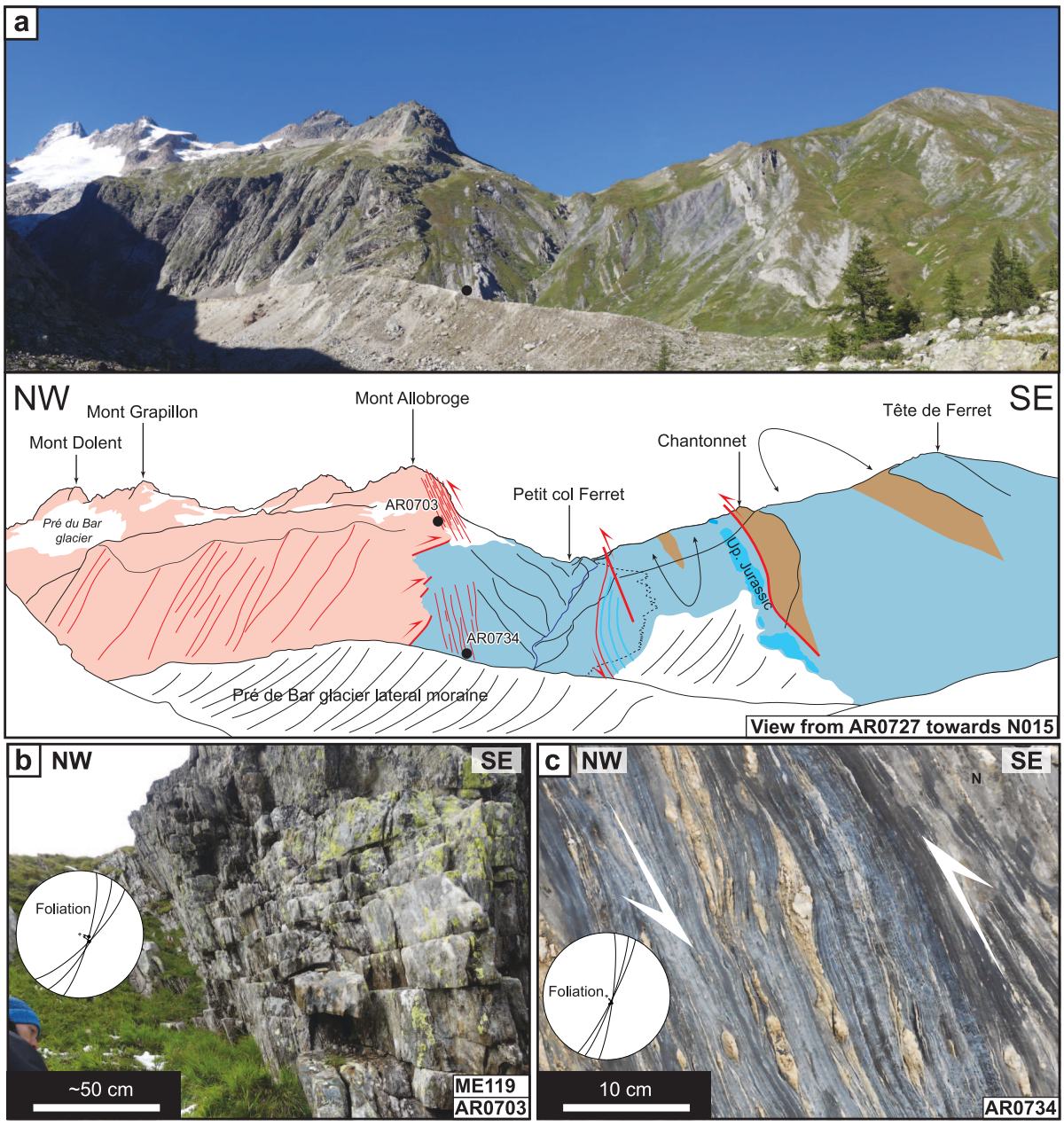

Figure 5.14. Cross section of the Italian side of the Petit Col Ferret. **a)** Panorama of the Col from the south: the deformation of the Helvetic Basal thrust affects the Mont-Blanc basement. The granites are mylonitized; **b)** Mylonitization of the basement: sample ME119 that has been used for dating the deformation; **c)** Foliated limestones above the basal thrust: intense marmorization and calcite vein boudinage.

5.4.3 Vallorcine-Miéville shear zone

At the macroscopic scale, the ARe293 sample consists of fine-grained mylonite (Fig. 5.15) with shear planes striking N3° ; 76° E with a lineation pitch of 86° N (az. N62°) (Fig. 5.15). S/C relationship indicates a normal sense of shear (east down). On a microscopic scale, the sample consists of fine-grained mica-supported mylonite with quartz porphyroclasts. Chemically, white micas are along the phengite-muscovite series in the Si vs Al plot with quite a large dispersion (Fig. 5.6). The composition map (Fig. 5.7) shows heterogeneity in the content of XMg. The ARe293 sample from the Vallorcine-Miéville shear zone also has chlorites crystallized as patches within the matrix.

After the exclusion of four $^{40}Ar/^{39}Ar$ data, the 15 remaining apparent ages range from 22.2 ± 0.6 to 40.2 ± 2.5 Ma. The large distribution of the data does not allow us to fit a significant normal distribution in the cumulative probability plot. The inverse isochron plot does not show any significant arrays.

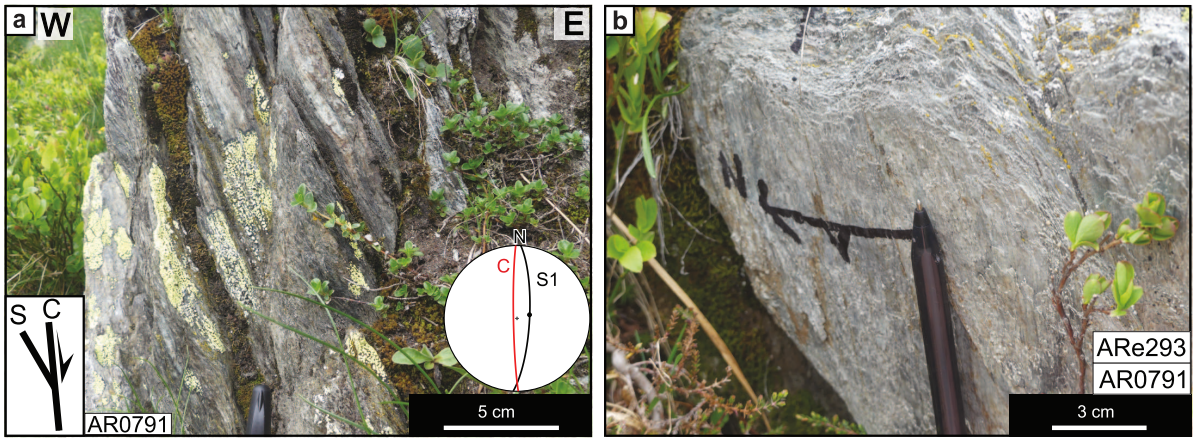

Figure 5.15. Field observations in the Vallorcine-Miéville shear zone. Foliation within the Vallorcine-Miéville shear zone at station AR0791, striking N3°;76°E bearing a lineation with a pitch of 86°N (azimuth N62°).

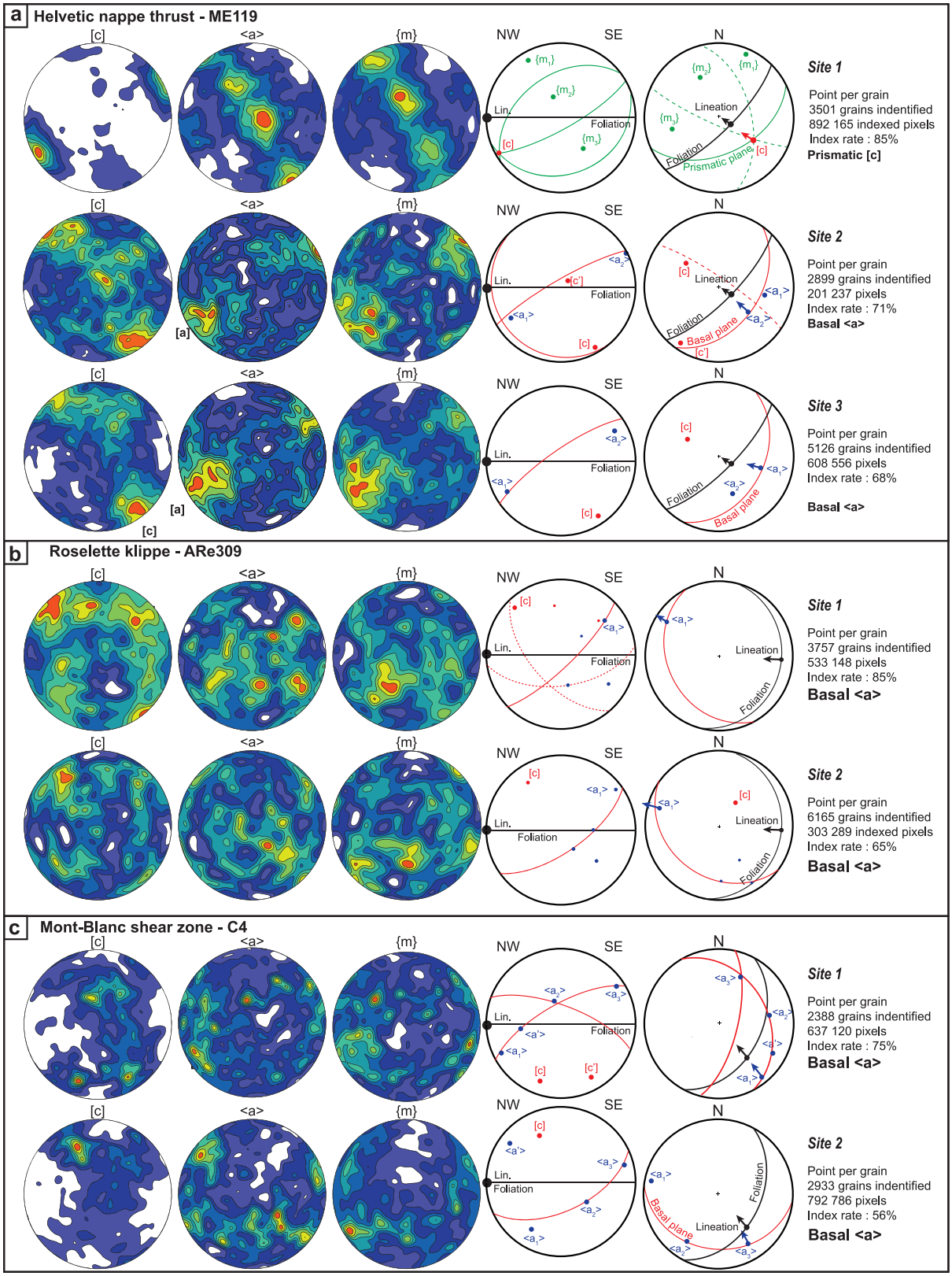

(Figure caption on next page)

Figure 5.16. Lattice preferred orientation of quartz ribbons with the dated mylonitic rocks. The stereographic plot reports the orientation density function of the crystallographic $[c]$ axis (left) and $< a >$ axis (center left) as well as the poles of prismatic planes $\{m\}$ (center right) of the mean orientation (equal area, lower hemisphere) of the grains in the reference frame. thin section. In the thin section reference frame, the foliation is vertically oriented E-W, and the lineation is horizontally oriented westward. The right stereo plots report the orientation of the measured maximums of the crystallographic axis, rotated back in the geographic reference frame, along with the foliation and the lineation measured in the field.

Table 5.4. Summary of ages and thermo-barometric estimated conditions. Mineral abbreviations according to Whitney and Evans (2009). In bold are the retained ages for interpretation.

Sample	Paragenesis	Apparent ages Ma $\pm 2\sigma$		Inverse isochron ages Ma $\pm 2\sigma$		Temperature estimate[1] °C	Pressure estimate[2] GPa
ARe001	Ms + Bt + Kfs + Ab + Qz + (Cal +Ttn)	14.9 ± 0.3	-	**14.9 ± 1.0**	24.6 ± 11.8	300 - 500	0.47 - 0.58 ± 0.15
ME147	Kfs + Ab + Ms + Bt + Qz	16.3 ± 3.0	29.3 ± 1.5	**17.3 ± 1.1**	25.8 ± 4.8	300 - 400	0.55 - 0.66 ± 0.19
C4	Ms + Bt + Qz + Ab + Kfs + (Cal + Ttn)	**16.4 ± 0.5**	-	Uninterpretable	21.3 ± 8.5	300 - 400	0.63- 0.74 ± 0.25
ME119	Ms + Kfs + Qz + Ab	14.3 ± 1.4	-	**13.7 ± 0.7**	-	> 550 and 300 - 400	0.74- 0.86 ± 0.26
ARe309	Ab + Ms + Qz	16.9 ± 0.5	-	**16.3 ± 3.1**	-	400 - 500	0.66 - 0.78 ± 0.26
ARe293	Ms + Ab + Chl + Qz	Uninterpretable		Uninterpretable		-	-

[1]Temperature of deformation estimated on quartz recrystallisation structures and LPO.

[2]Pressure estimation based on Si content in phengite (Massonne and Schreyer, 1987) in the temperature range.

5.5 Significance of the age data

Geochronological data give the time elapsed since the closure of the system: that is, the time since neither the father nor the daughter elements could move out from the considered mineral. Two major concepts have been proposed to explain the mobility of the radioactive and radiogenic isotopes, and thus the closure of the system. The first one is intracrystalline diffusion, which depends mainly on temperature and diffusion factors such as the activation energy, the pre-exponential factor, the diffusion radius (approximating grain size), and on the cooling rate (Dodson, 1973). In that case, the mineral-geochronologic method pair is considered to be a thermochronometer, i.e. the date reflects the timing at which the mineral cooled down to its closure temperature. The second is re-crystallization by dissolution and re-precipitation, e.g. (Putnis, 2009) in which case the mineral-geochronologic method pair is considered to be a hygrochronometer that dates the mineral re-crystallization (Villa, 2016).

The closure temperature of several geochronological method - mineral pairs has been calculated from empirical, experimental, and theoretical considerations giving rise to thermochronology that allows reconstructing the cooling path of rocks (e.g., Hurford, 1991; Reiners et al., 2005). Several studies have evaluated ^{40}Ar diffusion in muscovite to infer closure temperature under different conditions and cooling rates (Fig. 5.18). Pioneer studies (Hames and Bowring, 1994; Kirschner et al., 1996) have estimated that the closure temperature of ^{40}Ar in muscovite is about $350 \pm 50\ ^{\circ}\mathrm{C}$. Using experimental techniques, Harrison et al. (2009) measured the diffusion of ^{40}Ar in muscovite corresponding to a closure temperature of 405 $^{\circ}\mathrm{C}$ for a grain size of 100 $\mu\mathrm{m}$ radius and a cooling rate of 10 $^{\circ}\mathrm{C\,Ma^{-1}}$ at 0.5 GPa. Using the precise mapping of ages in undeformed white micas of a slowly cooling pluton (Nteme et al., 2023) evaluated ^{40}Ar diffusion parameters in muscovite corresponding to the closure temperature in the same range as in previous studies (Fig. 5.18). However, the diffusion parameters calculated for ideal muscovites correspond to much higher closure temperatures: 610 - 640 $^{\circ}\mathrm{C}$ for cooling rates ranging from 10 to 30 $^{\circ}\mathrm{C\,km^{-1}}$, grain sizes of 100 $\mu\mathrm{m}$, and null pressure (Nteme et al., 2022). Nteme et al. (2023) concluded that effective diffusion in natural white micas follows preferential paths even in undeformed minerals.

If a mineral crystallizes below its nominal closure temperature, its geochronological age should correspond to that of crystallization. However, this is not true if the system is later reopened by heating above the closure temperature, but also by another mechanism such as deformation or fluid dissolution. In several examples of highly deformed rocks, white micas have been suggested to crystallize below their nominal closure temperature for the K/Ar system, and their age was interpreted to reflect their crystallization in the S / C fabric, affecting the timing of deformation (e.g., Di Vincenzo et al., 2016; Laurent et al., 2021; Beaudoin et al., 2020; Rolland et al., 2008).

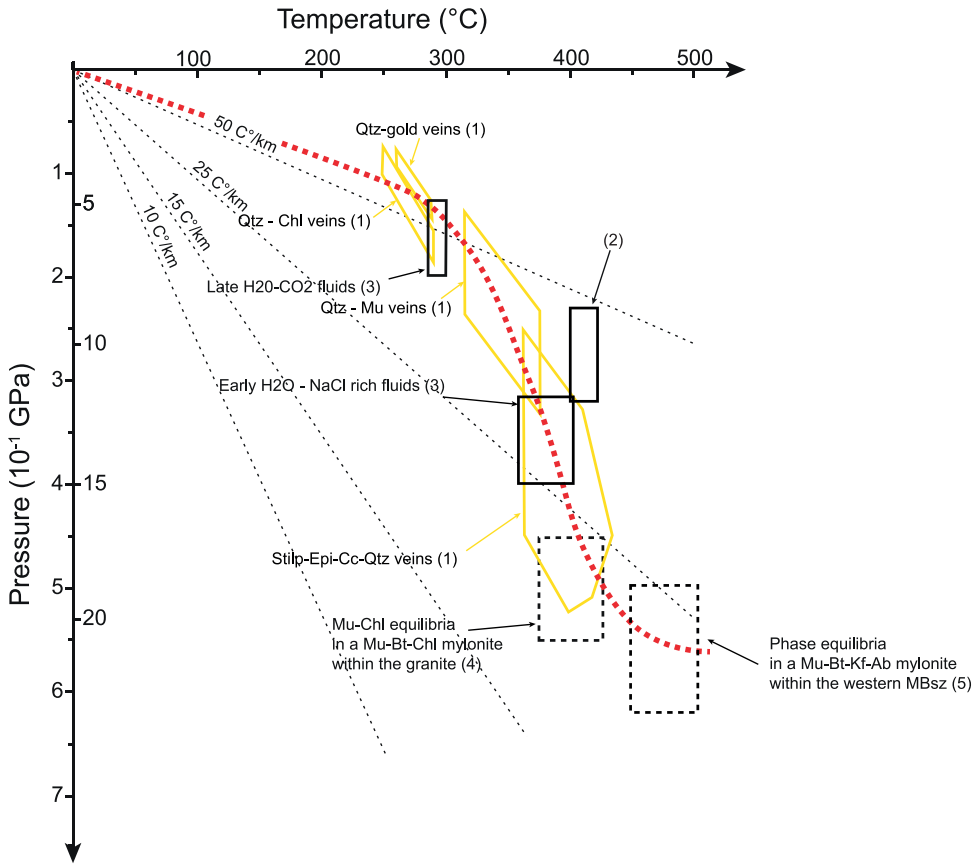

Figure 5.17. Pressure / temperature plot with the compilation of the published thermobarometric estimations for the Mont-Blanc massif. [1]: Marshall et al. (1998b); [2]: Poty et al. (1974); [3]:Poty et al. (1974): [4]: Rolland et al. (2003); [5]: This study

In the case of Mont-Blanc, few estimates of the P-T conditions reached within the basement during the alpine phase of deformation are available (Fig. 5.17). From the multi-equilibrium of muscovite + biotite + chlorite + epidote Rolland et al. (2003) calculated conditions of 0.50 ± 0.05 GPa and 400 ± 25 °C in a shear zone close to the eastern border of the range. Taking into account a crustal density of 2750 $\mathrm{kg\,m^{-3}}$, this pressure corresponds to a depth of 18.5 ± 1.8 km and a geothermal gradient of about 20 $\mathrm{°C\,km^{-1}}$. From the PerpleX calculation on the composition of white mica, we estimate conditions of about 500 °C and 0.47 to 0.66 GPa for the ARe001 sample, at the base of the Mont-Blanc shear zone (Fig. 5.9). This corresponds to a depth of 17 to 24 km and a geothermal gradient of 20 to 29 $\mathrm{°C\,km^{-1}}$. This difference in alpine exhumation is compatible with the fact that the Mont-Blanc is tilted towards the east (Mercier et al., 2023).

According to thermochronological studies of the area (Glotzbach et al., 2008; Glotzbach et al., 2011), the overall exhumation rate of the massif is on the order of 1 $\mathrm{km\,Ma^{-1}}$ since 22 Ma. Consequently, the cooling rate of the Mont-Blanc massif during the development of the shear zone is about 20 $\mathrm{°C\,Ma^{-1}}$.

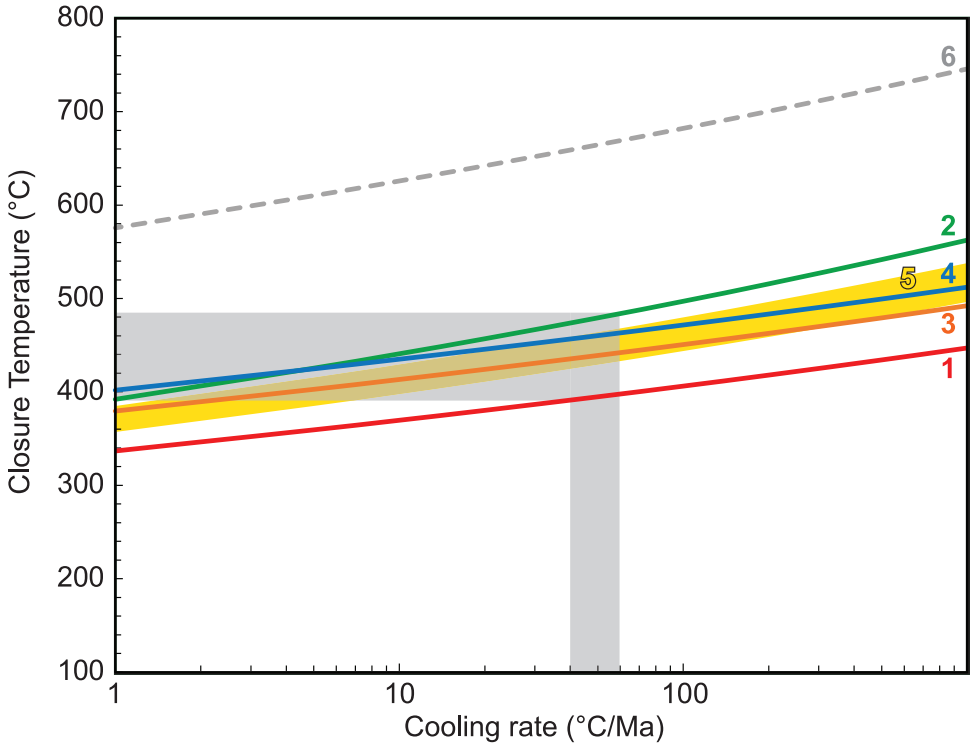

Figure 5.18. Recalculated variations of the closure temperature with cooling rate according to estimated Arrhenius parameters by: 1:Hames and Bowring (1994); 2: Lister and Baldwin (1996); 3: Kirschner et al. (1996); 4: Harrison et al. (2009); 5: Nteme et al. (2023) (including empirical defect-enhanced diffusion); 6: Nteme et al. (2022) (using perfect numerical muscovites). The recalculations are computed for a 150 µm cylindrical geometry diffusion model.

In our case, the grain sizes are about 100 µm in size, the estimated pressure is 0.50 ± 0.05 GPa, and the cooling rate is on the order of 20 $^{\circ}\mathrm{C\,Ma^{-1}}$. Estimates of Nteme et al. (2022) inferred the closure temperature of perfect numerical muscovites and obtained the closure temperature above 580 $^{\circ}\mathrm{C}$. In nature, muscovites have defaults that enhance diffusion and lower their effective closure temperature (Nteme et al., 2023). Using empirical diffusion domain defect-enhanced diffusion modeling of $40Ar$, Nteme et al. (2023) estimated a lower closure temperature in the range of results from other studies (Fig. 5.18). Therefore, we use 430 ± 30 $^{\circ}\mathrm{C}$, for the closure temperature of muscovite.

Mylonites from the Mont-Blanc shear zone (samples ARe001, ME147, and C4) show S/C relationships and asymmetric boudinage, with synkinematic recrystallized white mica, indicating a top-to-northwest sense of shear. $^{40}Ar/^{39}Ar$ *in situ* Inverse isochron ages range between 14.9 ± 1.0 and 17.0 ± 1.1 Ma in the three samples (Table 5.4, Fig. 5.11). In sample ME147 an older age component is present at 25.8 ± 4.9 Ma (Table 5.4, Fig. 5.11), while two older ages between 24 and 23 Ma are also present in sample ARe001. In all samples, the quartz microstructures suggest that bulging and subgrain rotation recrystallization occurred during deformation, implying a deformation temperature below 400 $^{\circ}\mathrm{C}$ (Fig. 5.12) (Stipp et al., 2002).

The quartz lattice preferred orientation analysis indicates a basal-$< a >$ type of slip during deformation for sample C4 (Fig. 5.16), which is estimated to occur below about 500 $^{\circ}$C (e.g., Pennacchioni et al., 2010; Takeshita, 1996). The temperature of deformation is lower than the nominal closure temperature of the white micas of 430 ± 30 $^{\circ}$C (see discussion above) and we consider that the younger age component dates deformation in the MBsz to have been active between 18 and 14 Ma. The presence of an inherited age component in ME147 suggests that deformation may have started earlier between 30 and 20 Ma.

Within the central part of the Mont-Blanc massif, Glotzbach et al. (2011) obtained thermochronological ages using fission tracks on zircon (ZFT) ranging from 11.2 ± 0.6 to 15.3 ± 0.3 Ma, depending on the elevation of the samples. Using a compilation of available thermochronological data from the Mont-Blanc and the Aiguilles Rouges massifs, in Pecube simulations, Mercier et al. (in preparation, see Chap. 6) propose the most probable exhumation histories for the Mont-Blanc range (see Fig. 6.19b, p. 289). The corresponding cooling histories can be retrieved for each sample. The dated samples of MBsz (ARe001, ME147, and C4) appear to be at temperatures below 400 $^{\circ}$C at the time corresponding to their $^{40}Ar/^{39}Ar$ ages (see Fig. 6.19c, p. 289). This independently confirms that the ages obtained are not cooling ages.

Sample ME119 from the base of the Helvetic thrusts on the eastern side of the Mont-Blanc massif, shows clear asymmetric crystallization of white mica around K-Feldspar during deformation (Fig. 5.4), suggesting a deformation temperature below 400 $^{\circ}$C. However, the lattice preferred orientation analysis performed with EBSD shows different activated slip systems depending on the zone considered (Fig. 5.16). The first zone produced a clear result that indicated the activation of the prismatic plane in the direction of the $< c >$ axis, typical of a higher deformation temperature, above $\approx$ 600 $^{\circ}$C (Takeshita, 1996; Mainprice et al., 1986; Lister and Dornsiepen, 1982; Pennacchioni et al., 2010, e.g.,). The shearing direction is top-to-N301° (Fig. 5.16a). The two other zones indicate the activation of the quartz basal plane in the $< a >$ direction, at a lower temperature, below 500 $^{\circ}$C (e.g., Pennacchioni et al., 2010; Takeshita, 1996) with a shear direction to N311° for site 2 and N284° for site 3 (Fig. 5.16a). These observations suggest that the top-to-NW shearing started at a temperature around 600 $^{\circ}$C and lasted until temperatures below 400 $^{\circ}$C, with a possible rotation of the direction of shearing to top-to-WNW at lower temperature. Following our earlier discussion we consider that the age of 13.7 ± 0.7 Ma dates the last increments of top-to-WNW / NW shearing, while the age of the higher temperature shearing stays unconstrained.

Crespo-Blanc et al. (1995), have performed $^{40}Ar/^{39}Ar$ on synkinematic white micas from mylonitized limestones near Sembrancher, about 20 km further north at the bottom of the Diableret nappe, the thrust above ME119 (Fig. 5.1a). They obtained plateaux ages ranging from 14.6 ± 0.2 to 18.5 ± 0.2 Ma within the shear zone similar to that of ME119 *in situ* age. These ages confirm our dating of the late deformation increments at 14 Ma, according to the

interpretation of Crespo-Blanc et al. (1995). These authors also performed the same dating on detrital white mica embedded in limestone about 15 m above the thrust, where the rocks are much less deformed and obtained age spectra with the first steps at about 15 Ma and the last at approximately 50 Ma (26.8 Ma for total gas release). The fact that the older age component is not completely reset in that sample suggests that the younger age reset is related to the thrust plane, possibly through enhanced fluid circulation, rather than with cooling.

Compared with the most probable cooling history for the central Mont-Blanc region (Mercier et al., in preparation, Chap. 6), the age of the ME119 sample corresponds to temperatures significantly lower than the nominal closure temperature of white micas (see Fig. 6.19b, p. 289). This appears to confirm our interpretation of that age as a crystallization age, not a cooling age. However, that reasoning could be biased as the modeled cooling histories assume a vertical uplift of the Mont-Blanc, that is tilted (Mercier et al., 2023, Chap. 4), so the cooling histories calculated for the northwestern part could not be valid for the southeastern part where the sample ME119 is located. But the ZFT ages at comparable altitudes are all between 11.2 and 12.5 Ma (Glotzbach et al., 2011; Seward and Mancktelow, 1994) suggesting that the tilt of the range is anterior to that time and that the cooling history of the northwestern part can be applied to the southeastern part, at least at that time.

Sample ARe309, located at the base of the Roselette klippe, on the eastern side of the Mont-Blanc and of the MBsz yields an age of 16.3 ± 3.1 Ma; slightly older than that of ME119, but within the same range taking uncertainties into account. The quartz lattice-preferred orientation analysis suggests an important simple shear component and a general asymmetry of the [c]-axis distribution, confirming the top-to-the-northwest (N$285°$ to N$303°$, Fig. 5.16b) sense of shear. The activated slip plane is the basal plane in the $< a >$ direction, suggesting a deformation temperature below 500 °C. It is difficult to constrain if deformation occurred just above or below the nominal closure temperature of white micas at 430 ± 30 °C. However, the facts that ARe309 and ME119 ages are similar, that both samples correspond to top-to-WNW shearing, and that the Roselette klippe does not root within but is cross-cut by the MBsz (Figs. 5.1 and 4.53d) lead us to propose that the two samples belong to the same structure, the basal Helvetic thrust that was active until 16 to 14 Ma.

5.6 Implications for the deformation sequence in the Western Alps

The new *in situ* $^{40}Ar/^{39}Ar$ age of synkinematic white micas allows to constrain the timing and thrust propagation sequence in the Mont-Blanc and subalpine massifs. Based on the 3D structural analysis of the structure (Mercier et al., 2023, Chap. 4, p. 117), we consider the

thrusting sequence of the area as an in-sequence history from east to west, with the particularity of the Helvetic nappe system working synchronously with the Mont-Blanc shear zone in a duplex-like system. Taking into account other published ages and the exhumation / cooling history of the range (Mercier et al., in preparation; Chap. 6), we propose the following scenario (Fig. 5.19):

1. The Penninic nappe system was active from the Eocene to the early Oligocene (Cenki-Tok et al., 2013; Simon-Labric et al., 2009; Egli et al., 2017). That thrust system emerged far to the west of the ECM and composed the Prealpine klippen (Chablais, Sulens, Annes) (see Fig. 4.27, p. 161).

2. The Helvetic thrust system includes the Wildhorn Nappe, Diableret Nappe, Morcles Nappe, and the Basal Thrust Nappe underlain by the Basal Helvetic Thrust (Leloup et al., 2005; Mercier et al., 2023; Egli et al., 2017, see also Chap. 4). The western front of that thrust system bounds the Miocene foreland deposits and is located west of the ECM (Kalifi et al., 2021) (see Fig. 4.27, p. 161). Part of the Helvetic nappes (Haut-Giffre, Aravis, Bornes, Beauges, eastern Chartreuse, and Moucherotte in eastern Vercors) located between that front and the western ECM (external Belledonne, Aiguilles Rouges) are large klippen (Doudoux et al., 1982; Kalifi et al., 2021; Mercier et al., 2023). The dating of the Miocene molasse constrains that thrust system to have been active before 21 Ma (Kalifi et al., 2021), and the absolute dating of micas within the nappes suggests that deformation started soon after the Penninic nappe system ended, at about 32 Ma (Cenki-Tok et al., 2013; Simon-Labric et al., 2009; Egli et al., 2017). Our new data constrain that it ended at 14 Ma.

3. The western Mont-Blanc shear zone is a steep reverse shear zone that cuts and offsets the Helvetic Nappes, and was therefore interpreted as younger (Leloup et al., 2005). However, our results show that it was active between 18 and 14 Ma. Previous geochronological data suggest that MBsz was active since about 22 Ma (Leloup et al., 2005; Rolland et al., 2008; Egli et al., 2017) as also suggested by the few inherited ages in sample C4. Such timing partly coincides with the low-angle thrust along the Helvetic nappes. Therefore, we propose that between 22 and 14 Ma, the western Mont-Blanc shear zones and the Helvetic nappes were part of the same duplex system, the basal thrust of the Helvetic nappes being a flat and the western Mont-Blanc shear zone being a ramp, as previously suggested by Mercier et al. (2023) and Gourlay and Ricou (1983). Furthermore, Leloup et al. (2005) documented brittle faults with dip-slip motion on the northwest flank of the Mont-Blanc massif (Nid d'Aigle), suggesting that the western Mont-Blanc shear zone may have lasted until more recent times when the Mont-Blanc massif was at shallower depth.

4. After 14 Ma, the western Mont-Blanc shear zone becomes a breach thrust that offsets the Helvetic Basal Thrust (Platt, 1984; Leloup et al., 2005; Mercier et al., 2023). Constraints on the timing of that breach thrust come mostly from low-temperature thermochronology and will be detailed in the next chapter.

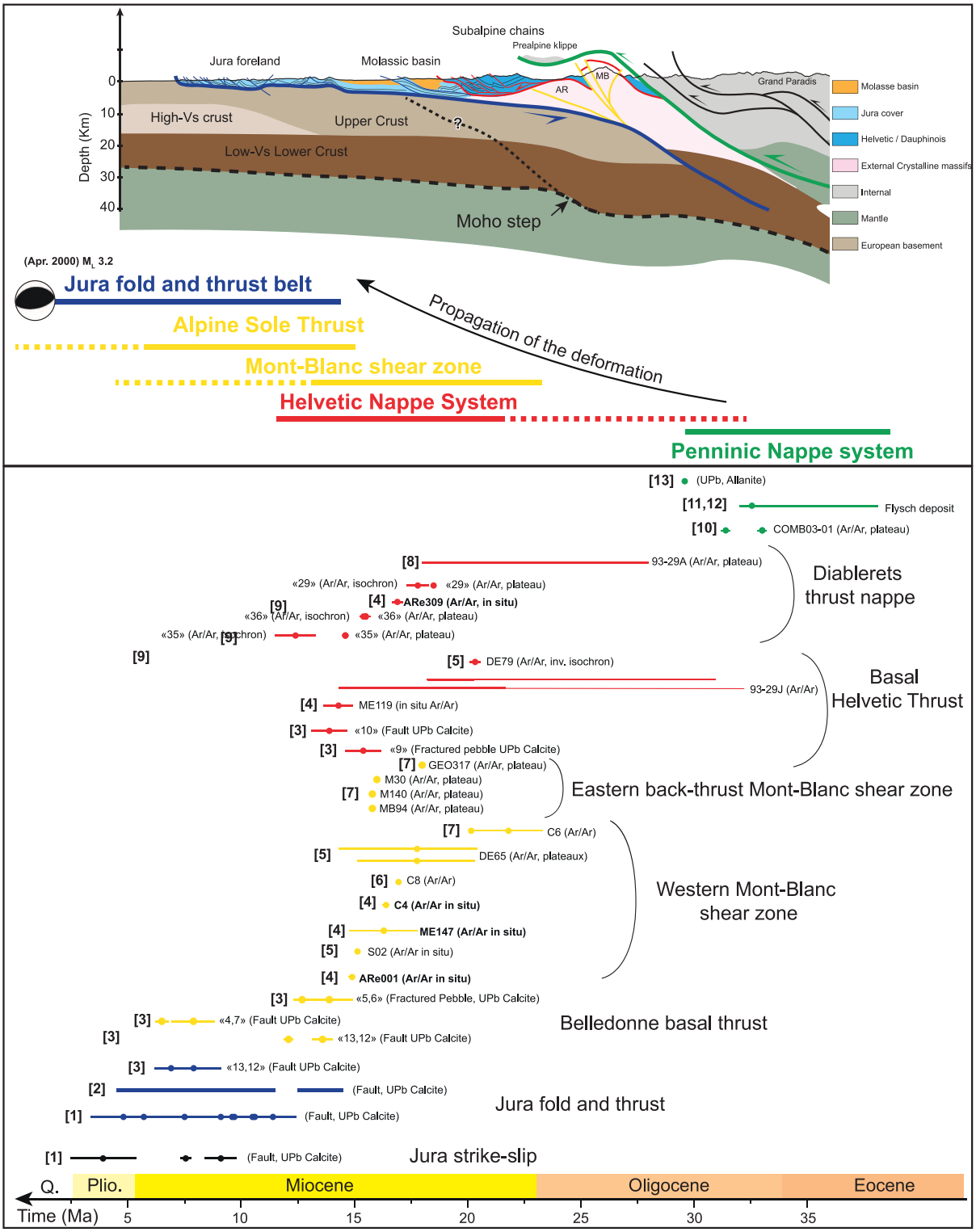

Figure 5.19. Compilation of the timing constraints on the main alpine deformations within the western Alps and Jura fold and thrust belt. [1]: Smeraglia et al. (2021); [2]: Looser et al. (2021); [3]:Bilau et al. (2023); [4]: This study; [5]: Egli et al. (2017); [6]: Leloup et al. (2005); [7]: Rolland et al. (2008); [8]: Kirschner et al. (1996) and Kirschner et al. (2003); [9]: Crespo-Blanc et al. (1995); [10]: Simon-Labric et al. (2009); [11,12]: Pfiffner et al. (2002) and Ruffini et al. (1997); [13]: Cenki-Tok et al. (2013).

5.7 Data availability

Stereographic plots were performed using Stereonet v.11 programs of Allmendinger et al. (2011) and Cardozo and Allmendinger (2013), freely available on Rick Allmendinger `https://www.rickallmendinger.net/stereonet`.

All data used in this publication: location of observations, measurements, samples, $^{40}Ar/^{39}Ar$ age data, and chemical analysis data are stored in a repository with the following `https://data.mendeley.com/datasets/b9xh763rsh/1`. $^{40}Ar/^{39}Ar$ data have been first processed using ArgonCalc software of Koppers (2002) together with scripts computed with MATLAB software (MATLAB, 2022).

Acknowledgments

This study was supported by INSU-CNRS through the 'FEI-UMR5276-Dotation Performance 2022'. It forms part of the Ph.D. project of Antoine Mercier at Université Claude Bernard Lyon 1, supported by the French Ministry of Research, Higher Education and Innovation. The authors thank the MATEIS laboratory of the INSA lab for giving us access to the Zeiss Supra SEM for EBSD analysis. The authors thank Valentina Batanova and Valérie Magnin from the ISTerre laboratory for the EPMA petrogeochemical analysis. Isterre MicroAnalytical Plateforme (IMAP) at the University of Grenoble Alpes was funded by grants from the European Research Council (ERC) under the Horizon H2020 research and innovation program of the European Union (Synergy Grant MEET, grant agreement no.856555); Auvergne-Rhône-Alpes region (2020 AURA P3 - CPER 2015/2020) and CNRS-INSU.

Chapter's key points

- Six mylonitic rocks from four distincts structure were dated using *in situ* $^{40}Ar/^{39}Ar$ dating method.
- The three samples from the western Mont-Blanc shear zone range in age from 14.9 to 17.3 Ma.
- The sample from the Helvetic nappes on top of the Mont-Blanc (eastern side) yields an age of 13.7 Ma.
- The sample from the Roselette klippe (south of Mont-Blanc) yields an age of 16.3 Ma.
- Thermobarometric conditions of the deformation were estimated by petrogeochemical quantification and lattice preferred orientation of quartz crystals and suggest that the deformation occurred below 500°C and between 0.47 and 0.74 GPa
- These new data are combined with previously published absolute dating to constrain the timing and thrust propagation sequence :
  1. The Helvetic nappe system started after the Penninic nappes system at about 32 Ma.
  2. The western Mont-Blanc shear zone develops from 22 Ma to 14 Ma synchronously with the Helvetic nappes in a duplex system.
  3. From 14, the Mont-Blanc shear zone becomes a breach thrust that intersects the Helvetic nappes.

Chapter 6

Exhumation history of Mont-Blanc and Aiguilles Rouges massifs

The Mont-Blanc summit, seen from Pointe Helbronner, Italy. Photo: Antoine Mercier (2020).

Abstract

We invert new thermochronological data to quantify the differential exhumation between the Mont-Blanc and Aiguilles Rouges massifs in the western Alps. The evolution of exhumation can be interpreted in terms of the interaction between internal (tectonic, isostasy) and external (erosion) processes. But the complexity of the interaction between driving forces and the exhumation leads to a non-unicity of the problem's solution, requiring the use of an advanced probabilistic method. We apply a method using Bayesian inference coupled with thermochronological simulation and the Pecube algorithm. Pecube is a software that performs numerical simulations of denudation on a crustal block, including relief amplification and faults. The inputs are observed thermochronological data, and the outputs are estimated thermochronological data depending on the parameters used for the simulation, such as the timing and magnitude of denudation, relief amplification, and thermal conditions. The estimated data can be compared to the observed data, and using inverse method the parameters are adjusted to reduce the difference between the two. After the first stage of parameter exploration by inversion (neighborhood algorithm), we resample the results obtained with a Bayesian method to obtain a posterior probability density function describing the models and parameter uncertainty. In addition, inversions of the data generated by direct models are used to assess the ability of the method and the data to quantify each parameter. We applied this methodology to the Mont-Blanc and Aiguilles Rouges massifs (French western Alps), enabling us to quantify the exhumation history of the two massifs and the differential exhumation between them and estimate the uncertainty of each parameter. The results indicate that (i) the Mont-Blanc massif was exhumed about 7 km more than the Aiguilles Rouges; (ii) the Mont-Blanc began to exhume after 21 Ma until 12 Ma, along with the activity of the Mont-Blanc shear zone; (iii) the Aiguilles Rouges began to exhume at 6 Ma, with differential exhumation between the two massifs stopping at 1 Ma, and (iv) the two massifs experienced a common acceleration phase, coeval with relief building and most likely related to climatic evolution.

Résumé

Nous inversons de nouvelles données thermochronologiques pour quantifier l'exhumation différentielle entre les massifs du Mont-Blanc et des Aiguilles Rouges dans les Alpes occidentales. L'exhumation peut être interprétée en termes d'interaction entre des processus internes (tectonique, isostasie) et externes (érosion). Mais la complexité de l'interaction entre les forces et l'exhumation conduit à une non-unicité de la solution, nécessitant l'utilisation d'une méthode statistique avancée. Dans ce travail nous appliquons une méthode utilisant l'inférence bayésienne couplée à la simulation numerique avec l'algorithme Pecube. Pecube est un logiciel qui simule numériquement la dénudation d'un bloc crustal en tenant compte de l'effet du relief et des failles. Les données de entrée sont des données thermochronologiques observées et les données en sortie sont des données thermochronologiques générée à partir des paramètres utilisés pour la simulation, tels que la chronologie et l'ampleur de la dénudation, l'amplification du relief et les conditions thermiques. Les données estimées peuvent être comparées aux données observées, et en utilisant la méthode inverse, les paramètres sont ajustés pour réduire la différence entre les deux. Après la première étape d'exploration des paramètres par inversion (algorithme de proches voisins), nous rééchantillonnons les résultats obtenus avec une méthode bayésienne pour obtenir une densité de probabilité décrivant les paramètres du modèles et leur incertitude. De plus, des inversions de données générées par un modèles directs (données synthétiques) sont utilisées pour évaluer la capacité de la méthode et des données à quantifier chaque paramètre. Nous avons appliqué cette méthodologie aux massifs du Mont-Blanc et des Aiguilles Rouges (Alpes occidentales françaises), ce qui nous a permis de quantifier l'histoire de l'exhumation des deux massifs et l'exhumation différentielle entre eux, et d'estimer l'incertitude de chaque paramètre. Les résultats indiquent que (i) le massif du Mont-Blanc a été exhumé environ 7 km de plus que celui des Aiguilles Rouges ; (ii) le Mont-Blanc a commencé à s'exhumer après 21 Ma jusqu'à 12 Ma, en même temps que l'activité de la zone de cisaillement du Mont-Blanc ; (iii) les Aiguilles Rouges ont commencé à s'exhumer après 6 Ma, l'exhumation différentielle entre les deux massifs s'arrêtant à 1 Ma, et (iv) les deux massifs ont connu une phase d'accélération commune, coïncidant avec l'édification du relief et vraisemblablement liée à l'incision glaciaire.

6.1 Introduction

The inverse method applied to thermochronological data can be used to quantify the history of rock exhumation (e.g., Hurford, 1991; Reiners et al., 2005). The evolution of exhumation can be interpreted in terms of the interaction between internal processes (tectonics, isostasy) and external processes (erosion) (Champagnac et al., 2007; Molnar and England, 1990). But the complexity of the interaction between driving forces and the exhumation leads to a non-unicity of the problem's solution, requiring the use of an advanced probabilistic method. Thermochronology is a technique that provides data on the thermal history of rocks, based on the accumulation of daughter product (isotope or damage) produced by the nuclear decay reaction (Dodson, 1973). The accumulation of decay products is controlled by diffusion, which is mainly dependent on temperature. Because the temperature increases with depth in the Earth's crust, thermochronological data record the depth of the rocks at a certain time. Internal driving forces, such as tectonics or isostatic rebound, can move the rock upward (rock uplift), while external driving forces, such as erosion or relief changes, can remove material from above and reach the topography surface. The interpretation of thermochronological ages depends on the thermal state of the crust, which means the geothermal gradient and its variations over time, and switching from thermochronological ages to rock exhumation requires reconstituting the thermal evolution over time, which depends on parameters such as the velocity and amplitude of exhumation, thermal advection, the topography and its evolution, heat transfer, etc. (Braun, 2002). Therefore, the relationship between the driving forces and the exhumation processes is highly non-linear and depends on many parameters.

Thermochronological numerical simulations, coupled with inverse methods, are proposed to quantify the numerous parameters that influence rock exhumation (e.g., Gallagher et al., 1998; Braun, 2003; Braun et al., 2012). However, the complexity of the interactions between the driving forces often leads to non-unicity of the problem solution (too many parameters), necessitating the use of a robust probabilistic method. In this work, we use the Pecube simulation code (Braun, 2003; Braun et al., 2012).

Pecube is a software that performs a numerical simulation of denudation of a crustal block that may take into account relief amplification and faults (Braun, 2003; Braun et al., 2012). The input is a tectono-geomorphologic scenario, and the outputs are estimated thermochronological data depending on the parameters used for the simulation, such as the timing and magnitude of denudation, relief amplification, and thermal conditions. The estimated data can be compared to the observed data, and using inverse method the parameters are adjusted to reduce the difference between the two. Furthermore, the use of synthetic data to test the ability of modeling to retrieve the exhumation history has been applied in several mountain belts and orogenic contexts (e.g., Valla et al., 2010; Robert et al., 2011) and seems to be a requirement to properly

understand the result of inverse problems.

In this work, we apply this method, that has proved beneficial in reconstructing the history of mountain belt exhumation (e.g., Van der Beek et al., 2010; Valla et al., 2011; Valla et al., 2012; Valla et al., 2010) in one of the most iconic external crystalline massifs of the western Alps: the Mont-Blanc massif. Exhumation histories of external crystalline massifs have been extensively studied using low-temperature thermochronology (e.g., Boutoux et al., 2016; Glotzbach et al., 2008; Glotzbach et al., 2011; Valla et al., 2010; Valla et al., 2011; Valla et al., 2012; Van der Beek et al., 2010; Girault et al., 2022; Seward and Mancktelow, 1994; Leloup et al., 2005; Soom, 1990; Rahn, 1994). Some authors argue that the external crystalline massifs experienced continuous exhumation since 18 Ma (Boutoux et al., 2016; Girault et al., 2022), while others suggest episodic exhumation of the massifs with a pulse of erosion between 6 and 5 Ma (Glotzbach et al., 2011; Van der Beek et al., 2010; Valla et al., 2011). The Mont-Blanc massif possesses one of the densest thermochronological datasets in the Alps (Fig. 6.4), allowing for a detailed investigation of its exhumation. On the west side of the Mont-Blanc, the Aiguilles Rouges massifs suffer from a lack of data, making the construction of its exhumation history complicated. Tectonic faults have been evidenced and characterized between these two massifs (Fig. 6.4). But we lack information about the rates and timings along the major faults, so we propose applying quantitative thermochronological analysis with thermokinematic modeling (Braun, 2003; Braun et al., 2012): Could thermochronological data quantify the differential exhumation between these two massifs ?

We first review the geological setting and exhumation history of the western Alps and then present the thermochronological dataset, combining our newly acquired data in the Aiguilles Rouges with the published dataset. A qualitative interpretation of the age-elevation relationship is performed with a pseudo-elevation plot. The ability of the data and the numerical simulation to infer the exhumation scenario is tested with synthetic data. The real thermochronological data are finally inverted with increasing complexity of parameterization, to look for the optimum solution. The differential exhumation between Mont-Blanc and Aiguilles Rouges is tested by including a fault that splits the dataset in the simulation or without. Finally, a choice of complexity is made according to the balance between simulation complexity and fit to the data, allowing us to infer the differential exhumation history of the Mont-Blanc and Aiguilles Rouges massifs.

6.2 Geological setting and exhumation of the Western Alps

The western Alps result from the Cenozoic collision between Europe and the continental margins of Apulia after the subduction of the Tethys initiated during the Middle Cretaceous and the collision began during the Paleogene. The orogen is structurally divided into two main

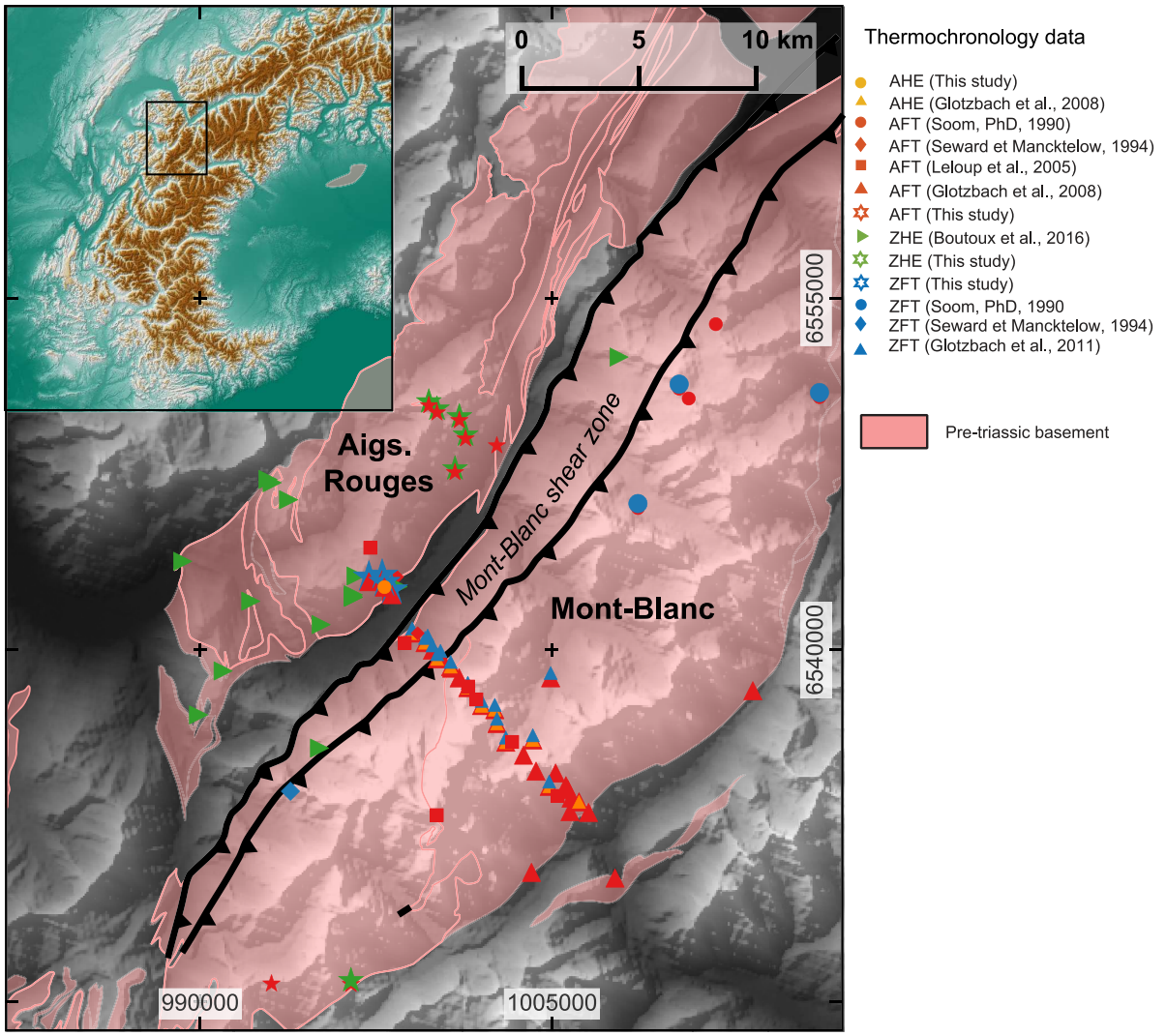

Figure 6.1. Simplified geological settings of the Mont-Blanc and Aiguilles Rouges basement massifs and associated thermochronological data. Thermochronological ages are localized (Glotzbach et al., 2008; Soom, 1990; Seward and Mancktelow, 1994; Leloup et al., 2005; Glotzbach et al., 2011; Boutoux et al., 2016; Valla et al., 2011)

parts according to the facies of metamorphism: the internal domain has been deformed at high temperature and deeply subducted during the Alpine orogeny (Chopin et al., 1987). On the other hand, the metamorphism along the external domain was limited to greenschist facies (e.g., Bousquet et al., 2004).

The external domain exposes basement of the External Crystalline Massifs (ECM) and their deformed sedimentary cover. The basement consists of Variscan metamorphic gneiss and granite. These massifs are characterized by some of the highest peaks of the Alpine orogen, with several summits higher than 4000 m (e.g., Mont-Blanc summit, Barre des Ecrins). Recent studies of the denudation history of the ECM have suggested continuous exhumation of the massifs since 18 to 20 Ma (Boutoux et al., 2016; Girault et al., 2022) with exhumation rates of about 1 $\mathrm{km\,Ma^{-1}}$, while others have proposed peaks in exhumation rate around 6 to 7 Ma (Bigot-Cormier et al., 2006; Glotzbach et al., 2008; Glotzbach et al., 2011). Sediment flux to the peri-Alpine basin has increased significantly since about 5 Ma, suggesting an increase in the exhumation rate (Kuhlemann et al., 2001; Kuhlemann et al., 2002).

Here, we focus on the Mont-Blanc and Aiguilles Rouges massif (Fig. 6.4) separated by the so-called Chamonix synclinorium where Mesozoic sediments outcrop. The Mont-Blanc massif has overthrust the Aiguilles Rouges and Chamonix synclinorium along a major shear zone characterized by southeast green-schist dipping foliation with inverse-dextral strike-slip motion (Bellière, 1956; Eltchaninoff, 1982; Butler, 1985; Leloup et al., 2005). The Mont-Blanc massif is also structured by a dense network of anastomosed shear zones (Rolland et al., 2008). These shear zones are proposed as the main tectonic forcing for the Mont-Blanc exhumation. On the other side, the Aiguilles Rouges have probably been exhumed through the blind Alpine Sole thrust (Leloup et al., 2005; Bellahsen et al., 2014), and the frontal Aiguilles Rouges thrust (Pfiffner et al., 1997), which both have a northwestern direction of thrust. But recent studies evidenced backthrusting in the Aiguilles Rouges (southeast direction of thrust), which could also exhume the massif (Leloup et al., 2005; Mercier et al., 2023, Chap. 4).

6.3 Quantification of denudation and relief histories

Inferring a rock exhumation history requires converting the thermal path of the rock sample in terms of exhumation, which means the velocity at which the sample has reached the surface and quantifying the processes responsible for the exhumation. In this framework, it seems important to clearly state and define the terms used. England and Molnar (1990) proposed the definitions of these terms (Fig. 6.2).

- **Surface height** refers to the elevation (altitude) of the Earth's surface from a given ellipsoid reference frame. Generally, the elevation reference frame is sea level.

- **Surface uplift** refers to the upward displacement of the earth's surface away from the geoid (gain in elevation).
- **Rock uplift** refers to the upward displacement of a block of rocks away from the geoid. Consequently, erosion-free rock uplift leads to a surface uplift of the same amount.
- **Exhumation** refers to the displacement of rocks with respect to the surface of the Earth. The *exhumation rate* is the time derivative of the material removal from above. In the same way, burial is the addition of materials from above (e.g.; nappe emplacement, basin filling).
- **Erosion** refers to the processes that remove materials from the surface of the Earth.

$$Surface\ Uplift = Rock\ Uplift - Exhumation$$

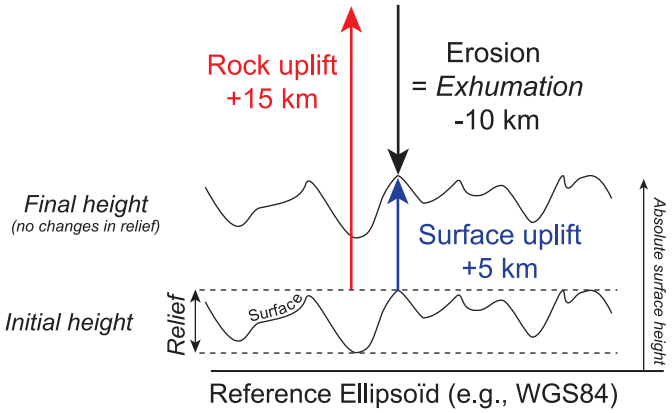

Figure 6.2. Balance of processes acting in the exhumation according to the terms defined by England and Molnar (1990). The surface uplift corresponds to the quantity of erosion removed from the rock uplift. Note that if the rock uplift is balanced by erosion, there are no changes in surface height.

Similarly, we define the terms used for the inverse problem:

- **Parameters** are the quantities that control the behavior of the numerical simulation. Accordingly, **parameterization** refers to a set of parameters (free or fixed) during an inversion.
- **Observed data** are thermochronological age measurements from a rock sample.
- **Estimated or generated data** are the thermochronological age calculated with numerical simulation using a specific set of parameters.
- **Model** refers to a specific set of parameters during a numerical simulation. A model is produced at each iteration during the inversion.

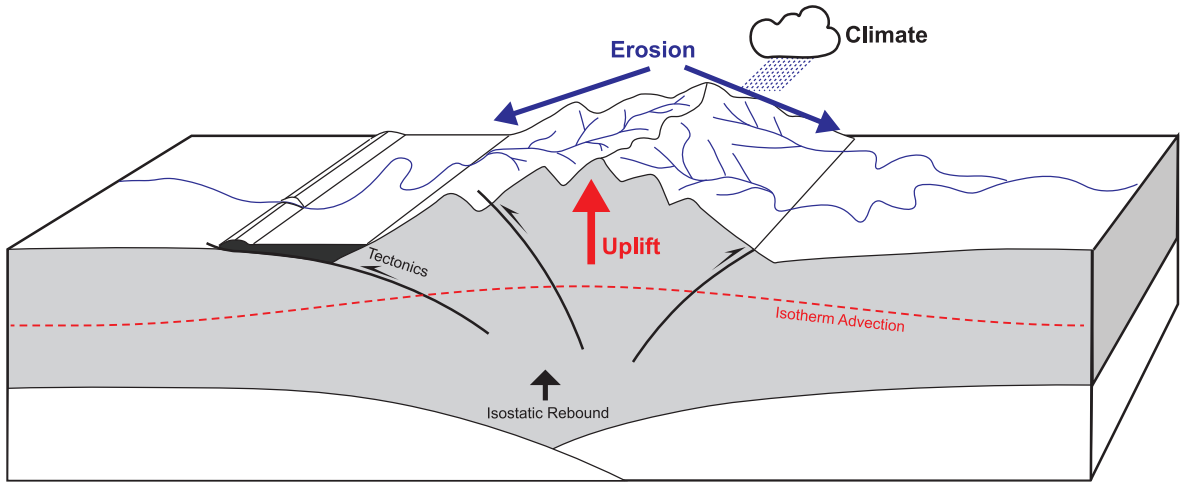

Figure 6.3. Surface processes acting in a collision orogen. Rock uplift moves upwards the surface with isostatic movements and tectonics, while the erosion processes move downwards the surface. The combination of both is rock exhumation. Simplified and redrawn from Wolf et al. (2022).

Understanding the evolution of the orogenic wedge requires reconstructing the exhumation history. From thermochronology we can reconstruct the thermal evolution of rocks but, as stated before, it is highly dependent on the geothermal gradient evolution. Estimating the thermal gradient is often difficult because of the factors that make it evolve in time and space: advection, relief changes, heat production, etc.

6.4 Thermochronology data

The apparent age of a rock is inferred from the decay of radioactive isotopes, resulting in the accumulation of daughter radiogenic nuclei. The amount of decay can then be directly estimated through the number of radiogenic isotope or the form of structural changes in the crystal induced by radioactivity (fission tracks) (Dodson, 1973). Theoretically, the apparent age corresponds to the time at which the daughter products are immobile and do not escape by diffusion from the host rock or mineral (Fig. 6.4). According to the Arrhenius equation, thermal diffusion increases with temperature: at higher temperatures, the daughter elements escape by diffusion as they are produced, they cannot accumulate in the mineral (Arrhenius, 1967). At lower temperatures, the diffusion escape rate becomes close to zero and the daughter elements accumulate in the mineral. The temperature at which the diffusion distance is smaller than the grain size defines the closure temperature, which depends on the thermochronological system considered (Fig. 6.5). In summary, the apparent age of a rock or mineral sample for a given thermochronological system corresponds to the time from the moment the sample cooled through the closure isotherm of its closure temperature. In detail, this timing is highly

dependent on the crystallization temperature of the mineral and the cooling rate of the rock.

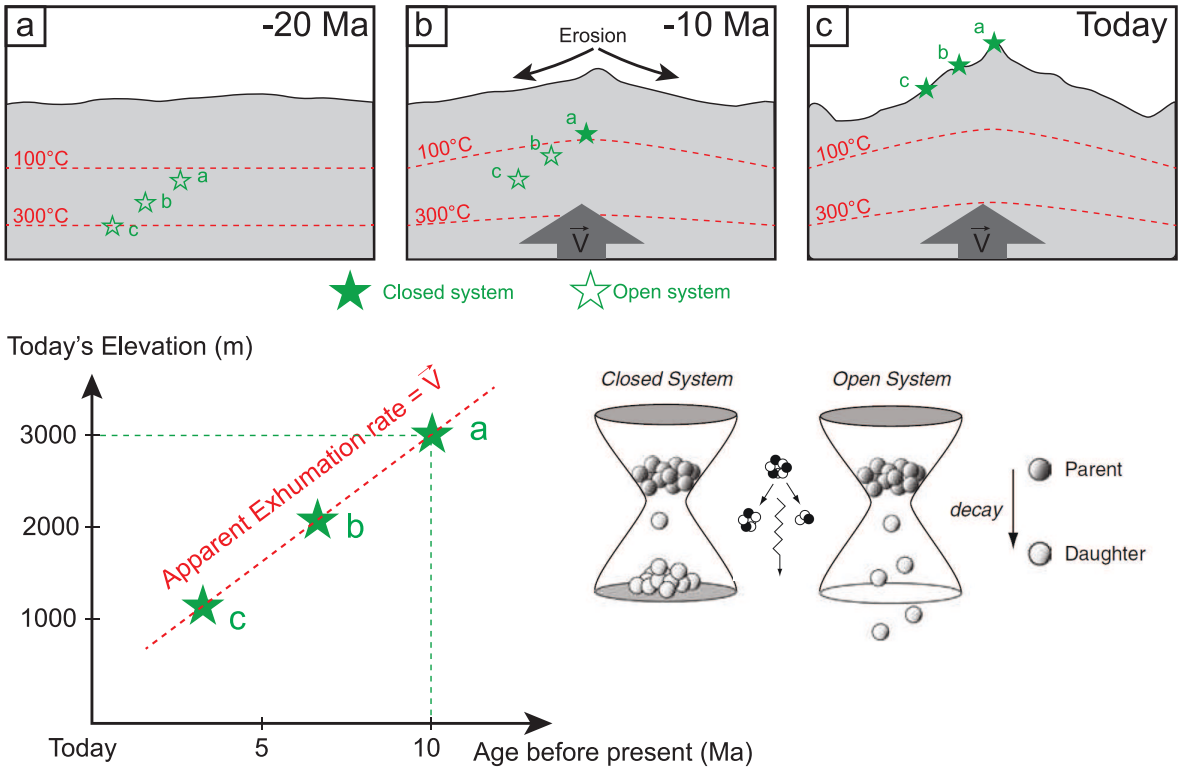

Figure 6.4. Schematic diagram illustrating the basis of the thermochronology method inferring exhumation histories. Hourglass analogies to open and closed thermochronological systems behaviors. In a closed system, the daughter product accumulated by the nuclear decay of a parent isotope is completely retained within the host mineral. In an open system, the daughter product is removed during its production. Samples from different elevations will close at different timing during the exhumation, leading to an apparent exhumation velocity. Modified from Braun et al. (2006).

The vast majority of published data have been collected exclusively in the Mont-Blanc massif (Seward and Mancktelow, 1994; Glotzbach et al., 2008; Glotzbach et al., 2011; Leloup et al., 2005; Boutoux et al., 2016; Rahn, 1994; Soom, 1990), therefore, we concentrated our sampling on the Aiguilles Rouges massifs since and only a few samples have been collected in the southern part of the Aiguilles Rouges (Seward and Mancktelow, 1994; Leloup et al., 2005; Boutoux et al., 2016) (Fig. 6.4). Our strategy was to perform a novel profile from the highest peak of the Aiguilles Rouges to the Mont-Blanc valley to better constrain the timing of exhumation. Ten new samples were collected in the southern Aiguilles Rouges massif, along two roughly northwest-southeast transects near the Brévent summit in the south and the Aiguille du Belvédère in the north. The northern transect runs from the Aiguille du Belvédère to the Chamonix Valley, between 1275 and 2920 m elevation (Fig. 6.6), and samples were collected every 250 - 300 m when possible. The Aiguilles Rouges basement in the sampling sites corresponds to migmatitic gneiss (Ayrton et al., 1987; Von Raumer and Bussy, 2004). Six

samples yielded sufficient apatites for AFT analysis and only five yielded enough zircons for (U-Th)/He analysis. We completed this new dataset with another transect further south in the Aiguilles Rouges that ran from the Brévent summit to the Chamonix Valley. This transect is made of migmatitic gneiss similar to the northern profile, has previously been collected by C. Glotzbach but has never been published. Three other samples have been collected in the south of the Mont-Blanc massif, in the migmatitic gneiss of the Mont-Blanc basement (Mennessier et al., 1977).

To better constrain the exhumation history, samples were collected for the application of four complementary thermochronological methods: (U-Th) / He in zircon (ZHE; T_c = 70 - 200 °C) and apatites (AHE; T_c = 40 - 70°C) and fission tracks in apatites (AFT; T_c = 70 - 120 °C) and zircons (ZFT; T_c = 200 - 300 °C).

Following the standard procedure used for thermochronology analyzes, the collected samples were crushed, apatite and zircon grains were separated from low-density grains using heavy liquid and magnetic separation techniques, and finally handpicked.

6.4.1 (U-Th)/He data

The (U-Th)/He thermochronological system is based on the production of He from the alpha nuclear decay reaction of ^{238}U, ^{232}Th and ^{147}Sm. Height nuclei of helium are produced from decay of ^{238}U, seven nuclei of helium are produced from decay in the chain of ^{235}U, six in the decay chain of ^{232}Th and a single nucleus in the chain of ^{147}Sm.

$$^{235}_{92}\mathrm{U} \xrightarrow{\alpha} {}^{231}_{90}\mathrm{Th} + \mathbf{{}^{4}_{2}He} \longrightarrow \cdots \longrightarrow {}^{207}_{81}\mathrm{Tl} \xrightarrow{\beta^-} {}^{207}_{82}\mathrm{Pb}_{\mathrm{stable}} \tag{6.1}$$

$$^{238}_{92}\mathrm{U} \xrightarrow{\alpha} {}^{234}_{90}\mathrm{Th} + \mathbf{{}^{4}_{2}He} \longrightarrow \cdots \longrightarrow {}^{210}_{84}\mathrm{Po} \xrightarrow{\alpha} {}^{206}_{82}\mathrm{Pb}_{\mathrm{stable}} + \mathbf{{}^{4}_{2}He} \tag{6.2}$$

$$^{232}_{90}\mathrm{Th} \xrightarrow{\alpha} {}^{228}_{88}\mathrm{Ra} + \mathbf{{}^{4}_{2}He} \longrightarrow \cdots \longrightarrow {}^{208}_{81}\mathrm{Tl} \xrightarrow{\beta^-} {}^{208}_{82}\mathrm{Pb}_{\mathrm{stable}} \tag{6.3}$$

$$^{147}_{62}\mathrm{Sm} \xrightarrow{\alpha} {}^{143}_{60}\mathrm{Nd}_{\mathrm{stable}} + \mathbf{{}^{4}_{2}He} \tag{6.4}$$

The use of (U-Th)/He decay for dating is valid only if (i) all decay chains are in secular equilibrium, which is the case for crystals formed more than 350 000 before the onset of alpha particle accumulation (Farley, 2000), and (ii) if there is no initial ^4He in the crystals. This ^4He could come from atmospheric contamination or fluid inclusions. In the case of minerals rich in U and Th, such as apatites and zircons, any amounts of initial ^4He are negligible compared with the ^4He produced. However, this may no longer be the case if the minerals are very young and the fluid inclusions are very rich in ^4He. Finally, the presence of Helium inherited from earlier thermal histories is unlikely, given the high diffusion velocities of Helium in crystals (Fabre

et al., 2002). The main challenge with using alpha particle production in thermochronometry is that these particles are emitted with enough kinetic energy to diffuse over a distance of several micrometers. With consequences, alpha particles can be expelled from the mineral, and the measured age will be younger than the actual age. In contrast, the mineral may have received alpha particles from a neighboring mineral, in which case the measured age will be older than the actual age. These effects are particularly critical for small crystals. For each alpha particle produced, we can therefore associate a zone into which it can be ejected. To take this effect into account and correct the measured ages, Farley et al. (1996) developed a quantitative model based on the measurement of the grain diameter, giving a correction factor called Ft. The notion of closure temperature should be handled with care in the case of apatites. Farley (2000) have shown that the closure temperature is a function of the grain size. In summary, the closure temperature for AHE dating is around 40 to 70°C, regardless of the cooling rate and grain size (Farley, 2000). As a result, AHE dating is particularly well suited to the study of low exhumation rates or, in the case of relatively young exhumations. In the thermochronological system (U-Th) / He, the daughter element is a noble gas that quickly escapes from the system. Therefore, it is considered that there is no daughter initially present and that the helium nucleus is only derived from the decay reaction. The closure temperature for the ZHE data is around 70 to 200°C Gérard et al. (2022). Note that apatites and zircons have not been analyzed in the same laboratory.

6.4.1.1 Apatite (U-Th)/He (AHE)

Analyzes have been performed at the University of Tübingen (Germany) following the procedure described in Danišík et al. (2012). U-Th-Sm contents were analyzed by ICP-MS at the University of Melbourne (Australia) (see details of the analytical technique and protocol in the appendix D.2 p.421). Three monograins of the sample (CGP54) located in the Aiguilles Rouges at an elevation of 1340 m yield an age range of 2.7 ± 0.3 to 5.5 ± 0.6. The oldest age has been excluded because it is older than the AFT age of the same sample. The weighted mean age obtained corresponds to 2.9 ± 0.3 Ma. From the Mont-Blanc massif, 14 published AHE ages have been obtained by Glotzbach et al. (2008) and range from 1.4 to 6.4 Ma.

6.4.1.2 Zircon (U-Th)/He (ZHE)

The analyzes were performed at the Laboratory of Géosciences Montpellier (France) (see details of the analytical technique and protocol in the appendix D.2 p.421). In the northern Aiguilles Rouges profile, five samples yielded enough zircon to perform a ZHE analysis. Four to seven monograin single grain age determinations were repeated for each of the five samples (Fig. 6.6 and table 6.2. These zircon grains have an eU content ranging mainly between 179 and 740 ppm, except sample ARe024 (2134 m), which contains one zircon with an eU value

of 1247 ppm. These samples do not display an important intra-sample age variation, with a maximum difference between the grain of less than 2 Ma, except sample ARe031 that has a dispersion of 3 Ma. We calculate the weighted mean ages of each sample with the replicates that range from 8.8 ± 0.7 to 10.0 ± 1.4. From the Mont-Blanc massif, only a single sample yielded sufficient zircons for ZHE analysis. Four grains were analyzed, having an eU content ranging from 553 to 1333 ppm, and showing a low dispersion of 8.6 ± 0.4 to 9.9 ± 0.5 Ma. Four other ages of ZHE ages have been published by Boutoux et al. (2016), ranging between 6.4 ± 0.4 and 8.1 ± 0.5 Ma.

6.4.2 Fission-track data

In the fission track system, we use the natural radiogenic decay of uranium. During radiogenic decay (mainly ^{238}U), the emission of high-energy particles damages the crystalline lattice of minerals, causing "fission tracks" (Gallagher et al., 1998). At high temperatures, the fission tracks heal and disappear completely by diffusion. The temperature at which the tracks do not heal corresponds to the closure temperature of the system. The fission track dating requires knowing the total amount of ^{238}U and evaluating the density of the fission tracks within a mineral gives the amount of ^{238}U that has fissioned.

$$t = \frac{1}{\lambda_{238}} Ln\left(\lambda_{238}\frac{\rho_s}{\rho_i}\rho_d \zeta g + 1\right) \tag{6.5}$$

With:

λ_{238}: Constant of radiogenic decay ^{238}U. (4.92×10^{-18}).

t: apparent age.

ρ_s: Spontaneous fission track density.

ρ_i: Radiation-induced fission tracks.

ρ_d: The density of traces in a dosimeter or the concentration in ^{238}U.

g: Geometric factor.

ζ: A proportionality constant.

6.4.2.1 Apatite fission tracks (AFT)

From the Aiguilles Rouges, we measured six AFT data from the northern profile and four from the southern profile. AFT analyzes were performed in the GEOPS laboratory (Université Paris Saclay, Orsay - France) for the samples (ARexx) and at the University of Tübingen (Germany) for the samples (CGPxx) (see details on the analytical technique and protocol in Appendix D.2 p. 421). The age ranges from 2.9 ± 0.1 Ma at the lowest elevation to 5.9 ± 1.7

Ma. The northern profile defines a reverse age - elevation relationship, as the oldest ages are from the bottom of the profile and the highest age from the top (expected for the lowest sample) (Fig. 6.6). In the Mont-Blanc massif, three samples were collected for AFT analysis in the southern part of the massif. These samples were collected between 2417 and 2860 m. AFT ages range from 3.1 ± 0.4 to 8.5 ± 1.6 Ma. Raw data and radial plots are available in appendix D.4 p. 423.

6.4.2.2 Zircon fission tracks (ZFT)

From the Aiguilles Rouges, ZFT data from the southern profile, resulting in ages ranging from 23.2 ± 1.4 to 45.8 ± 3.4 Ma. In the Mont-Blanc massif, the ZFT ages were previously obtained by Glotzbach et al. (2011) and are significantly younger than in the Aiguilles Rouges for a similar elevation, ranging from 11.2 ± 0.6 to 13.5 ± 0.3 Ma.

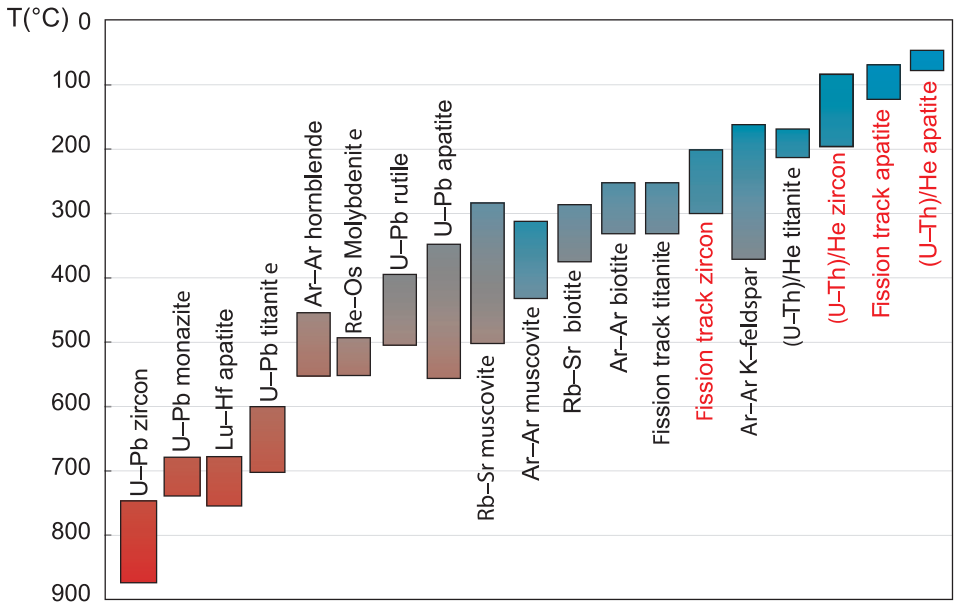

Figure 6.5. Effective closure temperatures for various commonly used thermochronometers from Chew and Spikings (2015). ZHE closure temperature has been modified after Gérard et al. (2022). The thermochronometer used in this study are highlighted in red.

Note that a third sampling profile was sampled in the eastern part of the massif, near the Petit Col Ferret in Italy, but none of the samples provided enough minerals for thermochronological analysis. This may be related to the basement facies in this area that is not granitic but rhyolitic.

Table 6.1. Apatite Fission Track Results From the Aiguilles Rouges and Mont-Blanc massifs, Western Alps

Sample ID	Latitude d.dd°	Longitude d.dd°	Elevation (m. a.s.l)	Lithology	Mineral	N_g^a	$p(\chi^2)^b$	FT Age $\pm 1\sigma$ (Ma)	MTL $\pm 1\sigma$ (µm)
Aig. Rouges									
ARe026	45.98733	6.873775	2920	Gneiss	Apatite	26	0.59	4.79 ± 0.4	
ARe031	45.98439	6.878031	2651	Gneiss	Apatite	17	0.39	5.26 ± 1.02	
ARe025	45.98103	6.890168	2369	Gneiss	Apatite	31	0.86	5.17 ± 0.5	
ARe024	45.97388	6.893069	2134	Gneiss	Apatite	23	0.077	5.72 ± 0.6	
ME130	45.96113	6.886376	1870	Gneiss	Apatite	25	0.63	5.86 ± 0.8	
ARe086	45.97062	6.910123	1275	Gneiss	Apatite	18	0.85	2.87 ± 0.5	
CGP51	45.91549	6.84838	1017	Gneiss	Apatite	26	0.78	5.0 ± 0.4	
CGP51	45.91549	6.84838	1017	Gneiss	Zircon	45	0.38	23.2 ± 1.4	114.41 ± 0.8
CGP52	45.92083	6.83608	1800	Gneiss	Apatite	25	0.99	4.9 ± 0.5	
CGP52	45.92083	6.83608	1800	Gneiss	Zircon	50	0.02	43.8 ± 2.9	114.41 ± 0.8
CGP53	45.92131	6.84342	1520	Gneiss	Apatite	20	0.98	5.5 ± 0.5	
CGP53	45.92131	6.84342	1520	Gneiss	Zircon	21	0.94	45.8 ± 3.4	
CGP54	45.91844	6.84448	1340	Gneiss	Apatite	37	1.0	4.4 ± 0.3	
CGP54	45.91844	6.84448	1340	Gneiss	Zircon	15	0.07	31.5 ± 2.9	
Mont-Blanc									
ARe184	45.76669	6.815500	2692	Gneiss	Apatite	18	0.96	3.24 ± 0.53	
ARe152	45.72738	6.711240	2417	Gneiss	Apatite	27	0.21	3.13 ± 0.21	
ARe165	45.76833	6.771957	2860	Gneiss	Apatite	33	0.51	8.47 ± 0.83	

Multi-column[a]Number of grains dated. [b]Probability obtaining chi-square value for ν degrees of freedom ($\nu = N - 1$).

Table 6.2. (U-Th)/He Results From the Aiguilles Rouges and Mont-Blanc massifs, Western Alps

Sample ID	Aliq.	4He (nccSTP/g)	U (ppm)	Th (ppm)	eU (ppm)	Th/U	Uncorr. Age (Ma)	1σ (Ma)	FT	Corr. Age (Ma)	1σ	Comment	Mean age (Ma)	1σ (Ma)
Aig. Rouges														
ARe026 (Zr)	#1	334114	474	110	500	0.232	5.53	0.06	0.711	7.78	0.39			
	#2	417730	479	93	502	0.195	6.89	0.07	0.713	9.66	0.48			
	#3	334107	442	115	470	0.261	5.88	0.06	0.658	8.94	0.45			
	#4	371502	483	107	509	0.222	6.04	0.06	0.651	9.28	0.46			
													8.8	**0.72**
ARe031 (Zr)	#1	367865	228	53	240	0.231	12.67	0.13	0.73	17.35	0.87	excluded		
	#2	336875	419	103	444	0.246	6.27	0.06	0.645	9.73	0.49			
	#3	419541	374	104	399	0.277	8.71	0.09	0.631	13.80	0.69	excluded		
	#4	351971	322	50	334	0.156	8.71	0.09	0.729	11.95	0.60			
	#5	234363	235	90	256	0.385	7.57	0.08	0.777	9.74	0.78			
	#6	305190	329	101	353	0.306	7.15	0.07	0.738	9.69	0.78			
	#7	146183	170	59	184	0.349	6.58	0.07	0.742	8.86	0.71			
													10.0	**1.40**
ARe025 (Zr)	#1	435224	451	54	463	0.119	7.77	0.08	0.762	10.19	0.51			
	#2	306388	359	52	371	0.146	6.83	0.07	0.793	8.61	0.43			
	#3	384696	564	156	602	0.276	5.29	0.05	0.615	8.60	0.43			
	#4	506088	512	73	530	0.142	7.90	0.08	0.746	10.60	0.53			
													9.3	**1.00**
ARe024 (Zr)	#1	1032925	1185	257	1247	0.217	6.90	0.10	0.797	8.60	0.70			
	#2	536338	594	61	609	0.103	7.28	0.07	0.751	9.70	0.48			
	#3	329341	370	88	391	0.239	6.97	0.07	0.798	8.74	0.44			
	#4	483629	711	116	739	0.164	5.42	0.05	0.559	9.69	0.59			
													9.2	**0.33**
ME130 (Zr)	#1	470966	475	238.9	533	0.503	7.32	0.07	0.725	10.10	0.51			
	#2	122141	145	139.6	179	0.963	5.67	0.06	0.691	8.21	0.41			
	#3	196782	253	45.5	264	0.180	6.16	0.06	0.673	9.15	0.46			
	#4	375376	394	258.6	457	0.656	6.81	0.07	0.74	9.20	0.46			
													9.1	**0.59**
CGP54 (Ap)	#2		25.9	10.6	44	0.041	2.2	0.3	0.81	2.7	0.3			
	#4		11.6	10.4	29	0.090	2.4	0.3	0.78	3.0	0.3			
	#5		9.3	9.4	26	0.101	4.0	0.6	0.73	5.5	0.6	excluded		
													2.9	**0.3**
Mont-Blanc														
ARe184 (Zr)	#1	993207	1240	387	1333	0.312	6.17	0.06	0.649	9.50	0.48			
	#2	477808	525	117	553	0.222	7.14	0.07	0.797	8.96	0.45			
	#3	763596	961	116	989	0.120	6.39	0.06	0.743	8.59	0.43			
	#4	1060084	1175	204	1224	0.174	7.16	0.07	0.718	9.98	0.50			
													9.2	**0.37**

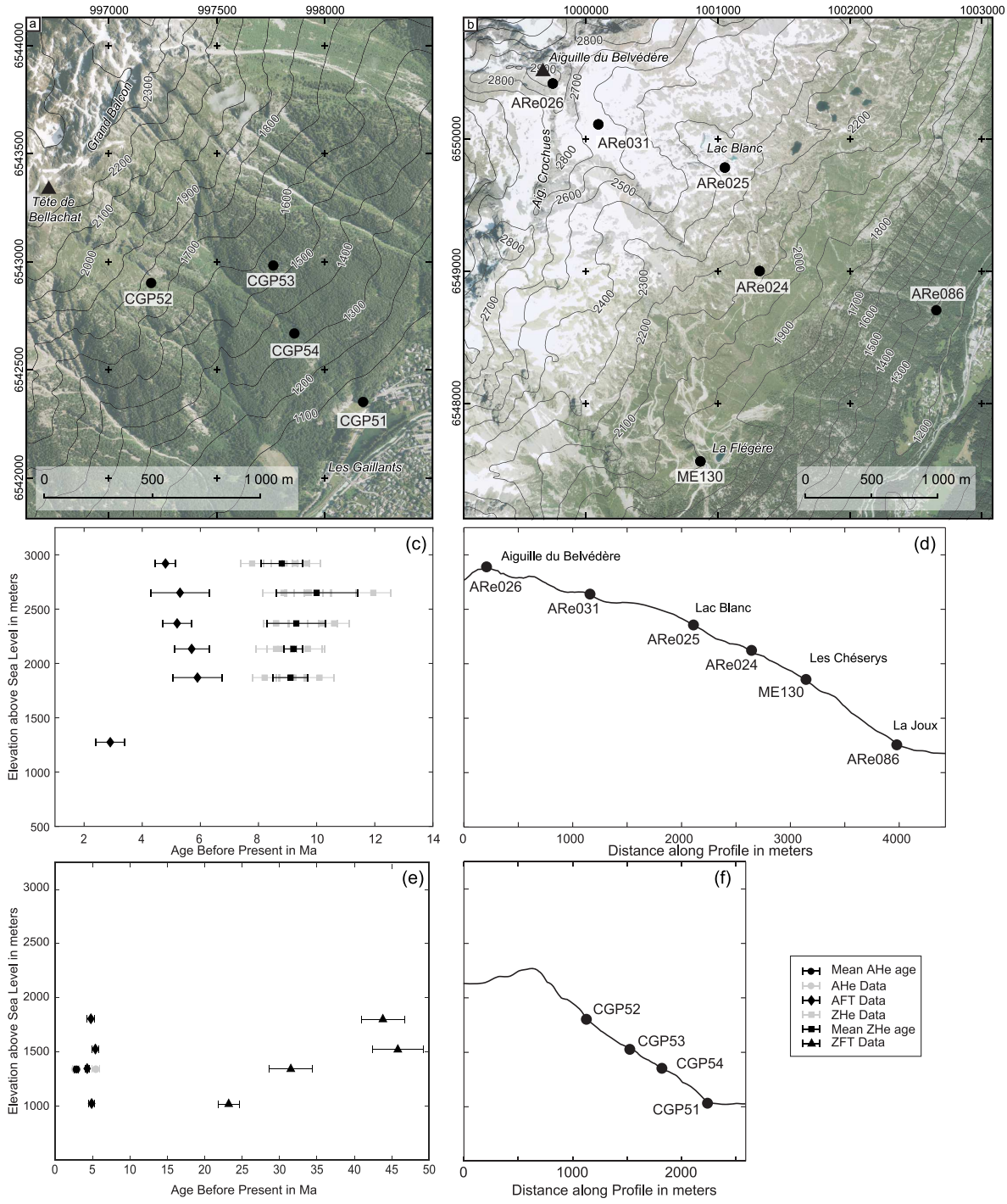

Figure 6.6. Location of the sampling regions. a-b) Aerial images of the sampling area: elevation contours from IGN 10-m resolution digital topography, overlain on orthorectified aerial photo mosaic from the Institut Géographique National, showing sample locations. Eastings and northings follow the Lambert93 grid in kilometers, projected on the RGF93 reference ellipsoid (RGF93/Lambert93 - EPSG2154); c and f show the age-elevation profile of both sampling sites along with (d and e) the associated topography profile (no vertical exaggeration) of the samples.

6.4.3 Qualitative interpretation

6.4.3.1 Age-Elevation relationship

From the Aiguilles Rouges, the AHE age-elevation relationship shows a nearly vertical slope (Figs. 6.6c and 6.7a), suggesting a rapid exhumation of the Aiguilles Rouges from 6 to 5 Ma that continued until 3 Ma. These results are in agreement with the AFT ages previously obtained in the Aiguilles Rouges (Seward and Mancktelow, 1994; Leloup et al., 2005) that obtained similar ages at similar elevations. Braun (2002) investigated the effects of relief changes on age elevation profiles and highlighted that a decrease in relief leads to a further overestimation of the exhumation rate and that a large decrease in relief can even lead to a negative slope. On the Mont-Blanc side, tens of AFT data have been obtained throughout the Mont-Blanc massif (Glotzbach et al., 2011; Leloup et al., 2005; Seward and Mancktelow, 1994; Soom, 1990), suggesting an exhumation from 7 to 5 Ma followed by a stagnation after 5 Ma. The AFTs of the Mont-Blanc massif show a clear positive correlation with elevation (Fig. 6.7). In the Aiguilles Rouges, the ZHE age elevation profile (Fig. 6.6) suggests a pulse in the exhumation rate in the Aiguilles Rouges ranging between 9 and 11 Ma. Boutoux et al. (2016) obtained ZHE ages ranging between 3.9 ± 0.2 and 7.8 ± 0.5 Ma in the Aiguilles Rouges, at lower elevation. Overall, the data, ZHE ages from the Aiguilles Rouges seem to be correlated with elevation and suggest an exhumation from 11 to 4 Ma. Other ZHE data have been obtained by Boutoux et al. (2016) at lower elevations in the massif, but the samples come from different parts of the massif and from a narrow elevation range (Δ = 302 m), making it difficult to interpret the age-elevation profile in terms of the apparent exhumation rate. ZFT data from the Mont-Blanc massif are significantly younger than those from the Aiguilles Rouges, suggesting that the Mont-Blanc was exhumed earlier. All AFT ages along the Mont-Blanc / Auguilles Rouges transect are similar between 3.4 and 4.5 Ma, implying that no differential movement has occurred since that time. All ZFT ages are similar between 11.2 and 13.5 Ma within the Mont-Blanc shear zone and the Mont-Blanc granite, suggesting that there is no significant vertical offset across the upper Mont-Blanc shear zone fault (angle fault) since then, as previously recognized by Glotzbach et al. (2008).

6.4.3.2 Pseudoelevation plot

We used newly acquired data and data from the literature to build a pseudoelevation plot (Fig. 6.6) (Reiners, 2003). The present elevation of the sample (H_s) is added to the depth at which its closure temperature (T_c) was at the time of closure for the closure temperatures used in the calculation). Pseudoelevation gives the elevation of the sample above its closure temperature (H_c) (Equation 6.6). The conversion from temperature to depth is given by an assumed fixed geothermal gradient. In the present case, we used 21 $^{\circ}\mathrm{C\,km^{-1}}$ (see Section

6.5.1.2). The value of the geothermal gradient is likely to change over time and with depth, which is a limitation of this graph.

$$H_c = \frac{T_c}{\Delta_g} + H_s \tag{6.6}$$

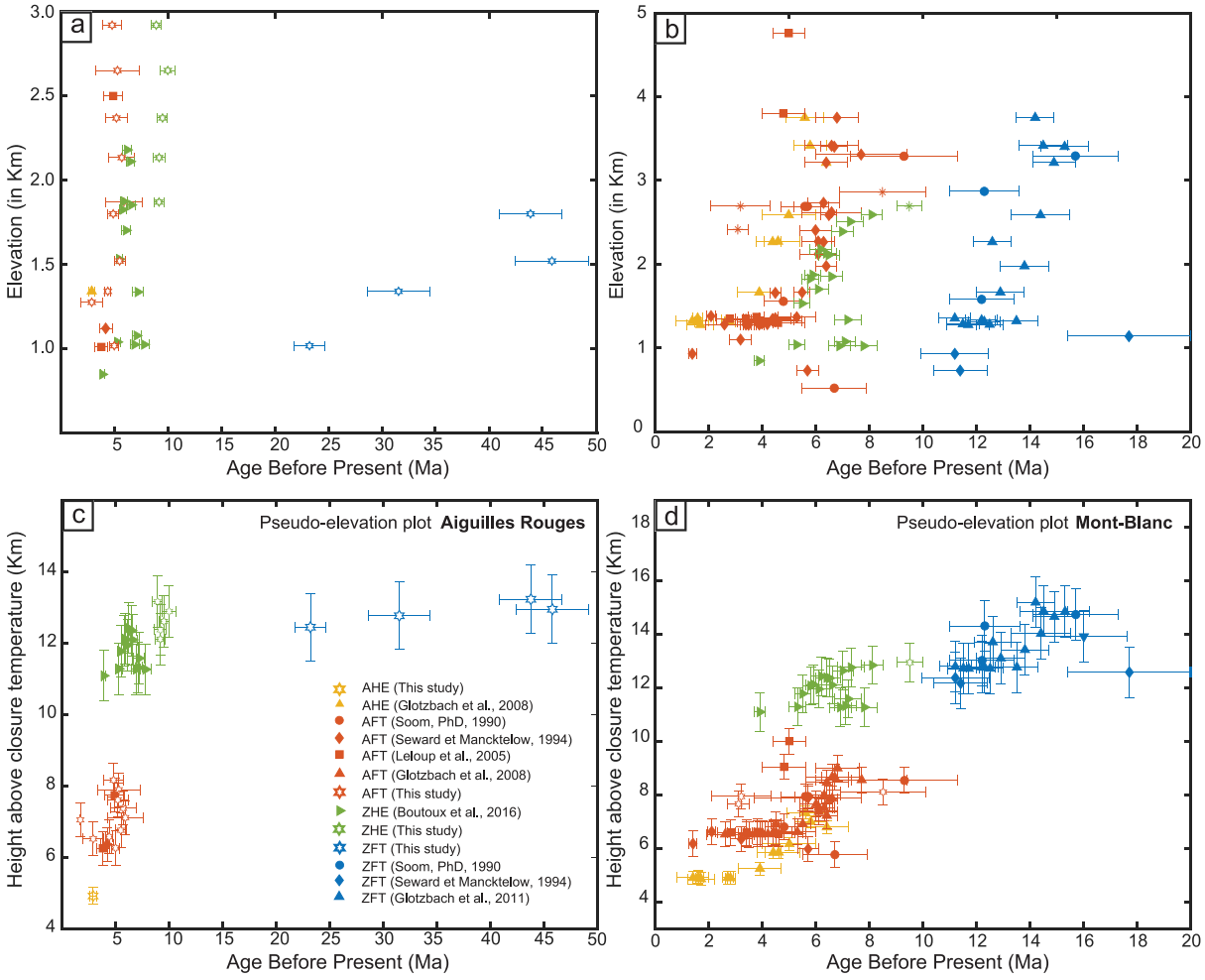

Figure 6.7. Age-elevation and pseudo-elevation plot for the Aiguilles Rouges and Mont-Blanc thermochronological data. a) Age-elevation plot of the Aiguilles Rouges data; b) Age-elevation plot for the Mont-Blanc data; c) Pseudo-elevation plot for the Aiguilles Rouges data, the present-day elevation of the sample is added to the depth at which its closure temperature was at the time of the closure. The geothermal gradient used to compute this plot is 21 $^{\circ}\mathrm{C\,km^{-1}}$ (see text for details.). Horizontal uncertainties are given by analytical error of the dating method, the error gives the vertical uncertainties on the closure temperature estimation; d) Pseudo-elevation plot for the Mont-Blanc data with the same characteristics as c. The legend is shared within the four plots.

The pseudo-elevation plot enables us to interpret the data in first order with all thermochronometers on the same plot. In Mont-Blanc, the peusdo elevation plot shows a coherent organization of the different thermochronometers according to the height above their closure temperature. The exhumation path displayed is stepped: the ZFT data show a slow dipping relation, suggesting that exhumation started from about 18 to 20 Ma. The ZHE data are quite

homogeneous at the same elevation above the closure temperature, suggesting a decrease in exhumation from 11 to 8 Ma. From 8 Ma, the AFT and AHE data are about 5 km lower in pseudo-elevation than the ZHE indicating an abrupt exhumation from approximately 8 Ma. In the Aiguilles Rouges, the ZFT ages range from 45.8 to 23.2 Ma, and within the uncertainties do not seem to display a change in their elevation above the closure temperature, suggesting that the massif has not experienced a particular cooling phase during this period. On the other hand, the ZHE and AFT data have similar ages ranging from 10.0 to 4.4 Ma, suggesting a rapid and late exhumation of the Aiguilles Rouges massif after about 10 Ma. In summary, from this qualitative interpretation, it seems that the Mont-Blanc experienced an exhumation from 18 to 20 Ma, while the exhumation of the Aiguilles Rouges does not seem to have started before about 10 Ma.

6.5 Methodology

Now that a qualitative interpretation of the observations has been carried out, let us further investigate and quantitatively estimate the exhumation of these massifs. To do so, we use numerical simulation to relate the exhumation history to observed thermochronological ages, and formulate an inverse problem to estimate the parameters describing the exhumation history.

6.5.1 Quantitative thermochronology through thermo-kinematic numerical simulation: *Pecube*

Thermochronological ages depend on the thermal evolution of the crust, which depends itself on the initial thermal structure, fault geometry, kinematics, and topographic surface evolution. To quantify this complex relationship, we performed a numerical simulation using the finite element code *Pecube*, originally developed by Braun (2003). The code is used for computing thermochronological data in terms of tectono-morphological scenarios by computing the thermal evolution of a crustal block. The thermal histories of rock samples are determined by solving the heat equation in three dimensions (Carslaw and Jaeger, 1947):

$$\rho c = \left(\frac{\partial T}{\partial t} + v_x \frac{\partial T}{\partial x} + v_y \frac{\partial T}{\partial y} + v_z \frac{\partial T}{\partial z} \right) = \frac{\partial}{\partial x} k \frac{\partial T}{\partial x} + \frac{\partial}{\partial y} k \frac{\partial T}{\partial y} + \frac{\partial}{\partial z} k \frac{\partial T}{\partial z} + \rho H \qquad (6.7)$$

- T: Temperature field (defined at each x, y, z position in space and t in time)
- ρ : The density of the crustal block ($\mathrm{kg\,m^{-3}}$).
- $v_{(x,y,z)}$: Components of rock velocity from the base of the crustal block (upward: denudation or downward: burial) representing exhumation ($\mathrm{km\,Ma^{-1}}$).

- k: Thermal conductivity ($\mathrm{W\,m^{-1}\,K^{-1}}$).
- H: Radioactive heat production rate ($\mathrm{W\,m^{-3}}$).

The performance and robustness of this algorithm for the simulation of thermal evolution have been demonstrated since the early studies and applied in various geological contexts (e.g., Braun, 2003; Braun et al., 2012; Robert et al., 2011; Van der Beek et al., 2010; Glotzbach et al., 2011; Glotzbach et al., 2008). The code has been upgraded and now considers the production of heat and the advection of the isotherm during exhumation (Braun et al., 2012). In this study, we used Pecube version 4.2.1 (`https://github.com/jeanbraun/Pecube`).

Geographically, the simulation encompasses an area of (40x40 km from $65.65°$E/$45.7°$N (southwest tip)) encompassing the Mont-Blanc and Aiguilles Rouges massifs. Temporarily, the simulation is defined with two clocks: one describing the timing of the topography evolution T^i_{topo} and one describing the timing of the denudation period or the activation of the fault (T^i_E, T^i_f, respectively). These two clocks may be tuned together or evolve independently. The evolution of relief during mountain construction may not be directly related to tectonic forcing. Therefore, it is necessary to let the two clocks evolve independently.

The general denudation rate (E_i) describes the uniform removal of material from the surface over the area. The topography amplitude (R_i) describes the elevation difference between the highest and lowest point. Thermochronology does not provide information on absolute surface elevation. Therefore, for each topographic time step (T^i_{topo}) the relief is expressed as a fraction of today's topography (h_{Today}) (Equation 6.8). *Pecube* considers an equilibrium between rock uplift velocity (V) and the erosion rate, implying that the rock uplift velocity field V is the exhumation rate. A fault divides the field velocity (and the data set) into a discrete plan. The fault motion (V_i) describes the velocity field parallel to the fault plane that affects one part of the crustal block. This fault velocity field is added to the general denudation. The surface topography digital elevation model (DEM) is provided by the Shuttle Radar Topography Mission (Farr et al., 2007), with a spatial resolution of approximately 650 m.

$$R_i = \frac{\Delta h_{Today}}{\Delta h_{TimeTopo_i}} \tag{6.8}$$

6.5.1.1 Fault parameters

The Mont-Blanc and Aiguilles Rouges massifs are separated by two major alpine thrust faults that have played an important role in their recent kinematics history: the Mont-Blanc shear zone and the Aiguilles Rouges back thrust (Fig. 6.4) (Leloup et al., 2005; Mercier et al., 2023). Since the code improvement of Robert et al. (2011), Pecube can split the crustal block and its velocity field with faults. The aim of this work is to investigate the differential

exhumation between these two massifs. We, therefore, implement a fictive vertical fault, running parallel to the Chamonix valley and that can vertically move the Mont-Blanc block in both senses (up or down). The velocity field associated with this fault adds up with the regional velocity field, leading to a differential exhumation between the two massifs at different time-step. Note that this approach is very similar to Bermudez et al. (2011).

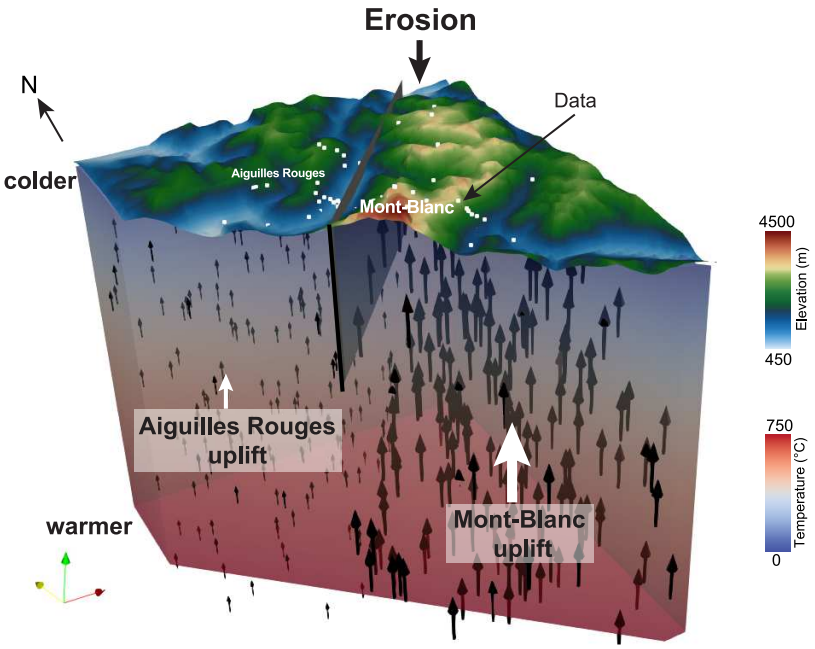

Figure 6.8. Crustal Thermal Pecube numerical simulation. The exhumation of the rocks results from regional erosion (the removal of materials from above). The rock uplift (induced by fault motion for example) moves upwards a block of material. The white spots are the rock samples dated in thermochronology used in the simulation. The fault used in the simulation crosses the entire block and is highlighted in black: the Mont-Blanc shear zone adds its velocity field to the regional velocity field to exhume faster than the Aiguilles Rouges. On the other way around, the Aiguilles Rouge back thrust permits to exhume faster the Aiguilles Rouges massif than the Mont-Blanc massif. The crustal thickness is of 35 km.

6.5.1.2 Thermal parameters

The thermal conditions of the crustal block are the key to properly simulate thermochronological ages because the cooling of the massif is directly dependent on these parameters (Seward and Mancktelow, 1994; Reiners et al., 2005). But the values of these thermal parameters are barely known in the crust and most likely evolved during orogen evolution. In an initial version of the simulation, we free the thermal parameters that control the basal temperature and the normalized heat production. The results lead the inversion to converge on an unrealistic exhumation scenario, largely overestimating the total exhumation. Subsequently, it was decided to fix the thermal parameters, based on the knowledge of the area.

From petrology, the highest pressure estimate during the Cenozoic in the Mont-Blanc

massif has been estimated at 0.50 ± 0.05 GPa and 400 ± 25 °C, determined based on independent mineral equilibria (Rolland et al., 2003). Using a crustal density of 2750 $\mathrm{kg\,m^{-3}}$, this pressure corresponds to a depth of about 19 km, estimating the maximum total amount of exhumation of the Mont-Blanc massif. Thermometric estimates from the bottom of sedimentary cover in the Morcles nappe above the Mont-Blanc massif have estimated that the temperature is 350 ± 20 °C from $\delta^{18}O$ in fluid inclusions (Kirschner et al., 1996). Using Raman spectroscopy applied to carbonic organic matter (RSCM), Girault et al. (2020) measured 325 ± 25 °C at a similar location. Further south in the Col du Bonhomme, in the southern tip of the Mont-Blanc massif, RSCM measurements gave 322 ± 18 °C and 336 ± 26 °C Dall'Asta et al., 2022. Finally, in the Aiguilles Rouges, the RSCM gave an estimate of 320 ± 25 °C (Boutoux et al., 2016). The estimation of the thickness of the overlying autochthonous and allochthonous sediments (Helvetic and Penninic nappes) eroded from above the massifs is approximately 12 to 15 km depending on the cross section considered (Leloup et al., 2005; Mercier et al., 2023). Extrapolating these values to the base of a 35 km thick crust corresponds to a geothermal gradient ranging from 21 to 29 $\mathrm{°C\,km^{-1}}$, typical of mountain building. In the following, the basal crustal temperature has been established at 730°C, corresponding to a geothermal gradient of 21 $\mathrm{°C\,km^{-1}}$. In comparison, thermal crustal models from Viganò and Martin (2007) have estimated the Moho temperature in the range of 700 to 800 °C. Heat production has been set to null because its importance in the upper part of the crust is negligible, as stated by previous simulations in the western Alps (Valla et al., 2010; Van der Beek et al., 2010).

In preliminary parameterizations, we used the isostatic rebound with free topography parameters, which led to a large over-exhumation (more than twice as expected) of the crustal block. Therefore, in the final results, the isostatic rebound has not been used, in the following parameterization, and thus set to null.

Parameter	Unit	Value
Crustal thickness	km	35
Crustal Density	$\mathrm{kg\,m^{-3}}$	2750
Mantle Density	$\mathrm{kg\,m^{-3}}$	3200
Thermal Diffusivity	$\mathrm{km^2\,Ma^{-1}}$	25
Temperature at sea level	°C	12.4
Atmospheric Lapse Rate	$\mathrm{°C\,km^{-1}}$	4.6
Nodes in z-direction		21
Grid spatial resolution	m	650m

Table 6.3. Thermal and crustal parameters sets within the Pecube numerical simulation.

6.5.2 Bayesian Inference: defining a posterior solution

As discussed above, thermochronological data depend on a wide variety of parameters, and these parameters are too numerous and cannot be inferred from the data. We will assume that some parameters remain fixed in the inversion and treat the others as unknown parameters to be estimated from the data. Hereafter, to explore the complex multidimensional parameter space, we used Pecube jointly with the Neighborhood Algorithm (NA) inversion code (Sambridge, 1999a), using the approach developed by (Braun and Robert, 2005; Valla et al., 2010; Van der Beek et al., 2010). NA inversion is used to find an optimum set of parameters to explain the data. Furthermore, coupled with Bayesian inference, this approach enables us to estimate the probability of model parameters m, given the observed data d_{obs}. From Bayes's Theorem, prior information on unknown parameters is combined with observed data to give the posterior probability function we are looking for (Fig. 6.9).

$$posterior \propto likelihood \times prior \tag{6.9}$$

$$p(m \mid d_{obs}) \propto p(d_{obs} \mid m) \times p(m) \tag{6.10}$$

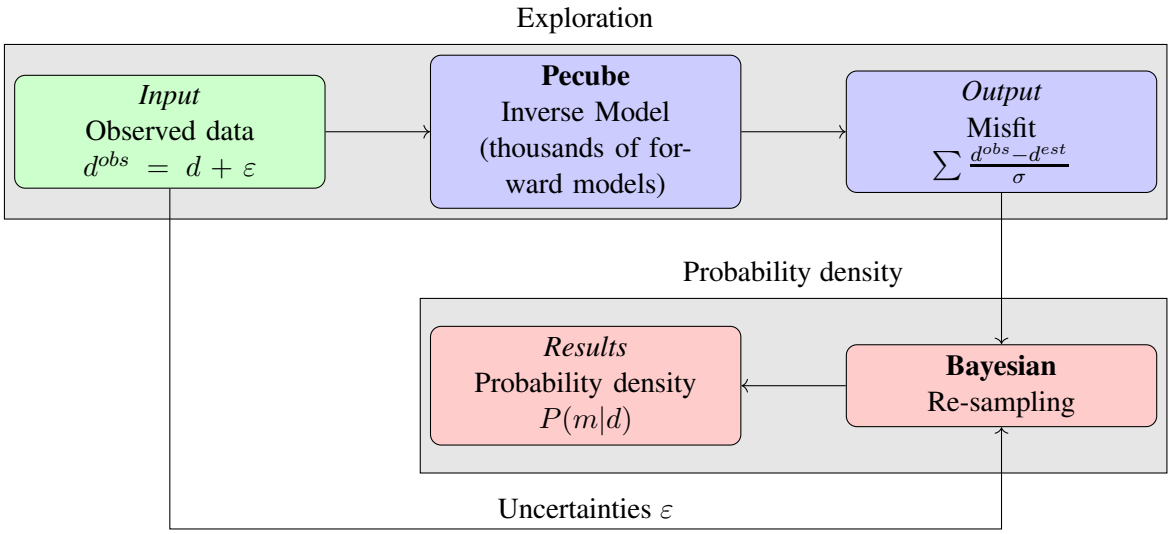

Figure 6.9. Modeling Workflow. The observed thermochronological data and their associated uncertainties are used as input in the Pecube code. Several direct models are performed by the neighborhood algorithm that explores the parameters. An associated misfit is calculated for each model calculation that quantifies the difference between the estimated and observed data. Next, the Bayesian Algorithm re-samples the models so that the model distribution is proportional to the probability density.

6.5.2.1 The likelihood function

For a given set of parameters, the likelihood distribution $p(d_{obs} \mid m)$ describes the probability of observing the thermochronological age data. To describe this distribution, uncertain-

ties must be associated with the data. That is, observed analytical errors (corresponding to the uncertainty bar on the plots) and an unknown theoretical error need to be estimated. In the following, we hypothesize that the unknown theoretical error is a Gaussian function.

$$d^{Obs} = d^{Pred} + \epsilon^{Obs} + \epsilon^{Theoretical} \tag{6.11}$$

$$L(o_i \mid p_i) = \frac{1}{\sqrt{2\pi\sigma_i^2}} exp\left(-\frac{o_i^2 - p_i^2}{2\sigma_i^2}\right) \tag{6.12}$$

6.5.2.2 The prior

The prior probability distribution describes the level of knowledge on the model parameters, independently of the data. Here, we choose to use a uniform distribution, and a *a priori* range is defined for each parameter. The parameter range to be explored must follow what we know from geology and what is physically realistic. Therefore, the topography amplification is set (fixed for all simulations) as null at the beginning of the simulation (no topography) and 1 at the end (present-day topography). The amplification is expected to occur during a single step from 20 Ma. Therefore, the time of amplification ranges from 20 to 0 in the inversion. The initiation of the simulation is also a free parameter that varies from 30 to 60 Ma.

6.5.3 Approximating the posterior probability distribution

6.5.3.1 Exploring the parameter space with the Neighborhood Algorithm

The NA explores the parameter space and runs thousands of forward models to find the set of parameters that maximize the posterior distribution, that is, parameter values that minimize the difference between observed (d_{obs}) and predicted data (d_{pred}).

To explore different parameterizations and the level of complexity, we performed simulations with increasing complexity (that is, number of unknown parameters) with a regionalized exhumation first for both Mont-Blanc and Aiguilles Rouges with uplift/burial rates ranging from -3 to 3 $\mathrm{km\,Ma^{-1}}$. Initiation of differential exhumation between massifs ranges from 30 to 15, with a time step ranging from 0 to 15. By qualitative interpretation, we do expect the end of motion along the Mont-Blanc shear zone to be around 11 to 12 Ma. The number of iterations was chosen according to the complexity of the model and the inspection of the evolution of the misfit during successive iterations, from 35 000 iterations for the simplest models to 55 000 for the most complex.

6.5.3.2 Sampling the posterior distribution

In the appraisal stage, the forward models resulting from the exploration stage are appraised with a Bayesian method that derives the posterior probability distribution of the parameters Sambridge, 1999b. In this case, the output ensemble of models is then distributed according to the target posterior probability distribution (see the input parameters of the Bayesian Neighborhood Algorithm in Table 6.4). In this way, plotting the distribution of the values selected for the ensemble solution can be used to represent marginals of the posterior probability, which are useful for interpretation. These distributions show the full knowledge we have about the model parameters, given the data. We combined the parameters for creating time evolution paths to build the output figures, shown as density plots.

Table 6.4. Input parameters for program Neighborhood Algorithm in the Bayesian stage

Forward Model Type	NA Approximation
Algorithm Type	Gibbs Sampler
Starting Point of 1st Random walk	Random
Quasi or Pseudo-random deviates	Pseudo
Seed for pseudo-random deviates	230728
Collection rate for accepting a model	1
Number of steps before refreshing distance list	2000

6.5.3.3 Choosing a level of complexity

The interpretation of the posterior solution in terms of geology requires the selection of a history. In terms of modeling results, we need to choose a model complexity. This step can be achieved using the Bayesian Inversion Criterion (BIC):

$$BIC = -2.lnL + k.ln(n) \tag{6.13}$$

With L the log-likelihood described above, k the number of free parameters, and n the number of observations. The BIC is computed from a single parametrization. The limitation of this criterion lies here: it is calculated from a single parametrization, although the aim of the Bayesian Inference is appraising the ensemble of models for extracting a probability. The best evaluation of the BIC would be to compute a BIC distribution along with the posterior distribution. This cannot be achieved with Pecube as the value of the likelihood function is not saved during the appraisal stage.

We computed the BIC using the median of the posterior distribution. Normally distributed variables are expressed as the mean $\pm$ standard deviation, while non-normally or skewed distributed variables are often expressed as the median and inter-quantile range. In our case, the

distributions are variable and often quasi-normally distributed, therefore we expressed the results of the posterior using the median of the distribution and a 65% deviation (1 σ). Moreover, the evaluation of the results with the BIC is one criterion for selecting the appropriate number of parameters, and the scientific pertinence of an output result regarding what is geologically realistic and what is known about an area must be taken into account to properly interpret the results.

6.5.4 Inversion of synthetic data: what can *Pecube* infer?

6.5.4.1 The design of a fictional scenario

To investigate the ability of our approach to retrieve exhumation history, we first performed inversions using synthetic data ($d^{Snthetic}$), generated using a known set of model parameters $g(m_{Scenario})$ and perturbed with a normally distributed random noise (ϵ) centered on 0 with a standard deviation of 0.8 Ma (parameterization SY002 to SY006). We also generated perturbed data using random noise with a standard deviation of 0.4 (parameterization SY008 to SY012) to quantify the effect of a lower perturbation on the result. The generated data are used as new input for inversion with the level of uncertainties in the data kept equal to the uncertainties in the observed data (= analytical uncertainty) (Fig. 6.10).

$$d^{Synthetic} = g(m_{Scenario}) + \epsilon \ (\mu = 0; \sigma = 0.8) \tag{6.14}$$

We design a true scenario with a complex but realistic exhumation history, implying a differential exhumation history between the Mont-Blanc and Aiguilles Rouges according to known faults in the massifs (Mont-Blanc shear zone and Aiguilles Rouges back thrusts). Recent studies have shown a Quaternary relief amplification (e.g., Valla et al., 2011), therefore, to evaluate the ability of the Pecube inversion to retrieve -or not- such a recent relief building, we conceptualized a synthetic model with a low topography before 5 Ma (less than 20% of today's topography) followed by a quick relief increase to reach the present topography. The designed scenario was chosen to generate realistic data similar to the observed data.

Inversions have been performed on the Aiguilles Rouges alone (parameterization ARxxx) and on the Mont-Blanc and Aiguilles Rouges together (parameterization MBxxx). Identically, the synthetic inversions have been performed in the Aiguilles Rouges alone (parameterization SYARx) and in the Mont-Blanc and Aiguilles Rouges together (parameterization SY00x).

6.5.4.2 Results on the inversion of synthetic data

In the simplest parameterization SYAR2 (Fig. 6.11), the inversion properly infers the latest exhumation rate (after about 10 Ma) and the topographic amplification. The burial phase

is always blurred and not properly inferred.

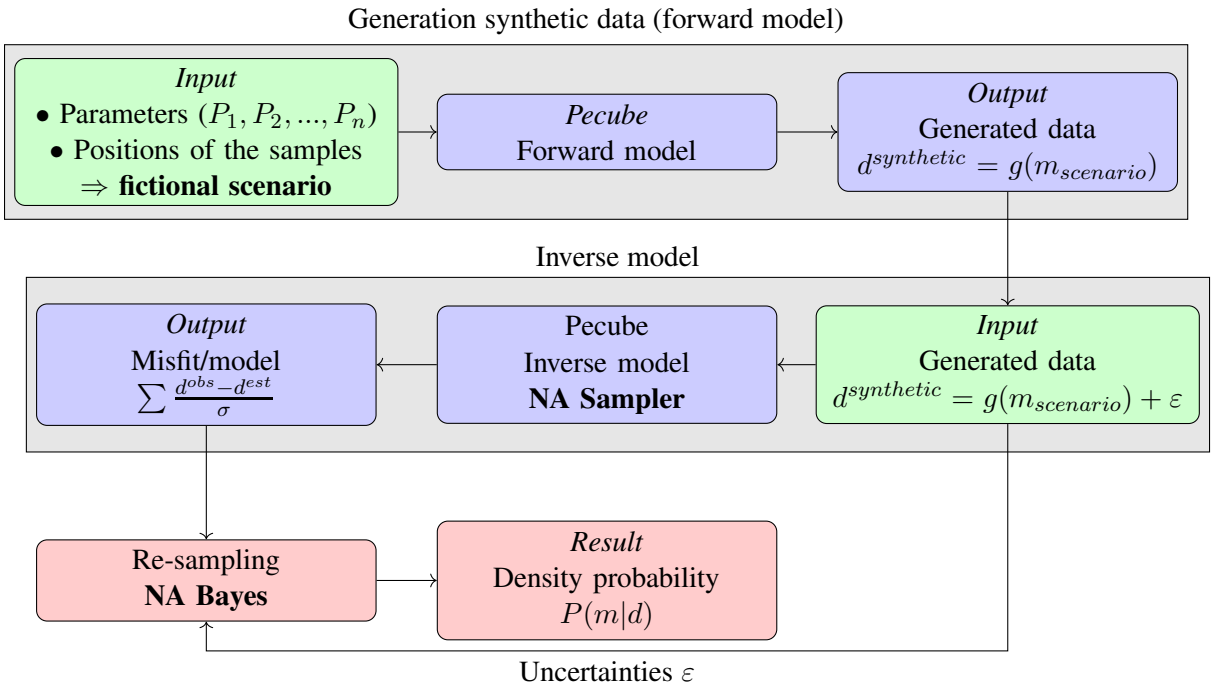

Figure 6.10. Workflow designed to generate synthetic data. The forward model is run with a fictional scenario (input parameters), with the location of the real measured samples. The output data are names *generated data*. A normally distributed random noise is added to these data and is now used as input data for the inverse modeling with the NA sample. The resampling is later performed with the NA Bayes, using the uncertainties of the initial data. The result is the probability density function $P(m|d)$.

From the Mont-Blanc massif, the best BIC is reached for the parameterization SY011, and the best fit is reached for the parameterization SY012. This last parameterization is the setup that has been used to generate the data, demonstrating that the inversion is able to reconstruct the "real" exhumation history because the dataset is sufficient. The inversion performed with the lowest random noise standard deviation (0.4) fit the data twice better, meaning that the fit is proportional to the dispersion. The exhumation rates are properly inferred, as well as the time changes. Interestingly, the topographic amplification occurs later than in the input scenario in the simplest parameterization (SY002 - SY004 and SY008 - SY010) but systematically earlier than in the synthetic scenario, for the parameterization SY005, SY006, SY011, and SY012. However, in these parameterizations, another probability maximum is highlighted at 5 Ma, the same as in the synthetic scenario.

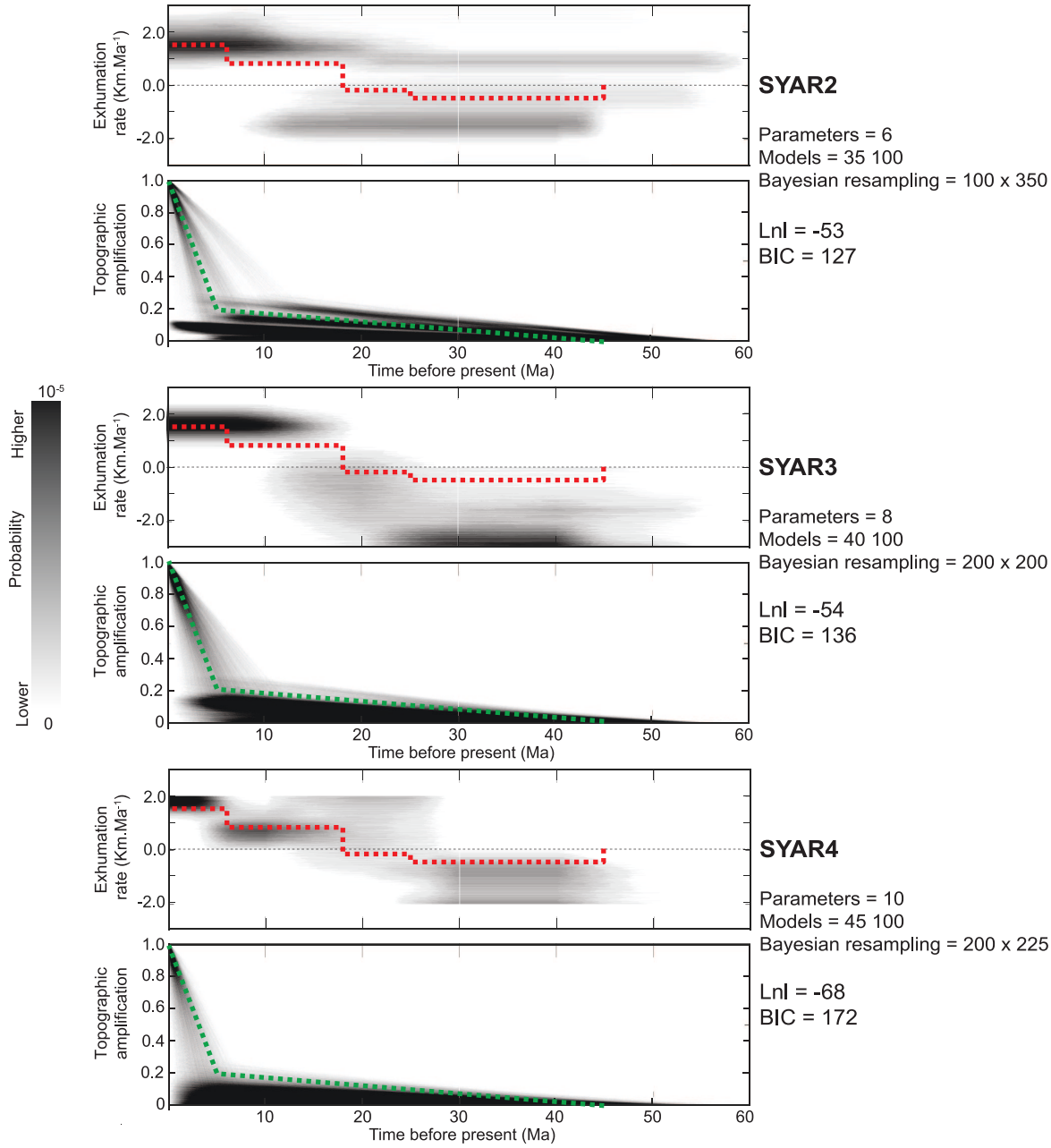

Figure 6.11. Inversion results of synthetic noised thermochronological data from the Aiguilles Rouges. For each inversion run, the ensemble solution for exhumation rate and topographic evolution is represented with a black-and-white density plot, giving an estimation of the posterior probability distribution. The red dotted line shows the true exhumation path of the massif and the green dotted line shows the true topographic evolution. The log-likelihood function and BIC are computed from the median value of the posterior probability distribution function.

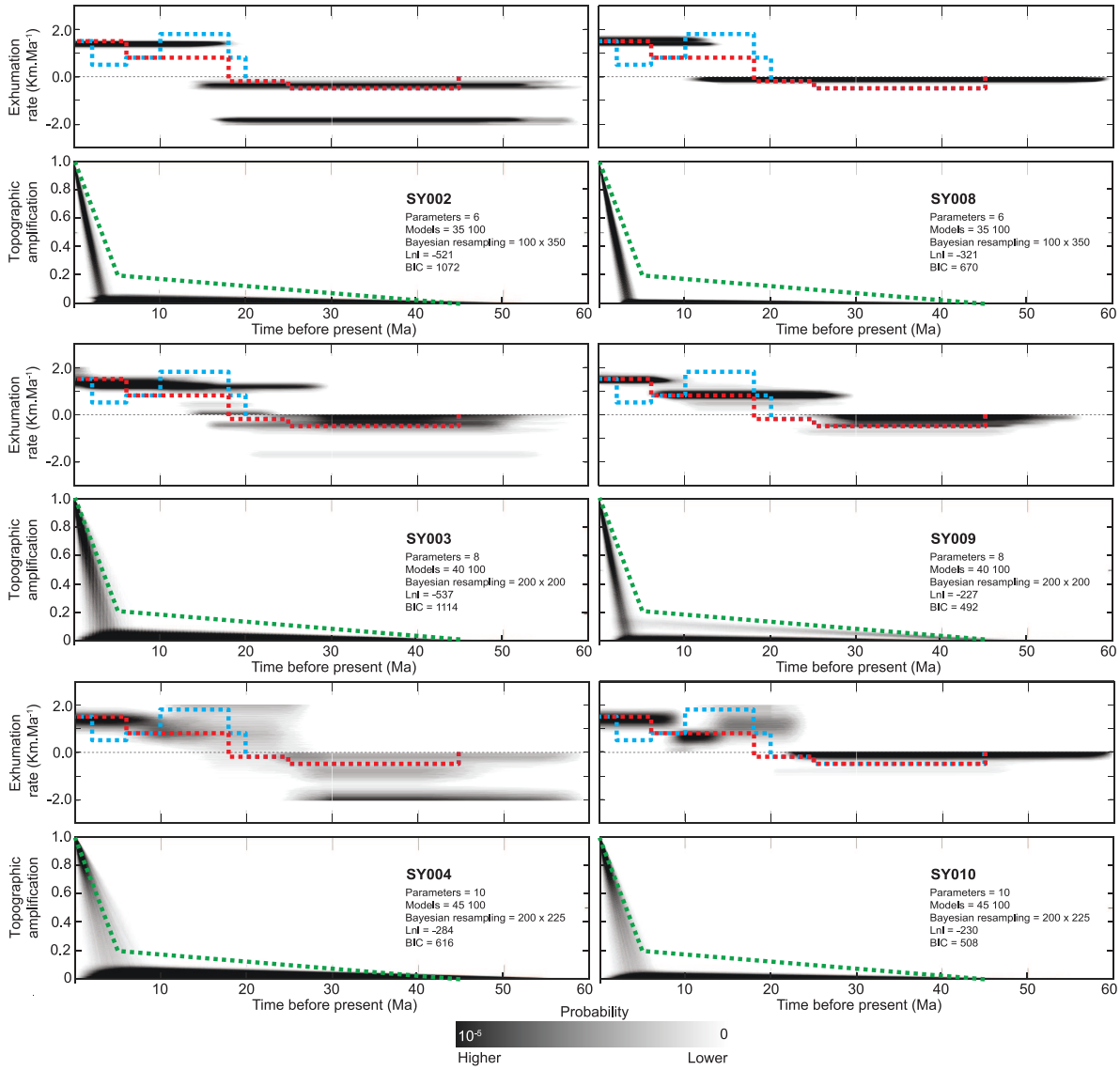

Figure 6.12. Inversion results of synthetic noised thermochronological data from the Mont-Blanc and Aiguilles Rouges with a regional exhumation. From parameterization SY002 to SY004 the random noise used to degrade the data has a standard deviation of 0.8, and 0.4 from parameterization SY008 to SY010. The ensemble solution for exhumation rate and topographic evolution is represented with a black-and-white density plot, giving an estimation of the posterior probability distribution. In the three presented parameterizations, the simulation does not allow a differential exhumation between Mont-Blanc and Aiguilles Rouges. The blue dotted line shows the true exhumation path of the Mont-Blanc massif, the red dotted line shows the true exhumation path of the Aiguilles Rouges massif and the green dotted line shows the true topographic evolution of both Mont-Blanc and Aiguilles Rouges. In all runs, the topographic amplification occurs later than in the true model.

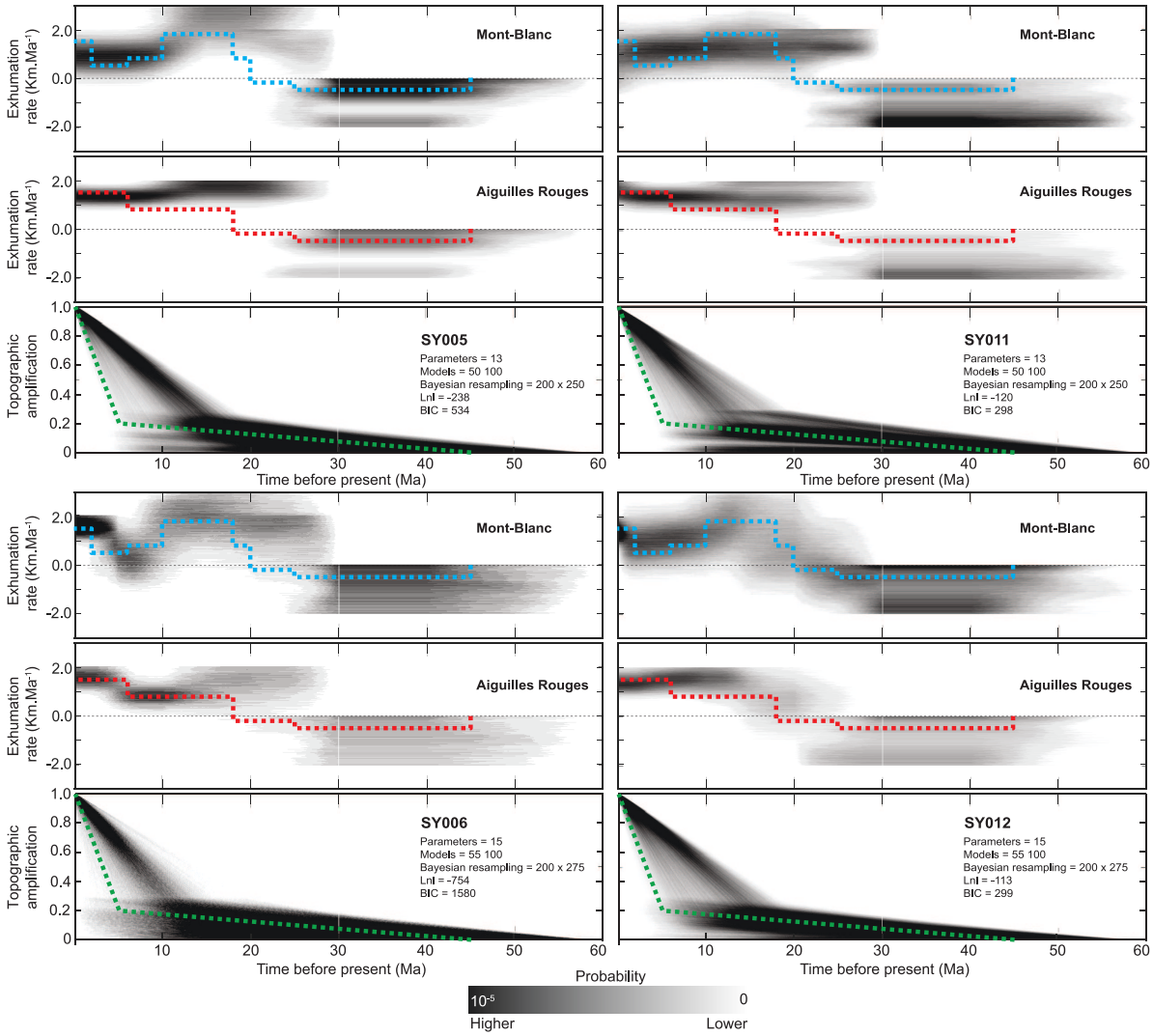

Figure 6.13. Inversion results of synthetic noised thermochronological data from the Mont-Blanc and Aiguilles Rouges with differential exhumation. In parameterization SY005 and SY006 the random noise used to degrade the data has a standard deviation of 0.8, and 0.4 from parameterization SY011 to SY012. The ensemble solution for exhumation rate and topographic evolution is represented with a black-and-white density plot, giving an estimation of the posterior probability distribution. In the presented parameterization, the simulation split the crustal blocks in two parts with the Aiguilles Rouges massif on one side and the Mont-Blanc massif on the other. The blue dotted line shows the true exhumation path of the Mont-Blanc massif, the red dotted line shows the true exhumation path of the Aiguilles Rouges massif and the green dotted line shows the true topographic evolution of both Mont-Blanc and Aiguilles Rouges. The best fit is reached with the more complex parameterization SY006. In these inversions, the topographic amplification occurs a bit earlier than in the true model.

6.6 Inversion of thermochronological data

The ability of our inversion approach to retrieve thermal histories has been evaluated for the current dataset; it is now possible to apply the same methodology to the real dataset. To do so, we performed the same inversion strategy on real data, starting with the Aiguilles Rouges alone and later encompassing both the Mont-Blanc and the Aiguilles Rouges.

6.6.1 Inversion results on the Aiguilles Rouges

The Aiguilles Rouges inversion explores the thermal-kinematic evolution of the massif with topographic evolution, exhumation, and burial during a period from 60 Ma before the present to today. The first parameterization investigates a burial phase before a single exhumation phase. The Aiguilles Rouges have been demonstrated to have been underthrusted below the Penninic Nappes first and later by the Helvetic Nappes before being exhumed by late steep thrusts (Leloup et al., 2005; Boutoux et al., 2016; Mercier et al., 2023). The transition timing between burial and exhumation is a free parameter ranging from 0 to 30 Ma and is estimated to be at 13.0 ± 1.0 Ma. The best BIC value is reached with the AR003 parameterization, with one phase of burial and two phases of exhumation. The results suggest that the massif began its exhumation at 11.1 ± 2.3 Ma with an exhumation rate of $1.3 \pm 0.2\ \mathrm{km\,Ma^{-1}}$. Finally, adding a third phase of possible exhumation (AR004 parameterization) does not improve the fit of the data. From all parameterizations, the topographic amplification occurs late, between 0.7 and 1.9 Ma. Comparison between observed data and predicted data computed from an exhumation model obtained from the median values of the posterior solution reveals that the data are relatively well predicted, except for ZFT data (Fig. 6.15). In brief, from the inversion results, the Aiguilles Rouges are most likely to have experienced an underthrusting phase before 11 Ma followed by a late and fast exhumation, with an exhumation rate greater than $1.3\ \mathrm{km\,Ma^{-1}}$).

6.6.2 Inversion results on the Mont-Blanc and Aiguilles Rouges

This inversion setup investigates the possibility of differential exhumation between the Mont-Blanc and Aiguilles Rouges massifs, due to the motion along the Mont-Blanc shear zone or the backthrust of the Aiguilles Rouges. First, inversions are performed without tectonic fault splitting the crustal block, to investigate the opposite hypothesis.

The first parameterization (MB002) investigates the transition time between burial and exhumation as a free parameter ranging from 0 to 60 Ma (Fig. 6.16 and Table 6.6). The results suggest a transition time at 21.1 ± 1.2 Ma. However, the estimated data poorly fit the observed data and therefore suggests that multiple exhumation phases are needed. The second parameterization (MB003) includes a second phase of exhumation that suggests a transition

Table 6.5. Thermal-kinematic (Pecube) inversion results of the Aiguilles Rouges models.

Parameters (unit)	Inversion Results								
	AR002			**AR003**			**AR004**		
	Range	Median	1σ	Range	Median	1σ	Range	Median	1σ
Relief Evolution									
T^1_{topo}	40 - 60	53.15	0.53	40 - 60	57.49	5.32	40 - 60	55.27	7.77
R_1	0	-	-	0	-	-	0	-	-
T^2_{topo}	0 - 20	1.32	0.36	0 - 20	0.71	2.18	0 - 20	1.88	2.83
R_2	0 - 0.3	0.098	0.011	0 - 0.3	0.12	0.18	0 - 0.3	0.090	0.12
Burial/Exhumation rate									
T^1_E (Ma)	40 - 60	T^1_{topo}	-	40 - 60	T^1_{topo}	-	40 - 60	T^1_{topo}	-
E_1 ($Km.Ma^{-1}$)	-3 - 0	-0.74	0.17	-3 - 0	-1.51	1.05	-3 - 0	-0.34	0.45
T^2_E (Ma)	0 - 30	13.00	0.95	20 - 40	34.76	6.09	20 - 40	33.74	14.90
E_2 ($Km.Ma^{-1}$)	0 - 3	1.20	0.081	-3 - 3	-0.18	0.57	-3 - 3	-0.14	0.87
T^3_E (Ma)	-	-	-	0 - 20	11.09	2.33	10 - 20	11.06	4.55
E_3 ($Km.Ma^{-1}$)	-	-	-	0 - 3	1.28	0.23	0 - 3	1.44	0.94
T^4_E (Ma)	-	-	-	-	-	-	0 - 10	2.36	6.21
E_4 ($Km.Ma^{-1}$)	-	-	-	-	-	-	0 - 3	0.70	0.89
Total exhumation (km)	-	15.60	-	-	14.17	-	-	14.23	-
Number of Models	35 100			40 100			45 100		
Bayesian re-sampling	100 x 350			200 x 200			200 x 225		
Number of Parameters	6			8			10		
Number of Data	36			36			36		
Log-likelihood	-209			-172			-277		
BIC	440			374			589		

Values of free parameters with 1σ uncertainty (65%) given by the NA-Bayes algorithm.
Log-likelihood and BIC are computed from the median value of the outputted distribution from the NA-Bayes algorithm.

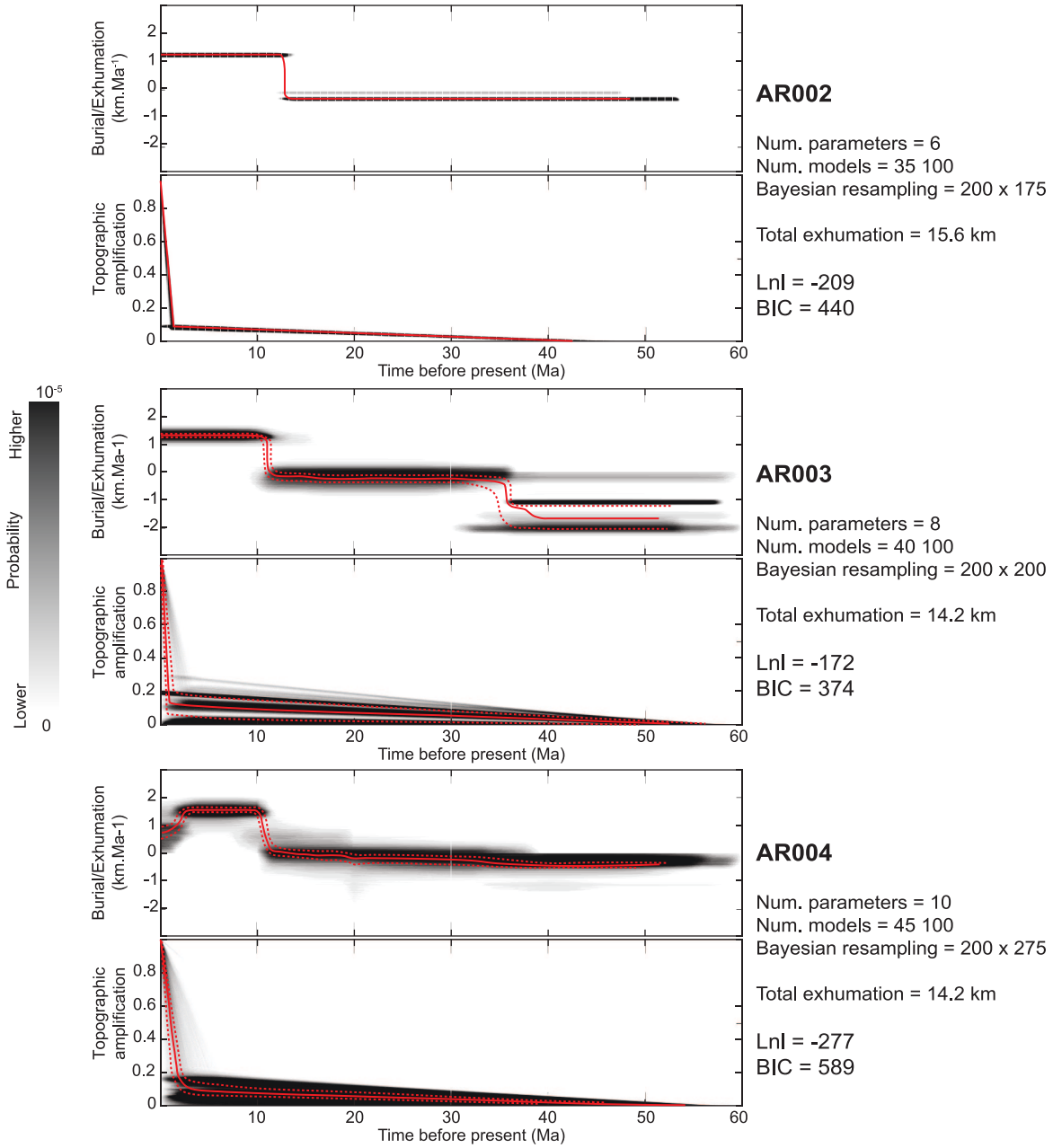

Figure 6.14. Results of the inversion of thermochronological data from the Aiguilles Rouges. For each parameterization (Table 6.5), the ensemble solution for exhumation rate and topographic evolution is represented with a black-and-white density plot, giving an estimation of the posterior probability distribution. The best BIC value is reached with the AR003 parameterization, with one phase of burial and two phases of exhumation. The results suggest that the massif began its exhumation at 11.1 ± 2.3 Ma with an exhumation rate of 1.3 ± 0.2 km Ma^{-1}.

from burial to exhumation at 28.8 ± 3.7 Ma with a low exhumation rate of 0.7 ± 0.2 km Ma^{-1} followed by a faster exhumation rate after 6.4 ± 1.9 Ma with an exhumation rate of 1.3 ± 0.2 km Ma^{-1}. The parameterization MB004 adds another exhumation phase that improves the fit to the data. The transition from burial to exhumation occurred after 25.5 ± 4.8 Ma with a rapid

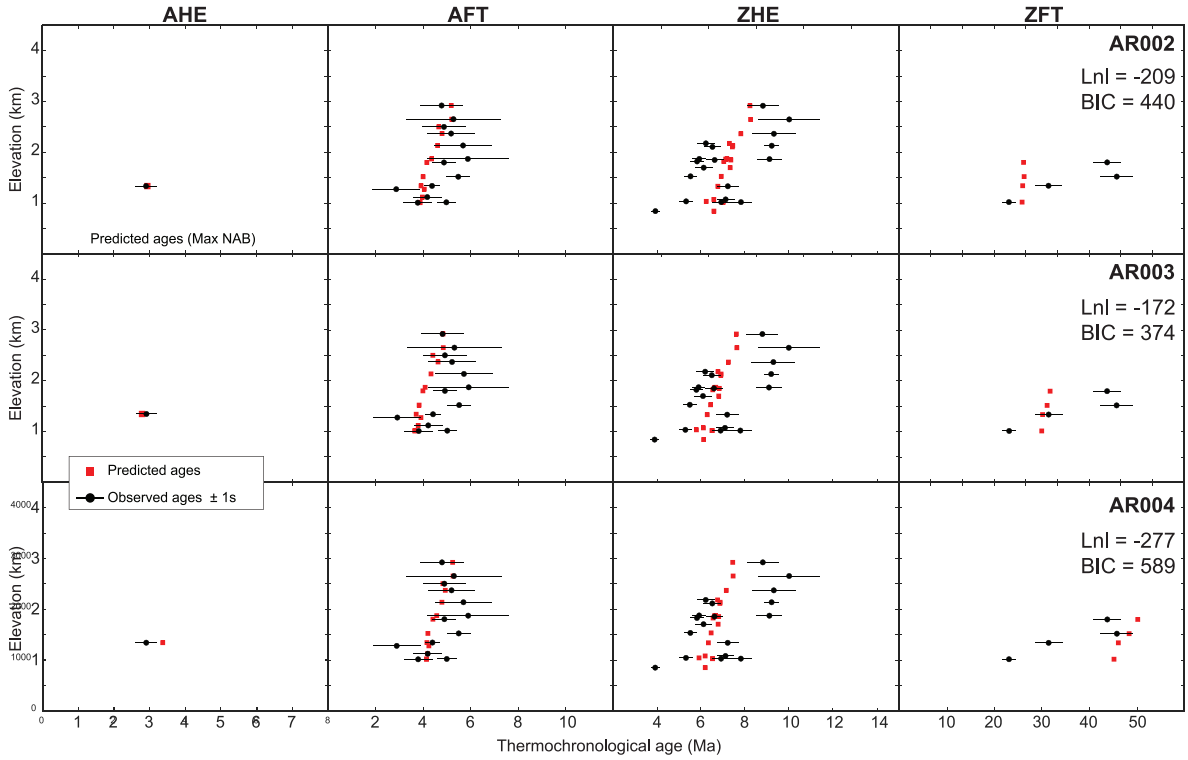

Figure 6.15. Comparison of observed and predicted thermochronological data from Aiguilles Rouges median solution of posterior distribution. The predicted ages are computed from the median values of the posterior solution on each parameter.

exhumation time period, followed by a slow exhumation at 13.6 ± 2.1 Ma. Finally, at 8.1 ± 1.5 the exhumation increases to 1.2 ± 0.3 km Ma^{-1}. In all of these first three parameterizations, the topography amplification starts from 16 to 18.5 Ma and progressively increases until today.

Parameterizations MB005 and MB006 split the crustal block into two parts using a fictive vertical fault that runs in the Chamonix valley. Parameterization MB005 reaches the best fit to the data, as well as the best BIC (Fig. 6.17 and Table 6.6). The results of this parameterization suggest an exhumation of the Aiguilles Rouges after 9.2 ± 2.7 Ma, Mont-Blanc was exhumed fast from 24.5 ± 4.7 to 12.8 ± 2.7 Ma and experienced a decrease in the exhumation rate until 9.2 ± 2.7 Ma, followed by an increase to 1.2 ± 0.5 to the present day. The results of the MB006 parameterization suggest that Aiguilles Rouges started to slowly exhume from 17.9 ± 6.2 at 0.3 ± 0.5 km Ma^{-1}. The exhumation increased after 5.6 ± 3.0 Ma to 1.5 ± 0.5 km Ma^{-1}. On the eastern side, Mont-Blanc was exhumed from 20.9 ± 7.4 to 12.1 ± 3.5 Ma, later experienced a drop in exhumation until 5.6 ± 3.0 and finally an increase in exhumation to 1.5 ± 0.5 km Ma^{-1} after 1.1 ± 1.9 Ma. Topographic amplification occurs after 16.5 ± 6.6 Ma in MB005, while in MB006 it occurs after 13.9 ± 11.5.

Table 6.6. Thermal-kinematic (Pecube) inversion results of the Mont-Blanc and Aiguilles Rouges models.

Parameters (unit)	Inversion Results														
	MB002			**MB003**			**MB004**			**MB005**			**MB006**		
	Range	Median	1σ	Range	Median	1σ	Range	Median	1σ	Range	Median	1σ	Range	Median	1σ
Relief Evolution															
Time Topo 1 (Ma)	40 - 60	41.42	13.47	40 - 60	56.04	14.24	40 - 60	55.52	6.31	40 - 60	45.76	7.55	40 - 60	47.02	8.57
Time Topo 2 (Ma)	0 - 20	18.50	2.04	0 - 20	16.36	3.67	0 - 20	18.29	4.84	0 - 20	16.54	6.57	0 - 20	13.94	11.50
Relief amplification	0 - 0.3	0.19	0.04	0 - 0.3	0.13	0.11	0 - 0.3	0.25	0.09	0 - 0.3	0.23	0.11	0 - 0.3	0.15	0.17
Burial/Exhumation rate															
Time step 1 (Ma)	40 - 60	T_{topo1}	-	40 - 60	T^1_{topo}	-	40 - 60	T^1_{topo}	-	40 - 60	T^1_{topo}	40 - 60	T^1_{topo}		
Burial rate 1($Km.Ma^{-1}$)	-3 - 0	-2.74	0.57	-2 - 0	-0.70	0.42	-2 - 0	-1.36	0.89	-2 - 0	-0.39	0.69	-2 - 0	-0.34	0.67
Time step 2 (Ma)	0 - 30	21.07	1.15	15 - 30	28.79	3.69	20 - 30	25.47	4.83	15 - 30	24.47	4.70	20 - 30	26.97	5.12
Exhumation rate 2($Km.Ma^{-1}$)	0 - 3	1.10	0.10	-2 - 2	0.65	0.20	-2 - 2	1.26	0.80	-2 - 2	0.12	0.69	-2 - 2	-0.08	1.09
Time step 3 (Ma)	-	-	-	0 - 15	6.42	0.62	10 - 20	13.64	2.06	0 - 15	9.21	2.70	10 - 20	17.89	6.17
Exhumation rate 3($Km.Ma^{-1}$)	-	-	-	0 -2	1.30	0.21	0 - 2	0.12	0.24	0 - 2	1.18	0.25	0 - 2	0.32	0.49
Time step 4 (Ma)	-	-	-	-	-	-	0 - 10	8.12	1.54	-	-	-	0 - 10	5.62	2.99
Exhumation rate 4($Km.Ma^{-1}$)	-	-	-	-	-	-	0 - 2	1.23	0.26	-	-	-	0 - 2	1.53	0.47
Differencial Exhumation (fault)															
Time start (Ma)	-	-	-	-	-	-	-	-	-	15 - 30	28.20	5.41	15 - 30	20.91	7.36
Velocity 1 ($Km.Ma^{-1}$)	-	-	-	-	-	-	-	-	-	-2 - 2	1.06	0.95	-2 - 2	1.38	1.07
Time step 2 (Ma)	-	-	-	-	-	-	-	-	-	0 - 15	12.82	2.74	0 - 15	12.05	3.49
Velocity 2 ($Km.Ma^{-1}$)	-	-	-	-	-	-	-	-	-	-2 - 2	0.03	0.46	-2 - 2	-0.81	1.24
Time end (Ma)	-	-	-	-	-	-	-	-	-	-	-	-	0 - 5	1.09	1.93
Total exhumation															
Mont-Blanc exhumation (Km)	-	23.12			22.96			24.80			28.00			19.03	
Aiguilles Rouges exhumation (Km)	-	-			-			-			12.70			12.50	
Number of parameters	6			8			10			12			15		
Number of Models	35 100			40 100			45 100			50 100			55 100		
Bayesian re-sampling	100 × 350			200 × 200			200 × 225			200 × 250			200 × 275		
Number of Data	117			117			117			117			117		
Log-likelihood	-968			-858			-844			-748			-776		
BIC	1974			1754			1738			1553			1624		

Values of free parameters with 1σ uncertainty (65%) given by the NA-Bayes algorithm.
Log-likelihood and BIC are computed from the median value of the outputted distribution from the NA-Bayes algorithm.

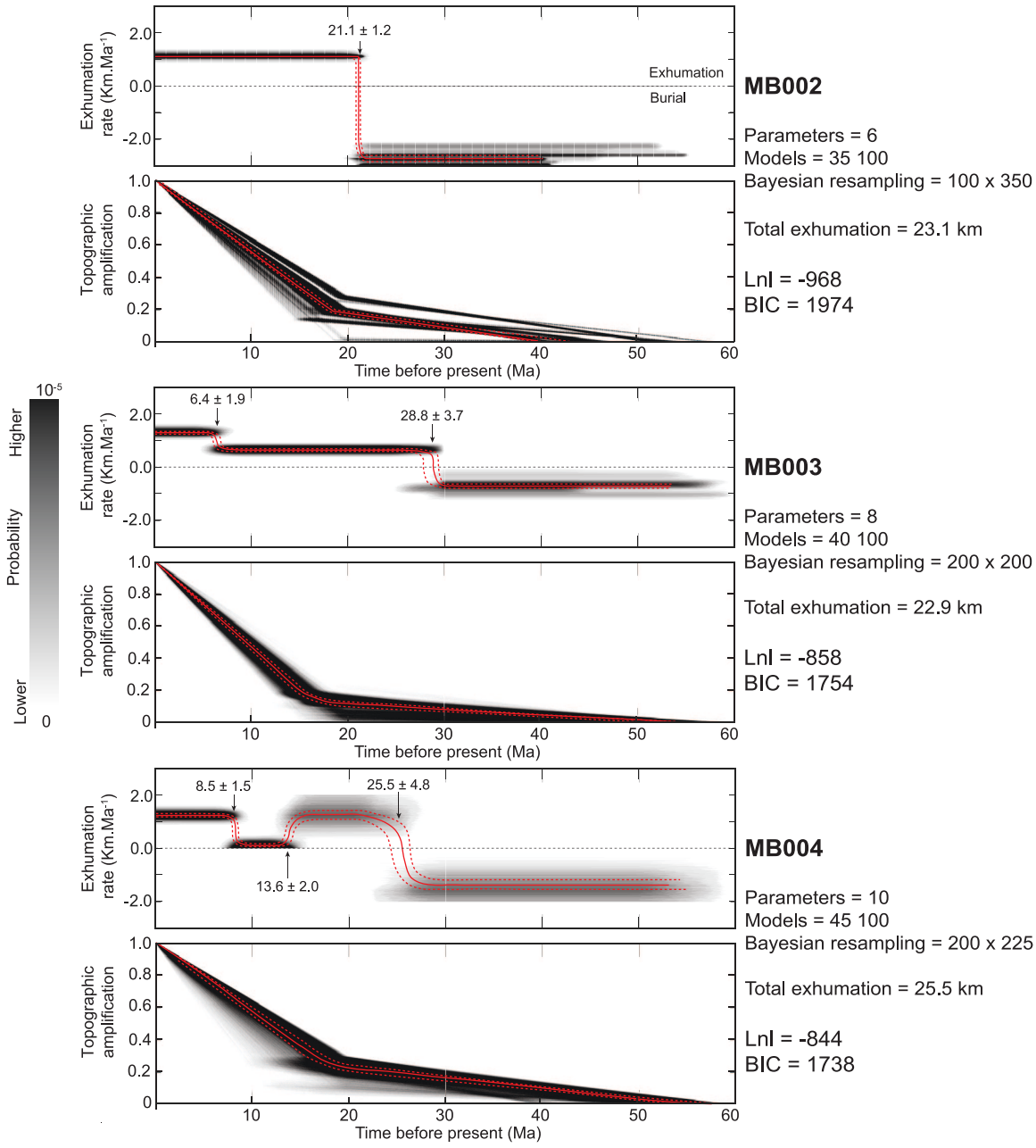

Figure 6.16. Results of the inversion of thermochronological data from the Mont-Blanc and Aiguilles Rouges **without** differential exhumation in between the two massifs. For each inversion run (MB002, MB003, and MB004), the ensemble solution for exhumation rate and topographic evolution is represented with a black-and-white density plot, giving an estimation of the posterior probability distribution. In the presented runs, the parameterization does not allow a differential exhumation between Mont-Blanc and Aiguilles Rouges. The red line shows the posterior median solution and the dotted line shows the 1σ uncertainties.

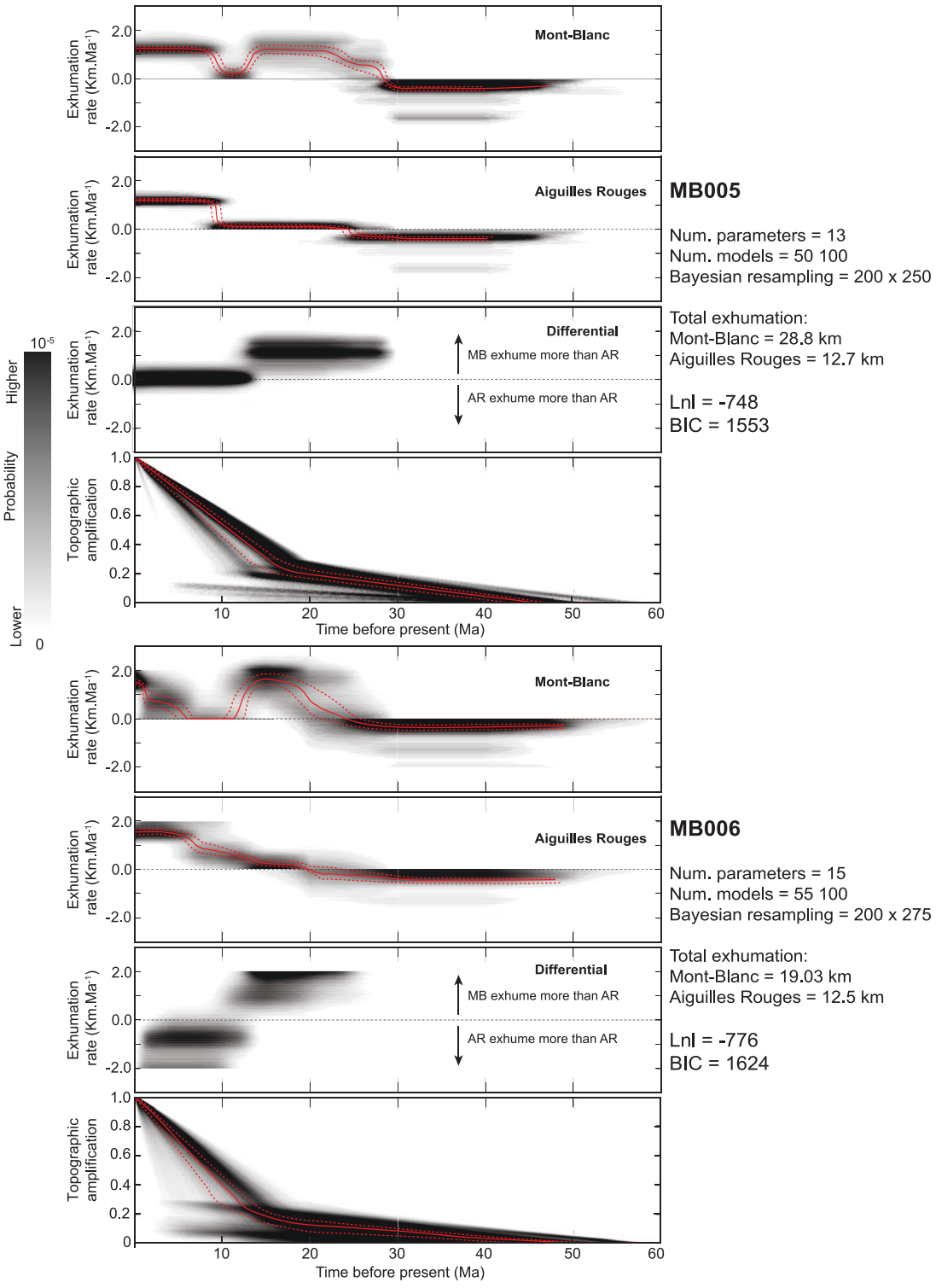

Figure 6.17. Results of the inversion of thermochronological data from the Mont-Blanc and Aiguilles Rouges **without** differential exhumation in between the two massifs. The ensemble solution for exhumation rate and topographic evolution is represented with a black-and-white density plot, giving an estimation of the posterior probability distribution. In the presented runs, the parameterization split the crustal blocks into two parts with the Aiguilles Rouges massif on one side and the Mont-Blanc massif on the other. The red line shows the posterior median solution and the dotted line shows the 1σ uncertainties.

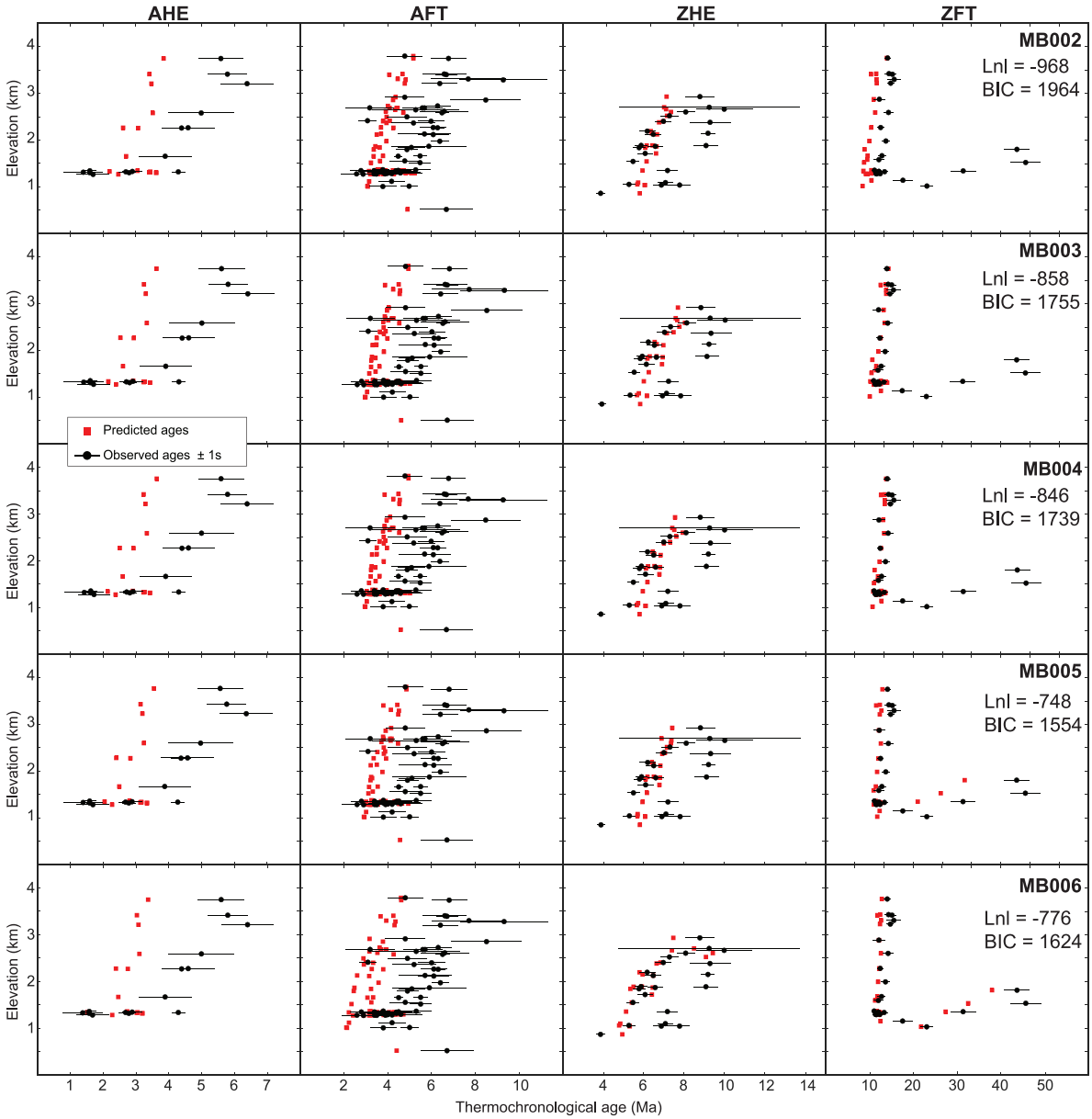

Figure 6.18. Comparison of observed and predicted thermochronological data for the parameter combination output from the median values of the posterior probability distribution functions.

6.7 Discussion

We performed inversions of thermochronological data from the Mont-Blanc and the Aiguilles Rouges massifs to unravel the exhumation history of these massifs. From the different parameterizations and levels of complexity, we need now to choose the most probable scenario. The best fit (lowest lnL value) is reached with parameterization MB005, however, the total amount of exhumation computed by this history for Mont-Blanc is largely overestimated (28 km), with respect to what is known about the exhumation of this massif: approximately 19 km (Rolland et al., 2003). Therefore, this scenario is likely unrealistic. However, the parameterization MB006 has a slightly lower fit to the data (higher lnL value), but the total amount of exhumation is more reasonable and corresponds to what is expected for this massif (19 km). Regarding the difference between observed and predicted data (Figs. 6.15 and 6.18), the fit of the data is high for several thermochronometers: the ZFT and ZHE are well estimated, even the oldest ages in the Aiguilles Rouges massif, but the predicted ages of AFT and AHE are systemically younger by about 2 Ma than the observed ages. This implies that the thermal histories and interpreted exhumation scenario could be erroneous inaccurate in the last millions years. Thermo-chronometers based on apatites are more sensitive to relief interaction. This difference could be due to oversimplified relief amplification modeling or to a varying geothermal gradient in the last million years of the exhumation history, as shown by the thermobarometric reconstruction of Leloup et al. (2005, fig. 7). Consequently, the increase in exhumation of both Mont-Blanc and Aiguilles Rouges after 1 Ma could, in fact occur earlier, between 4 to 6 Ma. In any case, further investigation is required to better predict the data, using more complex simulations for the relief evolution or improving Pecube to take into account varying geothermal gradients. Furthermore, the predicted ages presented in figure 6.18 result from a one parameterization with the median value of the posterior probability distribution, in the ensemble, the uncertainties in the estimation of the parameters reflect uncertainties in the observations. In summary, although the fit to the data and the BIC is slightly lower for the parameterization for MB006 than for MB005, the geological relevance of the result is a stronger argument, and thus the parameterization MB006 is the one retained to explain the exhumation of Mont-Blanc and Aiguilles Rouges.

The timing of amplification has a large uncertainty in the parameterization MB006, from the posterior probability density plot (Fig. 6.17), the topographic amplification has another maximum of amplification at about 5 Ma (Fig. D.5). In the inversion of synthetic data, topographic amplification was inferred to occur earlier. Therefore, there is the possibility that, in reality, the amplification occurred later than suggested by the inversion results.

The shear zone that separates the Aiguilles Rouges massif has been documented by several authors (e.g., Leloup et al., 2005; Egli et al., 2017). From thermobarometric estimates,

the differential exhumation between the Mont-Blanc and the Aiguilles Rouges was estimated between 2 and 8 km, in agreement with our findings. The absolute dating of synkinematic minerals crystallized during deformation along the Mont-Blanc shear zone yields ages from 14.30 to 21.8 (Leloup et al., 2005; Egli et al., 2017; Rolland et al., 2008) (see also Chap. 5). The timing of the differential exhumation between Mont-Bland and Aiguilles Rouges fits during the timing of activity along the Mont-Blanc shear zone, indicating that the exhumation is tectonically controlled during this period.

The findings are consistent with the inversion results presented by Glotzbach et al. (2011), which used the same approach to simulate the Mont-Blanc exhumation alone. Their results suggested an initiation of exhumation at 22 ± 2 Ma, followed by a decrease in exhumation at 6 ± 2 Ma, most likely lithologically controlled (crystalline rocks emerging through sedimentary cover) and a final increase in exhumation at 0.9 ± 0.8 Ma. On the contrary, our findings are not directly in agreement with the results of Boutoux et al. (2016), which used HeFTy to invert the ZHE data from the Aiguilles Rouges massif. The authors argue that Mont-Blanc reached its thermal peak at 10 to 15 Ma, while the Aiguilles Rouges reached its thermal peak between 5 and 10 Ma. Instead, we suggest that the Aiguilles Rouges reached their thermal peak earlier, at 12 to 17 Ma, underthrusted by the Mont-Blanc shear zone. In comparison, the Mont-Blanc reached its thermal peak at about 20 Ma, underthrusted by the Helvetic nappes and the Penninic nappes. Furthermore, Boutoux et al. (2016) proposed that Mont-Blanc and Aiguilles Rouges were exhumed together after 18 Ma, while we demonstrated that these massifs experienced differential exhumation. Their numerical simulation uses much fewer data (3 from Aiguilles Rouges and 3 from Mont-Blanc), and HeFTy does not allow splitting the dataset into several parts.

6.8 Conclusion

We have inverted thermochronological data to quantify the history of the exhumation of the Mont-Blanc and Aiguilles Rouges. The combined use of Pecube algorithm together with Bayesian inference overcomes the nonunicity of the problem and renders a density distribution function that quantifies the uncertainties in the parameters. The posterior distribution depends on the observational error (related to the analysis), the theoretical error (related to the incompatibility of Pecube to simulate the natural phenomena), and the number of observations (thermochronological data). We inverted synthetic data from known scenarios to evaluate the ability of the numerical simulation to retrieve the parameters.

The massifs probably experienced a differential exhumation history after an underthrusting phase until about 21 Ma (Fig. 6.19). The Mont-Blanc massif was quickly exhumed from 21 to 12 Ma, and later the massif experienced an abrupt drop in its exhumation. The Aigu-

illes Rouges started to exhume after 12 Ma, before an acceleration after 6 Ma. The differential exhumation between the two massifs stopped at about 1 Ma, and both experienced a fast exhumation phase. This last part of the scenario must be taken with caution because the data (AFT and AHE) are not well fit according to this scenario. Furthermore, the acceleration in the exhumation could have occurred earlier, possibly from 4 to 6 Ma. The total differential exhumation between Mont-Blanc and the Aiguilles Rouges is on the order of about 7 km. In the Miocene, the timing of differential exhumation between Mont-Bland and Aiguilles Rouges is coeval with the activity along the Mont-Blanc shear zone, indicating that the exhumation is controlled by tectonic forces during this period.

To broaden the discussion to the other External Crystalline massifs, Girault et al. (2022) suggested a continuous exhumation since 18 Ma, using a similar methodology of Boutoux et al. (2016) with QtQt (Gallagher, 2012). Using the inversion of thermochronological data applied in the Ecrins massifs (south of Belledonne), Van der Beek et al. (2010) found a drop in exhumation from 6.0 ± 3.3 Ma to 5.5 ± 3.3 Ma. Through this work we suggest that the approach of Pecube coupled with Bayesian inference (Sambridge, 1999a; Sambridge, 1999b) is more robust for inferring the exhumation in the case of the western Alps. Most likely because Pecube takes into account the relief amplification and QtQt much fewer data.

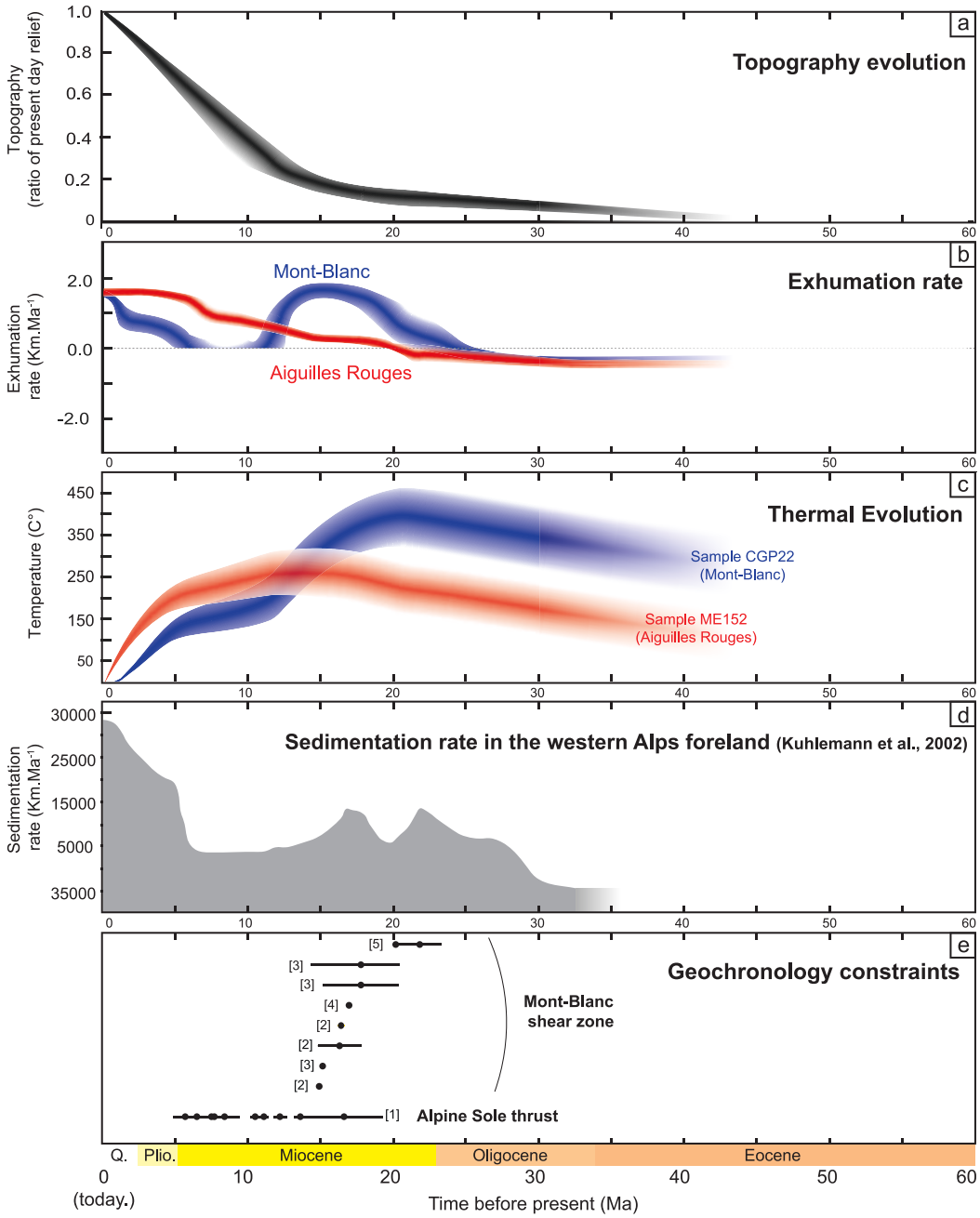

Figure 6.19. Overall exhumation history and topography evolution of Mont-Blanc and Aiguilles Rouges, computed from the parameterization MB006. a) Topography evolution; b) Exhumation rate evolution; c) Time-temperature path computed for samples CGP22 (at 2587 m of elevation) (Glotzbach et al., 2011) in the Mont-Blanc massif, and ME152 (Leloup et al., 2005) (at 2500 m of elevation) in the Aiguilles Rouges: the Mont-Blanc massif reached its thermal peak around 21 Ma while the Aiguilles Rouges reached its thermal peak around 12 to 17 Ma. d) Cumulative sediment discharge rates of the Western Alps (Kuhlemann et al., 2001; Kuhlemann et al., 2002); e) Geochronology $^{40}Ar/^{39}Ar$ data along the Mont-Blanc shear zone; references are: [1]: Bilau et al. (2023); [2]: This study; [3]: Egli et al. (2017); Rolland et al. (2008); [4]: Leloup et al. (2005); [5]: Rolland et al. (2003)

6.9 Data availability

All the data from this work, including the thermochronological data, input parameterization of Pecube, parameter exploration results, and Bayesian resampling are available in a repository at `https://data.mendeley.com/datasets/4dn8v2r2fc/1`.

Acknowledgments

This study was supported by INSU-CNRS through the "FEI-UMR5276-Dotation Performance 2022". It forms part of the Ph.D. project of Antoine Mercier at Université Claude Bernard Lyon 1, supported by the French Ministry of Research, Higher Education and Innovation. The computations were performed by the Geodcalctb cluster of the Laboratoire de Géologie de Lyon. The authors thank Jean Braun and Pierre Valla for the helpful discussions and advice that helped in this work.

Chapter's key points

- We inverted new thermochronological data to quantify the differential exhumation between the Mont-Blanc and Aiguilles Rouges massifs
- We applied a method using Bayesian inference coupled with thermochronological simulation and the Pecube algorithm.
- Inversion of synthetic data in general by known direct models has assessed the ability of the method and data to quantify each parameter.
- The Mont-Blanc massif was exhumed about 7 km more than the Aiguilles rouges.
- The Mont-Blanc began to exhume after 21 Ma, until 12 with the Mont-Blanc shear zone, while the Aiguilles Rouges did not exhume.
- The Aiguilles Rouges started to exhume after 12 Ma, before a phase of acceleration after 6 Ma.
- After 1 Ma, the two massifs experienced a common phase of rapid exhumation most likely related to glacial valley incision.

Part IV

DISCUSSION, IMPLICATIONS AND CONCLUSIONS

Chapter 7

Discussion and implications

Southwestern face of Petite and Grande Dents de Morcles (Valais, Switzerland). Photo: Philippe Hervé Leloup (august 2021).

In the following synthesis, we will discuss the total amount of exhumation of these massifs during the Cenozoic, later we will compile the constraints on the timing of Cenozoic deformations, and we will finally discuss the implications of these results on the evolution of the Alps and the Alpine orogenic wedge.

7.1 Implications in the structural evolution of Mont-Blanc and Aiguilles Rouges

7.1.1 Amount of Cenozoic Exhumation

The Cenozoic shortening has led to the exhumation and high altitude of the Aiguilles Rouges and Mont-Blanc ranges. It is now established that the basal layer of Triassic sandstone is widely distributed within the western external Alps and can be taken as a reference layer for post-Triassic deformations. This level is found subhorizontal at about -3000 m (asl.) in the Brizon well (46.03617N; 6.441525E [WGS84]), about 30 km north-west of Chamonix (Charollais and Jamet, 1990). Therefore, the altitude variation of the Triassic sandstone level can give a relative uplift with respect to that location. Atop the Aiguilles Rouges, below the Aiguille du Belvédère summit at 2965 m (asl.), it is found nearly horizontal (Fig. 4.17), implying approximately 6 km of relative uplift of the central Aiguilles Rouges (Fig. 7.1). Note that the altitude difference could be partly due to normal faulting from the Mesozoic or Eocene. However, the only normal faults that have been described between the Aiguilles Rouges and the Brizon well are from the Eocene and lead to negligible uplift of the Aiguilles Rouges (Butler et al., 2018).

The corresponding exhumation can also be estimated from the thickness of autochthonous and allochthonous sediments (Helvetic and Penninic nappes) that have been eroded at the top of the ranges. For the Aiguilles Rouges, it amounts to 12 to 15 km depending on the cross section considered (Escher et al., 1988; Escher et al., 1993; Pfiffner, 2014). The temperatures at the top of the basement before exhumation have been estimated to be between $350 \pm 20\ ^{\circ}\mathrm{C}$ from δ18O (Kirschner et al., 1995) and $325 \pm 25^{\circ}\mathrm{C}$ from RSCM (Girault et al., 2020) below the Morcles Nappe in Switzerland and $320 \pm 25^{\circ}\mathrm{C}$ from RSCM in the south of the Aiguilles Rouges (Boutoux et al., 2016). This corresponds to a thermal gradient between 20 and 31 $^{\circ}\mathrm{C\,km^{-1}}$, typical of mountain belts. Note that similar temperatures at the top of the basement in Morcles and the southern Aiguilles Rouges strongly suggest that both locations were buried at the same depth and therefore both overlaid by the Helvetic and Penninic nappes, confirming our description of the Morcles nappe at the top of the Aiguilles Rouges.

In Mont-Blanc, the Triassic sandstones outcrop both in the south (Col du Bonhomme) and the north (Catogne), but not at the top of the range, where they have been most likely eroded. The relative uplift of Mont-Blanc can be estimated with respect to the Brizon drill

hole: approximately 5.6 km in the south (Col du Bonhomme), ≥7.8 km near the Mont-Blanc summit, and 5.3 km in the north (Catogne) (Fig. 7.1). These values are lower bounds as they do not consider the layer tilt. Note that part of this uplift could result from Mesozoic and/or Cenozoic normal faulting. It is now well documented that part of the Mont-Blanc range was eroded during the Pliensbachian resulting in the sedimentation of "Grès Singuliers" and had therefore been exhumed before that time (Trumpy, 1971; Eltchaninoff, 1982; Ribes et al., 2020; Dall'Asta et al., 2022). However, no large normal fault has yet been found between the Mont-Blanc and the Aiguilles Rouges. The highest pressure estimate published in Mont-Blanc for the Cenozoic is 0.50 ± 0.05 GPa and 400 ± 25 °C (Rolland et al., 2003), from the MB140 sample at the Helbronner summit. This corresponds to a depth of 17 to 20 km, assuming a rock density of 2700 $\mathrm{kg\,m^{-3}}$ and implies an average thermal gradient of 18.5 to 26 $\mathrm{°C\,km^{-1}}$. These values imply 2 to 8 km more exhumation in the Mont-Blanc than in the Aiguilles Rouges. Note that this exhumation cannot be due to Mesozoic or Cenozoic normal faulting. From the PerpleX calculation on the composition of white mica, we estimate conditions of about 500°C and 0.47 to 0.66 GPa for the ARe001 sample, at the base of the Mont-Blanc shear zone (Fig. 5.9). This corresponds to a depth of 17 to 24 km and a geothermal gradient of 20 to 29 $\mathrm{°C\,km^{-1}}$, consistent with the estimate of Rolland et al. (2003). Three temperature estimates from RSCM measurements in the Col du Bonhomme area are between 322 ± 18 and 336 ± 26 °C (Dall'Asta et al., 2022), similar to those at the base of the Morcles nappe, suggesting a comparable amount of overlying autochthonous and allochthonous sediments (Helvetic and Penninic nappes) before exhumation.

Along the nearly horizontal transect (elevations between 1010 and 1350 m asl) perpendicular to the Chamonix valley at the level of the Mont-Blanc tunnel all zircon fission track ages are similar between 11.2 and 13.5 Ma within the Mont-Blanc shear zone (2 samples) and the Mont-Blanc granite (3 samples), suggesting that no significant vertical offset occurred across the Mont-Blanc shear zone and the Angle fault since that time (Glotzbach et al., 2011). From the Aiguilles Rouges, the ZFT newly acquired during this work gave ages ranging from 23.2 ± 1.4 to 45.8 ± 3.4 Ma (Fig. 6.7). This difference suggests that the Mont-Blanc massif has begun its exhumation before the Aiguilles Rouges massif. Glotzbach et al. (2011) proposed thermokinematic simulation with Pecube algorithm of a set of low-temperature thermochronology ages (Zircon and Apatite fission track and Apatite U/He) of the Mont-Blanc suggests an episodic exhumation with initiation at 22 ± 2 Ma with a rate of 0.80 ± 0.15 $\mathrm{km\,Ma^{-1}}$, which decreases to values of $0\,15(0\,65)$ $\mathrm{km\,Ma^{-1}}$ at $6(2)$ Ma, and finally increases to $2\,0(0\,6)$ $\mathrm{km\,Ma^{-1}}$ at $1\,7(0\,8)$ Ma (Glotzbach et al., 2011) (Fig.7.2). A phase of relatively fast cooling of the Mont-Blanc before 6 Ma followed by a slow cooling phase was also suggested from apatites fission track and U/He data alone (Glotzbach et al., 2008). The total amount of exhumation calculated from the most probable simulations of Glotzbach et al. (2011) is 21.6 km for the Mont-Blanc.

HeFTy models of one Zircon fission track, two Zircon U/He, one Apatite fission track and one Apatite U/He ages between 2500 and 2600 m of altitude within and in the hanging wall of the Mont-Blanc shear zone indicate continuous cooling since $18(2)$ Ma at an exhumation rate of approximately 1 $\mathrm{km\,Ma^{-1}}$ with possibly increased cooling at 18 to 14 and 8 to 4 Ma (Boutoux et al., 2016) (Fig.7.2). The average cooling histories of the Mont-Blanc and Aiguilles Rouges models converge at about 11 Ma (Boutoux et al., 2016), which could indicate the end of the motion along the Mont-Blanc shear zone and the back thrust of the Aiguilles Rouges. However, considering the full range of possible models, the cooling histories of the two ranges may have converged between 18 and 6 Ma.

Our findings (Chap. 6) confirm that Mont-Blanc and Aiguilles Rouges experienced a differential exhumation between 21 and 12 Ma, most likely due to motion along the Mont-Blanc shear zone. During this period, the Mont-Blanc was exhumed at a rate of approximately 1.7 $\mathrm{km\,Ma^{-1}}$. The Aiguilles Rouges slowly began to exhume after 12 Ma, before a phase of acceleration at a rate of approximately 1.5 $\mathrm{km\,Ma^{-1}}$ after 6 Ma. The numerical Pecube simulations estimated the total amount of exhumation to be on the order of 19 km for the Mont-Blanc massif and 12.5 km for the Aiguilles Rouges. Our estimation is slightly lower than the 22 km proposed by Glotzbach et al. (2011).

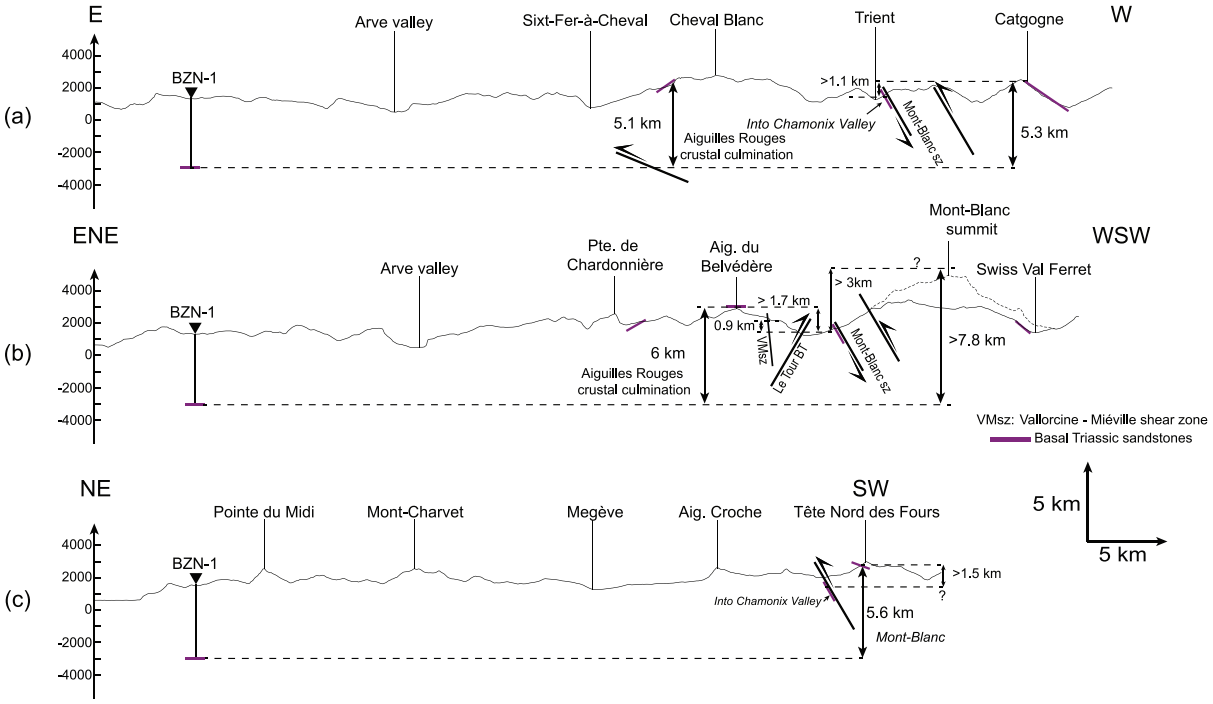

Figure 7.1. Sections highlighting the Triassic unconformity in order to estimate the amount of exhumation between the Aiguilles Rouges and Mont-Blanc massifs: (a) Section through Chablais, Haut-Giffre, Aiguiles Rouges and northern Mont-Blanc massif (Catogne); (b) Section through Désert de Platé, Aiguille du Belvédère and Mont-Blanc massif (Âmone); (c) Section through Aravis, Mont-Joly, Col du Bonhomme and southern Mont-Blanc massif (Tête Nord des Fours).

7.1.2 Constraints on the amount of absolute timing of Cenozoic deformations

7.1.2.1 Aiguilles Rouges backthrusts

The approximate 6 km of post-Triassic uplift of the Aiguilles Rouges from the Brizon drill hole is mostly the result of the uplift in the crustal culmination above the Alpine Sole Thrust (Leloup et al., 2005; Bellahsen et al., 2014), including the frontal Aiguilles Rouges thrust (Pfiffner et al., 1997) and the back thrusts (Fig. 7.1). We estimate that $\geq$1.7 km of this uplift has been accrued on the Vallorcine fault and the back thrusts (Fig. 7.1). The vertical offset of the Le Tour back trust alone is at least 935 m (elevation difference between the basement east of the Vallorcine Fault and the Chamonix valley (Fig. 7.1b). The offset on the Finhaut back thrust is more difficult to evaluate because it is very close to the Vallorcine fault (Fig. 4.8a).

Cooling histories modeled with HeFTy software and based on one Apatite Fission Track, the mean of two Zircon U/He, and one Apatite U/He ages from the central part of the Aiguilles Rouges suggest that cooling, and thus exhumation, started at about 18 Ma, and was faster ($\geq$ 25 $^{\circ}\mathrm{C\,Ma^{-1}}$) from 8 to 4 Ma (Boutoux et al., 2016) (Fig. 7.2). However, the cooling history is relatively poorly constrained and the exhumation could have started between $\approx$30 and 16 Ma. All apatite fission-track ages along a transect (elevations between 1010 and 1350 m a.s.l) perpendicular to the Chamonix valley at the level of the Mont-Blanc tunnel are similar between 3.4 and 4.5 Ma in the Aiguilles Rouges and the Mont-Blanc (Glotzbach et al., 2008). This implies that no significant movement has occurred on the Mont-Blanc shear zone or the Le Tour back thrust since then (Leloup et al., 2005; Glotzbach et al., 2008).

The Aiguilles Rouges back thrusts are mostly brittle and offset all the other structures, and are thus presumably relatively young. They appear coeval with a WNW-ESE compression phase but are possibly older than the present-day strike-slip regime. Unfortunately, the age of these deformation phases is unclear and no geochronological data are available on the back thrusts. Assuming that the back thrusts are linked to the most recent rapid cooling phase would imply that they were active between 8 and $\approx$ 4 Ma (Fig. 7.2).

7.1.2.2 Pormenaz - Merlet shear zone

The Pormenaz-Merlet shear zone is younger than the Helvetic nappes. The vertical offset across the Pormenaz - Merlet shear zone is $\geq$ 300 m (elevation difference between the basement east of the shear zone and the base of the Pormenaz klippe). The only thermochronological data that can constrain the absolute age of the shear zone are the samples MBZ10 and MBZ14 (Boutoux et al., 2016) that have similar elevations on both sides of the shear zone and give a similar mean Zircon U/He: 6.2 ± 0.4 and 6.3 ± 0.4 Ma, respectively. This implies that the

Pormenaz - Merlet shear zone offset is antecedent to that age and occurred at temperatures higher than the Zircon U/He closure temperature (70 to 200 $^{\circ}$C). If the motion on the shear zone contributed to the exhumation of the Aiguilles Rouges, it is therefore likely younger than 12 Ma (Fig. 7.2).

7.1.2.3 Mont-Blanc shear zone

The general direction of the Mont-Blanc shear zone is N34° with a N110° direction of thrusting on average. This geometry implies that the Mont-Blanc shear zone has mainly a thrust component (≈80%) and a slight dextral component (≈ 20%). The WNW-ESE direction of shortening (≈ N110° ductile structures) possibly rotated through time towards NNW-SSE (≈ N155° brittle structures) (Leloup et al., 2005). The vertical offset in the shear zone can be estimated from the offset of the Triassic sandstones across it: ≈ ≥1.5 km in the south (Col du Bonhomme), ≥ 3 km at the level of the Mont Blanc and ≈ ≥1 km in the north (Catogne) (Fig. 7.1). Pressure - Temperature estimates suggest that the differential exhumation between the Mont-Blanc and the Aiguilles Rouges is 2 to 8 km. Motion in the Mont-Blanc shear zone has increased that difference, while motion in the Le Tour back thrust decreased it. From the thermo-kinematic simulations, we infer the total amount of exhumation in the Aiguilles Rouges to be about 12 km, leading to a differential exhumation between Mont-Blanc and Aiguilles Rouges of 7 km.

$^{40}Ar/^{39}Ar$ mica ages have been performed within the Mont-Blanc shear zone, where the mylonitic foliation is underlain by chlorite ± white mica ± biotite. Biotite from sample C6 (Rolland et al., 2008) yields saddle age spectra suggestive of excess argon, with the youngest step at 19.75 ± 0.21 Ma, the inverse isochron age being 21.8 ± 0.3 Ma ($^{40}Ar/^{36}Ar = 316.1 \pm 4$, MSWD= 2.0) (Rolland et al., 2008) (Fig. 7.2, Table B.4). K-Feldspar from the nearby ME27 sample produces complex age spectra with a minimum age step of 10.61 ± 0.15 Ma (Leloup et al., 2005). Two duplicates of white micas from sample DE65 located further north along the Angle fault yield raising ages spectra, respectively, in the ranges of 14.30 to 20.41 and 15.13 to 20.32 Ma, both with a mini plateau at about 18 Ma (Table B.4) (Egli et al., 2017). Other $^{40}Ar/^{39}Ar$ ages from undeformed rocks yield constraints on the cooling history. The biotites of sample C8 of the undeformed Mont-Blanc granite yield an inverse isochron age of 16.6 ± 0.7 Ma that probably reflect the cooling of the hanging wall through $300 \pm 50^{\circ}$C (Leloup et al., 2005). K-feldspar from the same sample yields a minimum age step at 10.980 ± 0.002 Ma which could be interpreted as a maximum age for recrystallization of K-Feldspar at about 200°C (Leloup et al., 2005). All these samples do not give clear plateaux and the ages are difficult to interpret probably because the protolith is quite old (≥300 Ma) and the Alpine deformation temperature is below 450°C (Leloup et al., 2005; Rolland et al., 2008). In this work, the mylonites from the Mont-Blanc shear zone (samples ARe001, ME147, and C4), $^{40}Ar/^{39}Ar$ *in situ* inverse

isochron ages range between 14.9 ± 1.0 and 17.0 ± 1.1 Ma in the three samples (Fig. 5.11). The quartz microstructures and LPO suggest a deformation temperature below 400 to 500 $^{\circ}$C. These mylonites dates the deformation in the Mont-Blanc shear zone and suggest that it have been active between 18 and 14 Ma, however, the presence of an inherited age component in ME147 suggests that deformation may have started earlier between 30 and 20 Ma. All these ages are between approximately 22 and 11 Ma and could correspond to the time of deformation within the Mont-Blanc shear zone between 500 and 200°C.

White micas from sample S8 of Rolland et al. (2008) along the Vallorcine fault yield two $^{40}Ar/^{39}Ar$ mini-plateau ages at 14.3 ± 0.2 Ma (1σ) and 22.9 ± 0.9 Ma (2σ), Figs. 4.8a and 5.1b), that have been interpreted to reflect the duration of reverse faulting that would be contemporaneous with the Mont-Blanc shear zone (Rolland et al., 2008). From our analysis (sample ARe293, Fig. 5.10), after the exclusion of four *in situ* $^{40}Ar/^{39}Ar$ data, the 15 remaining apparent ages range from 22.2 ± 0.6 to 40.2 ± 2.5 Ma. In summary, the Vallorcine fault is a complicated shear zone that has a long and polyphase history, and the correspondence of ages with a given deformation phase is disputable.

Horizontal clefts with quartz + Chlorite $\pm$ fluorite $\pm$ adularia crystallizations are found within the Mont-Blanc and to a lesser extent in the Aiguilles Rouges (e.g., Poty et al., 1974; Rossi et al., 2005; Rossi and Rolland, 2014). These clefts are compatible with horizontal compression and are generally considered as coeval to the Mont-Blanc shear zone. Adularia from a cleft in central Mont-Blanc yields isochron ages $^{40}Ar/^{39}Ar$ of 10.6 - 13.6 Ma (MB03-70, 11.31 ± 0.68 for grain n1, 12.80 ± 0.78 for grain n2) (Fig. 7.2) (Rossi and Rolland, 2014). In the north of Mont-Blanc, clefts contain quartz + Stilpnomelane + Epidote + Calcite $\pm$ Adularia $\pm$ Gold, with the Adularia yielding a 9.9 ± 1.0 Ma $^{40}Ar/^{39}Ar$ isochron age (Marshall et al., 1998a) (Fig.7.2). Bergemann et al. (2019) applied the U-Th/Pb method on nine clefts containing monazite that yield ages between 12 and 6 Ma that relate three main growth events at 12 - 11, 11 - 9 and 9 - 6 Ma. Two veins are located in the Aiguilles Rouges, described as vertical and trending N190° and do not show the first growth stage. This was interpreted as evidence that the two last growth phases are linked with right-lateral shear along the NE - SW Rhône-Simplon fault (Bergemann et al., 2019). However, the orientation of these clefts is compatible with left-lateral, not right-lateral shear along a NE - SW fault, making that interpretation dubious.

In summary, the most probable structural scenario is that reverse / right lateral deformation started in the Mont-Blanc shear zone at about 500 $^{\circ}$C at about 22 Ma and most likely lasted until 11 Ma at lower temperature in a brittle regime (about 200 $^{\circ}$C). Because rapid cooling of the Mont-Blanc lasted until 6 ± 2 Ma, and crystallization in the horizontal clefts until 6.71 ± 0.23 Ma, thrusting may have possibly continued along the Lavancher fault until 6 ± 2 Ma but was over (as well as the Aiguilles Rouges back thrusts) at 4 Ma (Fig. 7.2). The end of motion in the Mont-Blanc shear zone possibly marks the initiation of the present-day brittle strike-slip stress

regime.

7.1.2.4 Helvetic Thrusts

Helvetic thrust deformation affects units from the basement to the Eocene sediments. Eocene sediments are Priabonian (Collet et al., 1952), implying a post-34 Ma deformation. Additionally, Taveyannaz volcaniclastic sandstones that were deposited before nappe stacking and folding contain 32.5 Ma andesitic clasts ($^{40}Ar/^{39}Ar$ in hornblendes), while biostratigraphic correlations suggest sedimentation between 32 and 29 Ma during Rupelien (Ruffini et al., 1997) implying post-Oligocene deformation.

No age data have been published on the Morcles nappe in France, but such ages are available from Switzerland. Fine-grained synkinematic white micas (2 - 6 μm) from five ductile carbonate mylonites at the base of the Morcles and Doldenhorm nappes in Switzerland yield staircase $^{40}Ar/^{39}Ar$ age spectra with apparent ages between 12 and 76 Ma, with 94% of the gas release, yielding ages between 32 and 14 Ma (Kirschner et al., 1996). Analysis of a larger set of 25 samples from the Helvetic nappes and comparison with the ages of Rb/Sr confirm that the $^{40}Ar/^{39}Ar$ ages result from variable mixtures of detrital and syntectonic (neoformed) micas, and that the ages tend to young from the structurally highest Helvetic thrusts (Mont Gond and Sublage) to the lowest (Diablerets and Morcles) (Kirschner et al., 2003). The age spectrum of sample 93-29-A from deformed Eocene sediments at the base of the Morcles nappe, yields a strong Miocene signal with two pseudo-plateaux at 19 and 21 Ma in the first 83% of gas release (Kirschner et al., 2003) (Fig. 7.2). The youngest ages (about 14 Ma) come from the base of the Morcles Nappe, at La Batiaz (Fig. 7.2), but correspond to less than 20% of the gas in a spectrum that does not show any plateau, so their significance is uncertain. These data suggest that the Morcles nappe was mostly placed between 21 and 19 Ma. Unfortunately, from the available data, it is unclear if that deformation ended at ≈19 Ma or lasted until ≈14 Ma.

At La Batiaz, white mica from sample DE79 from the Aiguilles Rouges gneiss with top-to-northwest thrusting evidence yields a plateau age of 20.28 ± 0.21 $^{40}Ar/^{39}Ar$ (inverse isochron: 20.18 ± 0.49 Ma) interpreted as related to motion in the Mont-Blanc shear zone (Egli et al., 2017). This interpretation is in the upper range of the ages discussed above for the Mont-Blanc shear zone. However, our structural mapping rather relates deformation at la Batiaz to the HBT, in the direct prolongation of the Forclaz fault, and we rather relate that age with those obtained at the base of the Morcles Nappe (Fig. 7.2). Closer to contact with sedimentary cover, sample S02 showing top-to-southeast normal shear criteria, yields a $^{40}Ar/^{39}Ar$ plateau age of 15.90 ± 0.15 (inverse isochron: 15.07 ± 0.23) that has been interpreted to correspond to the age of updoming of the Aiguilles Rouges postdating the Mont-Blanc shear zone (Egli et al., 2017). This timing is compatible with that of the uplift of the Aiguilles Rouges discussed above. *in situ* dating at the base of the Helvetic thrusts on the eastern side of the Mont-Blanc yield the

age of 13.7 ± 0.7 Ma (Chap. 5) most likely dating the last increments of top-to-WNW / NW shearing.

In summary, from the available geochronological data, we suggest that the Helvetic nappes were emplaced since 32 Ma. The Morcles nappe was mostly emplaced around 21-19 Ma, but lasting until about 14 Ma (Fig. 7.2).

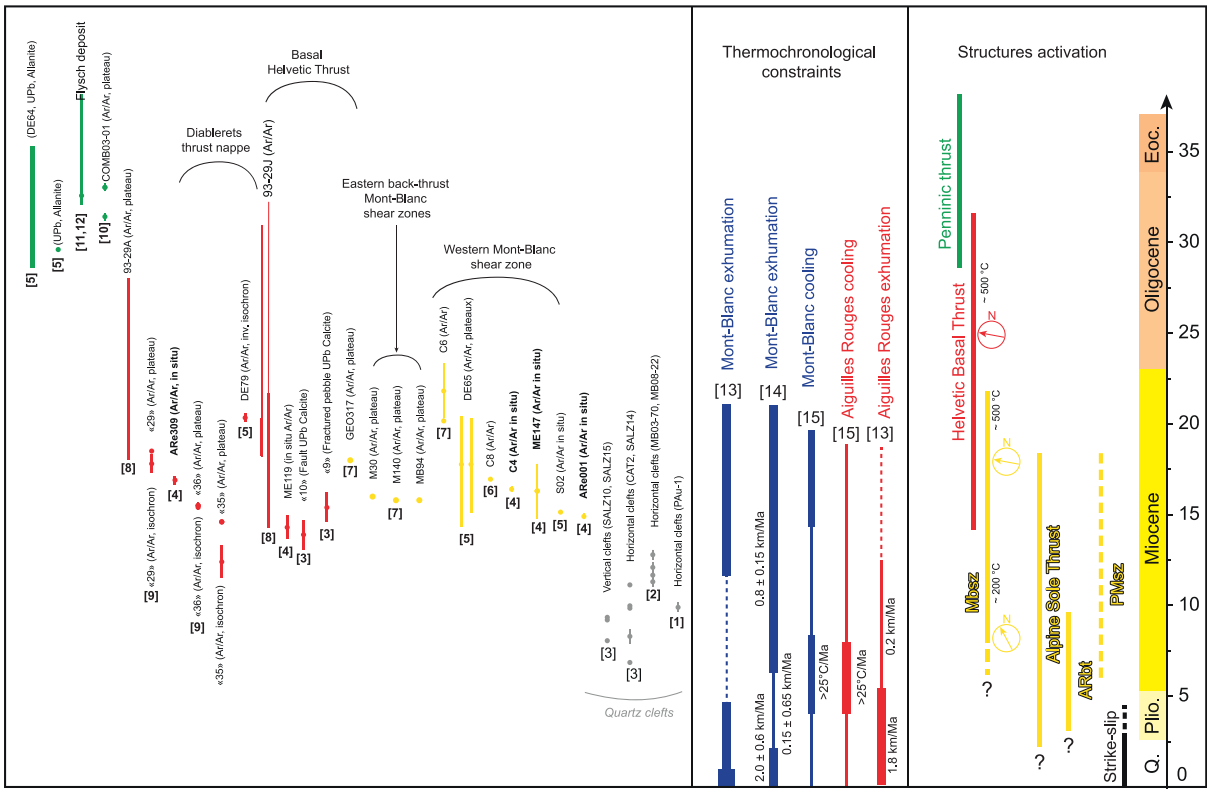

Figure 7.2. Time-Deformation constraints on the Cenozoic evolution of The Mont-Blanc and Aiguilles Rouges. Left, geochronological constraints, dots correspond to punctual ages and lines to age ranges of individual samples, data listed in Table S4. Center, Thermochronological constraints with exhumation estimate and cooling histories. The bold line indicates fast cooling/rapid exhumation. Right, the timing of the main structures, is dashed when uncertain. Colors refer to tectonic phases, arrow indicate the thrusting direction (see text for details). References: [1]: Marshall et al. (1998b); [2]: Rolland et al. (2008); [3]: Bergemann et al. (2019); [4]: This study (Chap. 5); [5]: Egli et al. (2017); [6]: Leloup et al. (2005); [7]: Rolland et al. (2008); [8]: Kirschner et al. (1996) and Kirschner et al. (2003); [9]: Crespo-Blanc et al. (1995); [10]: Simon-Labric et al. (2009); [11,12]: Pfiffner et al. (2002) and Ruffini et al. (1997); [13]: This study (Chap. 6) [14]: Glotzbach et al. (2011); [15]:Boutoux et al. (2016).

7.2 Implications of the structural evolution of the Alps

7.2.1 Shortening of the Helvetic nappes and lateral extent of the Helvetic thrusts

The Aiguilles Rouges have been underthrusted below the Penninic nappes along the Penninic thrust before ≈30 Ma (Simon-Labric et al., 2009; Pfiffner et al., 2002) (Fig. 7.2). As discussed above, the thrust at the base of the Helvetic nappes, along the Helvetic Basal Thrust (HBT), lasted until ≈19 Ma and possibly until ≈14 Ma. Above the HBT, several thrust sheets are found below the Penninic thrust that has been described in Switzerland and named the Helvetic and Ultrahelvetic nappes (Ramsay, 1981; Escher et al., 1988), and have possibly been activated in sequence from east to west (top to bottom) (Jeanbourquin, 1994) between ≈30 and ≈20 Ma (Kirschner et al., 2003).

The present 3D structural study implies that the Helvetic Basal thrust is a shear zone along which the overlying Morcles nappe was significantly detached from the underlying basement toward the WNW (N110° on average in the Aiguilles Rouges). This follows the interpretation of Paréjas (1925), Collet (1927), and Ramsay (1981) but not that of Escher et al. (1993) and Boutoux et al. (2016), which consider that the Morcles nappe is not significantly detached from the basement and is mostly restricted to Switzerland.

NW-SE shortening of the Urgonian limestone above the Helvetic Basal thrust can be estimated from the cross sections of (Ferrill and Groshong, 1993) and Butler et al. (2018) (Fig. 4.6a): 4.3 km (22%) and 3.7 km (24.5%) respectively. These are minimum estimates of the total shortening because they do not consider the offset on the basal helvetic thrust, which is difficult to constrain as it does not outcrop. From a 3D reconstruction based on the cross sections of Huggenberger (1985) and Faure et al. (1999), Affolter (2003) calculated a total shortening varying between 13 and 32 km from the NE to the SW of the Aiguilles Rouges (Fig.4.6a).

In the hypothesis of ductile folded basement (e.g., Escher et al., 1993), the Morcles nappe is expelled from a half-graben with the external Mont-Blanc at its core. The initial length of the cover was at least 21 km, while the current width of the external Mont-Blanc is only 3 km and implies more than 86% of shortening of the basement. However, the external Mont-Blanc is not a fold but a reverse shear zone. Moreover, from our results (Chap 5.) and other published ages (Rolland et al., 2008; Leloup et al., 2005; Egli et al., 2017; Kirschner et al., 1996) that shear zone is partly younger than the Morcles Nappe, implying that the nappe roots east of the Mont-Blanc, as well as the other Helvetic nappes. In such a case, the amount of internal shortening within the basement is independent of the amount of shortening along and above the Helvetic Basal thrust which could be quite large.

Southwest of the Mont-Blanc range, the sedimentary cover is interpreted as significantly detached from the basement by several authors. In the Mont Joly area (Fig.4.27), three flat thrust sheets have been described within the Mesozoic cover on a ≈1500 m thick succession from bottom to top: the Vervex, lower Mont-Joly (or Sangle) and Upper Mont-Joly units (Mennessier et al., 1977; Triboulet, 1980; Epard, 1990). These thrusts are the southward prolongation of the Helvetic nappes (Eltchaninoff, 1982; Epard, 1990), and are overlain by two other thrust sheets: the Roselend and Roselette nappes, both involving the basement (Mennessier et al., 1977; Eltchaninoff, 1982; Butler, 1985). The basal thrust, corresponding to the Helvetic Basal thrust, extends to the north-west, dipping north-west below the Aravis (Triboulet, 1980; Eltchaninoff, 1982; Butler, 1985; Epard, 1990; Bellahsen et al., 2014). The Helvetic Basal thrust underlies the folded Mesozoic cover and most probably emerges west of the Bornes Doudoux et al. (1982) between the Brizon (BZN-1) and Faucigny (FAY-1) deep wells (Charollais et al., 1996) (Fig.4.6a). This interpretation implies that the whole Aravis, Bornes, Bauges, and Semnoz massif corresponds to a large subalpine klippe above the Helvetic Basal thrust (Fig. 4.6). In the Brizon deep well the Tithonian limestones are found five times, attesting to a strong shortening of the cover (Charollais and Jamet, 1990). Bellahsen et al. (2014) estimate an NW-SE shortening of 17 km within the Bornes, while Affolter (2003) estimates a total thrusting of 30 to 36.5 km for the Helvetic nappes. Further south, Kalifi et al. (2021) propose a similar interpretation for the northern part of Vercors and the eastern part of Chartreuse. These massifs are klippes above a thrust they call Fault Zone 1 (FZ1), with shortening estimates between 14.1 and 5.8 in the north and south of Chartreuse, respectively. They further interpret FZ1 to have been active before ≈21 Ma has it created a relief that bounded the Miocene sea to the east (Kalifi et al., 2021; Kalifi et al., 2022). We propose that FZ1 of Kalifi et al. (2022) corresponds to the southern prolongation of the Helvetic Basal thrust that extends from Morcles Nappe to the northern Vercors.

7.2.2 Late reverse faults at the boundary of the external ranges

The subalpine klippe is bounded to the east by the external crystalline ranges of external Belledonne and the Aiguilles Rouges which are large basement windows (Fig. 4.6a). Most authors consider that the Jura and subalpine folds formed above thrusts that root below (west of) the external ranges (e.g., Burkhard and Sommaruga, 1998; Deville and Chauvière, 2000; Bellahsen et al., 2014). However, as described above, the Helvetic Basal thrust lies on top of the Aiguilles Rouges external crystalline range, thus implying that it roots above (east of) these ranges: in the Chamonix synclinorium and the synclinal médian of Belledonne (Fig.4.6) (e.g., Eltchaninoff, 1982; Leloup et al., 2005). Furthermore, the Helvetic Basal thrust roots east of the Mont-Blanc and has been cut and offset by later steep reverse faults including the Mont-Blanc shear zone.

Exhumation of the Mont-Blanc started at about 22 Ma in the hanging wall of the Mont-Blanc shear zone and lasted until at least 14 Ma, most likely probably up to 6 Ma, while the motion on the Helvetic Basal thrust was active at 21 - 14 Ma. The Mont-Blanc shear zone thus appears to be partly coeval with the Helvetic nappes that it offsets. A simple interpretation is that during this time range the Mont-Blanc shear zone was an imbricate thrust in the footwall of the Helvetic Basal thrust, before breaching out at 14 Ma (Fig.7.3).

The exhumation of the Aiguilles Rouges above the Alpine sole thrust started at 12 Ma (Fig. 7.2), inducing the bending of the Helvetic Basal thrust. Therefore, the period from 22 to 14 Ma corresponds to a major transition from the rooting of the main active thrusts from above (east) the external crystalline massifs in the Mont-Blanc area to thrusts rooted below (west) the external crystalline massifs (Alpine sole thrust).

Further south in Chartreuse, the molasse depocenter migrated at $\approx$18 Ma towards the west from the footwall of the HBT to the footwall of the Voreppe thrust rooting below Belledonne (Kalifi et al., 2021). This timing coincides with the onset of rapid exhumation of the external crystalline massif of Belledonne and is interpreted as the switch from distributed to localized (shear zones) deformation (Girault et al., 2022). However, that timing could also mark a major transition from rooting of the thrusts east (above) to west (below) of the external crystalline massifs as in the Aiguilles Rouges – Mont-Blanc, and we propose below a conceptual model for the Alpine deformation of the external crystalline massifs, based on our observations in the Aiguilles Rouges and Mont-Blanc massifs.

7.2.3 A conceptual model for Alpine External Crystalline Massifs deformation

We suggest that three major thrust systems with large horizontal displacement (so-called thin-skin tectonics) succeeded in the western Alps from the east (internal) to the west (external): the Penninic, Helvetic, and Basal thrust systems. In this interpretation, the Helvetic deformations are not limited to buckle folding, but are linked to a major thrust system more than 50 km long across-strike that absorbed between 13 and 36 km kilometers of ENE-WSW shortening: the Helvetic thrust system, with the Helvetic Basal Thrust at its base.

These thrusts induced large-scale folding of the Helvetic units with fold axis perpendicular to the thrust motion in the upper part of the thrust sheet, and sheath folds in the basal décollement level. Note that such sheath folds can barely be explained in a para-autochthonous hypothesis. That thrust system roots southeast (above) of the Mont-Blanc and Belledonne, close to, and possibly within, the Penninic thrust. The thrust system is composed of ramps usually located in the less deformable units (i.e., basement, Urgonian and Thithonian limestone), and long flats located in the less competent layers (i.e., Triassic siltites and dolostones, Liassic

marls). The main flat appears to be in the Triassic a few meters above the basement and has induced a large décollement of the cover with respect to the basement. Starting from a horizontal geometry would imply that no basement slice could be found along with the thrust within sedimentary rocks unless the thrust cuts down a section within the basement before climbing back up section, the so-called plucked basement slice (Platt, 1984), which seems unlikely. However, since the basement/cover interface was more likely to have rough geometry in part due to preexisting normal faults (either Jurassic or Eocene), the local cut-off of that interface, for example, at the tip of tilted blocks, can explain how basement pieces can be found within the sedimentary series (Fig.7.3e).

The helvetic thrust was active from 32 Ma to 14 Ma. During a first stage ($\approx$ 30 to $\approx$ 22 Ma) the HBT is rooted southeast of the Mont-Blanc (Fig.7.3a). To the west, the Helvetic Basal thrust thrust system bounded the Miocene Sea and was associated with the sedimentation of the Lower Freshwater Molasse in the Swiss Molasse basin (Garefalakis and Schlunegger, 2019) and the initial deposits of the Miocene Molasse in the Rhodano-Provencal Molasse basin (Kalifi et al., 2021; Kalifi et al., 2022). In a second stage ($\approx$ 22 to $\approx$ 18 Ma) a duplex formed (Fig.7.3b). The Mont-Blanc was the central bloc of that duplex bounded to the northwest by the Mont-Blanc shear zone and to the southeast by a ramp along the Helvetic Basal thrust. Note that the average nappe transport direction in the Helvetic nappe on the eastern and western side of the Mont-Blanc and Aiguilles Rouges (N110°) (Fig. 4.27) is identical to the thrusting direction of the western Mont-Blanc shear zone (N110°). At ≈18 Ma, the main deformation locus migrated to the west and the Alpine Sole thrust initiated rooting to the west (below) of the Aiguilles Rouges inducing uplift of the Aiguilles Rouges, while the Helvetic Basal thrust was still active (Fig.7.3c). This transition period ended at $\approx$ 14 Ma when the activity of the Helvetic Basal thrust ended, but several steep faults began in the Alpine Sole Thrust hanging wall (Fig.7.3d). Some of the Helvetic Basal thrust ramps eventually became breach thrusts that cut up a section across their previous flat (Platt, 1984). This was the case for the Mont-Blanc shear zone that was active together with the Helvetic Basal thrust between ≈22 and 14 Ma, before offsetting that structure between 14 and possibly 6 Ma. The activation of such a breach thrust is correlated with that of the back-thrusts and the formation of horizontal clefts and would correspond to the transition of thin-skin to thick-skin tectonics in the Mont-Blanc, while thin-skin tectonics takes place in the Jura. Note that this model does not imply any major strike-slip motion along the Chamonix synclinorium, nor the synclinal median in Belledonne before $\approx$ 6 Ma.

7.3 Implications on the Alpine orogenic wedge

Mountain belts are often described as orogenic wedges with the internal part of the belt consisting of a structural culmination formed by the basal accretion of crystalline thrust sheets and an external part of imbricated thrusts formed by frontal accretion of sedimentary units (Pfiffner, 2017, for a review). In the case of the external Alps, the External Crystalline Massifs have been interpreted as such a culmination (e.g., Lacassin et al., 1990; Pfiffner et al., 1997; Menard and Thouvenot, 1987).

Analog and numerical experiments have emphasized the importance of décollement layers, erosion, and sedimentation in the formation of such orogenic wedges and their influence on the deformation style. In analog sandbox experiments, a geometry similar to the external alps has been obtained with an antiformal culmination that refolds previous flat thrust sheets (e.g., Konstantinovskaya and Malavieille, 2005; Bonnet et al., 2007). In that case, the culmination is achieved by basal accretion of basement slices in a duplex and back thrust in the internal part (Bonnet et al., 2007). The same kind of geometry is obtained in viscoelastoplastic numerical models when there are two levels of flat décollement with the upper one weaker than the basal one (Dal Zilio et al., 2020). In some of these cases, the antiformal culmination uplift is achieved not by basal accretion, but by out-of-sequence breach thrusting at the front of the culmination and back thrusting at the back (Model M5 Dal Zilio et al., 2020). In all cases, the vertical growth of the culmination is enhanced by strong erosion. Basic features of our conceptual model, such as the up-doming and breach thrusting of a previously flat décollement, are obtained in some of these wedge models. However, these models correspond to a brittle wedge over a rigid basement, as rheology is independent of temperature, and one can question their applicability to Mont-Blanc, where the Miocene temperature may have reached 450 - 500 °C (Poty et al., 1974; Rolland et al., 2003, Chap. 5).

Numerical thermomechanical simulations with viscoelastoplastic rheology have been designed to discuss the mechanical parameters that control the style of deformation (thin skin versus thick skin) during nappe formation (Spitz et al., 2020; Bauville and Schmalholz, 2015; Kiss et al., 2020). The authors evaluated the mechanical parameters that control thin-skin vs. thick-skin tectonics style in nappe formation (i.e. folding versus thrusting). To do so, they compared simulations with different parameters (viscosity contrasts between cover and basement, thermal control, etc.). Their general results suggest that the deformation style is mainly controlled by the viscosity contrast between the basement and the sedimentary cover. In the absence of any softening mechanism, strain localization occurs along weak layers and is thus mainly controlled by the viscosity contrast between the basement (high viscosity) and the cover (low viscosity) and the initial geometry of that boundary. Flat low viscosity layers (e.g. evaporite layer or temperature-softened layers) promote the transport of a large horizontal thrust

nappe, while steep boundaries (that is, inherited normal fault) promote folding of the basement and sediments (Spitz et al., 2020; Bauville and Schmalholz, 2015; Kiss et al., 2020). These models suggest that for a basement with high viscosity ($\geq$1023 Pa.s) and in the absence of any localization mechanism, shortening of a previous graben can produce basement folding and squeeze out sediments with a geometry comparable to the basement fold nappe proposed for the Morcles Nappe by Escher et al. (1988) (Fig. 4.7a); while in the absence of graben thrust nappe with large horizontal transport such as the Wildhorn and Glarus nappes develop. In our study area, there is no clear evidence for a Mesozoic normal fault, no evidence of basement folding, and clear evidence of décollement of the cover with respect to the basement along the Helvetic Basal thrust, and the situation is thus comparable to that of the Glarus, but with a later deformation phase, inducing thrust of the basement in the internal part of the system (Fig. 4.7b). The presence of pieces of basement inside the Helvetic Basal thrust shear zone (Fig. 4.11) suggests that, even in the absence of a deep basin, the basement / cover interface had a rough geometry and the basement heights have been cut (Fig.7.3e).

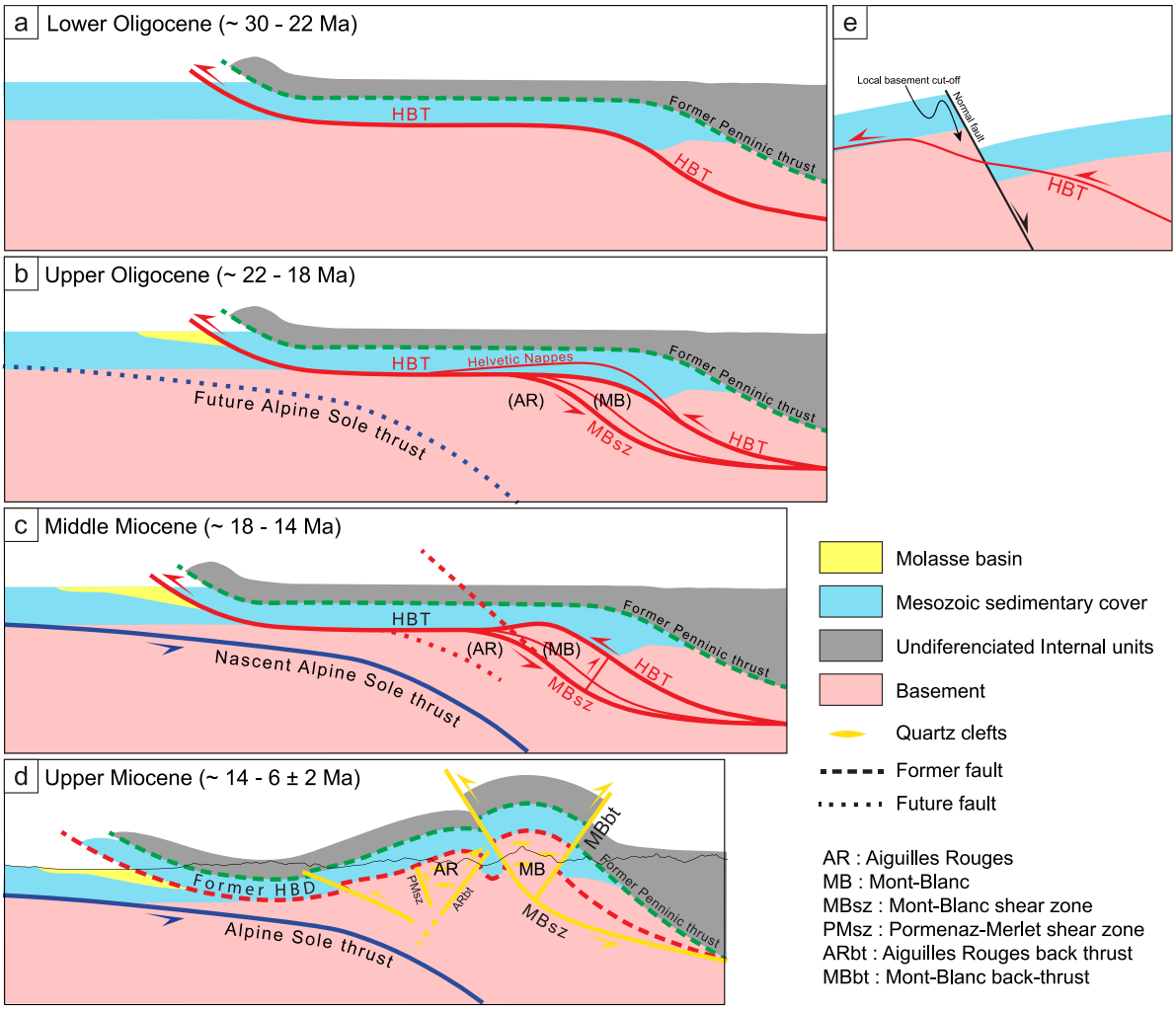

Figure 7.3. A conceptual model for western Alps External Crystalline massifs deformation. a) Lower Oligocene (30-22 Ma) stage of Helvetic nappe stacking (thin shinned). Helvetic Basal Décollement at the base of the Helvetic nappes taking root southeast (above) of the Mont-Blanc. b) Upper Oligocene (22-18 Ma) stage of further Helvetic nappe stacking with duplexing. The external crystalline massifs are structured in duplexes between two branches of the Helvetic Basal thrust where the deformation is more (Mont-Blanc) or less (Aar) localized. c) Middle Miocene (18-14 Ma) transition stage. The Helvetic Basal thrust is buckled at the top of the duplex where back-thrusting takes place. Initiation of the Alpine Sole thrust initiate Aiguilles Rouges exhumation. d) Upper Miocene (14-6 Ma) stage of breach thrust and steep faults (thick skin), the main stage of the external crystalline massifs exhumation above the Alpine Sole thrust that roots northwest (below) the external crystalline massifs. The Mont-Blanc shear zone becomes a breach thrust through the former Helvetic Basal thrust coevally with back-thrusting of the Mont-Blanc and Aiguilles Rouges. Horizontal quartz clefts open within the external crystalline massifs. Note that the basal sole thrust induces thin skin tectonics in the Jura at the same time. e) Sketch of a possible configuration with a roughed geometry of the cover/basement interface leading to the incorporation of basement pieces within the sedimentary series at the base of the thrust.

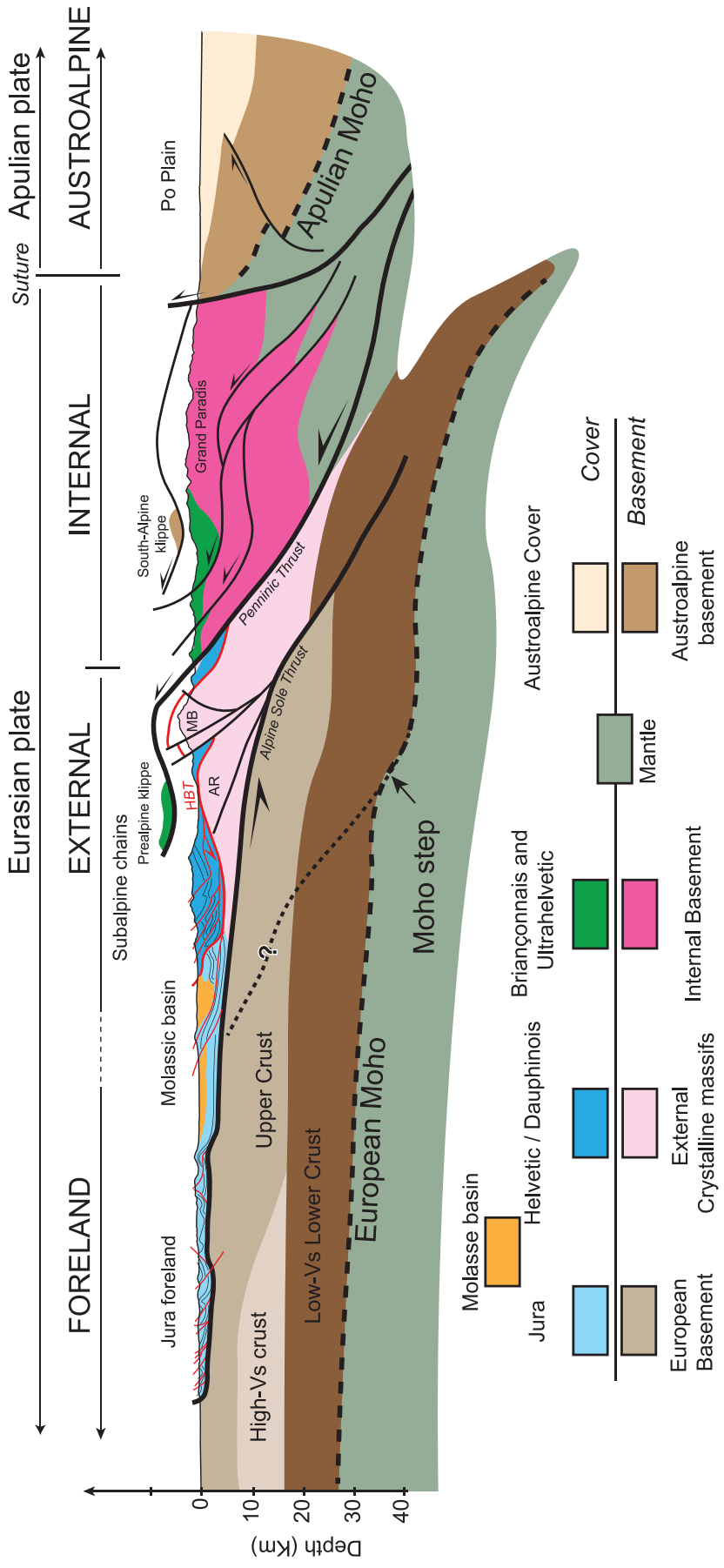

Figure 7.4. Cross section through the Alps along the ECORS-CROP transect (Guellec et al., 1990) and the northern CIFALP transect (Paul et al., 2022; Malusà et al., 2021).

CONCLUSIONS AND PERSPECTIVES

This Ph.D. work proposes reconstructing the deformations in an orogenic belt: the Alps. To do so, we reconstructed the 3D geometry of the structures with field observation, microstructural characterization of the deformation, and structural data, combined with 3D geological modeling. The timing has been constrained using *in situ* $^{40}Ar/^{39}Ar$ dating technique applied on synkinematic micas from shear zones within the massif, and the conditions of deformations from Quartz deformation analysis and chemical analysis . The quantification of the exhumation and the reconstruction of the thermal history of the massif have been constrained using thermochronological modeling coupled with Beyasian inference to evaluate the most probabilistic scenario of exhumation. The study focuses on the Mont-Blanc and Aiguilles Rouges area, two of the external crystalline massifs of the western Alps.

What is the cover / basement relationship in the Mont-Blanc and Aiguilles Rouges ?

A décollement thrust is evidenced and characterized at the bottom of the Helvetic nappes. This décollement is part of the Helvetic nappe system, which is a major thrust system active mainly between ∼30 and ∼14 Ma, in an ∼N110° direction, with a total shortening between 13 and 36 km. Above the Aiguilles Rouges a flat is located within the Triassic a few meters above the basement and another within the Liassic shales. The décollement is an apparent normal fault on the northwestern flank of the Aiguilles Rouges, because it has been tilted during the later uplift of the Aiguilles Rouges most likelly above the external Alpine Sole Thrust. The most basal Helvetic thrust extends below the Haut-Giffre and most probably emerges west of the Prealps klippe. During the Miocene, it was cut by several steep reverse faults: the Aiguilles Rouges back thrusts, the Merlet-Pormenaz shear zone, and the Mont-Blanc shear zone. The Helvetic nappes were uplifted and folded above the basement culminations of the external crystalline massifs, which mostly shape the map geometry of the present-day external crystalline massifs. These late deformations obscured the continuity of the décollement and precluded its recognition as a major structure, even if it was previously described in several localities. The basal Helvetic thrust partly roots in the Chamonix synclinorium, but its internal

roots are found on the eastern side (above) of the Mont-Blanc due to the late offset by the breach faults and back thrusts.

What is the thrust propagation sequence in the western Alps ?

We propose a tectonic scenario in which the Mont-Blanc shear zone acted as a ramp of the helvetic nappes between ∼22 and 14 Ma, before becoming a breach thrust between 14 and 6 Ma. The period between ∼22 and 14 Ma was a transition of the major thrust system between the helvetic nappes that root southeast (above) of the external crystalline massifs to the Alpine Sole thrust that roots northwest (below) of the external crystalline massifs.

The main structural characteristics of the Mont-Blanc area can most probably be extrapolated in the southwest, with the external Belledonne, Synclinal Median, and Internal Belledonne being an equivalent of the Aiguilles Rouges, the Chamonix Synclinorium, and the Mont-Blanc, respectively. We suggest that the Helvetic nappes extend in the Chablais, the Bornes, eastern Chartreuse, and northeast Vercors, defining a large klippe that roots east (above) Belledonne. After ∼ 18 Ma, a major transition occurred with the Alpine sole thrust rooting west (below) the external crystalline massifs and steep reverse faults shaping the Belledonne range geometry.

How many thrust systems shaped the external crystalline massifs of the western Alps ?

This new tectonic model has several implications: the first is that three major thrust systems, not only two, have shaped the external western Alps: the Penninic, Helvetic and Alpine Sole thrust systems. These thrust systems have propagated in sequence from the internal (east) part to the external one (west). Because the Helvetic phase has been overlooked, shortening in the external Alps has been underestimated. The second implication is that the exhumation of the external ranges of the western Alps was mostly controlled by steep reverse faults, including back thrust and limited folding above the more external thrust system since ∼18 Ma. At that time, thick-skin deformation in the more internal part of the belt coincides with thin-skin deformation in the external part.

What are the implications in the evolution of the alpine orogenic wedge?

Such evolution of the orogenic wedge is in good agreement with the experimental and numerical models of the deformation in the evolution of the orogenic wedge (Konstantinovskaya and Malavieille, 2005; Dal Zilio et al., 2020; Bonnet et al., 2007; Bonnet et al., 2008). The paleo-structures should have a major influence on the localization of the décollement and propagation of the thrust system. This is true but not as systematic as previously suggested: the ramps

of the thrust systems are not always located on previous normal faults, and intense folding of the lower Mesozoic sediments is not always due to the inversion of narrow thick sedimentary basins, but rather to intense shearing within a décollement level. However, the complex 3D geometry of the cover / basement interface, mostly due to Mesozoic and Eocene normal faults played a role in the detailed geometry of the thrusts, with pieces of the basement being cut off locally and incorporated within the sediments, inducing that thrusts may locally appear as substractive faults.

Perpectives

This multidisciplinary approach proposes unraveling the alpine deformation in the western Alps and has revealed important aspects that would be interesting to investigate in the future.

Shortening estimations

We did not estimate the amount of shortening from our sections, mainly because of an insufficient time during this Ph.D. Furthermore, the shortening estimates based on restaurations of sections form the 3D GeoModel is not straightforward. Using the flexural slip restauration model, that seems to be applicable in the case of Aravis and Bornes fold and thrust belt, the sections must be rework to preserve the areas of the units along the sections. Indeed the 3D GeoModel does not preserve the volumes, but interpolates the surfaces.

Geochronological constraints

The presented work investigated the timing of deformation using *in situ* $^{40}Ar/^{39}Ar$ on synkinematic white micas in six mylonites of three major shear zones within the Mont-Blanc massif. However, further investigation of the timing of deformation in this massif could be performed:

- **Penninic thrust:** the most reliable dating of the Penninc thrust is located in the Ecrins massif (about 100 km further south) using step heating $^{40}Ar/^{39}Ar$ (Simon-Labric et al., 2009). In the Mont-Blanc, Egli et al. (2017) used the same technique and obtained a wide age range of about 7 Ma, between 28 and 35 Ma. We sampled mylonites from the Penninic thrust in the same area as Egli et al. (2017) (Col de la Seigne) and further south east of the Col du Bonhomme; maybe using *in situ* $^{40}Ar/^{39}Ar$ we could better estimate the timing of the deformation.
- **Pormenaz-Merlet shear zone:** This shear zone was described for the first time in this Ph.D. work and has never been dated. The relative timing suggests that the shear zone

was active in the Cenozoic because it offsets the base of the Helvetic nappes in the Crête Blanche klippe (see Fig. 4.19, p. 151). However, nearby, we observed folding in the Carboniferous shales uncomformably overlayed by the Triassic, suggesting a deformation that occured prior to the Triassic and later than the Carboniferous deposition, thus most likely Saalian, as suggested by previous authors (Pilloud, 1991; Pairis et al., 1992). The Pormenaz-Merlet shear zone could have experienced a complex history of deformation, maybe polyphased, and precise timing could be investigated using *in situ* $^{40}Ar/^{39}Ar$ argon dating. Moreover, we selected samples of mylonites whithin this shear zone that are currently prepared for datation.

- **Mont-Blanc backthrust:** backthrusting ductile shear zones of Mont-Blanc have been dated by Rolland et al. (2008) to be active around 16 Ma in a thrust / dextral motion. Backthrusting deformation was described on the eastern side of the Mont-Blanc in this Ph.D. work at the contact between the Mont-Blanc granite and the overturned Jurassic series (see Fig. 4.33, p. 4.33). We sampled mylonites rocks at the contact that could be dated using *in situ* $^{40}Ar/^{39}Ar$ to better constrain the activity of backthrusting in Mont-Blanc and the eventual migration of the deformation from inner Mont-Blanc to outer (eastern) Mont-Blanc.

- **Aiguilles Rouges backthrust:** The backthrusting in the Aiguilles Rouges was previously described by Leloup et al. (2005) and reaffirmed and characterized in this Ph.D. work. The relative timing indicates that the activity of these thrusts was post-Helvetic nappes, but there is no absolute dating. Dating these structures will not be easy, as there are not many outcroping mylonites. We sampled oriented mylonitic rocks in the Le Tour area and north of Les Praz (under the Flégère cablecar) that could be used for absoulte dating.

- **Basal thrust of the Morcles nappe:** Although the Morcles nappe is a well-known structure, there are only a few absolute datings of this nappe above the Aiguilles Rouges: Kirschner et al. (1996) dated thinny micas in the marmorized limestones, and Egli et al. (2017) dated mylonites in the basement of the Aiguilles Rouges below the thrust. We identified mylonitized basement slices within the thrust that could be dated using *in situ* $^{40}Ar/^{39}Ar$ and better constrain the deformation and its relationship to the western Mont-Blanc shear zone.

- **Brittle strike-slip faults:** In this work, we measured and characterized normal faults of various orientations (see Fig. 4.52, p. 198). Some of these faults show calcite crystallization that could be dated using the U-Th/Pb dating method (e.g., Bilau et al., 2023). The investigation of the activation time of these faults is important and could complete the deformation sequence of the massif.

Influence of structural inheritance in the localization of the deformation

It has been proposed that the deformation of the external crystalline massifs is mainly controlled by the geometry of inherited Jurassic normal faults (e.g., Escher et al., 1993; Burkhard and Sommaruga, 1998; Bellahsen et al., 2014). We stated before that this is true, but not as systematic as previously suggested. In this Ph.D. work, we highlighted several Eocene normal faults that have been deformed during the thrusting but not reused by the thrusts. We only found one Jurassic fault in the Col du Bonhomme area (see Fig.4.28, p. 164). Boutoux et al. (2016) suggested that the Chamonix Valley (and the Morcles basin) is bounded in the west by a Jurassic normal fault, while such a fault has never been characterized. In fact, the Morcles sedimentary basin, which is always described as a Jurassic basin, is mainly an Eocene sedimentation basin (e.g., Héli, 1972) that could have influence the deformation style of the nappe. A further investigation of these normal faults (mainly Eocene and eventually Jurassic) is absolutely necessary, with precise mapping and absolute dating.

Petro-geochemical and thermochronological study of Belledonne

Finally, a similar work could be performed further south in the Belledonne massif. I partly supervised a master thesis during this work that estimated the thermobarometric conditions of the deformation in the Belldonne massif to be at $440 \pm 30°\mathrm{C}$ and 0.59 ± 0.06 GPa (Gunia, 2023). This is in the same range as our results in the Mont-Blanc massif. Now, an absolute dating of the thrusts in the Belledonne massifs is necessary to further constrain the precise timing of deformation in the external crystalline massifs. Although now exhumation is better constrained in the external crystalline massifs (including this work), a deeper study of the Belledonne massif would allow us to refine the exhumation scenario and confirm the diachronism in the beginning of the exhumation from south to north in the external crystalline massifs, as suggested by Girault et al. (2022). Furthermore, the role of the synclinal median as a thrust has been characterized by Gunia (2023) but the differential exhumation accommodated by this thrust is unclear and requires further investigations.

Late steps in the exhumation of the ECM

From our work (Chap. 6) the last step (before 4 Ma) of the exhumation is not well constrained by the simulation. Mélis (2023) investigated the paleo-altimetry of the Mont-Blanc and Belledonne massif and found that the massifs were most likelly at low elevation until 12 Ma, suggesting a late increase in the relief. These results tends, along with recent thermochronological and drainage development studies (Valla et al., 2012; Lemot et al., 2023) to demonstrate that the relief in the western alps built up relatively recently, coevally with the Alpine Sole Thrust activity.

Bibliography

ABD ELMOLA, Ahmed; MONIÉ, Patrick; LABAUME, Pierre; TEIXELL, Antonio; CHARPENTIER, Delphine and BUATIER, Martine, 2022. Deformation conditions and 40Ar/39Ar dating of thrusting recorded by clay minerals: An example of the Lakora thrust (west-central Pyrenees). *Journal of Structural Geology*. Vol. 165, p. 104744. ISSN 0191-8141. Available from DOI: 10.1016/j.jsg.2022.104744.

AFFOLTER, Thomas, 2003. *Étude des déformations et restauration 3D d'un bassin de front de chaîne : l'exemple du Jura et des massifs subalpins français*. PhD thesis. Université Joseph-Fourier - Grenoble I.

AFFOLTER, Thomas, 2004. Map view retrodeformation of an arcuate fold-and-thrust belt: The Jura case. *Journal of Geophysical Research*. Vol. 109, no. B3. Available from DOI: 10.1029/2002jb002270.

AFFOLTER, Thomas; FAURE, Jean-Luc; GRATIER, Jean-Pierre and COLLETTA, Bernard, 2008. Kinematic models of deformation at the front of the Alps: new data from map-view restoration. *Swiss Journal of Geosciences*. Vol. 101, no. 2, pp. 289–303. Available from DOI: 10.1007/s00015-008-1263-3.

ALLÉGRE, C. J.; COURTILLOT, V.; TAPPONNIER, P.; HIRN, A.; MATTAUER, M.; COULON, C.; JAEGER, J. J.; ACHACHE, J.; SCHÄRER, U.; MARCOUX, J.; BURG, J. P.; GIRARDEAU, J.; ARMIJO, R.; GARIÉPY, C.; GÖPEL, C.; TINDONG, Li; XUCHANG, Xiao; CHENFA, Chang; GUANGQIN, Li; BAOYU, Lin; JIWEN, Teng; NAIWEN, Wang; GUOMING, Chen; TONGLIN, Han; XIBIN, Wang; WANMING, Den; HUAIBIN, Sheng; YOUGONG, Cao; JI, Zhou; HONGRONG, Qiu; PEISHENG, Bao; SONGCHAN, Wang; BIXIANG, Wang; YAOXIU, Zhou and XU, Ronghua, 1984. Structure and evolution of the Himalaya–Tibet orogenic belt. *Nature*. Vol. 307, no. 5946, pp. 17–22. Available from DOI: 10.1038/307017a0.

ALLMENDINGER, Richard W; CARDOZO, Nestor and FISHER, Donald M, 2011.
Structural geology algorithms: Vectors and tensors. Cambridge University Press.

AMBERGER, G. F., 1959.
L' autochtone de la partie Nord-Ouest du massif des Aiguilles Rouges: Haute-Savoie et Valais.
Doctoral dissertation. University of Geneva.

ANGELIER, Jacques; CHU, Hao-Tsu; LEE, Jian-Cheng and HU, Jyr-Ching, 2000.
Active faulting and earthquake hazard: The case study of the Chihshang Fault, Taiwan.
Journal of Geodynamics. Vol. 29, no. 3, pp. 151–185. ISSN 0264-3707.
Available from DOI: 10.1016/S0264-3707(99)00045-9.

ANGRAND, Paul and MOUTHEREAU, Frédéric, 2021.
Evolution of the Alpine orogenic belts in the Western Mediterranean region as resolved by the kinematics of the Europe-Africa diffuse plate boundary.
Bulletin de la Société Géologique de France. Vol. 192, no. 1. ISSN 0037-9409.
Available from DOI: 10.1051/bsgf/2021031.42.

ANTOINE, P.; FÉRAUD, J. and POULAIN, P. A., 1979.
Carte géologique de la France, feuille du Mont-Blanc (Sheet 704, scale 1:50,000).
French geological survey: Bureau de Recherches Géologiques et Minières.

ANTOINE, Pierre; PAIRIS, Jean-Louis and PAIRIS, Bernard, 1975.
Quelques observations nouvelles sur la structure de la couverture sédimentaire interne du massif du Mont-Blanc, entre le col Ferret (frontière italo-suisse) et la Tête des Fours (Savoie, France).
Géologie Alpine. Vol. 51, pp. 5–23.

ARGAN, E., 1916. Sur l'arc des Alpes occidentales. *Eclogae geologicae Helveticae*.
Vol. 14, pp. 145–192.

ARRHENIUS, S., 1967.
ON THE REACTION VELOCITY OF THE INVERSION OF CANE SUGAR BY ACIDS. In:
Selected Readings in Chemical Kinetics. Elsevier, pp. 31–35.
Available from DOI: 10.1016/b978-0-08-012344-8.50005-2.

AUSTIN, Nicholas; EVANS, Brian; HERWEGH, Marco and EBERT, Andreas, 2008.
Strain localization in the Morcles nappe (Helvetic Alps, Switzerland).
Swiss Journal of Geosciences. Vol. 101, no. 2, pp. 341–360.
Available from DOI: 10.1007/s00015-008-1264-2.

AVANZINI, Marco and CAVIN, Lionel, 2009. A new Isochirotherium trackway from the Triassic of Vieux Emosson, SW Switzerland: stratigraphic implications. *Swiss Journal of Geosciences*. Vol. 102, no. 2, pp. 353–361. Available from DOI: 10.1007/s00015-009-1322-4.

AVOUAC, J. P. and BUROV, E. B., 1996.
Erosion as a driving mechanism of intracontinental mountain growth.
Journal of Geophysical Research: Solid Earth. Vol. 101, no. B8, pp. 17747–17769.
Available from DOI: 0.1029/96JB01344.

AVOUAC, Jean-Philippe, 2003.
Mountain building, erosion, and the seismic cycle in the Nepal Himalaya.
Advances in geophysics. Vol. 46, pp. 1–80.

AYRTON, S.; BARFÉTY, J.; BELLIÈRE, J.; GUBLER, Y. and JEMELIN, L., 1987.
Carte géologique de la France, feuille de Chamonix (Sheet 680, scale 1:50,000).
French geological survey: Bureau de Recherches Géologiques et Minières.

AYRTON, Stephen, 1972. Sur la prolongation de la nappe de Morcles en France.
Eclogae Geologicae Helvetiae. Available from DOI: 10.5169/SEALS-164096.

AYRTON, Stephen, 1980. La géologie de la zone Martigny - Chamonix (versant suisse) et l'origine de la nappe de Morcles (un exemple de subduction continentale). *Eclogae Geolicae Helvetiae*. Vol. 73, no. 1, pp. 137–172. Available also from: https://hal-insu.archives-ouvertes.fr/insu-00925393.

BACHMANN, F.; HIELSCHER, Ralf and SCHAEBEN, Helmut, 2010.
Texture Analysis with MTEX – Free and Open Source Software Toolbox.
Solid State Phenomena. Vol. 160, pp. 63–68.
Available from DOI: 10.4028/www.scientific.net/ssp.160.63.

BACHMANN, Florian; HIELSCHER, Ralf and SCHAEBEN, Helmut, 2011.
Grain detection from 2d and 3d EBSD data—Specification of the MTEX algorithm.
Ultramicroscopy. Vol. 111, no. 12, pp. 1720–1733. ISSN 0304-3991.
Available from DOI: 10.1016/j.ultramic.2011.08.002.

BADOUX, H; BURRI, M; GALLUS, JH; KRUMMENACHER, D; LOUP, G and SUBLET, P, 1971.
Feuille 1305 Dent de Mordes. *Atlas géologique de la Suisse*. No. 25,000.

BAUVILLE, Arthur and SCHMALHOLZ, Stefan M., 2015.
Transition from thin- to thick-skinned tectonics and consequences for nappe formation: Numerical simulations and applications to the Helvetic nappe system, Switzerland.

Tectonophysics. Vol. 665, pp. 101–117.
Available from DOI: 10.1016/j.tecto.2015.09.030.

BEAUDOIN, Alexandre; SCAILLET, Stéphane; MORA, Nicolas; JOLIVET, Laurent and AUGIER, Romain, 2020. In Situ and Step-Heating $^{40}Ar/^{39}$ Ar Dating of White Mica in Low-Temperature Shear Zones (Tenda Massif, Alpine Corsica, France). *Tectonics*. Vol. 39, no. 12. Available from DOI: 10.1029/2020tc006246.

BEAUMONT, C.; JAMIESON, R. A.; NGUYEN, M. H. and LEE, B., 2001. Himalayan tectonics explained by extrusion of a low-viscosity crustal channel coupled to focused surface denudation. *Nature*. Vol. 414, no. 6865, pp. 738–742. Available from DOI: 10.1038/414738a.

BELLAHSEN, N.; JOLIVET, L.; LACOMBE, O.; BELLANGER, M.; BOUTOUX, A.; GARCIA, S.; MOUTHEREAU, F.; POURHIET, L. Le and GUMIAUX, C., 2012.
Mechanisms of margin inversion in the external Western Alps: Implications for crustal rheology. *Tectonophysics*. Vol. 560-561, pp. 62–83.
Available from DOI: 10.1016/j.tecto.2012.06.022.

BELLAHSEN, N.; MOUTHEREAU, F.; BOUTOUX, A.; BELLANGER, M.; LACOMBE, O.; JOLIVET, L. and ROLLAND, Y., 2014. Collision kinematics in the western external Alps. *Tectonics*. Vol. 33, no. 6, pp. 1055–1088. Available from DOI: 10.1002/2013tc003453.

BELLANGER, M.; AUGIER, R.; BELLAHSEN, N.; JOLIVET, L.; MONIÉ, P.; BAUDIN, T. and BEYSSAC, O., 2015. Shortening of the European Dauphinois margin (Oisans Massif, Western Alps): New insights from RSCM maximum temperature estimates and 40Ar/39Ar in situ dating. *Journal of Geodynamics*. Vol. 83, pp. 37–64.
Available from DOI: 10.1016/j.jog.2014.09.004.

BELLIERE, Jacques, 1988. On the age of mylonites within the Mont Blanc massif. *Geodinamica Acta*. Vol. 2, no. 1, pp. 13–16. Available from DOI: 10.1080/09853111.1988.11105151.

BELLIÈRE, J., 1956.
Caractère de la déformation alpine dans les schistes cristallins du massif du Mont-Blanc. *Bulletin de la Société Géologique de France*. Vol. VI, pp. 691–6988.

BERGEMANN, Christian A.; GNOS, Edwin and WHITEHOUSE, Martin J., 2019.
Insights into the tectonic history of the Western Alps through dating of fissure monazite in the Mont Blanc and Aiguilles Rouges Massifs. *Tectonophysics*. Vol. 750, pp. 203–212.
Available from DOI: 10.1016/j.tecto.2018.11.013.

BERMUDEZ, Mauricio A.; BEEK, Peter van der and BERNET, Matthias, 2011.
Asynchronous Miocene–Pliocene exhumation of the central Venezuelan Andes. *Geology*. Vol. 39, no. 2, pp. 139–142. ISSN 0091-7613. Available from DOI: 10.1130/G31582.1.

BERTHÉ, Didier; CHOUKROUNE, Pierre and GAPAIS, Denis, 1979.
Orientations préférentielles du quartz et orthogneissification progressive en régime cisaillant : l'exemple du cisaillement sud-armoricain. *Bulletin de Minéralogie*.
Vol. 102, no. 2-3, pp. 265–272. Available also from: https://www.persee.fr/doc/bulmi_0180-9210_1979_act_102_2_7287.

BERTINI, G.; MARCUCCI, M.; NEVINI, R.; PASSERINI, P. and SGUAZZONI, G., 1985.
Patterns of faulting in the Mont Blanc granite. *Tectonophysics*. Vol. 111, no. 1-2, pp. 65–106. Available from DOI: 10.1016/0040-1951(85)90066-6.

BERTRAND, M., 1881. Failles de la lisière du Jura entre Besançon et Salins. *Bull. Soc. Géol. Fr.* Vol. 3, no. 10, pp. 114–126.

BIGOT-CORMIER, Florence; SOSSON, Marc; POUPEAU, Gérard; STÉPHAN, Jean-François and LABRIN, Erika, 2006.
The denudation history of the Argentera Alpine External Crystalline Massif (Western Alps, France-Italy): an overview from the analysis of fission tracks in apatites and zircons. *Geodinamica Acta*. Vol. 19, no. 6, pp. 455–473.
Available from DOI: 10.3166/ga.19.455-473.

BILAU, Antonin; BIENVEIGNANT, Dorian; ROLLAND, Yann; SCHWARTZ, Stéphane; GODEAU, Nicolas; GUIHOU, Abel; DESCHAMPS, Pierre; MANGENOT, Xavier; BRIGAUD, Benjamin; BOSCHETTI, Louise and DUMONT, Thierry, 2023. The Tertiary structuration of the Western Subalpine foreland deciphered by calcite-filled faults and veins. *Earth-Science Reviews*. Vol. 236, p. 104270. ISSN 0012-8252.
Available from DOI: 10.1016/j.earscirev.2022.104270.

BILLANT, Jérémy; HIPPOLYTE, Jean-Claude and BELLIER, Olivier, 2015. Tectonic and geomorphic analysis of the Belledonne border fault and its extensions, Western Alps. *Tectonophysics*. Vol. 659, pp. 31–52. ISSN 0040-1951.
Available from DOI: 10.1016/j.tecto.2015.07.025.

BOLLINGER, L.; AVOUAC, J. P.; BEYSSAC, O.; CATLOS, E. J.; HARRISON, T. M.; GROVE, M.; GOFFÉ, B. and SAPKOTA, S., 2004.
Thermal structure and exhumation history of the Lesser Himalaya in central Nepal. *Tectonics*. Vol. 23, no. 5. Available from DOI: 10.1029/2003TC001564.

BONNET, Cécile; MALAVIEILLE, Jacques and MOSAR, Jon, 2007.
Interactions between tectonics, erosion, and sedimentation during the recent evolution of the Alpine orogen: Analogue modeling insights. *Tectonics*. Vol. 26, no. 6.
Available from DOI: 10.1029/2006TC002048.

BONNET, Cécile; MALAVIEILLE, Jacques and MOSAR, Jon, 2008.
Surface processes versus kinematics of thrust belts: impact on rates of erosion, sedimentation, and exhumation – Insights from analogue models. *Bulletin de la Société Géologique de France*. Vol. 179, no. 3, pp. 297–314. ISSN 0037-9409.
Available from DOI: 10.2113/gssgfbull.179.3.297.

BOUSQUET, R.; ENGI, M.; GOSSO, G.; OBERHÄNSLI, R.; BERGER, A.; SPALLA, M. I. and GOFFÉ, B., 2004. Explanatory notes to the map: metamorphic structure of the Alps transition from the Western to the Central Alps.
Mitteilungen Der Österreichischen Mineralogischen Gesellschaft. Vol. 134, no. 1, pp. 279–298.

BOUSQUET, Romain; OBERHÄNSLI, Roland; SCHMID, Stefan; BERGER, Alfons; WIEDERKEHR, Michael; MOELLER, Andreas; ROSENBERG, Claudio; ZEILINGER, Gerold; MOLLI, Giancarlo and KOLLER, Friedrich, 2012. *Metamorphic structure of the Alps*.

BOUTOUX, A.; BELLAHSEN, N.; NANNI, U.; PIK, R.; VERLAGUET, A.; ROLLAND, Y. and LACOMBE, O., 2016.
Thermal and structural evolution of the external Western Alps: Insights from (U–Th–Sm)/He thermochronology and RSCM thermometry in the Aiguilles Rouges/Mont Blanc massifs. *Tectonophysics*. Vol. 683, pp. 109–123.
Available from DOI: 10.1016/j.tecto.2016.06.010.

BOUTOUX, Alexandre; BELLAHSEN, Nicolas; LACOMBE, Olivier; VERLAGUET, Anne and MOUTHEREAU, Frédéric, 2014. Inversion of pre-orogenic extensional basins in the external Western Alps: Structure, microstructures and restoration. *Journal of Structural Geology*. Vol. 60, pp. 13–29. Available from DOI: 10.1016/j.jsg.2013.12.014.

BOYER, S. E. and ELLIOTT, D., 1982. Thrus Systems.
The American Association of Petroleum Geologists Bulletin. Vol. 66, no. 9, pp. 1196–1230.
Available from DOI: 10.1016/j.jsg.2013.12.014.

BRÄNDLEIN, P.; NOLLAU, G. and SHARP, Z., 1994.
Petrography and geochemistry of the Vallorcine granite (Aiguilles Rouges massif, Western Alps). *Schweizerische mineralogische und petrographische Mitteilungen*. Vol. 74, pp. 227–243.
Available from DOI: 10.5169/SEALS-56344.

BRAUN, Jean, 2002. Quantifying the effect of recent relief changes on age–elevation relationships. *Earth and Planetary Science Letters*. Vol. 200, no. 3, pp. 331–343. ISSN 0012-821X. Available from DOI: 10.1016/S0012-821X(02)00638-6.

BRAUN, Jean, 2003. Pecube: a new finite-element code to solve the 3D heat transport equation including the effects of a time-varying, finite amplitude surface topography. *Computers & Geosciences*. Vol. 29, no. 6, pp. 787–794. Available from DOI: 10.1016/s0098-3004(03)00052-9.

BRAUN, Jean and ROBERT, Xavier, 2005. Constraints on the rate of post-orogenic erosional decay from low-temperature thermochronological data: application to the Dabie Shan, China. *Earth Surface Processes and Landforms*. Vol. 30, no. 9, pp. 1203–1225. Available from DOI: 10.1002/esp.1271.

BRAUN, Jean; VAN DER BEEK, Peter and BATT, Geoffrey, 2006. *Quantitative Thermochronology: Numerical Methods for the Interpretation of Thermochronological Data*. Cambridge University Press. Available from DOI: 10.1017/CBO9780511616433.

BRAUN, Jean; VAN DER BEEK, Peter; VALLA, Pierre; ROBERT, Xavier; HERMAN, Frédéric; GLOTZBACH, Christoph; PEDERSEN, Vivi; PERRY, Claire; SIMON-LABRIC, Thibaud and PRIGENT, Cécile, 2012. Quantifying rates of landscape evolution and tectonic processes by thermochronology and numerical modeling of crustal heat transport using PECUBE. *Tectonophysics*. Vol. 524-525, pp. 1–28. Available from DOI: 10.1016/j.tecto.2011.12.035.

BURCHFIEL, B. C. and ROYDEN, L H., 1985. North-south extension within the convergent Himalayan region. *Geology*. Vol. 13, no. 10, p. 679. Available from DOI: 10.1130/0091-7613(1985)13<679:newtch>2.0.co;2.

BURCHFIEL, Burrell C.; ZHILIANG, Chen; HODGES, Kip V.; YUPING, Liu; ROYDEN, Leigh H.; CHANGRONG, Deng and JIENE, Xu, 1992. The South Tibetan Detachment System, Himalayan Orogen: Extension Contemporaneous With and Parallel to Shortening in a Collisional Mountain Belt. In: *Geological Society of America Special Papers*. Geological Society of America, pp. 1–41. Available from DOI: 10.1130/spe269-p1.

BURG, J.P.; BRUNEL, M.; GAPAIS, D.; CHEN, G.M. and LIU, G.H., 1984. Deformation of leucogranites of the crystalline Main Central Sheet in southern Tibet (China). *Journal of Structural Geology*. Vol. 6, no. 5, pp. 535–542. Available from DOI: 10.1016/0191-8141(84)90063-4.

BURG, Jean-Pierre, 1983. *Carte Géologique du sud du Tibet*.
Ministère de la Géologie, République Populaire de Chine.

BURKHARD, Martin and SOMMARUGA, Anna, 1998.
Evolution of the western Swiss Molasse basin: structural relations with the Alps and the Jura belt.
Geological Society, London, Special Publications. Vol. 134, no. 1, pp. 279–298.
Available from DOI: 10.1144/gsl.sp.1998.134.01.13.

BUROV, Evgene B. and DIAMENT, Michel, 1995.
The effective elastic thickness (T e) of continental lithosphere: What does it really mean?
Journal of Geophysical Research: Solid Earth. Vol. 100, no. B3, pp. 3905–3927.
Available from DOI: 10.1029/94JB02770.

BURRI, M; JEMELIN, L; OULIANOFF, N; AYRTON, S; GRASMÜCK, K; KRUMMENACHER, D; RAUMER, J von; STALDER, P; TRÜMPY, R and WUTZ, B, 1983. Feuille 1325 Sembrancher.
Atlas géologique de la Suisse. Vol. 1, no. 25,000.

BUSSY, François; HERNANDEZ, Jean and VON RAUMER, Jürgen, 2000.
Bimodal magmatism as a consequence of the post-collisional readjustment of the thickened Variscan continental lithosphere (Aiguilles Rouges-Mont Blanc Massifs, Western Alps).
Earth and Environmental Science Transactions of the Royal Society of Edinburgh.
Vol. 91, no. 1-2, pp. 221–233. Available from DOI: 10.1017/s0263593300007392.

BUSSY, François and RAUMER, Jürgen Von, 1993.
U-Pb dating of Palaeozoic events in the Mont-Blanc crystalline massif, Western Alps.
Terra Nova. Vol. 5, no. 1, pp. 56–57.

BUTLER, Robert W.H., 1985. The restoration of thrust systems and displacement continuity around the Mont Blanc massif, NW external Alpine thrust belt. *Journal of Structural Geology*.
Vol. 7, no. 5, pp. 569–582. Available from DOI: 10.1016/0191-8141(85)90029-x.

BUTLER, Robert W.H.; BOND, Clare E.; COOPER, Mark A. and WATKINS, Hannah, 2018.
Interpreting structural geometry in fold-thrust belts: Why style matters.
Journal of Structural Geology. Vol. 114, pp. 251–273.
Available from DOI: 10.1016/j.jsg.2018.06.019.

BYRNE, T.; CHAN, Y.-C.; RAU, R.-J.; LU, C.-Y.; LEE, Y.-H. and WANG, Y.-J., 2011.
The Arc–Continent Collision in Taiwan. In: *Arc-Continent Collision*.
Berlin, Heidelberg: Springer Berlin Heidelberg, pp. 213–245. ISBN 978-3-540-88558-0.
Available from DOI: 10.1007/978-3-540-88558-0_8.

CALCAGNO, P.; CHILÈS, J.P.; COURRIOUX, G. and GUILLEN, A., 2008.
Geological modelling from field data and geological knowledge.
Physics of the Earth and Planetary Interiors. Vol. 171, no. 1-4, pp. 147–157.
Available from DOI: 10.1016/j.pepi.2008.06.013.

CAMPANI, Marion; MANCKTELOW, Neil and COURRIOUX, Gabriel, 2014.
The 3D interplay between folding and faulting in a syn-orogenic extensional system: the Simplon Fault Zone in the Central Alps (Switzerland and Italy). *Swiss Journal of Geosciences*. Vol. 107, no. 2-3, pp. 251–271. Available from DOI: 10.1007/s00015-014-0163-y.

CAMPANI, MMarion; MANCKTELOW, Neil; SEWARD, Diane; ROLLAND, Yann; MÜLLER, W. and GUERRA, I., 2010.
Geochronological evidence for continuous exhumation through the ductile-brittle transition along a crustal-scale low-angle normal fault: Simplon Fault Zone, central Alps. *Tectonics*. Vol. 29, no. 3. Available from DOI: 10.1029/2009tc002582.

CAPUZZO, Nicola and BUSSY, François, 2000.
High-precision dating and origin of synsedimentary volcanism in the Late Carboniferous Salvan-Dorénaz basin (Aiguilles-Rouges Massif, Western Alps).
Schweizerische mineralogische und petrographische Mitteilungen. Vol. 80, pp. 147–167.
Available from DOI: 10.5169/SEALS-60958.

CAPUZZO, Nicola; HANDLER, Robert; NEUBAUER, Franz and WETZEL, Andreas, 2003.
Post-collisional rapid exhumation and erosion during continental sedimentation: the example of the late Variscan Salvan-Dorénaz basin (Western Alps). *International Journal of Earth Sciences*. Vol. 92, no. 3, pp. 364–379. Available from DOI: 10.1007/s00531-003-0332-0.

CAPUZZO, Nicola and WETZEL, Andreas, 2004. Facies and basin architecture of the Late Carboniferous Salvan-Dorénaz continental basin (Western Alps, Switzerland/France).
Sedimentology. Vol. 51, no. 4, pp. 675–697.
Available from DOI: 10.1111/j.1365-3091.2004.00642.x.

CARA, Michel; VAN DER WOERD, Jérôme; ALASSET, Pierre-Jean; BENJUMEA, Juan and MÉRIAUX, Anne-Sophie, 2017. The 1905 Chamonix earthquakes: active tectonics in the Mont Blanc and Aiguilles Rouges massifs. *Swiss Journal of Geosciences*. Vol. 110, no. 2, pp. 631–651.
Available from DOI: 10.1007/s00015-017-0262-7.

CARDOZO, Nestor and ALLMENDINGER, Richard W, 2013.
Spherical projections with OSXStereonet. *Computers & Geosciences*. Vol. 51, pp. 193–205.
Available from DOI: 10.1016/j.cageo.2012.07.021.

CARENA, Sara; SUPPE, John and KAO, Honn, 2002. Active detachment of Taiwan illuminated by small earthquakes and its control of first-order topography. *Geology*. Vol. 30, no. 10, pp. 935–938. ISSN 0091-7613. Available from DOI: 10.1130/0091-7613(2002)030<0935:ADOTIB>2.0.CO;2.

CARR, J. C.; BEATSON, R. K.; CHERRIE, J. B.; MITCHELL, T. J.; FRIGHT, W. R.; MCCALLUM, B. C. and EVANS, T. R., 2001. Reconstruction and Representation of 3D Objects with Radial Basis Functions. In: *Proceedings of the 28th Annual Conference on Computer Graphics and Interactive Techniques*. New York, NY, USA: Association for Computing Machinery, pp. 67–76. SIGGRAPH '01. ISBN 158113374X. Available from DOI: 10.1145/383259.383266.

CARSLAW, H. S. and JAEGER, J. C., 1947. *Conduction of heat in solids*.

CENKI-TOK, Bénédicte; DARLING, James R.; ROLLAND, Yann; DHUIME, Bruno and STOREY, Craig D., 2013. Direct dating of mid-crustal shear zones with synkinematic allanite: new in situ U-Th-Pb geochronological approaches applied to the Mont Blanc massif. *Terra Nova*. Vol. 26, no. 1, pp. 29–37. Available from DOI: 10.1111/ter.12066.

CERIANI, Stefano; FÜGENSCHUH, Bernhard and SCHMID, Stefan M., 2001. Multi-stage thrusting at the "Penninic Front" in the Western Alps between Mont Blanc and Pelvoux massifs. *International Journal of Earth Sciences*. Vol. 90, no. 3, pp. 685–702. Available from DOI: 10.1007/s005310000188.

CHALLANDES, Nathalie; MARQUER, Didier and VILLA, Igor M., 2008. P-T-t modelling, fluid circulation, and 39Ar-40Ar and Rb-Sr mica ages in the Aar Massif shear zones (Swiss Alps). *Swiss Journal of Geosciences*. Vol. 101, no. 2, pp. 269–288. Available from DOI: 10.1007/s00015-008-1260-6.

CHAMBERLIN, Rollin T., 1925. The Wedge Theory of Diastrophism. *The Journal of Geology*. Vol. 33, no. 8, pp. 755–792. Available from DOI: 10.1086/623259.

CHAMBERLIN, T. C., 1899. An Attempt to Frame a Working Hypothesis of the Cause of Glacial Periods on an Atmospheric Basis. *The Journal of Geology*. Vol. 7, no. 6, pp. 545–584. Available from DOI: 10.1086/608449.

CHAMPAGNAC, J.D.; MOLNAR, P.; ANDERSON, R.S.; SUE, C. and DELACOU, B., 2007. Quaternary erosion-induced isostatic rebound in the western Alps. *Geology*. Vol. 35, no. 3, p. 195. Available from DOI: 10.1130/g23053a.1.

CHAROLLAIS, J.; DAVAUD, E. and JAMET, M., 1996. Evolution of the southeastern Jura plateform-margin between the upper Jurassic and the Oligocene: new data from three oil wells. *Géologie de la France*. Vol. 1, no. 3, pp. 25–42.
Available also from: http://geolfrance.brgm.fr/sites/default/files/upload/documents/revues_articles_gf3-1-1996.pdf.

CHAROLLAIS, Jean and JAMET, Marc, 1990.
Principaux résultats géologiques du forage Brizon 1 (BZN 1) Haute-Savoie, France.
Mémoires de la Société géologique de France (1833). Vol. 156, pp. 185–202.

CHEW, David M. and SPIKINGS, Richard A., 2015. Geochronology and Thermochronology Using Apatite: Time and Temperature, Lower Crust to Surface. *Elements*. Vol. 11, no. 3, pp. 189–194. ISSN 1811-5209. Available from DOI: 10.2113/gselements.11.3.189.

CHI, WR, 1981. Stratigraphic record of plate interactions in the Coastal Range of eastern Taiwan. *Memoir of the Geological Society of China*. Vol. 4, pp. 155–194.

CHOPIN, C.; GIBBONS, W.; PLATT, J. P.; ARTYUSHKOV, E. V.; OXBURGH, Ernest Ronald; YARDLEY, B. W. D. and ENGLAND, Philip Christopher, 1987. Very-high-pressure metamorphism in the western Alps: implications for subduction of continental crust. *Philosophical Transactions of the Royal Society of London. Series A, Mathematical and Physical Sciences*. Vol. 321, no. 1557, pp. 183–197.
Available from DOI: 10.1098/rsta.1987.0010.

CHOUKROUNE, Pierre and GAPAIS, Denis, 1983. Strain pattern in the Aar Granite (Central Alps): orthogneiss developed by bulk inhomogeneous flattening.
In: COBBOLD, P.R.; SCHWERDTNER, W.M. and TREAGUS, S.H. (eds.).
Strain Patterns in Rocks. Pergamon, pp. 411–418. ISBN 978-0-08-030273-7.
Available from DOI: doi.org/10.1016/B978-0-08-030273-7.50019-7.

COBBOLD, P.R. and QUINQUIS, H., 1980. Development of sheath folds in shear regimes. *Journal of Structural Geology*. Vol. 2, no. 1-2, pp. 119–126.
Available from DOI: 10.1016/0191-8141(80)90041-3.

COLLET, L. W., 1927. *The Structure of the Alps*. Edward Arnold, London. ISBN 9781118708118.

COLLET, L. W. and PARÉJAS, Ed., 1920. *The Structure of the Alps*.
Available from DOI: 10.5169/SEALS-742613.

COLLET, Léon W.; OULIANOFF, N. and REINHARD, M., 1952.
carte géologique Suisse : feuille de Finhaut n°525 (scale 1 :25,000).
Commission géologique Suisse.

COLLOMBET, M.; THOMAS, J. C.; CHAUVIN, A.; TRICART, P.; BOUILLIN, J. P. and GRATIER, J. P., 2002. Counterclockwise rotation of the western Alps since the Oligocene: New insights from paleomagnetic data. *Tectonics*. Vol. 21, no. 4, pp. 14-1-14–15.
Available from DOI: 10.1029/2001TC901016.

CONNOLLY, J. A. D., 1990.
Multivariable phase diagrams; an algorithm based on generalized thermodynamics.
American Journal of Science. Vol. 290, no. 6, pp. 666–718.
Available from DOI: 10.2475/ajs.290.6.666.

CONNOLLY, J. A. D. and PETRINI, K., 2002. An automated strategy for calculation of phase diagram sections and retrieval of rock properties as a function of physical conditions.
Journal of Metamorphic Geology. Vol. 20, no. 7, pp. 697–708.
Available from DOI: 10.1046/j.1525-1314.2002.00398.x.

CORBIN, P. and OULIANOFF, N., 1928.
carte géologique du Mont-Blanc : feuille Des Tines (scale 1:20,000).
Institut de Géologie et de Paléontologie. Available also from: https://hal-insu.archives-ouvertes.fr/insu-01026264.

COTTLE, John M.; SEARLE, Michael P.; HORSTWOOD, Matthew S. A. and WATERS, David J., 2009. Timing of Midcrustal Metamorphism, Melting, and Deformation in the Mount Everest Region of Southern Tibet Revealed by U(-Th)-Pb Geochronology. *The Journal of Geology*. Vol. 117, no. 6, pp. 643–664. Available from DOI: 10.1086/605994.

COWAN, EJ; BEATSON, RK; FRIGHT, WR; MCLENNAN, TJ and MITCHELL, TJ, 2002.
Rapid geological modelling. In:
Applied structural geology for mineral exploration and mining, international symposium, pp. 23–25.

CRESPO-BLANC, Anne; MASSON, Henri; SHARP, Zachary; COSCA, Michael and HUNZIKER, Johannes, 1995. A stable and 40Ar/39Ar isotope study of a major thrust in the Helvetic nappes (Swiss Alps): Evidence for fluid flow and constraints on nappe kinematics. *GSA Bulletin*. Vol. 107, no. 10, pp. 1129–1144. ISSN 0016-7606.
Available from DOI: 10.1130/0016-7606(1995)107<1129:ASAAAI>2.3.CO;2.

DAHLEN, F. A., 1984. Noncohesive critical Coulomb wedges: An exact solution.
Journal of Geophysical Research: Solid Earth. Vol. 89, no. B12, pp. 10125–10133.
Available from DOI: 10.1029/jb089ib12p10125.

DAL ZILIO, Luca; RUH, Jonas and AVOUAC, Jean-Philippe, 2020.
Structural Evolution of Orogenic Wedges: Interplay Between Erosion and Weak Décollements.
Tectonics. Vol. 39, no. 10, e2020TC006210. Available from DOI: 10.1029/2020TC006210.

DALL'ASTA, Nicolas; HOAREAU, Guilhem; MANATSCHAL, Gianreto; CENTRELLA, Stephen; DENÈLE, Yoann; RIBES, Charlotte and KALIFI, Amir, 2022.
Structural and petrological characteristics of a Jurassic detachment fault from the Mont-Blanc massif (Col du Bonhomme area, France). *Journal of Structural Geology*. Vol. 159, p. 104593.
ISSN 0191-8141. Available from DOI: 10.1016/j.jsg.2022.104593.

DANIŠÍK, Martin; KUHLEMANN, Joachim; DUNKL, István; EVANS, Noreen J.; SZÉKELY, Balázs and FRISCH, Wolfgang, 2012.
Survival of Ancient Landforms in a Collisional Setting as Revealed by Combined Fission Track and (U-Th)/He Thermochronometry: A Case Study from Corsica (France).
The Journal of Geology. Vol. 120, no. 2, pp. 155–173. Available from DOI: 10.1086/663873.

DE LEPINAY, Bernard ; Paris 6 (Degree-grantor), 1981.
Etude géologique de la région des Gets et de Samoens, Haute Savoie. Les rapports entre les Préalpes du Chablais (nappe de la Brèche et nappe des Gêts) et les unités delphino-helvétiques.
ISSN 0755-1347. PhD thesis.

DE SAUSSURE, Horace Benedict, 1796. *Voyages dans les Alpes*. Vol. 3.

DECELLES, P.G.; GEHRELS, G.E.; NAJMAN, Y.; MARTIN, A.J.; CARTER, A. and GARZANTI, E., 2004. Detrital geochronology and geochemistry of Cretaceous–Early Miocene strata of Nepal: implications for timing and diachroneity of initial Himalayan orogenesis.
Earth and Planetary Science Letters. Vol. 227, no. 3, pp. 313–330. ISSN 0012-821X.
Available from DOI: 10.1016/j.epsl.2004.08.019.

DECELLES, Peter G.; ROBINSON, Delores M. and ZANDT, George, 2002.
Implications of shortening in the Himalayan fold-thrust belt for uplift of the Tibetan Plateau.
Tectonics. Vol. 21, no. 6, pp. 12-1-12–25. Available from DOI: 10.1029/2001TC001322.

DEMATHIEU, G. and WEIDMANN, M., 1982.
Les empreintes de pas de reptiles dans le Trias du Vieux Emosson (Finhaut, Valais, Suisse).
Eclogae Geologicae Helvetiae. Vol. 75, no. 3, pp. 721–757.

DEVILLE, Éric and CHAUVIÈRE, Alain, 2000. Thrust tectonics at the front of the western Alps: constraints provided by the processing of seismic reflection data along the Chambéry transect. *Comptes Rendus de l'Académie des Sciences - Series IIA - Earth and Planetary Science*. Vol. 331, no. 11, pp. 725–732. Available from DOI: 10.1016/s1251-8050(00)01463-4.

DEWEY, John F.; PITMAL, Walter C.; RYAN, William B. F. and BONNIN, Jean, 1973. Plate Tectonics and the Evolution of the Alpine System. *Geological Society of America Bulletin*. Vol. 84, no. 10, p. 3137. Available from DOI: 10.1130/0016-7606(1973)84<3137:ptateo>2.0.co;2.

DÈZES, P.; SCHMID, S.M. and ZIEGLER, P.A., 2004. Evolution of the European Cenozoic Rift System: interaction of the Alpine and Pyrenean orogens with their foreland lithosphere. *Tectonophysics*. Vol. 389, no. 1, pp. 1–33. ISSN 0040-1951. Available from DOI: 10.1016/j.tecto.2004.06.011.

DI VINCENZO, Gianfranco; GRANDE, Antonietta; PROSSER, Giacomo; CAVAZZA, William and DECELLES, Peter G., 2016. 40Ar–39Ar laser dating of ductile shear zones from central Corsica (France): Evidence of Alpine (middle to late Eocene) syn-burial shearing in Variscan granitoids. *Lithos*. Vol. 262, pp. 369–383. ISSN 0024-4937. Available from DOI: 10.1016/j.lithos.2016.07.022.

DIELFORDER, A. and HAMPEL, A., 2021. Force-Balance Analysis of Stress Changes During the Subduction-Collision Transition and Implications for the Rise of Mountain Belts. *Journal of Geophysical Research: Solid Earth*. Vol. 126, no. 3, e2020JB020914. Available from DOI: 10.1029/2020JB020914. e2020JB020914 2020JB020914.

DIELFORDER, Armin, 2017. Constraining the strength of megathrusts from fault geometries and application to the Alpine collision zone. *Earth and Planetary Science Letters*. Vol. 474, pp. 49–58. Available from DOI: 10.1016/j.epsl.2017.06.021.

DIELFORDER, Armin; HETZEL, Ralf and ONCKEN, Onno, 2020. Megathrust shear force controls mountain height at convergent plate margins. *Nature* [online]. Vol. 582, no. 7811, pp. 225–229 [visited on 2022-10-25]. ISSN 0028-0836, ISSN 1476-4687. Available from DOI: 10.1038/s41586-020-2340-7.

DOBMEIER, Christoph and VON RAUMER, Jürgen, 1995. Significance of Latest-Variscan and Alpine Deformation For the Evolution of Montagne de Pormenaz (SouthWestern Aiguilles-Rouges massif, Western Alps. *Eclogae Geologicae Helvetiae*. Vol. 88, no. 2, pp. 267–279.

DODSON, Martin H., 1973.
Closure temperature in cooling geochronological and petrological systems.
Contributions to Mineralogy and Petrology. Vol. 40, no. 3, pp. 259–274.
Available from DOI: 10.1007/bf00373790.

DOUDOUX, B.; LEPINAY, B. Mercier de and TARDY, M., 1982.
Une interprétation nouvelle de la structure des massifs subalpins savoyards (Alpes occidentales): nappes de charriage oligocènes et déformations superposées.
Comptes Rendus de l'Académie des Sciences de Paris. Vol. II, no. 64, pp. 63–68.

DOUDOUX, Bernard; BARFETY, JC; CARFANTAN, JC; TARDY, M; NICOUD, G and ROSSET, J, 1992. Annecy-Ugine. *Carte Géologique de la France*. No. 50,000.

DUMONT, T.; LEMOINE, M. and TRICART, P., 1984. Tectonique synsedimentaire triasico-jurassique et rifting tethysien dans l'unite prepiemontaise de Rochebrune au Sud-Est de Briancon.
Bulletin de la Société Géologique de France. Vol. S7-XXVI, no. 5, pp. 921–933.
ISSN 0037-9409. Available from DOI: 10.2113/gssgfbull.S7-XXVI.5.921.

DUMONT, T.; SCHWARTZ, S.; GUILLOT, S.; SIMON-LABRIC, T.; TRICART, P. and JOURDAN, S., 2012.
Structural and sedimentary records of the Oligocene revolution in the Western Alpine arc.
Journal of Geodynamics. Vol. 56-57, pp. 18–38. ISSN 0264-3707.
Available from DOI: 10.1016/j.jog.2011.11.006. Geodynamics and Orogenesis.

DUMONT, Thierry, 1988. Late Triassic-Early Jurassic evolution of the Western Alps and of their European foreland; initiation of the Tethyan rifting. *Bulletin de la Société Géologique de France*. Vol. IV, no. 4, pp. 601–611. ISSN 0037-9409.
Available from DOI: 10.2113/gssgfbull.IV.4.601.

DUMONT, Thierry; CHAMPAGNAC, Jean-Daniel; CROUZET, Christian and ROCHAT, Philippe, 2008. Multistage shortening in the Dauphiné zone (French Alps): the record of Alpine collision and implications for pre-Alpine restoration. *Swiss Journal of Geosciences*.
Vol. 101, no. S1, pp. 89–110. Available from DOI: 10.1007/s00015-008-1280-2.

DUMONT, Thierry; SIMON-LABRIC, Thibaud; AUTHEMAYOU, Christine and HEYMES, Thomas, 2011. Lateral termination of the north-directed Alpine orogeny and onset of westward escape in the Western Alpine arc: Structural and sedimentary evidence from the external zone. *Tectonics*.
Vol. 30, no. 5. Available from DOI: 10.1029/2010TC002836.

DUPARC, L.; LUGEON, M.; MICHEL-LÉVY, A. and MRAZEC, L, 1966.
Carte géologique de la France, feuille de Vallorcine Mont-Blanc (Sheet 160, scale 1:80,000). *French geological survey: Bureau de Recherches Géologiques et Minières*.

EBERT, Andreas; HERWEGH, Marco; EVANS, Brian; PFIFFNER, Adrian; AUSTIN, Nick and VENNEMANN, Torsten, 2007.
Microfabrics in carbonate mylonites along a large-scale shear zone (Helvetic Alps). *Tectonophysics*. Vol. 444, no. 1, pp. 1–26. ISSN 0040-1951.
Available from DOI: doi.org/10.1016/j.tecto.2007.07.004.

EGLI, Daniel and MANCKTELOW, Neil, 2013.
The structural history of the Mont Blanc massif with regard to models for its recent exhumation. *Swiss Journal of Geosciences*. Vol. 106, no. 3, pp. 469–489.
Available from DOI: 10.1007/s00015-013-0153-5.

EGLI, Daniel; MANCKTELOW, Neil and SPIKINGS, Richard, 2017.
Constraints from 40Ar/39Ar geochronology on the timing of Alpine shear zones in the Mont Blanc-Aiguilles Rouges region of the European Alps. *Tectonics*. Vol. 36, no. 4, pp. 730–748.
Available from DOI: 10.1002/2016TC004450.

ELMI, S, 1984. Bordure vivaro-cevenole. In: Mem. BRGM, Orleans, pp. 143–146.

ELTCHANINOFF, Catherine, 1982. *Étude géologique entre Belledonne et Mont Blanc: la terminaison septentrionale du massif de Belledonne et les terrains de son enveloppe - Alpes françaises*. ISSN 0037-9409. Available from DOI: 10.2113/gssgfbull.S7-XXIV.4.817.
PhD thesis.

ELTCHANINOFF-LANCELOT, Catherine; TRIBOULET, Sylvette; DOUDOUX, Bernard; FUDRAL, Serge; RAMPNOUX, Jean-Paul and TARDY, Marc, 1980.
Stratigraphie et tectonique des unites delphino-helvetiques comprises entre Mont-Blanc et Belledonne (Savoie-Alpes occidentales); Implications regionales. Doctoral dissertation.
Université Pierre et Marie Curie de Paris.

ENGLAND, Philip and MOLNAR, Peter, 1990.
Surface uplift, uplift of rocks, and exhumation of rocks. *Geology*.
Vol. 18, no. 12, pp. 1173–1177. ISSN 0091-7613.
Available from DOI: 10.1130/0091-7613(1990)018<1173:SUUORA>2.3.CO;2.

ENGLAND, Philip and MOLNAR, Peter, 1993. Cause and effect among thrust and normal faulting, anatectic melting and exhumation in the Himalaya.

Geological Society, London, Special Publications. Vol. 74, no. 1, pp. 401–411.
Available from DOI: 10.1144/gsl.sp.1993.074.01.27.

EPARD, Jean Luc, 1990. *La nappe de Morcles au sud-ouest du Mont-Blanc*.
Available also from: https://tel.archives-ouvertes.fr/tel-00923347.
PhD thesis. Université de Lausanne. Mémoires de Géologie (Lausanne) No. 8, 1990.

EPARD, Jean-Luc, 1986.
Le contact entre le socle du Mont-Blanc et la zone de Chamonix: implications tectoniques.
Bulletin de la société Vaudoise des sciences naturelles. Vol. 288, pp. 225–245.

ESCHER, Arthur; MASSON, Henri and STECK, Albrecht, 1988.
Coupes géologiques des Alpes occidentales Suisses. *Mémoires des laboratoires de géologie, minéralogie, géophysique et du musée géologique de l'Université de Lausanne*. Vol. 2.

ESCHER, Arthur; MASSON, Henri and STECK, Albrecht, 1993.
Nappe geometry in the Western Swiss Alps. *Journal of Structural Geology*.
Vol. 15, no. 3-5, pp. 501–509. Available from DOI: 10.1016/0191-8141(93)90144-y.

FABRE, Cécile; BOIRON, Marie-Christine; DUBESSY, Jean; CATHELINEAU, Michel and BANKS, David A, 2002. Palaeofluid chemistry of a single fluid event: a bulk and in-situ multi-technique analysis (LIBS, Raman Spectroscopy) of an Alpine fluid (Mont-Blanc).
Chemical Geology. Vol. 182, no. 2-4, pp. 249–264.
Available from DOI: 10.1016/s0009-2541(01)00293-5.

FARLEY, K. A., 2000.
Helium diffusion from apatite: General behavior as illustrated by Durango fluorapatite.
Journal of Geophysical Research: Solid Earth. Vol. 105, no. B2, pp. 2903–2914.
Available from DOI: 10.1029/1999JB900348.

FARLEY, K.A.; WOLF, R.A. and SILVER, L.T., 1996.
The effects of long alpha-stopping distances on (U-Th)/He ages.
Geochimica et Cosmochimica Acta. Vol. 60, no. 21, pp. 4223–4229. ISSN 0016-7037.
Available from DOI: 10.1016/S0016-7037(96)00193-7.

FARR, Tom G.; ROSEN, Paul A.; CARO, Edward; CRIPPEN, Robert; DUREN, Riley; HENSLEY, Scott; KOBRICK, Michael; PALLER, Mimi; RODRIGUEZ, Ernesto; ROTH, Ladislav; SEAL, David; SHAFFER, Scott; SHIMADA, Joanne; UMLAND, Jeffrey; WERNER, Marian; OSKIN, Michael; BURBANK, Douglas and ALSDORF, Douglas, 2007.
The Shuttle Radar Topography Mission. *Reviews of Geophysics*. Vol. 45, no. 2.
Available from DOI: 10.1029/2005rg000183.

FAURE, J. L.; COLLETTA, B.; DEVILLE, E. and LECOMTE, J. C., 1999.
Méthodologie d'équilibrage de coupes structurales en zones compressives: la coupe de la vallée de l'Arve et lacoupe du massif des Bornes (profil Ecors Alp1 et Alp2). Tech. rep.
Etude FSH. (139 pages, 102 figures). Rapport IFP 45584.

FAURE, Michel, 1995. Late orogenic carboniferous extensions in the Variscan French Massif Central. *Tectonics*. Vol. 14, no. 1, pp. 132–153. Available from DOI: 10.1029/94TC02021.

FEDERAL GEOGRAPHIC DATA COMMITTEE, 2006. *FGDC Digital Cartographic Standard for Geologic Map Symbolization (PostScript Implementation)*. U.S. Geological Survey.
Available also from: https://pubs.usgs.gov/tm/2006/11A02/.

FERRANDINI, J; GATTACCECA, J; FERRANDINI, M; DEINO, A and JANIN, M-C, 2003.
Chronostratigraphie et paléomagnétisme des dépôts oligo-miocènes de Corse: implications géodynamiques pour l'ouverture du bassin liguro-provençal.
Bulletin de la Société géologique de France. Vol. 174, no. 4, pp. 357–371.

FERRILL, David A and GROSHONG, Richard H, 1993.
Kinematic model for the curvature of the northern Subalpine Chain, France.
Journal of Structural Geology. Vol. 15, no. 3-5, pp. 523–541.
Available from DOI: 10.1016/0191-8141(93)90146-2.

FRÉCHET, Julien; THOUVENOT, François; FROGNEUX, Michel; DEICHMANN, Nicolas and CARA, Michel, 2010. The Mw 4.5 Vallorcine (French Alps) earthquake of 8 September 2005 and its complex aftershock sequence. *Journal of Seismology*. Vol. 15, no. 1, pp. 43–58.
Available from DOI: 10.1007/s10950-010-9205-8.

GAILLARDET, J.; DUPRÉ, B.; LOUVAT, P. and ALLÈGRE, C.J., 1999. Global silicate weathering and CO2 consumption rates deduced from the chemistry of large rivers. *Chemical Geology*. Vol. 159, no. 1, pp. 3–30. ISSN 0009-2541.
Available from DOI: 10.1016/S0009-2541(99)00031-5.

GALLAGHER, Kerry, 2012.
Transdimensional inverse thermal history modeling for quantitative thermochronology.
Journal of Geophysical Research: Solid Earth. Vol. 117, no. B2, n/a–n/a.
Available from DOI: 10.1029/2011jb008825.

GALLAGHER, Kerry; BROWN, Roderick and JOHNSON, Christopher, 1998.
FISSION TRACK ANALYSIS AND ITS APPLICATIONS TO GEOLOGICAL PROBLEMS.
Annual Review of Earth and Planetary Sciences. Vol. 26, no. 1, pp. 519–572.
Available from DOI: 10.1146/annurev.earth.26.1.519.

GAPAIS, D. and BARBARIN, B., 1986.
Quartz fabric transition in a cooling syntectonic granite (Hermitage Massif, France).
Tectonophysics. Vol. 125, no. 4, pp. 357–370. ISSN 0040-1951.
Available from DOI: 10.1016/0040-1951(86)90171-X.

GAPAIS, Denis, 1989. Shear structures within deformed granites: Mechanical and thermal indicators.
Geology. Vol. 17, no. 12, pp. 1144–1147. ISSN 0091-7613.
Available from DOI: 10.1130/0091-7613(1989)017<1144:SSWDGM>2.3.CO;2.

GARDIEN, Véronique; MARTELAT, Jean-Emmanuel; LELOUP, Philippe-Herve; MAHÉO, Gweltaz; BEVILLARD, Benoit; ALLEMAND, Pascal; MONIÉ, Patrick; PAQUETTE, Jean-Louis; GROSJEAN, Anne-Sabine; FAURE, Michel; CHELLE-MICHOU, Cyril and FELLAH, Clémentine, 2022. Fast exhumation rate during late orogenic extension: The new timing of the Pilat detachment fault (French Massif Central, Variscan belt). *Gondwana Research*. Vol. 103, pp. 260–275. ISSN 1342-937X.
Available from DOI: 10.1016/j.gr.2021.10.007.

GAREFALAKIS, Philippos and SCHLUNEGGER, Fritz, 2019.
Tectonic processes, variations in sediment flux, and eustatic sea level recorded by the 20 Myr old Burdigalian transgression in the Swiss Molasse basin. *Solid Earth*.
Vol. 10, no. 6, pp. 2045–2072. Available from DOI: 10.5194/se-10-2045-2019.

GASQUET, Dominique; BERTRAND, Jean-Michel; PAQUETTE, Jean-Louis; LEHMANN, Jérémie; RATZOV, Gueorgui; GUEDES, Roger De Ascencao; TIEPOLO, Massimo; BOULLIER, Anne-Marie; SCAILLET, Stéphane and NOMADE, Sébastien, 2010.
Miocene to Messinian deformation and hydrothermal activity in a pre-Alpine basement massif of the French western Alps: new U-Th-Pb and argon ages from the Lauzière massif.
Bulletin de la Société Géologique de France. Vol. 181, no. 3, pp. 227–241.
Available from DOI: 10.2113/gssgfbull.181.3.227.

GATTACCECA, J.; DEINO, A.; RIZZO, R.; JONES, D.S.; HENRY, B.; BEAUDOIN, B. and VADEBOIN, F., 2007. Miocene rotation of Sardinia: New paleomagnetic and geochronological constraints and geodynamic implications. *Earth and Planetary Science Letters*.
Vol. 258, no. 3, pp. 359–377. ISSN 0012-821X.
Available from DOI: doi.org/10.1016/j.epsl.2007.02.003.

GAUTHERON, C.; PINNA-JAMME, R.; DERYCKE, A.; AHADI, F.; SANCHEZ, C.; HAURINE, F.; MONVOISIN, G.; BARBOSA, D.; DELPECH, G.; MALTESE, J.; SARDA, P. and TASSAN-GOT, L., 2021.
Technical note: Analytical protocols and performance for apatite and zircon (U–Th)/He analysis on quadrupole and magnetic sector mass spectrometer systems between 2007 and 2020.

Geochronology. Vol. 3, no. 1, pp. 351–370.
Available from DOI: 10.5194/gchron-3-351-2021.

GAUTHERON, Cécile and TASSAN-GOT, Laurent, 2010.
A Monte Carlo approach to diffusion applied to noble gas/helium thermochronology.
Chemical Geology. Vol. 273, no. 3, pp. 212–224. ISSN 0009-2541.
Available from DOI: 10.1016/j.chemgeo.2010.02.023.

GE, Chenglong; LELOUP, Philippe Hervé; ZHENG, Yong; SCAILLET, Stéphane; AIRAGHI, Laura; DUVAL, Florian; ZHANG, Jinjiang and LI, Haibing, 2023.
Cenozoic kinematics of the Wenchuan-Maoxian fault implies crustal stacking rather than channel flow extrusion at the eastern margin of Tibetan plateau (Longmen Shan).
Tectonophysics. Vol. 857, p. 229816. ISSN 0040-1951.
Available from DOI: 10.1016/j.tecto.2023.229816.

GENIER, Florian; BUSSY, François; EPARD, Jean-Luc and BAUMGARTNER, Lukas, 2008.
Water-assisted migmatization of metagraywackes in a Variscan shear zone, Aiguilles-Rouges massif, western Alps. *Lithos*. Vol. 102, no. 3-4, pp. 575–597.
Available from DOI: 10.1016/j.lithos.2007.07.024.

GÉRARD, Benjamin; ROBERT, Xavier; GRUJIC, Djordje; GAUTHERON, Cécile; AUDIN, Laurence; BERNET, Matthias and BALVAY, Mélanie, 2022. Zircon (U-Th)/He Closure Temperature Lower Than Apatite Thermochronometric Systems: Reconciliation of a Paradox. *Minerals*. Vol. 12, no. 2, p. 145. Available from DOI: 10.3390/min12020145.

GILLCRIST, Ralph; COWARD, Mike and MUGNIER, Jean-Louis, 1987.
Structural inversion and its controls: examples from the Alpine foreland and the French Alps.
Geodinamica Acta. Vol. 1, no. 1, pp. 5–34.
Available from DOI: 10.1080/09853111.1987.11105122.

GIRAULT, J. B.; BELLAHSEN, N.; BERNET, M.; PIK, R.; LOGET, N.; LASSEUR, E.; ROSENBERG, C.L.; BALVAY, M. and SONNET, M., 2022.
Exhumation of the Western Alpine collisional wedge: New thermochronological data.
Tectonophysics. Vol. 822, p. 229155. ISSN 0040-1951.
Available from DOI: 10.1016/j.tecto.2021.229155.

GIRAULT, J. B.; BELLAHSEN, N.; BOUTOUX, A.; ROSENBERG, C. L.; NANNI, U.; VERLAGUET, A. and BEYSSAC, O., 2020. The 3D Thermal Structure of the Helvetic Nappes of the European Alps: Implications for Collisional Processes. *Tectonics*.
Vol. 39, no. 3, e2018TC005334. Available from DOI: 10.1029/2018TC005334.
e2018TC005334 2018TC005334.

GLOTZBACH, Christoph; REINECKER, J.; DANIŠÍK, M.; RAHN, M.; FRISCH, W. and SPIEGEL, C., 2008. Neogene exhumation history of the Mont Blanc massif, western Alps. *Tectonics*. Vol. 27, no. 4. Available from DOI: 10.1029/2008TC002257.

GLOTZBACH, Christoph; VAN DER BEEK, Peter and SPIEGEL, Cornelia, 2011. Episodic exhumation and relief growth in the Mont Blanc massif, Western Alps from numerical modelling of thermochronology data. *Earth and Planetary Science Letters*. Vol. 304, no. 3-4, pp. 417–430. Available from DOI: 10.1016/j.epsl.2011.02.020.

GNOS, Edwin; MULLIS, Josef; RICCHI, Emmanuelle; BERGEMANN, Christian A.; JANOTS, Emilie and BERGER, Alfons, 2021. Episodes of fissure formation in the Alps: connecting quartz fluid inclusion, fissure monazite age, and fissure orientation data. *Swiss Journal of Geosciences*. Vol. 114, no. 1. Available from DOI: 10.1186/s00015-021-00391-9.

GODIN, Laurent, 2003. Structural evolution of the Tethyan sedimentary sequence in the Annapurna area, central Nepal Himalaya. *Journal of Asian Earth Sciences*. Vol. 22, no. 4, pp. 307–328. ISSN 1367-9120. Available from DOI: 10.1016/S1367-9120(03)00066-X.

GOURLAY, P. and RICOU, L., 1983. Dextral strike-slip tectonics along the Chamonix suture zone (French and swiss Alps). *Comptes rendus de l'académie des sciences*. Vol. 296.

GOURLAY, Pierre, 1986. La deformation du socle et des couvertures delphino-helvetiques dans la region du Mont-Blanc (Alpes Occidentales). *Bulletin de la Société Géologique de France*. Vol. II, no. 1, pp. 159–169. ISSN 0037-9409. Available from DOI: 10.2113/gssgfbull.II.1.159.

GRACIANSKY, P. C. de; DARDEAU, G.; LEMOINE, M. and TRICART, P., 1989. The inverted margin of the French Alps and foreland basin inversion. *Geological Society, London, Special Publications*. Vol. 44, no. 1, pp. 87–104. Available from DOI: 10.1144/GSL.SP.1989.044.01.06.

GRAND, T., 1988. Mesozoic extensional inherited structures on the European margin of the Ligurian Tethys; the example of the Bourg d'Oisans Half-graben, Western Alps. *Bulletin de la Société Géologique de France*. Vol. IV, no. 4, pp. 613–621. ISSN 0037-9409. Available from DOI: 10.2113/gssgfbull.IV.4.613.

GRASEMANN, Bernhard; FRITZ, Harry and VANNAY, Jean-Claude, 1999. Quantitative kinematic flow analysis from the Main Central Thrust Zone (NW-Himalaya, India): implications for a decelerating strain path and the extrusion of orogenic wedges.

Journal of Structural Geology. Vol. 21, no. 7, pp. 837–853.
Available from DOI: 10.1016/s0191-8141(99)00077-2.

GRAVELEAU, Fabien; MALAVIEILLE, Jacques and DOMINGUEZ, Stéphane, 2012.
Experimental modelling of orogenic wedges: A review. *Tectonophysics*. Vol. 538-540, pp. 1–66.
ISSN 0040-1951. Available from DOI: 10.1016/j.tecto.2012.01.027.

GRUJIC, Djordje; CASEY, Martin; DAVIDSON, Cameron; HOLLISTER, Lincoln S.;
KÜNDIG, Rainer; PAVLIS, Terry and SCHMID, Stefan, 1996. Ductile extrusion of the Higher Himalayan Crystalline in Bhutan: evidence from quartz microfabrics. *Tectonophysics*.
Vol. 260, no. 1-3, pp. 21–43. Available from DOI: 10.1016/0040-1951(96)00074-1.

GUÉGUEN, Philippe; JANEX, Gael; NOMADE, Jérôme; LANGLAIS, Mickael;
HELMSTETTER, Agnès; COUTANT, Olivier; SCHWARTZ, Stéphane and DOLLET, Cyrielle, 2021. Unprecedented seismic swarm in the Maurienne valley (2017–2019) observed by the SISmalp Alpine seismic network: operational monitoring and management.
Comptes Rendus. Géoscience. Vol. 353, no. S1, pp. 517–534.
Available from DOI: 10.5802/crgeos.70.

GUELLEC, S.; MUGNIER, J.L.; TADRY, M. and ROURE, F., 1990. Neogene evolution of the western Alpine foreland in ligth of ECORS data and balanced cross-section.
Mémoires de la Société Géologique de la France. Vol. 156, pp. 165–184.

GUERMANI, A. and PENNACCHIONI, G., 1998. Brittle precursors of plastic deformation in a granite: an example from the Mont Blanc massif (Helvetic, western Alps).
Journal of Structural Geology. Vol. 20, no. 2, pp. 135–148. ISSN 0191-8141.
Available from DOI: 10.1016/S0191-8141(97)00080-1.

GUILLOT, Stéphane; PAOLA, Silvia di; MÉNOT, René-Pierre; LEDRU, Patrick;
SPALLA, Maria Iole; GOSSO, Guido and SCHWARTZ, Stéphane, 2009.
Suture zones and importance of strike-slip faulting for Variscan geodynamic reconstructions of the External Crystalline Massifs of the western Alps.
Bulletin de la Société Géologique de France. Vol. 180, no. 6, pp. 483–500. ISSN 0037-9409.
Available from DOI: 10.2113/gssgfbull.180.6.483.

GUNIA, Maureen, 2023.
Étude pétrologique et structurale pendant l'orogénèse alpine du massif de Belledonne.
Master dissertation. Université Claude Bernard Lyon 1.

HAMES, W.E. and BOWRING, S.A., 1994.
An empirical evaluation of the argon diffusion geometry in muscovite.

Earth and Planetary Science Letters. Vol. 124, no. 1, pp. 161–169. ISSN 0012-821X. Available from DOI: 10.1016/0012-821X(94)00079-4.

HANMER, S. and PASSCHIER, C., 1991. Shear-sense indicators: a review. *Geological Survey of Canada*. Vol. 130, no. 3. Available from DOI: 10.1017/s0016756800020112.

HARRISON, T. Mark; CÉLÉRIER, Julien; AIKMAN, Amos B.; HERMANN, Joerg and HEIZLER, Matthew T., 2009. Diffusion of 40Ar in muscovite. *Geochimica et Cosmochimica Acta*. Vol. 73, no. 4, pp. 1039–1051. ISSN 0016-7037. Available from DOI: 10.1016/j.gca.2008.09.038.

HÉLI, Badoux, 1972. Tectonique de la nappe de Morcles, entre Rhône et Lizerne. *Mater. Carte Geol. Suisse*. Vol. 143, pp. 1–78.

HIELSCHER, R. and SCHAEBEN, H., 2008. A novel pole figure inversion method: specification of the MTEX algorithm. *Journal of Applied Crystallography*. Vol. 41, no. 6, pp. 1024–1037. Available from DOI: 10.1107/s0021889808030112.

HILTON, Robert G. and WEST, A. Joshua, 2020. Mountains, erosion and the carbon cycle. *Nature Reviews Earth & Environment*. Vol. 1, no. 6, pp. 284–299. Available from DOI: 10.1038/s43017-020-0058-6.

HODGES, K. V.; PARRISH, R. R. and SEARLE, M. P., 1996. Tectonic evolution of the central Annapurna Range, Nepalese Himalayas. *Tectonics*. Vol. 15, no. 6, pp. 1264–1291. Available from DOI: 10.1029/96tc01791.

HOMEWOOD, Peter, 1983. Palaeogeography of alpine flysch. *Palaeogeography, Palaeoclimatology, Palaeoecology*. Vol. 44, no. 3-4, pp. 169–184. Available from DOI: 10.1016/0031-0182(83)90101-3.

HUBBARD, Mary and MANCKTELOW, Neil S., 1992. Lateral displacement during Neogene convergence in the western and central Alps. *Geology*. Vol. 20, no. 10, pp. 943–946. ISSN 0091-7613. Available from DOI: 10.1130/0091-7613(1992)020<0943:LDDNCI>2.3.CO;2.

HUGGENBERGER, Peter, 1985. *Faltenmodelle und Verformungsverteilung in Deckenstrukturen am Beispiel der Morcles-Decke (Helvetikum der Westschweiz)*. ETH Zurich. Available from DOI: 10.3929/ETHZ-A-000365939. PhD thesis.

HURFORD, Anthony J., 1990. Standardization of fission track dating calibration: Recommendation by the Fission Track Working Group of the I.U.G.S. Subcommission on Geochronology. *Chemical Geology: Isotope Geoscience section*. Vol. 80, no. 2, pp. 171–178. ISSN 0168-9622. Available from DOI: 10.1016/0168-9622(90)90025-8.

HURFORD, Anthony J., 1991. Uplift and cooling pathways derived from fission track analysis and mica dating: a review. *Geologische Rundschau*. Vol. 80, no. 2, pp. 349–368. Available from DOI: 10.1007/bf01829371.

HURFORD, Anthony J. and GREEN, Paul F., 1982. A users' guide to fission track dating calibration. *Earth and Planetary Science Letters*. Vol. 59, no. 2, pp. 343–354. ISSN 0012-821X. Available from DOI: 10.1016/0012-821X(82)90136-4.

JANOTS, Emilie; GRAND'HOMME, Alexis; BERNET, Matthias; GUILLAUME, Damien; GNOS, Edwin; BOIRON, Marie-Christine; ROSSI, Magali; SEYDOUX-GUILLAUME, Anne-Magali and GUEDES, Roger De Ascenção, 2019. Geochronological and thermometric evidence of unusually hot fluids in an Alpine fissure of Lauzière granite (Belledonne, Western Alps). *Solid Earth*. Vol. 10, no. 1, pp. 211–223. Available from DOI: 10.5194/se-10-211-2019.

JEANBOURQUIN, Pascal, 1994. Early deformation of ultrahelvetic mélanges in the helvetic nappes (Western Swiss Alps). *Journal of Structural Geology*. Vol. 16, no. 10, pp. 1367–1383. Available from DOI: 10.1016/0191-8141(94)90003-5.

KALIFI, A.; LELOUP, P. H.; SORREL, P.; GALY, A.; DEMORY, F.; SPINA, V.; HUET, B.; QUILLÉVÉRÉ, F.; RICCIARDI, F.; MICHOUX, D.; LECACHEUR, K.; GRIME, R.; PITTET, B. and RUBINO, J.-L., 2021. Chronology of thrust propagation from an updated tectono-sedimentary framework of the Miocene molasse (western Alps). *Solid Earth*. Vol. 12, no. 12, pp. 2735–2771. Available from DOI: 10.5194/se-12-2735-2021.

KALIFI, Amir; SORREL, Philippe; LELOUP, P. H.; SPINA, Vincenzo; HUET, Bastien; GALY, Albert; RUBINO, Jean-Loup and PITTET, Bernard, 2020. Changes in hydrodynamic process dominance (wave, tide or river) in foreland sequences: The subalpine Miocene Molasse revisited (France). *Sedimentology*. Vol. 67, no. 5, pp. 2455–2501. Available from DOI: 10.1111/sed.12708.

KALIFI, Amir; SORREL, Philippe; LELOUP, Philippe-Hervé; GALY, Albert; SPINA, Vincenzo; HUET, Bastien; RUSSO, Séverine; PITTET, Bernard and RUBINO, Jean-Loup, 2022. Tectonic control on the palaeogeographical evolution of the Miocene Seaway along the Western

Alpine foreland basin. *Geological Society, London, Special Publications*, SP523–2021–78. Available from DOI: 10.1144/sp523-2021-78.

KELLEY, S.P.; ARNAUD, N.O. and TURNER, S.P., 1994.
High spatial resolution investigations using an ultra-violet laser probe extraction technique. *Geochimica et Cosmochimica Acta*. Vol. 58, no. 16, pp. 3519–3525.
Available from DOI: 10.1016/0016-7037(94)90103-1.

KEMPF, Oliver and PFIFFNER, Adrian, 2004. Early Tertiary evolution of the North Alpine Foreland Basin of the Swiss Alps and adjoining areas. *Basin Research*. Vol. 16, no. 4, pp. 549–567.
Available from DOI: 10.1111/j.1365-2117.2004.00246.x.

KERRICH, Robert; ALLISON, Iain; BARNETT, Robert L.; MOSS, Stephen and STARKEY, John, 1980. Microstructural and chemical transformations accompanying deformation of granite in a shear zone at Mieville, Switzerland, with implications for stress corrosion cracking and superplastic flow. *Contributions to Mineralogy and Petrology*. Vol. 73, no. 3, pp. 221–242.
Available from DOI: 10.1007/bf00381442.

KETCHAM, Richard A.; GAUTHERON, Cécile and TASSAN-GOT, Laurent, 2011.
Accounting for long alpha-particle stopping distances in (U–Th–Sm)/He geochronology: Refinement of the baseline case. *Geochimica et Cosmochimica Acta*.
Vol. 75, no. 24, pp. 7779–7791. ISSN 0016-7037.
Available from DOI: 10.1016/j.gca.2011.10.011.

KINDLER, Pascal, 1988. *Géologie des wildflyschs entre Arve et Giffre (Haute-Savoie, France).*
Available from DOI: 10.13097/ARCHIVE-OUVERTE/UNIGE:109974. PhD thesis.
Université de Genève.

KIRSCHNER, David L.; COSCA, Michael A.; MASSON, Henri and HUNZIKER, Johannes C., 1996.
Staircase $^{40}Ar/^{39}Ar$ spectra of fine-grained white mica: Timing and duration of deformation and empirical constraints on argon diffusion. *Geology*. Vol. 24, no. 8, pp. 747–750.
ISSN 0091-7613.
Available from DOI: 10.1130/0091-7613(1996)024<0747:SAASOF>2.3.CO;2.

KIRSCHNER, David L.; MASSON, Henri and COSCA, Michael A., 2003.
An $^{40}Ar/^{39}Ar$, and stable isotope study of micas in low-grade fold-and-thrust belt: an example from the Swiss Helvetic Alps. *Contributions to Mineralogy and Petrology*.
Vol. 145, no. 4, pp. 460–480. Available from DOI: 10.1007/s00410-003-0461-2.

KIRSCHNER, David L.; SHARP, Zachary D. and MASSON, Henri, 1995.
Oxygen isotope thermometry of quartz-calcite veins: Unraveling the thermal-tectonic history of

the subgreenschist facies Morcles nappe (Swiss Alps). *Geological Society of America Bulletin*. Vol. 107, no. 10, pp. 1145–1156.
Available from DOI: 10.1130/0016-7606(1995)107<1145:OITOQC>2.3.CO;2.

KISS, Dániel; DURETZ, Thibault and SCHMALHOLZ, Stefan Markus, 2020.
Tectonic inheritance controls nappe detachment, transport and stacking in the Helvetic nappe system, Switzerland: insights from thermomechanical simulations. *Solid Earth*. Vol. 11, no. 2, pp. 287–305. Available from DOI: 10.5194/se-11-287-2020.

KONSTANTINOVSKAYA, E. and MALAVIEILLE, J., 2011.
Thrust wedges with décollement levels and syntectonic erosion: A view from analog models. *Tectonophysics*. Vol. 502, no. 3-4, pp. 336–350.
Available from DOI: 10.1016/j.tecto.2011.01.020.

KONSTANTINOVSKAYA, Elena and MALAVIEILLE, J., 2005.
Accretionary orogens: Erosion and exhumation. *Geotectonics*. Vol. 39, no. 1, pp. 69–86.

KOPPERS, Anthony A.P., 2002. ArArCALC—software for 40Ar/39Ar age calculations. *Computers & Geosciences*. Vol. 28, no. 5, pp. 605–619. ISSN 0098-3004.
Available from DOI: 10.1016/S0098-3004(01)00095-4.

KUHLEMANN, J; FRISCH, W; DUNKL, I and SZÉKELY, B, 2001. Quantifying tectonic versus erosive denudation by the sediment budget: the Miocene core complexes of the Alps. *Tectonophysics*. Vol. 330, no. 1, pp. 1–23. ISSN 0040-1951.
Available from DOI: 10.1016/S0040-1951(00)00209-2.

KUHLEMANN, J.; FRISCH, W.; SZÉKELY, B.; DUNKL, I. and KÁZMÉR, M., 2002.
Post-collisional sediment budget history of the Alps: tectonic versus climatic control. *International Journal of Earth Sciences*. Vol. 91, no. 5, pp. 818–837.
Available from DOI: 10.1007/s00531-002-0266-y.

LACASSIN, R.; TAPPONNIER, R. and BOURJOT, L., 1990. Culminations anticlinales d'échelle crustale et imbrication de la lithosphère dans les Alpes, apports du profil ECORS-CROP. *Comptes rendus de l'Académie des sciences. Série 2, Mécanique, Physique, Chimie, Sciences de l'univers, Sciences de la Terre*. Vol. 310, no. 6, pp. 807–814.

LACASSIN, Robin, 1988. Large-scale foliation boudinage in gneisses. *Journal of Structural Geology*. Vol. 10, no. 6, pp. 643–647. Available from DOI: 10.1016/0191-8141(88)90030-2.

LACASSIN, Robin and MATTAUER, Maurice, 1985.
Kilometre-scale sheath fold at Mattmark and implications for transport direction in the Alps.
Nature. Vol. 315, no. 6022, pp. 739–742. Available from DOI: 10.1038/315739a0.

LAJAUNIE, Christian; COURRIOUX, Gabriel and MANUEL, Laurent, 1997. Foliation fields and 3D cartography in geology: Principles of a method based on potential interpolation.
Mathematical Geology. Vol. 29, no. 4, pp. 571–584.
Available from DOI: 10.1007/bf02775087.

LANARI, Pierre; LAUGHTON, Joshua; TEDESCHI, Mahyra and MARKMANN, Thorsten, 2023.
XMapTools 4.1. Zenodo. Available from DOI: 10.5281/ZENODO.7656958.

LANARI, Pierre; VHO, Alice; BOVAY, Thomas; AIRAGHI, Laura and CENTRELLA, Stephen, 2019.
Quantitative compositional mapping of mineral phases by electron probe micro-analyser.
Geological Society, London, Special Publications. Vol. 478, no. 1, pp. 39–63.
Available from DOI: 10.1144/SP478.4.

LANARI, Pierre; VIDAL, Olivier; DE ANDRADE, Vincent; DUBACQ, Benoît; LEWIN, Eric; GROSCH, Eugene G. and SCHWARTZ, Stéphane, 2014. XMapTools: A MATLAB-based program for electron microprobe X-ray image processing and geothermobarometry.
Computers & Geosciences. Vol. 62, pp. 227–240. ISSN 0098-3004.
Available from DOI: 10.1016/j.cageo.2013.08.010.

LANDRY, Patrice, 1976.
Contribution à l'étude géologique de la région de Roselend (Savoie) - Alpes françaises.
Available also from: https://theses.hal.science/tel-00562487. Theses.
Université Scientifique et Médicale de Grenoble.

LANDRY, Patrice, 1978. Données nouvelles sur la couverture sédimentaire des massifs cristallins externes au Sud du Mont-Blanc. *Géologie Alpine*. Vol. 54, pp. 83–110.

LASLETT, G.M.; GLEADOW, A.J.W. and DUDDY, I.R., 1984.
The relationship between fission track length and track density in apatite.
Nuclear Tracks and Radiation Measurements (1982). Vol. 9, no. 1, pp. 29–38. ISSN 0735-245X.
Available from DOI: 10.1016/0735-245X(84)90019-X.

LAUBSCHER, HP, 1961. Die fernschubhypothese der jurafaltung. *Eclogae Geologicae Helvetiae*. Vol. 54, no. 1, pp. 222–282.

LAUBSCHER, HP, 1973. Jura mountains. *Gravity and Tectonics*, pp. 217–227.

LAURENT, Valentin; SCAILLET, Stéphane; JOLIVET, Laurent; AUGIER, Romain and ROCHE, Vincent, 2021. 40Ar behaviour and exhumation dynamics in a subduction channel from multi-scale 40Ar/39Ar systematics in phengite. *Geochimica et Cosmochimica Acta*. Vol. 311, pp. 141–173. Available from DOI: 10.1016/j.gca.2021.06.001.

LE BRETON, Eline; HANDY, Mark R.; MOLLI, Giancarlo and USTASZEWSKI, Kamil, 2017. Post-20 Ma Motion of the Adriatic Plate: New Constraints From Surrounding Orogens and Implications for Crust-Mantle Decoupling. *Tectonics*. Vol. 36, no. 12, pp. 3135–3154. Available from DOI: 10.1002/2016TC004443.

LE PICHON, Xavier, 1968. Sea-floor spreading and continental drift. *Journal of Geophysical Research (1896-1977)*. Vol. 73, no. 12, pp. 3661–3697. Available from DOI: h10.1029/JB073i012p03661.

LELOUP, P. H.; ARNAUD, N.; SOBEL, E. R. and LACASSIN, R., 2005. Alpine thermal and structural evolution of the highest external crystalline massif: The Mont Blanc. *Tectonics*. Vol. 24, no. 4. Available from DOI: 10.1029/2004tc001676.

LELOUP, P.H.; MAHÉO, G.; ARNAUD, N.; KALI, E.; BOUTONNET, E.; LIU, Dunyi; XIAOHAN, Liu and HAIBING, Li, 2010. The South Tibet detachment shear zone in the Dinggye area: Time constraints on extrusion models of the Himalayas. *Earth and Planetary Science Letters*. Vol. 292, no. 1, pp. 1–16. ISSN 0012-821X. Available from DOI: 10.1016/j.epsl.2009.12.035.

LELOUP, Philippe Hervé, 2023. Comment on the paper "Structural and petrological characteristics of a Jurassic detachment fault from the Mont-Blanc massif (Col du Bonhomme area, France) » by Dall'Asta et al. Published in Journal of Structural Geology 159 (2022). *Journal of Structural Geology*. Vol. 168, p. 104811. ISSN 0191-8141. Available from DOI: 10.1016/j.jsg.2023.104811.

LEMOINE, M. and TRICART, P., 1986. Les Schistes lustrés piémontais des Alpes occidentales: approche stratigraphique, structurale et sédimentologique. *Eclogae Geologicae Helvetiae*. Vol. 79, no. 2, pp. 271–294.

LEMOINE, Marcel and TRUMPY, Rudolf, 1987. Pre-oceanic rifting in the Alps. *Tectonophysics*. Vol. 133, no. 3, pp. 305–320. ISSN 0040-1951. Available from DOI: 10.1016/0040-1951(87)90272-1. Deep Internal Processes and Continental Rifting.

LEMOT, François; VALLA, Pierre G.; VAN DER BEEK, Peter; JAGERCIKOVA, Marianna; NIEDERMANN, Samuel; CARCAILLET, Julien; SOBEL, Edward R.; ANDÒ, Sergio;

GARZANTI, Eduardo; ROBERT, Xavier; BALVAY, Mélanie; BERNET, Matthias; GLODNY, Johannes and MOCOCHAIN, Ludovic, 2023. Miocene cave sediments record topographic, erosional and drainage development in the Western European Alps. *Earth and Planetary Science Letters*. Vol. 621, p. 118344. ISSN 0012-821X. Available from DOI: https://doi.org/10.1016/j.epsl.2023.118344.

LILLIE, A., 1937. Les Préalpes internes entre Arve et Giffre. *Rev. Géogr. phys. Géol. dyn.* Vol. 9, no. 3, pp. 233–298.

LIN, A. T.; WATTS, A. B. and HESSELBO, S. P., 2003. Cenozoic stratigraphy and subsidence history of the South China Sea margin in the Taiwan region. *Basin Research*. Vol. 15, no. 4, pp. 453–478. Available from DOI: 10.1046/j.1365-2117.2003.00215.x.

LISTER, G.S and DORNSIEPEN, U.F, 1982. Fabric transitions in the Saxony granulite terrain. *Journal of Structural Geology*. Vol. 4, no. 1, pp. 81–92. ISSN 0191-8141. Available from DOI: 10.1016/0191-8141(82)90009-8.

LISTER, G.S. and PRICE, G.P., 1978. Fabric development in a quartz-feldspar mylonite. *Tectonophysics*. Vol. 49, no. 1-2, pp. 37–78. Available from DOI: 10.1016/0040-1951(78)90097-5.

LISTER, Gordon S. and BALDWIN, Suzanne L., 1996. Modelling the effect of arbitrary P-T-t histories on argon diffusion in minerals using the MacArgon program for the Apple Macintosh. *Tectonophysics*. Vol. 253, no. 1-2, pp. 83–109. Available from DOI: 10.1016/0040-1951(95)00059-3.

LOOSER, N.; MADRITSCH, H.; GUILLONG, M.; LAURENT, O.; WOHLWEND, S. and BERNASCONI, S. M., 2021. Absolute Age and Temperature Constraints on Deformation Along the Basal Décollement of the Jura Fold-and-Thrust Belt From Carbonate U-Pb Dating and Clumped Isotopes. *Tectonics*. Vol. 40, no. 3. Available from DOI: 10.1029/2020tc006439.

MAINPRICE, David; BOUCHEZ, Jean-Luc; BLUMENFELD, Philippe and TUBIÀ, José Maria, 1986. Dominant c slip in naturally deformed quartz: Implications for dramatic plastic softening at high temperature. *Geology*. Vol. 14, no. 10, pp. 819–822. ISSN 0091-7613. Available from DOI: 10.1130/0091-7613(1986)14<819:DCSIND>2.0.CO;2.

MALAVIEILLE, J.; GUIHOT, P.; COSTA, S.; LARDEAUX, J.M. and GARDIEN, V., 1990. Collapse of the thickened Variscan crust in the French Massif Central: Mont Pilat extensional shear zone and St. Etienne Late Carboniferous basin. *Tectonophysics*.

Vol. 177, no. 1, pp. 139–149. ISSN 0040-1951.
Available from DOI: 10.1016/0040-1951(90)90278-G.
International IGCP Conference Project 233.

MALAVIEILLE, Jacques, 2010. Impact of erosion, sedimentation, and structural heritage on the structure and kinematics of orogenic wedges: Analog models and case studies. *GSA Today*, pp. 4–10. Available from DOI: 10.1130/gsatg48a.1.

MALAVIEILLE, Jacques; LALLEMAND, Serge E; DOMINGUEZ, Stephane; DESCHAMPS, Anne; LU, Chia-Yu; LIU, Char-Shine; SCHNURLE, P and CREW, AS, 2002.
Arc-continent collision in Taiwan: New marine observations and tectonic evolution.
Special Papers-Geological Society of America, pp. 187–211.

MALLET, J. L, 1992. GOCAD: A computer aided design program for geological applications. In: *Three-dimensional modeling with geoscientific information systems*.
Kluwer Academic Publishers, Dordrecht, NATO-ASI. Vol. 354, pp. 123–142.

MALUSÀ, M. G.; GUILLOT, S.; ZHAO, L.; PAUL, A.; SOLARINO, S.; DUMONT, T.; SCHWARTZ, S.; AUBERT, C.; BACCHESCHI, P.; EVA, E.; LU, Y.; LYU, C.; PONDRELLI, S.; SALIMBENI, S.; SUN, W. and YUAN, H., 2021.
The Deep Structure of the Alps Based on the CIFALPS Seismic Experiment: A Synthesis.
Geochemistry, Geophysics, Geosystems. Vol. 22, no. 3, e2020GC009466.
Available from DOI: 10.1029/2020GC009466. e2020GC009466 2020GC009466.

MALUSKI, H. and MONIÉ, P., 1988. 40Ar-39Ar laser probe multi-dating inside single biotites of a Variscan orthogeneiss (Pinet, Massif Central, France).
Chemical Geology: Isotope Geoscience section. Vol. 73, no. 3, pp. 245–263. ISSN 0168-9622.
Available from DOI: 10.1016/0168-9622(88)90005-X.

MANCKTELOW, Neil S. and PENNACCHIONI, Giorgio, 2004.
The influence of grain boundary fluids on the microstructure of quartz-feldspar mylonites.
Journal of Structural Geology. Vol. 26, no. 1, pp. 47–69. ISSN 0191-8141.
Available from DOI: 10.1016/S0191-8141(03)00081-6.

MARCONATO, L; LELOUP, P. H.; LASSERRE, C; JOLIVET, R; CARITG, S; GRANDIN, R; MÉTOIS, M; CAVALIÉ, O and AUDIN, L, 2021.
Insights on fault reactivation during the 2019 November 11, Mw4.9 Le Teil earthquake in southeastern France, from a joint 3-D geological model and InSAR time-series analysis.
Geophysical Journal International. Vol. 229, no. 2, pp. 758–775.
Available from DOI: 10.1093/gji/ggab498.

MARQUER, Didier; CALCAGNO, Philippe; BARFETY, Jean-Claude and BAUDIN, Thierry, 2006. 3D Modeling and Kinematics of the External Zone of the French Western Alps (Belledonne and Grand Châtelard Massifs, Maurienne Valley, Savoie). *Eclogae Geologicae Helvetiae*. Vol. 99, no. 2, pp. 211–222. Available from DOI: 10.1007/s00015-006-1183-z.

MARSHALL, D.; MEISSER, N. and TAYLOR, R. P., 1998a. Fluid inclusion, stable isotope and Ar-Ar evidence for the age and origin of gold-bearing quartz veins at Mont Chemin, Switzerland. *Mineralogy and Petrology*. Vol. 62, no. 3-4, pp. 147–165. Available from DOI: 10.1007/bf01178027.

MARSHALL, D.; PFEIFER, H. R.; HUNZIKER, J. C. and KIRSCHNER, D., 1998b. A pressure-temperature-time path for the NE Mont-Blanc massif; fluid-inclusion, isotopic and thermobarometric evidence. *European Journal of Mineralogy*. Vol. 10, no. 6, pp. 1227–1240. ISSN 0935-1221.

MARTINI, Jacques, 1966. *Etude pétrographique des grés de Taveyanne entre Arve et Giffre (Haute Savoie, France) . Alpes*. Available also from: https://theses.hal.science/tel-00904871. Theses. Université de Genève.

MASSONNE, Hans -Joachim and SCHREYER, Werner, 1987. Phengite geobarometry based on the limiting assemblage with K-feldspar, phlogopite, and quartz. *Contributions to Mineralogy and Petrology*. Vol. 96, no. 2, pp. 212–224. Available from DOI: 10.1007/bf00375235.

MATHERON, Georges, 1963. Principles of geostatistics. *Economic Geology*. Vol. 58, no. 8, pp. 1246–1266. ISSN 0361-0128. Available from DOI: 10.2113/gsecongeo.58.8.1246.

MATLAB, 2022. *MATLAB version: 9.13.0 (R2022b)*. Natick, Massachusetts, United States: The MathWorks Inc. Available also from: https://www.mathworks.com.

MATTAUER, Maurice, 1975. Sur le mecanisme de formation de la schistosite dans l'himalaya. *Earth and Planetary Science Letters*. Vol. 28, no. 2, pp. 144–154. ISSN 0012-821X. Available from DOI: 10.1016/0012-821X(75)90222-8.

MCDOUGALL, Ian and HARRISON, T Mark, 1999. In: *Geochronology and Thermochronology by the $^{40}Ar/^{39}Ar$ Method*. Oxford University Press. ISBN ISBN 0-19-504302-2.

MÉLIS, Raphaël, 2023.
Quand la pluie piégée dans les inclusions fluides permet de reconstituer les paléoreliefs.
Doctoral dissertation. University Claude Bernard Lyon 1.

MENARD, Gilles and THOUVENOT, François, 1987.
Coupes équilibrées crustales : méthodologie et application aux Alpes occidentales.
Geodinamica Acta. Vol. 1, no. 1, pp. 35–45.
Available from DOI: 10.1080/09853111.1987.11105123.

MENNESSIER, G.; CARME, F.; BELLIERE, J.; DHELLEMES, R.; ANTOINE, P.;
DABROWSKI, H.; MELOUX, J. and BORDET, C., 1977.
Carte géologique de la France, feuille de Saint-Gervais-les-Bains (Sheet 703, scale 1:50,000).
French geological survey: Bureau de Recherches Géologiques et Minières.

MERCIER, Antoine; LELOUP, Philippe Hervé; COURRIOUX, Gabriel; CARITG, Séverine;
LOPEZ, Simon; GRANDJEAN, Philippe; PASSOT, Sophie and KALIFI, Amir, 2023.
Large thrusting and late faulting shape the Aiguilles Rouges crystalline massif (Western Alps),
structural implications. *Tectonophysics*. Vol. 847, p. 229691.
Available from DOI: 10.1016/j.tecto.2022.229691.

MERCIER, Jonathan; BRAUN, Jean and VAN DER BEEK, Peter, 2017.
Do along-strike tectonic variations in the Nepal Himalaya reflect different stages in the accretion
cycle? Insights from numerical modeling. *Earth and Planetary Science Letters*.
Vol. 472, pp. 299–308. ISSN 0012-821X.
Available from DOI: 10.1016/j.epsl.2017.04.041.

MERLE, Olivier and MICHON, Laurent, 2001. The formation of the West European Rift; a new model
as exemplified by the Massif Central area. *Bulletin de la Société Géologique de France*.
Vol. 172, no. 2, pp. 213–221. ISSN 0037-9409. Available from DOI: 10.2113/172.2.213.

MINETTO, Riccardo; HELMSTETTER, Agnès; SCHWARTZ, Stéphane; LANGLAIS, Mickaël;
NOMADE, Jérôme and GUÉGUEN, Philippe, 2022. Analysis of the Spatiotemporal Evolution
of the Maurienne Swarm (French Alps) Based on Earthquake Clustering.
Earth and Space Science. Vol. 9, no. 7, e2021EA002097.
Available from DOI: 10.1029/2021EA002097. e2021EA002097 2021EA002097.

MOLLI, G. and MALAVIEILLE, J., 2010.
Orogenic processes and the Corsica/Apennines geodynamic evolution: insights from Taiwan.
International Journal of Earth Sciences. Vol. 100, no. 5, pp. 1207–1224.
Available from DOI: 10.1007/s00531-010-0598-y.

MOLLI, Giancarlo; WHITE, Joseph Clancy; KENNEDY, Lori and TAINI, Veronica, 2011.
Low-temperature deformation of limestone, Isola Palmaria, northern Apennine, Italy – The role of primary textures, precursory veins and intracrystalline deformation in localization.
Journal of Structural Geology. Vol. 33, no. 3, pp. 255–270. ISSN 0191-8141.
Available from DOI: 10.1016/j.jsg.2010.11.015.

MOLNAR, Peter and ENGLAND, Philip, 1990.
Late Cenozoic uplift of mountain ranges and global climate change: chicken or egg? *Nature*.
Vol. 346, no. 6279, pp. 29–34. Available from DOI: 10.1038/346029a0.

MORET, L., 1922.
Observations nouvelles sur la région des klippes du Plateau de Châtillon (Haute-Savoie).
C.R. Soc. géol. France, pp. 142–144.

MOSAR, J., 1989. Deformation interne dans les Prealpes medianes (Suisse).
Eclogae Geologicae Helvetiae. Vol. 82, no. 3, pp. 765–793.

MOUTHEREAU, Frédéric; LACOMBE, Olivier; DEFFONTAINES, Benoit; ANGELIER, Jacques and BRUSSET, Stéphane, 2001. Deformation history of the southwestern Taiwan foreland thrust belt: insights from tectono-sedimentary analyses and balanced cross-sections. *Tectonophysics*.
Vol. 333, no. 1, pp. 293–322. ISSN 0040-1951.
Available from DOI: 10.1016/S0040-1951(00)00280-8.

MOUTHEREAU, Frédéric; WATTS, Anthony B. and BUROV, Evgueni, 2013.
Structure of orogenic belts controlled by lithosphere age. *Nature Geoscience*.
Vol. 6, no. 9, pp. 785–789. Available from DOI: 10.1038/ngeo1902.

MUGNIER, J.-L.; GAJUREL, A.; HUYGHE, P.; JAYANGONDAPERUMAL, R.; JOUANNE, F. and UPRETI, B., 2013.
Structural interpretation of the great earthquakes of the last millennium in the central Himalaya.
Earth-Science Reviews. Vol. 127, pp. 30–47. ISSN 0012-8252.
Available from DOI: 10.1016/j.earscirev.2013.09.003.

MUGNIER, Jean-Louis; GUELLEC, Stephane; MENARD, Gilles; ROURE, François; TARDY, Marc and VIALON, Pierre, 1990. A crustal scale balanced cross-section through the external Alps deduced from the ECORS profile. *Mémoires de la Société géologique de France (1833)*.
Vol. 156, pp. 203–216.

NICOLAS, A; POLINO, R; HIRN, A and NICOLICH, R., 1990.
ECORS-CROP traverse and deep structure of the western Alps: A synthesis.
Mémoires de la Société géologique de France. Vol. 156, no. 1833, pp. 15–27.

NOUIBAT, A; STEHLY, L; PAUL, A; SCHWARTZ, S; BODIN, T; DUMONT, T; ROLLAND, Y; BROSSIER, R; TEAM, Cifalps and GROUP, AlpArray Working, 2021.
Lithospheric transdimensional ambient-noise tomography of W-Europe: implications for crustal-scale geometry of the W-Alps. *Geophysical Journal International*.
Vol. 229, no. 2, pp. 862–879. ISSN 0956-540X.
Available from DOI: 10.1093/gji/ggab520.

NTEME, Jehiel; SCAILLET, Stéphane; BRAULT, Pascal and TASSAN-GOT, Laurent, 2022.
Atomistic simulations of 40Ar diffusion in muscovite. *Geochimica et Cosmochimica Acta*.
Vol. 331, pp. 123–142. ISSN 0016-7037.
Available from DOI: 10.1016/j.gca.2022.05.004.

NTEME, Jehiel; SCAILLET, Stéphane; GARDÉS, Emmanuel; DUVAL, Florian; NABELEK, Peter and MOTTOLESE, Angelo, 2023. Defect-controlled Ar40 diffusion-domain structure of white micas from high-resolution Ar40/Ar39 crystal-mapping in slowly-cooled muscovite.
Geochimica et Cosmochimica Acta. Vol. 342, pp. 84–107. ISSN 0016-7037.
Available from DOI: 10.1016/j.gca.2022.12.004.

OKUDAIRA, Takamoto; TAKESHITA, Toru; HARA, Ikuo and ANDO, Jun-ichi, 1995.
A new estimate of the conditions for transition from basal ⟨a⟩ to prism [c] slip in naturally deformed quartz. *Tectonophysics*. Vol. 250, no. 1-3, pp. 31–46.
Available from DOI: 10.1016/0040-1951(95)00039-4.

PAIRIS, B.; PAIRIS, J. L. and PORTHAULT, B., 1973. Présence de Crétacé supérieur reposant sur le socle dans le massif des Aiguilles Rouges, Alpes de Haute Savoie.
Comptes rendus de l'Académie des Sciences de Paris. Vol. 276, pp. 1131–1134.

PAIRIS, Bernard and PAIRIS, JL, 1975.
Précisions nouvelles sur le Tertiaire du massif de Platé (Haute-Savoie). *Géologie Alpine*.
Vol. 51, pp. 83–127.

PAIRIS, J. L.; PAIRIS, B; BELLIÈRE, J.; ROSSET, J.; DÉTRAZ, H.; MULLER, A.; MULLER, D.; VILLARS, F.; MENNESSIER, G.; CHAROLLAIS, J.; KINDLER, P.; PIERRE, X. and USELLE, J. P., 1992.
Carte géologique de la France, feuille de Cluses, (Sheet 679, scale 1:50,000).
French geological survey: Bureau de Recherches Géologiques et Minières.

PARÉJAS, Ed., 1925. La tectonique du Mont Joly (Haute-Savoie). *Eclogae Geologicae Helvetiae*.
Vol. 19, no. 2, pp. 420–503. Available from DOI: 10.5169/SEALS-158423.

PARÉJAS, Edouard, 1922.
Géologie de la zone de Chamonix comprise entre le Mont-Blanc et les Aiguilles rouges.
Mémoires de la Société de Physique et d'Histoire naturelle de Genève.
Vol. 39, no. 7, pp. 374–442.

PASSCHIER, C.W. and TROUW, R.A.J., 2005. *Microtectonics*. 2nd ed. Springer Berlin, Heidelberg.
ISBN 978-3-540-64003-5. Available from DOI: 10.1007/3-540-29359-0.

PAUL, Anne; MALUSÀ, Marco G.; SOLARINO, Stefano; SALIMBENI, Simone; EVA, Elena; NOUIBAT, Ahmed; PONDRELLI, Silvia; AUBERT, Coralie; DUMONT, Thierry; GUILLOT, Stéphane; SCHWARTZ, Stéphane and ZHAO, Liang, 2022. Along-strike variations in the fossil subduction zone of the Western Alps revealed by the CIFALPS seismic experiments and their implications for exhumation of (ultra-) high-pressure rocks.
Earth and Planetary Science Letters. Vol. 598, p. 117843.
Available from DOI: 10.1016/j.epsl.2022.117843.

PAUL, Corbin and NICOLAS, Oulianoff, 1926. sur les elements des deux tectoniques, hercynienne et alpine, observables dans la protogine du mont-blanc.
Comptes Rendus de l'académie des Sciences. Vol. 182, pp. 935–936.

PENNACCHIONI, Giorgio; MENEGON, Luca; LEISS, Bernd; NESTOLA, Fabrizio and BROMILEY, Geoffrey, 2010. Development of crystallographic preferred orientation and microstructure during plastic deformation of natural coarse-grained quartz veins.
Journal of Geophysical Research: Solid Earth. Vol. 115, no. B12.
Available from DOI: 10.1029/2010JB007674.

PEVERELLI, Veronica; EWING, Tanya; RUBATTO, Daniela; WILLE, Martin; BERGER, Alfons; VILLA, Igor Maria; LANARI, Pierre; PETTKE, Thomas and HERWEGH, Marco, 2021.
U - Pb geochronology of epidote by laser ablation inductively coupled plasma mass spectrometry (LA-ICP-MS) as a tool for dating hydrothermal-vein formation. *Geochronology*.
Vol. 3, no. 1, pp. 123–147. Available from DOI: 10.5194/gchron-3-123-2021.

PFIFFNER, O. A, 2011. Structural Map of the Helvetic Zone of the Swiss Alps, including Vorarlberg (Austria) and Haute Savoie (France) (1:100 000), Explanatory Notes. *Geological Special Map*.
Vol. 128.

PFIFFNER, O. A.; BURKHARD, M.; HÄNNI, R.; KAMMER, A.; KLIGFIELD, R.; MANCKTELOW, N. S.; MENKVELD, J. W.; RAMSAY, J. G.; SCHMID, S. M. and ZURBRIGGEN, R., 2011. Structural Map of the Helvetic Zone of the Swiss Alps, including Vorarlberg (Austria) and Haute Savoie (France) (1:100 000). *Geological Special Map*. Vol. 128.

PFIFFNER, O. A.; ELLIS, S. and BEAUMONT, C., 2000.
Collision tectonics in the Swiss Alps: Insight from geodynamic modeling. *Tectonics*. Vol. 19, no. 6, pp. 1065–1094. Available from DOI: 10.1029/2000TC900019.

PFIFFNER, O. A.; SCHLUNEGGER, F. and BUITER, S. J. H., 2002. The Swiss Alps and their peripheral foreland basin: Stratigraphic response to deep crustal processes. *Tectonics*. Vol. 21, no. 2, pp. 3–16. Available from DOI: 10.1029/2000tc900039.

PFIFFNER, O. Adrian, 1993.
The structure of the Helvetic nappes and its relation to the mechanical stratigraphy. *Journal of Structural Geology*. Vol. 15, no. 3-5, pp. 511–521.
Available from DOI: 10.1016/0191-8141(93)90145-z.

PFIFFNER, O. Adrian, 2017. Thick-Skinned and Thin-Skinned Tectonics: A Global Perspective. *Geosciences*. Vol. 7, no. 3, p. 71. Available from DOI: 10.3390/geosciences7030071.

PFIFFNER, O. Adrian; LEHNER, Peter; HEITZMANN, Peter; MUELLER, Stephan and STECK, Albrecht, 1997. *Deep structure of the Swiss Alps: results of NRP 20*. Birkhäuser. ISBN ISBN 3-7643-5254-X.

PFIFFNER, Othmar Adrian, 2014. Tectonic Structure of the Alps. In: *Geology of the Alps*.
Revised and updated translation of Geologie der Alpen, Second Edition.
Ed. by JOHN WILEY & SONS, Ltd.
Chichester, West Sussex, PO19 8SQ, UK: Wiiley Blackwell, chap. 5, pp. 169–281.
ISBN 978-1-118-70812-5. Available also from: https://www.wiley.com/en-ie/Geology+of+the+Alps-p-9781118708125.

PILLOUD, Claude, 1991. *Structures de deformation alpines dans le synclinal de Permo-Carbonifère de Salvan-Dorenaz (massif des Aiguilles Rouges, Valais)*.
Available also from: https://theses.hal.science/tel-00923357. Theses. Université de Lausanne.

PLANCHEREL, R.; BROQUET, P. and CARON, C., 1998.
Carte géologique de la France, feuille de Samoens-Pas-de-Morgins (Sheet 655, scale 1:50,000). *French geological survey: Bureau de Recherches Géologiques et Minières*.

PLATT, J. P., 1986. Dynamics of orogenic wedges and the uplift of high-pressure metamorphic rocks. *GSA Bulletin*. Vol. 97, no. 9, pp. 1037–1053. ISSN 0016-7606.
Available from DOI: 10.1130/0016-7606(1986)97<1037:DOOWAT>2.0.CO;2.

PLATT, J.P., 1984. Balanced cross-sections and their implications for the deep structure of the northwest Alps: discussion. *Journal of Structural Geology*. Vol. 6, no. 5, pp. 603–606. ISSN 0191-8141. Available from DOI: 10.1016/0191-8141(84)90072-5.

POTY, B.; STADLER, H. A. and WEISBORD, A. M., 1974. Fluid inclusions studies in quartz from fissures of western and central Alps. *Schweizerische Mineralogische und Petrographische Mitteilungen*. Vol. 54, pp. 717–752.

PRICE, Raymond A., 1986. The southeastern Canadian Cordillera: Thrust faulting, tectonic wedging, and delamination of the lithosphere. *Journal of Structural Geology*. Vol. 8, no. 3-4, pp. 239–254. Available from DOI: 10.1016/0191-8141(86)90046-5.

PRUVOST, Pierre, 1956. La phase orogénique saalienne en France. *Zeitschrift der Deutschen Geologischen Gesellschaft*. Vol. 108, no. 3, pp. 102–106. Available from DOI: 10.1127/zdgg/108/1956/102.

PUTNIS, A., 2009. Mineral Replacement Reactions. *Reviews in Mineralogy and Geochemistry*. Vol. 70, no. 1, pp. 87–124. Available from DOI: 10.2138/rmg.2009.70.3.

QGIS DEVELOPMENT TEAM, 2023. *QGIS Geographic Information System*. QGIS Association. Available also from: https://www.qgis.org.

QUINQUIS, H.; AUDREN, CL.; BRUN, J. P. and COBBOLD, P. R., 1978. Intense progressive shear in Ile de Groix blueschists and compatibility with subduction or obduction. *Nature*. Vol. 273, no. 5657, pp. 43–45. Available from DOI: 10.1038/273043a0.

RAHN, M., 1994. *Incipient metamorphism of the Glarus Alps: Petrology of the Taveyanne Greywacke and fission track dating*. Doctoral dissertation. University of Basel.

RAMSAY, John G., 1981. Tectonics of the Helvetic Nappes. *Geological Society, London, Special Publications*. Vol. 9, no. 1, pp. 293–309. Available from DOI: 10.1144/gsl.sp.1981.009.01.26.

RAYMO, M. E. and RUDDIMAN, W. F., 1992. Tectonic forcing of late Cenozoic climate. *Nature*. Vol. 359, no. 6391, pp. 117–122. Available from DOI: 10.1038/359117a0.

RAYMO, Maureen E.; RUDDIMAN, William F. and FROELICH, Philip N., 1988. Influence of late Cenozoic mountain building on ocean geochemical cycles. *Geology*. Vol. 16, no. 7, p. 649. Available from DOI: 10.1130/0091-7613(1988)016<0649:iolcmb>2.3.co;2.

RAYMOND, O.; DUCLAUX, G.; BOISVERT, E.; CIPOLLONI, C.; COX, S.; LAXTON, J.; LETOURNEAU, F.; RICHARD, S.; RITCHIE, A.; SEN, M.; SERRANO, J. -J.; SIMONS, B. and VUOLLO, J., 2012.
GeoSciML v3.0 - a significant upgrade of the CGI-IUGS geoscience data model. In: *EGU General Assembly Conference Abstracts*, p. 2711.
EGU General Assembly Conference Abstracts.

REINERS, P. W., 2003. Post-orogenic evolution of the Dabie Shan, eastern China, from (U-Th)/He and fission-track thermochronology. *American Journal of Science*. Vol. 303, no. 6, pp. 489–518. Available from DOI: 10.2475/ajs.303.6.489.

REINERS, Peter W.; EHLERS, Todd A. and ZEITLER, Peter K., 2005.
Past, Present, and Future of Thermochronology. *Reviews in Mineralogy and Geochemistry*. Vol. 58, no. 1, pp. 1–18. ISSN 1529-6466. Available from DOI: 10.2138/rmg.2005.58.1.

REINHARD, M. and PREISWERK, H., 1927.
Über Granitmylonite in Aiguilles-Rouges Massiv (westl. Wallis).
Verhandlungen der Naturforschenden Gesellschaft Basel. Vol. 38, pp. 188–200.

REYER, Eduard, 1892. *Ursachen der Deformationen und der Gebirgsbildung*. W. Engelmann.

RIBES, Charlotte; GHIENNE, Jean-François; MANATSCHAL, Gianreto; DALL'ASTA, Nicolas; STOCKLI, Daniel F.; GALSTER, Federico; GILLARD, Morgane and KARNER, Garry D., 2020. The Grès Singuliers of the Mont Blanc region (France and Switzerland): stratigraphic response to rifting and crustal necking in the Alpine Tethys.
International Journal of Earth Sciences. Vol. 109, no. 7, pp. 2325–2352.
Available from DOI: 10.1007/s00531-020-01902-z.

RICCHI, E.; BERGEMANN, C.A.; GNOS, E.; BERGER, A.; RUBATTO, D. and WHITEHOUSE, M.J., 2019. Constraining deformation phases in the Aar Massif and the Gotthard Nappe (Switzerland) using Th-Pb crystallization ages of fissure monazite-(Ce). *Lithos*. Vol. 342-343, pp. 223–238. Available from DOI: 10.1016/j.lithos.2019.04.014.

ROBERT, Xavier; VAN DER BEEK, Peter; BRAUN, Jean; PERRY, Claire and MUGNIER, Jean-Louis, 2011.
Control of detachment geometry on lateral variations in exhumation rates in the Himalaya: Insights from low-temperature thermochronology and numerical modeling.
Journal of Geophysical Research: Solid Earth. Vol. 116, no. B5.
Available from DOI: 10.1029/2010JB007893.

ROLLAND, Y.; CORSINI, M.; ROSSI, M.; COX, S. F.; PENNACCHIONI, G.; MANCKTELOW, N. and BOULLIER, A. M., 2007. *Tectonics*. Vol. 26, no. 2.
Available from DOI: 10.1029/2006TC001956.

ROLLAND, Y.; COX, S.; BOULLIER, A. M.; PENNACCHIONI, G and MANCKTELOW, N., 2003. Rare earth and trace element mobility in mid-crustal shear zones: insights from the Mont Blanc Massif (Western Alps). *Earth and Planetary Science Letters*. Vol. 214, no. 1-2, pp. 203–219.
Available from DOI: 10.1016/s0012-821x(03)00372-8.

ROLLAND, Y.; ROSSI, M.; COX, S. F.; CORSINI, M.; MANCKTELOW, N.; PENNACCHIONI, G.; FORNARI, M. and BOULLIER, A. M., 2008. 40Ar/39Ar dating of synkinematic white mica: insights from fluid-rock reaction in low-grade shear zones (Mont Blanc Massif) and constraints on timing of deformation in the NW external Alps.
Geological Society, London, Special Publications. Vol. 299, no. 1, pp. 293–315.
Available from DOI: 10.1144/sp299.18.

ROLLAND, Yann; BILAU, Antonin; CARDINAL, Thibaut; NOUIBAT, Ahmed; BIENVEIGNANT, Dorian; BOSCHETTI, Louise; SCHWARTZ, Stéphane and BERNET, Matthias, 2022. Bridging the Gap between Long-Term Orogenic Evolution ($>$ 10 Ma Scale) and Geomorphological Processes That Shape the Western Alps: Insights from Combined Dating Approaches. *Geosciences*. Vol. 12, no. 11. ISSN 2076-3263.
Available from DOI: 10.3390/geosciences12110393.

ROLLAND, Yann; CORSINI, Michel and DEMOUX, Antoine, 2009.
Metamorphic and structural evolution of the Maures-Tanneron massif (SE Variscan chain): evidence of doming along a transpressional margin. *Bulletin de la Société Géologique de France*. Vol. 180, no. 3, pp. 217–230. ISSN 0037-9409.
Available from DOI: 10.2113/gssgfbull.180.3.217.

ROSSI, M. and ROLLAND, Y., 2014.
Stable isotope and Ar/Ar evidence of prolonged multiscale fluid flow during exhumation of orogenic crust: Example from the Mont Blanc and Aar Massifs (NW Alps). *Tectonics*.
Vol. 33, no. 9, pp. 1681–1709. Available from DOI: 10.1002/2013TC003438.

ROSSI, M.; ROLLAND, Y.; VIDAL, O. and COX, S. F., 2005.
Geochemical variations and element transfer during shear-zone development and related episyenites at middle crust depths: insights from the Mont Blanc granite (French — Italian Alps). *Geological Society of London, Special Publications*. Vol. 245, no. 1, pp. 373–396.
Available from DOI: 10.1144/GSL.SP.2005.245.01.18.

RUFFINI, R; POLINO, R; CALLEGARI, E; HUNZIKER, JC and PFEIFER, HR, 1997.
Volcanic clast-rich turbidites of the Taveyanne sandstones from the Thônes syncline (Savoie, France): Records for a Tertiary postcollisional volcanism.
Schweizerische mineralogische und petrographische Mitteilungen. Vol. 77, no. 2, pp. 161–174.

SAMBRIDGE, Malcolm, 1999a.
Geophysical inversion with a neighbourhood algorithm—I. Searching a parameter space.
Geophysical Journal International. Vol. 138, no. 2, pp. 479–494.
Available from DOI: 10.1046/j.1365-246x.1999.00876.x.

SAMBRIDGE, Malcolm, 1999b.
Geophysical inversion with a neighbourhood algorithm—II. Appraising the ensemble.
Geophysical Journal International. Vol. 138, no. 3, pp. 727–746.
Available from DOI: 10.1046/j.1365-246x.1999.00900.x.

SANCHEZ, Guillaume; ROLLAND, Yann; SCHNEIDER, Julie; CORSINI, Michel; OLIOT, Emilien; GONCALVES, Philippe; VERATI, Chrystèle; LARDEAUX, Jean-Marc and MARQUER, Didier, 2011. Dating low-temperature deformation by 40Ar/39Ar on white mica, insights from the Argentera-Mercantour Massif (SW Alps). *Lithos*.
Vol. 125, no. 1-2, pp. 521–536. Available from DOI: 10.1016/j.lithos.2011.03.009.

SCARPONI, M; HETÉNYI, G; BERTHET, T; BARON, L; MANZOTTI, P; PETRI, B; PISTONE, M and MÜNTENER, O, 2020. New gravity data and 3-D density model constraints on the Ivrea Geophysical Body (Western Alps). *Geophysical Journal International*.
Vol. 222, no. 3, pp. 1977–1991. ISSN 0956-540X.
Available from DOI: 10.1093/gji/ggaa263.

SCHETTINO, Antonio and TURCO, Eugenio, 2009.
Breakup of Pangaea and plate kinematics of the central Atlantic and Atlas regions.
Geophysical Journal International. Vol. 178, no. 2, pp. 1078–1097. ISSN 0956-540X.
Available from DOI: 10.1111/j.1365-246X.2009.04186.x.

SCHMID, S. M. and CASEY, M., 1986.
Complete fabric analysis of some commonly observed quartz C-axis patterns. In:
Mineral and Rock Deformation: Laboratory Studies.
American Geophysical Union, pp. 263–286. Available from DOI: 10.1029/gm036p0263.

SCHMID, S. M. and KISSLING, E., 2000.
The arc of the western Alps in the light of geophysical data on deep crustal structure. *Tectonics*.
Vol. 19, no. 1, pp. 62–85. Available from DOI: 10.1029/1999TC900057.

SEN, Marcus and DUFFY, Tim, 2005.
GeoSciML: Development of a generic GeoScience Markup Language.
Computers & Geosciences. Vol. 31, no. 9, pp. 1095–1103. ISSN 0098-3004.
Available from DOI: 10.1016/j.cageo.2004.12.003.
Application of XML in the Geosciences.

SEWARD, Diane and MANCKTELOW, Neil S., 1994.
Neogene kinematics of the central and western Alps: Evidence from fission-track dating.
Geology. Vol. 22, no. 9, pp. 803–806. ISSN 0091-7613.
Available from DOI: 10.1130/0091-7613(1994)022<0803:NKOTCA>2.3.CO;2.

SHYU, J. Bruce H.; SIEH, Kerry; CHEN, Yue-Gau and LIU, Char-Shine, 2005.
Neotectonic architecture of Taiwan and its implications for future large earthquakes.
Journal of Geophysical Research: Solid Earth. Vol. 110, no. B8.
Available from DOI: 10.1029/2004JB003251.

SIBUET, Jean-Claude and HSU, Shu-Kun, 2004. How was Taiwan created? *Tectonophysics*.
Vol. 379, no. 1-4, pp. 159–181. Available from DOI: 10.1016/j.tecto.2003.10.022.

SIMOES, Martine; AVOUAC, Jean Philippe; BEYSSAC, Olivier; GOFFÉ, Bruno;
FARLEY, Kenneth A. and CHEN, Yue-Gau, 2007.
Mountain building in Taiwan: A thermokinematic model.
Journal of Geophysical Research: Solid Earth. Vol. 112, no. B11.
Available from DOI: 10.1029/2006JB004824.

SIMOES, Martine; BEYSSAC, Olivier and CHEN, Yue-Gau, 2012.
Late Cenozoic metamorphism and mountain building in Taiwan: A review.
Journal of Asian Earth Sciences. Vol. 46, pp. 92–119. ISSN 1367-9120.
Available from DOI: 10.1016/j.jseaes.2011.11.009.

SIMON-LABRIC, T.; ROLLAND, Y.; DUMONT, T.; HEYMES, T.; AUTHEMAYOU, C.;
CORSINI, M. and FORNARI, M., 2009. $^{40}Ar/^{39}Ar$ dating of Penninic Front tectonic
displacement (W Alps) during the Lower Oligocene (31–34 Ma). *Terra Nova*.
Vol. 21, no. 2, pp. 127–136.
Available from DOI: 10.1111/j.1365-3121.2009.00865.x.

SIMONETTI, M.; CAROSI, R.; MONTOMOLI, C.; COTTLE, J. M. and LAW, R. D., 2020.
Transpressive Deformation in the Southern European Variscan Belt: New Insights From the
Aiguilles Rouges Massif (Western Alps). *Tectonics*. Vol. 39, no. 6.
Available from DOI: 10.1029/2020tc006153.

SIMONS, Bruce; BOISVERT, Eric; BRODARIC, Boyan; COX, Simon; DUFFY, Tim R.; JOHNSON, Bruce R.; LAXTON, John L. and RICHARD, Steve, 2006. GeoSciML: Enabling the Exchange of Geological Map Data. *ASEG Extended Abstracts*. Vol. 2006, no. 1, pp. 1–4. Available from DOI: 10.1071/aseg2006ab162.

SINCLAIR, H. D., 1997. *Geological Society of America Bulletin*. Vol. 109, no. 3, p. 0324. Available from DOI: 10.1130/0016-7606(1997)109<0324:tmfupf>2.3.co;2.

SMERAGLIA, Luca; LOOSER, Nathan; FABBRI, Olivier; CHOULET, Flavien; GUILLONG, Marcel and BERNASCONI, Stefano M., 2021. U–Pb dating of middle Eocene–Pliocene multiple tectonic pulses in the Alpine foreland. *Solid Earth*. Vol. 12, no. 11, pp. 2539–2551. Available from DOI: 10.5194/se-12-2539-2021.

SOLARINO, Stefano; MALUSÀ, Marco G.; EVA, Elena; GUILLOT, Stéphane; PAUL, Anne; SCHWARTZ, Stéphane; ZHAO, Liang; AUBERT, Coralie; DUMONT, Thierry; PONDRELLI, Silvia; SALIMBENI, Simone; WANG, Qingchen; XU, Xiaobing; ZHENG, Tianyu and ZHU, Rixiang, 2018. Mantle wedge exhumation beneath the Dora-Maira (U)HP dome unravelled by local earthquake tomography (Western Alps). *Lithos*. Vol. 296-299, pp. 623–636. ISSN 0024-4937. Available from DOI: 10.1016/j.lithos.2017.11.035.

SOOM, M. A., 1990. *Abkühlungs- und Hebungsgeschichte der Externmassive und der penninischen Decken beidseits der Simplon-Rhone-Linie seit dem Oligozän: Spaltspurdatierung an Apatit/Zirkon und K-Ar-Datierungen an Biotit/Muskovit (westliche Zentralalpen)*. PhD thesis. University of Bern.

SPITZ, Richard; BAUVILLE, Arthur; EPARD, Jean-Luc; KAUS, Boris J. P.; POPOV, Anton A. and SCHMALHOLZ, Stefan M., 2020. Control of 3-D tectonic inheritance on fold-and-thrust belts: insights from 3-D numerical models and application to the Helvetic nappe system. *Solid Earth*. Vol. 11, no. 3, pp. 999–1026. Available from DOI: 10.5194/se-11-999-2020.

STECK, A. and VOCAT, D., 1973. Zur Mineralogie der Granitmylonite von Miéville, Aiguilles Rouges Massiv. *Schweizerische Mineralogische und Petrographische Mitteilungen*. Vol. 54, pp. 474–477.

STEYRER, Hans Peter and STURM, Robert, 2002. Stability of zircon in a low-grade ultramylonite and its utility for chemical mass balancing: the shear zone at Miéville, Switzerland. *Chemical Geology*. Vol. 187, no. 1-2, pp. 1–19. Available from DOI: 10.1016/s0009-2541(02)00010-4.

STILLE, Hans, 1940. Einfuhrung in den Bau Amerikas: Berlin. *Gebruder Borntraeger*.

STINGL, Volkmar, 1989. Marginal marine sedimentation in the basal alpine Buntsandstein (Scythian) in the western part of the Northern Calcareous Alps (Tyrol/Salzburg, Austria). *Palaeogeography, Palaeoclimatology, Palaeoecology*. Vol. 72, pp. 249–262. ISSN 0031-0182. Available from DOI: 10.1016/0031-0182(89)90145-4. XIIth INQUA Congress.

STIPP, Michael; STÜNITZ, Holger; HEILBRONNER, Renée and SCHMID, Stefan M., 2002. The eastern Tonale fault zone: a 'natural laboratory' for crystal plastic deformation of quartz over a temperature range from 250 to 700°C. *Journal of Structural Geology*. Vol. 24, no. 12, pp. 1861–1884. ISSN 0191-8141. Available from DOI: 10.1016/S0191-8141(02)00035-4.

STRZERZYNSKI, Pierre; GUILLOT, Stéphane; COURRIOUX, Gabriel and LEDRU, Patrick, 2005. Modélisation géométrique 3D des granites stéphaniens du massif du Pelvoux (Alpes, France). *Comptes Rendus Geoscience*. Vol. 337, no. 14, pp. 1284–1292. Available from DOI: 10.1016/j.crte.2005.06.008.

TAKESHITA, Toru, 1996. Estimate of the physical conditions for deformation based on c-axis fabric transitions in naturally deformed quartzite. *Journal-Geological Society of Japan*. Vol. 102, pp. 211–222.

TAPPONNIER, P.; PELTZER, G. and ARMIJO, R., 1986. On the mechanics of the collision between India and Asia. *Geological Society, London, Special Publications*. Vol. 19, no. 1, pp. 113–157. Available from DOI: 10.1144/GSL.SP.1986.019.01.07.

THORNTON, James M.; MARIETHOZ, Gregoire and BRUNNER, Philip, 2018. A 3D geological model of a structurally complex Alpine region as a basis for interdisciplinary research. *Scientific Data*. Vol. 5, no. 1. Available from DOI: 10.1038/sdata.2018.238.

THOUVENOT, F; SENECHAL, G; TRUFFERT, C and GUELLEC, S, 1996. Comparison between two techniques of line-drawing migration (ray-tracing and common tangent method). *Mémoires-Société Géologique de France*, pp. 53–60.

THOUVENOT, François; FRÉCHET, Julien; JENATTON, Liliane and GAMOND, Jean-François, 2003. The Belledonne Border Fault: identification of an active seismic strike-slip fault in the western Alps. *Geophysical Journal International*. Vol. 155, no. 1, pp. 174–192. ISSN 0956-540X. Available from DOI: 10.1046/j.1365-246X.2003.02033.x.

THOUVENOT, FRANçois; PAUL, ANNE; SENECHAL, Guy; HIRN, ALFRED and NICOLICH, RINALDo, 1990.
ECORS-CROP wide-angle reflection seismics: constraints on deep interfaces beneath the Alps. *Mém. Soc. Géol. France*. Vol. 156, pp. 97–106.

TOY, Virginia G.; PRIOR, David J. and NORRIS, Richard J., 2008.
Quartz fabrics in the Alpine Fault mylonites: Influence of pre-existing preferred orientations on fabric development during progressive uplift. *Journal of Structural Geology*.
Vol. 30, no. 5, pp. 602–621. ISSN 0191-8141.
Available from DOI: 10.1016/j.jsg.2008.01.001.

TRAP, Pierre; ROGER, Françoise; CENKI-TOK, Bénédicte and PAQUETTE, Jean-Louis, 2016.
Timing and duration of partial melting and magmatism in the Variscan Montagne Noire gneiss dome (French Massif Central). *International Journal of Earth Sciences*.
Vol. 106, no. 2, pp. 453–476. Available from DOI: 10.1007/s00531-016-1417-x.

TRÉPIED, L.; DOUKHAN, J. C. and PAQUET, J., 1980.
Subgrain boundaries in quartz theoretical analysis and microscopic observations.
Physics and Chemistry of Minerals. Vol. 5, no. 3, pp. 201–218. ISSN 1432-2021.
Available from DOI: 10.1007/BF00348570.

TRIBOULET, Sylvette, 1980. *Etude geologique entre Belledonne et Mont Blanc : la terminaison septentrionale du massif de Belledonne et les terrains de son enveloppe - Alpes françaises*.
Available also from: https://tel.archives-ouvertes.fr/tel-00616709.
PhD thesis. Université Pierre et Marie Curie - Paris VI.

TRUMPY, R., 1971. Sur le Jurassique de la zone helvétique en Suisse.
Annales of the Geological Institute of Hungary. Vol. 54, no. 2, pp. 370–382.

VALLA, Pierre; HERMAN, Frédéric; VAN DER BEEK, Peter and BRAUN, Jean, 2010.
Inversion of thermochronological age-elevation profiles to extract independent estimates of denudation and relief history — I: Theory and conceptual model.
Earth and Planetary Science Letters. Vol. 295, no. 3-4, pp. 511–522.
Available from DOI: 10.1016/j.epsl.2010.04.033.

VALLA, Pierre; VAN DER BEEK, Peter and BRAUN, Jean, 2011.
Rethinking low-temperature thermochronology data sampling strategies for quantification of denudation and relief histories: A case study in the French western Alps.
Earth and Planetary Science Letters. Vol. 307, no. 3-4, pp. 309–322.
Available from DOI: 10.1016/j.epsl.2011.05.003.

VALLA, Pierre G.; VAN DER BEEK, Peter A.; SHUSTER, David L.; BRAUN, Jean; HERMAN, Frédéric; TASSAN-GOT, Laurent and GAUTHERON, Cécile, 2012. Late Neogene exhumation and relief development of the Aar and Aiguilles Rouges massifs (Swiss Alps) from low-temperature thermochronology modeling and 4He/3He thermochronometry. *Journal of Geophysical Research: Earth Surface*. Vol. 117, no. F1. Available from DOI: 10.1029/2011JF002043.

VAN DER BEEK, Peter; VALLA, Pierre; HERMAN, Frédéric; BRAUN, Jean; PERSANO, Cristina; DOBSON, Katherine J. and LABRIN, Erika, 2010. Inversion of thermochronological age–elevation profiles to extract independent estimates of denudation and relief history — II: Application to the French Western Alps. *Earth and Planetary Science Letters*. Vol. 296, no. 1, pp. 9–22. ISSN 0012-821X. Available from DOI: 10.1016/j.epsl.2010.04.032.

VANARDOIS, Jonas; ROGER, Françoise; TRAP, Pierre; GONCALVES, Philippe; LANARI, Pierre; PAQUETTE, Jean-Louis; MARQUER, Didier; CAGNARD, Florence; BAYON, Benjamin Le; MELLETON, Jérémie and BAROU, Fabrice, 2022. Exhumation of deep continental crust in a transpressive regime: The example of Variscan eclogites from the Aiguilles-Rouges massif (Western Alps). *Journal of Metamorphic Geology*. Available from DOI: 10.1111/jmg.12659.

VARGA, M. de la; SCHAAF, A. and WELLMANN, F., 2019. GemPy 1.0: open-source stochastic geological modeling and inversion. *Geoscientific Model Development*. Vol. 12, no. 1, pp. 1–32. Available from DOI: 10.5194/gmd-12-1-2019.

VIGANÒ, Alfio and MARTIN, Silvana, 2007. Thermorheological model for the European Central Alps: brittle?ductile transition and lithospheric strength. *Terra Nova*. Vol. 19, no. 5, pp. 309–316. Available from DOI: 10.1111/j.1365-3121.2007.00751.x.

VILLA, Igor M., 2016. Diffusion in mineral geochronometers: Present and absent. *Chemical Geology*. Vol. 420, pp. 1–10. Available from DOI: 10.1016/j.chemgeo.2015.11.001.

VILLARS, F; MULLER, D and LATELIN, O, 1988. Analyse de la structure du Mont Charvin (Haute-Savoie) en termes de tectonique synsédimentaire paléogène. Conséquences pour l'interprétation structurale des chaînes subalpines septentrionales. *Comptes rendus de l'Académie des sciences. Série 2, Mécanique, Physique, Chimie, Sciences de l'univers, Sciences de la Terre*. ISSN 0764-4450.

VON RAUMER, Jürgen and BUSSY, F., 2004. Mont Blanc and Aiguilles Rouges geology of their polymetamorphic basement (external massifs, Westerns Alps, France-Switzerland).

Mémoires de Géologie (Lausanne). Vol. 42, pp. 1–210.
Available also from: https://folia.unifr.ch/global/documents/299595.

WEBB, A. Alexander G.; YIN, An; HARRISON, T. Mark; CÉLÉRIER, Julien and BURGESS, W. Paul, 2007. The leading edge of the Greater Himalayan Crystalline complex revealed in the NW Indian Himalaya: Implications for the evolution of the Himalayan orogen. *Geology*. Vol. 35, no. 10, p. 955. Available from DOI: 10.1130/g23931a.1.

WELLMANN, Florian and CAUMON, Guillaume, 2018.
3-D Structural geological models: Concepts, methods, and uncertainties.
In: SCHMELZBACH, Cedric (ed.). *Advances in Geophysics*. Elsevier. Vol. 59, pp. 1–121.
Available from DOI: 10.1016/bs.agph.2018.09.001.

WHITNEY, D. L. and EVANS, B. W., 2009. Abbreviations for names of rock-forming minerals. *American Mineralogist*. Vol. 95, no. 1, pp. 185–187.
Available from DOI: 10.2138/am.2010.3371.

WIECZOREK, John; BLOOM, David; GURALNICK, Robert; BLUM, Stan; DÖRING, Markus; GIOVANNI, Renato; ROBERTSON, Tim and VIEGLAIS, David, 2012.
Darwin Core: An Evolving Community-Developed Biodiversity Data Standard. *PLOS ONE*. Vol. 7, no. 1, pp. 1–8. Available from DOI: 10.1371/journal.pone.0029715.

WILSON, J. Tuzo, 1966. Did the Atlantic Close and then Re-Open? *Nature*. Vol. 211, no. 5050, pp. 676–681. Available from DOI: 10.1038/211676a0.

WOLF, Sebastian G.; HUISMANS, Ritske S.; BRAUN, Jean and YUAN, Xiaoping, 2022. Topography of mountain belts controlled by rheology and surface processes. *Nature*. Vol. 606, no. 7914, pp. 516–521. Available from DOI: 10.1038/s41586-022-04700-6.

YIN, An, 2006. Cenozoic tectonic evolution of the Himalayan orogen as constrained by along-strike variation of structural geometry, exhumation history, and foreland sedimentation. *Earth-Science Reviews*. Vol. 76, no. 1-2, pp. 1–131.
Available from DOI: 10.1016/j.earscirev.2005.05.004.

ZAHOREC, P.; PAPČO, J.; PAŠTEKA, R.; BIELIK, M.; BONVALOT, S.; BRAITENBERG, C.; EBBING, J.; GABRIEL, G.; GOSAR, A.; GRAND, A.; GÖTZE, H.-J.; HETÉNYI, G.; HOLZRICHTER, N.; KISSLING, E.; MARTI, U.; MEURERS, B.; MRLINA, J.; NOGOVÁ, E.; PASTORUTTI, A.; SALAUN, C.; SCARPONI, M.; SEBERA, J.; SEOANE, L.; SKIBA, P.; SZŰCS, E. and VARGA, M., 2021.
The first pan-Alpine surface-gravity database, a modern compilation that crosses frontiers.

Earth System Science Data. Vol. 13, no. 5, pp. 2165–2209.
Available from DOI: 10.5194/essd-13-2165-2021.

APPENDICES

Annexe A

SYNTHÈSE EN FRANÇAIS

Reconstitution 4D des déformations alpines dans les Alpes occidentales
Implications sur l'évolution du prisme orogénique

A.1 Objectif

Cette thèse de doctorat a pour objectif de reconstituer l'évolution au Cénozoïque du prisme orogénique dans les Alpes occidentales à travers un exemple particulièrement complexe, emblématique et controversé : le massif du Mont-Blanc. Cette région a été largement étudiée depuis les premiers travaux pionniers de De Saussure (1796) et la première conceptualisation de la déformation des roches liée à des processus géologiques. Depuis lors, les concepts tectoniques de déformation et de failles ont progressé, et de nouvelles observations de terrain restent essentielles pour formuler, confronter et évaluer les principaux modèles conceptuels. Depuis les années 1990, la contribution des grands projets géophysiques pour l'imagerie de la structure à grande échelle des Alpes a jeté une lumière nouvelle sur l'évolution de la collision (e.g., Guellec et al., 1990 ; Malusà et al., 2021 ; Pfiffner et al., 1997). Simultanément, les progrès des performances informatiques nous permettent désormais de construire des modèles numériques plus complexes pour simuler les processus naturels. L'utilisation combinée de ces compétences permet l'élaboration d'un modèle géologique géométrique et cinématique de l'évolution des chaînes de montagnes, basé sur des observations.

A.2 Méthodologie

En géologie structurale, il est souvent très difficile de retrouver les données d'origines utilisées pour l'interprétation des cartes géologiques ou des coupes après leur publication. Cette limite rend impossible l'évaluation du degré de contrainte des modèles, ou la compilation de

l'ensemble de données par d'autres auteurs, voire la proposition d'autres modèles basés sur les mêmes données. Pour résoudre ce problème, nous devons tout d'abord élaborer une base de données permettant aux géologues structuralistes de partager leurs données avec la communauté scientifique (Chapitre 3).

Une bonne compréhension de la géométrie précise des structures est fondamentale. Trop souvent, les géologues sont limités à l'espace 2D par le biais de cartes et de coupes transversales, principalement parce que le matériel de travail est en 2D (cahier, feuille de papier, écran d'ordinateur). Cette approche peut être suffisante lorsque la géologie est géométriquement simple, cylindrique et que la direction de raccourcissement est constante dans le temps, et lorsque les données sont acquises régulièrement le long des coupes. Cependant, les données géologiques sont souvent éparses et distribuées de manière irrégulière dans la zone d'étude et une simple interpolation des données de surface dans des coupes n'est pas suffisante.

Nous devons donc construire un modèle géologique 3D basé sur des mesures de terrain pour évaluer cette géométrie complexe. Depuis les années 1990, les progrès de la géostatistique ont révolutionné la géologie structurale en introduisant des techniques de modélisation 3D qui sortent de la représentation graphique et qui répondent à des règles géologiques (Mallet, 1992 ; Lajaunie et al., 1997 ; Calcagno et al., 2008). Dans ce travail, nous utilisons le logiciel *GeoModeller* qui modélise les surfaces avec la méthode d'interpolation du co-krigeage (Chapitre 4).

Au delà de la compréhension de la géométrie, la tectonique a également une notion de mouvement : étant donné que les chaînes de montagnes évoluent au cours du temps, il est nécessaire de combiner la géométrie 3D avec une reconstruction cinématique pour aborder la solution **4D** dans son ensemble (géométrie 3D + temps 1D). À l'échelle régionale, notre étude structurale repose principalement sur des cartes géologiques publiées, que nous complétons et mettons à jour par d'abondantes observations, mesures et cartographies sur le terrain. À l'échelle de l'affleurement, nous caractérisons le style, l'intensité et la géométrie de la déformation par une observation qualitative et des mesures précises de l'orientation des structures (stratigraphie, schistosité, plans de cisaillement, linéations, etc.). Nous sélectionnons méticuleusement des échantillons orientés et coupons des lames minces orientées pour caractériser la déformation à l'échelle microscopique. Les principaux critères de cisaillement utilisés sont la relation entre les plans de cisaillement et de clivage (Berthé et al., 1979), le boudinage asymétrique (Lacassin, 1988), les queues de cristallisation des porphyroclastes (δ et σ) (Hanmer and Passchier, 1991), et l'orientation préférentielle des cristaux de quartz (Gapais and Barbarin, 1986 ; Passchier and Trouw, 2005 ; Stipp et al., 2002). Les contraintes temporelles absolues sont obtenues d'abord obtenues à l'aide de la chronologie relative des structures et à l'aide de la datation absolue. En outre, les conditions thermobarométriques de la déformation sont estimées par quantification pétrogéochimique à la microsonde électronique (Chapitre 5).

Pour quantifier la quantité et la chronologie de l'exhumation des massifs, nous utilisons des données thermochronologiques qui enregistrent le refroidissement des roches. Des simulations numériques thermochronologiques, couplées à des méthodes inverses, sont proposées pour quantifier les nombreux paramètres qui influencent l'exhumation et le refroidissement des roches et, par conséquent, pour évaluer les processus dynamiques responsables de cette exhumation (e.g., Gallagher et al., 1998 ; Braun, 2003 ; Braun et al., 2012). Cependant, la complexité des interactions entre les forces motrices conduit souvent à la non-unicité de la solution du problème (trop de paramètres), ce qui nécessite l'utilisation d'une méthode probabiliste robuste. Dans ce travail, nous utilisons le code de simulation Pecube (Braun, 2003 ; Braun et al., 2012) (Chapitre 6).

A.3 Cadre géologique (Chapitre 1 et 2)

Les chaines de montagnes continentales sont le résultat de l'accrétion de deux continents en collision. Le modèle de Coulomb a été proposé pour expliquer l'évolution tectonique de chaines de montagnes : ce modèle est basé sur la forme triangulaire de la collision en coupe et sur le fait que la convergence est accommodée par un mega-chevauchement marquant l'interface entre les plaques. Lors de la collision, la déformation migre progressivement en séquence vers la partie externe de la chaîne. Ce modèle mécanique permet de calculer l'orientation des contraintes principales maximales et de prédire les conditions de contrainte sous lesquelles le prisme est mécaniquement stable ou instable. Grâce à l'étude de trois exemples naturels de prismes orogéniques (Taïwan, Himalaya, Alpes), et bien que les orogènes soient différentes et présentent des spécificités, nous avons identifié un scénario commun de déformation pendant la collision : subduction continentale, empilement crustal et exhumation de la partie interne, puis propagation de la déformation dans l'avant-pays. Les modèles analogiques et numériques simulent la propagation de la déformation dans un prisme orogénique. Ces modèles ont mis en évidence l'influence de l'érosion/sédimentation, de la rhéologie de la croûte, de la localisation des décollements ainsi que de la prés-tructuration héritée sur l'évolution du prisme orogénique.

Dans les cas des Alpes occidentales, la chaîne est considérée comme un prisme orogénique résultant de la convergence entre l'Europe et la marge continentales Apulienne pendant le Cénozoïque. Le prisme collisionnel est divisé en deux parties : d'un côté le domaine interne, incluant des roches déformées à haute température profondément enfouies pendant l'orogenèse alpine, et de l'autre le domaine externe, où le métamorphisme alpin est resté limité au faciès schistes verts. Avant la collision alpine, la marge européenne a hérité de la pré-structuration résultant de :

1. **De l'extension post-varisque** prenant place au début du Carbonifère et caractérisée par une direction d'étirement NW-SE dans le Massif central (e.g., Faure, 1995). Une

deuxième phase d'extension s'en est suivie, se produisant à la fin du Carbonifère et au début du Permien, avec une direction d'ouverture NNE-SSW. Des auteurs ont proposé qu'elle soit liée à un effondrement post-orogénique reflétant la croûte sur-épaissie (e.g., Malavieille et al., 1990 ; Gardien et al., 2022).

2. L**La compression Saalienne** : (Stille, 1940 ; Pruvost, 1956) Cette phase est située entre le Cisuralien et le Guadalupien pendant le Permien. Dans les Alpes, Pilloud (1991) a rattaché des déformations dans le Carbonifère à la phase de déformation Saalienne. Plus tard, Pairis et al. (1992) ont attribué la déformation des sédiments carbonifères dans la région à Pormenaz (Aiguilles Rouges) à cette même phase. Cette compression est peu documentée en France et pourrait avoir joué un rôle important dans la structuration des Alpes.

3. **L'extension Mésozoïque** : Les déformations associées au rifting Méosoïque sont principalement décrites dans les massifs de l'Oisans et des Ecrins et sont caractérisées par un réseau de failles normales qui lient des blocs basculés (e.g., Graciansky et al., 1989 ; Lemoine and Tricart, 1986 ; Lemoine and Trumpy, 1987 ; Dumont, 1988). Bien que l'extension jurassique semble bien documentée dans les Alpes occidentales, la caractérisation tectonique *in situ* et les mesures de telles failles normales sont assez éparses. A partir de mesures microtectoniques dans la région de Bourg d'Oisans, Grand (1988) a estimé un changement dans la direction de l'extension de N-S à la fin du Trias, à WNW-ESE pendant le Jurassique inférieur. D'autres ont suggéré que la direction principale de l'extension varie de N-S à NE-SW (Lemoine and Trumpy, 1987 ; Dumont et al., 1984 ; Dumont et al., 2008). Dans la vallée de Chamonix, Boutoux et al. (2016) fait référence à une "faille normale mésozoïque de Chamonix" limitant le côté ouest du synclinal de Chamonix, mais une telle faille normale n'a jamais été caractérisée par des preuves tectoniques sur le terrain.

4. **L'extension Eocène-Oligocène** : Cette phase d'extension est probablement liée à l'ouverture du rift ouest-européen et s'est propagée vers le sud, en même temps qu'une compression dans les Alpes occidentales (Dèzes et al., 2004). La première phase d'extension, de 35 à 23 Ma, correspond à une extension orientée E-W (Merle and Michon, 2001). À partir de 23 Ma, la seconde phase d'extension a provoqué l'ouverture du golfe du Lion et du bassin liguro-provençal, associée à la rotation du bloc Corso-Sarde (Ferrandini et al., 2003 ; Gattacceca et al., 2007).

À partir de là, différents modèles ont été proposés pour expliquer la séquence de déformation pendant la collision alpine : dans le domaine externe, la collision aurait commencé à l'Éocène avec le chevauchement Pennique, qui a chevauché la partie interne du prisme sur la partie externe. Ensuite, la déformation a migré vers le nord-est dans les massifs cristallins

externes et les nappes subalpines et helvetiques. Dans le cas du massif du Mont-Blanc, de nombreux modèles de déformation ont été proposés, basés sur différentes interprétations, des observations et des données de terrain. Au final, la séquence, la chronologie, le style et l'ampleur de la déformation dans ce massif restent mal compris.

A.4 Développement d'une base de donnée relationnelle : *DataGeol* (Chapitre 3)

Nous avons conçu une base de données relationnelle spécifiquement destinée au stockage et au traitement des données issues de la géologie structurale : *DataGeol*. La base de données organise efficacement les données dans différentes tables, garantit l'unicité des données avec des clés primaires (PK) et l'intégrité des tables entre elles avec des clés étrangères (FK). Les tables sont standardisées à l'aide de vocabulaires et de normes qui garantissent l'échange au sein de la communauté scientifique. La base de données est codée en *standard querry language* (SQL) à l'aide du système open source PostgreSQL. En pratique, au retour d'une mission de terrain, l'utilisateur saisit les informations qu'il a renseigné dans son carnet de terrain dans les différentes tables dédiées (affleurements, mesures, observations, échantillons, etc.). Les tables sont organisées, reliées et fusionnées en tables de sortie appelés "vues", ce qui permet d'exporter les données dans différents formats pour les traiter et les afficher dans un SIG ou les utiliser dans des modèles géologiques 3D. Cette base de données a été créée pour le stockage et l'organisation des données structurales 3D provenant des Alpes occidentales. Ces données ont permis la construction d'un modèle géologique 3D de 65 x 63 km basé sur l'interpolation de champs de potentiels. L'ensemble des données inclut les localisations des affleurements, les descriptions lithologiques, les mesures des structures géologiques, les échantillons et les analyses. Les données proviennent de différentes missions de terrain effectuées dans la zone d'étude. Les affleurements ont été géoréférencés à l'aide d'un GPS de randonnée et les mesures géologiques ont été effectuées à l'aide de boussoles géologiques professionnelles. Ce jeu de données compile également des données publiées dans la même zone par d'autres auteurs. Cette base de données a également pour but de servir d'exemple pour le stockage et l'archivage de données structurales dans la communauté scientifique internationale.

Depuis 2020, l'Union Européenne a révolutionné la diffusion et l'organisation des données issues de la recherche scientifique avec les principes FAIR. Cet acronyme décrit la manière dont les données de recherche devraient être organisées, afin qu'elles puissent être plus facilement trouvées (***F**indable*), accessibles (***A**ccessible*), échangées (***I**nteroperable*), et réutilisées (*Reusable*) par la communauté scientifique. Conformément à cet objectif et parce que ce travail a été entièrement financé par des subventions de recherche publiques, toutes les données produites sont mises à disposition par le biais de répertoires de stockages de confiance.

A.5 Construction d'un modèle géologique 3D (Chapitre 4)

Dans les Alpes externes, deux modèles de déformation complètement différents sont proposés. Pour la plupart des auteurs, la géométrie actuelle des massifs est le résultat du plissement intense de la couverture sédimentaire mésozoïque, déposée à l'origine dans des demi-grabens, avec le socle dans une nappe de plissement ductile (e.g., Escher et al., 1993). Selon cette hypothèse, la géométrie des grabens guide les déformations postérieures, et la couverture est considérée comme para-autochtone car les déplacements horizontaux à l'interface socle / couverture sont modérés (e.g., Escher et al., 1993 ; Burkhard and Sommaruga, 1998 ; Bellahsen et al., 2014). L'autre hypothèse proposée est que la couverture mésozoïque est fortement déplacée vers l'ouest au-dessus d'un chevauchement en décollement (e.g., Leloup et al., 2005 ; Pfiffner, 2014).

L'existence d'un tel chevauchement est importante non seulement pour la compréhension de la géologie régionale mais a également des implications sur : i) l'estimation du raccourcissement total dans les Alpes externes ; ii) la chronologie et le mécanisme d'exhumation des chaînes externes ; iii) la chronologie et les mécanismes de déformation dans les chaines subalpines ; iv) la façon dont le raccourcissement est absorbé dans un milieu stratifié avec une rhéologie contrastée (couverture sédimentaire vs. socle) ; et v) l'influence de la géométrie initiale (paléo-topographie : horst et grabens) sur le style de la déformation.

Nous présentons ici une étude structurale 3D détaillée des relations couverture/sous-sol dans les massifs du Mont-Blanc, Aiguilles Rouges, chaînes subalpines et nappes helvétiques. L'étude structurale est accompagnée de la modélisation géologique 3D, permettant de quantifier les relations structurales 3D. Le modèle géologique 3D a été construit avec le logiciel *GeoModeller* qui interpole les données d'orientation et de contact à l'aide de l'algorithme de co-krigeage (Lajaunie et al., 1997 ; Calcagno et al., 2008). Le modèle mesure 65 x 63 km et comprend 1500 données structurales mesurées, 2 profils sismiques, 3 forages, 4 conduites souterraines et même des données issues de la spéléologie. Les résultats mettent en évidence un chevauchement de la couverture sédimentaire mésozoïque au-dessus des massifs cristallins du Mont-Blanc et des Aiguilles Rouges avec une localisation de la déformation à l'interface couverture / socle (décollement), mais qui, localement mylonitise le socle. Ces résultats suggèrent un changement dans le style de déformation entre la nappe de Morcles et la nappe subalpine : la nappe de Morcles correspondant à un grand pli couché et intensément cisaillé à sa base, alors qu'au sud la déformation dans la nappe subalpine est essentiellement localisée à l'interface couverture / socle avec un niveau décollement plus efficace. Plus tardivement, les nappes helvétiques sont déformées par l'exhumation du Mont-Blanc et des Aiguilles Rouges. Dans le Mont-Blanc, c'est la zone de cisaillement ouest du massif qui semble concentrer la majeure partie de la déformation, alors qu'a l'est, la déformation est plus distribuée le long de zones de

cisaillement anastomosées. De leur côté, les Aiguilles Rouges sont structurées par une série de rétro-chevauchements.

A.6 Chronologie de la déformation (Chaptitre 5)

Le massif du Mont-Blanc a fait l'objet de plusieurs études géochronologiques, et aujourd'hui il est communément admis que les principales phases de déformation se sont produites de l'Oligocène au Miocène (Kirschner et al., 2003 ; Leloup et al., 2005 ; Rolland et al., 2008 ; Egli et al., 2017). Cependant, certains points clés de la séquence de déformation ne sont toujours pas clairs. Par exemple, la question de savoir si un seul événement de plissement est responsable de la formation de la Nappe de Morcles et de la zone de cisaillement du Mont-Blanc (Buckle folding) (e.g., Ramsay, 1981 ; Escher et al., 1988), ou si les deux structures se sont succédées dans le temps (Leloup et al., 2005), ou encore si le décollement horizontal à la base de la Nappe de Morcles et la zone de cisaillement du Mont-Blanc ont été en partie synchrones dans un duplex. L'objectif de cette partie est de déterminer la chronologie de la déformation et d'établir un lien entre les deux structures.

Pour contraindre la chronologie de la déformation, nous avons réalisé une étude détaillée de six roches mylonitiques du massif du Mont-Blanc provenant de trois structures distinctes (nappes Helvétiques de part et d'autre du Mont-Blanc, la zone de cisaillement ouest du Mont-Blanc, la zone de cisaillement de Vallorcine - Miéville). Les conditions de déformation pression-température sont estimées dans chaque échantillon par la combinaison d'études : (i) micro structurales basée sur la description de la microstructure et sur l'orientation préférentielle du quartz obtenue par diffraction électronique rétrodiffusée (EBSD) et (ii) micro-chimique, basée sur des analyses à la microsonde électronique. Les données d'âge sont obtenues en utilisant la méthode de datation par ablation laser $^{40}Ar/^{39}Ar$ *in situ*.

Les trois échantillons de la zone de cisaillement du Mont-Blanc ont fourni des âges allant de 14.9 à 17.3 Ma. L'échantillon provenant des nappes helvétiques au dos du Mont-Blanc (Est) donne un âge de 13.7 Ma et l'échantillon de la klippe de Roselette (au sud du Mont-Blanc) et attribué aux nappes helvétiques, donne un âge de 16.3 Ma. Les résultats des analyses suggèrent que la déformation s'est produite en dessous de 500°C et entre 0,47 et 0,74 GPa. La similitude des âges de la zone de cisaillement du Mont-Blanc et des nappes helvétiques au dessus conduisent à la conclusion que les nappes helvétiques fonctionnaient simultanément avec la zone de cisaillement du Mont-Blanc dans un système de type duplex.

Les nouvelles données d'âge *in situ* $^{40}Ar/^{39}Ar$ sur micas blancs syn-cinématiques permettent de contraindre la chronologie et la séquence de propagation des chevauchements dans les massifs du Mont-Blanc et chines subalpines. Sur la base de la relation structurale 3D entre

les structures (Cf. partie précédente, Chap. 4), nous considérons la séquence de chevauchements comme une histoire en séquence d'est en ouest, avec la particularité du système des nappes Helvétiques fonctionnant de manière synchrone avec la zone de cisaillement du Mont-Blanc dans un système de type duplex. En tenant compte des autres âges publiés et de l'histoire de l'exhumation et du refroidissement de la chaîne (Cf. partie suivante, Chap. 6), nous proposons le scénario suivant (Fig. 5.19) :

1. Le système chevauchement des nappes Penniques est actif de l'Éocène jusqu'au début de l'Oligocène (Cenki-Tok et al., 2013 ; Simon-Labric et al., 2009 ; Egli et al., 2017). Ce système de chevauchement a émergé loin à l'ouest des massifs cristallins externes (MCE) au niveau des klippes préalpines (Chablais, Sulens, Annes) (voir Fig. 4.27, p. 161).

2. Le système de chevauchement Helvétique comprend la nappe du Wildhorn, la nappe des Diableret, la nappe de Morcles reposant sur chevauchement helvétique basal (Leloup et al., 2005 ; Mercier et al., 2023 ; Egli et al., 2017). Le front occidental de ce système de chevauchement limite les dépôts de l'avant-pays Miocène et se situe à l'ouest des MCE (Kalifi et al., 2021) (voir Fig. 4.27, p. 161). Une partie des nappes Helvétiques (Haut-Giffre, Aravis, Bornes, Beauges, Chartreuse orientale, Moucherotte dans le Vercors oriental) situées entre ce front et les MCE (Belledonne externe, Aiguilles Rouges) sont en fait de grandes klippes (Doudoux et al., 1982 ; Kalifi et al., 2021 ; Mercier et al., 2023). La datation de la molasse miocène contraint ce système de chevauchement à avoir été actif avant 21 Ma (Kalifi et al., 2021), et la datation absolue des micas dans les nappes suggère que la déformation a commencé peu après la fin du système de nappes Penniques, vers 32 Ma (Cenki-Tok et al., 2013 ; Simon-Labric et al., 2009 ; Egli et al., 2017). Nos nouvelles données indiquent qu'il s'est terminé à 14 Ma.

3. La zone de cisaillement du Mont-Blanc occidental (MBsz) est une zone de cisaillement inverse abrupte qui recoupe et décale les nappes helvétiques, et a donc été interprétée comme une faille plus jeune (Leloup et al., 2005). Cependant, nos résultats montrent qu'elle a été active entre 18 et 14 Ma. Les données géochronologiques publiées suggèrent que le MBsz était active depuis environ 22 Ma (Leloup et al., 2005 ; Rolland et al., 2008 ; Egli et al., 2017). Cette période coïncide en partie avec le chevauchelent plat le long des nappes helvétiques. Par conséquent, nous proposons qu'entre 22 et 14 Ma, les zones de cisaillement du Mont-Blanc occidental et des nappes helvétiques faisaient partie d'un même système de chevauchement en duplex. Le chevauchement basal des nappes helvétiques étant un plat et la zone de cisaillement du Mont-Blanc occidental étant une rampe, comme l'ont suggéré précédemment Mercier et al. (2023) et Gourlay and Ricou (1983). De plus, Leloup et al. (2005) a documenté des failles cassantes avec un mouvement en dip-lsip sur le flanc nord-ouest du massif du Mont-Blanc (au niveau du Nid d'Aigle), suggérant que la zone de cisaillement du Mont-Blanc occidental a pu durer

jusqu'à une époque plus récente, lorsque le massif du Mont-Blanc était à une profondeur plus faible.

4. Après 14 Ma, la zone de cisaillement occidentale du Mont-Blanc devient un chevauchement qui émerge et décale le chevauchement basal helvétique (Platt, 1984 ; Leloup et al., 2005 ; Mercier et al., 2023). Les contraintes sur la chronologie de ce chevauchement proviennent principalement de la thermochronologie à basse température (voir section suivante).

A.7 Histoire d'exhumation du Mont-Blanc et des Aiguilles Rouges (Chapitre 6)

L'histoire de l'exhumation des massifs cristallins externes a été largement étudiée à l'aide de la thermochronologie basse température (e.g., Boutoux et al., 2016 ; Glotzbach et al., 2008 ; Glotzbach et al., 2011 ; Valla et al., 2010 ; Valla et al., 2011 ; Valla et al., 2012 ; Van der Beek et al., 2010 ; Girault et al., 2022 ; Seward and Mancktelow, 1994 ; Leloup et al., 2005 ; Soom, 1990 ; Rahn, 1994). Certains auteurs proposent que les massifs cristallins externes (MCE) ont connu une exhumation continue depuis 18 Ma (Boutoux et al., 2016 ; Girault et al., 2022), tandis que d'autres suggèrent une exhumation épisodique des massifs avec une impulsion d'érosion entre 6 et 5 Ma (Glotzbach et al., 2011 ; Van der Beek et al., 2010 ; Valla et al., 2011). Le massif du Mont-Blanc possède l'un des ensembles de données thermochronologiques les plus denses des Alpes, ce qui permet une étude détaillée de son exhumation. En revanche, le massif des Aiguilles Rouges souffre d'un manque de données, ce qui complique la construction de son histoire d'exhumation. Des failles ont été mises en évidence et caractérisées entre ces deux massifs, mais nous manquons d'informations sur les la chronologie relative et la quantité d'exhumation de ces massifs. C'est pourquoi nous proposons d'appliquer une analyse thermochronologique quantitative avec une modélisation thermocinématique (Braun, 2003 ; Braun et al., 2012).

Pour quantifier la quantité et la chronologie de l'exhumation des massifs, nous utilisons des données thermochronologiques qui enregistrent le trajet de refroidissement des roches. Cependant, la relation entre le refroidissement des roches et l'exhumation n'est pas simple et combinée à l'interaction complexe entre l'érosion et la tectonique. Pour quantifier le rôle de chaque, nous pouvons simuler numériquement le processus d'exhumation à l'aide d'algorithmes spécifiquement conçus pour cela (e.g., Gallagher et al., 1998 ; Braun, 2003 ; Braun et al., 2012). Nous appliquons la simulation numerique avec l'algorithme Pecube. Pecube est un logiciel qui simule numériquement la dénudation d'un bloc crustal en tenant compte de l'effet de l'évolution du relief sur l'advection des isotherme et des failles qui recoupe les données. Les données

d'entrée de la simulation sont des âges thermochronologiques observés, et les données de sortie sont des âges thermochronologiques estimés qui dépendent des paramètres utilisés pour la simulation. Les données estimées peuvent être comparées aux données observées et, à l'aide de méthodes inverses, les paramètres de la simulation sont ajustés pour réduire la différence entre les deux. Cependant, la complexité du problème entraîne une non-unicité de la convergence, c'est pourquoi nous utilisons une méthode en deux étapes : après une première étape d'exploration des paramètres par inversion (algorithme des proches voisins) (Sambridge, 1999a), nous ré-échantillonnons les résultats obtenus avec une méthode Bayésienne pour obtenir une distribution de la densité de probabilité qui décrit les paramètres de la simulation et les incertitudes associées (Sambridge, 1999b). En outre, des inversions de données synthétiques générées par des modèles directs (dont nous connaissons les paramètres d'entrée) sont utilisées pour évaluer la capacité de l'inversion et des données à quantifier chaque paramètre de la simulation.

Les résultats indiquent que (i) le massif du Mont-Blanc a été exhumé environ 7 km de plus que celui des Aiguilles Rouges ; (ii) le Mont-Blanc a commencé à s'exhumer après 21 Ma jusqu'à 12 Ma, en même temps que l'activité le long de la zone de cisaillement du Mont-Blanc ; (iii) les Aiguilles Rouges ont commencé à s'exhumer doucement après 12 Ma, avant une phase de brusque accélération après 6 Ma. L'exhumation différentielle entre les deux massifs s'arrête à 1 Ma, et (iv) les deux massifs ont connu une phase d'accélération commune, coïncidant avec l'édification du relief et vraisemblablement liée à l'incision glaciaire.

A.8 Conclusions et implications

A.8.1 Implications à l'échelle du Mont-Blanc et des Aiguilles Rouges

Un décollement est mis en évidence et caractérisé à la base des nappes helvétiques. Ce décollement fait partie du système des nappes helvétiques qui est un système de chevauchement majeur et actif principalement entre $\sim$30 et $\sim$14 Ma, dans une direction N110° et avec un raccourcissement total compris entre 13 et 36 km. Au-dessus des Aiguilles Rouges, le chevauchement le plus basal est localisé dans le Trias à quelques mètres au-dessus du socle et un deuxième est à la base des schistes liasiques. Le chevauchement de base est en apparence une faille normale sur le flanc NW des Aiguilles Rouges parce qu'il a été basculé lors du soulèvement des Aiguilles Rouges au-dessus du chevauchement du socle alpin. Le chevauchement Helvetique Basal s'étend sous le Haut-Giffre et les chaines subalpines et émerge très probablement à l'ouest de la klippe des Préalpes. Au cours du Miocène, ce chevauchement a été recoupé par plusieurs failles inverses raides : dans les Aiguilles Rouge : la zone de cisaillement de Merlet-Pormenaz, les rétro-chevauchements des Aiguilles Rouges, et la zone de cisaillement du Mont-Blanc. Plus tard, les nappes helvétiques ont été soulevées et bombées au-dessus

du socle des massifs cristallins externes, et ce sont ces failles tardives qui façonnent principalement la géométrie actuelle des massifs cristallins externes. Ces déformations tardives ont masqué la continuité des nappes Helvétiques et ont empêché sa reconnaissance en tant que structure majeure, même si elle a été décrite antérieurement.

A.8.2 Quelle est la séquence de déformation dans les Alpes externes

Nous proposons un nouveau scénario tectonique dans lequel la zone de cisaillement ouest du Mont-Blanc a servi de rampe au nappes Helvétiques entre 22 et 14 Ma, avant de devenir un chevauchement recoupant les nappes entre 14 et 6 Ma. La période comprise entre 22 et 14 Ma correspond à une transition d'un système de chevauchement s'enracinant au sud-est (au-dessus) des massifs cristallins externes vers un le chevauchement basal alpin s'enracinant au nord-ouest (au-dessous) des massifs cristallins externes.

Les principales caractéristiques structurales de la région du Mont-Blanc peuvent très probablement être extrapolées au sud-ouest, avec Belledonne externe, le Synclinal médian, Belledonne interne étant un équivalent des Aiguilles Rouges, du Synclinorium de Chamonix, et du Mont-Blanc respectivement. Nous suggérons que les nappes helvétiques au-dessus du HBT s'étendent dans le Chablais, les Bornes, la Chartreuse orientale et le nord-est du Vercors, définissant une grande klippe qui s'enracine à l'est (au-dessus) de Belledonne. Après 18 Ma, une transition majeure s'est produite au sein de la sole alpine qui enracine à l'ouest (en dessous) les massifs cristallins externes et les failles inverses abruptes qui façonnent la géométrie de Belledonne.

A.8.3 Implication à l'échelle des Alpes occidentales

Nous proposont un nouveau modèle tectonique, qui a plusieurs implications à l'échelles des Alpes occidentales : la première est que trois grands systèmes de chevauchement, et non deux, ont façonné les Alpes occidentales : le système de chevauchement Pennique, le système Helvétique et le chavauchement basal alpin. Ces grands systèmes de chevauchement se sont propagés en séquence de la partie interne (est) vers la partie externe (ouest). Jusqu'à présent, la phase Helvétique ayant été négligée, le raccourcissement dans les Alpes externes a probablement été sous-estimé. La deuxième implication est que l'exhumation des massifs cristallins externes a été principalement contrôlée par des failles inverses raides (parfois en hors-séquence), des rétro-chevauchements et un bombement de faible ampleur au-dessus des chevauchements externes depuis 18 Ma. Pendant cette période d'exhumation, la déformation en *thick-skin* dans la partie la plus interne de la chaine est contemporaine avec de la déformation *thin-skin* dans la partie externe plus externe (Jura).

A.8.4 Implications à l'échelle du Prisme orogénique

L'évolution du prisme orogénique que nous proposons est concordante avec les simulations expérimentales et numériques de la déformation des prismes orogéniques (Konstantinovskaya and Malavieille, 2005 ; Dal Zilio et al., 2020 ; Bonnet et al., 2007 ; Bonnet et al., 2008). Dans les Alpes externes il est souvent proposé que les paléo-structures heritées ont une influence majeure sur la localisation de la déformation. Ceci est vrai mais probablement pas aussi systématiquement que ce qui est suggéré : les rampes des systèmes de chevauchements ne sont pas toujours localisées sur d'anciennes failles normales et le plissement intense des sédiments du Mésozoïques n'est pas toujours dû à l'inversion de bassins sédimentaires, mais plutôt à un cisaillement intense à l'intérieur d'un niveau de décollement. En revanche, la géométrie 3D complexe de l'interface couverture / socle, compliquée principalement par les failles normales du Mésozoïque et de l'Éocène, a joué un rôle dans la géométrie des chevauchements, des morceaux du socle pouvant être localement arrachés et incorporés dans les sédiments, ce qui fait que les chevauchements peuvent localement apparaître comme des failles soustractives.

Appendix B

Supporting information for chapter 4

Contents of this file

1. Tables B.1 to B.4.
2. Figures B.1.

Table B.1. Locations of outcrops used in section 4.3.

Location	Sites	Longitude	Latitude	Elevation	Verbatim Locality
AR0025	FF1	6.950569	46.02661	1965	Col des Posettes, Vallorcine, France
AR0027	FF1	6.953102	46.02507	2008	Col des Posettes, Chamonix-Mont-Blanc, France
AR0139	HGT6	6.874016	45.98791	2955	Aiguille du Belvedere, Chamonix-Mont-Blanc, France
AR0141	HGT6	6.873149	45.987858	2966	Aiguille du Belvedere, Chamonix-Mont-Blanc, France
AR0152	TB1	6.883872	45.94979	1287	Aiguilles Rouges, Les Praz, Chamonix-Mont-Blanc, France
AR0162		6.87577	46.019135	2630	Mont-Oreb, Aiguilles Rouges, Vallon de Berard, Vallorcine, France
AR0178	HGT2	6.861869	46.01774	2532	Mont-Buet, Aiguilles Rouges, Vallon de Berard, Vallorcine, France
AR0184		6.857506	46.01343	2454	Mont-Buet, Aiguilles Rouges, Vallon de Berard, Vallorcine, France
AR0184b		6.857152	46.013	2450	Mont-Buet, Aiguilles Rouges, Vallon de Berard, Vallorcine, France
AR0190	FF3	6.999964	46.05488	1490	Forclaz pass, Valais, Switzerland
AR0271	FF2	6.97485	46.04682	2040	Carraye, Les Tseppes, Valais, Switzerland
AR0358	FB1	6.973778	46.08449	1360	Aiguilles Rouges, Finhaut, Valais, Switzerland
AR0359	FB1	6.976246	46.085842	1332	Aiguilles Rouges, Finhaut, Valais, Switzerland
AR0370b		6.96539	46.06789	1070	Aiguilles Rouges, Finhaut, Valais, Switzerland
AR0391	TB2	6.93418	46.000328	1517	Montroc, Chamonix-Mont-Blanc, France
AR0392	TB2	6.934502	46.000233	1509	Montroc, Chamonix-Mont-Blanc, France
AR0393	TB2	6.935156	46.000435	1488	Montroc, Chamonix-Mont-Blanc, France
AR0394	TB2	6.934862	46.000626	1488	Montroc, Chamonix-Mont-Blanc, France
AR0395	TB2	6.935742	46.000843	1500	Montroc, Chamonix-Mont-Blanc, France
AR0396	TB2	6.936321	46.001965	1525	Montroc, Chamonix-Mont-Blanc, France
AR0411	TB1	6.889766	45.95017	1153	Aiguilles Rouges, Les Praz, Chamonix-Mont-Blanc, France
AR0447	PMsz2	6.791885	45.95824	2059	Crete Blanche, Pormenaz, Servoz, France
AR0453	PMsz2	6.79339	45.95871	2076	Crete Blanche, Pormenaz, Servoz, France
AR0454	PMsz2	6.793369	45.958714	2082	Crete Blanche, Pormenaz, Servoz, France
AR0455	PMsz2	6.793432	45.958782	2082	Crete Blanche, Pormenaz, Servoz, France
AR0482	PMsz1	6.806119	45.90461	1365	Le Coupeau, Les Houches, France
AR0483	PMsz1	6.80579	45.904827	1346	Le Coupeau, Les Houches, France
AR0484	PMsz1	6.805527	45.9048	1347	Le Coupeau, Les Houches, France
AR0485	PMsz1	6.805086	45.90484	1337	Le Coupeau, Les Houches, France
AR0486	PMsz1	6.804257	45.90493	1326	Le Coupeau, Les Houches, France
AR0765	FB2	6.917144	45.9997	1733	Les Cheserys, Aiguilles Rouges, Chamonix-Mont-Blanc, France
AR0779	FB2	6.918403	46.00137	1688	Les Cheserys, Aiguilles Rouges, Chamonix-Mont-Blanc, France
AR0874	FB3	6.922863	46.07913	1986	Eastern side of Emosson lake, Valais, Switzerland
AR0875	FB3	6.9227004	46.08043	1976	Eastern side of Emosson lake, Valais, Switzerland
AR0892	HBT4	6.906337	46.09824	1986	North of Emosson lake, Valais, Switzerland
AR0894	FB3	6.922009	46.083485	1971	Aiguilles Rouges, Eastern side of Emosson lake, Valais, Switerland
AR0895	FB3	6.924889	46.07647	1996	Aiguilles Rouges, Eastern side of Emosson lake, Valais, Switerland
AR0896	FB3	6.924889	46.07618	1994	Aiguilles Rouges, Eastern side of Emosson lake, Valais, Switerland
AR0897	FB3	6.916172	46.075157	1997	Aiguilles Rouges, Eastern side of Emosson lake, Valais, Switerland
AR0903		6.928097	46.099403	2269	Col de Barberine, Valais, Switzerland
AR0909		6.92832	46.09988	2283	Col de Barberine, Valais, Switzerland
AR0905	HBT1	6.928226	46.09963	2280	Col de Barberine, Valais, Switzerland
AR0906	HBT1	6.928317	46.099693	2279	Col de Barberine, Valais, Switzerland
AR0907	HBT1	6.928324	46.099777	2280	Col de Barberine, Valais, Switzerland
AR0912	HBT1	6.928404	46.100166	2298	Col de Barberine, Valais, Switzerland
AR0914	HBT1	6.928567	46.100517	2314	Col de Barberine, Valais, Switzerland
AR0915	HBT1	6.92848	46.10068	2342	Col de Barberine, Valais, Switzerland
AR0916	HBT1	6.928534	46.1008	2346	Col de Barberine, Valais, Switzerland
AR0917	HBT1	6.928748	46.100895	2355	Col de Barberine, Valais, Switzerland
AR0919	PMsz3	6.796878	45.95758	2189	Pointe Noire de Pormenaz, Servoz, France
AR1451		6.837431	46.0711	1003	Haut-Giffre, Nant des Pères, Sixt-Fer-a-Cheval, France
AR1470		6.8435555	46.072613	1056	Haut-Giffre, Nant des Pères, Sixt-Fer-a-Cheval, France
AR1472	HGT5	6.813543	45.977247	2159	Moede d'Anterne, Passy, France
AR1925	HGT3	6.813335	45.977212	2170	Moede d'Anterne, Passy, France
AR1926	HGT3	6.81643	45.979589	2179	Moede d'Anterne, Passy, France

Table B.2. Measures plotted in the stereographic diagrams in Figure 4.8. HGT: Haut-Giffre Thrust; TB: Tour Back Thrust; PMsz: Pormenaz-Merlet shear zone; FB: Finhaut back thrust; FF: Forclaz fault.

Site	Mean Fault Plane	Mean Lineation
	Strike ; Dip ; Quadrant	Trend/Plunge
HGT1	N019 ; 23° W	285/25
HGT2	N020 ; 33° W	280/32
HGT3	N045 ; 13° W	288/05
HGT5	N038 ; 32° E	-
HGT6	N058 ; 9° NW	288/05
TB1	N179 ; 50° W	309/39
TB2	N003 ; 39° W	303/31
PMsz1	N157 ; 34° E	96/55
PMsz2	N006 ; 72° SE	105/80
PMsz3	N055 ; 22° SE	96/55
FB1	N013 ; 43° W	297/42
FB2	N019 ; 75° W	285/75
FB3	N015 ; 67° W	304/62
FF1	N031 ; 62° E	95/60
FF2	N008 ; 28° E	133/24
FF3	N030 ; 77° E	186/61

Table B.3. Summarizing measurement conditions, details of used instruments, and sample preparation during Electron BackScattered Diffraction (EBSD) analysis.

Instrument	FIB Zeiss NVision 40
Location	INSA Lyon
Working conditions	Acceleration voltage 340 kV
	Acquisition speed 10 Hz
	Exposure time 20 ms
Acquisition software	Oxford Instruments Channel 5.0
Sample ID	ARe42
Sample preparation	Polished carbon-coated (5 microns) thin section (30 μm)
Image resolution	385x292 px
Mean indexing	72.5%
Optical step size	6 μm
Field width	2
Field height	1.74 μm
Number of data points	111 650

Table B.4. Details on datations samples from figure 7.2.

Sample	Latitude	Longitude	Location	Tectonic Unit	Mineral	Plateaux Ages	Inv. Isochrone Age	Age Range
	Decimal (EPSG:4326)				(Ma, 2σ)	(Ma, 2σ)	(Ma)	
C6[1]	45.89639	6.87835	Plan de l'Aiguille	MBsz	Biotite	19.75 ± 0.21	21.8 ± 3	
S68[1]	46.05072	6.94603	Vallorcine	VMsz	Phengite	14.3 ± 0.2 & 22.9 ± 0.9	14.5 ± 0.3 & 23.4 ± 0.4	
ME27[2]	45.89951	6.88742	Plan de l'Aiguille	MBsz	K-Feldspar	10.61 ± 0.15 (min age)		
C8[2]	45.89534	6.89365	Plan de l'Aiguille	MBsz	Biotite	16.6 ± 0.7		
C8[2]	45.89534	6.89365	Plan de l'Aiguille	MBsz	K-Feldspar	10.98 ± 0.2 (min age)		
DE65[3]	46.06699	7.07607	Angle Fault	MBsz	White mica			14.30 - 20.41
DE79[3]	46.10759	7.06844	La Bâtiaz	HBT	White mica	20.28 ± 0.21	20.18 ± 0.49	
S02[3]	46.10666	7.06827	Sur le Sex	HBT	White mica	15.09 ± 0.15	15.07± 0.23	
93-29-A[4]	46.17236	7.12788	Morcles	HBT	2-6 µm mica	ĩ9 & 21		
92-29-J[4]	46.10615	7.06903	Morcles	HBT	2-6 µm mica			13.6 - 22.7
	[1] Rolland et al., 2008							
	[2] Leloup et al., 2005							
	[3] Egli et al., 2017							
	[4] Kirschner et al., 2003							
	MBsz : Mont-Blanc shear zone							
	VMsz : Vallorcine Miéville shear zone							
	HBT : Helvetic Basal Thrust							

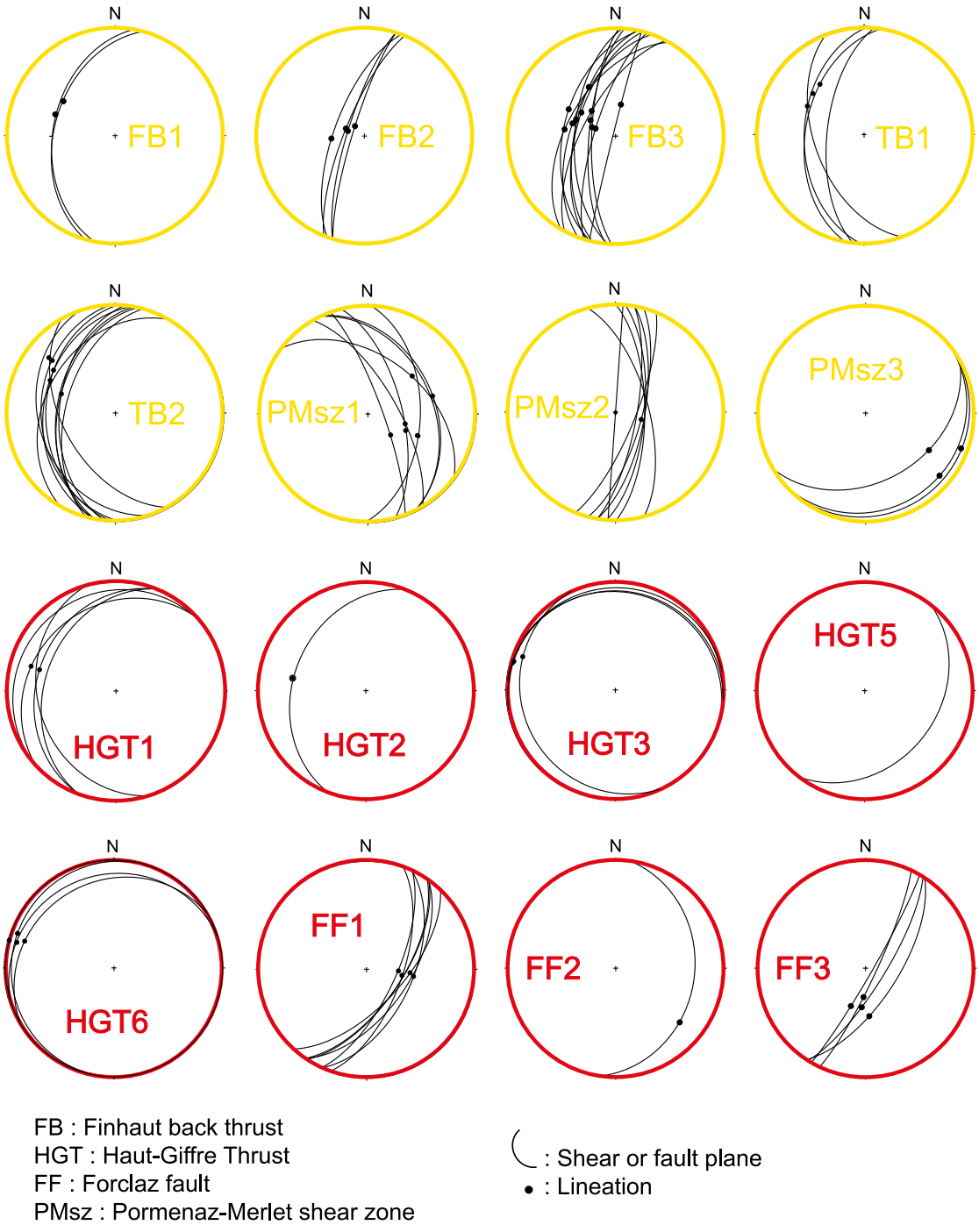

Figure B.1. Data used for calculating the mean plane and mean lineation in the stereo plots used in Figure 3a. Stereoplots are in the lower hemisphere, equal area, north up.

Appendix C

Supporting information for chapter 5

Contents of this file

1. Text C.1 detailing the argon dating method.
2. Text C.2 detailing the treatement of EBSD data with MTex algorithm and MATLAB.
3. Figures C.10 to C.19
4. Tables C.1 to C.7

C.1 Basis of $^{40}Ar/^{39}Ar$ dating method

Geochronological methods are based on the decay of radiogenic isotopes through time. The rate of decay of a radioactive isotope follows an exponential law, with the number N of radiogenic atoms present at time t proportional to the number of radiogenic atoms present initially N_0 at time t_0.

$$N = N_0\, e^{-\lambda t} \tag{C.1}$$

With λ, the decay constant represents the fraction of a parent radioactive atom decaying per unit of time. Thus, the half-life $t_{1/2}$ is the time required for several radiogenic atoms to decay to half that initial quantity ($t_{1/2} = \frac{ln2}{\lambda}$).

Thereafter, the initial number of parent atoms (at t_0) corresponds to the number of daughter atoms (D) generated plus today's number of parent atoms (N).

$$N_0 = N + D \tag{C.2}$$

Using both equations leads to:

$$N = (N + D)e^{-\lambda t} \;\Leftrightarrow\; t = \frac{1}{\lambda} ln\left(1 + \frac{D}{N}\right) \tag{C.3}$$

The $^{40}Ar/^{39}Ar$ dating method is derived from the $K - Ar$ method. ^{40}K is a naturally occurring isotope with an abundance of 0.012% and has the particularity to have two decay modes: β^- (89%) and β^+ (11%) giving two different stable daughter isotopes: $^{40}Ca^*$ and $^{40}Ar^*$ respectively. Although $^{40}Ca^*$ is rarely used in rock dating because of its abundance in nature, ^{40}Ar may be useful for mineral dating. Because of this dual decay, the basic equation requires adaptations to be applied to this decay scheme.

$$t = \frac{1}{\lambda_{Ar} + \lambda_{Ca}}\, ln\left(1 + \frac{\lambda_{Ar} + \lambda_{Ca}}{\lambda_{Ar}} \frac{^{40}Ar^*}{^{40}K}\right) \tag{C.4}$$

As the decay constants λ_A and λ_C are known, measuring the amount of $^{40}Ar^*$ and ^{40}K can lead to calculating the age since the system's closure. However, the major problem with this technique is linked with the analytical measure: the ^{39}K and ^{36}Ar must be measured separately in two different spectrometers. A solution arises by artificially transforming the ^{39}K into ^{39}Ar by inducing the decay into a nuclear reactor.

As the ratio $\frac{^{40}K}{^{39}K}$ is constant in nature, the $\frac{^{40}Ar^*}{^{39}K}$ ratio is proportional to the age.

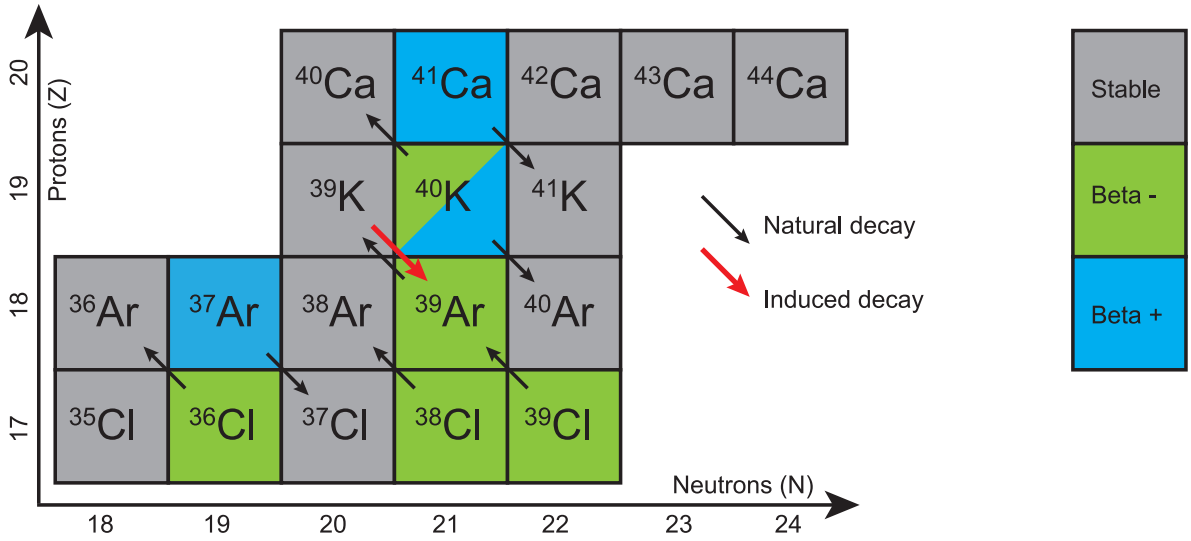

Figure C.1. Chart of isotopes decay of Chlorine, Argon, Potassium, and Calcium. Gray boxes are stable isotopes, green boxes are isotopes with β^- decay mode and blue boxes are isotopes with β^+ decay mode. Note that ^{40}K has two decay modes.

$$^{39}K + n \rightarrow {}^{39}Ar_K + p \tag{C.5}$$

n is a neutron bombarded from the reactor to induce the decay and p is a proton outputted from the β decay. The amount of $39Ar_K$ produced from the induced decay is proportional to the amount of ^{39}K present before the irradiation according to irradiation conditions:

$$^{39}Ar_K = {}^{39}K\Delta \int \Phi(E)\sigma(E)dE \tag{C.6}$$

With Δ the duration of the irradiation, $\Phi(E)$ the neutron flux at energy E, and σ(E) the neutron capture cross section at energy E. Because determining precisely each of these values independently is difficult, Merrihue and Turner 1966 suggested that irradiating a standard sample with its age accurately known at the same time as the sample studied can determine a parameter J, known as the irradiation parameter that gives the "flux" of produced $^{39}Ar_K$ from the standard. Assuming derivation of equations (see McDougall and Harrison (1999)), J can be expressed as follow:

$$J = e^{(\lambda_{Ar}+\lambda_{Ca})t_{std}} - 1 \frac{[^{39}Ar_K]_{std}}{[^{40}Ar^*]_{std}} \tag{C.7}$$

This value of J is then used in Eq. ?? together with the express the $\frac{^{40}Ar^*}{^{39}Ar_K}$ ratio measured in the unknown sample irradiated at the same time, to determine the age as follows:

$$t = \frac{1}{\lambda_{Ar} + \lambda_{Ca}} ln \left(1 + J \frac{^{40}Ar^*}{^{39}Ar_K} \right) \tag{C.8}$$

As mass spectrometers do not measure absolute abundances but ratios, some standardization procedures are required. The isotopic composition of atmospheric argon has been determined by Nier (1950).

$$\left(\frac{^{40}Ar}{^{36}Ar} \right)_{Atmo} = 295.5 \tag{C.9}$$

$$^{40}Ar_{Tot} \; = \; ^{40}Ar_{Atmo} + ^{40}\,Ar^* \;\; \Leftrightarrow \;\; 295.5 \times ^{36}\,Ar_{Atmo} + ^{40}\,Ar^* \tag{C.10}$$

A problem with normal isochrone is that ^{36}Ar is the isotope measured with the poorest precision, therefore the error associated with the fit is important. Another limitation arises: the samples where ^{36}Ar has not been detected are plotted approaching infinity, thus the radiogenic enriched samples will dominate the regression.

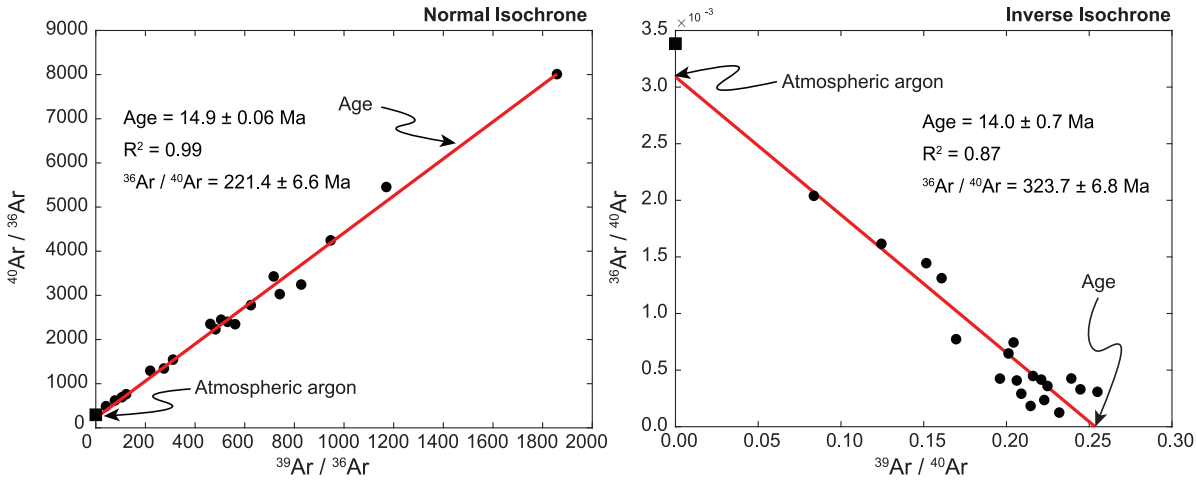

Figure C.2. Illustration of isochrones plots (left) and inverse isochrone plot (right). In the regular isochrone, the age is given by the slope of the regression, which gives the $\frac{^{40}Ar^*}{[^{39}Ar_K]}$ ratio; the atmospheric argon value is given by the y-intercept. In the inverse isochrone, the age is given by the inverse of the x-intercept value; the inverse of the y-intercept gives the atmospheric argon.

C.1.1 Extraction procedure and analysis

1. **Laser ablation**: V1 closed, V2 and V3 opened; pump2 maintaining vacuum.

2. **Stop pumping**: V1 and V3 opened, V2 closed. Gas is relaxing in the line between the ablation cell and valve V4.

3. **Purification**: Closure of V3 and opening of V2. The gas is purified by the *getters* between V3 and V4.
4. **Balancing**: Opening of V4, the gas is relaxing between V3 and the spectrometer.
5. **Pumping**: Closure of V4, pumping of the line by pump1 between V4 and ablation cell. The gas goes in the spectrometer.
6. **Analysis** By the spectrometer.
7. **Pumping**: End of the analysis, pumping of the spectrometer and the line by pump1 and 2.

The two *getters*, are aside from the line and composed of alloys of Zinc and aluminum. These two extractors aim to clean the extracted gas from the sample, they break the hydrocarbon chains and extract the following compounds: H_2O, H_2, CO, N_2 et O_2.

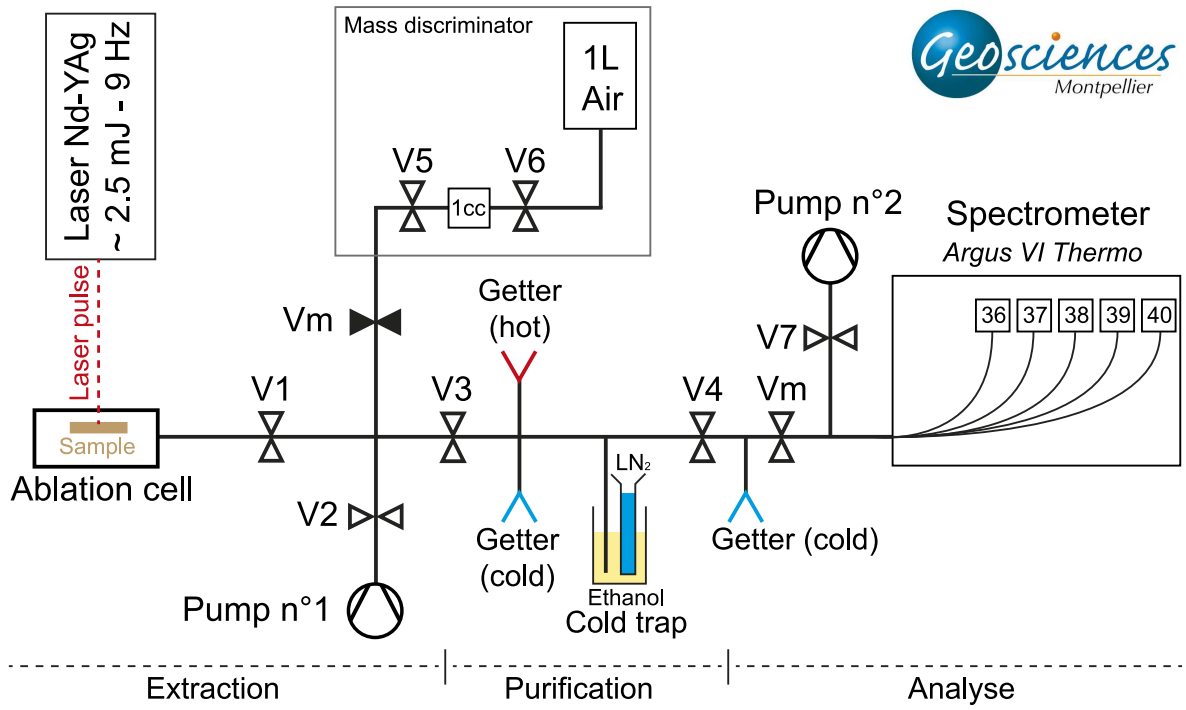

Figure C.3. Operating diagram of the extraction line for $^{40}Ar/^{39}Ar$ dating at *Geosciences Montpellier laboratory*.

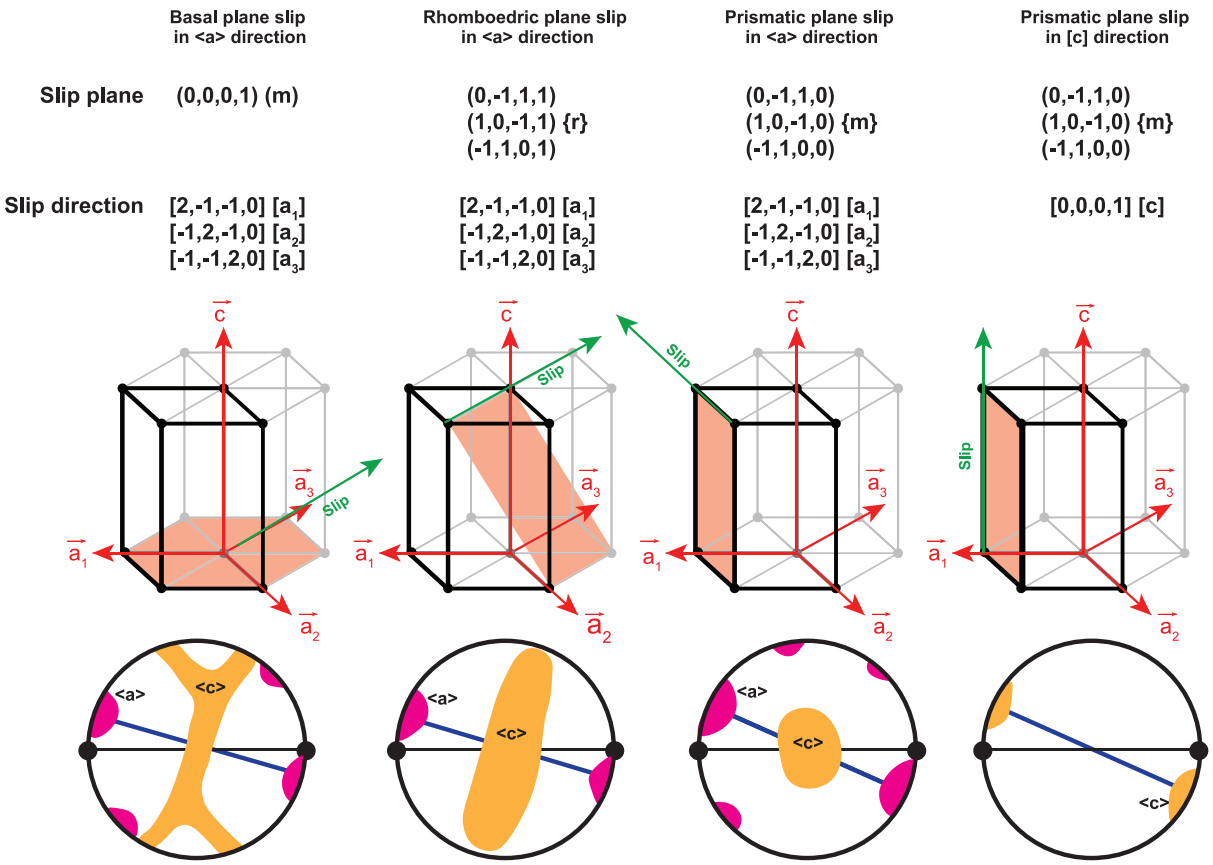

Figure C.4. Quartz slip systems, modified after Passchier and Trouw (2005).

C.2 Treatment of EBSD data with MTex

MTex is a Matlab code designed by Hielscher and Schaeben (2008) to process EBSD data. In the following, we will detail the processing of the EBSD data with the Matlab command lines supplied by the MTex package, based on our own processing and the MTex user guide.

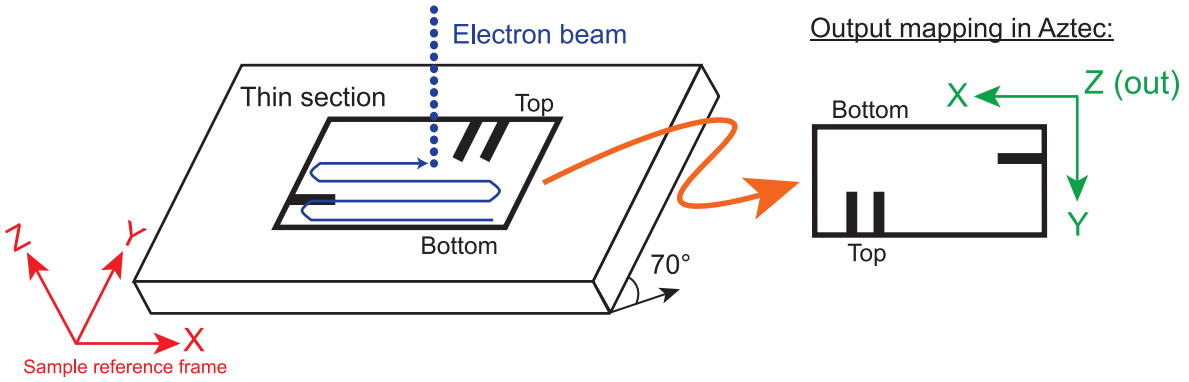

Figure C.5. EBSD analysis reference frame

Import Data Load the predefined crystal coordinate system with the crystallographic axis, lengths, and angles [α, β and γ]:

```
%% Specify Crystal and Specimen Symmetries
CS = {...
  'notIndexed',...
  crystalSymmetry('321', [4.9 4.9 5.5], 'X||a*', 'Y||b', 'Z||c*',...
  'mineral','Quartz-new', 'color', [0.53 0.81 0.98])};
```

By default, the Euclidean reference frame is oriented with the E_z axis aligned with the crystallographic $< c >$ axis, the Euclidean E_y axis along the crystallographic $< b >$ axis and the Euclidean E_x crystallographic $< a >$.

To rotate the data back in the section reference frame, it is necessary to apply the following plotting convention: setting the x-axis towards the east and the z-axis out-of-plane.

```
setMTEXpref('xAxisDirection','east');
setMTEXpref('zAxisDirection','outofPlane');
```

Specify the names of the files to be imported and create a variable 'ebsd' containing the data:

```
%% Specify File Names
sampleName = 'ME119-MAP1.crc';

% path to files
pname = pwd;

% which files to be imported
fname = [pname '\' sampleName];

% Import the data and create an EBSD variable
ebsd = EBSD.load(fname,CS,'interface','crc',...
  'convertSpatial2EulerReferenceFrame');
ebsd = ebsd('indexed');
```

Extract and plot crystals orientation map Extract the orientation indexed for each pixel of the map.

Plot the crystal c-axis orientation map

```
figure
cdk = HSVDirectionKey(specimenSymmetry('2'));
cdk.whiteCenter=zvector;
cdk.refl = zvector;
h = Miller({0,0,0,1},ebsd('indexed').CS);
cdir = ebsd.orientations.*h;
cdir.antipodal=1;
color = cdk.direction2color(cdir);
plot(ebsd,color)

figure
plot(cdk)
```

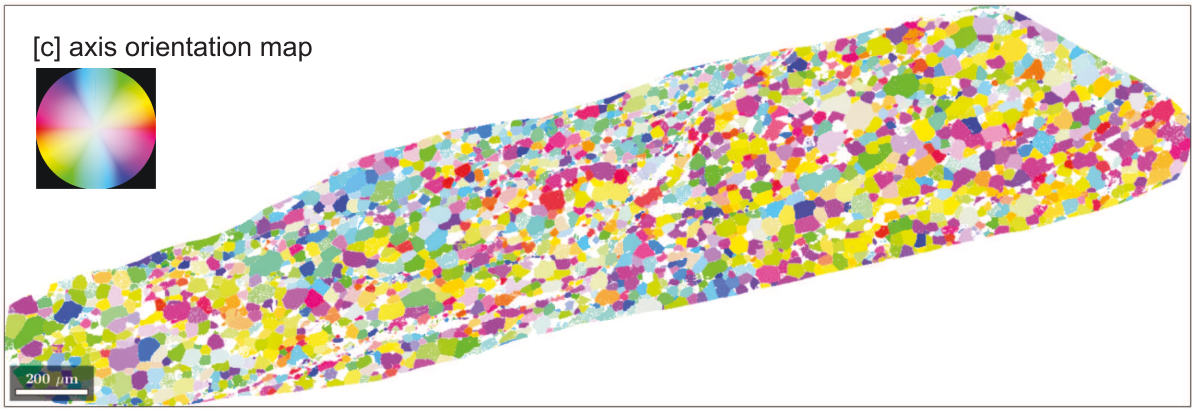

Figure C.6. c-axis orientation map

Grain Reconstruction The grains boundaries are reconstructed, using a misorientation threshold of 10° degrees. Wild spikes (grains smaller than one pixel) are removed:

```
%% Calculates grain boundaries
% 1. Construct grains using a critical misorientation of 10 degrees
[grains,ebsd.grainId,ebsd.mis2mean] = calcGrains(ebsd, ...
    'angle',10*degree);

% 2. Remove wild spikes
ebsd(grains(grains.grainSize == 1 )) = [];

% 3. Smooth grains boundaries
F = halfQuadraticFilter;
ebsd = smooth(ebsd,F);

% 4. Reconstruct grains without wild-spikes
[grains,ebsd.grainId,ebsd.mis2mean] = calcGrains(ebsd, ...
    'angle',10*degree);

% 5. Remove grains smaller than 4 pixels
grains(grains.grainSize <= 4) = [];

grains = smooth(grains,5);
```

Plot the crystal c-axis orientation map with calculated grain boundaries:

```
figure
cdk = HSVDirectionKey(specimenSymmetry('2'));
cdk.whiteCenter=zvector;
cdk.refl = zvector;
h = Miller({0,0,0,1},ebsd('indexed').CS);
cdir = ebsd.orientations.*h;
cdir.antipodal=1;
color = cdk.direction2color(cdir);
plot(ebsd,color)
hold on
plot(grains.boundary,'linewidth',2)

figure
plot(cdk)
```

Pole Figures Pole figures are key for the interpretation and analysis of the orientations. Crystal directions are reported in a pole figure, with the variable h defining the planes that are aligned with respect to specimen directions.

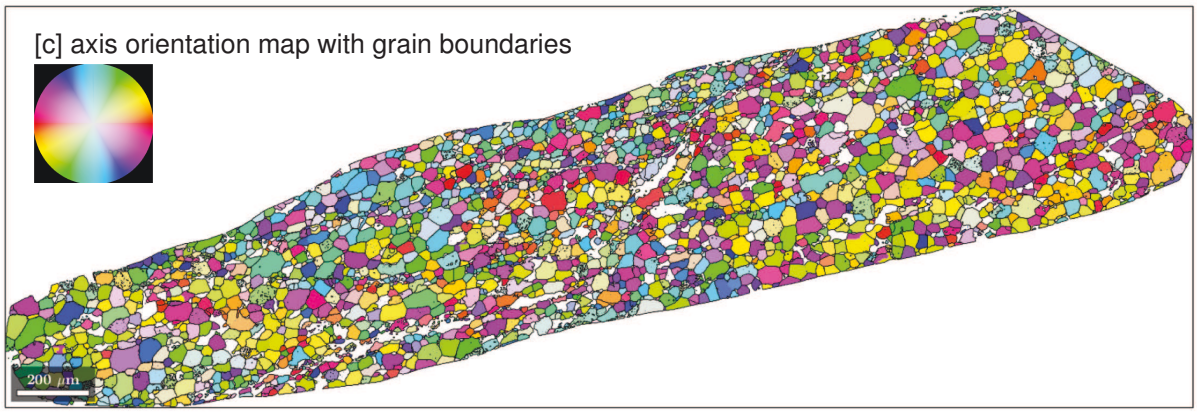

Figure C.7. c-axis orientation map with reconstructed grains

```
%% Pole figure

cs = loadCIF('quartz');
h = Miller({0,0,0,1},{2,-1,-1,0},{1,0,-1,0},{1,0,-1,1},{0,1,-1,1},cs);
odf = calcDensity(grains.meanOrientation,'halfwidth',6*degree);
plotPDF(odf,h,'lower','contourf')
```

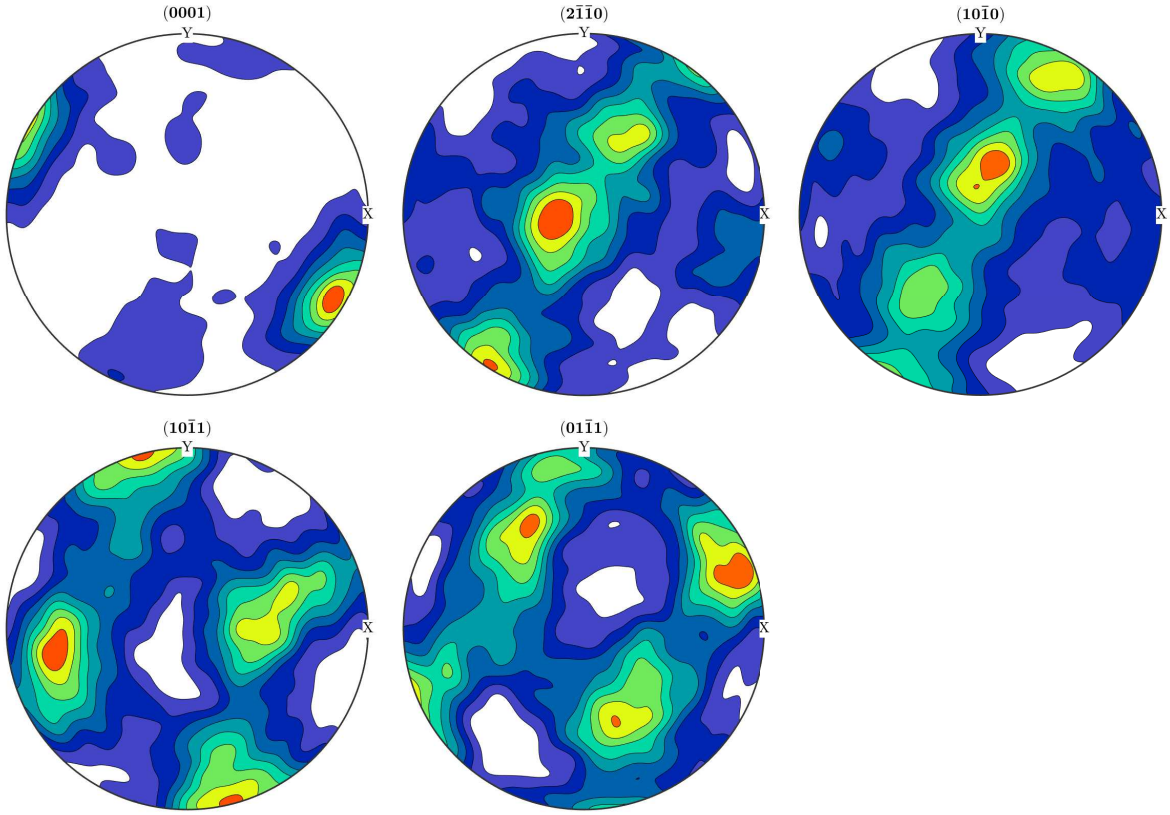

Figure C.8. Pole figure of the c-axis and a-axis orientation

Compute and plot the distribution of the grain size blka

```
d = 2*equivalentRadius(nonbordergrains);

edges = [0:5:150]; % Set the histogram bin widths
loglim = [0 150 0 0.15]; % Set the histogram axis limits

figure
histogram(d,edges,'Normalization','probability',...
    'facecolor',[0.5 0.5 0.5]);
    xlabel('Grain size (\mum)')
    ylabel('Relative frequency (%)')
    axis(loglim)
    set(gca,'xtick',[0:50:150])
```

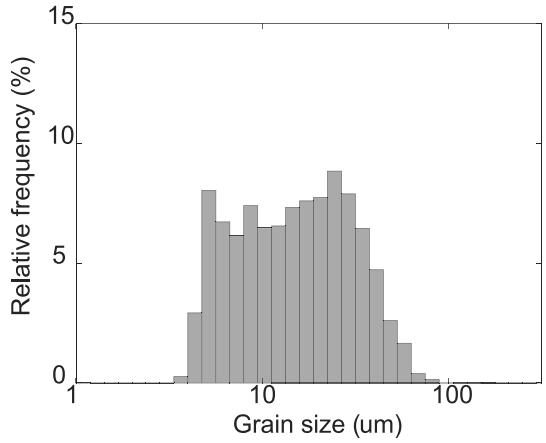

Figure C.9. Equivalent radius of the grain size distribution

C.3 EBSD results

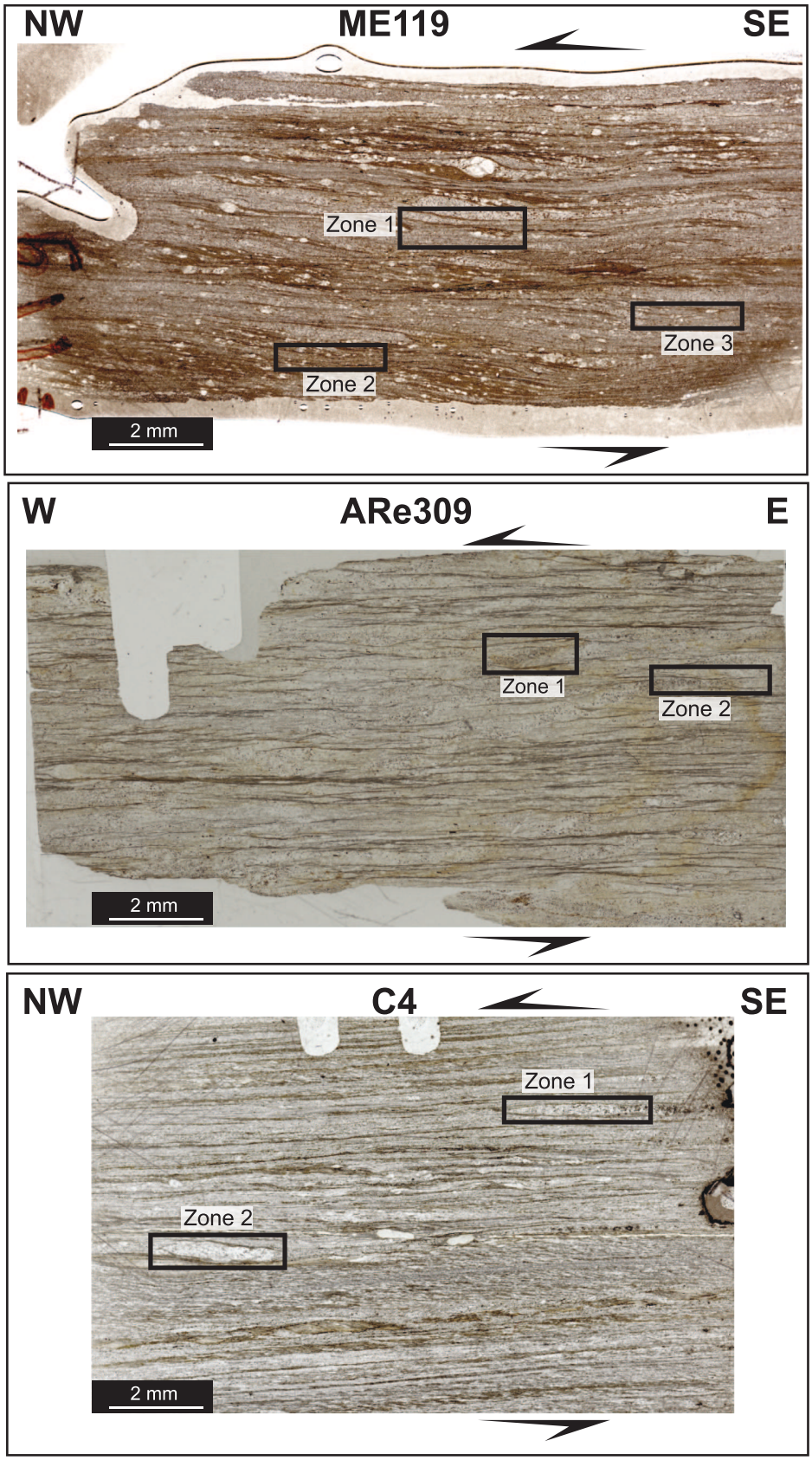

Figure C.10. Mapped zones with EBSD within the thin section.

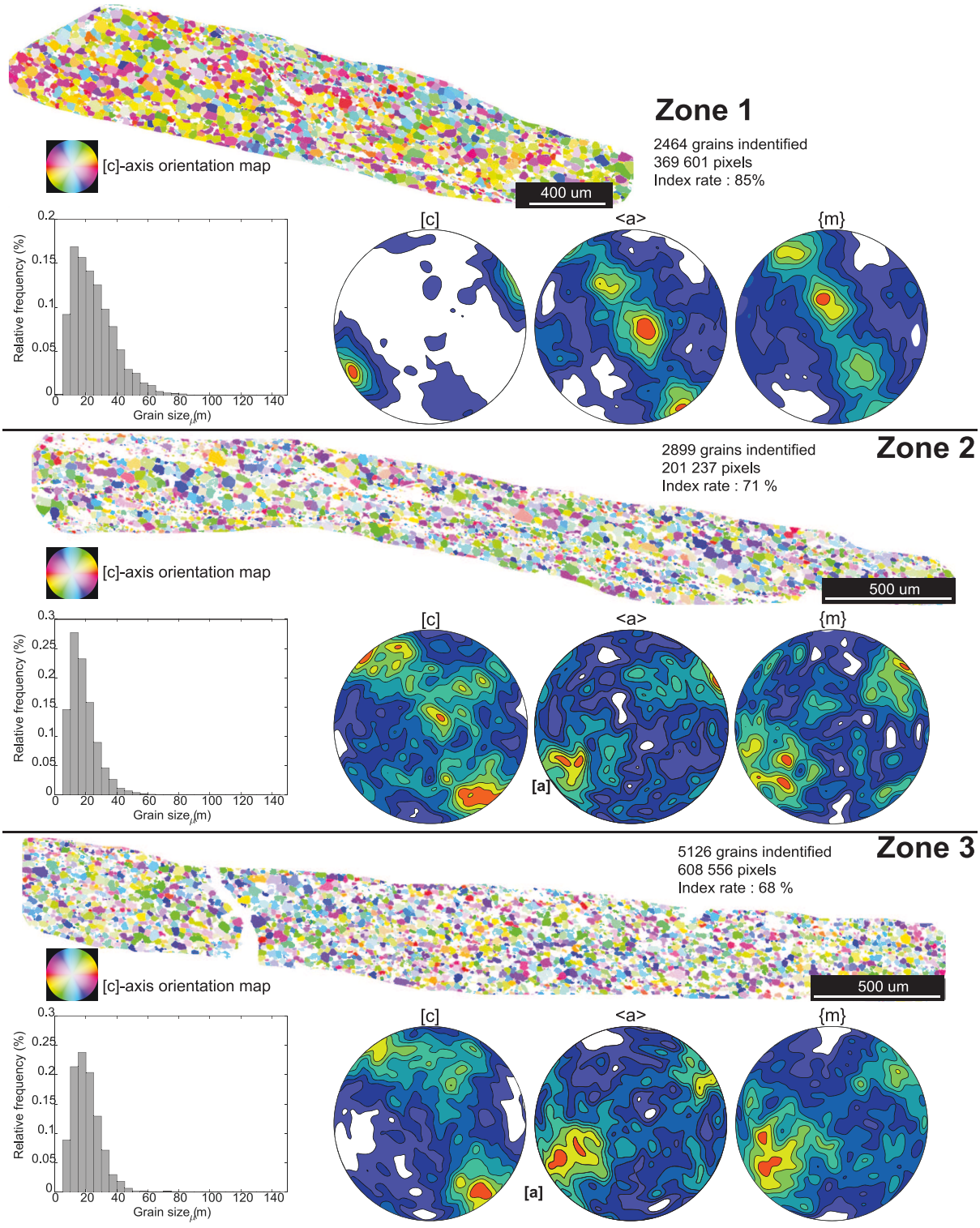

Figure C.11. EBSD results of sample ME119. [c]-axis maps, grain size distribution and crystallographic axis orientations in a stereographic projection (lower hemisphere, equal area).

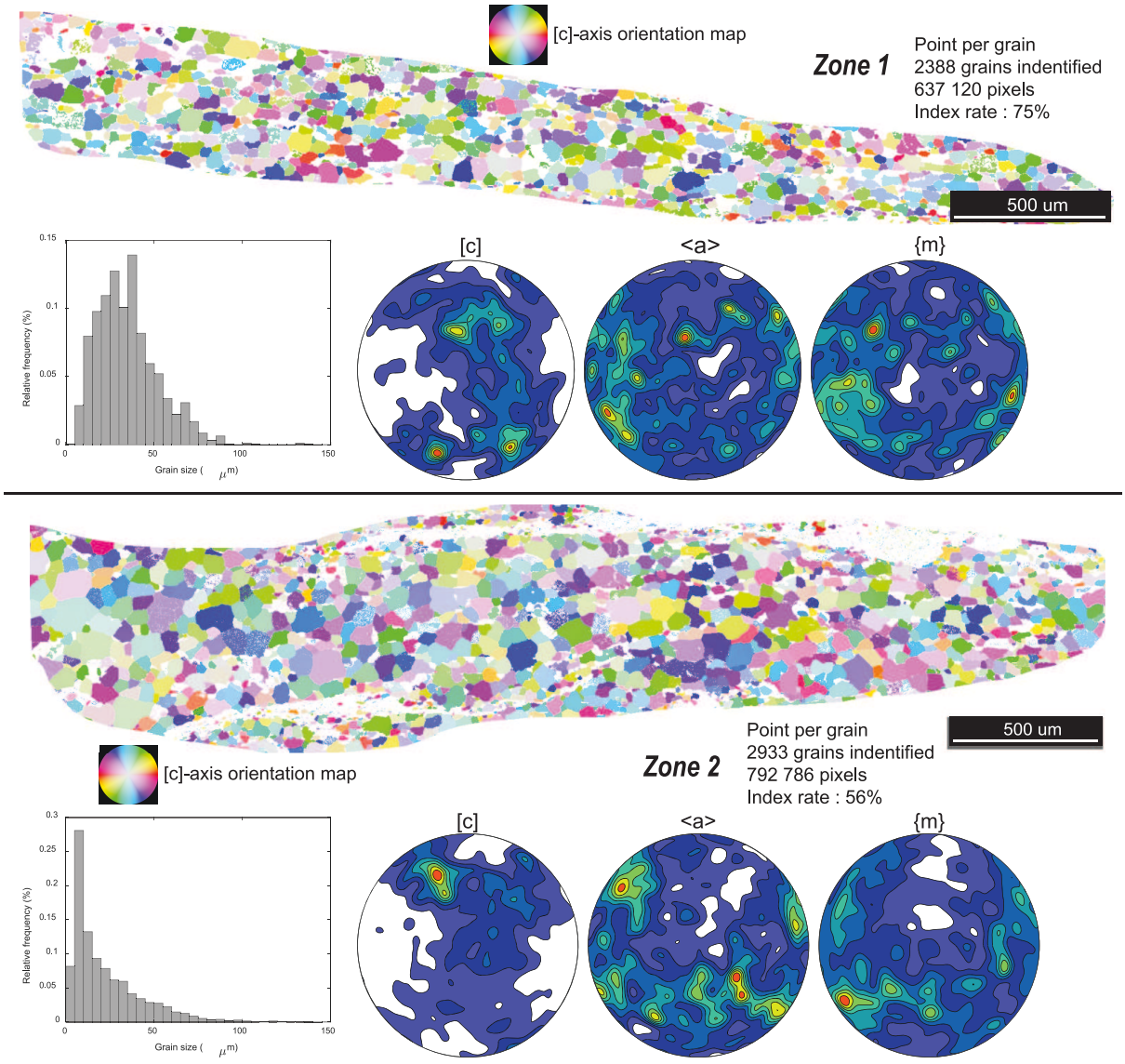

Figure C.12. EBSD results of sample C4. [c]-axis maps, grain size distribution and crystallographic axis orientations in a stereographic projection (lower hemisphere, equal area).

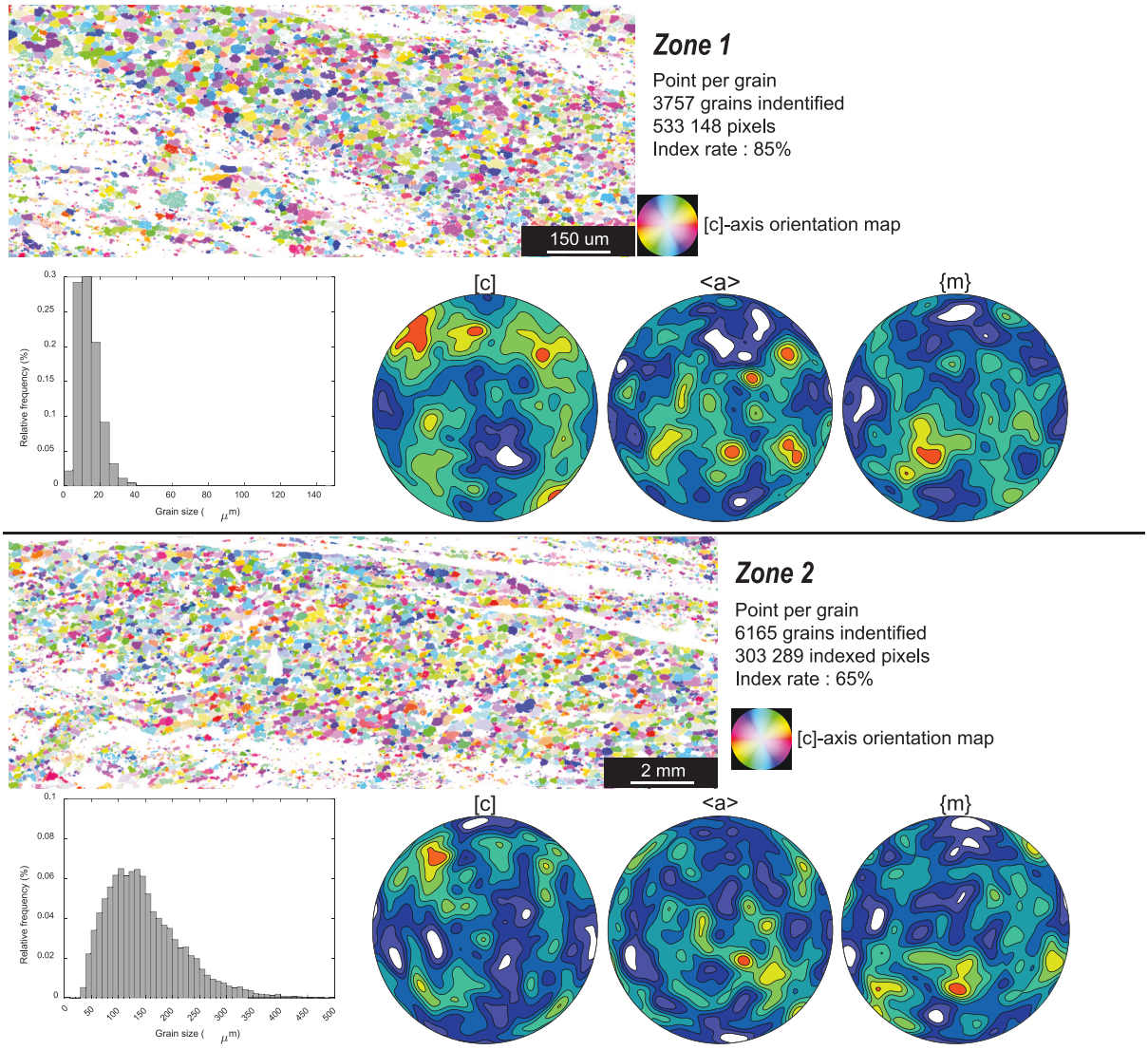

Figure C.13. EBSD results of sample ARe309. [c]-axis maps, grain size distribution and crystallographic axis orientations in a stereographic projection (lower hemisphere, equal area).

C.4 *In situ* laser ablation maps

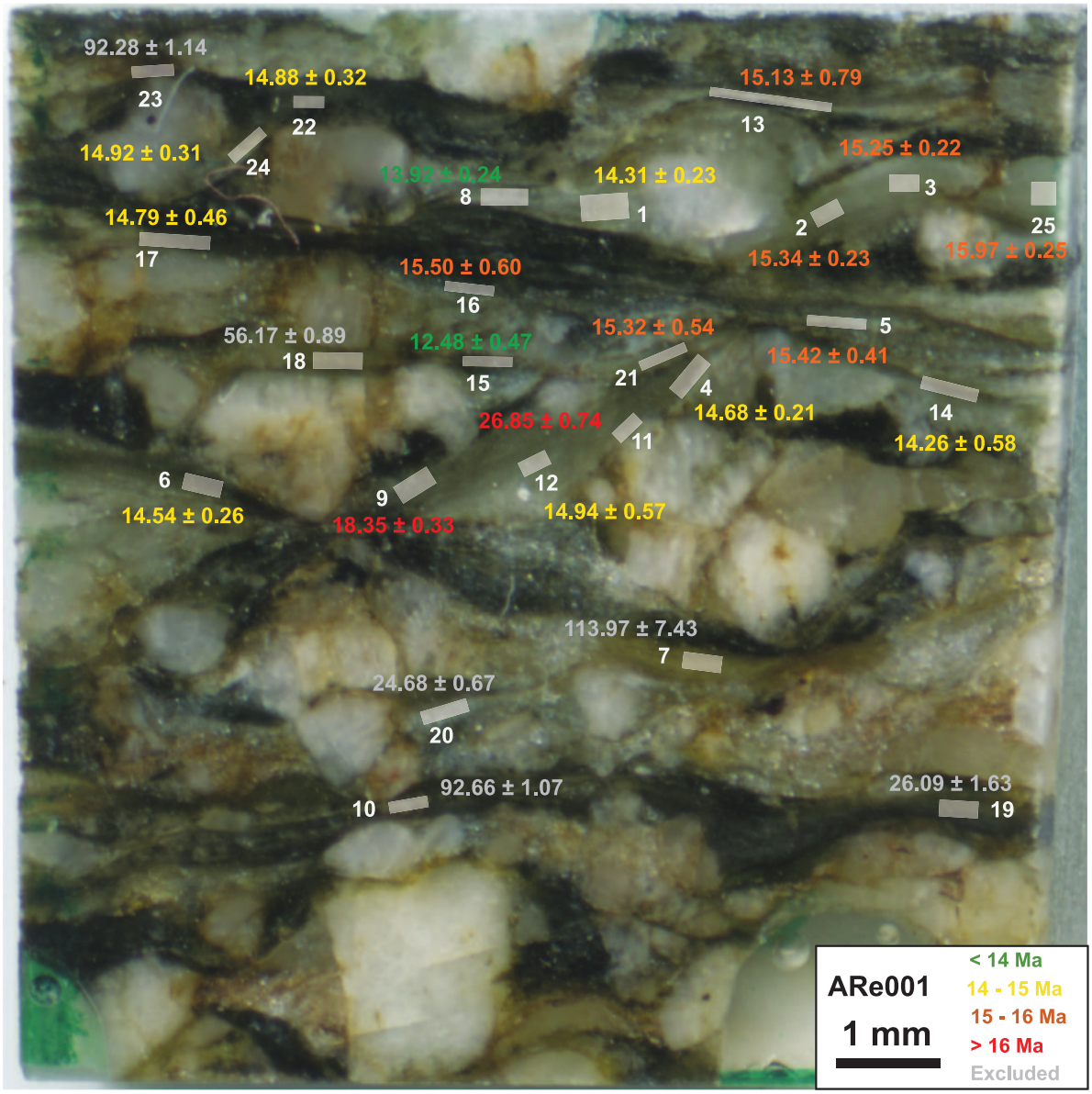

Figure C.14. *In situ* laser ablation map with spot numbers for sample ARe001. Spot colors refer to apparent ages.

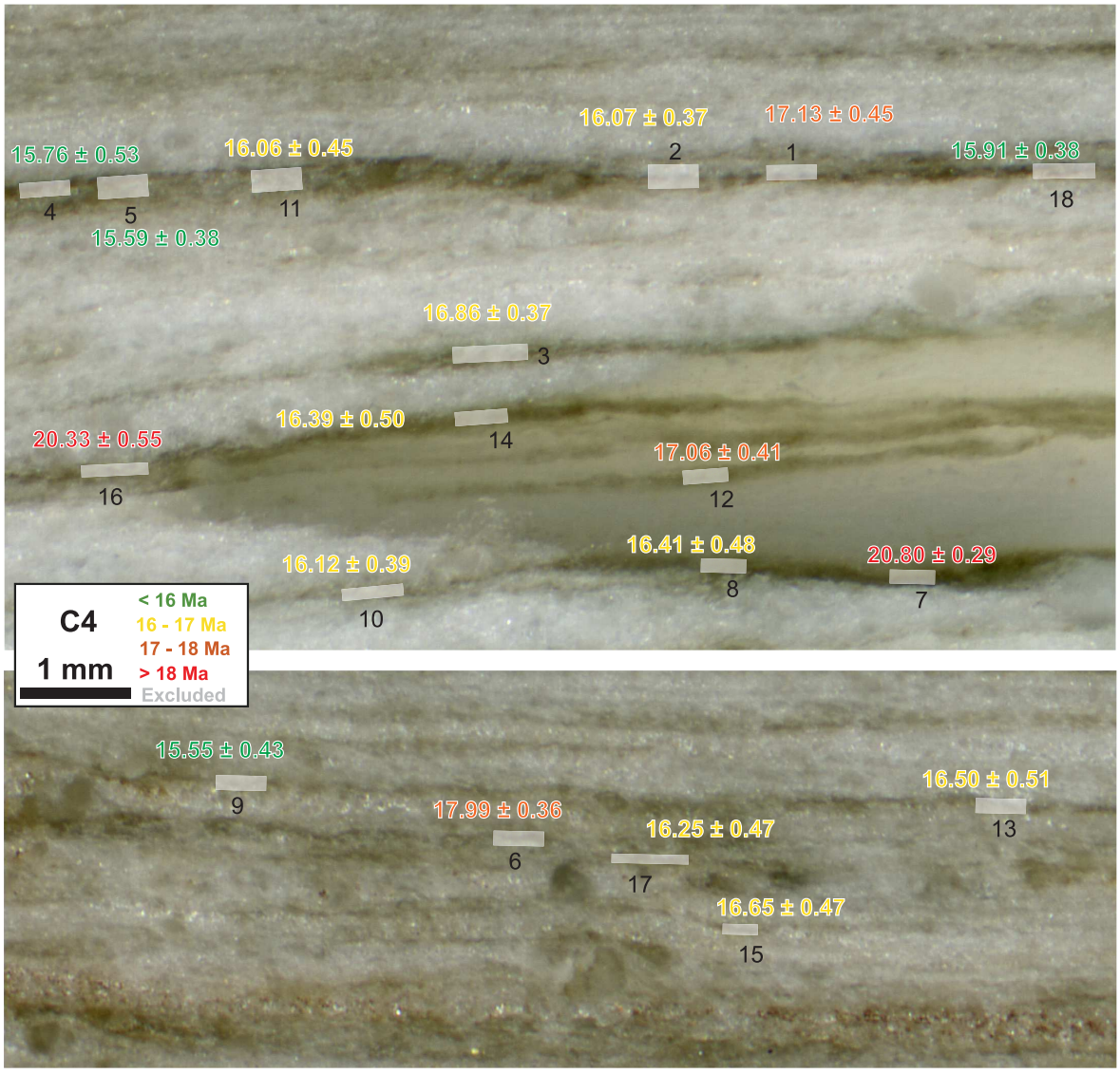

Figure C.15. *In situ* laser ablation map with spot numbers for sample C4. Spot colors refer to apparent ages.

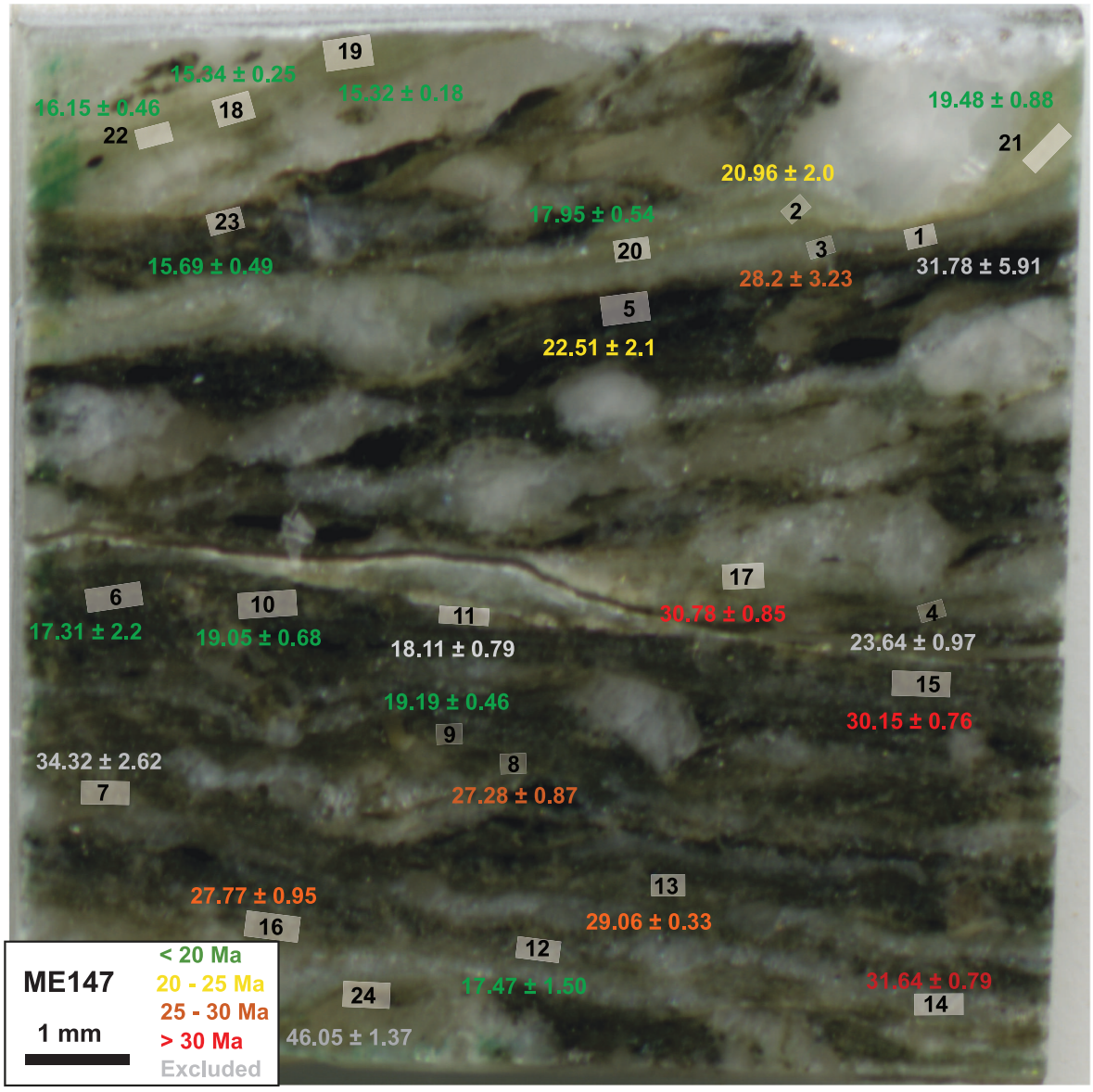

Figure C.16. *In situ* laser ablation map with spot numbers for sample ME147. Spot colors refer to apparent ages.

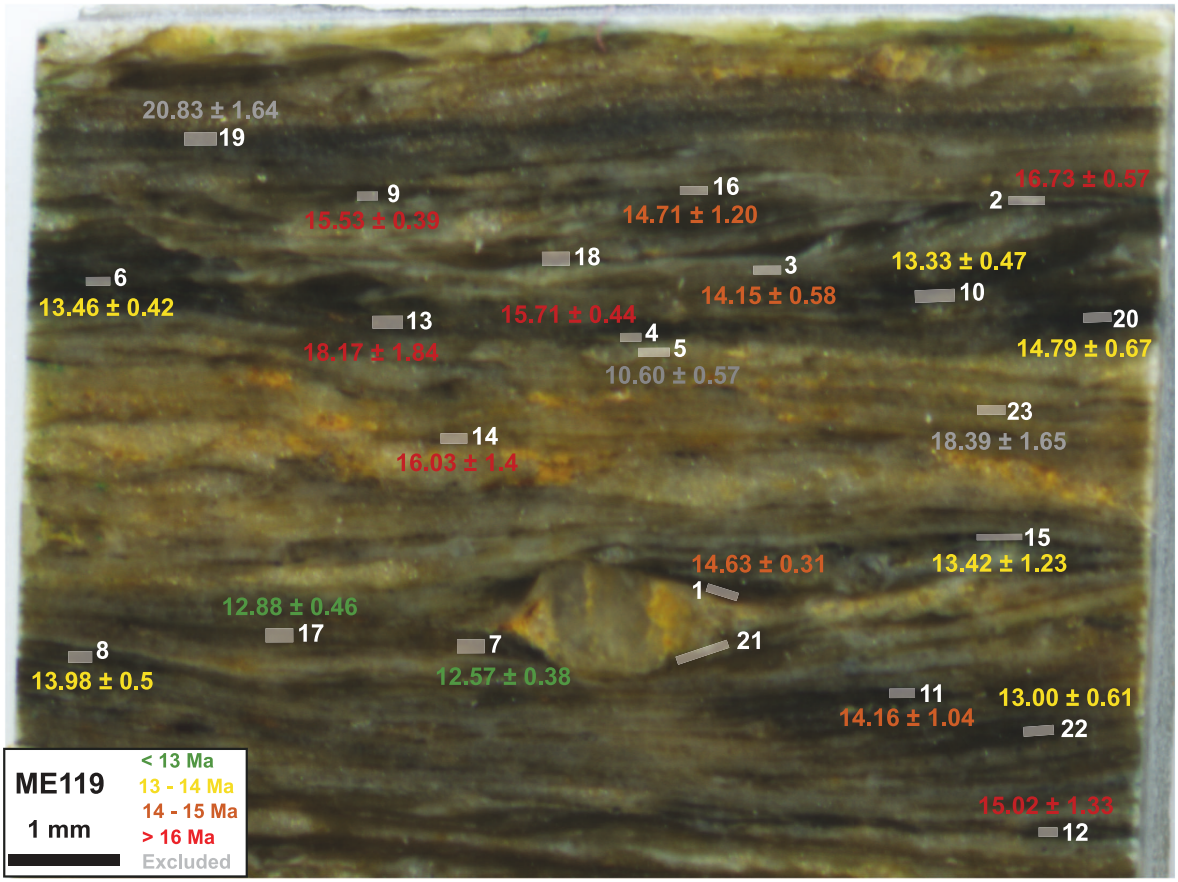

Figure C.17. *In situ* laser ablation map with spot numbers for sample ME119. Spot colors refer to apparent ages.

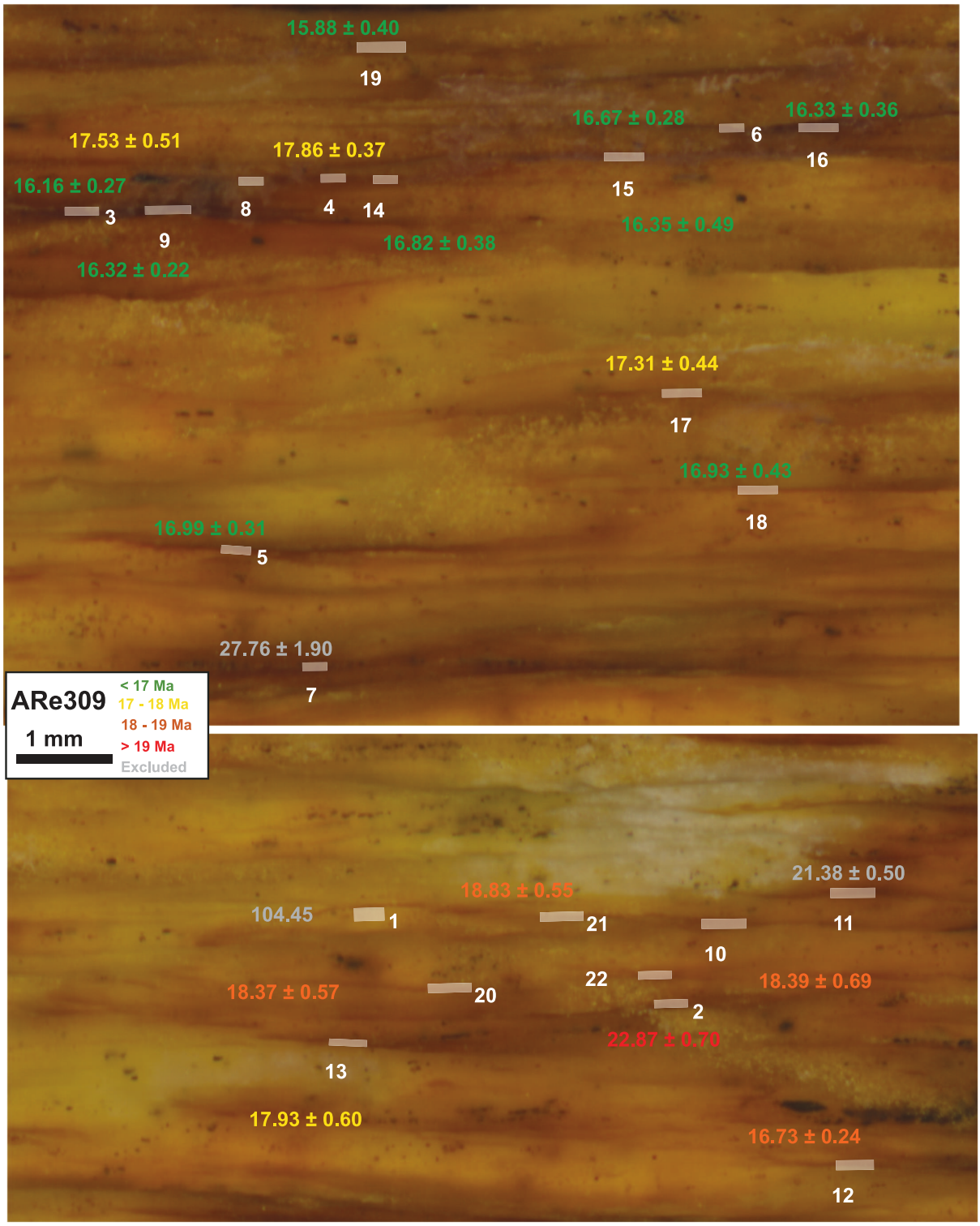

Figure C.18. *In situ* laser ablation map with spot numbers for sample ARe309. Spot colors refer to apparent ages.

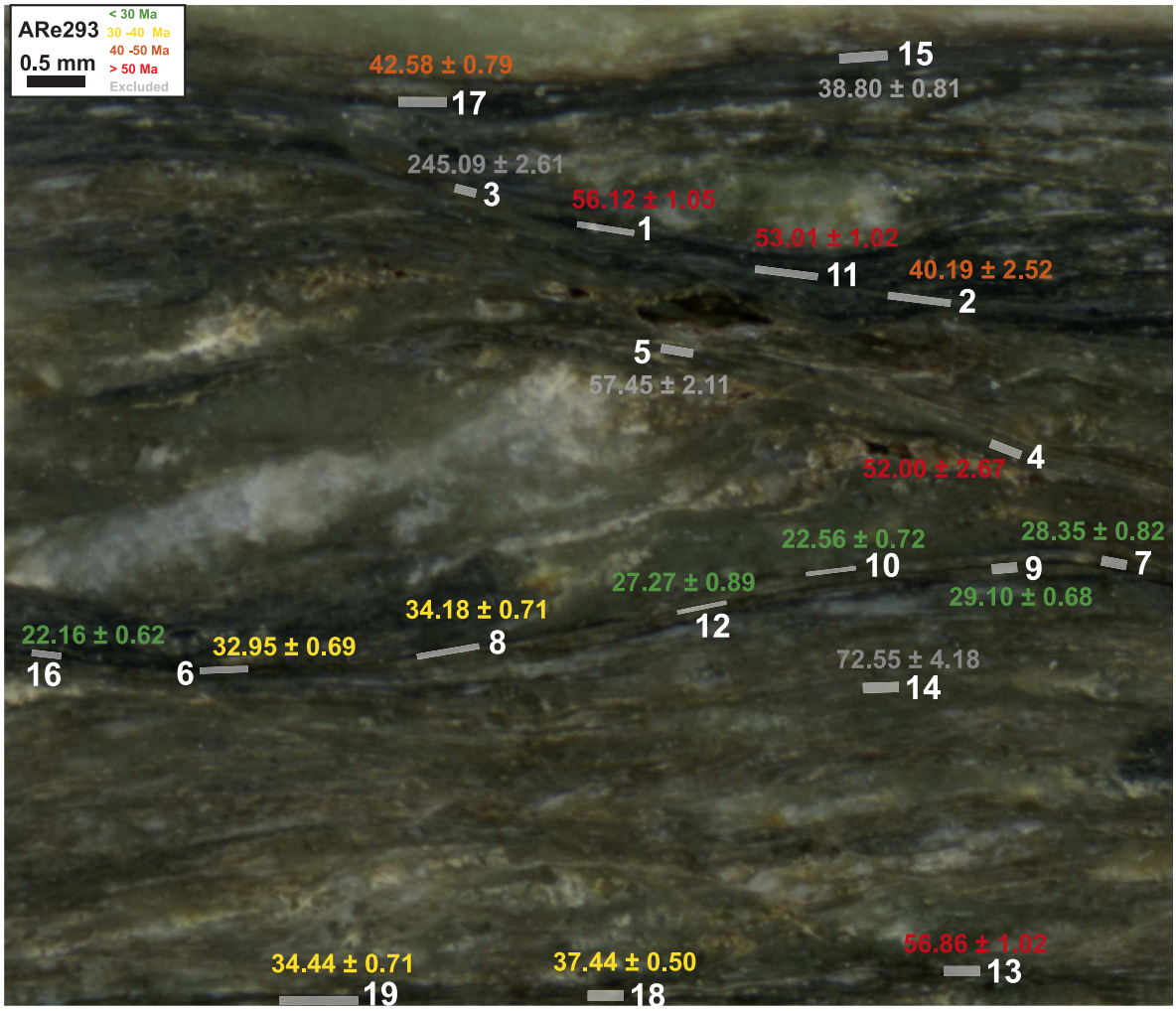

Figure C.19. *In situ* laser ablation map with spot numbers for sample ARe293. Spot colors refer to apparent ages.

C.5 EBSD measurement details

Table C.1. Summarizing measurement conditions, details of used instruments, and sample preparation during Electron BackScattered Diffraction (EBSD) analysis.

Sample ID	ME119			ARe309		C4	
	Site 1	Site 2	Site 3	Site 1	Site 2	Site 1	Site 2
Acceleration voltage (kV)	15	15	15	20	20	20	20
Acquisition speed (Hz)	198.8	198.8	198.8	325.7	327.7	322.3	327.7
Image size	1637x545	1823x350	1833x322	1950x780	1724x620	1813x352	1724x620
Field width (mm)	3.27	3.65	3.67	2.05	2.24	3.63	2.24
Field height (mm)	1.09	0.7	0.66	1.15	0.81	0.7	0.81
Step size (μm)	2	2	2	1.3	1.3	2	1.3
Index rate (%)	85.1	70.5	68.2	45.5	55.8	75.1	55.8
Working distance (mm)	15.7	15.6	16.1	14.3	13.7	23.3	13.7
Tilt (°)	70	70	70	70	70	70	70
Exposure time (ms)	5	5	5	3	3	3	3
Number of data points	892 165	201 237	227 733	533 148	579 233	241 703	465 897
Number of grains	2349	2899	3075	3757	6165	884	1619
Instrument	Zeiss Supra 55VP						
Location	MATEIS Laboratory - INSA Lyon						
Samples preparation	No carbon coating						

C.6 In-situ $^{40}Ar/^{39}Ar$ raw data on white mica

Table C.2. In-situ $^{40}Ar/^{39}Ar$ data on white mica from sample **ARe001**.

Spot ID	$^{36}Ar_a$ [V]	1σ %	$^{37}Ar_{Ca}$ [V]	1σ %	$^{38}Ar_{Cl}$ [V]	1σ %	$^{39}Ar_K$ [V]	1s %	$^{40}Ar_{Rad}$ [V]	1σ %	Age Ma	2σ Ma	$^{40}Ar_{Rad}$ %	$^{39}Ar_K$ %	Comment
1	0.0032	8.8618	b.d.l	0.1249	b.d.l	b.d.l	3.2515	0.4284	13.3692	0.6705	14.31	0.23	93.1619	4.1381	
2	0.0025	13.4416	0.1078	126.8512	0.0115	157.7111	3.9502	0.4308	17.4085	0.5998	15.34	0.23	95.7328	5.0274	
3	0.0027	11.2949	b.d.l	0.1349	b.d.l	b.d.l	3.7766	0.4700	16.5467	0.5696	15.25	0.22	95.2369	4.8065	
4	0.0023	13.7323	b.d.l	0.1380	b.d.l	b.d.l	3.7621	0.3744	15.8601	0.6159	14.68	0.21	95.7017	4.7879	
5	0.0023	13.5340	b.d.l	0.1637	b.d.l	b.d.l	2.0821	0.8265	9.2231	1.0424	15.42	0.41	93.0208	2.6498	
6	0.0016	18.3830	b.d.l	0.1207	b.d.l	b.d.l	3.2654	0.5928	13.6436	0.6943	14.54	0.26	96.3240	4.1559	
7	0.0232	1.3993	b.d.l	0.1218	b.d.l	b.d.l	0.5249	3.3145	17.6683	0.5763	113.97	7.43	71.8351	0.6681	Excluded
8	0.0028	10.2865	b.d.l	0.1142	b.d.l	b.d.l	3.0928	0.4841	12.3684	0.7286	13.92	0.24	93.5652	3.9362	
9	0.0482	0.7790	0.1584	75.9120	b.d.l	b.d.l	3.2055	0.5740	16.9159	0.7021	18.35	0.33	53.9562	4.0796	
10	0.0264	2.0046	0.5927	38.8535	0.0498	38.5704	5.4080	0.5712	147.1038	0.1593	92.66	1.07	94.8763	6.8827	
11	0.0216	2.1427	0.0576	300.7077	0.0366	47.9320	2.9445	1.0125	22.7905	0.9562	26.85	0.74	77.8471	3.7475	
12	0.0139	3.3407	b.d.l	0.2014	0.0164	117.6452	3.1218	0.9785	13.3955	1.6321	14.94	0.57	76.2088	3.9731	
13	0.0112	4.5052	b.d.l	0.1820	b.d.l	b.d.l	2.2965	1.3056	9.9812	2.2653	15.13	0.79	74.7204	2.9227	
14	0.0017	26.7750	0.0970	171.8079	b.d.l	b.d.l	3.0116	1.0464	12.3339	1.7508	14.26	0.58	95.8559	3.8328	
15	0.0019	23.9684	0.1458	131.5975	b.d.l	b.d.l	3.5347	0.8604	12.6658	1.6912	12.48	0.47	95.5670	4.4986	
16	0.0032	14.7240	0.0262	680.6849	0.0112	172.0997	2.9638	1.0092	13.2833	1.6463	15.60	0.60	93.1309	3.7720	
17	0.0021	21.7451	0.2284	130.6150	b.d.l	b.d.l	3.8884	0.7938	16.5226	1.3280	14.79	0.46	96.1264	4.9487	
18	0.0131	3.5748	b.d.l	0.1824	0.0018	1402.6670	4.0679	0.7383	66.3973	0.3296	56.17	0.89	94.4034	5.1771	
19	0.0019	27.9599	2.9706	6.8885	0.0604	28.9211	1.4065	2.2492	10.5742	2.1964	26.09	1.63	94.7653	1.7900	Excluded
20	0.0068	6.7945	b.d.l	0.1912	0.0321	79.2075	3.1888	0.9741	22.6714	0.9580	24.68	0.67	91.7234	4.0583	
21	0.0021	21.0720	b.d.l	0.1929	0.0336	70.3232	3.3521	0.9747	14.7584	1.4748	15.32	0.54	95.6362	4.2662	
22	0.0031	8.7433	0.6573	17.8721	0.0480	31.6674	2.8100	0.7807	12.0127	0.7641	14.88	0.32	92.6005	3.5763	
23	0.0376	0.9689	0.1184	155.0068	0.0815	16.0871	3.5468	0.6140	97.1441	0.1192	93.28	1.14	89.6052	4.5139	
24	0.0032	8.6684	0.2359	54.6416	0.0131	130.4347	2.7927	0.7420	11.9733	0.7460	14.92	0.31	92.4835	3.5543	
25	b.d.l	b.d.l	0.3202	35.0943	b.d.l	b.d.l	3.3288	0.7241	15.2744	0.2719	15.97	0.25	99.7909	4.2365	

b.d.l: Below detection limit

Table C.3. In-situ $^{40}Ar/^{39}Ar$ data on white mica from sample **ME147**.

Spot	$^{36}Ar_a$ [V]	1σ %	$^{37}Ar_{Ca}$ [V]	1σ %	$^{38}Ar_{Cl}$ [V]	1σ %	$^{39}Ar_K$ [V]	1s %	$^{40}Ar_{Rad}$ [V]	1σ %	Age Ma	2σ Ma	$^{40}Ar_{Rad}$ %	$^{39}Ar_K$ %	Comment
1	0.0046	43.1589	0.2011	52.8141	0.0447	65.8600	0.9361	3.8893	8.6167	7.9891	31.78	5.60	86.0961	1.3716	Excluded
2	b.d.l	b.d.l	0.2078	51.1335	b.d.l	b.d.l	1.3709	2.4057	8.2994	4.1382	20.96	2.00	99.8441	2.0087	
3	0.0071	27.3703	0.2473	37.1519	0.0440	66.5782	1.4950	2.1512	12.2051	5.5320	28.21	3.32	85.0915	2.1906	
4	0.0474	4.1752	0.2967	29.5964	0.0202	134.2176	5.1021	0.6639	34.8542	1.9602	23.64	0.97	71.0656	7.4759	
5	0.0107	18.3384	0.9212	12.1409	0.0284	93.8343	2.3228	1.3473	15.1050	4.4936	22.51	2.10	82.4509	3.4035	
6	0.0027	71.1815	0.5126	21.5850	0.0242	110.9262	2.0687	1.5135	10.3299	6.5011	17.31	2.30	92.5598	3.0311	
7	0.0127	4.0610	0.3489	33.7149	0.0161	189.7419	0.7797	1.9230	7.7547	3.3440	34.32	2.62	67.0533	1.1424	Excluded
8	0.0139	1.8706	0.0475	184.1053	b.d.l	b.d.l	1.9735	0.7313	15.5764	1.4263	27.28	0.87	78.8750	2.8916	
9	0.0158	2.4416	b.d.l	0.1483	b.d.l	b.d.l	3.9118	0.5229	21.6729	1.1010	19.20	0.47	81.9813	5.7318	
10	0.0037	9.5795	0.6981	20.0921	b.d.l	b.d.l	2.5605	0.5868	14.0779	1.6696	19.05	0.67	92.6371	3.7518	
11	0.1227	0.5504	0.3324	42.4675	b.d.l	b.d.l	2.6910	0.6810	14.0631	2.0798	18.11	0.79	27.7204	3.9430	
12	0.0134	2.0578	b.d.l	0.1137	b.d.l	b.d.l	3.4606	0.4259	17.2982	1.2937	17.33	0.47	81.0480	5.0707	
13	0.0329	1.1541	b.d.l	0.1141	b.d.l	b.d.l	3.3421	0.3929	28.1065	0.4099	29.06	0.33	74.0651	4.8970	
14	0.0262	1.8879	0.8469	17.9155	0.0110	201.3951	2.4397	0.9503	22.3616	0.8204	31.65	0.79	74.0604	3.5748	
15	0.0182	2.0867	0.2413	88.6779	0.0167	100.2786	2.4202	1.0178	21.1285	0.7482	30.15	0.76	79.4849	3.5463	
16	0.0121	3.9493	0.5449	30.8418	0.0010	3674.5585	1.9515	1.2795	15.6784	1.1486	27.77	0.95	81.1479	2.8595	
17	0.0369	1.3307	0.2354	65.7519	0.0027	979.6724	2.2756	1.0684	20.2863	0.9027	30.79	0.85	64.7649	3.3344	
18	0.0066	6.0886	0.6997	21.5077	0.0136	117.3793	5.2858	0.4381	23.3780	0.6943	15.34	0.25	92.0345	7.7450	
19	0.0085	4.6746	0.4293	18.2807	b.d.l	b.d.l	5.9941	0.4047	26.4865	0.4546	15.33	0.19	91.0453	8.7829	
20	0.0042	15.9282	b.d.l	0.1790	0.0035	437.7593	3.5542	0.7522	18.4087	1.3079	17.95	0.54	93.4780	5.2079	
21	0.0132	4.9954	1.1440	14.8026	b.d.l	b.d.l	2.1842	1.1786	12.2789	1.9302	19.48	0.88	75.5524	3.2005	
22	0.0066	9.8715	0.6471	26.3591	0.0218	74.3813	3.9556	0.6728	18.4187	1.2729	16.15	0.46	90.1935	5.7961	
23	0.0019	34.9625	0.9466	17.9659	b.d.l	b.d.l	3.7142	0.7367	16.8066	1.4009	15.69	0.49	96.5866	5.4422	
24	0.0237	2.9318	b.d.l	0.1849	0.0561	31.3973	2.1472	1.2454	28.7533	0.8549	46.05	1.37	80.2225	3.1462	

b.d.l: Below detection limit

Table C.4. In-situ $^{40}Ar/^{39}Ar$ data on white mica from sample **C4**.

Spot	$^{36}Ar_a$ [V]	1σ %	$^{37}Ar_{Ca}$ [V]	1σ %	$^{38}Ar_{Cl}$ [V]	1σ %	$^{39}Ar_K$ [V]	1s %	$^{40}Ar_{Rad}$ [V]	1σ %	Age Ma	2σ Ma	$^{40}Ar_{Rad}$ %	$^{39}Ar_K$ %	Comment
1	0.0047	9.5476	0.3534	65.4246	b.d.l	b.d.l	4.1528	0.5611	20.3470	1.1975	17.13	0.45	93.4142	5.2781	
2	0.0055	8.0141	0.3999	57.2329	b.d.l	b.d.l	5.0285	0.5250	23.0992	1.0411	16.07	0.37	93.1801	6.3912	
3	0.0039	11.5901	0.4537	49.9188	0.0290	52.8938	4.9856	0.4728	24.0311	1.0092	16.86	0.37	95.1584	6.3367	
4	0.0060	7.5806	0.6699	34.0149	0.0379	45.0105	3.4789	0.6581	15.6701	1.5439	15.76	0.53	89.6312	4.4216	
5	0.0051	9.2375	0.2051	196.4675	0.0034	461.7041	4.8410	0.4760	21.5789	1.1364	15.59	0.38	93.2355	6.1529	
6	0.0050	9.2079	0.1089	266.4530	0.0140	120.9958	4.1628	0.5748	21.4180	1.1342	17.99	0.46	93.3711	5.2909	
7	0.0045	9.3008	0.7049	33.1729	b.d.l	b.d.l	6.5471	0.3572	38.9756	0.6085	20.80	0.29	96.4917	8.3213	
8	0.0050	8.8437	0.5456	41.4759	0.0084	182.2166	3.7828	0.6149	17.7496	1.3495	16.41	0.48	92.1409	4.8079	
9	0.0049	8.8762	0.1573	154.5799	b.d.l	b.d.l	4.2435	0.5708	18.8649	1.2675	15.55	0.43	92.6874	5.3935	
10	0.0035	12.9527	0.1467	157.2016	b.d.l	b.d.l	4.7155	0.4985	21.7311	1.1126	16.12	0.39	95.2554	5.9934	
11	0.0034	12.7452	0.2539	95.3096	b.d.l	b.d.l	4.0455	0.5853	18.5775	1.2796	16.06	0.45	94.7007	5.1418	
12	0.0041	11.2127	0.2431	97.2094	b.d.l	b.d.l	4.4985	0.4963	21.9465	1.1145	17.06	0.41	94.4913	5.7176	
13	0.0043	10.0874	0.0618	399.2105	b.d.l	b.d.l	3.6219	0.6450	17.0898	1.4045	16.50	0.51	92.7666	4.6034	
14	0.0061	7.1395	0.0628	366.6326	b.d.l	b.d.l	3.6957	0.6760	17.3226	1.3835	16.39	0.50	90.3574	4.6972	
15	0.0040	12.0963	0.5289	47.3478	b.d.l	b.d.l	4.0580	0.6286	19.3156	1.2830	16.65	0.47	93.9980	5.1576	
16	0.0177	2.5953	0.2393	101.6295	b.d.l	b.d.l	3.8786	0.6848	22.5731	1.0851	20.33	0.52	80.9623	4.9296	
17	0.0058	8.4255	0.1608	139.3284	b.d.l	b.d.l	3.9929	0.5804	18.5524	1.3370	16.25	0.47	91.3039	5.0750	
18	0.0061	7.1916	0.2062	120.3505	b.d.l	b.d.l	4.9491	0.5547	22.5045	1.0679	15.91	0.38	92.3488	6.2903	

b.d.l: Below detection limit

Table C.5. Infrared laser in-situ $^{40}Ar/^{39}Ar$ data on white mica from sample **ME119**.

Spot	$^{36}Ar_a$ [V]	1σ %	$^{37}Ar_{Ca}$ [V]	1σ %	$^{38}Ar_{Cl}$ [V]	1σ %	$^{39}Ar_K$ [V]	1s %	$^{40}Ar_{Rad}$ [V]	1σ %	Age Ma	2σ Ma	$^{40}Ar_{Rad}$ %	$^{39}Ar_K$ %	Comment
1	0.0040	10.7379	b.d.l	0.1161	0.0041	654.4563	7.4309	0.1946	30.8631	1.0325	14.63	0.31	96.1084	7.3424	
2	0.1097	0.6339	b.d.l	0.1286	0.0240	106.3792	4.4973	0.2945	21.3672	1.6880	16.73	0.57	39.4408	4.4438	
3	0.0083	5.8165	b.d.l	0.1436	b.d.l	b.d.l	4.0023	0.3652	16.0729	2.0302	14.15	0.58	86.4702	3.9546	
4	0.0112	3.6851	b.d.l	0.1282	b.d.l	b.d.l	5.1665	0.2886	23.0449	1.3767	15.71	0.44	87.1869	5.1050	
5	0.0065	7.2041	0.1165	96.3530	0.0082	283.2335	4.0271	0.3911	12.0986	2.6801	10.60	0.57	86.0221	3.9791	
6	0.0196	2.1100	b.d.l	0.1198	b.d.l	b.d.l	5.3811	0.2673	20.5494	1.5463	13.46	0.42	77.6644	5.3170	
7	0.0074	6.3543	0.1353	95.2655	b.d.l	b.d.l	6.1228	0.2262	21.8292	1.4850	12.57	0.38	90.5959	6.0498	
8	0.0088	5.6219	b.d.l	0.1434	0.0036	680.1583	4.6703	0.3058	18.5318	1.7687	13.98	0.50	87.3941	4.6147	
9	0.0050	8.6896	b.d.l	0.1249	b.d.l	b.d.l	5.8522	0.2810	25.7939	1.2411	15.53	0.39	94.3260	5.7825	
10	0.0470	0.9880	b.d.l	0.1214	b.d.l	b.d.l	4.9303	0.3143	18.6438	1.7373	13.33	0.47	56.9655	4.8716	
11	0.0162	10.6138	0.2114	43.9890	0.0193	81.0454	5.0366	0.4732	20.2447	3.6527	14.16	1.04	80.5766	4.9767	
12	0.0078	21.8993	0.0268	318.4415	b.d.l	b.d.l	3.9389	0.4986	16.7966	4.4013	15.02	1.33	87.5987	3.8920	
13	0.0233	7.4685	0.4010	32.3582	0.0248	87.3404	2.8515	0.6726	14.7174	5.0523	18.17	1.84	67.8519	2.8175	
14	0.0172	10.1561	0.4519	20.9632	0.0034	542.5037	3.7717	0.4976	17.1619	4.3466	16.03	1.40	76.8226	3.7267	
15	0.0346	4.9906	0.3048	36.4156	0.0256	75.3693	4.2397	0.4304	16.1442	4.5922	13.42	1.23	60.8855	4.1892	
16	0.0046	37.9167	0.2909	31.3732	0.0192	111.5567	4.3516	0.3863	18.1723	4.0811	14.71	1.20	92.8412	4.2998	
17	0.0084	10.9017	b.d.l	0.1544	b.d.l	b.d.l	4.7156	0.2902	17.2355	1.7689	12.88	0.46	87.1357	4.6595	
18	0.0087	10.4730	0.1211	127.9147	b.d.l	b.d.l	5.4341	0.3230	21.6041	1.4048	14.01	0.40	89.1253	5.3694	
19	0.0128	7.0584	b.d.l	0.1497	0.0484	40.0173	1.3690	1.3499	8.1095	3.7333	20.83	1.64	67.8837	1.3527	Excluded
20	0.0439	2.1754	b.d.l	0.1443	b.d.l	b.d.l	3.3823	0.3974	14.1991	2.2318	14.79	0.67	51.9189	3.3420	
21	0.0071	12.8809	0.1141	126.5224	b.d.l	b.d.l	5.0873	0.3696	22.2469	1.3709	15.40	0.44	91.1349	5.0267	
22	0.0049	18.7172	0.0054	2633.9134	0.0204	66.1993	3.6312	0.4395	13.3922	2.3022	13.00	0.61	89.8640	3.5879	
23	0.0080	11.2383	0.3711	40.3379	b.d.l	b.d.l	1.3151	1.0959	6.8707	4.3848	18.39	1.65	74.1049	1.2994	Excluded

b.d.l: Below detection limit

Table C.6. Infrared laser in-situ $^{40}Ar/^{39}Ar$ data on white mica from sample **ARe309**.

Spot	$^{36}Ar_a$ [V]	1σ %	$^{37}Ar_{Ca}$ [V]	1σ %	$^{38}Ar_{Cl}$ [V]	1σ %	$^{39}Ar_K$ [V]	1s %	$^{40}Ar_{Rad}$ [V]	1σ %	Age Ma	2σ Ma	$^{40}Ar_{Rad}$ %	$^{39}Ar_K$ %	Comment
1	0.0211	1.0892	0.1044	158.7726	0.0336	44.8883	0.1376	11.4837	4.1601	1.8431	104.45	23.61	39.7960	0.2903	Excluded
2	0.0166	2.1949	b.d.l	0.1770	0.0242	61.0965	1.5288	0.9852	9.8979	1.1839	22.87	0.70	66.5515	3.2259	
3	0.0032	8.3289	b.d.l	0.2696	0.0304	47.3308	3.0184	0.4470	13.7823	0.6325	16.16	0.25	93.2508	6.3693	
4	0.0016	16.1056	0.0663	252.0712	b.d.l	b.d.l	2.3134	0.6999	11.6795	0.7519	17.86	0.37	95.8255	4.8817	
5	0.0049	5.3824	b.d.l	0.1872	0.0073	218.0288	2.6701	0.5873	12.8178	0.6850	16.99	0.31	89.5042	5.6342	
6	0.0023	12.3502	0.3419	49.3650	b.d.l	b.d.l	2.8132	0.4633	13.2477	0.6914	16.67	0.28	94.8590	5.9363	
7	0.0269	0.8499	0.1574	94.8125	0.0051	553.0207	0.5209	2.8558	4.0984	1.9205	27.76	1.90	33.8130	1.0993	Excluded
8	0.0018	14.6538	0.2791	65.0575	b.d.l	b.d.l	1.6145	0.9796	8.0012	1.0838	17.53	0.51	93.5101	3.4068	
9	0.0013	15.3731	0.0924	164.2949	b.d.l	b.d.l	3.1172	0.5023	14.3745	0.4647	16.32	0.22	97.2723	6.5777	
10	0.0037	7.4706	b.d.l	0.1610	0.0086	200.3113	2.3139	0.4529	11.6596	0.7644	17.83	0.32	91.2659	4.8827	
11	0.0037	5.9021	0.1112	219.0448	b.d.l	b.d.l	1.3601	0.7335	8.2275	0.9121	21.38	0.50	87.9141	2.8701	
12	0.0058	3.7871	0.0840	261.1882	0.0018	837.1272	2.8209	0.4700	13.3354	0.5628	16.73	0.24	88.3919	5.9524	
13	0.0024	11.2610	0.1163	110.8196	0.0387	75.7261	1.7570	1.3132	8.9043	1.0543	17.93	0.60	92.3663	3.7075	
14	0.0018	15.3490	b.d.l	0.1484	0.0021	1363.3547	2.7167	0.8478	12.9087	0.7409	16.82	0.38	95.8237	5.7327	
15	0.0029	9.7608	0.0111	1970.3314	0.0283	100.5244	2.1779	1.1354	10.0590	0.9757	16.35	0.49	91.8505	4.5956	
16	0.0034	8.6271	b.d.l	0.1472	0.0097	320.7915	2.8908	0.8029	13.3398	0.7751	16.33	0.36	92.7622	6.1000	
17	0.0049	6.1904	b.d.l	0.1446	b.d.l	b.d.l	2.4888	0.9572	12.1727	0.8420	17.31	0.44	89.1563	5.2517	
18	0.0041	6.9463	b.d.l	0.1323	0.0184	161.9863	2.4878	0.9657	11.9020	0.8181	16.93	0.43	90.5130	5.2495	
19	0.0038	7.6647	b.d.l	0.1453	0.0348	84.2039	2.6170	0.9356	11.7378	0.8416	15.88	0.40	91.0156	5.5222	
20	0.0102	3.0677	b.d.l	0.1184	b.d.l	b.d.l	2.0637	1.2047	10.7153	0.9769	18.37	0.57	77.7682	4.3546	
21	0.0072	5.0397	b.d.l	0.1606	0.0031	889.8922	2.1605	1.0549	11.5035	1.0385	18.83	0.55	84.1211	4.5590	
22	0.0129	2.8228	b.d.l	0.1257	b.d.l	b.d.l	1.8011	1.4051	9.3617	1.2690	18.39	0.69	70.8074	3.8005	

b.d.l: Below detection limit

Table C.7. Infrared laser in-situ $^{40}Ar/^{39}Ar$ data on white mica from sample **ARe293**.

Spot	$^{36}Ar_a$ [V]	1σ %	$^{37}Ar_{Ca}$ [V]	1σ %	$^{38}Ar_{Cl}$ [V]	1σ %	$^{39}Ar_K$ [V]	1s %	$^{40}Ar_{Rad}$ [V]	1σ %	Age Ma	2σ Ma	$^{40}Ar_{Rad}$ %	$^{39}Ar_K$ %	Comment
1	0.0069	13.0318	0.3780	45.6783	0.0086	321.1649	3.1290	0.6445	50.0888	0.7034	56.12	1.05	95.9968	5.2627	
2	0.0087	10.4445	0.3238	51.6090	0.0079	370.8919	1.2448	1.9688	14.2074	2.4900	40.19	2.52	84.5267	2.0937	
3	0.0216	4.2313	0.3600	49.5978	0.0040	716.8825	0.2387	9.0720	17.5989	2.0259	245.09	42.61	73.1381	0.4015	Excluded
4	0.0092	10.0191	0.3642	46.6804	0.0236	125.6361	1.3235	1.8488	19.6103	1.8277	52.00	2.67	87.6297	2.2261	
5	0.7087	0.2110	0.1541	124.3592	0.0013	2190.1251	2.0311	0.8792	33.2976	1.6464	57.45	2.11	13.5955	3.4161	Excluded
6	0.0112	7.9403	b.d.l	0.1994	b.d.l	b.d.l	3.9842	0.4726	37.2045	0.9435	32.95	0.69	91.6367	6.7012	
7	0.0041	23.6514	0.6045	35.2665	0.0320	86.3284	3.4324	0.5912	27.5444	1.3307	28.35	0.82	95.6742	5.7732	
8	0.0063	14.1586	0.2365	81.2697	b.d.l	b.d.l	3.9064	0.4992	37.8559	0.9261	34.18	0.71	95.1805	6.5704	
9	0.0096	9.3780	0.3053	56.7337	0.0069	398.3063	3.9803	0.4601	32.7899	1.0759	29.10	0.68	91.8627	6.6946	
10	0.0057	15.6182	0.1568	104.6505	b.d.l	b.d.l	3.6247	0.5396	23.1093	1.5215	22.56	0.72	92.9749	6.0965	
11	0.0034	26.3732	0.0318	522.4307	0.0139	206.3799	3.2977	0.6732	49.8225	0.7106	53.01	1.02	97.9331	5.5466	
12	0.0472	2.1476	0.3715	49.7965	0.0072	411.0423	3.2957	0.6790	25.4351	1.4943	27.27	0.89	64.3211	5.5431	
13	0.0074	12.0094	b.d.l	0.1693	0.0139	219.9540	3.3782	0.6426	54.8073	0.6409	56.86	1.02	96.0481	5.6819	
14	0.0221	4.2301	b.d.l	0.2017	0.0523	56.4302	0.9879	2.3558	20.5396	1.7536	72.55	4.18	75.6923	1.6616	Excluded
15	0.1066	0.9677	0.0851	209.1822	0.0158	174.0540	3.8918	0.5431	42.8682	0.8993	38.80	0.81	57.3672	6.5459	Excluded
16	0.0285	3.2735	b.d.l	0.1763	0.0173	158.9118	4.3303	0.4745	27.1158	1.3281	22.16	0.62	76.0358	7.2834	
17	0.0057	15.8273	0.0728	239.8585	b.d.l	b.d.l	3.0996	0.6124	43.7538	0.8045	49.58	0.99	96.2187	5.2133	
18	0.0878	1.1320	0.2750	60.9833	0.1824	14.9458	6.2101	0.3488	65.9803	0.5716	37.44	0.50	71.5197	10.4451	
19	0.0282	3.1543	b.d.l	0.1768	0.1267	22.2796	4.0686	0.5394	39.7308	0.8826	34.44	0.71	82.4341	6.8431	

b.d.l: Below detection limit

Appendix D

Supporting information for chapter 6

Contents of this file

1. Tables D.1 to D.3: Inversion results of synthetic data.
2. Figures D.1 to D.5: 1D posterior probability functions of Pecube parameterization.
3. Text D.2: analytical protocol for thermochronological data.
4. Tables D.4 to D.12: Raw data from AFT analysis.
5. Figures D.6 to D.7: Radial plot from AFT analysis

Table D.1. Thermal-kinematic (Pecube) inversion results of the synthetic Aiguilles Rouges models.

Parameters (unit)	Inversion Results								
	SYAR2			**SYAR3**			**SYAR4**		
	Range	Median	1σ	Range	Median	1σ	Range	Median	1σ
Relief Evolution									
T^1_{topo}	40 - 60	48.16	13.83	40 - 60	45.07	12.24	40 - 60	44.29	7.09
R_1	0	-	-	0	-	-	0	-	-
T^2_{topo}	0 - 20	4.06	6.35	0 - 20	5.07	5.80	0 - 20	2.80	4.40
R_2	0 - 0.3	0.10	0.13	0 - 0.3	0.11	0.14	0 - 0.3	0.062	0.11
Burial/Exhumation rate									
T^1_E (Ma)	40 - 60	T^1_{topo}	-	40 - 60	T^1_{topo}	-	40 - 60	T^1_{topo}	-
E_1 ($Km.Ma^{-1}$)	-3 - 0	-0.74	2.66	-3 - 0	-2.34	1.48	-3 - 0	-1.062	1.15
T^2_E (Ma)	0 - 30	12.32	12.05	20 - 40	27.91	11.10	20 - 40	27.043	5.88
E_2 ($Km.Ma^{-1}$)	0 - 3	1.55	0.88	-3 - 3	-0.88	2.09	-3 - 3	-1.062	1.15
T^3_E (Ma)	-	-	-	0 - 20	13.34	6.76	0 - 20	13.55	6.02
E_3 ($Km.Ma^{-1}$)	-	-	-	0 - 3	1.56	0.65	0 - 3	0.61	1.98
T^4_E (Ma)	-	-	-	-	-	-	0 - 20	4.72	3.21
E_4 ($Km.Ma^{-1}$)	-	-	-	-	-	-	0 - 3	1.73	0.40
Number of Models	35 100			40 100			45 100		
Bayesian re-sampling	100 x 350			200 x 200			200 x 225		
Number of Parameters	6			8			10		
Number of Data	36			36			36		
Log-likelihood	-53			-54			-68		
BIC	127			136			172		

Values of free parameters with 1σ uncertainty (65%) given by the NA-Bayes algorithm.
Log-likelihood and BIC are computed from the median value of the outputted distribution from the NA-Bayes algorithm.
Framed BIC corresponds to the lowest BIC value, giving the most efficient inversion.

Table D.2. Thermal-kinematic (Pecube) inversion results of the synthetic models from SY008 to SY0012, using a normally distributed noise in the data centered on 0 with a standard deviation of 0.4.

Parameters (unit)	Inversion Results															
	SY000	**SY008**			**SY009**			**SY010**			**SY011**			**SY012**		
		Range	Median	1σ	Range	Median	1σ	Range	Median	1σ	Range	Median	1σ	Range	Median	1σ
Relief Evolution																
Time Topo 1 (Ma)	45	40 - 60	58.10	3.25	40 - 60	50.26	7.27	40 - 60	58.10	10.42	40 - 60	53.39	12.63	40 - 60	48.27	10.17
Time Topo 2 (Ma)	5	0 - 20	3.39	1.09	0 - 20	3.22	1.55	0 - 20	3.45	3.22	0 - 20	12.72	8.05	0 - 20	12.08	10.53
Relief amplification	0.2	0 - 0.3	0.0069	0.013	0 - 0.3	0.01	0.023	0 - 0.3	0.02	0.03	0 - 0.3	0.16	0.17	0 - 0.3	0.15	0.14
Burial/Exhumation rate																
Time step 1 (Ma)	T_{topo1}	0 - 60	T_{topo1}	-	40 - 60	T^1_{topo}	-	40 - 60	T^1_{topo}	-	40 - 60	T^1_{topo}	40 - 60	T^1_{topo}		
Burial rate 1 ($\mathrm{km\,Ma^{-1}}$)	-0.5	-3 - 0	-0.11	0.14	-2 - 0	-0.25	0.44	-2 - 0	-0.13	0.96	-2 - 0	-1.40	1.27	-2 - 0	-0.99	1.43
Time step 2 (Ma)	25	0 - 30	12.55	2.32	15 - 30	26.82	4.67	20 - 30	23.09	2.46	15 - 30	26.53	7.78	20 - 30	23.91	5.99
Exhumation rate 2 ($\mathrm{km\,Ma^{-1}}$)	-0.2	0 - 3	1.49	0.25	-2 - 2	0.80	0.32	-2 - 2	1.13	0.96	-2 - 2	1.28	0.84	-2 - 2	1.42	0.78
Time step 3 (Ma)	18	-	-	-	0 - 15	7.39	2.71	10 - 20	13.41	2.49	0 - 15	8.46	11.62	10 - 20	14.69	4.08
Exhumation rate 3 ($\mathrm{km\,Ma^{-1}}$)	0.8	-	-	-	0 -2	1.44	0.18	0 - 2	0.60	0.46	0 - 2	1.52	0.57	0 - 2	1.42	0.78
Time step 4 (Ma)	6	-	-	-	-	-	-	0 - 10	8.85	1.73	-	-	-	0 - 10	7.11	5.27
Exhumation rate 4 ($\mathrm{km\,Ma^{-1}}$)	1.5	-	-	-	-	-	-	0 - 2	1.38	0.43	-	-	-	0 - 2	1.32	0.58
Fault motion																
Time start (Ma)	20	-	-	-	-	-	-	-	-	-	15 - 30	27.18	4.84	15 - 30	27.14	10.13
Velocity 1 ($Km.Ma^{-1}$)	1	-	-	-	-	-	-	-	-	-	-2 - 2	0.00	1.21	-2 - 2	1.06	1.50
Time step 2 (Ma)	10	-	-	-	-	-	-	-	-	-	0 - 15	3.74	9.46	0 - 15	10.36	5.27
Velocity 2 ($Km.Ma^{-1}$)	-1	-	-	-	-	-	-	-	-	-	-2 - 2	-0.63	1.32	-2 - 2	-0.44	1.17
Time end (Ma)	2	-	-	-	-	-	-	-	-	-	-	-	-	0 - 5	0.53	0.94
Number of parameters		6			8			10			12			15		
Number of Models		35 100			40 100			45 100			50 100			55 100		
Bayesian re-sampling		100x350			200x200			200x225			200x250			200x275		
Number of Data		117			117			117			117			117		
Log-likelihood		-321			-277			-230			-120			-113		
BIC		670			492			508			298			299		

Values of free parameters with 1σ uncertainty (65%) given by the NA-Bayes algorithm.
Log-likelihood and BIC are computed from the median value of the outputted distribution from the NA-Bayes algorithm.

Table D.3. Thermal-kinematic (Pecube) inversion results of the synthetic models from SY002 to SY006, using a normally distributed noise in the data centered on 0 with a standard deviation of 0.8.

Parameters (unit)	Inversion Results															
	SY000	**SY002**			**SY003**			**SY004**			**SY005**			**SY006**		
		Range	Median	1σ	Range	Median	1σ	Range	Median	1σ	Range	Median	1σ	Range	Median	1σ
Relief Evolution																
Time Topo 1 (Ma)	45	40 - 60	54.22	6.33	40 - 60	50.45	8.31	40 - 60	55.13	13.71	40 - 60	47.23	11.04	40 - 60	50.63	12.29
Time Topo 2 (Ma)	5	0 - 20	3.36	1.28	0 - 20	3.22	3.07	0 - 20	3.72	4.30	0 - 20	13.73	9.82	0 - 20	10.29	9.69
Relief amplification	0.2	0 - 0.3	0.015	0.03	0 - 0.3	0.02	0.04	0 - 0.3	0.025	0.05	0 - 0.3	0.15	0.17	0 - 0.3	0.14	0.19
Burial/Exhumation rate																
Time step 1 (Ma)	T_{topo1}	0 - 60	T_{topo1}	-	40 - 60	T^1_{topo}	-	40 - 60	T^1_{topo}	-	40 - 60	T^1_{topo}	40 - 60	T^1_{topo}		
Burial rate 1 ($\mathrm{km\,Ma^{-1}}$)	-0.5	-3 - 0	-0.65	1.52	-2 - 0	-0.32	0.54	-2 - 0	-1.00	1.52	-2 - 0	-0.59	1.33	-2 - 0	-0.85	1.27
Time step 2 (Ma)	25	0 - 30	16.00	3.44	15 - 30	22.49	12.22	20 - 30	25.98	4.33	15 - 30	24.79	5.97	20 - 30	26.82	5.74
Exhumation rate 2 ($\mathrm{km\,Ma^{-1}}$)	-0.2	0 - 3	1.36	0.12	-2 - 2	1.12	0.95	-2 - 2	0.74	1.77	-2 - 2	1.61	0.58	-2 - 2	1.09	1.58
Time step 3 (Ma)	18	-	-	-	0 - 15	9.98	11.79	10 - 20	12.00	4.94	0 - 15	9.44	6.30	10 - 20	13.35	5.74
Exhumation rate 3 ($\mathrm{km\,Ma^{-1}}$)	0.8	-	-	-	0 -2	1.43	0.49	0 - 2	0.98	0.68	0 - 2	1.34	0.47	0 - 2	0.81	0.60
Time step 4 (Ma)	6	-	-	-	-	-	-	0 - 10	6.71	6.70	-	-	-	0 - 10	4.83	3.01
Exhumation rate 4 ($\mathrm{km\,Ma^{-1}}$)	1.5	-	-	-	-	-	-	0 - 2	1.35	0.45	-	-	-	0 - 2	1.53	0.55
Fault motion																
Time start (Ma)	20	-	-	-	-	-	-	-	-	-	15 - 30	27.43	5.41	15 - 30	26.85	10.00
Velocity 1 ($Km.Ma^{-1}$)	1	-	-	-	-	-	-	-	-	-	-2 - 2	1.02	1.54	-2 - 2	1.06	1.50
Time step 2 (Ma)	10	-	-	-	-	-	-	-	-	-	0 - 15	12.86	4.53	0 - 15	8.76	4.15
Velocity 2 ($Km.Ma^{-1}$)	-1	-	-	-	-	-	-	-	-	-	-2 - 2	-0.44	0.84	-2 - 2	-0.62	1.13
Time end (Ma)	2	-	-	-	-	-	-	-	-	-	-	-	-	0 - 5	4.27	2.35
Number of parameters		6			8			10			12			15		
Number of Models		35 100			40 100			45 100			50 100			55 100		
Bayesian re-sampling		100x350			200x200			200x225			200x250			200x275		
Number of Data		117			117			117			117			117		
Log-likelihood		-521			-537			-471			-238			-754		
BIC		1072			1114			990			534			1581		

Values of free parameters with 1σ uncertainty (65%) given by the NA-Bayes algorithm.
Log-likelihood and BIC are computed from the median value of the outputted distribution from the NA-Bayes algorithm.

D.1 1D posterior probability functions

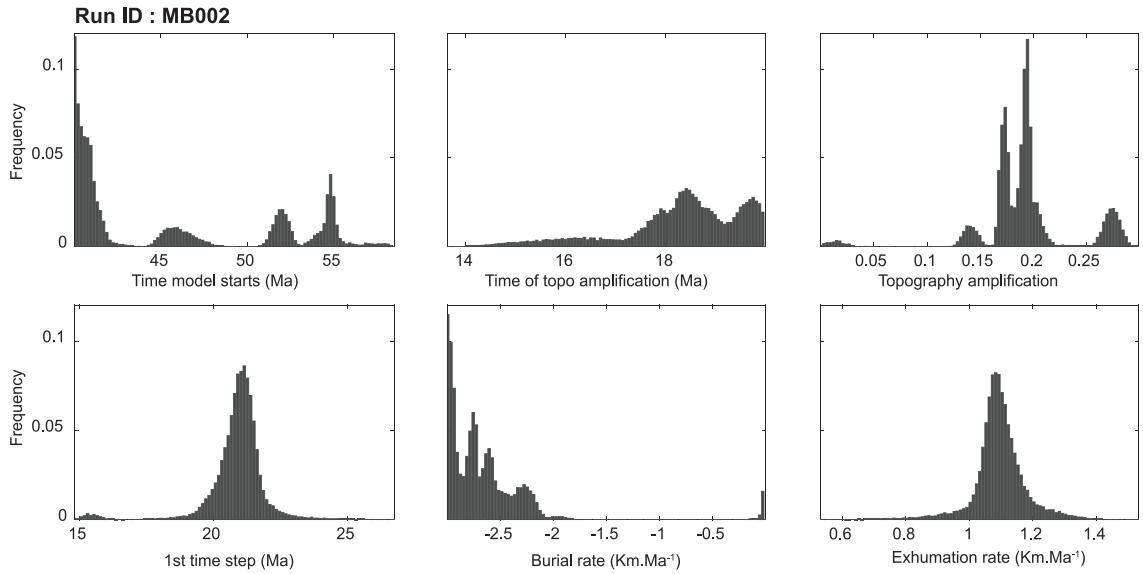

Figure D.1. Posterior probability functions from parameterization MB002.

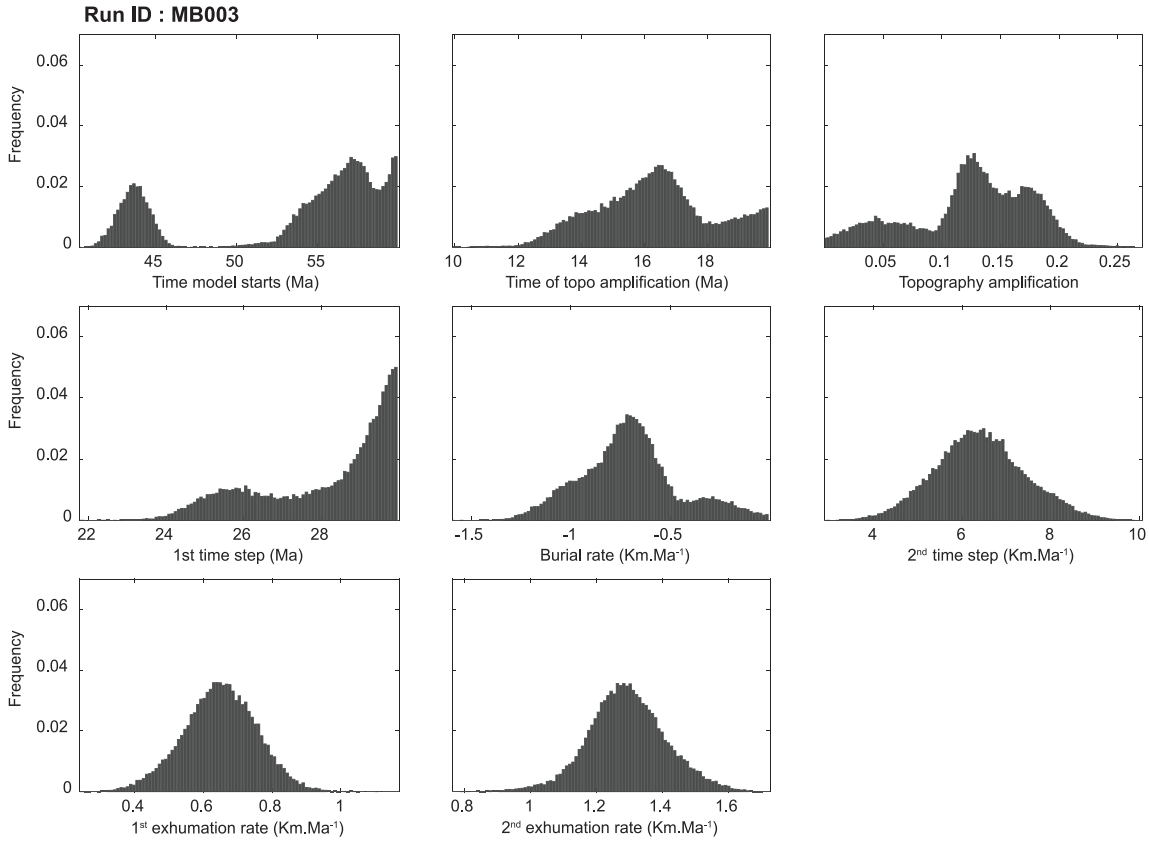

Figure D.2. Posterior probability functions from parameterization MB003.

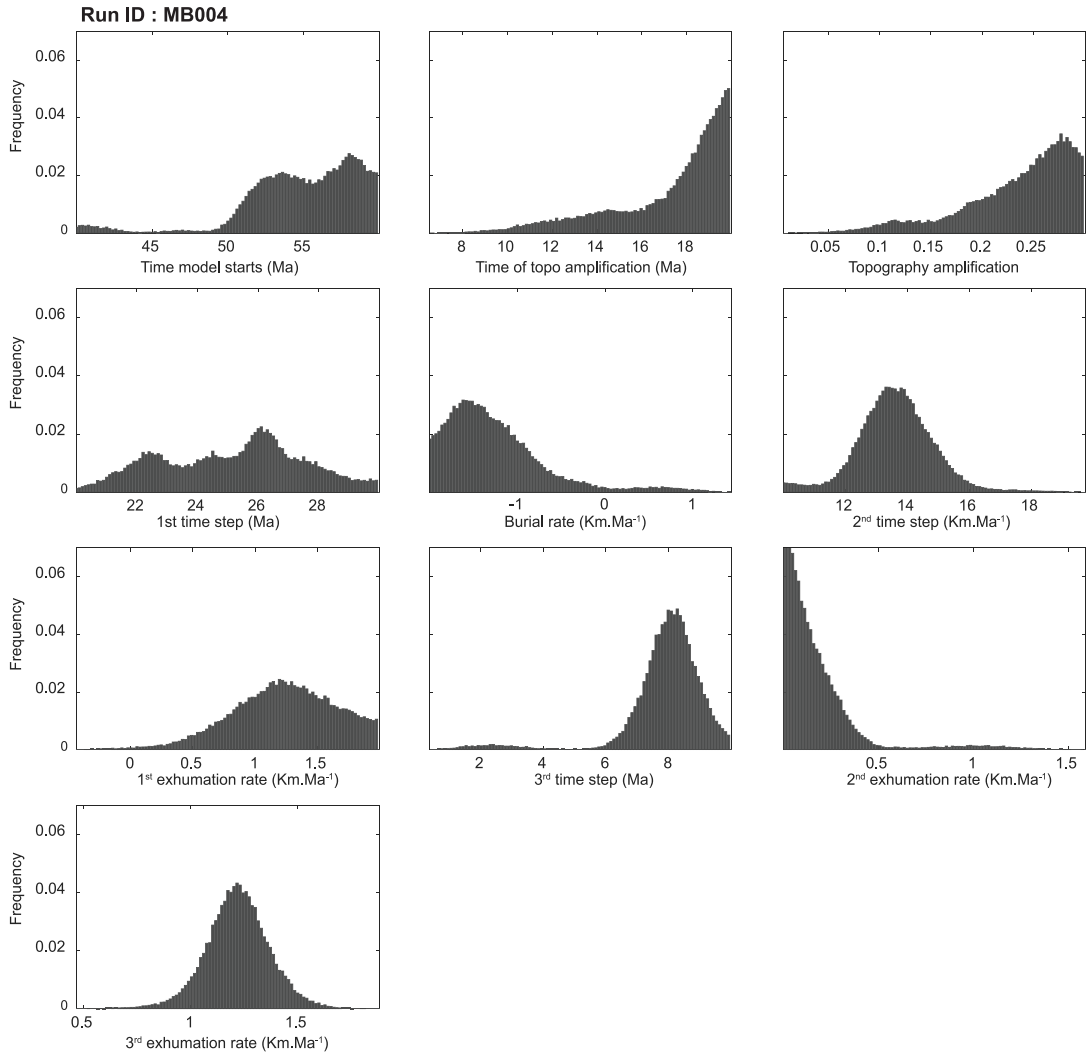

Figure D.3. Posterior probability functions from parameterization MB004.

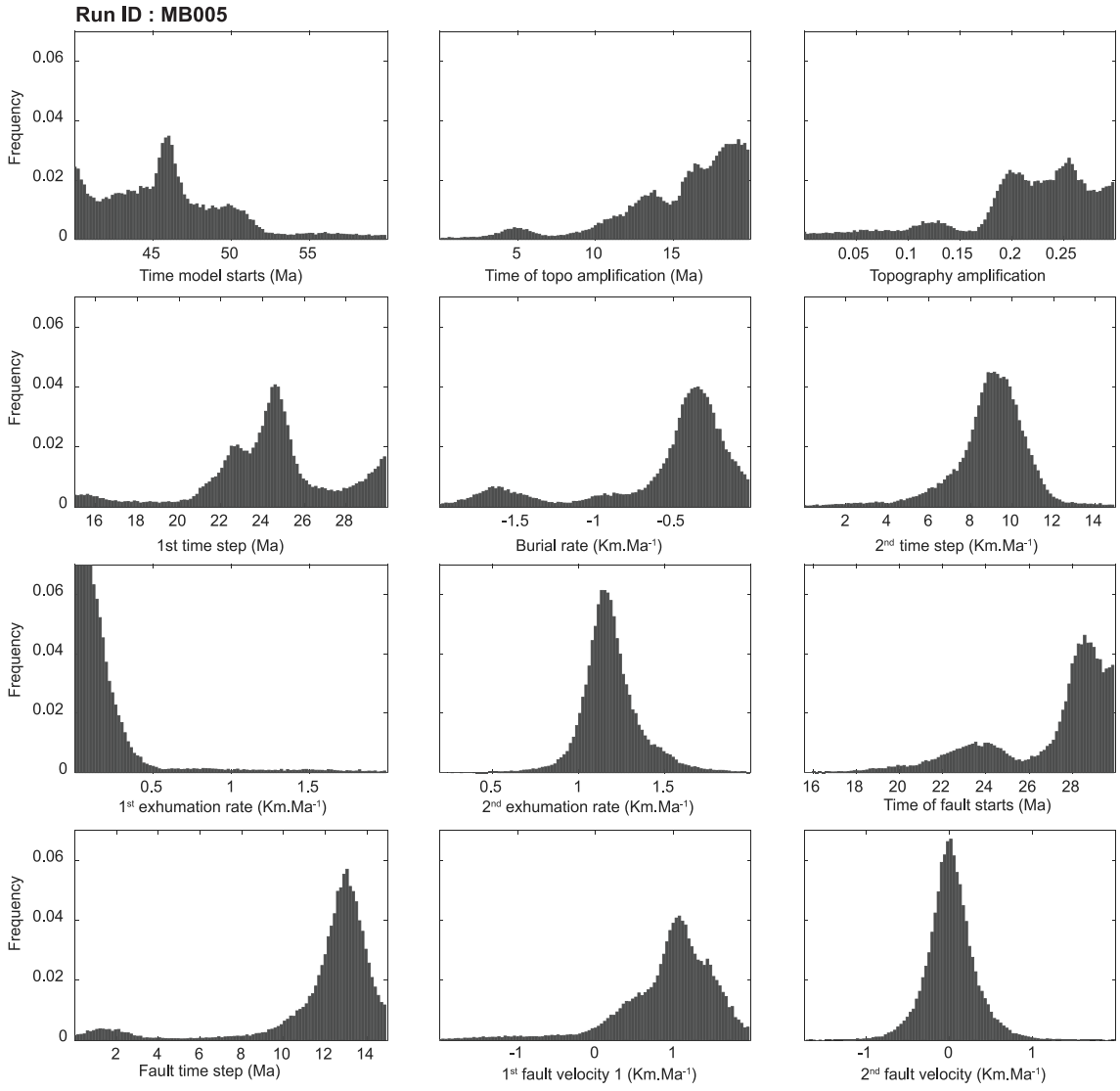

Figure D.4. Posterior probability functions from parameterization MB005.

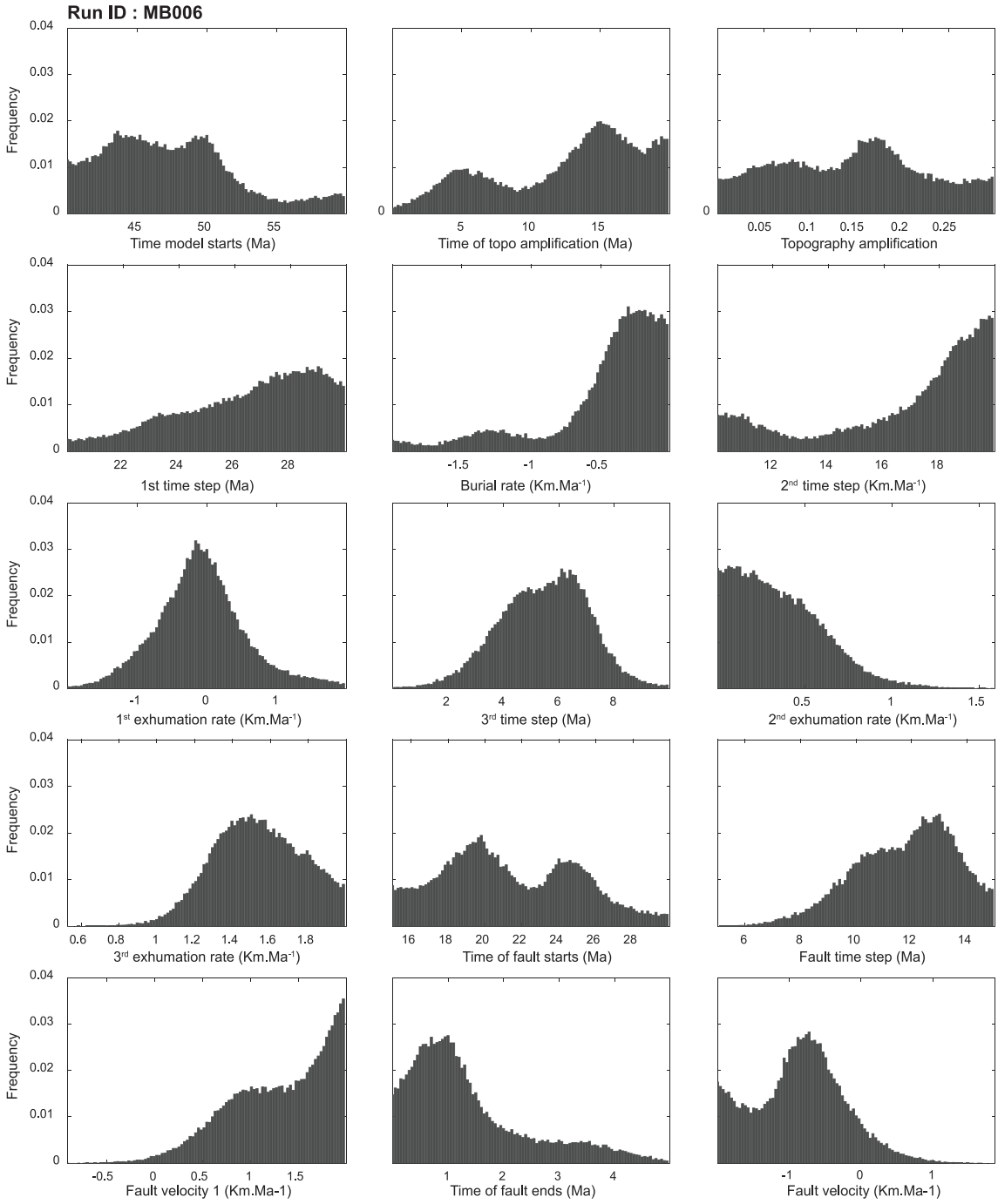

Figure D.5. Posterior probability functions from parameterization MB006.

D.2 Protocols

AHE

Apatite grains were hand picked from apatite concentrates under a stereomicroscope with focus on morphology, size and purity for (U-Th)/He analyses. Selected grains were further inspected for inclusions at $\times$800 magnification under cross-polarized light. Grains free of visible inclusions were digitally photographed and their dimensions were measured parallel and perpendicular to the crystallographic c-axis in order to calculate α-correction factors (Ft) (Farley et al., 1996; Ketcham et al., 2011). Grains were loaded into Pt-tubes and degassed by laser-heating at 160 to 960°C for 5 min, spiked with 3He and analyzed with a Pfeiffer Prisma QMS-200 mass spectrometer using the He-line at the University of Tübingen (Germany) following the procedure described in (Danišík et al., 2012). U-Th-Sm contents were analyzed by isotope dilution ICP-MS at the University of Melbourne (Australia).

ZHE

Zircon (U-Th)/He (ZHE) were performed at the Laboratory of Géosciences Montpellier (France). Each single grain was packed in Nb tube for zircon, placed under vacuum, and heated with a 1 090 nm fiber laser operating at 4.0 W (1 100°C) during 15 minnutes. After 3He spiking, gas purification was achieved by a cryogenic trap and two SAES AP-10-N getters, and helium content was measured on a quadrupole PrismaPlus QMG 220. The 4He content was determined by the peak height method and was 10–10,000 times above typical blank levels. A second heating run using the same analytical procedure was systematically conducted to verify that more than 99% of 4He was extracted during the first run. After helium extraction, Nb tubes were retrieved from the sample chamber and transferred in a 2 ml polypropylene conical tube. Samples were doubly spiked (230Th and 233U) and dissolved using procedures previously described Gautheron et al. (2021). The resulting solutions were diluted, and U (233U and 238U) and Th (230Th and 232Th) were measured by using isotope dilution ICPMS. For age calculation, alpha ejection correction (Farley et al., 1996) was calculated using the Ft software (Gautheron and Tassan-Got, 2010).

AFT

Samples ARexx Apatite fission track were performed in the GEOPS laboratory (Université Paris Saclay, Orsay - France). Crystals were mounted in epoxy, polished to expose the surface crystal, and etched at 5 M HNO_3 for 20 s at 20 ± 1°C. Apatite crystals were covered with low U-muscovite sheets and three glass CN-5 dosimeters as well as two apatite standards (Durango and Fish Canyon Tuff Hurford, 1990). To estimate the abundance of ^{238}U, we used the exter-

nal detector method: the sample is irradiated with neutron flux, inducing fission tracks from the decay of ^{235}U. The number of traces induced irradiation estimates the abundance of ^{235}U. Samples were irradiated at the Garching facility (München, Germany) with a nominal fluence of 5.0×10^{-15} neutrons/cm^2. The tracks were counted and measured with a $\times 1.250$ magnification using a digitized tablet coupled with an optical microscope (Laslett et al., 1984). Fission track ages were calculated using the zeta calibration method described in Hurford and Green (1982) and we report central ages with two-sigma errors. The zeta of the laser is of $141(6)$. No track lengths were measured. ICP-MS analyses were performed in the Geosciences Rennes laboratory.

Samles CGPxx Fission-track analysis, apatite and zircon concentrates were embedded in epoxy and PFA Teflon, respectively, and then ground and polished to 4π geometry. Apatites were etched in 166 5M HNO3 for 20 s at 20°C and zircons were etched in a eutectic melt of KOH-NaOH for 69-h at 215°C [Zaun and Wagner, 1985] to reveal spontaneous tracks. The etching efficiency of ZFTs depends on the accumulated radiation damage; tracks first appear in grains with higher radiation damage and associated lower closure temperatures [e.g. Rahn et al., 2004]. To account for intra-sample variations in annealing kinetics, we prepared two ZFT mounts per each sample, which we etched for different times. We periodically controlled the etching progress (every 6-10 hours), and stopped etching of the first mount when sufficient ($>$20) grains revealed well-etched, clearly visible ($\sim$1 μm wide), and countable tracks. We continued etching of the second mount and thereby over-etched or even lost some grains with higher radiation damage. Etching of the second mount was stopped 175 when last $\sim$20 grains most resistant against etching revealed countable tracks ($\sim$1 μm wide). Both mounts per each sample were dated with the external detector method [Naeser, 1978] using the ζ-calibration approach [Hurford and Green, 1983]. They were irradiated with thermal neutrons at the 179 FRM-II reactor facility in Garching (Technical University Munich, Germany). To reveal induced tracks, mica external detectors were etched with 40% HF at 20°C for 40 min. Fission tracks were counted on an Olympus BX-51 microscope under $\times$1000 magnification using a dry objective. The kinetic properties of apatite crystals were estimated via measurement of Dpar values; the length of the etch pit parallel to the crystallographic c-axis [Burtner et al.,1984 1994]

Table D.4. Apatite fission track data for sample **ARe024**

Sample	#grains	Ns	$\Sigma\, p_i\Omega_i$	$1\sigma\ \Sigma\, p_i\Omega_i$	ζ ICP	2σ ζICP	χ^2	$P(\chi^2)$	Pooled age	2σ Ma
ARe024	23	127	1.71E-05	1.1823E-07	0.70	0.03	32.06	0.08	**5.2**	**1.0**

Grain	Ns	Area (cm^2)	$^{238}U/^{43}$Ca	Weighted $^{238}U/^{43}Ca$	2σ abs	$p_i\Omega_i$	$p_i\Omega_i 1\sigma$	FT Age	2σ
ARe024-G01	9	4.90E-05	1.44E-02	1.45E-02	4.28E-04	7.09E-07	2.09544E-08	8.9	5.97
ARe024-G02	4	2.50E-05	1.63E-02	1.68E-02	4.99E-04	4.19E-07	1.24843E-08	6.7	6.72
ARe024-G03	2	2.50E-05	1.50E-02	1.52E-02	4.42E-04	3.80E-07	1.10439E-08	3.7	5.25
ARe024-G04	9	4.90E-05	2.08E-02	2.08E-02	6.04E-04	1.02E-06	2.96081E-08	6.2	4.15
ARe024-G05	4	2.50E-05	1.95E-02	1.96E-02	5.66E-04	4.91E-07	1.41477E-08	5.7	5.74
ARe024-G06	6	2.50E-05	1.31E-02	1.43E-02	4.41E-04	3.58E-07	1.10219E-08	11.8	9.64
ARe024-G07	5	3.60E-05	2.16E-02	2.15E-02	6.37E-04	7.73E-07	2.29385E-08	4.6	4.08
ARe024-G08	3	4.90E-05	1.47E-02	1.48E-02	4.46E-04	7.25E-07	2.18559E-08	2.9	3.36
ARe024-G09	8	5.00E-05	2.83E-02	2.98E-02	8.86E-04	1.49E-06	4.42828E-08	3.8	2.67
ARe024-G10	9	3.60E-05	1.85E-02	1.85E-02	5.47E-04	6.65E-07	1.96812E-08	9.5	6.36
ARe024-G11	9	5.00E-05	1.80E-02	1.79E-02	5.32E-04	8.96E-07	2.65915E-08	7.1	4.73
ARe024-G12	6	5.00E-05	3.52E-02	3.52E-02	1.05E-03	1.76E-06	5.23047E-08	2.4	1.96
ARe024-G13	4	3.60E-05	1.91E-02	1.91E-02	5.55E-04	6.89E-07	1.9963E-08	4.1	4.09
ARe024-G14	4	3.60E-05	2.49E-02	2.46E-02	7.25E-04	8.86E-07	2.61009E-08	3.2	3.18
ARe024-G15	6	3.60E-05	2.15E-02	2.16E-02	6.21E-04	7.76E-07	2.23495E-08	5.4	4.45
ARe024-G16	9	3.60E-05	1.97E-02	1.96E-02	5.71E-04	7.05E-07	2.05577E-08	9.0	6.00
ARe024-G17	9	2.40E-05	2.22E-02	2.24E-02	6.56E-04	5.39E-07	1.57415E-08	11.7	7.85
ARe024-G18	4	2.50E-05	1.67E-02	1.65E-02	4.90E-04	4.13E-07	1.22436E-08	6.8	6.82
ARe024-G19	2	2.50E-05	1.53E-02	1.48E-02	4.43E-04	3.70E-07	1.10667E-08	3.8	5.37
ARe024-G20	5	2.00E-05	7.60E-02	7.59E-02	2.23E-03	1.52E-06	4.45594E-08	2.3	2.08
ARe024-G21	5	2.40E-05	1.49E-02	1.49E-02	4.41E-04	3.58E-07	1.0576E-08	9.8	8.79
ARe024-G22	2	3.60E-05	1.61E-02	1.61E-02	4.76E-04	5.78E-07	1.71391E-08	2.4	3.44
ARe024-G23	3	3.60E-05	1.84E-02	1.68E-02	5.23E-04	6.05E-07	1.884E-08	3.5	4.03

Table D.5. Apatite fission track data for sample **ARe025**

Sample	#grains	Ns	$\Sigma\, p_i\Omega_i$	$1\sigma\ \Sigma\, p_i\Omega_i$	ζ ICP	$2\sigma\ \zeta$ICP	χ^2	$P(\chi^2)$	Pooled age	2σ Ma
ARe025	31	107	1.66E-05	1.03225E-07	0.70	0.03	25.23	0.71	4.5	0.9

Grain	Ns	Area (cm^2)	$^{238}U/^{43}$Ca	Weighted $^{238}U/^{43}Ca$	2σ abs	$p_i\Omega_i$	$p_i\Omega_i 1\sigma$	FT Age	2σ
ARe025-G01	1	2.50E-05	7.23E-03	7.64E-03	2.26E-04	1.91E-07	5.65468E-09	3.7	7.37
ARe025-G02	3	2.50E-05	1.47E-02	1.47E-02	4.24E-04	3.67E-07	1.05958E-08	5.8	6.65
ARe025-G03	2	3.60E-05	1.30E-02	1.32E-02	3.84E-04	4.76E-07	1.38235E-08	3.0	4.18
ARe025-G04	6	2.50E-05	3.46E-02	3.48E-02	1.02E-03	8.71E-07	2.5412E-08	4.8	3.97
ARe025-G05	4	4.90E-05	3.04E-02	3.23E-02	9.74E-04	1.58E-06	4.77356E-08	1.8	1.78
ARe025-G06	3	4.00E-05	1.87E-02	1.84E-02	5.36E-04	7.38E-07	2.14505E-08	2.9	3.31
ARe025-G07	2	2.50E-05	2.21E-02	2.17E-02	6.28E-04	5.42E-07	1.56976E-08	2.6	3.67
ARe025-G08	4	3.60E-05	2.14E-02	2.17E-02	6.37E-04	7.83E-07	2.29354E-08	3.6	3.60
ARe025-G09	3	4.20E-05	1.55E-02	1.53E-02	4.56E-04	6.42E-07	1.91431E-08	3.3	3.80
ARe025-G10	3	3.60E-05	1.06E-02	1.02E-02	3.01E-04	3.68E-07	1.08315E-08	5.7	6.63
ARe025-G11	3	2.80E-05	1.19E-02	1.24E-02	3.67E-04	3.49E-07	1.02744E-08	6.1	7.00
ARe025-G12	6	3.00E-05	1.85E-02	1.85E-02	5.35E-04	5.56E-07	1.60397E-08	7.6	6.21
ARe025-G13	3	2.40E-05	1.92E-02	1.85E-02	5.40E-04	4.44E-07	1.29587E-08	4.8	5.50
ARe025-G14	10	6.40E-05	1.35E-02	1.35E-02	3.88E-04	8.61E-07	2.48218E-08	8.2	5.18
ARe025-G15	3	4.00E-05	9.76E-03	9.72E-03	2.83E-04	3.89E-07	1.13226E-08	5.4	6.27
ARe025-G16	6	3.60E-05	1.32E-02	1.31E-02	3.78E-04	4.71E-07	1.35937E-08	9.0	7.32
ARe025-G17	2	4.80E-05	1.73E-02	1.70E-02	4.92E-04	8.15E-07	2.36234E-08	1.7	2.44
ARe025-G18	3	3.00E-05	2.31E-02	1.87E-02	7.18E-04	5.62E-07	2.15277E-08	3.8	4.34
ARe025-G19	4	4.00E-05	1.30E-02	1.39E-02	4.47E-04	5.55E-07	1.78755E-08	5.1	5.08
ARe025-G20	5	3.00E-05	1.72E-02	1.64E-02	4.81E-04	4.91E-07	1.4434E-08	7.2	6.41
ARe025-G21	1	2.50E-05	8.83E-03	8.84E-03	2.69E-04	2.21E-07	6.73318E-09	3.2	6.37
ARe025-G22	2	3.00E-05	8.73E-03	8.97E-03	2.61E-04	2.69E-07	7.82235E-09	5.2	7.40
ARe025-G23	0	2.50E-05	1.42E-02	8.76E-03	1.01E-03	2.19E-07	2.52194E-08	1.6	4.52
ARe025-G24	3	2.40E-05	7.41E-03	8.06E-03	2.61E-04	1.94E-07	6.26221E-09	10.9	12.60
ARe025-G25	2	2.50E-05	1.03E-02	1.06E-02	3.08E-04	2.64E-07	7.7004E-09	5.3	7.53
ARe025-G26	5	3.50E-05	1.40E-02	1.40E-02	4.05E-04	4.91E-07	1.41773E-08	7.2	6.42
ARe025-G27	3	2.50E-05	1.78E-02	1.78E-02	5.16E-04	4.45E-07	1.29096E-08	4.7	5.48
ARe025-G28	2	3.60E-05	1.88E-02	1.82E-02	5.29E-04	6.57E-07	1.90482E-08	2.1	3.03
ARe025-G29	2	3.60E-05	2.26E-02	1.94E-02	6.48E-04	6.99E-07	2.33368E-08	2.0	2.85
ARe025-G30	2	3.60E-05	1.12E-02	1.01E-02	3.14E-04	3.62E-07	1.1312E-08	3.9	5.50
ARe025-G31	9	3.60E-05	1.97E-02	1.99E-02	5.73E-04	7.17E-07	2.06346E-08	8.8	5.90

Table D.6. Apatite fission track data for sample **ARe026**

Sample	#grains	Ns	$\Sigma\ p_i\Omega_i$	$1\sigma\ \Sigma\ p_i\Omega_i$	ζ ICP	2σ ζICP	χ^2	$P(\chi^2)$	Pooled age	2σ Ma
ARe026	26	119	1.87E-05	1.24962E-07	0.70	0.03	14.85	0.94	4.5	0.8

Grain	Ns	Area (cm^2)	$^{238}U/^{43}$Ca	Weighted $^{238}U/^{43}Ca$	2σ abs	$p_i\Omega_i$	$p_i\Omega_i 1\sigma$	FT Age	2σ
ARe026-G01	2	3.60E-05	2.16E-02	2.48E-02	8.43E-04	8.91E-07	3.03377E-08	1.6	2.23
ARe026-G02	8	4.90E-05	2.74E-02	2.63E-02	8.43E-04	1.29E-06	4.12992E-08	4.4	3.09
ARe026-G03	1	3.00E-05	1.07E-02	1.04E-02	3.08E-04	3.11E-07	9.23101E-09	2.3	4.52
ARe026-G04	3	3.50E-05	1.24E-02	1.26E-02	3.73E-04	4.39E-07	1.30487E-08	4.8	5.55
ARe026-G05	4	3.60E-05	1.09E-02	1.16E-02	3.52E-04	4.18E-07	1.2659E-08	6.7	6.74
ARe026-G06	5	3.60E-05	1.57E-02	1.57E-02	4.57E-04	5.64E-07	1.6455E-08	6.2	5.59
ARe026-G07	4	4.20E-05	1.59E-02	1.59E-02	4.67E-04	6.66E-07	1.96008E-08	4.2	4.23
ARe026-G08	6	6.00E-05	1.72E-02	1.60E-02	4.85E-04	9.59E-07	2.90983E-08	4.4	3.60
ARe026-G09	3	4.20E-05	1.39E-02	1.34E-02	3.98E-04	5.63E-07	1.67139E-08	3.7	4.33
ARe026-G10	9	4.90E-05	2.70E-02	2.60E-02	7.62E-04	1.28E-06	3.73149E-08	5.0	3.32
ARe026-G11	4	2.50E-05	1.26E-02	1.45E-02	5.37E-04	3.61E-07	1.34355E-08	7.8	7.80
ARe026-G12	2	3.60E-05	1.17E-02	1.18E-02	4.11E-04	4.25E-07	1.48126E-08	3.3	4.69
ARe026-G13	3	4.00E-05	1.75E-02	1.69E-02	5.03E-04	6.78E-07	2.01326E-08	3.1	3.60
ARe026-G14	5	4.90E-05	1.11E-02	1.12E-02	3.31E-04	5.48E-07	1.62273E-08	6.4	5.75
ARe026-G15	3	4.90E-05	1.70E-02	1.76E-02	5.21E-04	8.62E-07	2.55071E-08	2.4	2.83
ARe026-G16	11	1.00E-04	1.58E-02	1.60E-02	4.80E-04	1.60E-06	4.79693E-08	4.8	2.93
ARe026-G17	3	4.80E-05	1.74E-02	1.80E-02	5.37E-04	8.65E-07	2.57791E-08	2.4	2.82
ARe026-G18	8	5.00E-05	1.22E-02	1.26E-02	3.84E-04	6.32E-07	1.91949E-08	8.9	6.31
ARe026-G19	13	1.00E-04	1.64E-02	1.65E-02	4.83E-04	1.65E-06	4.83356E-08	5.5	3.09
ARe026-G20	1	3.60E-05	1.11E-02	1.16E-02	3.56E-04	4.17E-07	1.28332E-08	1.7	3.38
ARe026-G21	4	2.00E-05	3.71E-02	3.71E-02	1.11E-03	7.41E-07	2.21171E-08	3.8	3.80
ARe026-G22	2	1.60E-05	1.27E-02	1.16E-02	3.62E-04	1.85E-07	5.78781E-09	7.6	10.73
ARe026-G23	4	4.20E-05	1.23E-02	1.29E-02	3.96E-04	5.43E-07	1.66414E-08	5.2	5.19
ARe026-G24	3	7.00E-05	9.20E-03	9.34E-03	2.79E-04	6.54E-07	1.9533E-08	3.2	3.73
ARe026-G25	4	4.00E-05	1.65E-02	1.66E-02	5.23E-04	6.63E-07	2.09202E-08	4.2	4.25
ARe026-G26	4	3.50E-05	1.36E-02	1.43E-02	4.31E-04	5.02E-07	1.50768E-08	5.6	5.61

Table D.7. Apatite fission track data for sample **ARe031**

Sample	#grains	Ns	$\Sigma\, p_i\Omega_i$	$1\sigma\, \Sigma\, p_i\Omega_i$	ζ ICP	2σ ζICP	χ^2	$P(\chi^2)$	Pooled age	2σ Ma
ARe031	17	25	4.02E-06	4.00111E-08	0.70	0.03	4.73	1.00	4.4	1.8

Grain	Ns	Area (cm^2)	$^{238}U/^{43}$Ca	Weighted $^{238}U/^{43}Ca$	2σ abs	$p_i\Omega_i$	$p_i\Omega_i 1\sigma$	FT Age	2σ
ARe031-G01	8	5.00E-05	2.12E-02	2.15E-02	6.20E-04	1.07E-06	3.10033E-08	5.2	3.71
ARe031-G02	2	2.00E-05	5.06E-03	5.24E-03	1.57E-04	1.05E-07	3.13552E-09	13.4	19.00
ARe031-G03	3	3.60E-05	9.15E-03	9.14E-03	2.67E-04	3.29E-07	9.62458E-09	6.4	7.41
ARe031-G04	1	3.50E-05	8.42E-03	6.87E-03	2.45E-04	2.41E-07	8.58243E-09	2.9	5.85
ARe031-G05	1	3.50E-05	5.23E-03	5.32E-03	1.53E-04	1.86E-07	5.36311E-09	3.8	7.56
ARe031-G06	1	3.60E-05	4.63E-03	4.59E-03	1.35E-04	1.65E-07	4.8514E-09	4.3	8.52
ARe031-G07	1	3.60E-05	5.31E-03	5.33E-03	1.55E-04	1.92E-07	5.58323E-09	3.7	7.34
ARe031-G08	1	3.60E-05	5.60E-03	5.44E-03	1.67E-04	1.96E-07	6.01248E-09	3.6	7.18
ARe031-G09	1	2.80E-05	4.53E-03	4.50E-03	1.31E-04	1.26E-07	3.66519E-09	5.6	11.17
ARe031-G10	0	2.50E-05	4.23E-03	3.77E-03	1.20E-04	9.43E-08	3.00416E-09	3.7	10.55
ARe031-G11	0	2.50E-05	1.63E-02	1.40E-02	4.64E-04	3.51E-07	1.16067E-08	1.0	2.83
ARe031-G12	0	1.60E-05	9.14E-03	8.19E-03	3.15E-04	1.31E-07	5.03785E-09	2.7	7.59
ARe031-G13	1	2.00E-05	4.82E-03	4.73E-03	1.37E-04	9.46E-08	2.74045E-09	7.4	14.86
ARe031-G14	2	1.60E-05	7.58E-03	7.86E-03	2.29E-04	1.26E-07	3.65719E-09	11.2	15.83
ARe031-G15	1	2.50E-05	7.14E-03	7.66E-03	2.29E-04	1.92E-07	5.72952E-09	3.7	7.35
ARe031-G16	1	2.00E-05	7.25E-03	7.35E-03	2.13E-04	1.47E-07	4.25461E-09	4.8	9.58
ARe031-G17	1	4.20E-05	5.57E-03	6.42E-03	2.25E-04	2.70E-07	9.46435E-09	2.6	5.22

Table D.8. Apatite fission track data for sample **ARe086**

Sample	#grains	Ns	$\Sigma\, p_i\Omega_i$	$1\sigma\ \Sigma\, p_i\Omega_i$	ζ ICP	2σ ζICP	χ^2	$P(\chi^2)$	Pooled age	2σ Ma
ARe086	18	32	9.78E-06	9.13666E-08	0.70	0.03	12.99	0.74	2.3	0.8

Grain	Ns	Area (cm^2)	$^{238}U/^{43}$Ca	Weighted $^{238}U/^{43}Ca$	2σ abs	$p_i\Omega_i$	$p_i\Omega_i 1\sigma$	FT Age	2σ
ARe086-G01	3	5.00E-05	1.66E-02	1.70E-02	4.95E-04	8.52E-07	2.47535E-08	2.5	2.86
ARe086-G02	1	3.60E-05	1.98E-02	1.97E-02	5.68E-04	7.11E-07	2.04425E-08	1.0	1.98
ARe086-G03	1	2.50E-05	1.01E-02	9.04E-03	2.84E-04	2.26E-07	7.09766E-09	3.1	6.23
ARe086-G04	1	3.60E-05	1.01E-02	1.04E-02	3.04E-04	3.75E-07	1.09322E-08	1.9	3.75
ARe086-G05	1	2.00E-05	1.35E-02	1.28E-02	4.00E-04	2.56E-07	8.00241E-09	2.7	5.49
ARe086-G06	0	4.90E-05	1.43E-02	1.40E-02	4.55E-04	6.88E-07	2.22755E-08	0.5	1.45
ARe086-G07	2	3.20E-05	1.56E-02	1.99E-02	8.50E-04	6.36E-07	2.72087E-08	2.2	3.13
ARe086-G08	1	3.60E-05	8.96E-03	8.97E-03	2.60E-04	3.23E-07	9.34461E-09	2.2	4.36
ARe086-G09	6	1.00E-04	2.03E-02	2.11E-02	6.18E-04	2.11E-06	6.17705E-08	2.0	1.64
ARe086-G10	3	1.00E-04	6.36E-03	6.18E-03	1.83E-04	6.18E-07	1.82688E-08	3.4	3.95
ARe086-G11	1	7.00E-05	1.50E-02	1.34E-02	4.34E-04	9.40E-07	3.03527E-08	0.7	1.50
ARe086-G13	2	2.50E-05	7.77E-03	7.59E-03	2.25E-04	1.90E-07	5.61937E-09	7.4	10.49
ARe086-G14	1	1.60E-05	1.35E-02	1.47E-02	4.52E-04	2.35E-07	7.22438E-09	3.0	5.98
ARe086-G15	1	2.50E-05	1.03E-02	1.00E-02	2.92E-04	2.51E-07	7.29243E-09	2.8	5.60
ARe086-G16	1	3.50E-05	7.93E-03	7.31E-03	2.25E-04	2.56E-07	7.89214E-09	2.8	5.50
ARe086-G17	2	2.00E-05	1.42E-02	1.64E-02	5.75E-04	3.27E-07	1.14951E-08	4.3	6.08
ARe086-G18	2	3.60E-05	1.63E-02	1.72E-02	5.07E-04	6.18E-07	1.82463E-08	2.3	3.22
ARe086-G19	3	2.50E-05	6.75E-03	6.84E-03	1.98E-04	1.71E-07	4.95349E-09	12.3 14.25	

Table D.9. Apatite fission track data for sample **ARe152**

Sample	#grains	Ns	$\Sigma\, p_i\Omega_i$	$1\sigma\ \Sigma\, p_i\Omega_i$	ζ ICP	2σ ζICP	χ^2	$P(\chi^2)$	Pooled age	2σ Ma
ARe152	27	292	6.89E-05	4.48704E-07	0.70	0.03	31.63	0.21	3.0	0.4

Grain	Ns	Area (cm^2)	$^{238}U/^{43}$Ca	Weighted $^{238}U/^{43}Ca$	2σ abs	$p_i\Omega_i$	$p_i\Omega_i 1\sigma$	FT Age	2σ
ARe152-G01	7	2.00E-05	5.64E-02	6.86E-02	2.84E-03	1.37E-06	5.68295E-08	3.6	2.72
ARe152-G02	5	3.00E-05	6.05E-02	6.07E-02	1.75E-03	1.82E-06	5.24187E-08	1.9	1.73
ARe152-G03	7	2.50E-05	1.09E-01	1.08E-01	3.10E-03	2.71E-06	7.7451E-08	1.8	1.38
ARe152-G04	21	4.90E-05	8.59E-02	8.65E-02	2.50E-03	4.24E-06	1.22466E-07	3.5	1.53
ARe152-G05	5	2.50E-05	2.93E-02	2.92E-02	8.44E-04	7.30E-07	2.11087E-08	4.8	4.32
ARe152-G06	14	5.00E-05	7.62E-02	8.05E-02	2.48E-03	4.03E-06	1.24159E-07	2.4	1.31
ARe152-G07	10	4.00E-05	4.24E-02	4.45E-02	1.33E-03	1.78E-06	5.3007E-08	4.0	2.51
ARe152-G08	11	3.50E-05	8.70E-02	8.86E-02	2.63E-03	3.10E-06	9.21047E-08	2.5	1.51
ARe152-G09	8	3.60E-05	3.35E-02	3.65E-02	1.12E-03	1.31E-06	4.04646E-08	4.3	3.04
ARe152-G10	6	4.90E-05	3.74E-02	3.69E-02	1.07E-03	1.81E-06	5.23883E-08	2.3	1.91
ARe152-G11	18	5.00E-05	9.76E-02	9.66E-02	2.78E-03	4.83E-06	1.38923E-07	2.6	1.24
ARe152-G12	4	5.00E-05	1.94E-02	1.95E-02	5.60E-04	9.73E-07	2.79892E-08	2.9	2.90
ARe152-G13	11	3.60E-05	1.21E-01	1.21E-01	3.62E-03	4.36E-06	1.30194E-07	1.8	1.07
ARe152-G14	17	2.40E-05	1.04E-01	1.03E-01	3.04E-03	2.48E-06	7.29792E-08	4.8	2.35
ARe152-G15	11	3.50E-05	1.01E-01	9.78E-02	2.90E-03	3.42E-06	1.01482E-07	2.3	1.37
ARe152-G16	20	3.50E-05	1.08E-01	1.11E-01	3.20E-03	3.88E-06	1.11848E-07	3.6	1.63
ARe152-G17	9	2.00E-05	9.57E-02	8.52E-02	2.72E-03	1.70E-06	5.43259E-08	3.7	2.48
ARe152-G18	18	4.90E-05	6.21E-02	6.78E-02	2.04E-03	3.32E-06	9.99377E-08	3.8	1.81
ARe152-G19	13	4.00E-05	4.26E-02	4.28E-02	1.29E-03	1.71E-06	5.14736E-08	5.3	2.98
ARe152-G20	16	3.00E-05	9.79E-02	9.50E-02	2.76E-03	2.85E-06	8.27778E-08	4.0	1.99
ARe152-G21	8	4.90E-05	2.10E-02	2.12E-02	6.14E-04	1.04E-06	3.0071E-08	5.4	3.84
ARe152-G22	5	2.50E-05	3.83E-02	3.92E-02	1.14E-03	9.81E-07	2.8471E-08	3.6	3.21
ARe152-G23	12	3.00E-05	1.19E-01	1.15E-01	3.38E-03	3.44E-06	1.01482E-07	2.5	1.42
ARe152-G24	8	3.00E-05	9.32E-02	9.43E-02	2.74E-03	2.83E-06	8.22373E-08	2.0	1.41
ARe152-G25	10	1.60E-05	9.46E-02	1.10E-01	3.79E-03	1.75E-06	6.06759E-08	4.0	2.54
ARe152-G26	14	4.20E-05	1.09E-01	1.25E-01	4.23E-03	5.27E-06	1.77708E-07	1.9	1.00
ARe152-G27	4	1.60E-05	7.68E-02	7.23E-02	2.15E-03	1.16E-06	3.43334E-08	2.4	2.43

Table D.10. Apatite fission track data for sample **ARe165**

Sample	#grains	Ns	$\Sigma\, p_i\Omega_i$	$1\sigma\, \Sigma\, p_i\Omega_i$	ζ ICP	2σ ζICP	χ^2	$P(\chi^2)$	Pooled age	2σ Ma
ARe165	33	103	1.03E-05	1.03449E-07	0.70	0.03	29.58	0.59	7.1	1.4

Grain	Ns	Area (cm^2)	$^{238}U/^{43}$Ca	Weighted $^{238}U/^{43}Ca$	2σ abs	$p_i\Omega_i$	$p_i\Omega_i 1\sigma$	FT Age	2σ
ARe165-G01	1	3.60E-05	3.32E-03	3.79E-03	1.30E-04	1.37E-07	4.67933E-09	5.1	10.30
ARe165-G02	0	2.50E-05	4.18E-03	3.00E-03	1.50E-04	7.51E-08	3.75217E-09	4.7	13.24
ARe165-G03	1	2.50E-05	9.07E-03	9.36E-03	2.79E-04	2.34E-07	6.98446E-09	3.0	6.02
ARe165-G04	3	3.60E-05	1.27E-02	1.36E-02	4.13E-04	4.90E-07	1.48856E-08	4.3	4.98
ARe165-G05	1	1.60E-05	4.85E-03	4.94E-03	1.47E-04	7.90E-08	2.34672E-09	8.9	17.80
ARe165-G06	3	3.60E-05	6.07E-03	6.47E-03	2.01E-04	2.33E-07	7.22329E-09	9.1	10.47
ARe165-G07	1	3.60E-05	5.21E-03	5.04E-03	1.51E-04	1.81E-07	5.42175E-09	3.9	7.76
ARe165-G08	2	1.00E-04	5.35E-03	4.95E-03	1.54E-04	4.95E-07	1.53945E-08	2.8	4.02
ARe165-G09	4	5.00E-05	7.14E-03	6.98E-03	2.02E-04	3.49E-07	1.01059E-08	8.1	8.07
ARe165-G10	6	2.40E-05	1.28E-02	1.30E-02	3.85E-04	3.11E-07	9.24947E-09	13.5	11.08
ARe165-G11	0	3.60E-05	7.40E-03	7.16E-03	2.10E-04	2.58E-07	7.56641E-09	1.4	3.86
ARe165-G12	5	2.80E-05	8.92E-03	8.76E-03	2.56E-04	2.45E-07	7.17504E-09	14.3	12.83
ARe165-G13	7	1.00E-04	3.00E-03	3.15E-03	9.56E-05	3.15E-07	9.56047E-09	15.6	11.84
ARe165-G14	2	4.20E-05	7.51E-03	8.62E-03	5.48E-04	3.62E-07	2.30031E-08	3.9	5.51
ARe165-G15	4	2.50E-05	9.59E-03	9.48E-03	2.80E-04	2.37E-07	6.98877E-09	11.9	11.88
ARe165-G16	5	5.00E-05	9.55E-03	9.39E-03	2.79E-04	4.70E-07	1.3961E-08	7.5	6.71
ARe165-G17	2	5.00E-05	6.04E-03	6.05E-03	1.78E-04	3.03E-07	8.91001E-09	4.6	6.58
ARe165-G18	4	2.50E-05	6.71E-03	6.23E-03	1.92E-04	1.56E-07	4.79955E-09	18.1	18.08
ARe165-G19	4	5.00E-05	7.55E-03	7.91E-03	2.37E-04	3.96E-07	1.18262E-08	7.1	7.12
ARe165-G20	2	6.00E-05	1.36E-02	1.44E-02	1.42E-03	8.62E-07	8.53475E-08	1.6	2.31
ARe165-G21	4	3.60E-05	8.41E-03	8.69E-03	2.58E-04	3.13E-07	9.30304E-09	9.0	9.00
ARe165-G22	5	1.00E-04	5.93E-03	5.87E-03	1.72E-04	5.87E-07	1.72062E-08	6.0	5.37
ARe165-G23	1	2.50E-05	8.70E-03	8.69E-03	2.53E-04	2.17E-07	6.33499E-09	3.2	6.48
ARe165-G24	3	3.60E-05	8.09E-03	8.08E-03	2.33E-04	2.91E-07	8.37251E-09	7.3	8.39
ARe165-G25	1	2.50E-05	7.37E-03	7.89E-03	2.37E-04	1.97E-07	5.93187E-09	3.6	7.13
ARe165-G26	2	0.000025	6.46E-03	6.76E-03	2.03E-04	1.69E-07	5.06281E-09	8.3	11.78
ARe165-G27	3	0.00004	3.87E-03	3.74E-03	1.13E-04	1.49E-07	4.5356E-09	14.1	16.31
ARe165-G28	5	0.000036	7.20E-03	7.32E-03	2.18E-04	2.63E-07	7.86375E-09	13.3	11.96
ARe165-G29	6	0.000049	1.24E-02	1.28E-02	3.77E-04	6.28E-07	1.84737E-08	6.7	5.50
ARe165-G30	2	0.00005	5.61E-03	5.23E-03	1.59E-04	2.62E-07	7.96881E-09	5.4	7.61
ARe165-G31	5	0.00004	4.80E-03	5.01E-03	1.51E-04	2.00E-07	6.05362E-09	17.5	15.72
ARe165-G32	4	0.00005	5.05E-03	5.52E-03	1.71E-04	2.76E-07	8.54246E-09	10.2	10.21
ARe165-G33	5	0.00006	8.55E-03	8.64E-03	2.55E-04	5.18E-07	1.52874E-08	6.8	6.08

Table D.11. Apatite fission track data for sample **ARe184**

Sample	#grains	Ns	$\Sigma\, p_i\Omega_i$	$1\sigma\ \Sigma\, p_i\Omega_i$	ζ ICP	2σ ζICP	χ^2	$P(\chi^2)$	Pooled age	2σ Ma
ARe184	18	37	9.20E-06	6.88487E-08	0.70	0.03	7.64	0.97	2.8	0.9

Grain	Ns	Area (cm^2)	$^{238}U/^{43}$Ca	Weighted $^{238}U/^{43}Ca$	2σ abs	$p_i\Omega_i$	$p_i\Omega_i 1\sigma$	FT Age	2σ
ARe184-G01	2	2.50E-05	2.36E-02	2.32E-02	6.65E-04	5.80E-07	1.66159E-08	2.4	3.43
ARe184-G02	2	2.00E-05	1.28E-02	1.20E-02	3.58E-04	2.41E-07	7.16887E-09	5.8	8.28
ARe184-G03	2	2.50E-05	1.05E-02	1.03E-02	2.99E-04	2.58E-07	7.47359E-09	5.5	7.72
ARe184-G04	5	4.20E-05	2.26E-02	2.19E-02	6.35E-04	9.20E-07	2.66841E-08	3.8	3.42
ARe184-G05	2	2.80E-05	1.67E-02	1.63E-02	4.70E-04	4.55E-07	1.31547E-08	3.1	4.37
ARe184-G06	0	3.50E-05	1.17E-02	1.14E-02	3.28E-04	3.98E-07	1.14698E-08	0.9	2.50
ARe184-G07	1	2.40E-05	1.63E-02	1.62E-02	4.66E-04	3.89E-07	1.11856E-08	1.8	3.62
ARe184-G08	1	1.20E-05	2.77E-02	2.70E-02	7.89E-04	3.24E-07	9.46844E-09	2.2	4.34
ARe184-G09	1	2.50E-05	1.48E-02	1.50E-02	4.31E-04	3.74E-07	1.07746E-08	1.9	3.77
ARe184-G10	4	3.00E-05	1.64E-02	1.67E-02	4.87E-04	5.01E-07	1.46028E-08	5.6	5.62
ARe184-G11	3	4.90E-05	1.68E-02	1.69E-02	4.95E-04	8.27E-07	2.42377E-08	2.6	2.95
ARe184-G12	1	2.80E-05	2.40E-02	2.43E-02	6.98E-04	6.81E-07	1.95346E-08	1.0	2.07
ARe184-G13	2	2.80E-05	1.73E-02	1.73E-02	4.98E-04	4.83E-07	1.39335E-08	2.9	4.12
ARe184-G14	2	1.80E-05	1.77E-02	1.73E-02	5.06E-04	3.12E-07	9.11487E-09	4.5	6.39
ARe184-G15	2	3.00E-05	9.60E-03	9.66E-03	2.78E-04	2.90E-07	8.35494E-09	4.9	6.87
ARe184-G16	2	2.50E-05	2.83E-02	2.93E-02	8.73E-04	7.32E-07	2.18181E-08	1.9	2.72
ARe184-G17	2	2.40E-05	3.67E-02	3.95E-02	1.18E-03	9.48E-07	2.82409E-08	1.5	2.10
ARe184-G18	3	2.50E-05	2.05E-02	1.95E-02	5.75E-04	4.88E-07	1.43665E-08	4.3	5.00

Table D.12. Apatite fission track data for sample **ME130**

Sample	#grains	Ns	$\Sigma\, p_i\Omega_i$	$1\sigma\ \Sigma\, p_i\Omega_i$	ζ ICP	2σ ζICP	χ^2	$P(\chi^2)$	Pooled age	2σ Ma
ME130	25	47	7.00E-06	4.63191E-08	0.70	0.03	12.93	0.97	4.7	1.4

Grain	Ns	Area (cm^2)	$^{238}U/^{43}$Ca	Weighted $^{238}U/^{43}Ca$	2σ abs	$p_i\Omega_i$	$p_i\Omega_i 1\sigma$	FT Age	2σ
ME130-G01	0	3.60E-05	5.74E-03	5.79E-03	1.73E-04	2.08E-07	6.24542E-09	1.7	4.77
ME130-G02	1	1.60E-05	3.02E-02	3.26E-02	9.98E-04	5.22E-07	1.59687E-08	1.3	2.70
ME130-G03	0	2.50E-05	9.62E-03	9.59E-03	2.82E-04	2.40E-07	7.05754E-09	1.5	4.15
ME130-G04	2	2.50E-05	8.74E-03	8.72E-03	2.52E-04	2.18E-07	6.31146E-09	6.5	9.13
ME130-G05	1	1.20E-05	8.70E-03	8.92E-03	2.61E-04	1.07E-07	3.12821E-09	6.6	13.14
ME130-G06	3	4.00E-05	7.17E-03	7.09E-03	2.07E-04	2.84E-07	8.29301E-09	7.4	8.60
ME130-G07	2	3.50E-05	1.08E-02	1.08E-02	3.20E-04	3.79E-07	1.11965E-08	3.7	5.25
ME130-G08	2	2.50E-05	8.92E-03	9.03E-03	2.70E-04	2.26E-07	6.74741E-09	6.2	8.82
ME130-G09	1	6.40E-05	8.70E-03	8.71E-03	2.55E-04	5.58E-07	1.632E-08	1.3	2.52
ME130-G10	1	2.50E-05	7.63E-03	7.69E-03	2.22E-04	1.92E-07	5.5615E-09	3.7	7.32
ME130-G11	2	1.50E-05	6.05E-03	6.04E-03	1.93E-04	9.06E-08	2.88927E-09	15.5	21.96
ME130-G12	1	2.50E-05	1.39E-02	1.36E-02	4.11E-04	3.39E-07	1.0284E-08	2.1	4.15
ME130-G13	0	2.50E-05	7.10E-03	7.14E-03	2.10E-04	1.78E-07	5.23882E-09	2.0	5.57
ME130-G14	3	2.50E-05	1.07E-02	1.07E-02	3.12E-04	2.67E-07	7.79542E-09	7.9	9.14
ME130-G15	4	3.60E-05	9.17E-03	9.22E-03	2.74E-04	3.32E-07	9.87113E-09	8.5	8.49
ME130-G16	2	1.50E-05	6.74E-03	6.68E-03	1.98E-04	1.00E-07	2.9722E-09	14.0	19.84
ME130-G17	5	6.40E-05	9.59E-03	9.59E-03	2.78E-04	6.14E-07	1.7793E-08	5.7	5.13
ME130-G18	3	1.60E-05	2.50E-02	2.47E-02	7.17E-04	3.95E-07	1.14764E-08	5.3	6.18
ME130-G19	1	1.60E-05	9.70E-03	9.68E-03	2.88E-04	1.55E-07	4.60798E-09	4.5	9.09
ME130-G20	1	3.60E-05	7.33E-03	7.34E-03	2.13E-04	2.64E-07	7.66088E-09	2.7	5.33
ME130-G21	3	3.60E-05	7.02E-03	7.13E-03	2.09E-04	2.57E-07	7.52268E-09	8.2	9.51
ME130-G22	2	2.50E-05	8.06E-03	8.01E-03	2.37E-04	2.00E-07	5.927E-09	7.0	9.94
ME130-G23	1	2.40E-05	6.92E-03	6.88E-03	2.02E-04	1.65E-07	4.85274E-09	4.3	8.53
ME130-G24	3	6.00E-05	8.37E-03	8.04E-03	2.46E-04	4.82E-07	1.4779E-08	4.4	5.06
ME130-G25	3	2.40E-05	9.60E-03	9.57E-03	2.78E-04	2.30E-07	6.67739E-09	9.2	10.62

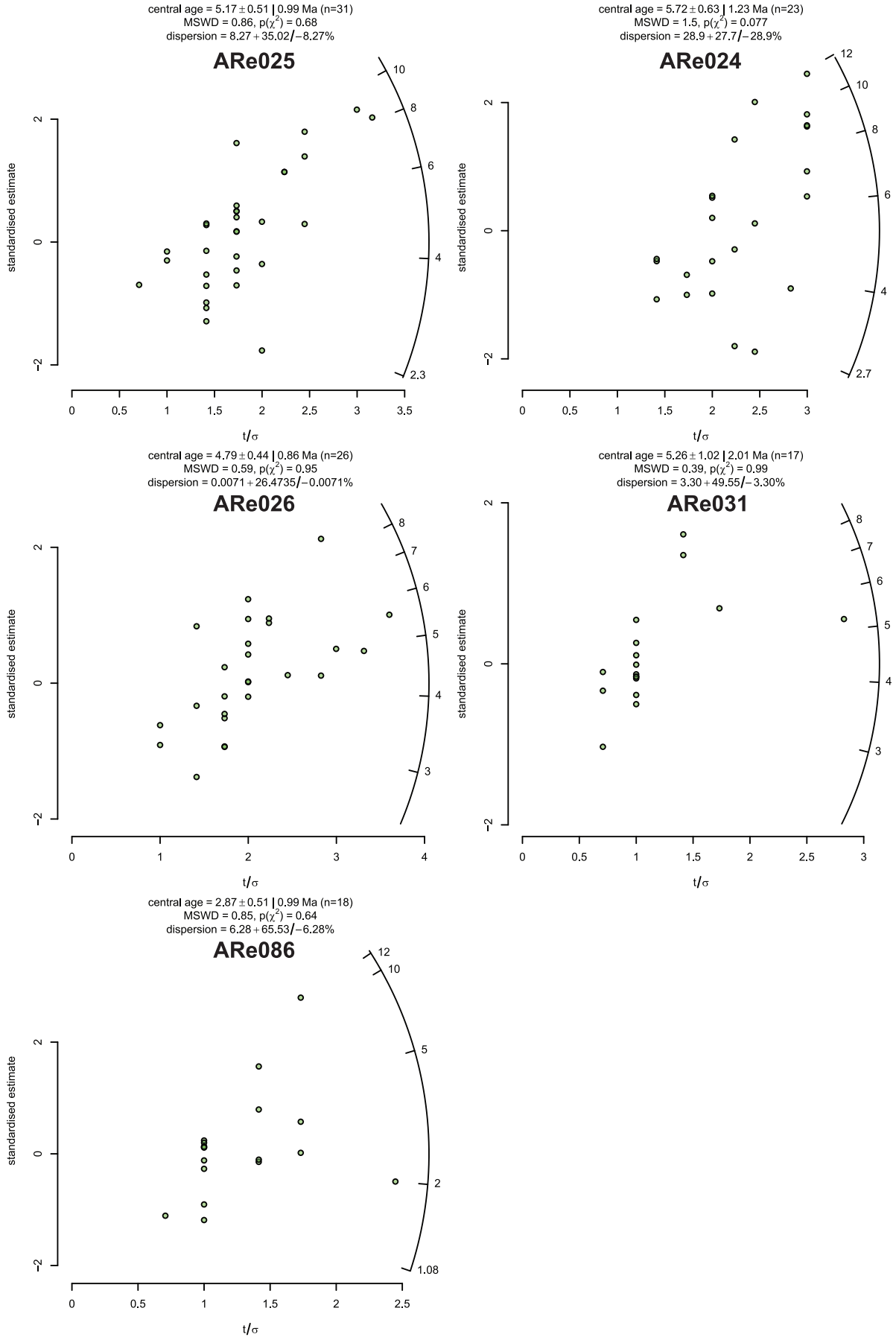

Figure D.6. Radial plots from AFT analysis.

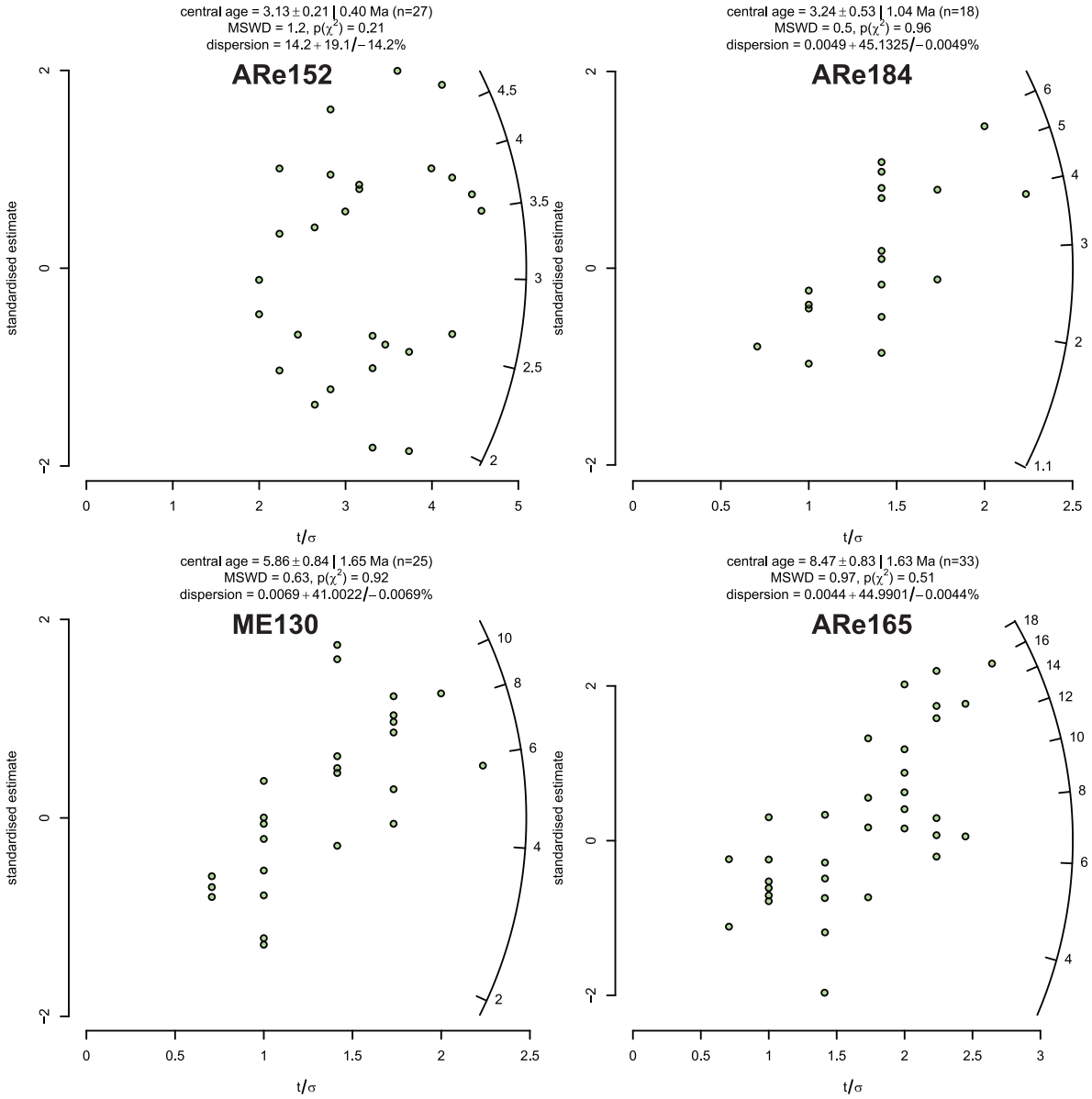

Figure D.7. Radial plots from AFT analysis.

Appendix E

Sciences communications

Accepted or in preparation research articles

Mercier, A., Leloup, P. H., Courrioux, G., Caritg, S., Lopez, S., Grandjean, P., Passot, S., and Kalifi, A. (2023). Large thrusting and late faulting shape the Aiguilles Rouges crystalline massif (Western Alps), structural implications. *Tectonophysics*, 847, 229691, doi: 10.1016/j.tecto.2022.229691.

Mercier, A., Leloup, P. H., Monié, P., Mahéo, G., Iemmolo, A., Fellah, C., Langlois, C., and Douillard, T. (2023). Timing of deformation in the western Alps: implications from $^{40}Ar/^{39}Ar$ laser dating of synkinematics white micas. *In Prep. for Tectonics*

Mercier A., Bodin T., Leloup P .H., Mahéo G., Monié P., Barbarand J., Glotzbach C. and Robert X. (2023). Quantification of Alpine exhumation and relief changes with Bayesian inversion. The case study of the Mont-Blanc and Aiguilles Rouges massifs. *In Prep. for JGR: Solid Earth.*

Mercier A., Leloup P. H., Guina M., Courrier T., and Libier Y. (2023). Development of a relational database to organize geological field data: *DataGeol*. *In Prep. to Data In Brief.*

Oral Communications

- **EGU21**: Gather Online - 19–30 April 2021 (International)
- **RST2021**: Lyon - 1-5 November 2021 (National)
- **RST2023**: Rennes - 30 October to 3 November 2023 (National)
- **AGU23**: San Fransisco, CA - 19–30 April 2021 (International)
- **Public Conference**: Argentière (74400) - 8th August 2023 (Vulgarization)

EGU21: Gather Online - 19–30 April 2021

Session TS7.8: *The Alps and neighboring mountain belts (Pyrenees, Apennines, Dinarides, Carpathians): a multidisciplinary vision (AlpArray).*

Rediscovery of a major alpine thrust: the Helvetic Basal Décollement

A. Mercier[1], P H. Leloup[1], G. Courrioux[2], S. Caritg[2], S. Lopez[2], A. Kalifi[1]

[1]Laboratoire de Géologie de Lyon – Terre, planètes et environnement (LGL-TPE) – CNRS : UMR5276, Université de Lyon - France. [2] Bureau de Recherches Géologiques et Minières (BRGM) - France

For two centuries the European Alps are a natural laboratory to study continental lithosphere deformation during mountain building. Since the early studies, a constant question has been to evaluate the importance of vertical versus horizontal displacements in the building of reliefs. Whilst the occurrence of large thrust sheets, as initially proposed from field observations, is now well explained in the frame of plate tectonics, controversies still arise on the precise geometry, amount, and timing of major thrusting during the orogeny. We present a new detailed 3D structural study of the cover/basement relationships in the Chamonix synclinorium in between the Mont-Blanc (MB) and Aiguilles Rouges (AR) ranges. These massifs are two of the main external basement ranges of the western Alps. The study allows deciphering the area structural history: the Mesozoic sedimentary cover has been thrust at least 10km NW above the Helvetic Basal Décollement (HBD) before being offset by late steep thrusts during exhumation in the Miocene.

Such interpretation fundamentally diverges from the classical view of the sedimentary cover of the Chamonix synclinorium being expulsed from a former graben during a single deformation phase and implies that a major thrust phase lasting 10 Ma has been overlooked. Our observations show that the HBD was a major thrust system active between 30 and 20 Ma, possibly until 15 Ma, with a shortening of more than 10km in the south to 20km in the north. It extends below most of the subalpine ranges and emerges in front of the Bauges and within the Chartreuse and Vercors massifs, and was rooted east of the External Crystalline Massifs (Mont-Blanc and Belledonne). During the Miocene, the HBD was cut by steep reverse faults and uplifted above the basement culmination of the External Crystalline Massifs obscuring its continuity and precluding its recognition as a major structure even if it was previously described at several localities.

EGU21-8595

https://doi.org/10.5194/egusphere-egu21-8595

EGU General Assembly 2021

Réunion des Sciences de la Terre, Lyon - novembre 2021

Session T1.2: *Orogènes : Système Tibet-Himalaya, Chaînes Alpines péri-méditerranéennes et Pyrénées*

Rediscovery of a major alpine thrust: the Helvetic Basal Decollement

A. Mercier[1], P H. Leloup[1], G. Courrioux[2], S. Caritg[2], S. Lopez[2], A. Kalifi[1]

[1]Laboratoire de Géologie de Lyon – Terre, planètes et environnement (LGL-TPE) – CNRS : UMR5276, Université de Lyon - France. [2] Bureau de Recherches Géologiques et Minières (BRGM) - France

For two centuries the European Alps are a natural laboratory to study continental lithosphere deformation during mountain building. Since the early studies, a constant question has been to evaluate the importance of vertical versus horizontal displacements in the building of reliefs. Although the occurrence of large thrust sheets, as initially proposed from field observations, is now well explained in the frame of plate tectonics, controversies still arise on the precise geometry, amount, and timing of major thrusting during the orogeny.

We present a new detailed 3D structural study of the cover/basement relationships in the Chamonix synclinorium in between the Mont-Blanc (MB) and Aiguilles Rouges (AR) ranges. These massifs are two of the main external basement ranges of the western Alps. The study allows deciphering the area structural history: the Mesozoic sedimentary cover has been thrust at least 10km NW above the Helvetic Basal Décollement (HBD) before being offset by late steep thrusts during exhumation in the Miocene.

Such interpretation fundamentally diverges from the classical view of the sedimentary cover of the Chamonix synclinorium being expulsed from a former graben during a single deformation phase and implies that a major thrust phase lasting 10 Ma has been overlooked. Our observations show that the HBD was a major thrust system active between 30 and 20 Ma, possibly until 15 Ma, with a shortening of more than 10km in the south to 20km in the north. It extends below most of the subalpine ranges and emerges in front of the Bauges and within the Chartreuse and Vercors massifs, and was rooted east of the External Crystalline Massifs (Mont-Blanc and Belledonne). During the Miocene, the HBD was cut by steep reverse faults and uplifted above the basement culmination of the External Crystalline Massifs obscuring its continuity and precluding its recognition as a major structure even if it was previously described at several localities.

RST2021

sciencesconf.org:rst2020-lyon:329970

Réunion des Sciences de la Terre 2021

Réunion des Sciences de la Terre, Rennes - novembre 2023

Session 4.3: *Studying the orogenic system through the analyses and integration of geophysical and geological data*

Datations absolues et modèles thermo-cinématiques contraignent l'histoire d'exhumation du Mont-Blanc et quantifient les mécanismes associés

A. Mercier[1], P H. Leloup[1], T. Bodin[1], P. Monié[2], J. Barbarand[3], G. Mahéo[1], C. Glotzbach[4], X. Robert[5]

[1]Univ Lyon, Université Claude Bernard Lyon 1, ENSL, UJM, CNRS, Laboratoire de géologie de Lyon: Terre, Planètes, Environnement, Villeurbanne Cedex, France. [2]Université de Montpellier, CNRS, Géosciences Montpellier, Montpellier Cedex 05, France. [3]Universite Paris Sud, GEOPS, Paris, France. [4]University of Tübingen, Department of Geosciences, Tübingen, Germany. [5]University Grenoble Alpes, ISTerre, Grenoble, France.

La thermochronologie, couplée à la modélisation numérique, permettent de quantifier l'exhumation des roches. L'évolution de l'exhumation permet de discuter de l'interaction entre les processus internes (tectonique, isostasie) et externes (érosion). Cependant, la complexité des forçages et par conséquent le nombre de paramètres à modéliser conduisent souvent à une non-unicité de la solution. Les méthodes inverses peuvent répondre à ce problème en cherchant les paramètres optimaux par itérations successives. Cependant, l'ensemble de solutions possibles n'est pas toujours perceptible. Dans ce travail nous appliquons une méthode utilisant l'inférence bayésienne couplée à la simulation numerique (Pecube). Après une phase d'exploration des paramètres par inversion (Neighborhood Algorithm), nous ré-échantillonnons les résultats obtenus avec une méthode Bayésienne pour obtenir une densité de probabilité décrivant les modèles et l'incertitude des paramètres. De plus, des inversions de données générées par des modèles directs, permettent d'évaluer la capacité de la méthode et du jeu de données à quantifier chaque paramètre. L'application de cette démarche aux massifs du Mont-Blanc et des Aiguilles Rouges permet (i) de quantifier l'histoire d'exhumation des deux massifs et du différentiel d'exhumation entre eux (ii) d'estimer l'incertitude sur chaque paramètre de la modélisation. Indépendamment, nous avons réalisé des datations absolues par la méthode Ar/Ar par ablation laser in situ, sur 6 mylonites. Les résultats des deux méthodes concordent et indiquent que (i) Le Mont-Blanc a été exhumé de l'ordre de 7 km de plus que les Aiguilles Rouges. (ii) Le Mont-Blanc commence son exhumation après 21 Ma et jusqu'à 12 Ma, pendant l'activité de la zone de cisaillement du Mont-Blanc. (iii) Les Aiguilles Rouges s'exhument elles à partir de 12 Ma, avant une phase d'accélération après 5 Ma, l'exhumation différentielle s'arrêtant à 1 Ma. Cette phase et liée à l'activation du rétro-chevauchement du Tour. (iv) Les deux massifs subissent une phase d'accélération commune, contemporaine avec la formation du relief, liée à l'évolution climatique.

RST2023

sciencesconf.org:rst2023-rennes:484203

Réunion des Sciences de la Terre 2023

AGU23: San Fransico, CA & Online 11-15 December 2023

Session T026: *Reconstructing Tectonics, Climate and Erosion of Mountain Belts*

Unraveling the Exhumation History of the Western Alps: Insights from Thermo-Kinematic Simulations and Absolute Dating of Deformation

A. Mercier[1], P H. Leloup[1], T. Bodin[1], P. Monié[2], J. Barbarand[3], G. Mahéo[1], C. Glotzbach[4], X. Robert[5]

[1]Univ Lyon, Université Claude Bernard Lyon 1, ENSL, UJM, CNRS, Laboratoire de géologie de Lyon: Terre, Planètes, Environnement, Villeurbanne Cedex, France. [2]Université de Montpellier, CNRS, Géosciences Montpellier, Montpellier Cedex 05, France. [3]Universite Paris Sud, GEOPS, Paris, France. [4]University of Tübingen, Department of Geosciences, Tübingen, Germany. [5]University Grenoble Alpes, ISTerre, Grenoble, France.

We apply both geochronology and thermochronology methods to the Mont-Blanc and Aiguilles Rouges crystalline massifs to decipher the structural evolution of the western Alps.

On the one hand, we invert new and published thermochronological data to quantify the differential exhumation between the two massifs by using a thermal-kinematic simulation (Pecube) coupled with Bayesian inference. We also performed inversions of synthetic data generated from known forward models to assess the ability of the data and of the simulations to quantify each parameter including relief and fault slip rate evolution.

On the other hand, three mylonites from the Mont-Blanc shear zone (MBsz) in between the two ranges, and two mylonites from the Helvetic thrust system above them are dated using in situ 40Ar/39Ar on synkinematic white micas. Thermobarometric conditions of the deformation were estimated from petro-geochemical quantification and lattice preferred orientation of quartz to be below 500°C and between 0.47 and 0.74 GPa. The MBsz samples range in age from 14.9 to 17.3 Ma. The samples from the Helvetic thrust system on the eastern and western sides of the Mont-Blanc yield ages of 13.7 and 16.3 Ma, respectively.

The results of the two methods are consistent and imply four deformation phases: (i) From 21 Ma to 14 Ma, the Mont-Blanc is exhumed in a duplex of the Helvetic thrust system; (ii) Between 14 Ma and approximately 11 Ma, the MBsz becomes a breach thrust that crosscut the Helvetic thrust system; (iii) At 6 Ma the Aiguilles Rouges begin to exhume above back thrusts. At that time, thick-skin deformation in the Mont-Blanc is coeval with thin-skin deformation in the foreland; (iv) The two massifs experience a common recent phase of high exhumation since about 1 Ma, coeval with relief building and most likely related to glacial valley incision.

This work emphasizes the benefits of coupling thermochronology with geochronology. The results imply that three major thrust systems have propagated in sequence in the western alps: the Penninic, the Helvetic, and the Alpine Sole Thrusts.

Conférence grand public à Argentière - 8 aout 2023

Association des Réserves Naturelles des Aiguilles Rouges

L'histoire géologique mouvementée du Mont-Blanc: Que sait-on? Comment le sait-on?

A. Mercier

Pourquoi étudier la formation des Alpes ? Les chaines de montagnes intriguent les géologues depuis des siècles, mais leur formation est encore mal comprise et de nombreuses questions restent en suspens : Quelle-est la chronologie précise des évènements ? Comment et quand s'est formé le relief ? Comment les roches ont été déformées ? Aujourd'hui les méthodes numériques et la modélisation enrichissent la compréhension des concepts et aident les géologues à quantifier les phénomènes, mais l'observation et la description naturaliste reste une étape clé avant la quantification. Comment font les géologues pour mieux comprendre l'histoire des Alpes et en particulier celle du Mont-Blanc et des Aiguilles Rouges ? Quelles méthodes utilisent-ils ? Où en est la recherche scientifique sur ce domaine en 2023 ?.

Appendix F

Tectonophysics

Original research article published in *Tectonophysics* journal with the following co-authors and reference:

Mercier, A., Leloup, P. H., Courrioux, G., Caritg, S., Lopez, S., Grandjean, P., Passot, S., and Kalifi, A. (2023). Large thrusting and late faulting shape the Aiguilles Rouges crystalline massif (Western Alps), structural implications. *Tectonophysics*, 847, 229691
doi:10.1016/j.tecto.2022.229691.

Tectonophysics 847 (2023) 229691

Contents lists available at ScienceDirect

Tectonophysics

journal homepage: www.elsevier.com/locate/tecto

Large thrusting and late faulting shape the Aiguilles Rouges crystalline massif (Western Alps), structural implications

A. Mercier [a,*], P.H. Leloup [a], G. Courrioux [b], S. Caritg [b], S. Lopez [b], P. Grandjean [a], S. Passot [a], A. Kalifi [a]

[a] Univ Lyon, Université Claude Bernard Lyon 1, ENSL, UJM, CNRS, Laboratoire de Géologie de Lyon: Terre, Planètes et Environnement, 2 rue Raphaël Dubois, F-69622 Villeurbanne, France

[b] Bureau de Recherches Géologiques et Minières, Direction des Géoressources, 3 av. Claude-Guillemin, BP 36009 45060 Orléans Cedex 2, France

ARTICLE INFO

Keywords:
Alpine geology
Microtectonics
Orogenesis
3D geological modeling
Helvetic Basal Thrust
Crystalline External Massifs

ABSTRACT

Although the Helvetic nappes of the Western Alps have been widely studied, their style, amount, and timing of deformation during the Alpine orogeny remain a subject of controversy. The discussion partly arises from various interpretations of the external crystalline massifs geometry and of the cover/basement relationships. Here, we apply structural analysis based on new field data, microtectonics, and 3D geological modeling on the Aiguilles Rouges and Mont-Blanc massifs, to better quantify their tectonic evolution and their relationship with the nappe stacking. Our results show large thrusting of the Helvetic Mesozoic sedimentary cover above the Aiguilles Rouges basement towards the WNW. The basal contact of the Helvetic nappes, which we call the Helvetic Basal thrust (HBT), often corresponds to a décollement level localized above the Triassic unconformity, but that locally also affects the basement. We suggest that most of the subalpine ranges are klippes above the HBT, and estimate the shortening of the thrust from previously published cross-sections to be between 13 and 32 km. According to published ages, we argue that the HBT was active in the Oligo-Miocene, between ~30 and ~14 Ma. After ~14 Ma and until ~6 Ma, the HBT is offset by late steep out-of-sequence faults, including back-thrusts and the Mont-Blanc shear zone that was previously a ramp of the HBT. The transition of the major thrust system from the HBT rooting above (east) of the Mont-Blanc to the Alpine sole thrust rooting below (west) of the Aiguilles Rouges occurred between 18 and 14 Ma.

1. Introduction

For two centuries the European Alps are a natural laboratory to study continental lithosphere deformation during mountain building. Since the early studies, a constant question has been to evaluate the importance of vertical versus horizontal displacements in the building of reliefs. Although the occurrence of large thrust sheets, as initially proposed from field observations (e.g., Bertrand, 1881; Argand, 1916), are now well explained in the frame of plate tectonics, controversies still arise on the precise geometry, amount, and timing of major thrusting during the orogeny.

Two completely different views are proposed in the external domain of the belt's western part. For most authors, the present-day geometry, results from the intense folding of the Mesozoic sedimentary cover, originally deposited in half grabens, together with the basement in a ductile basement fold nappe (e.g., Escher et al., 1993). In such a case the geometry of the half grabens guides later deformation(s), and the cover is considered para-autochthonous because horizontal displacements are moderate (e.g., Escher et al., 1993; Burkhard and Sommaruga, 1998; Bellahsen et al., 2014). Alternatively, it is proposed that the Mesozoic cover is significantly displaced to the west above a thrust: the Helvetic Basal Thrust (HBT) (e.g., Leloup et al., 2005; Pfiffner, 2014).

The existence and kinematics of such thrust are important not only for the understanding of the regional geology but also have implications on a) the estimate of total shortening in the external Alps; b) the timing and mechanism of uplift of the external ranges; c) the timing and mechanism of folding within the subalpine belts; d) the way shortening is absorbed in a layered media with contrasting rheology (sedimentary cover vs. basement); e) the influence of the initial geometry (paleo-topography: horst and grabens) on the deformation style.

Abbreviations: HBT, Helvetic Basal Thrust.

* Corresponding author.
E-mail addresses: antoine.mercier@univ-lyon1.fr, antoine.mercier@gmx.com (A. Mercier).

https://doi.org/10.1016/j.tecto.2022.229691
Received 27 June 2022; Received in revised form 19 December 2022; Accepted 22 December 2022
Available online 28 December 2022
0040-1951/© 2023 Elsevier B.V. All rights reserved.

Here, we present a detailed 3D structural study of the cover/basement relationships in the Chamonix synclinorium between the Mont-Blanc and Aiguilles Rouges ranges. These field observations are key to characterize the deformation within the orogenic wedge, and thus to discuss the outcome of rheological models (e.g. Spitz et al., 2020; Bauville and Schmalholz, 2015).

2. Geological setting

The western Alps are an accretionary wedge resulting from the Cenozoic convergence between Europe and Apulia continental margins. The anterior subduction of the ocean started during the mid-Cretaceous and led to the collision in the Paleogene. The wedge is split into two parts: the internal domain containing ophiolites and rocks that have been deformed at high temperature and/or deeply subducted during the Alpine orogeny, and the external domain where Alpine metamorphism is limited to green-schist facies (e.g., Bousquet et al., 2004). The internal domain is thrust above the external one along the west verging Penninic thrust, with the Prealps being interpreted as a klippe of the internal domain (e.g., Mosar, 1989) (Fig. 1). Such interpretation implies at least 95 km of thrusting to the NW above the Penninic thrust, which has been later folded upward to expose a window of the external domain in the Mont-Blanc/Aiguilles Rouges area (Fig. 1). Motion on the Penninic thrust was coeval with the sedimentation of flysch deposits in a flexural basin during the Upper Eocene/Lower Oligocene (e.g., Homewood, 1983; Ruffini et al., 1997) and ended at ~30 Ma (e.g., Pfiffner et al., 2002).

The external domain exposes both basement ridges, the external crystalline massifs, and their folded sedimentary cover (Fig. 1). The basement consists of Variscan (≥300 Ma) metamorphic gneisses, granites, and Carboniferous/Permian sedimentary rocks. The overlying sedimentary cover span in age from Triassic to Miocene. The external crystalline massifs straddle for 330 km along the belt from Aar to Ecrins and form slivers separated by sedimentary rocks (Fig. 1) that have been interpreted either as paleo-horsts inherited from Mesozoic rifting (e.g., Lemoine and Tricart, 1986), crustal culminations above thrust ramps (e.g., Lacassin et al., 1990; Pfiffner et al., 1997; Menard and Thouvenot, 1987), anticline cores (e.g., Escher et al., 1993), or a combination of those. The sedimentary cover is folded and locally forms the Helvetic nappes whose extent, geometry, and timing are still discussed.

The Mont-Blanc and Aiguilles Rouges ranges are two NE-SW trending external crystalline massifs separated by a narrow structure filled with Mesozoïc sediments: the so-called Chamonix synclinorium, trending N030°(Fig. 1). From the early 1920s, it has been suggested that the Chamonix synclinorium corresponds to the root of the Morcles Nappe, the lowest of the Helvetic nappes (Collet and Paréjas, 1920; Paréjas, 1922; Eltchaninoff, 1982; Butler, 1985). However, thrusting at the bottom of the Morcles Nappe has been minimized or even denied. For example, Ayrton (1980) proposes that the synclinorium is the contact zone between the autochthonous sedimentary cover of the Mont-Blanc and that of the Aiguilles Rouges. Several authors propose that the Morcles nappe is para-autochthonous, being the reverse limb of a buckle anticline, whose core consists of the folded basement (so-called external Mont-Blanc) and the periphery of cover rocks expulsed from a Mesozoic Half-graben (Ramsay, 1981; Epard, 1986; Escher et al., 1993; Burkhard and Sommaruga, 1998; Egli and Mancktelow, 2013; Bellahsen et al., 2014) (Fig. 2a).

Alternatively, it has been proposed a two phases scenario, with first, thrusting towards the NW of most of the cover and part of the basement; and second exhumation of the Mont-Blanc along the steep reverse Mont-blanc shear zone and doming of the Aiguilles Rouges above a deeper thrust (Leloup et al., 2005) (Fig. 2b).

Yet others consider that the linear shape of the Chamonix Synclinorium, and of the Mont-Blanc range, partly results from right-lateral strike-slip faulting along the Simplon Rhône fault system (Gourlay and Ricou, 1983; Hubbard and Mancktelow, 1992; Seward and Mancktelow, 1994) connected to the Simplon low - angle detachment fault that was active between ~18.5 and 4 Ma (Campani et al., 2010).

In the northwestern Alps, the instrumental earthquakes are best explained by a strike-slip state of stress with σ1 trending WNW-ESE (Fréchet et al., 2011). The most significant instrumental earthquake in the Aiguilles Rouges area was the M_w 4.5 Vallorcine earthquake (8th September 2005) that activated the N060° trending right-lateral Gros-Nol Fault (Fréchet et al., 2011) (Fig. 3a). That fault is oblique to the Chamonix synclinorium that trends ~N030°.

3. Data and methods

3.1. Structural analysis

At the regional scale, the structural study is mainly based on published geological maps at the 1:500000 scale in France (Corbin and Oulianoff, 1928; Ayrton et al., 1987; Pairis et al., 1992) and 1:25000 in Switzerland (Collet et al., 1952), that we completed and updated with field observations, measurements, and mapping. At the outcrop scale, we characterize the style, intensity, and geometry of the deformation by qualitative observation and precise measurements of the orientation of the structural features (stratigraphy, cleavage, shear planes, lineations, etc.). We meticulously select oriented samples and produce oriented thin sections to characterize the deformation at a microscopic scale. The main shear criteria used are the relationship between cleavage and shear planes (Berthé et al., 1979), asymmetrical boudinage (Lacassin, 1988), delta and sigma porphyroclasts (Hanmer and Passchier, 1991), and lattice preferred orientation in quartz (Gapais and Barbarin, 1986; Passchier and Trouw, 2005).

Field data (observations, measurements, samples, photos, etc.) are managed in a relational database, *DataGeol*, that we specifically designed for the processing of structural geology field data. *DataGeol* efficiently organizes, stores, and archives the data into different tables that are standardized with vocabularies, structured with constraints (primary keys), and linked together with foreign keys. The database is coded with the Structured Query Language (SQL) through the open-source system PostgreSQL with PGadmin graphical interface, which is a powerful programming language for object-relational databases. The use of a database and the SQL language allows interrogations and queries of the data for different applications purpose either for mapping in a GIS, structural analysis, 3D modeling, or any other export tables. Note that DataGeol is fully compatible with the vocabularies of the Open Geospatial Consortium (OGC) and the data model standard of the Darwin Core.

3.2. 3D geological modeling

Classically, the geometry of the geological structure deduced from observations at the surface and at depth is depicted through surface mapping and vertical cross-sections. When numerous cross-sections are performed, a relatively precise idea of the 3D geometry can be given. However, the cross-sections are only 2D projected representations of the surrounding data, and the original 3D data position, orientation, and uncertainty are lost.

The 3D geological approach of GeoModeller implements numerically geological concepts to build an implicit 3D model based on geological rules (Calcagno et al., 2008). The interface between two geological formations corresponds to an isopotential surface described by a potential field. That potential field is interpolated from the measured orientation data (stratification, cleavage, or foliation) using the geostatistical method developed by Lajaunie et al. (1997). The method uses the structural orientation data, that locally defines the gradient of the potential field. The interface is the isopotential surface passing through the contact point(s) observed in the field. Formations with interfaces that are sub-parallel to each other and thus share the same potential field are grouped into a series. Defining a series interface necessitates at least

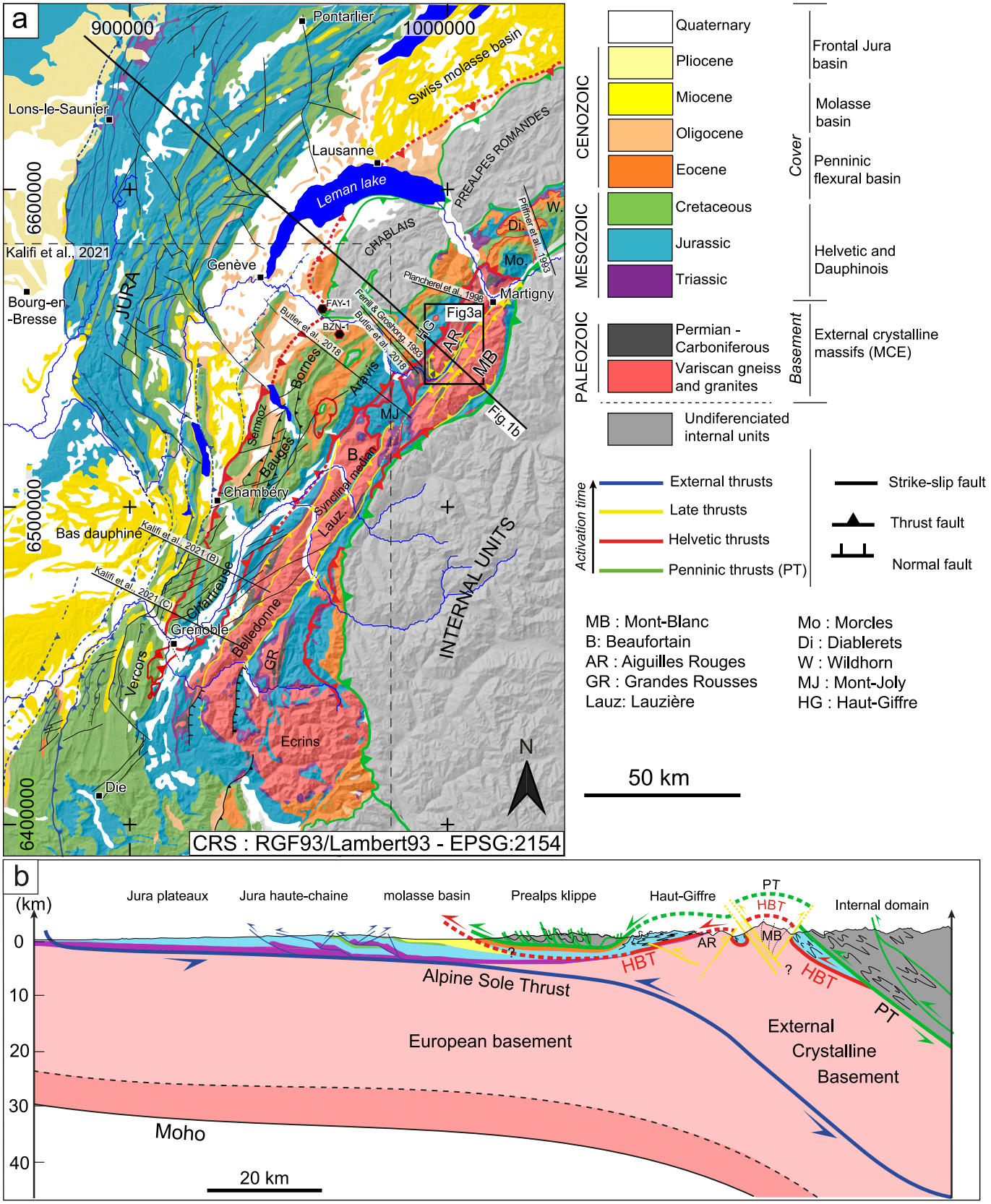

Fig. 1. Structural frame of the western Alps. a) Structural map with the main thrust systems: Penninic thrust, Helvetic thrust, Alpine Sole Thrust, and late thrusts. The black frame corresponds to the location of Fig. 3a. Location of cross-sections that are discussed in the text is indicated with the reference therein (Plancherel et al., 1998; Ferrill and Groshong Jr, 1993; Butler et al., 2018; Kalifi et al., 2021). b) Synthetic cross-section of the western Alps. The crustal structure is from Lacassin et al. (1990) and Pfiffner et al. (1997), the Jura deformation from Affolter (2004); Affolter et al. (2008), the structure of the Prealps klippe is from Mosar (1989), the structure of the Aiguilles Rouges and Mont-Blanc area is from this study, and Leloup et al. (2005); the structure in the internal domain is from Ceriani et al. (2001). Cross section trace is located in the map (a).

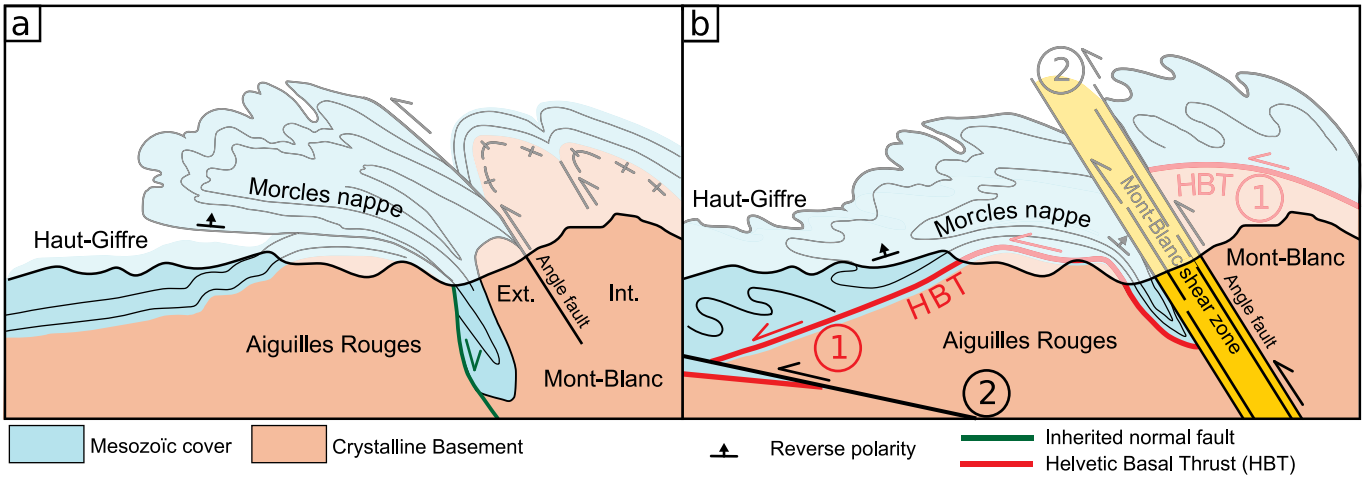

Fig. 2. Contrasting models for Alpine deformation of the external crystalline massifs and their cover, as exemplified in the Aiguilles Rouges and Mont-Blanc massifs. a) One-stage folding of a thick sedimentary series located within half grabens, resulting in parautochtonous folds (basement fold nappe). The external Mont-Blanc basement is tightly folded and the normal limb of the cover roots in the Angle Fault (e.g., Escher et al., 1988, 1993). b) Two stages of deformation model. 1st stage: Thrusting (mostly décollement of the cover with respect to the basement) towards the west. 2nd stage: offset of the thrust level by a reverse shear zone (Mont-Blanc shear zone) and updoming of the Aiguilles Rouges (e.g., Leloup et al., 2005).

one structural measurement (orientation) within the series and one contact point (location). This is well adapted to model sedimentary series but can also be used in magmatic and metamorphic rocks when their internal structures are parallel to their interface (Calcagno et al., 2008). A relative chronology must be defined for the formations within the series to satisfy the geological concept of superposition. Further, a relationship between the series that are not parallel to each other, must be defined: erode if the series crosscuts the oldest ones and onlap if it does not (Calcagno et al., 2008). Faults are discontinuities that offset the potential fields, their relative timing must be defined to respect the cross-cutting relationships.

The 3D geological model encompasses a 14.3 × 20.3 km zone (Figs. 3 and 4) and is based on new structural measurements at 432 locations at the surface. Some structural measurements are taken from published geological maps, (Corbin and Oulianoff, 1928; Amberger, 1959; Ayrton et al., 1987; Pairis et al., 1992). Other subsurface observations are taken along water penstock pipes provided by Emosson SA company (Fig. 3a). The resulting model has been built by distinguishing eight geological formations (Fig. 4) with their structural relationships defined according to the geology observed in the field and described in the bibliography. Model views are shown in Figs. 4, 11, and 14. To better characterize the precise geometry of the synclinorium in its central part, we performed a smaller geomodel that allows a more detailled visualization of the synclinorium, distinguishing four formations within the Mesozoic series (Figs. 3a, 11 and 12). The 3D GeoModels and their associated data are provided in the repository.

4. Structures and cover/basement relationships in the Mont-Blanc/Aiguilles Rouges area

4.1. Geological background

4.1.1. Basement of the Aiguilles Rouges and Mont-Blanc ranges

Within the Aiguilles Rouges, the basement corresponds to gneiss and granites with a polymetamorphic Variscan history and overlain by Carboniferous/Permian sediments (e.g., Von Raumer and Bussy, 2004). During the Variscan history, the Aiguilles Rouges followed a clockwise P-T path with the formation of eclogites at maximum metamorphic conditions of ≥60 km depth and 700 ± 75 °C (Vanardois et al., 2022) possibly at ~395 Ma. High-K calc-alkaline granite emplacement occurred at 332 ± 2 Ma in the south of the massif (Bussy et al., 2000), with peak temperature, probably reached at 327 ± 2 Ma (Bussy et al., 2000) during crustal thickening. Migmatitisation occurred at 320 ± 1 Ma during decompression in part within the transpressive NE-SW right-lateral Berard-Emosson shear zone (Bussy et al., 2000; Genier et al., 2008; Simonetti et al., 2020). The long and narrow Vallorcine granite intruded that shear zone at 306.5 ± 1.5 Ma (Bussy et al., 2000). Its emplacement is interpreted to take place during NE-SW dextral strike-slip deformation (Brändlein et al., 1994). The granite is bounded in the south-east by the Vallorcine-Mieville shear zone (Fig. 3a) that is interpreted to be a late Variscan strike-slip shear zone (Reinhard and Preiswerk, 1927; Steck and Vocat, 1973) partly reactivated during the Alpine orogeny under low-grade metamorphic conditions (Kerrich et al., 1980; Steyrer and Sturm, 2002; Rolland et al., 2008). The precise history of that fault is most likely polyphase and still discussed. Post-Variscan cooling and exhumation were very fast, and sedimentation in the Salvan Dorénaz basin started at 308 ± 3 Ma (Moscovian, Carboniferous) by coarse detrital deposits and lasted until at least 295 ± 3 Ma (Asselian, Permian) (Capuzzo and Bussy, 2000; Capuzzo et al., 2003; Capuzzo and Wetzel, 2004). The Variscan gneiss and granites are unconformably overlain by Triassic sandstones. Within the Aiguilles Rouges Alpine metamorphism and deformation are milder than in the Mont-Blanc with a maximum temperature of 320 °C in the Carboniferous rock (Boutoux et al., 2016), and mostly brittle deformation (e.g., Von Raumer and Bussy, 2004).

Within the Mont-Blanc massif, the basement is very similar to the Aiguilles Rouges. The massif is mainly composed of a calc-alkaline granite intruding Variscan metamorphic gneiss. The granite has been dated by U/Pb on zircons at 304 ± 3 Ma (Bussy and Von Raumer, 1993).

4.1.2. Cover of the Aiguilles Rouges and Mont-Blanc ranges

On the western margin of the Aiguilles Rouges massif, the bottom of the Mesozoic sedimentary cover corresponds to a sandstone layer dipping 15° to 35° to the north-west that can be followed continuously for about 25 km (e.g., Amberger, 1959; Ayrton et al., 1987; Pairis et al., 1992) (Fig. 3a and b). The layer marks a clear stratigraphic and angular unconformity as it rests on Variscan gneiss with steep foliation (average N012, 70°E) (Fig. S3). The sandstone level is overlain conformably by red and green siltites, dolostones, and cargneule attributed to the Triassic (Collet et al., 1952; Ayrton et al., 1987; Pairis et al., 1992). The same succession is found at several localities along the unconformity and defines the Triassic autochthonous cover of the Aiguilles Rouges. Locally, white limestone is found above this series (Fig. 3a) and is attributed either to the Upper Jurassic (Collet et al., 1952; Ayrton, 1972)

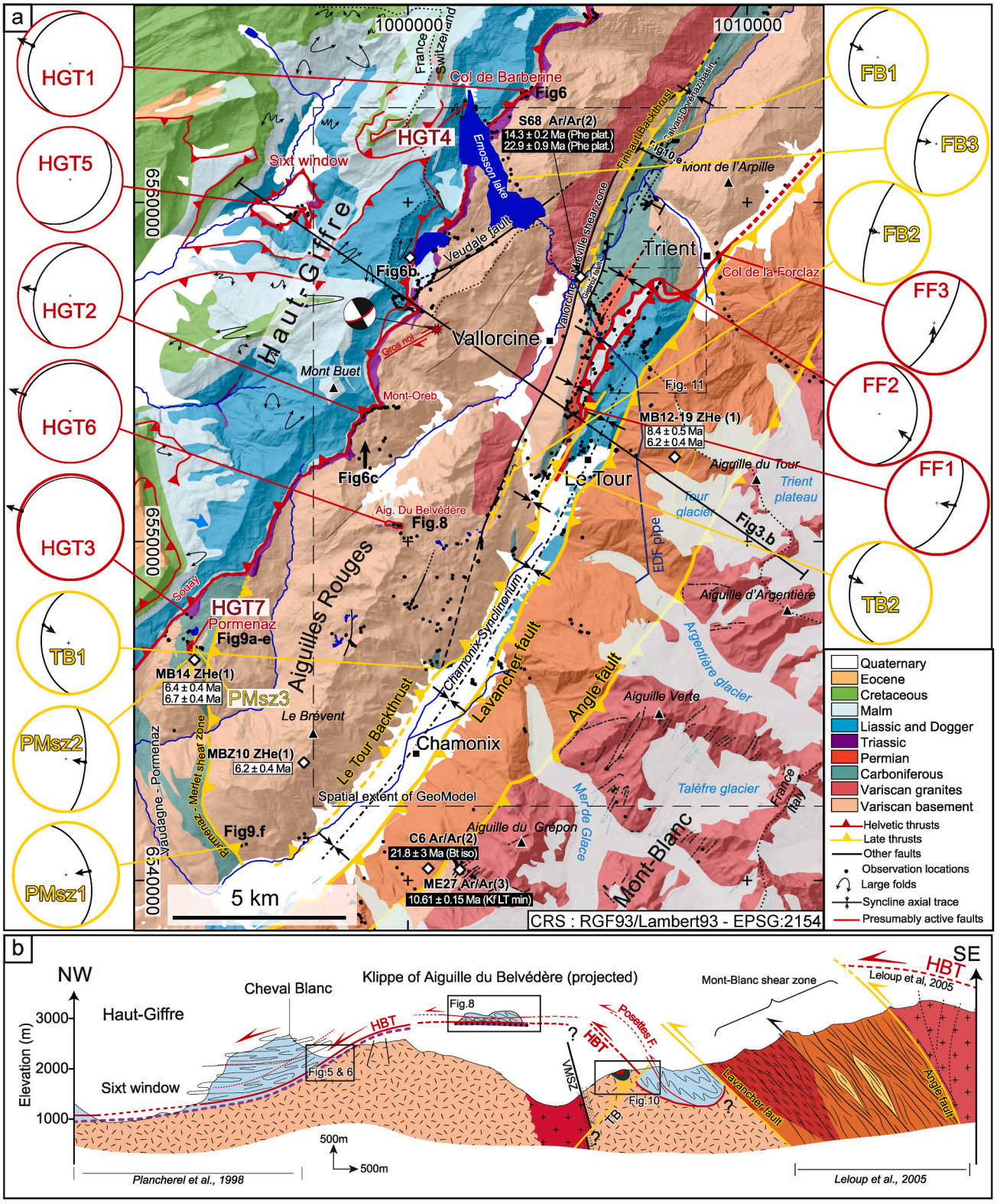

Fig. 3. Structure of the Chamonix Synclinorium. a) Structural map. Location in Fig. 1a. Structure of the Haut-Giffre cover is from Pfiffner et al. (2010). HGTx, TBx, PMszx, FFx, FBx are acronyms for sites corresponding to several locations (HBT: Haut-Giffre Décollement, TB: Le Tour back thrust, PMsz: Pormenaz-Merlet shear zone, FF: Forclaz fault, FB: Finhaut back thrust). Samples and datations references are (1: Boutoux et al., 2016; 2: Rolland et al., 2008 and 3: Leloup et al., 2005). ZHe: U/Th/He technique on Zircons; Ar/Ar: $^{40}Ar/^{39}Ar$ method. Bt.: Biotite; Kf.: Potassium-rich feldspar; Phe.: Phengite; Min.: Minimum age; Plat.: Plateau age; Iso.: Inverse isochrone age. The map without stereo plots and surcharge is available as Fig. S1. Stereo plots show mean fault or shear plane kinematics in each site (lower hemisphere equal-area projection, arrows showing upper bloc motion). Precise locations and sites are given in Table S1. Mean shear or fault plane measures reported in the stereo-plots are available in Table S2. Stereoplots with all the data from each site are available in Fig. S2. Dashed black frames correspond to the spatial extent of the GeoModel (Fig. 4) and the zoom in the Posettes area (Fig. 11) Cross-section. Location and legend on (a). All structural data, locations, sites, samples, and 3D GeoModels are provided in a repository, see Data Availability statement.

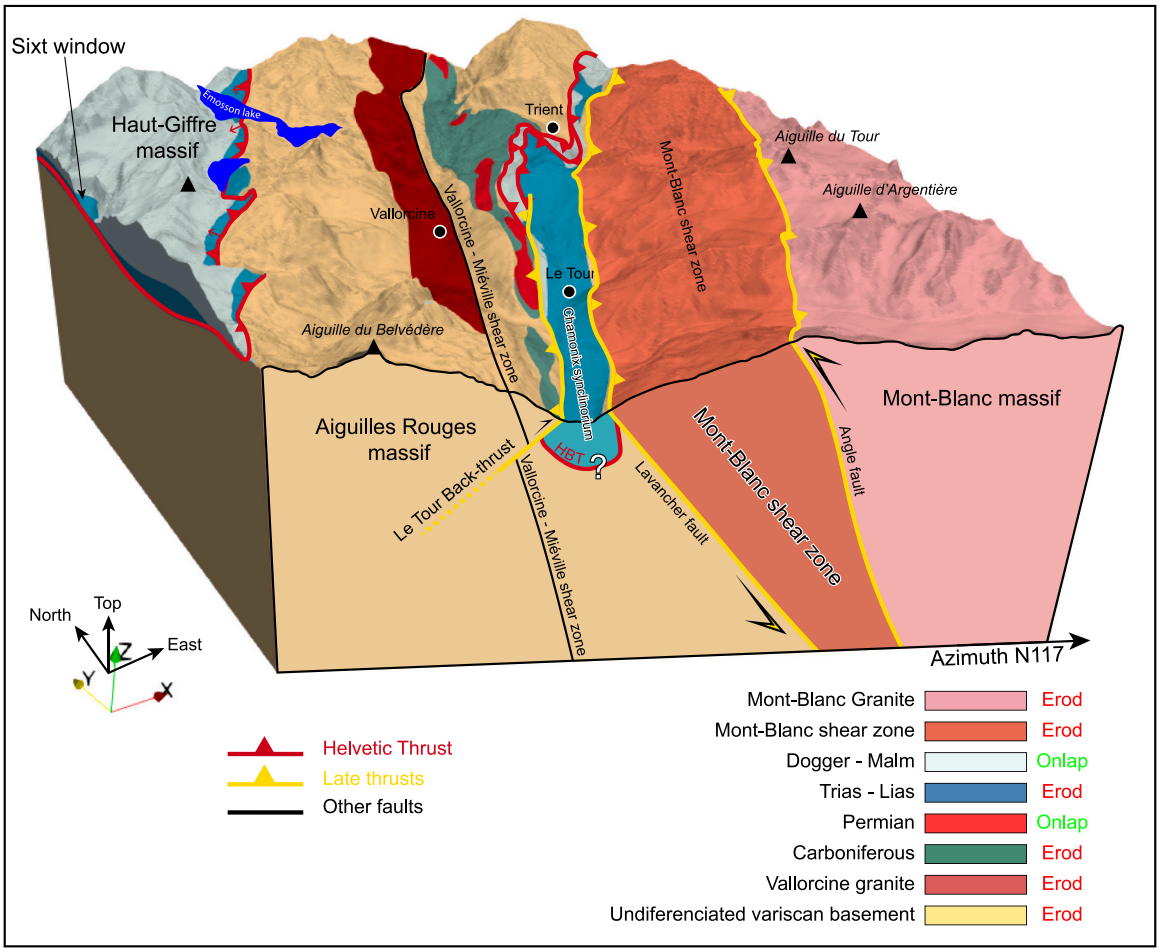

Fig. 4. View of the 3D GeoModel. The model is cross-cut perpendicularly to the structures across the Chamonix Synclinorium south of Le Tour village. See the associated stratigraphic pile and their relation that were used in the modeling.

or the Cretaceous (Ayrton et al., 1987, B. Pairis et al., 1973, Pairis et al., 1992). At other locations the succession is topped by Aalenian black slates, (Ayrton et al., 1987; Collet et al., 1952; Pairis et al., 1992). That Mesozoic series has been interpreted as an incomplete stratigraphic succession resulting from condensed sedimentation atop a Mesozoic horst (e.g., Corbin and Oulianoff, 1928; Ayrton et al., 1987).

The autochthonous/allochthonous nature of the cover above the Aiguilles Rouges basement is debated since decades. On the western flank of the Aiguilles Rouges the Mesozoic series above the Triassic have been considered as the para-autochthonous cover of the Mont-Blanc, belonging to the Morcles fold-nappe with insignificant thrusting with respect to the underlying basement (e.g., Escher et al., 1988; Bellahsen et al., 2014). In the highest peak of the Aiguilles Rouges, (Fig. 3a), Collet and Paréjas (1920) proposed that the Aalenian is thrust atop the Triassic, but the associated folds were later interpreted as local structures of minor importance (e.g., Corbin and Oulianoff, 1928; Ayrton et al., 1987). Similarly, white limestones in Pormenaz (Fig. 3a) have been considered allochthonous (Duparc et al., 1966; Dobmeier and Von Raumer, 1995) or autochthonous (Pairis et al., 1992).

The complex geometry of the Chamonix synclinorium has led to several interpretations. Some consider that the western boundary of the Chamonix synclinorium corresponds to the Triassic basal unconformity atop the Variscan gneiss (Ayrton, 1980; Ayrton et al., 1987). In the para-autochthonous hypothesis, that boundary is a Mesozoic normal fault bounding a half-graben filled by a thick series of *syn*-rift sediments, while the top of the horst presents an incomplete stratigraphic succession (e.g., Bellahsen et al., 2014; Boutoux et al., 2016). However, such a normal fault has never been characterized with direct evidence. Further north, in the Morcles massif, Badoux (1972) suggests that the Chamonix synclinorium corresponds to a deep Priabonian basin with detrital deposits sourced from the Aiguilles Rouges cover. Some argue that the Mesozoic sediments are not autochthonous but are thrust above the basement (Leloup et al., 2005; Pfiffner et al., 2010). Others consider that a major thrust within the Chamonix synclinorium separates the Mont-Blanc and Aiguilles Rouges autochthonous covers (Ayrton, 1980; Ayrton et al., 1987).

For most authors, the Chamonix synclinorium corresponds to the Morcles nappe root, but the interpretation varies on the style of deformation and amount of motion at the base on the nappe. For some, the Morcles nappe is a large anticline affecting both the basement and the cover (ductile basement fold nappe), the eastern boundary of the Chamonix synclinorium corresponding to the reverse limb of the fold, the external Mont-Blanc being the core of the fold and the normal limb rooting in the Angle fault (e.g., Epard, 1990; Escher et al., 1988, 1993) (Fig. 2a). However, no clear evidence of the folding of the Mont-Blanc basement has ever been published. Others propose that the external Mont-Blanc is not folded but corresponds to an Alpine reverse shear zone that brings the basement on top of the synclinorium (e.g., Bellière, 1956; Eltchaninoff, 1982; Butler, 1985; Leloup et al., 2005) (Fig. 2a). This ~3 km wide deformation zone is characterized by south-east dipping greenschist foliation trending from N000° to N066° (N034°; 53°E on average). Previously interpreted as resulting from three distinct Variscan deformation events (Belliere, 1988), this deformation is rather interpreted as a network of Alpine shear zones affecting Variscan mylonites, gneisses, and granites (Leloup et al., 2005). Shear criteria in the Alpine mylonites indicate top to the northwest thrusting (Leloup

et al., 2005). As the mineral and stretching lineation have pitches between 90° to 60° E (Average azimuth N100°), this corresponds to a thrust with a minor dextral component. The upper part of the Mont-Blanc shear zone corresponds to the Angle fault (e.g., Corbin and Oulianoff, 1928), and the lower one to the Lavancher fault (Fig. 3). The Mont-Blanc shear zone dies out southwest and northeast of the Mont-Blanc with a maximum offset between Chamonix and l'Argentière (Leloup et al., 2005). In that interpretation, the overturned stratigraphic sequence along the eastern boundary of the Chamonix synclinorium is a drag fold below the reverse fault. A variation of the basement fold nappe model is that the Mont-Blanc massif is part of a large anticline with the Mont-Blanc shear zone constituting the western reverse limb of that fold (e.g., Egli et al., 2017). Yet others consider that the linear shape of the Chamonix Synclinorium, and of the Mont-Blanc range, partly results from right-lateral strike-slip faulting along the Simplon Rhône - Belledonne fault system (Gourlay and Ricou, 1983; Hubbard and Mancktelow, 1992; Seward and Mancktelow, 1994).

4.2. Thrusting evidences in the Aiguilles Rouges

4.2.1. Thrusting along the western margin of the Aiguilles Rouges

In the north of the Aiguilles Rouges, next to the Col de Barberine (site HGT1, Fig. 3a), the autochthonous Triassic is folded, brecciated, and overlain by a sliver of Variscan migmatitic gneiss itself overlain by Triassic quartzite (Fig. 5a). While the sliver of gneiss does not appear to have been deformed at low temperatures the upper part of the Triassic level is strongly deformed, affected by recumbent folds (Fig. 5b), and strongly brecciated at the contact (Fig. 5a). The Triassic is overlain by a slice of limestone attributed to the Eocene, directly overlain by the limestones attributed to the Upper Jurassic (Collet et al., 1952) (Fig. 5a). The stratigraphic series is isoclinaly folded and foliated with S/C relationships suggesting a top to N285° shearing (Fig. 5c). These observations imply both the duplication of the Triassic/basement contact and intense top to the northwest shearing of a reverse stratigraphic series.

Further south, in the Mont-Oreb area (site HGT2, Fig. 3a), above the Triassic, white limestones attributed to the Upper Jurassic are strongly deformed. The limestones are metamorphosed to marbles and a strong west-dipping schistosity affects both the limestone and calcite veins (Fig. 6a). The cleavage bears a stretching lineation trending N280° (Fig. S4a) and asymmetry of the folds suggests a top to the west shear sense intensively sheared within a major decollement (Fig. 6c). At nearby location AR0184 (Fig. 6c), the underlying Triassic sandstones are also strongly deformed, affected by an isoclinal fold with the axial plane and axis parallel to the cleavage and stretching lineation respectively (Fig. S4b). The limestones are overlain by strongly foliated and folded black slates attributed to the Aalenian, implying decoupling between the two units and thus another fault at the top of the limestones (Fig. 6c). The same fault is visible atop the white limestones at several locations, for example near the Vieux Emosson lake (Fig. 3, Fig. 6b). Further south along the Souay river, (site HGT3, Fig. 3a), above the Carboniferous sediments of the Pormenaz basin, Triassic brecciated cargneules are overlain by white limestones that are metamorphosed to marbles and mylonitized (Fig. S5a). The marbles bear a well-visible stretching lineation, trending N288° and are also asymmetrically folded with an axis trending N032° (Fig. S5b). The lineation, shear plane, and asymmetry of the fold suggest a direction of shear towards the WNW.

Above the white limestone, the Aalenian black slates are affected by numerous spectacular isoclinal folds. The folds do not show a systematic vergence (Fig. 7a, b) and are even sometimes closed (Fig. 7d). Given the steepness of the topographic slopes, few measurements of these folds

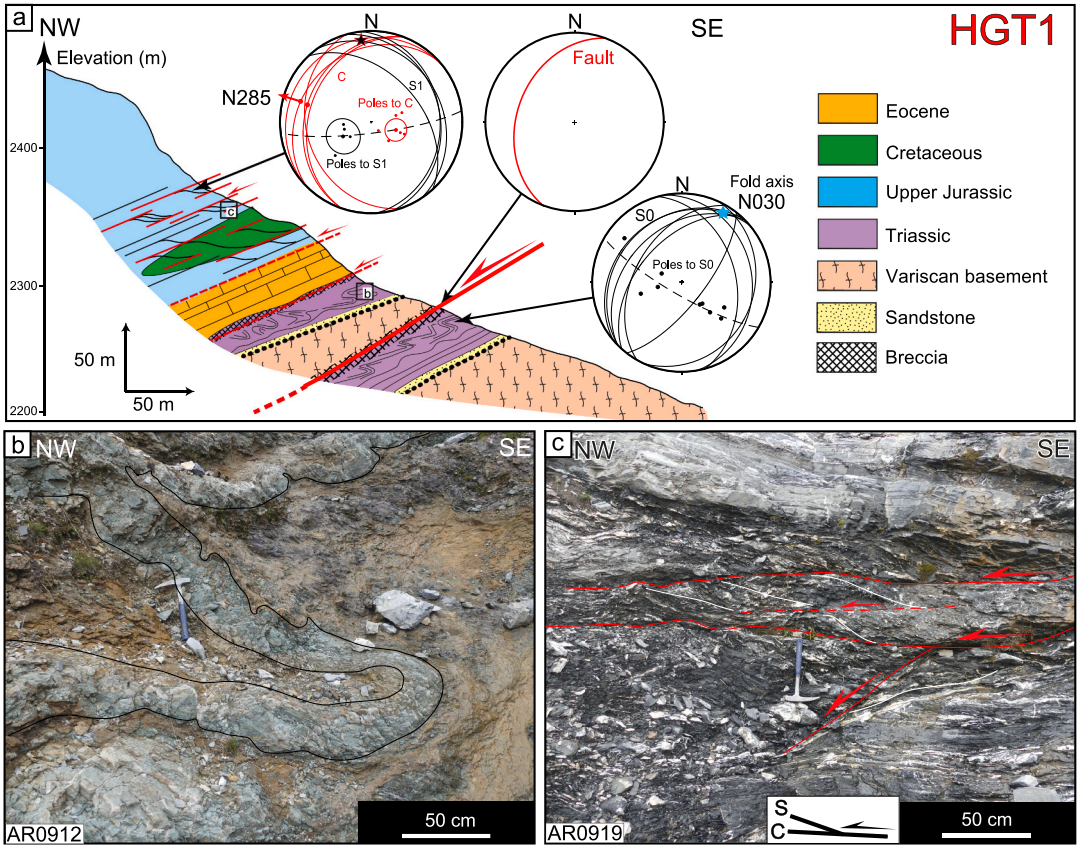

Fig. 5. Cover/basement relationships at the col. de Barberine (Aiguilles Rouges, site HGT1). a) Field cross-section along a talweg 300 m west of the Barberine pass. Stratigraphic ages from Collet et al. (1952). Stereo plots (equal-area, lower hemisphere projection) show the geometry of structures in b and c. b) Recumbent fold in red and green Triassic siltites at location AR0912. The fold axis trends N030°. b) Strongly sheared black shales at location AR0919. S/C relationships indicate top to the N285° shearing. (For interpretation of the references to colour in this figure legend, the reader is referred to the web version of this article.)

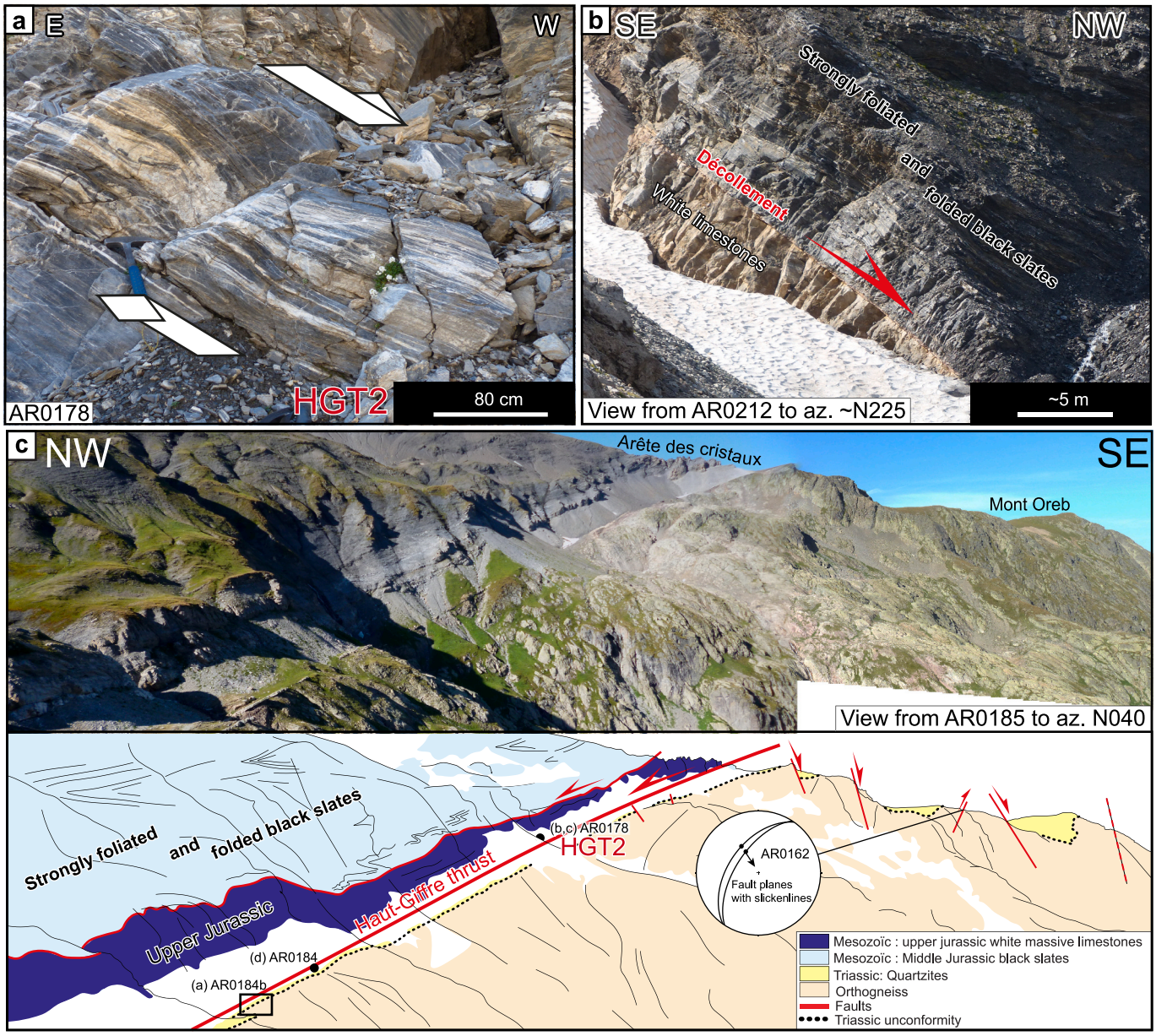

Fig. 6. Cover/basement relationships in the western side of Aiguilles Rouges. a) Shear zone at the base of the Mesozoic sedimentary cover, above the Triassic unconformity at site HGT2; b) Localized decollement above white limestones. The decollement is associated with a shear zone in the Aalenian slates; c) Picture at the top and interpreted panoramic view at the bottom of the Haut-Giffre thrust (view from location AR0185, towards ~N040°). The Upper Jurassic white limestones are visible as well as intense folding within the lower Mesozoic slates above.

have been performed, but north of the Emosson lake (Site HGT4, Fig. 3a) stratification and cleavage measurements indicate two families of fold axis trending N209° and N280° and sharing an almost horizontal axial plane (Fig. 7c). Such folds are widespread in the Haut-Giffre Mesozoic cover (Fig. 3a).

We interpret all these field observations as reflecting a major ~500 m thick shear zone affecting the Mesozoic cover above the Aiguilles Rouges basement. We term the base of that shear zone the Haut-Giffre Thrust (HGT). The direction of shearing is given by the orientation of the stretching lineation and the shear sense is top to the WNW motion (Fig. 3a). Within the shear zone, several folds are sheath folds that have highly curvilinear axes, with some axis parallel to the direction of transport. Such folds occur in shear zones with a high simple shear strain ($\gamma \geq 10$) (Cobbold and Quinquis, 1980; Quinquis et al., 1978; Lacassin and Mattauer, 1985).

The present-day dip of the HGT with its top to the WNW motion would correspond to a normal fault configuration (Fig. 6c). But local basement duplication implies that the fault is an additive as it duplicates formations and is thus more probably a tilted thrust. Slices of relatively young formations (Upper Jurassic in the south, Eocene in the north) near the base of the shear zone suggest that it is a sheared reverse limb, equivalent to the reverse limb of the Morcles nappe outcropping <15 km to the northeast (e.g., Escher et al., 1993).

West of the Aiguilles Rouges, the Giffre river has dug a deep valley in the Mesozoic sediments. In this valley, 4 km northeast of Sixt-Fer-a-Cheval village, there is a small outcrop of the basement (Site HGT5, Fig. 3a). There, the Variscan basement corresponds to chlorite bearing schist with a nearly horizontal foliation and is topped unconformably by Triassic sandstones (Fig. S6a). Above, the Triassic succession (sandstone, dolostone, green and red siltites) is nearly horizontal, itself overlain by intensively folded and sheared black slates with shear planes trending N038°; 32 SE (Fig. S6b). This outcrop is therefore a window through the

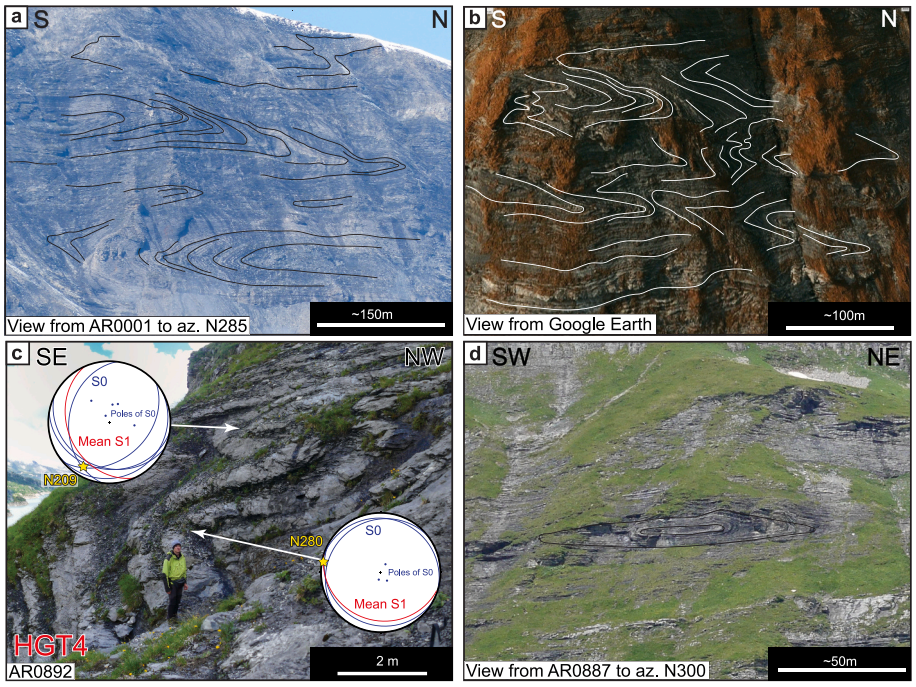

Fig. 7. Folding of the Mesozoic cover on the western flank of the Aiguilles Rouges. Locations in Fig. 3a. a) Large isoclinal folds on the Haut-Giffre massif seen from the Montagne des Posettes. Some stratifications are highlighted in black. b) Google Earth™ view of the slope above the Emosson lake. Some stratifications are highlighted in white; c) Two different types of folds affecting the Mesozoic cover above the Emosson lake (site HGT4): stereo plots (equal-area, lower hemisphere projection) show the bedding and cleavage of the folds: one with N280 trending axis, and the other with N209 trending axis.; d) Entirely closed sheath fold above Emosson lake (view from location AR0887, towards azimuth ~N300°).

Haut Giffre thrust. That window is an important constraint for the geometry of the 3D GeoModel (Fig. 3b, Fig. 4).

4.2.2. *Thrusting atop the Aiguilles Rouges*

Atop the Aiguilles Rouges (Aiguille du Belvédère, site HGT6), outcrops Mesozoic sediments interpreted as a buttress of an autochthonous incomplete series deposited atop a Mesozoic horst (e.g., Corbin and Oulianoff, 1928; Ayrton et al., 1987). However, if the basal part of the series is the autochthonous level of Triassic sandstone described above, the overlying dolostone layers are affected by intense northwest-verging folds with N032° trending axis and south-east dipping axial planes (Fig. 8a, b, and c), while the upper part of the summit is composed of flat-lying (sub-horizontal) black slates, with a stretching lineation striking N285° (Fig. S7a). Our interpretation is thus rather that the Mesozoic cover at this location is affected by two main top-to-the-NW flat faults (Fig. 8a), with transport direction towards ~N310° (Fig. S7b) for the bottom one and ~N285° for the top one (Fig. S7a). These faults most likely connect with the Haut-Giffre thrust located <2.5 km away (Fig. 3). Because the peak is in a high-mountain area, access is quite challenging. Therefore, we acquired high-resolution drone images, to build a 3D photogrammetric digital elevation model (DEM). Fig. 8a is a screenshot of the model. See data Availability for more information and links to visualize and download the model.

Seven kilometers southwest of the Aiguille du Belvédère, another buttress of limestones atop the basement is described at the Crête Blanche de Pormenaz (site HGT7, Fig. 3a). At this location, the Triassic sandstones rest on dark Carboniferous series and are overlain by white limestones (Fig. 9a). The Triassic sandstones are affected by a cataclastic foliation (Fig. 9b). The bottom of the limestone is also deformed and marmorized, with indications of foliation boudinage (Fig. 9c), suggesting that the basal contact of the limestones and the Triassic is tectonic rather than stratigraphic. This implies that the Mesozoic forms a small klippe. We thus interpret the basal contact as part of the Haut-Giffre décollement rather than an undeformed stratigraphic contact.

4.2.3. *Thrusting of the cover on the eastern side of the Aiguilles Rouges: The Forclaz Fault*

In the northwest of the Chamonix synclinorium, the Mesozoic sediments rest on top of the Aiguilles Rouges basement along an east-dipping contact: the Forclaz Fault (Fig. 3, and Fig. 10a). At site FF1 the Mesozoic rocks rest on top of Carboniferous sandstones and are strongly deformed with a cleavage steeply dipping to the east and a downdip lineation. A few kilometers further north at the foot of the Croix de Fer summit (site FF2, Fig. 3a), the contact cannot be observed directly but the overlying upper limestones appear much less steep and bear a well-printed stretching lineation trending N130° (Fig. 10a). The basal contact is well exposed at location AR0190 (site FF3, Fig. 3a, 10b, and c) along the road to the Forclaz pass, where Mesozoic sediments are separated from gneiss by a 50 cm thick quartz level (Fig. 10b). This quartz level was previously interpreted as the basal Triassic sandstone layer resting unconformably atop the Variscan gneiss (Ayrton, 1980; Ayrton et al., 1987). A thin section of the sample Are042, from that quartz layer, has been cut perpendicular to the fault contact and parallel to the lineation. At the micro-scale, the quartz grains are angular with a size below 100 μm. This suggests that the layer more likely corresponds to a deformed level separating the sedimentary rocks from the basement (Fig. 10d). Crystallographic Preferred Orientation (CPO) analysis of quartz using Electron back-scattered diffraction (EBSD) of sample ARe042 thin section has been performed (Fig. 10c) (technical information about the analysis is provided in Table S3). Data were processed with the MTex algorithm (Hielscher and Schaeben, 2008), 5788 grains were identified on 343,007 pixels, using a misorientation threshold of 15° and minimal grain size of 5 pixels. The presented stereographic plot (equal area, lower hemisphere) shows the orientations of the crystallographic axis (<a> and <c>), with colour according to point density (one point per grain identified). The CPO suggests the activation of the quartz crystallographic basal plane, at about 350° – 400 °C (Passchier and Trouw, 2005), with a top to the west reverse shearing along the <a1> axis trending N122° (Fig. 11c and d).

We interpret the Forclaz fault as a west verging thrust because (i) site FF3 shows a top to the northwest thrusting of the Mesozoic sediments above the Aiguilles Rouges basement (Fig. 10b and c). (ii) As already pointed out by Ayrton (1980), folds within the overlying Mesozoic have an NW vergence.

4.2.4. *Thrusting within the Chamonix synclinorium: The Posettes fault*

Within the Mesozoic synclinorium, the Posettes fault dips to the southeast, runs subparallel to the Forclaz Fault, and brings Middle

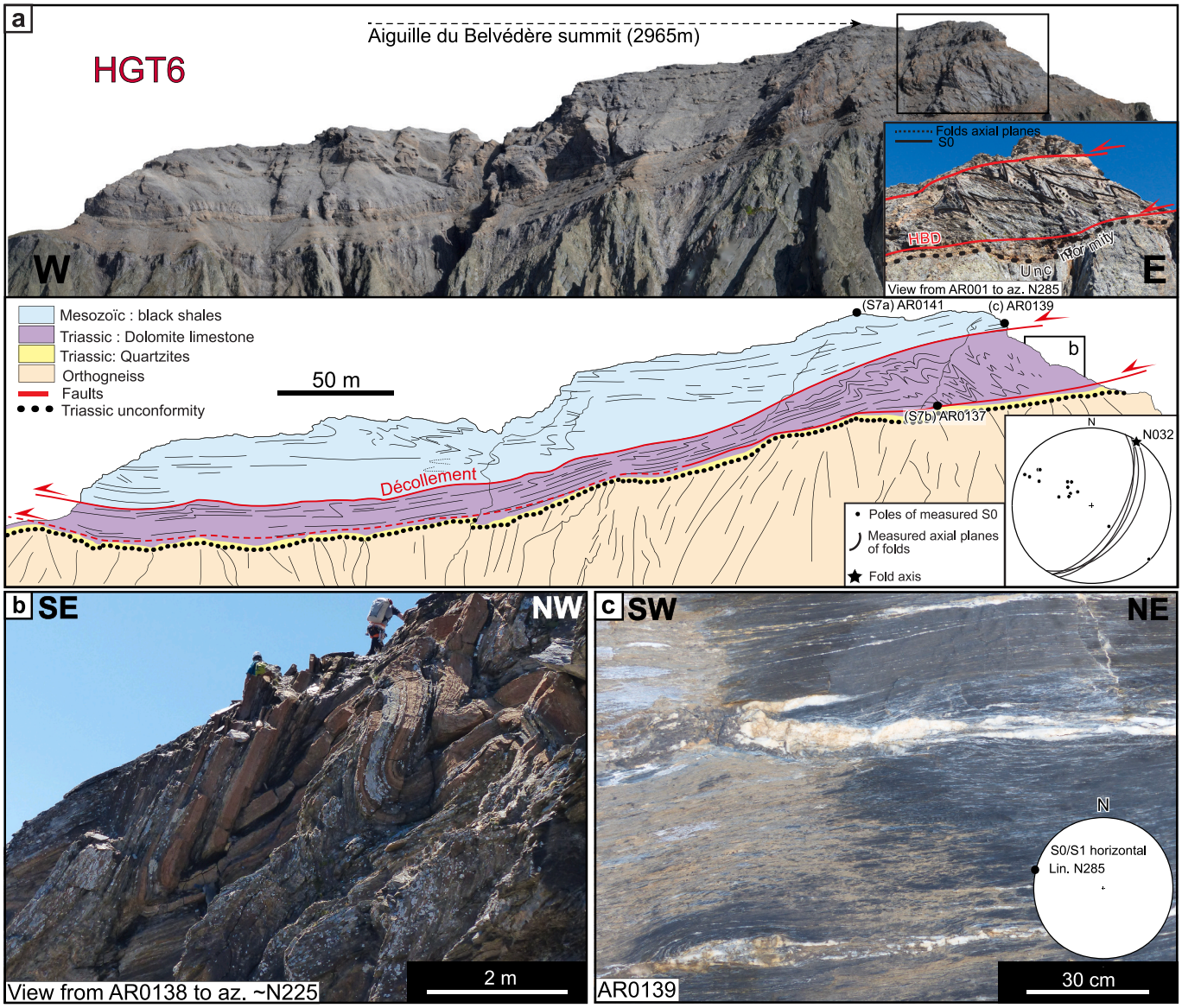

Fig. 8. Cover/basement relationships at the Aiguille du Belvédère. a) Panorama of the summit view from the south. Top: a screenshot of the 3D photogrammetric model. Bottom: geological interpretation. Insets: picture and stereo-plot (equal area, lower hemisphere projection) of northwest verging folds within the Triassic dolostones. The folds have an axis trending N032°. b) Tight northwest verging folds within the Triassic sedimentary cover (view from location AR0138, towards azimuth N225°). The folded dolostones bears a stretching lineation striking N130° (see Fig. S7b); c) Highly deformed mesozoïc black slates with calcite isoclinal folding and boudinage (location AR0139) bearing a stretching lineation striking N285° (see Fig. S7a).

Jurassic black slates on top of strongly folded Upper Jurassic limestones (Fig. 10a, Fig. 3a and b). This geometry is well-constrained in the 3D models, particularly in the Montagne des Posettes zoom-in model (Fig. 11). The black slates are also strongly folded, describing a large fold with a steep axis (~ trend 70° / plunge 68°) and with a core of middle Jurassic limestones that constitute the Croix de Fer summit (Ayrton, 1980). Further east the Mesozoic series dip to the southeast and are cut by the Mont-Blanc shear zone that rises the Mont-Blanc basement (Leloup et al., 2005) (Fig. 10a).

The folds with steep axis have been interpreted as reflecting strike-slip motion along the Rhône valley being part of the Simplon-Rhône dextral fault (Hubbard and Mancktelow, 1992). As Ayrton (1980) we rather interpret them as large sheath folds, like those observed in the Haut-Giffre, some of them with axis nearly parallel to that of the shearing direction within the cover décollement zone. In this interpretation, the base of the Mesozoic cover of the Chamonix synclinorium corresponds to the same Haut-Giffre Thrust.

4.2.5. *Synthesis on the thrusting above the Aiguilles Rouges*

To sum up, the faults and shear zones found on the western limb (Haut-Giffre thrust - HGT), atop (Pormenaz and Belvédère klippes), and on the eastern limb (Forclaz fault) are segments of the same thrust at the base of the Helvetic nappes: the Helvetic basal Thrust (HBT) (Fig. 3b). Motion on the HBT is everywhere top to the WNW and its antiformal shape results from the later updoming of the Aiguilles Rouges. The HBT is nearly parallel to the cover/basement interface and is the base of a strongly sheared reverse limb of a recumbent fold. It corresponds to the base of the Morcles Nappe. It affects the Jurassic and Triassic series, and even locally the basement.

4.3. *Reverse faults in the Aiguilles Rouges range and the Chamonix Synclinorium*

4.3.1. *Pormenaz-Merlet shear zone*

The southwest side of the Aiguilles Rouges is characterized by the

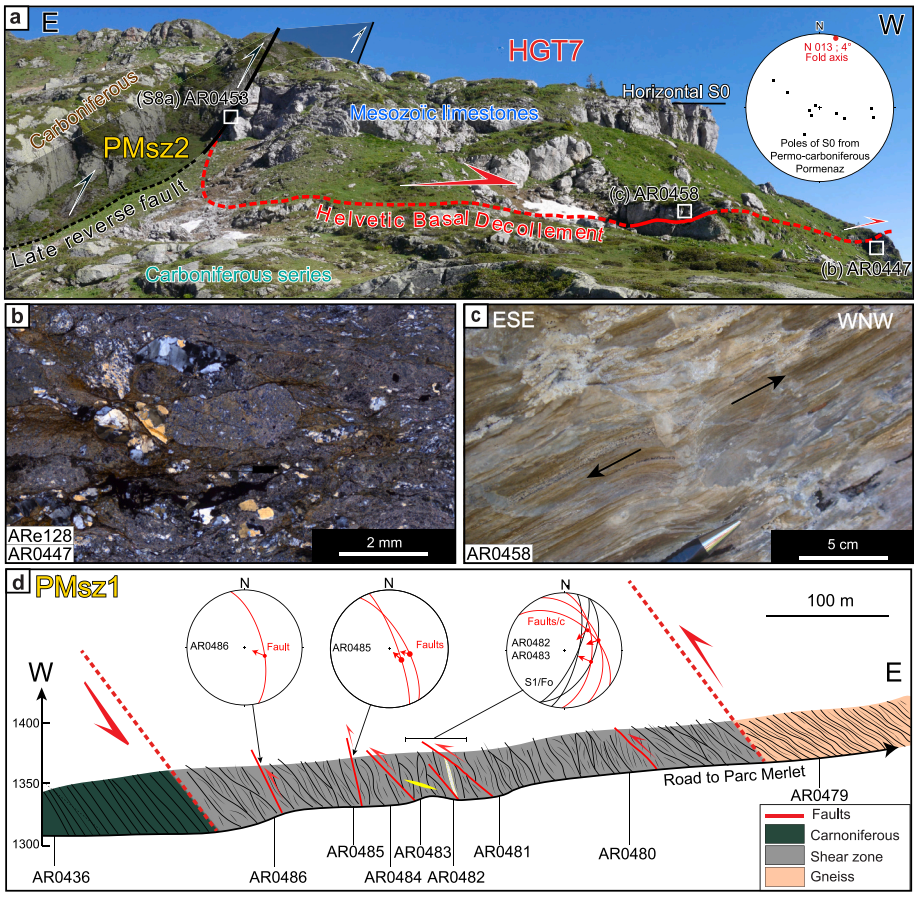

Fig. 9. Cover/basement relationships near Pormenaz (Aiguilles Rouges massif). a-c) The Crête Blanche klippe. a) General view of the klippe, the limestones are thrusted westward above a basal thurst, before being offset by a late steep thrust (See also fig. S8a). Stereo-plot (lower hemisphere, equal area) on the right shows poles of bedding planes of the Carboniferous sediments in the Pormenaz zone: average folds axis dips ~4° to N013°. B) Foliation and metamorphosed quartzite (location AR0447). c) Marmorized limestones showing foliation boudinage, indicating ESE-WNW-oriented stretching (location AR0458). d) Cross-section of the Merlet-Pormenaz shear zone along the road to the Merlet parc. Stereo-plots (lower hemisphere, equal area) show fault planes and shear planes along the section.

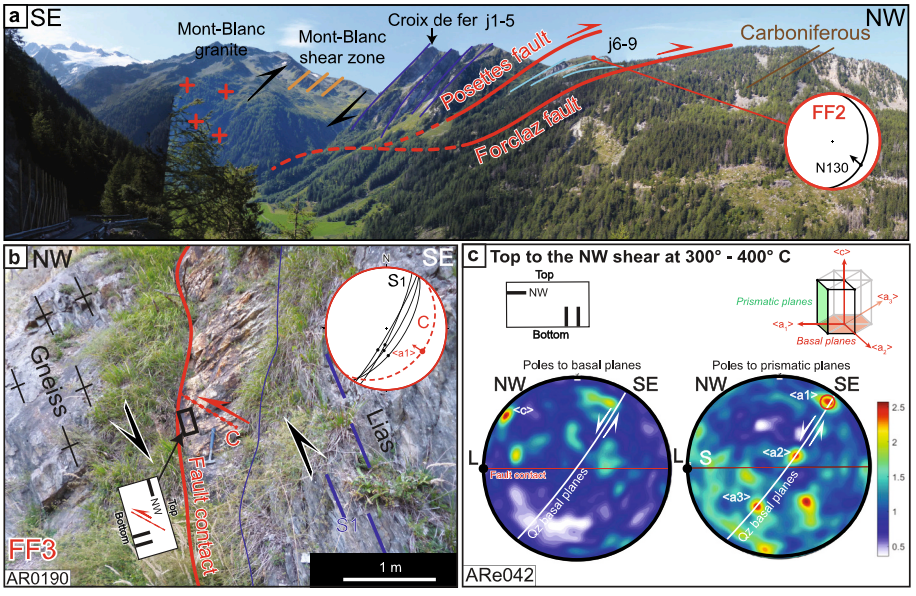

Fig. 10. Cover/basement relationships in the north of the Chamonix Synclinorium. a) The Mont-Blanc shear zone, Posettes, and Forclaz fault viewed from the north. b) Forclaz Fault quartz layer at site FF3 (location AR0190). Plotted S1 refers to the cleavage in the Liassic slates, dashed red line corresponds to the shear plane inferred from CPO analysis, plotted lineation refers to the <a1> direction; c) Crystallographic preferred orientations (CPO) of <c> and <a> axis of quartz sample ARe042 measured with EDSD technique. Equal area projection, lower hemisphere, colour as a function of the measurement density, fault contact is plotted as horizontal (red line) and the lineation is in the NW-SE direction (black circle). The pattern suggests an activation of the crystallographic basal plane along the <a1> direction, compatible with a top to northwest sense of shear. (For interpretation of the references to colour in this figure legend, the reader is referred to the web version of this article.)

contact zone between gneiss and Carboniferous sediments (Site PMsz1, Fig. 3a). The contact corresponds to a 350 m wide shear zone with foliation north-south striking and steeply dipping (~70°) to the west (Fig. 9d). Shallower shear planes trend from N156° to N182° and bear lineations trending N050° to N130°, indicating a top to the west thrusting (Fig. 9d).

Returning to the Pormenaz Crête-Blanche (Site PMsz2, Fig. 3a), the white limestones described in Section 4.2.2 abut against the Carboniferous series. This contact corresponds to a steep reverse fault trending N003°;70 SE that brings the Carboniferous on top of the Mesozoïc limestones (Fig. 9a, Fig. S8a). A few decameters to the east the same shear zone brings the Variscan gneiss of the Aiguilles Rouges on top of the Carboniferous (Site PMsz3 Fig. 3a). There, flat reverse faults with striation trending N130° affect the carboniferous, showing top-to-the-

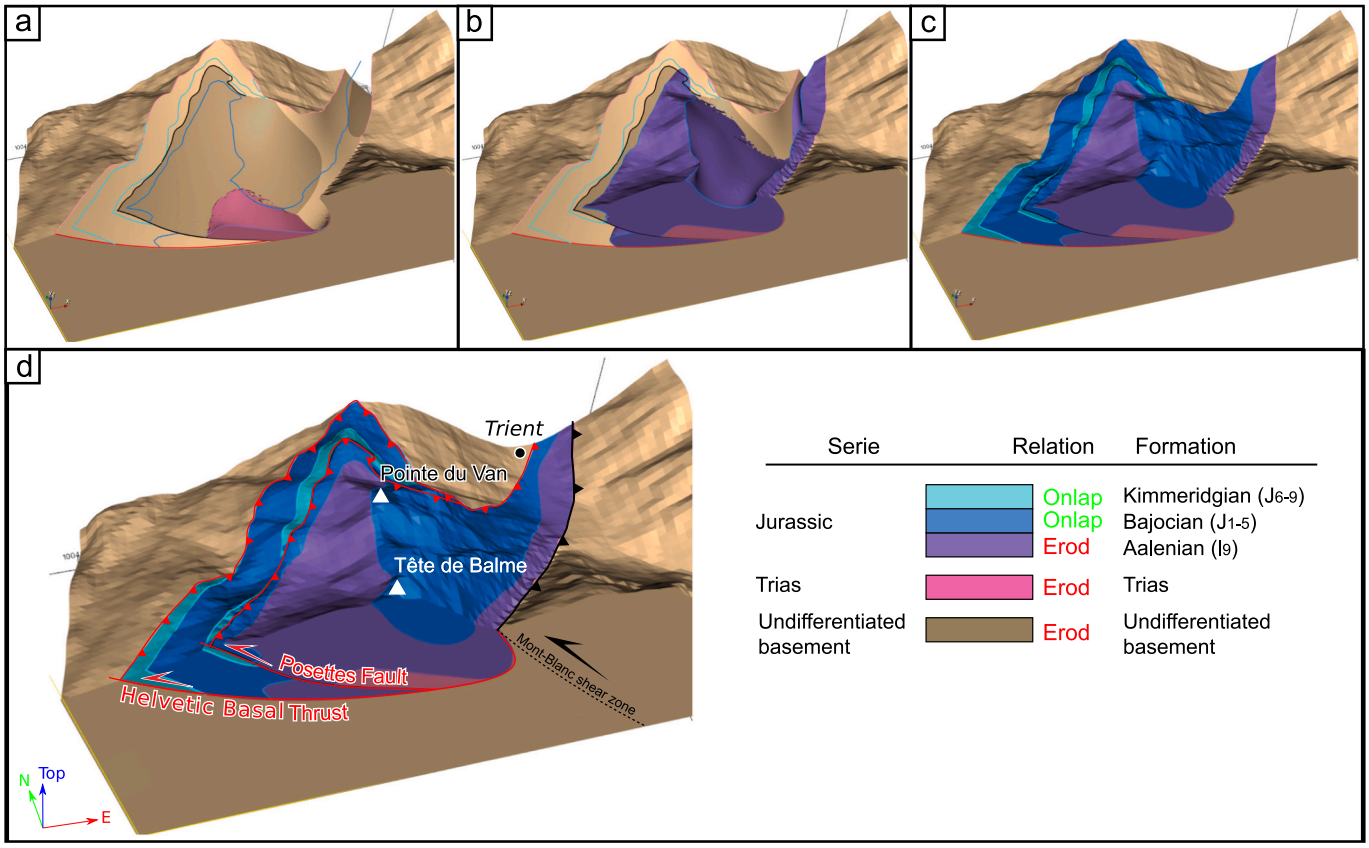

Fig. 11. Views of 3D GeoModel, from the central part of the synclinorium: the Montagne des Posettes. a) to d), views of the GeoModel with the different layers removed. The basal decollement and the Posettes thrust are highlighted in red. The Mont-Blanc shear zone is not modeled here, however, its position is shown in the figure. The stratigraphic pile of the model as well as the relationship between them is shown in d. (For interpretation of the references to colour in this figure legend, the reader is referred to the web version of this article.)

north-western shearing (Fig. S8b).

These observations lead to the interpretation of the eastern boundary of the Carboniferous sediments as a continuous reverse shear zone, as already suggested by J. L. Pairis et al. (1992) and Dobmeier and Von Raumer (1995). The fact that the shear zone bounds the Crête-Blanche klippe imply it is younger than the Haut-Giffre Thrust. The Carboniferous sediments below the shear zone are affected by folds with an axis striking N013° (Fig. 9a), suggesting an ~*E*-W direction of compression, compatible with the measures of the faults above.

4.3.2. *Back thrusting on the eastern side of the Aiguilles Rouges*

North of the Aiguilles Rouges, at the limit between the Salvan-Dorenaz Carboniferous – Permian basin and the Aiguilles Rouges basement (Site FB1, Fig. 3a) the Permian sediments show an ~N032° subvertical schistosity and west-dipping reverse shear planes trending N012° on average (Fig. 12a and b). These observations indicate that at this location the Variscan basement is thrust towards the east over the Salvan-Dorenaz basin, along a previously unreported thrust fault that we name Finhaut back thrust. According to the published geological map (Collet et al., 1952), the Finhaut back-thrust probably extends 5 km to the south (Fig. 3a). Within the basin, the sediments are strongly folded with folds axis trending ~N030° and steep axial plane schistosity trending N020° on average (Fig. 12c). Similar folds are found in the Carboniferous/Permian sediments of the Posettes area on the other side of the valley. A previously unreported ~N020° trending normal fault, the Gietroz fault, offsets the basin (Fig. 12c). A thin section of sample ARe096 (Fig. S9) indicates a normal shear sense on the fault. Both the Finhaut back thrust and the folds affecting the Salvan-Dorenaz basin could have formed coevally during an ~N110° compression phase, while the Gietroz fault is probably younger.

West-dipping reverse faults and shear zones trending ~N020°, whilst never described in the literature, are relatively common in the eastern part of the Aiguilles Rouges. Another example can be found further south (site FB2, Fig. 3a), where reverse faults trend N017;77°W with clear evidence of thrusting towards the southeast. Numerous such faults are also visible on the eastern shore of the Emosson Lake (site FB3, Fig. 3a) striking on average N015°; 59°W with striations azimuth trending ~N105°. Such a fault trending ~N033; 60°W with a striation with a pitch of 75°N is also visible at site HGT1 (location AR0162) in between possibly earlier normal faults (Fig. 6c).

The brittle regime of these faults suggests they are occurring at low pressure/temperature conditions and could be related to recent deformations. These observations suggest that back thrusting in the Aiguilles Rouges has been overlooked and may play an important role in the structuration and exhumation of the massif.

Further south in the Chamonix valley, most of the synclinorium western border is hidden by Quaternary deposits. However, a large outcrop of limestones attributed to the Jurassic (Ayrton et al., 1987) is visible at site TB1 (Fig. 3a). These limestones are affected by a schistosity that trends N072°;40°N and are overlain by the Aiguilles Rouges basement composed of Variscan gneiss and a Permo-Carboniferous tight syncline (Fig. 13a). Just above the contact, the Permian green siltites are foliated (N002°;44°E) and a bear mineral lineation (N126°). The thin section cut parallel to the lineation shows a clear thrust top to the southeast with S/C criteria (sample ARe033, Fig. 13c). At this location, the Aiguilles Rouges basement is therefore thrust above the cover.

Six kilometers further north near le Tour village (site TB2, Fig. 3a) Mesozoic sediments are also found below the Aiguilles Rouges basement. The Permian green siltites are foliated, with S/C criteria indicating a top to the southeast reverse shear (Fig. 13b and d). That contact

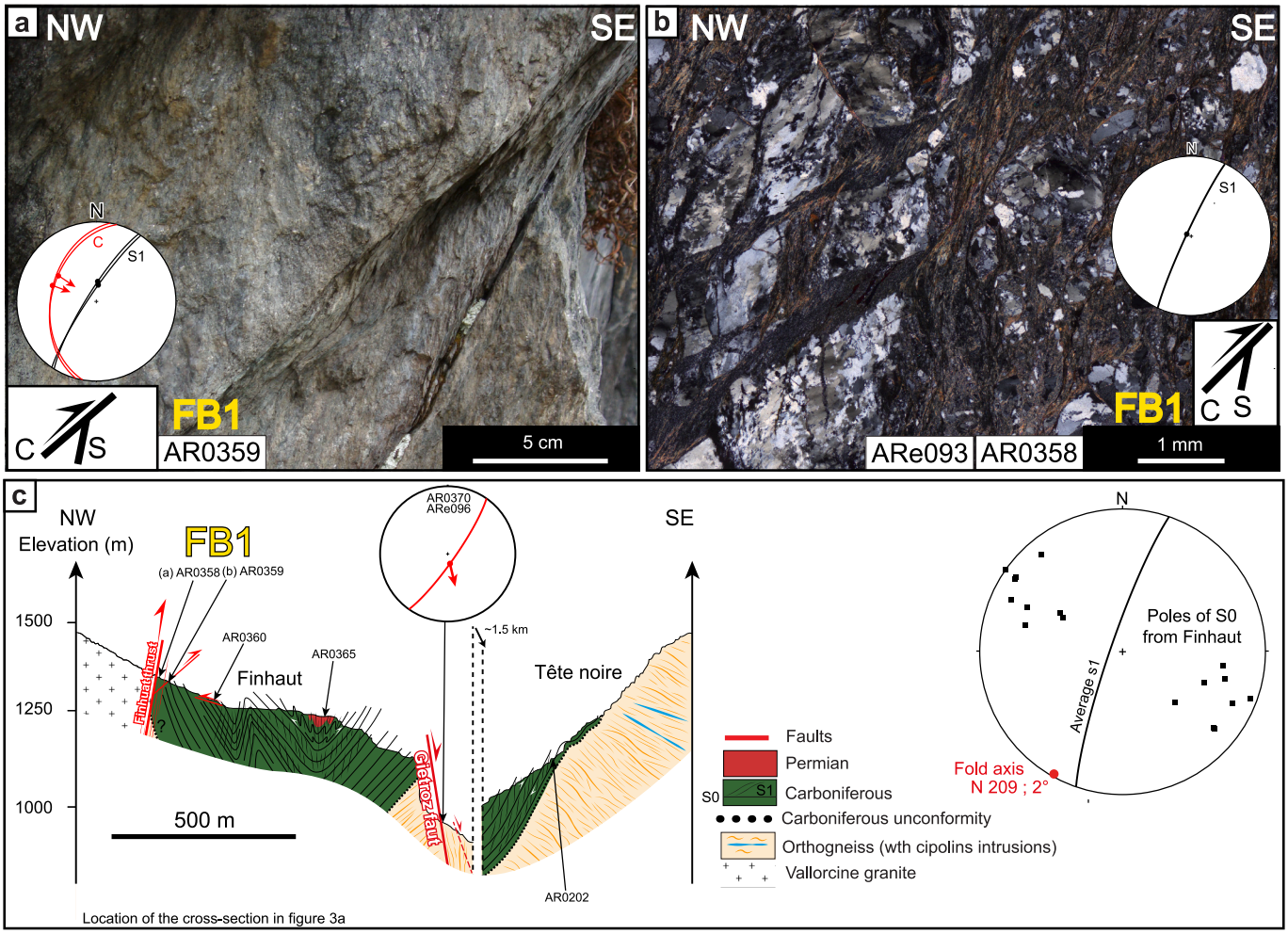

Fig. 12. The Finhaut back thrust. a) Thin section of sample ARe093 of the Finhaut thrust (site FB1, Fig. 3a). Greenschist foliation strike N025°; 85°W and S/C relationships imply a reverse motion. b) Shear planes within Carboniferous sediments in the footwall of the Finhaut back-thrust at location AR0359. Shear planes (C) strike N010°; 42°W, C/S relation implies a top to the south-east sense of shear. c) Cross-section across the Salvan-Dorénaz basin, see Fig. 3a for location. Stereo plots (equal area, lower hemisphere projection) in the Finhaut area the average folds axis dips 2° to N209°.

continues ~2 km towards the northeast (Fig. 3a). The two faults at sites TB1 and TB2 have the same direction and the same kinematics and are interpreted as a back-thrust fault of the Aiguille Rouges above the Chamonix synclinorium that we call the Le Tour Back thrust (Fig. 3a).

Further south there is no outcrop of Mesozoic sediments and the Tour back-thrust cannot be mapped. We infer that this fault is hidden by the Quaternary deposits (Fig. 3a). Cartographically the Tour back thrust is parallel to the Finhaut back thrust, thus they have possibly been activated at the same time. Le Tour back thrust is seen in the GeoModel, bringing the Posettes Permo-Carboniferous syncline atop the Chamonix Synclinorium (Fig. 4 and Fig. 14a, b, and c).

5. Implications on the structural evolution of the Mont-Blanc and Aiguilles Rouges massifs

5.1. Relative timing of the main structures

After the deposition of Mesozoic and Cenozoic sediments, the first widespread shortening tectonic phase in the area involved thrusting of the Mesozoic/Cenozoic cover towards the west along a relatively flat structure that we term the Helvetic basal thrust (HBT) (HBD of Leloup et al., 2005). That structure was later cut and offset by steeper thrusts on both sides of the Chamonix synclinorium: the Mont-Blanc shear zone on the western edge of the Mont-Blanc (Eltchaninoff, 1982; Butler, 1985; Leloup et al., 2005; Egli and Mancktelow, 2013) and the Le Tour (Leloup et al., 2005) and Finhaut back thrusts along the eastern edge of the Aiguilles Rouges.

The relative chronology of the Pormenaz-Merlet shear zone is difficult to establish. Towards the south, the shear zone appears to be cut by the Le Tour back thrust and/or the Mont-Blanc shear zone as it is not seen on the southern side of the Chamonix valley, but the precise field relationships are obscured by Quaternary deposits (Fig. 3). The shear zone cuts and offset the Crête Blanche klippe that we interpret as part of the HBT (Fig. 9a), but further to the north the shear zone does not significantly offset the HBT (Fig. 3). We interpret this apparent inconsistency as due to a decrease of the Merlet-Pormenaz shear-zone offset towards the north, whilst this point still requires further field investigations. We thus infer that the Merlet-Pormenaz shear zone is younger that the HBT and older that the Mont-Blanc shear zone. It is thus an Alpine structure that has never been described as such.

The Vallorcine fault has a polyphase history and corresponds in fact to several structures active both before and during the Cenozoic, but it appears to not significantly offset the Le Tour back-thrust.

The Gietroz normal fault has a limited extent and offsets (Fig. 12c) which renders its relative timing difficult to determine. The main extension phases in the area (Early Jurassic and Eocene-Oligocene) are antecedent to the Alpine shortening phases, but the fault seems to offset the folds associated with the Finhaut back thrust (Fig. 12c).

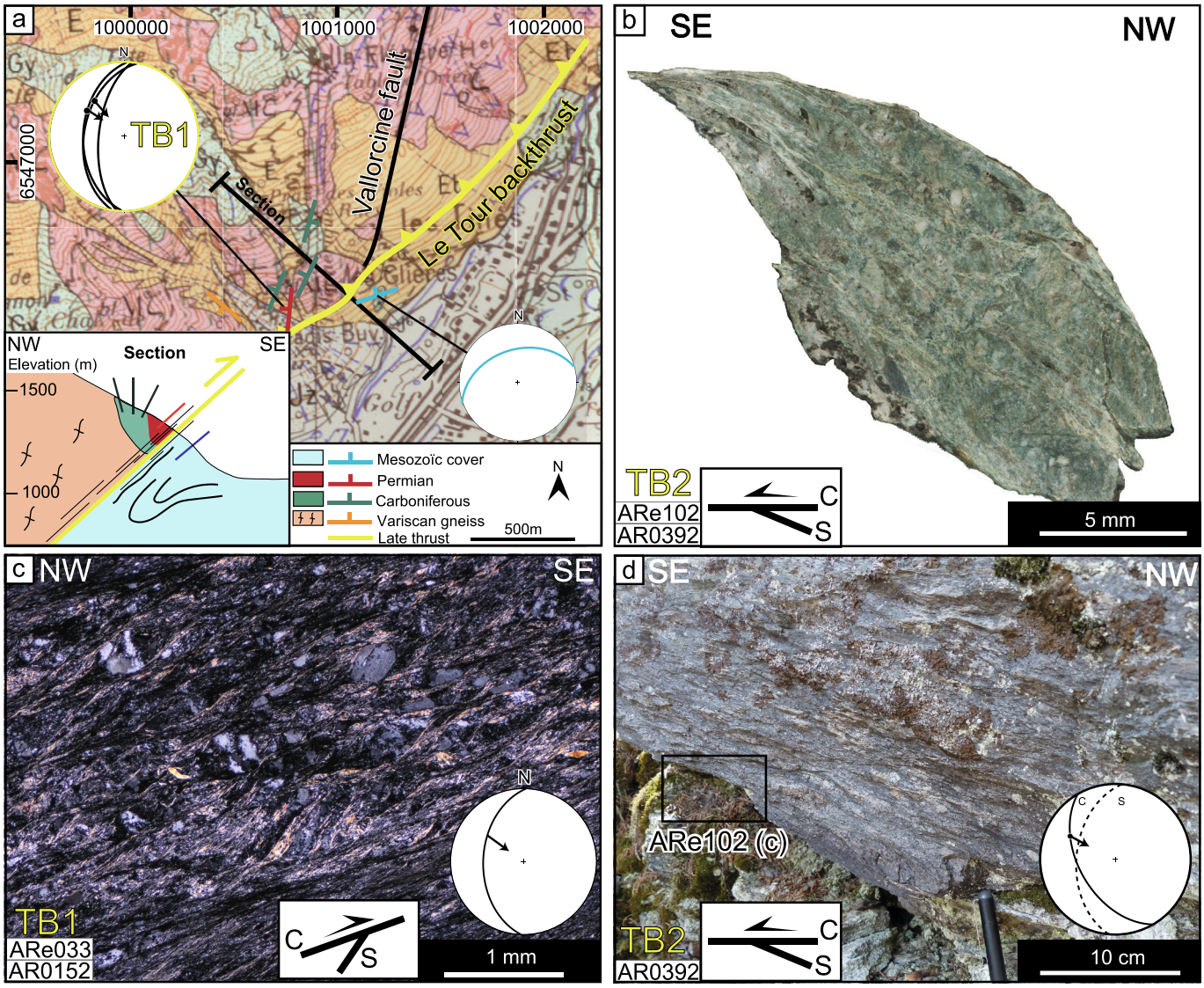

Fig. 13. Le Tour back thrust. a) Structural map and cross-section (inset). The background is the 1:50.000 geological map (Ayrton et al., 1987). Stereo-plots (lower hemisphere, equal-area projection) show the orientations of the schistosity in the Mesozoic sediments in the over-thrusting Permian schists. b) Thin section of the sample ARe102, S/C relationship suggests top to the south-east reverse sense of shear; c) Thin section of sample ARe033 cut parallel to lineation. S/C relationship suggests top to the south-east reverse sense of shear. d) Location of sample ARe102 from location AR0392, S/C relationships indicates top to the south-east sense of shear.

5.2. Amounts of Cenozoic exhumation

The Cenozoic shortening has led to the exhumation and high altitude of the Aiguilles Rouges and Mont-Blanc ranges. It is now established that the Triassic sandstone basal layer is widely distributed within the western external Alps and can be taken as a reference layer for post-Triassic deformations. That level is found sub-horizontal at about -3000 m (a.s.l.) in the Brizon well (46.03617 N; 6.441525E [WGS84]), about 30 km north-west of Chamonix (Charollais and Jamet, 1990). Altitude variation of the Triassic sandstone level can thus give a relative uplift with respect to that location. Atop the Aiguilles Rouges, below the Aiguille du Belvédère summit at 2965 m (a.s.l.), it is found nearly horizontal (Fig. 8) implying about 6 km of relative uplift of the central Aiguilles Rouges (Fig. S10). Note that the altitude difference could partly result from Mesozoic or Eocene normal faulting. However, the only normal faults that have been described between the Aiguilles Rouges and the Brizon well are Eocene and lead to negligible uplift of the Aiguilles Rouges (Butler et al., 2018).

The corresponding exhumation can also be estimated from the thickness of autochthonous and allochthonous (Helvetic and Penninic nappes) sediments that have been eroded at the top of the ranges. For the Aiguilles Rouges, it amounts to ~12–15 km depending on the cross-section considered (Escher et al., 1988, 1993; Pfiffner, 1993). Temperatures at the top of the basement before exhumation have been estimated at 350 ± 20 °C from δ18O (Kirschner et al., 1995) and 325 ± 25 °C from RSCM (Girault et al., 2020) below the Morcles Nappe in Switzerland, and 320 ± 25 °C from RSCM in the south of the Aiguilles Rouges (Boutoux et al., 2016). This corresponds to a thermal gradient of ~ 20–31 °C/km, typical of mountain belts. Note that similar temperatures at the top of the basement in Morcles and the southern Aiguilles Rouges strongly suggest that both locations were buried at the same depth and thus both overlain by the Helvetic and Penninic nappes, confirming our description of the Morcles Nappe at the top of the Aiguilles Rouges.

In the Mont-Blanc, the Triassic sandstones outcrop both in the south (Col du Bonhomme) and the north (Catogne) but not at the top of the range where they have been most likely eroded. Mont-Blanc relative uplift can be estimated with respect to the Brizon well: about 5.6 km in

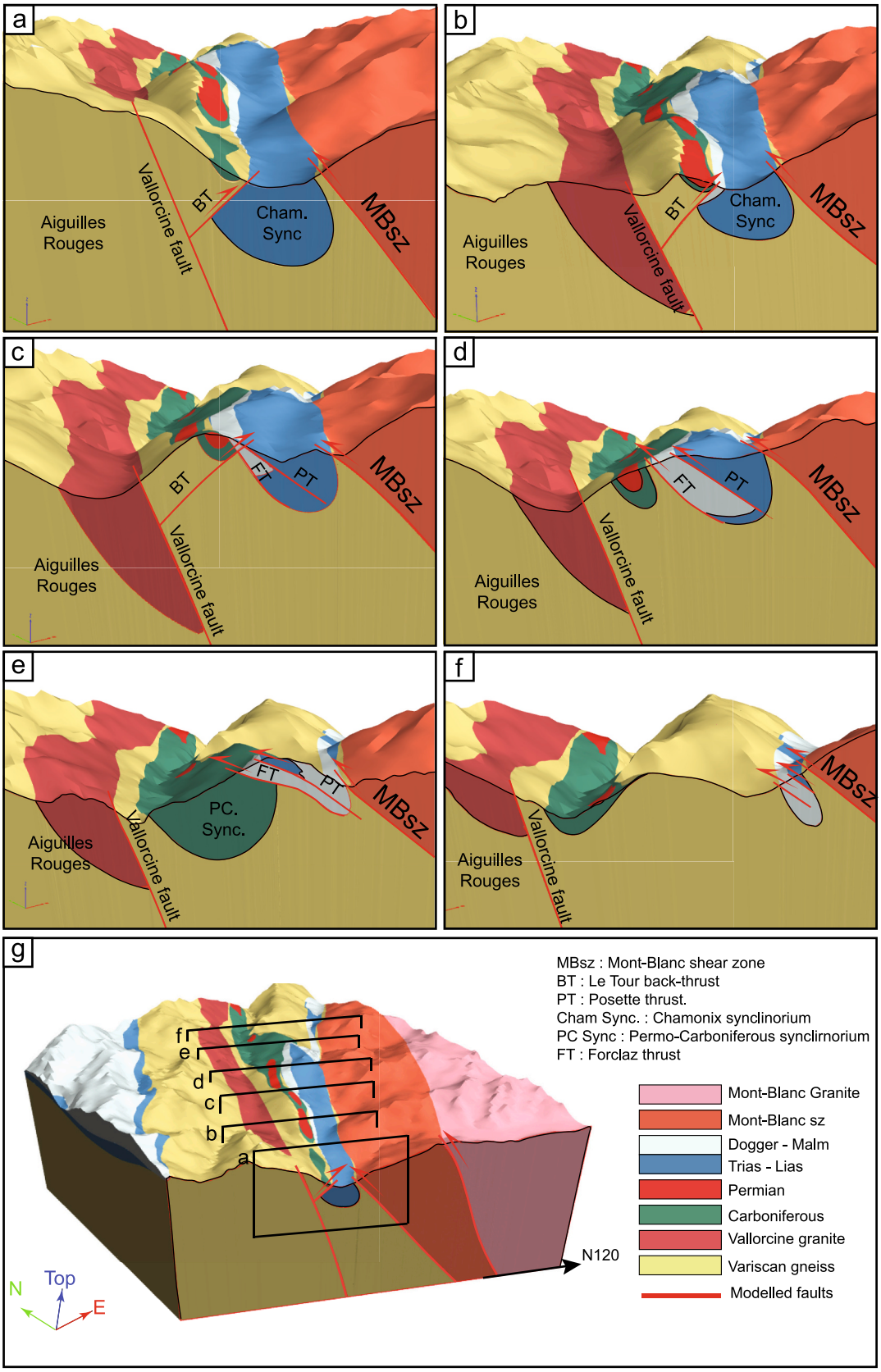

Fig. 14. Cross-sections of the Argentiere 3D GeoModel highlighting the structural continuity of the Chamonix synclinorium. a to f: successive cross-sections from south to north. Note that Finhaut thrust has not been included in this model, and that the precise shape of the Chamonix synclinorium is not constrained at depth.

the south (Col du Bonhomme), ≥ 7.8 km near the Mont-Blanc summit, and 5.3 km in the north (Catogne) (Fig. S10). These values are lower bounds as they do not consider the layer tilt. Note that part of this uplift could result from Mesozoic and/or Cenozoic normal faulting. It is now well documented that part of the Mont-Blanc range was eroded during the Pliensbachian yielding to the Grès Singuliers sedimentation and had thus been exhumed before that time (Trumpy, 1971; Eltchaninoff, 1982; Ribes et al., 2020). However, no large normal fault has yet been found between the Mont-Blanc and the Aiguilles Rouges. The highest pressure estimate in the Mont-Blanc for the Cenozoic is 0.5 ± 0.05 GPa and 400 ± 25 °C (Rolland et al. (2003), sample MB140, Helbronner area). This corresponds to a depth of 17 to 20 km assuming a rock density of 2.7 and implies an average thermal gradient of 18.5 to 26 °C/km. These values imply 2 to 8 km more exhumation in the Mont-Blanc than in the Aiguilles Rouges. Note that this exhumation cannot be due to Mesozoic nor Cenozoic normal faulting. Three temperature estimates from RSCM measurements in the Col du Bonhomme area are between 322 ± 18 and 336 ± 26 °C (Dall'Asta et al., 2022), similar to those at the base of the Morcles nappe thus suggesting a comparable amount of overlying autochthonous, and, allochthonous (Helvetic and Penninic nappes) sediments before the exhumation.

5.3. Constraints on the amount and absolute timing of Cenozoic deformations

5.3.1. Le Tour and Finhaut back-thrusts

The approximate 6 km of post-Triassic uplift of the Aiguilles Rouges from the Brizon well mostly results from the uplift in the crustal culmination above the Alpine Sole Thrust (Leloup et al., 2005; Bellahsen et al., 2014), including the frontal Aiguilles Rouges thrust (Pfiffner et al., 1997) and the back thrusts (Fig. 1b and Fig. S10). We estimate that ≥1.7 km of this uplift has been accrued on the Vallorcine fault and the back thrusts (Fig. S10). The vertical offset of the Le Tour back trust alone is 935 m at the very least (elevation difference between the basement east of the Vallorcine Fault and the Chamonix valley (Fig. S10b). The offset on the Finhaut back thrust is more difficult to evaluate because it is very close to the Vallorcine fault (Fig. 3a).

Cooling histories modeled with the HeFTy software and based on one Apatite Fission Track, the mean of two Zircon U/He, and one Apatite U/He ages from the central part of the Aiguilles Rouges suggest that cooling, and thus exhumation, started at about 18 Ma, and was faster (≥25 °C/Ma) from 8 to 4 Ma (Boutoux et al., 2016) (Fig. 15). However, the cooling history is relatively poorly constrained and exhumation could have started between ~ 30 and 16 Ma. All apatite fission tracks ages along a transect (elevations between 1010 and 1350 m asl) perpendicular to the Chamonix valley at the level of the Mont-Blanc tunnel are similar between 3.4 and 4.5 Ma in the Aiguilles Rouges and the Mont-Blanc (Glotzbach et al., 2008). This implies that no significant

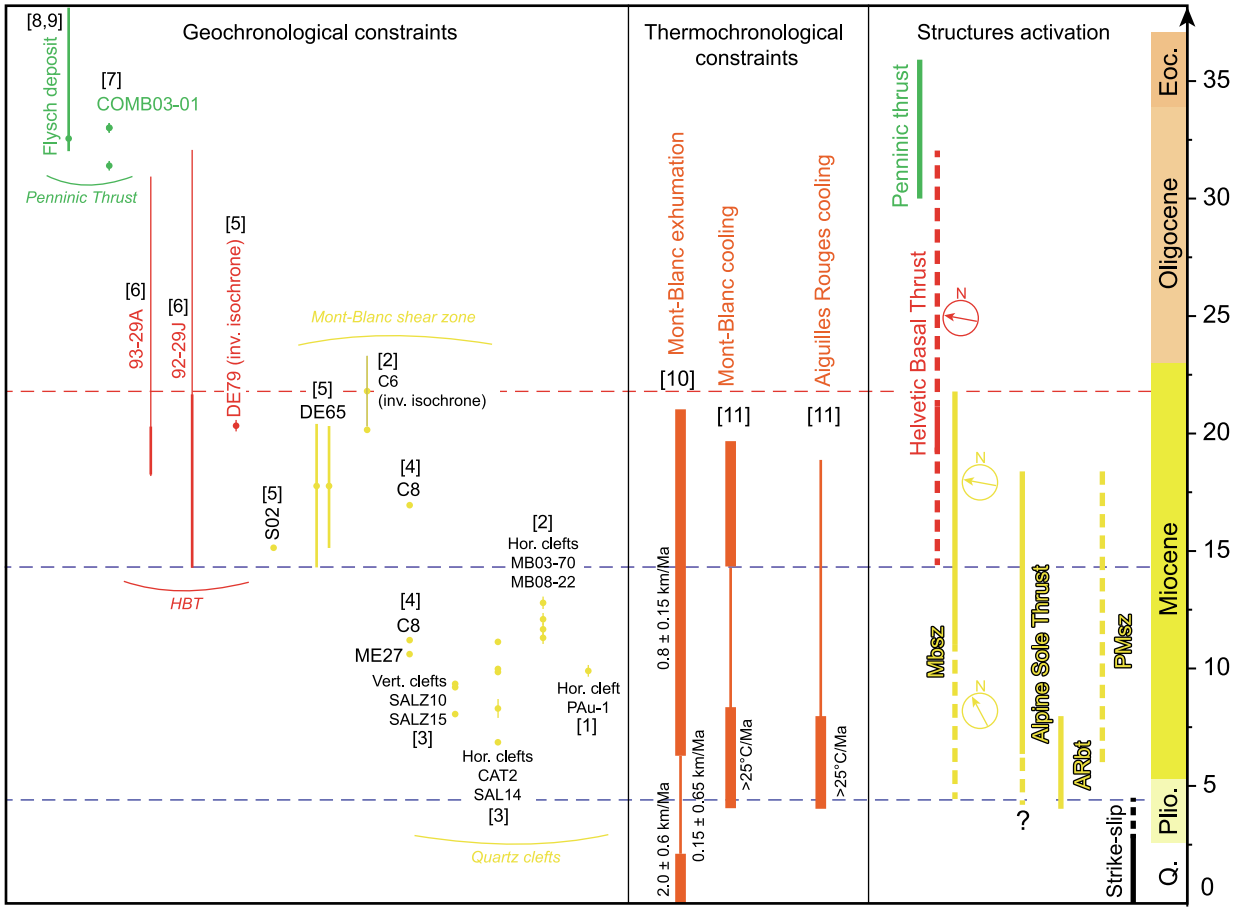

Fig. 15. Time-Deformation constraints on the Cenozoic evolution of The Mont-Blanc and Aiguilles Rouges. Left, geochronological constraints, dots correspond to individual ages and lines to age ranges of individual samples, data listed in Table S4. Center, Thermochronological constraints with exhumation estimate and cooling histories. Bold line indicates fast cooling/rapid exhumation. Right, timing of the main structures, dashed when uncertain. Colors refer to tectonic phases, arrow indicate the thrusting direction (see text for details). References: [1]: Poty et al. (1974). [2]: Rolland et al. (2008). [3]: Bergemann et al., (2019). [4]: Leloup et al. (2005). [5]: Egli et al. (2017). [6]: Kirschner et al. (1996, 2003). [7]: Simon-Labric et al. (2009). [8]: Pfiffner et al., 2002. [9]: Ruffini et al. (1997); [10]: Glotzbach et al. (2011). [11]: Boutoux et al. (2016).

movement has occurred on the Mont-Blanc shear zone nor the Le Tour back thrust since that time (Leloup et al., 2005; Glotzbach et al., 2008).

The Aiguilles Rouges back thrusts are mostly brittle and offset all the other structures and are thus presumably relatively young. They appear coeval with a WNW-ESE compression phase but are possibly older than the present-day strike-slip regime. Unfortunately, the age of these deformation phases is yet unclear and no geochronological data are available on the back thrusts. Assuming that the back thrusts are linked to the most recent rapid cooling phase would imply that they were active between 8 and ~4 Ma (Fig. 15).

5.3.2. Pormenaz-Merlet shear zone

As discussed above, the shear zone is younger than the HBT but presumably older than the Mont-Blanc shear zone. Vertical offset across the Pormenaz-Merlet shear zone is ≥300 m (elevation difference between the basement east of the shear zone and the base of the Pormenaz klippe). The only thermochronology data that can help to constrain the absolute age of the shear zone are samples MBZ10 and MBZ14 (Boutoux et al., 2016) that have similar elevations on both sides of the shear zone and give similar Zircon U/He mean ages: 6.2 ± 0.4 and 6.3 ± 0.4 Ma respectively. This implies that the shear zone offset is antecedent to that age and occurred at temperatures higher than the Zircon U/He closure temperature (140–195 °C). Motion on the shear zone contributed to the exhumation of the Aiguilles Rouges and is thus most likely younger than ~18 Ma (Fig. 15).

5.3.3. Mont-Blanc shear zone

The overall direction of the Mont-Blanc shear zone is N034° with a N110° direction of thrusting on average. This geometry implies that the Mont-Blanc shear zone has mainly a thrust component (~80%) and a slight dextral component (~20%). The WNW-ESE direction of shortening (~N110° ductile structures) possibly rotated through time towards NNW-SSE (~N155° brittle structures) (Leloup et al., 2005). The vertical offset on the shear zone may be estimated from the offset of the Triassic sandstones across it: ~ ≥ 1.5 km in the south (Col du Bonhomme), ≥3 km at the level of the Mont Blanc, and ~ ≥ 1 km in the north (Catogne) (Fig. S10). Pressure-Temperature estimates suggest that the differential exhumation between the Mont-Blanc and the Aiguilles Rouges is 2 to 8 km. Motion on the Mont-Blanc shear zone has increased that difference, while motion on the Le Tour back thrust decreased it.

$^{40}Ar/^{39}Ar$ mica ages have been performed within the Mont-Blanc shear zone, where the mylonitic foliation is underlain by chlorite ± white mica ± biotite. Biotite from sample C6 (Rolland et al., 2008) yields saddle age spectra suggestive of excess argon, with the youngest step at 19.75 ± 0.21 Ma, the inverse isochrone age being 21.8 ± 3 Ma (40/36i = 316.1 ± 4, MSWD = 2.0) (Rolland et al., 2008) (Fig. 15, Table S4). K-Feldspar from nearby sample ME27 yields complex age spectra with a minimum age step at 10.61 ± 0.15 Ma (Leloup et al., 2005). Two duplicates of white micas from sample DE65 located further north along the Angle fault yield raising ages spectra, respectively in the ranges, 14.30–20.41 and 15.13–20.32 Ma, both with a mini plateau at ~18 Ma (Table S4) (Egli et al., 2017). Other $^{40}Ar/^{39}Ar$ ages from undeformed rocks yield constraints on the cooling history. Biotites of sample C8 from the undeformed Mont-Blanc granite yield an inverse isochron age of 16.6 ± 0.7 Ma (Fig. 15, Table S4) that probably reflect the cooling of the hanging wall through 300 ± 50 °C (Leloup et al., 2005). K-feldspar from the same sample yields a minimum age step at 10.98 ± 0.2 Ma which could be interpreted as a maximum age for K-Feldspar recrystallization at about 200 °C (Leloup et al., 2005). All these samples do not give clear plateaux and the ages are difficult to interpret probably because the protolith is quite old (≥300 Ma) and the Alpine deformation temperature is below 450 °C (Leloup et al., 2005; Rolland et al., 2008). However, all these ages are between ~ 22 and ~ 11 Ma and could correspond to the timing of deformation within the Mont-Blanc shear zone between ~ 400 and ~ 200 °C (Fig. 15, Table S4).

White micas from sample S8 along the Vallorcine fault yield two $^{40}Ar/^{39}Ar$ mini-plateau ages at 14.3 ± 0.2 Ma (1σ) and 22.9 ± 0.9 Ma (2σ) (sample S68 of Rolland et al. (2008), Fig. 3a, Fig. 15, Table S4), that have been interpreted to reflect the duration of reverse faulting that would be coeval with the Mont-Blanc shear zone (Rolland et al., 2008). However, the Vallorcine fault has a long and polyphase history and the correspondence of the ages with a given deformation phase is disputable.

Along the nearly horizontal transect (elevations between 1010 and 1350 m asl) perpendicular to the Chamonix valley at the level of the Mont-Blanc tunnel all zircon fission-track ages, are similar between 11.2 and 13.5 Ma within the Mont-Blanc shear zone (2 samples) and the Mont-Blanc granite (3 samples) suggesting that no significant vertical offset occurred across the Mont-Blanc shear zone and the Angle fault since that time (Glotzbach et al., 2011). The absence of Zircon fission track age in the Aiguilles Rouges, precludes a similar discussion on the Lavancher fault and the Le Tour back-thrust. Pecube model of a set of low-temperature thermochronology ages (Zircon and Apatite fission track and Apatite U/He) of the Mont-Blanc suggests an episodic exhumation with initiation at 22 ± 2 Ma with a rate of 0.8 ± 0.15 km/Ma, that decreases to values of 0.15 ± 0.65 km/Ma at 6 ± 2 Ma, and finally increase up to 2.0 ± 0.6 km/Ma at 1.7 ± 0.8 Ma. (Glotzbach et al., 2011) (Fig. 15). A phase of relatively fast cooling of the Mont-Blanc before ~ 6 Ma followed by a slow cooling phase was also suggested from apatites fission-track and U/He data alone and HeFTy models (Glotzbach et al., 2008). HeFTy models of one Zircon fission track, two Zircon U/He, one Apatite fission track, and one Apatite U/He ages between 2500 and 2600 m of altitude within and in the hanging wall of the Mont-Blanc shear zone indicate a continuous cooling since 18 ± 2 Ma with possibly increased cooling at 18–14 and 8–4 Ma (Boutoux et al., 2016) (Fig. 15). The average model cooling histories of the Mont-Blanc and Aiguilles Rouges converge at about 11 Ma (Boutoux et al., 2016) which could indicate the end of motion along the Mont-Blanc shear zone and Le Tour back thrust. However, if considering the full range of possible models, the cooling histories of the two ranges may have converged between 18 and 6 Ma.

Horizontal clefts with quartz + Chlorite ± fluorite ± adularia crystallizations are found within the Mont-Blanc and to a lesser extent in the Aiguilles Rouges (e.g., Poty and Cathelineau, 1974; Rossi et al., 2005; Rossi and Rolland, 2014). These clefts are compatible with horizontal compression and are generally considered as coeval to the Mont-Blanc shear zone. Adularia from one cleft in the central Mont-Blanc yields $^{40}Ar/^{39}Ar$ isochron ages of 10.6–13.6 Ma (MB03–70, 11.31 ± 0.68 for grain n°1, 12.8 ± 0.78 for grain n°2) (Fig. 15) (Rossi and Rolland, 2014). In the north of the Mont-Blanc, clefts contain quartz + Stilpnomelane + Epidote + Calcite ± Adularia ± Gold, with the Adularia yielding a 9.9 ± 1 Ma $^{40}Ar/^{39}Ar$ isochron age (Marshall et al., 1998) (Fig. 15). Bergemann et al. (2019) applied the U-Th/Pb method on nine clefts containing monazite that yield ages between 12 and 6 Ma that relate three main growth events at 12–11,11–9 and 9–6 Ma. The two veins located in the Aiguilles Rouges are described as vertical and trending N190° and do not show the first growth stage. This was interpreted as evidence that the two last growth phases are linked with right-lateral shear along the NE-SW Rhône-Simplon fault (Bergemann et al., 2019). However, the orientation of these clefts is compatible with left-lateral, not right-lateral shear along a NE-SW fault, making that interpretation dubious.

From all these data the most probable structural scenario is that reverse/right-lateral deformation started in the Mont-Blanc shear zone at 400 °C at ~22 Ma and lasted until ~11 Ma at ~200 °C. Because rapid cooling of the Mont-Blanc lasted until 6 ± 2 Ma, and crystallization in the horizontal clefts until 6.71 ± 0.23 Ma., thrusting may have continued along the Lavancher fault until 6 ± 2 Ma but was over (as well as the Le Tour back-thrust) at ~4 Ma (Fig. 15). Exhumation in the central Mont-Blanc at 0.8 ± 0.15 km/Ma implies 7.2 ± 1.3 km between 20 and 11 Ma and 4 ± 0.5 km between 11 and 6 Ma, corresponding to a total of 9.5–13 km. This is similar to the thickness of possible overlying nappes and compatible with the offset of the Triassic (≥3 km in central

Mont-Blanc). This is however much lower than the estimate from the petrographic analysis (18.5 ± 1.85 km from sample MB140, Rolland et al. (2003)). The end of motion on the Mont-Blanc shear zone possibly marks the initiation of the present-day strike-slip stress regime.

5.3.4. Helvetic thrusts

Helvetic thrust deformation affects units from the basement to the Eocene sediments. The Eocene sediments are Priabonian (Collet et al., 1952) thus implying a post-34 Ma deformation. Further, the Taveyannaz volcaniclastic sandstones that were deposited before the nappe stacking and folding contain 32.5 Ma andesitic clasts ($^{40}Ar/^{39}Ar$ on hornblendes), while biostratigraphic correlations suggest sedimentation between 32 and 29 Ma during the Rupelien (Ruffini et al., 1997) implying a post-Oligocene deformation.

No age data have been published on the Morcles nappe in France, but such ages are available from Switzerland. Fine-grained *syn*-kinematic white micas (2–6 μm) from five ductile carbonate mylonites at the base of the Morcles and Doldenhorm nappes in Switzerland yield staircase $^{40}Ar/^{39}Ar$ age spectra with apparent ages between 12 and 76 Ma with 94% of the gas release yielding ages between 32 and 14 Ma (Kirschner et al., 1996). Analysis of a larger set of twenty-five samples from the Helvetic nappes and comparison with Rb/Sr ages confirm that the $^{40}Ar/^{39}Ar$ ages result from variable mixtures of detrital and syntectonic (neoformed) micas, and that ages tend to young from the highest Helvetic thrusts (Mont Gond and Sublage) to the lowest (Diableret and Morcles) (Kirschner et al., 2003). The age spectrum of sample 93–29-A from deformed Eocene sediments at the base of the Morcles Nappe, yields a strong Miocene signal with two pseudo-plateaux at 19 and 21 Ma in the first 83% of gas release (Kirschner et al., 2003) (Fig. 15). The youngest ages (about 14 Ma) come from the base of the Morcles Nappe, at la Batiaz (Fig. 15) but correspond to <20% of the gas in a spectrum that does not show any plateau, so their significance is uncertain. These data suggest that the Morcles nappe mostly emplaced at 21–19 Ma. Unfortunately, from the available data, it is unclear if that deformation ended at ~19 Ma or lasted until ~14 Ma.

At la Batiaz, white mica from sample DE79 from the Aiguilles Rouges gneiss with top to the north-west thrusting evidence yield a 20.28 ± 0.21 $^{40}Ar/^{39}Ar$ plateau age (inverse isochrone: 20.18 ± 0.49 Ma) interpreted as related to motion on the Mont-Blanc shear zone (Egli et al., 2017). This interpretation is in the upper range of the ages discussed above for the Mont-Blanc shear zone. However, our structural mapping rather relates deformation at la Batiaz to the HBT, in the direct prolongation of the Forclaz fault, and we rather relate that age with those obtained at the base of the Morcles Nappe (Fig. 15). Closer to the contact with the sedimentary cover, sample S02 showing top to the south-east normal shear criteria, yields a $^{40}Ar/^{39}Ar$ plateau age of 15.9 ± 0.15 (inverse isochrone: 15.07 ± 0.23) that has been interpreted to correspond to the age of updoming of the Aiguilles Rouges postdating the Mont-Blanc shear zone (Egli et al., 2017). This timing is compatible with that of the uplift of Aiguilles Rouges discussed above.

Available geochronological data thus suggest that the Helvetic nappes in Switzerland emplaced since ~32 Ma, with the Morcles nappe mostly around 21–19 Ma but lasting possibly until ~14 Ma (Fig. 15). In the absence of any absolute age in our study area, we infer that the timing was the same a few km southwest along-strike, but this deserves further study.

6. Implications on the structural evolution of the Alps

6.1. Shortening of the Helvetic nappes and lateral extent of the Helvetic Basal Thrust

The Aiguilles Rouges have been underthrusted below the Penninic nappes along the Penninic thrust until ~30 Ma (Simon-Labric et al., 2009; Pfiffner et al., 2002) (Fig. 15). As discussed above, thrusting at the base of the Helvetic nappes, along the Helvetic Basal Thrust (HBT), lasted until ~19 Ma and possibly until ~14 Ma. Above the HBT, several thrusts sheets are found below the Penninic thrust that has been described in Switzerland and named the Helvetic and Ultrahelvetic nappes (Ramsay, 1981; Escher et al., 1988), and have possibly been activated in sequence from east to west (top to bottom) (Jeanbourquin, 1994) between ~30 and ~20 Ma (Kirschner et al., 2003).

The present 3D structural study implies that the HBT is a shear zone along which the overlying Morcles nappe was significantly detached from the underlying basement towards the WNW (N110° on average in the Aiguilles Rouges). This follows the interpretation of Paréjas (1925), Collet (1927), and Ramsay (1981) but not that of Escher et al. (1993) and Boutoux et al. (2016), which consider that the Morcles nappe is not significantly detached from the basement and is mostly restricted to Switzerland.

NW-SE shortening of the Urgonian limestone above the HBT can be estimated from the cross-sections of Ferrill and Groshong Jr (1993) and Butler et al. (2018) (Fig. 1a): 4.3 km (22%) and 3.7 km (24.5%) respectively. These are minimum estimates of the total shortening because they do not consider the offset on the HBT which is difficult to constrain as it does not outcrops. From a 3D reconstruction based on the cross-sections of Huggenberger (1985) and Faure et al. (1999), Affolter (2003) calculate a total shortening varying between 13 and 32 km from the NE to the SW of the Aiguilles Rouges (Fig. 1a).

In the ductile folded basement hypothesis (e.g., Escher et al., 1993), the Morcles nappe is expelled from a half-graben with the external Mont-Blanc at its core. The initial length of the cover was at least 21 km while the present-day width of the external Mont-Blanc is only 3 km and it implies >86% of shortening of the basement. However, the External Mont-Blanc is not a fold but a reverse shear zone. Moreover, that shear zone is younger than the Morcles Nappe, implying that the nappe roots east of the Mont-Blanc as well as the other Helvetic nappes. In such a case, the amount of internal shortening within the basement is independent of the amount of shortening along and above the HBT which could be quite large.

Southwest of the Mont-Blanc range the sedimentary cover is interpreted as significantly detached from the basement by several authors. In the Mont Joly area (Fig. 1a), three flat thrust sheets have been described within the Mesozoic cover on a ~ 1500 m thick succession from bottom to top: the Vervex, lower Mont-Joly (or Sangle) and Upper Mont-Joly units (Mennessier et al., 1977; Triboulet, 1980; Epard, 1990). These thrusts are the southward prolongation of the Helvetic nappes (Eltchaninoff, 1982; Epard, 1990), and are overlain by two other thrust sheets: the Roselend and Roselette nappes, both involving the basement (Mennessier et al., 1977; Eltchaninoff, 1982; Butler, 1985). The basal thrust, corresponding to the HBT, prolongs to the north-west, dipping north-west below the Aravis (Triboulet, 1980; Eltchaninoff, 1982; Butler, 1985; Epard, 1990; Bellahsen et al., 2014). The HBT underlies the folded Mesozoic cover and most probably emerges west of the Bornes (Doudoux et al., 1982) between the Brizon (BZN-1) and Faucigny (FAY-1) deep wells (Charollais et al., 1996) (Fig. 1a). That interpretation implies that the whole Aravis, Bornes, Bauges, and Semnoz massif corresponds to a large subalpine klippe above the HBT (Fig. 1). In the Brizon deep well the Tithonian limestones are found five times attesting to strong shortening of the cover (Charollais and Jamet, 1990). Bellahsen et al. (2014) estimate an NW-SE shortening of 17 km within the Bornes, while Affolter (2003) estimates a total thrusting of 30 to 36.5 km for the Helvetic nappes. Further south, Kalifi et al. (2021) propose a similar interpretation for the northern part of Vercors and the eastern part of Chartreuse. These massifs are klippes above a thrust they call Fault Zone 1 (FZ1), with shortening estimates between 14.1 and 5.8 in the north and south of Chartreuse respectively. They further interpret FZ1 to have been active before ~21 Ma has it created a relief that bounded the Miocene sea to the east (Kalifi et al., 2021, 2022). We propose that the FZ1 of Kalifi et al. (2022) corresponds to the southern prolongation of the HBT that extend from the Morcles Nappe to the northern Vercors.

6.2. Late reverse faults at the boundary of the external ranges

The subalpine klippe is bounded to the east by the external crystalline ranges of external Belledonne and the Aiguilles Rouges which are large basement windows (Fig. 1a). Most authors consider that the Jura and subalpine folds formed above thrusts that root below (west of) the external ranges (e.g., Burkhard and Sommaruga, 1998; Deville and Chauvière, 2000; Bellahsen et al., 2014). However, as described above, the Helvetic basal décollement lies on top of the Aiguilles Rouges external crystalline range, thus implying that it roots above (east of) these ranges: in the Chamonix Synclinorium and the synclinal médian (Fig. 1) (e.g., Eltchaninoff, 1982; Leloup et al., 2005). Further, as discussed above, the HBT roots east of the Mont-Blanc and has been cut and offset by later steep reverse faults including the Mont-Blanc shear zone.

Exhumation of the Mont-Blanc started at ~22 Ma in the hanging wall of the Mont-Blanc shear zone and lasted until at least ~11 Ma, very probably until 6 Ma, while motion on the HBT was active at 21–19 Ma and possibly until ~14 Ma. The Mont-Blanc shear zone thus appears to be partly coeval with the HBT that it offsets for a time range between 3 and 8 Ma depending on the timing of the end of motion on the HBT (19 or 14 Ma) (Fig. 15). A simple interpretation is that during this time range the Mont-Blanc shear zone was an imbricate thrust in the footwall of the HBT, before breaching out at ~19 or 14 Ma and starting to offset the HBT (Fig. 16).

Exhumation of the Aiguilles Rouges above the Alpine sole thrust started at ~18 Ma (Fig. 15), inducing the bending of the HBT that was possibly still active during ~5 Ma. The period from ~22 to ~19 or 14 Ma thus corresponds to a major transition from the rooting of the main active thrusts from above (east) the external crystalline massifs in the Mont-Blanc area (HBT) to thrusts rooted below (west) of the external crystalline massifs (Alpine sole thrust).

Further south in Chartreuse, the molasse depocenter migrated at ~18 Ma towards the west from the footwall of the HBT to the footwall of the Voreppe thrust rooting below Belledonne (Kalifi et al., 2021). This

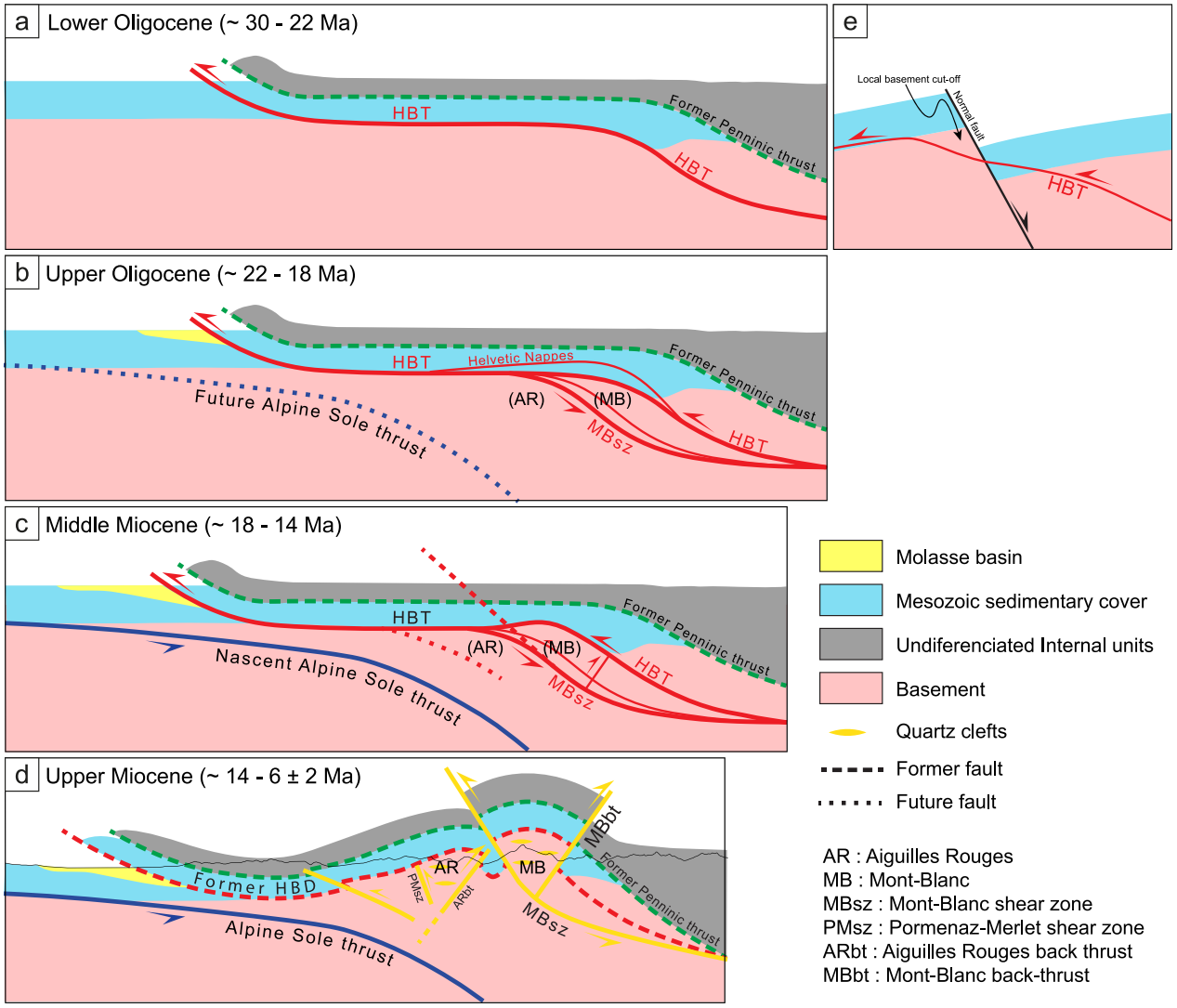

Fig. 16. A conceptual model for western Alps External Crystalline massifs deformation. a) Lower Oligocene (30–22 Ma) stage of Helvetic nappe stacking (thin shin). Helvetic Basal Décollement at the base of the Helvetic nappes taking root southeast (above) of the Mont-Blanc. b) Upper Oligocene (22–18 Ma) stage of further Helvetic nappe stacking with duplexing. The external crystalline massifs are structured in duplexes between two branches of the HBT where the deformation is more (Mont-Blanc) or less (Aar, Belledonne) localized. c) Middle Miocene (18–14 Ma) transition stage. The HBT is bent at the top of the duplex where back-thrusting takes place. Initiation of the Alpine Sole thrust induces Aiguilles Rouges exhumation. d) Upper Miocene (14–6 Ma) stage of breach thrust and steep faults (thick skin), the main stage of the external crystalline massifs exhumation above the Alpine Sole thrust that roots northwest (below) the external crystalline massifs. The Mont-Blanc shear zone becomes a breach thrust through the former HBT coevally with back-thrusting of the Mont-Blanc and Aiguilles Rouges. Horizontal quartz clefts open within the external crystalline massifs. Note that the Alpine sole thrust induces thin skin tectonics in the Jura at the same time. e) Sketch of a possible configuration with a roughed geometry of the cover/basement interface leading to the incorporation of basement pieces within the sedimentary series at the base of the thrust.

timing is coeval with the onset of rapid exhumation of the Belledonne external crystalline massif and is interpreted as the switch from distributed to localized (shear zones) deformation (Girault et al., 2022). However, that timing could as well mark a major transition from rooting of the thrusts east (above) to the west (below) of the external crystalline massifs as in the Aiguilles Rouges – Mont-Blanc, and we propose below a conceptual model for the external crystalline massifs Alpine deformation, based on our observations in the Aiguilles Rouges and Mont-Blanc massifs.

6.3. A conceptual model for Alpine External Crystalline Massifs deformation

We suggest that three major thrust systems with large horizontal displacement (so-called thin-skin tectonics) succeeded in the western Alps from the east (internal) to the west (external): the Penninic, Helvetic, and Basal thrust systems. In this interpretation, the Helvetic deformations are not limited to a buckle folding but are linked to a major thrust system >50 km long across-strike that absorbed between 13 and 36 km kilometers of ENE-WSW shortening: the Helvetic thrust system, with the Helvetic Basal Thrust at its base.

These thrusts induced large-scale folding of the Helvetic units with fold axis perpendicular to the thrust motion in the upper part of the thrust sheet, and sheath folds in the basal décollement level. Note that such sheath folds can barely be explained in a para-autochthonous hypothesis. That thrust system roots southeast (above) of the Mont-Blanc and Belledonne, close to, and possibly within the Penninic thrust. The thrust system is composed of ramps usually located in the less deformable units (i.e., basement, Urgonian and Thithonian limestone), and long flats located in the less competent layers (i.e., Triassic siltites and dolostones, Liassic marls). The main flat appears to be in the Triassic a few meters above the basement and has induced a large décollement of the cover with respect to the basement. Starting from a horizontal geometry would imply that no basement slice could be found along with the thrust within sedimentary rocks unless the thrust does cut downsection within the basement before climbing up section, the so-called plucked basement slice (Platt, 1984), which seems unlikely. However, as the basement/cover interface had more likely a roughed geometry in part because of preexisting normal faults (either Jurassic or Eocene), the local cutoff of that interface, for example at the tip of tilted blocks, can explain how basement pieces can be found within the sedimentary series (Fig. 16e).

Helvetic thrusting lasted from ~30 Ma to ~14 Ma. During a first stage (~30 to ~22 Ma) the HBT is rooted southeast of the Mont-Blanc (Fig. 16a). To the west, the HBT thrust system bounded the Miocene Sea and was coeval with the sedimentation of the Lower Freshwater molasse in the Swiss molasse basin (Garefalakis and Schlunegger, 2019) and the initial deposits of the Miocene molasse in the Rhodano–Provencal molasse basin (Kalifi et al., 2021, 2022). In a second stage (~22 to ~18 Ma) a duplex formed (Fig. 16b). The Mont-Blanc was the central bloc of that duplex bounded to the northwest by the Mont-Blanc shear zone, and to the southeast by a ramp along the HBT. At ~18 Ma, the main locus of deformation migrated towards the west and the Alpine Sole thrust initiated rooting west (below) the Aiguilles Rouges inducing uplift of the Aiguilles Rouges, while the HBT was still active (Fig. 16c). This transition period ended at ~14 Ma when the HBT ended, but several steep faults initiated in the Alpine Sole Thrust hanging wall (Fig. 16d). Some of the HBT ramps eventually became breach thrusts that cut up-section across their previous flat (Platt, 1984). This was the case for the Mont-Blanc shear zone that was active together with the HBT between ~22 and 14 Ma, before offsetting that structure between 14 and ~6 Ma. The activation of such breach thrust is coeval with that of the back-thrusts and the formation of horizontal clefts and would correspond to the transition of thin-skin to thick-skin tectonics in the Mont-Blanc, while thin-skin tectonics takes place in the Jura. Note that this model does not imply any major strike-slip motion along the Chamonix Synclinorium, nor the synclinal median in Belledonne before ~6 Ma.

6.4. Implications on the Alpine orogenic wedge

Mountain belts are often described as orogenic wedges with the internal part of the belt consisting of a structural culmination formed by basal accretion of crystalline thrust sheets, and an external part of imbricated thrusts formed by frontal accretion of sedimentary units (Pfiffner, 2017, for a review). In the case of the external Alps, the External Crystalline Massifs have been interpreted as such a culmination (e.g., Lacassin et al., 1990; Pfiffner et al., 1997; Menard and Thouvenot, 1987). Analog and numerical experiments have emphasized the importance of décollement layers, erosion, and sedimentation in the formation of such orogenic wedges and their influence on the deformation style. In analog sandbox experiments, a geometry similar to the external alps has been obtained with an antiformal culmination refolding previous flat thrust sheets (e.g., Konstantinovskaya and Malavieille, 2005; Bonnet et al., 2007). In that case, the culmination is achieved by basal accretion of basement slices in a duplex, and back thrusting in the internal part (Bonnet et al., 2007). The same kind of geometry is obtained in visco-elastoplastic numerical models when two flat decollement levels are present with the upper one weaker than the basal one (Dal Zilio et al., 2020). In some of these cases, the uplift of the antiformal culmination is achieved not by basal accretion but by out-of-sequence breach thrusting at the front of the culmination and back thrusting at the back (Model M5, Dal Zilio et al., 2020). In every case, the vertical growth of the culmination is enhanced by strong erosion. Basic features of our conceptual model, such as the up doming and breach thrusting of a previously flat décollement, are obtained in some of these wedge models. However, these models correspond to a brittle wedge over a rigid basement as rheology is independent of temperature, and one can question their applicability to the Mont-Blanc where the Miocene temperature may have reached 400 °C (Poty et al., 1974; Poty and Cathelineau, 1974; Rolland et al., 2003). Numerical thermo-mechanical simulations with visco-elastoplastic rheology have been designed to discuss the mechanical parameters that control the deformation style (thin-skin versus thick-skin) during nappe formation (Spitz et al., 2020; Bauville and Schmalholz, 2015; Kiss et al., 2020). In these simulations in the absence of any softening mechanism, strain localization occurs along weak layers and is thus mainly controlled by the viscosity contrast between the basement (high viscosity) and the cover (low viscosity), and the initial geometry of that boundary. Flat low viscosity layers (i.e., evaporite layer) promote large horizontal thrust nappe transport, while steep boundaries (i.e. inherited normal fault) promote folding of the basement and sediments (Spitz et al., 2020; Bauville and Schmalholz, 2015; Kiss et al., 2020). These models suggest that for a basement with high viscosity ($\geq 10^{23}$ Pa.s) and in the absence of any localization mechanism, shortening of a previous graben can yield folding of the basement and squeeze out of the sediments with a geometry comparable to the basement fold nappe proposed for the Morcles Nappe by Escher et al. (1988) (Fig. 2a); while in the absence of graben thrust nappe with large horizontal transport such as the Wildhorn and Glarus nappes develop. In our study area, there is no clear evidence for a Mesozoic normal fault, no evidence of basement folding, and clear evidence for décollement of the cover with respect to the basement along the HBT, and the situation is thus comparable to that of the Glarus, but with a later deformation, phase inducing thrusting of the basement in the internal part of the system (Fig. 2b). The presence of basement pieces inside the HBT shear zone (Fig. 6) suggests that, even in the absence of a deep basin, the basement/cover interface had a roughed geometry, and basement highs have been cut off (Fig. 16e).

7. Conclusions

A décollement thrust is evidenced at the bottom of the Helvetic

nappes (named the Helvetic Basal Thrust or HBT). The HBT was a major thrust system active mostly between ~30 and ~14 Ma, in an ~N110° direction, with a total shortening between 13 and 36 km. An HBT flat is located within the Triassic a few meters above the basement and another within the Liassic shales. The HBT is an apparent normal fault on the NW flank of the Aiguilles Rouges, but this is because it has been tilted during the later uplift of the Aiguilles Rouges above the more external Alpine Sole Thrust. The HBT extends below the Haut-Giffre and most probably emerges west of the Prealps klippe during the Miocene, the HBT was cut by several steep reverse faults: in the Aiguilles Rouges the Merlet-Pormenaz shear zone, the Le Tour and Finhaut back thrust, and the Mont-Blanc shear zone in the Mont-Blanc. The HBT was uplifted and folded above the basement culminations of the external crystalline massifs, and it is these late faults that mostly shape the present-day external crystalline massifs map geometry. These late deformations obscured the HBT continuity and precluded its recognition as a major structure even if it was previously described at several localities. The HBT roots in the Chamonix synclinorium, but its internal roots have in fact to be found on the eastern side (above) of the Mont-Blanc because of the late offset by the breach faults, and back thrusts.

We propose a tectonic scenario where the Mont-Blanc shear zone acted as a ramp of the HBT between ~22 and 14 Ma, before becoming a breach thrust between 14 and 6 Ma. The period between ~22 and 14 Ma was a transition of the major thrust system between the HBT rooting southeast (above) of the external crystalline massifs to the Alpine Sole thrust rooting northwest (below) of the external crystalline massifs. Before ~6 Ma, there is no evidence of large strike-slip motion along the Chamonix synclinorium, thus no direct connection through the Rhône fault between exhumation in the Mont-Blanc and the footwall of the Simplon normal fault.

The main structural characteristics of the Mont-Blanc area can most probably be extrapolated in the southwest, with the external Belledonne, Synclinal Median, Internal Belledonne being an equivalent of the Aiguilles Rouges, the Chamonix Synclinorium, and the Mont-Blanc respectively. We suggest that the Helvetic nappes above the HBT extend in the Chablais, the Bornes, eastern Chartreuse, and northeast Vercors defining a large klippe that roots east (above) Belledonne. After ~18 Ma a major transition occurred within the Alpine sole thrust rooting west (below) the external crystalline massifs, and steep reverse faults shaping the Belledonne geometry.

This re-discovery of a major thrust system has several implications: the first one is that three major thrust systems, not only two, have shaped the external western Alps: the Penninic, Helvetic, and Alpine Sole thrust systems. These thrust systems have propagated in sequence from the internal (east) part to the external one (west). Because the Helvetic phase has been overlooked, shortening in the external Alps has been underestimated. The second implication is that the exhumation of the external ranges of the western Alps was mostly controlled by steep reverse faults, including back thrusting and limited folding above the more external thrust system since ~18 Ma. At that time, thick-skin deformation in the more internal part of the belt was coeval with thin-skin deformation in the external part.

CRediT authorship contribution statement

A. Mercier: Data curation, Methodology, Investigation, Visualization, Formal analysis, Writing – original draft, Writing – review & editing. **P.H. Leloup:** Supervision, Conceptualization, Investigation, Formal analysis, Writing – original draft, Writing – review & editing, Funding acquisition. **G. Courrioux:** Methodology, Software. **S. Caritg:** Methodology, Software. **S. Lopez:** Data curation, Software. **P. Grandjean:** Investigation, Visualization. **S. Passot:** Data curation, Visualization, Software. **A. Kalifi:** Formal analysis.

Declaration of Competing Interest

The authors declare the following financial interests/personal relationships which may be considered as potential competing interests:

Antoine Mercier reports financial support was provided by Référenciel Géologique de la France. Antoine Mercier reports financial support was provided by Institut National des Sciences de l'Univers (Proframme SYSTER).

Antoine Mercier reports financial support was provided by the french ministry of Research, Higher Education and Innovation through its Ph.D project.

Data availability

GeoModeller software used in this research is available for download at https://www.intrepid-geophysics.com/product/geomodeller/ with a valid commercial or research Licence. 3D Geological models are provided in GeoModeller native format (.xml). The models are also provided in a 3D portable document format (.pdf) that can be opened with free Acrobat Reader software. See data repository.

Samples are identified with a persistent identifier of the International Geo Sample Number (IGSN:https://www.igsn.org/): these numbers are indicated in the Samples.csv table in the data repository.

Stereographic plots were performed using the Stereonet v.11 programs of Allmendinger et al. (2011) and Cardozo and Allmendinger (2013), freely available at https://www.rickallmendinger.net/stereonet.

3D photogrammetric digital elevation model (DEM) of the Aiguille du Belvédère is built from 260 shots with a spatial resolution of about 6 cm, acquired by drone, assembled with Agistoft Metashape 1.7.3 software. The model is visible online with annotations and detailed images in the Sketchfab platform at the following link: https://skfb.ly/o9Wsw. The high-resolution source of the model is retrievable in the data repository.

All data used in this publication: location of observations, measurements, samples, GeoModels source format, and 3D photogrammetric models are stored in a repository with the following link: https://data.mendeley.com/datasets/snx9zkrvts/1

Acknowledgments

This study was partly supported by INSU-CNRS through the "SYSTER-FEI-UMR5276-Dotation Performance 2022" and the RGF "Alpes et bassins périphériques" from the French Geological Survey. It forms part of the Ph.D. project of Antoine Mercier at Université Claude Bernard Lyon 1, supported by the French Ministry of Research, Higher Education and Innovation. The authors thank B. Boulicaut and J. Jacquod from the Emosson SA company for providing the geological sections along the water penstock pipes. We also thank Clémentine Fellah, Cyril Langlois, and Thierry Douillard from the INSA Lyon laboratory that performed the EBSD experiment for the quartz LPO analysis. Finally, we thank the conservatory of natural areas (ASTER), for authorizing the drone surveying (n°DDT-2020-1166) above the Aiguille du Belvedere in the Aiguilles Rouges massif, and especially the guard Laurent Delomez for coming us in the field. A. Pfiffner and an anonymous reviewer are thanked for reviews that enriched and helped to clarify the manuscript.

Appendix A. Supplementary data

Supplementary data to this article can be found online at https://doi.org/10.1016/j.tecto.2022.229691.

References

Affolter, T., 2003. Étude des déformations et restauration 3D d'un bassin de front de chaîne: l'exemple du Jura et des massifs subalpins français (Doctoral dissertation).. Université Joseph-Fourier Grenoble I.

Affolter, T., 2004. Map view retrodeformation of an arcuate fold-and-thrust belt: the Jura case. J. Geophys. Res. 109 (B3) https://doi.org/10.1029/2002jb002270.

Affolter, T., Faure, J.-L., Gratier, J.-P., Colletta, B., 2008. Kinematic models of deformation at the front of the Alps: new data from map-view restoration. Swiss J. Geosci. 101 (2), 289–303. https://doi.org/10.1007/s00015-008-1263-3.

Allmendinger, R.W., Cardozo, N., Fisher, D.M., 2011. Structural Geology Algorithms: Vectors and Tensors. Cambridge University Press.

Amberger, G.F., 1959. L' autochtone de la partie Nord-Ouest du massif des Aiguilles Rouges: Haute-Savoie et Valais (Doctoral dissertation).. University of Geneva.

Argand, E., 1916. Sur l'arc des Alpes occidentales. Eclogae Geol. Helv. 14, 145–192.

Ayrton, S., 1972. Sur la prolongation de la nappe de Morcles en France. Eclogae Geol. Helv. https://doi.org/10.5169/SEALS-164096.

Ayrton, S., 1980. La géologie de la zone Martigny Chamonix (versant suisse) et l'origine de la nappe de Morcles (un exemple de subduction continentale). Eclogae Geolicae Helvetiae 73 (1), 137–172. Retrieved from. https://hal-insu.archives-ouvertes.fr/insu-00925393.

Ayrton, S., Barféty, J., Bellière, J., Gubler, Y., Jemelin, L., 1987. Carte géologique de la France, feuille de Chamonix (Sheet 680, scale 1:50,000). French geological survey: Bureau de Recherches Géologiques et Minières.

Badoux, H., 1972. Tectonique de la nappe de Morcles entre Rhône et Lizerne. Mat. Carte géol. Suisse 143.

Bauville, A., Schmalholz, S.M., 2015. Transition from thin-to thick-skinned tectonics and consequences for nappe formation: numerical simulations and applications to the Helvetic nappe system, Switzerland. Tectonophysics 665, 101–117. https://doi.org/10.1016/j.tecto.2015.09.030.

Bellahsen, N., Mouthereau, F., Boutoux, A., Bellanger, M., Lacombe, O., Jolivet, L., Rolland, Y., 2014. Collision kinematics in the western external Alps. Tectonics 33 (6), 1055–1088. https://doi.org/10.1002/2013tc003453.

Bellière, J., 1956. Caractère de la déformation Alpine dans les schistes cristallins du massif du Mont-Blanc. Bull. Soc. Géol. France VI, 691–6988.

Belliere, J., 1988. On the age of mylonites within the Mont Blanc massif. Geodin. Acta 2 (1), 13–16.

Bergemann, C.A., Gnos, E., Whitehouse, M.J., 2019. Insights into the tectonic history of the Western Alps through dating of fissure monazite in the Mont Blanc and Aiguilles Rouges Massifs. Tectonophysics 750, 203–212.

Berthé, D., Choukroune, P., Gapais, D., 1979. Orientations préférentielles du quartz et orthogneissification progressive en régime cisaillant: l'exemple du cisaillement sud-armoricain. Bull. Minér. 102 (2–3), 265–272.

Bertrand, M., 1881. Failles de la lisière du Jura entre Besançon et Salins. Bull. Soc. Géol. France 3 (10), 114–126.

Bonnet, C., Malavieille, J., Mosar, J., 2007. Interactions between tectonics, erosion, and sedimentation during the recent evolution of the Alpine orogen: analogue modeling insights. Tectonics 26 (6). https://doi.org/10.1029/2006TC002048.

Bousquet, R., Engi, M., Gosso, G., Oberhänsli, R., Berger, A., Spalla, M.I., Goffé, B., 2004. Explanatory notes to the map: metamorphic structure of the Alps transition from the Western to the Central Alps. Mitteilungen Der Österreichischen Mineralogischen Gesellschaft 134 (1), 279–298.

Boutoux, A., Bellahsen, N., Nanni, U., Pik, R., Verlaguet, A., Rolland, Y., Lacombe, O., 2016. Thermal and structural evolution of the external Western Alps: insights from (U–Th–Sm)/He thermochronology and RSCM thermometry in the Aiguilles Rouges/Mont Blanc massifs. Tectonophysics 683, 109–123. https://doi.org/10.1016/j.tecto.2016.06.010.

Brändlein, P., Nollau, G., Sharp, Z., 1994. Petrography and geochemistry of the Vallorcine granite (Aiguilles Rouges massif, Western Alps). Schweiz. Mineral. Petrogr. Mitt. 74, 227–243. https://doi.org/10.5169/SEALS-56344.

Burkhard, M., Sommaruga, A., 1998. Evolution of the western Swiss Molasse basin: structural relations with the Alps and the Jura belt. Geol. Soc. Lond., Spec. Publ. 134 (1), 279–298. https://doi.org/10.1144/gsl.sp.1998.134.01.13.

Bussy, F., Von Raumer, J., 1993. U–Pb dating of Palaeozoic events in the Mont-Blanc crystalline massif, Western Alps. Terra Nova 5 (1), 56–57.

Bussy, F., Hernandez, J., Von Raumer, J., 2000. Bimodal magmatism as a consequence of the post-collisional readjustment of the thickened Variscan continental lithosphere (Aiguilles Rouges-Mont Blanc Massifs, Western Alps). Earth Environ. Sci. Trans. R. Soc. Edinb. 91 (1–2), 221–233. https://doi.org/10.1017/s0263593300007392.

Butler, R.W., 1985. The restoration of thrust systems and displacement continuity around the Mont Blanc massif, NW external Alpine thrust belt. J. Struct. Geol. 7 (5), 569–582. https://doi.org/10.1016/0191-8141(85)90029-x.

Butler, R.W., Bond, C.E., Cooper, M.A., Watkins, H., 2018. Interpreting structural geometry in fold-thrust belts: why style matters. J. Struct. Geol. 114, 251–273. https://doi.org/10.1016/j.jsg.2018.06.019.

Calcagno, P., Chilès, J., Courrioux, G., Guillen, A., 2008. Geological modelling from field data and geological knowledge. Phys. Earth Planet. Inter. 171 (1–4), 147–157. https://doi.org/10.1016/j.pepi.2008.06.013.

Campani, M., Herman, F., Mancktelow, N., 2010. Two-and three-dimensional thermal modeling of a low-angle detachment: exhumation history of the Simplon Fault Zone, central Alps. J. Geophys. Res. Solid Earth 115 (B10). https://doi.org/10.1029/2009JB007036.

Capuzzo, N., Bussy, F., 2000. High-precision dating and origin of synsedimentary volcanism in the late Carboniferous Salvan-Dorénaz basin (Aiguilles-Rouges Massif, Western Alps). Schweiz. Mineral. Petrogr. Mitt. 80, 147–167. https://doi.org/10.5169/SEALS-60958.

Capuzzo, N., Wetzel, A., 2004. Facies and basin architecture of the Late Carboniferous Salvan-Dorénaz continental basin (Western Alps, Switzerland/France). Sedimentology 51 (4), 675–697. https://doi.org/10.1111/j.1365-3091.2004.00642.x.

Capuzzo, N., Handler, R., Neubauer, F., Wetzel, A., 2003. Post-collisional rapid exhumation and erosion during continental sedimentation: the example of the late Variscan Salvan-Dorénaz basin (Western Alps). Int. J. Earth Sci. 92 (3), 364–379. https://doi.org/10.1007/s00531-003-0332-0.

Cardozo, N., Allmendinger, R.W., 2013. Spherical projections with OSXStereonet. Comput. Geosci. 51, 193–205. https://doi.org/10.1016/j.cageo.2012.07.021.

Ceriani, S., Fügenschuh, B., Schmid, S.M., 2001. Multi-stage thrusting at the "Penninic Front" in the Western Alps between Mont Blanc and Pelvoux massifs. Int. J. Earth Sci. 90 (3), 685–702. https://doi.org/10.1007/s005310000188.

Charollais, J., Jamet, M., 1990. Principaux résultats géologiques du forage Brizon 1 (BZN1) Haute-Savoie, France. Mém. Soc. Géol. France 1833 (156), 185–202.

Charollais, J., Davaud, E., Jamet, M., 1996. Evolution of the southeastern Jura plateform-margin between the upper Jurassic and the Oligocene: new data from three oil wells. Géol. Fr. 1 (3), 25–42.

Cobbold, P.R., Quinquis, H., 1980. Development of sheath folds in shear regimes. J. Struct. Geol. 2 (1–2), 119–126.

Collet, L.W., 1927. The Structure of the Alps. Edward Arnold, London.

Collet, L.W., Paréjas, E., 1920. The Structure of the Alps. https://doi.org/10.5169/SEALS-742613.

Collet, L.W., Oulianoff, N., Reinhard, M., 1952. Carte géologique Suisse: feuille de Finhaut n°525 (scale 1:25,000). Commission géologique Suisse.

Corbin, P., Oulianoff, N., 1928. carte géologique du mont-blanc: feuille des tines (scale 1: 20,000). Institut de Géologie et de Paléontologie. Retrieved from. https://hal-insu.archives-ouvertes.fr/insu-01026264.

Dal Zilio, L., Ruh, J., Avouac, J.-P., 2020. Structural evolution of orogenic wedges: Interplay between erosion and weak décollements. Tectonics 39 (10). https://doi.org/10.1029/2020TC006210 e2020TC006210.

Dall'Asta, N., Hoareau, G., Manatschal, G., Centrella, S., Denèle, Y., Ribes, C., Kalifi, A., 2022. Structural and petrological characteristics of a Jurassic detachment fault from the Mont-Blanc massif (Col du Bonhomme area, France). J. Struct. Geol. 159, 104593 https://doi.org/10.1016/j.jsg.2022.104593.

Deville, E., Chauvière, A., 2000. Thrust tectonics at the front of the western Alps: constraints provided by the processing of seismic reflection data along the Chambéry transect. Compt. Rend. Acad. Sci. Ser. IIA Earth Planet. Sci. 331 (11), 725–732. https://doi.org/10.1016/s1251-8050(00)01463-4.

Dobmeier, C., Von Raumer, J., 1995. Significance of latest-Variscan and Alpine deformation for the evolution of Montagne de Pormenaz (SouthWestern Aiguilles-Rouges massif, Western Alps). Eclogae Geol. Helvetiae 88 (2), 267–279.

Doudoux, B., de Lepinay, B.M., Tardy, M., 1982. Une interprétation nouvelle de la structure des massifs subalpins savoyards (Alpes occidentales): nappes de charriage oligocènes et déformations superposées. Compt. Rend. Acad. Sci. Paris, II 64, 63–68.

Duparc, L., Lugeon, M., Michel-Lévy, A., Mrazec, L., 1966. Carte géologique de la France, feuille de Vallorcine Mont-Blanc (Sheet 160, scale 1:80,000). French geological survey: Bureau de Recherches Géologiques et Minières.

Egli, D., Mancktelow, N., 2013. The structural history of the Mont Blanc massif with regard to models for its recent exhumation. Swiss J. Geosci. 106 (3), 469–489. https://doi.org/10.1007/s00015-013-0153-5.

Egli, D., Mancktelow, N., Spikings, R., 2017. Constraints from $^{40}Ar/^{39}Ar$ geochronology on the timing of Alpine shear zones in the Mont-Blanc Aiguilles Rouges region of the European Alps. Tectonics 36 (4), 730–748. https://doi.org/10.1002/2016TC004450.

Eltchaninoff, C., 1982. Etude géologique entre Belledonne et Mont Blanc: la terminaison septentrionale du massif de Belledonne et les terrains de son enveloppe Alpes françaises. Bull. Soc. Géol. France S7-XXIV (4), 817–830. https://doi.org/10.2113/gssgfbull.S7-XXIV.4.817.

Epard, J.L., 1986. Le contact entre le socle du Mont-Blanc et la zone de Chamonix: implications tectoniques. Bull. Soc. Vaudoise Sci. Nat. 288, 225–245.

Epard, J.L., 1990. La nappe de Morcles au sud-ouest du Mont-Blanc (Doctoral dissertation, Université de Lausanne). Retrieved from. https://tel.archives-ouvertes.fr/tel-00923347.

Escher, A., Masson, H., Steck, A., 1988. Coupes géologiques des Alpes occidentales Suisses. In: Mémoires des laboratoires de géologie, minéralogie, géophysique et du musée géologique de l'Université de Lausanne, 2.

Escher, A., Masson, H., Steck, A., 1993. Nappe geometry in the western swiss Alps. J. Struct. Geol. 15 (3–5), 501–509. https://doi.org/10.1016/0191-8141(93)90144-y.

Faure, J.L., Colletta, B., Deville, E., Lecomte, J.C., 1999. Méthodologie d'équilibrage de coupes structurales en zones compressives: la coupe de la vallée de l'Arve et la coupe du massif des Bornes (profil Ecors Alp1 et Alp2). (Tech. Rep.). Etude FSH. (139 pages, 102 figures). Rapport IFP 45584.

Ferrill, D.A., Groshong Jr., R.H., 1993. Kinematic model for the curvature of the northern Subalpine Chain, France. J. Struct. Geol. 15 (3–5), 523–541. https://doi.org/10.1016/0191-8141(93)90146-2.

Fréchet, J., Thouvenot, F., Frogneux, M., Deichmann, N., Cara, M., 2011. The Mw 4.5 Vallorcine (French Alps) earthquake of 8 September 2005 and its complex aftershock sequence. J. Seismol. 15 (1), 43–58. https://doi.org/10.1007/s10950-010-9205-8.

Gapais, D., Barbarin, B., 1986. Quartz fabric transition in a cooling syntectonic granite (Hermitage Massif, France). Tectonophysics 125 (4), 357–370. https://doi.org/10.1016/0040-1951(86)90171-X.

Garefalakis, P., Schlunegger, F., 2019. Tectonic processes, variations in sediment flux, and eustatic sea level recorded by the 20 myr old burdigalian transgression in the

swiss molasse basin. Solid Earth 10 (6), 2045–2072. Retrieved from. https://doi.org/10.5194/se-10-2045-2019.
Genier, F., Bussy, F., Epard, J.-L., Baumgartner, L., 2008. Water-assisted migmatization of metagraywackes in a Variscan shear zone, Aiguilles-Rouges massif, western Alps. Lithos 102 (3–4), 575–597. https://doi.org/10.1016/j.lithos.2007.07.024.
Girault, J.B., Bellahsen, N., Boutoux, A., Rosenberg, C.L., Nanni, U., Verlaguet, A., Beyssac, O., 2020. The 3D thermal structure of the Helvetic Nappes of the European Alps: implications for collisional processes. Tectonics 39 (3). https://doi.org/10.1029/2018TC005334 e2018TC005334.
Girault, J.B., Bellahsen, N., Bernet, M., Pik, R., Loget, N., Lasseur, E., Sonnet, M., 2022. Exhumation of the Western Alpine collisional wedge: new thermochronological data. Tectonophysics 822, 229155. https://doi.org/10.1016/j.tecto.2021.229155.
Glotzbach, C., Reinecker, J., Danisik, M., Rahn, M., Frisch, W., Spiegel, C., 2008. Neogene exhumation history of the Mont Blanc massif, western Alps. Tectonics 27 (4). https://doi.org/10.1029/2008TC002257.
Glotzbach, C., van der Beek, P., Spiegel, C., 2011. Episodic exhumation and relief growth in the Mont Blanc massif, Western Alps from numerical modelling of thermochronology data. Earth Planet. Sci. Lett. 304 (3–4), 417–430. https://doi.org/10.1016/j.epsl.2011.02.020.
Gourlay, P., Ricou, L., 1983. Dextral strike-slip tectonics along the Chamonix suture zone (French and swiss Alps). C. R. Acad. Sci. 296.
Hanmer, S., Passchier, C., 1991. Shear-sense indicators: a review. Geol. Surv. Can. 130 (3) https://doi.org/10.1017/s0016756800020112.
Hielscher, R., Schaeben, H., 2008. A novel pole figure inversion method: specification of the MTEX algorithm. J. Appl. Crystallogr. 41 (6), 1024–1037. https://doi.org/10.1107/s0021889808030112.
Homewood, P., 1983. Palaeogeography of Alpine flysch. Palaeogeogr. Palaeoclimatol. Palaeoecol. 44 (3–4), 169–184. https://doi.org/10.1016/0031-0182(83)90101-3.
Hubbard, M., Mancktelow, N.S., 1992. Lateral displacement during Neogene convergence in the western and central Alps. Geology 20 (10), 943–946. https://doi.org/10.1130/0091-613(1992)020⟨0943:LDDNCI⟩2.3.CO;2.
Huggenberger, P., 1985. Faltenmodelle und verformungsverteilung in deckenstrukturen am beispiel der morcles-decke (helvetikum der westschweiz) (Doctoral dissertation). https://doi.org/10.3929/ETHZ-A-000365939.
Jeanbourquin, P., 1994. Early deformation of Ultrahelvetic mélanges in the Helvetic nappes (Western Swiss Alps). J. Struct. Geol. 16 (10), 1367–1383.
Kalifi, A., Leloup, P.H., Sorrel, P., Galy, A., Demory, F., Spina, V., Rubino, J.-L., 2021. Chronology of thrust propagation from an updated tectono-sedimentary framework of the Miocene molasse (western Alps). Solid Earth 12 (12), 2735–2771. https://doi.org/10.5194/se-12-2735-2021.
Kalifi, A., Sorrel, P., Leloup, P.-H., Galy, A., Spina, V., Huet, B., Rubino, J.-L., 2022. Tectonic control on the palaeogeographical evolution of the miocene seaway along the western Alpine foreland basin. In: Geological Society, London, Special Publications, SP523–2021–78. https://doi.org/10.1144/sp523-2021-78.
Kerrich, R., Allison, I., Barnett, R.L., Moss, S., Starkey, J., 1980. Microstructural and chemical transformations accompanying deformation of granite in a shear zone at Mieville, Switzerland, with implications for stress corrosion cracking and superplastic flow. Contrib. Mineral. Petrol. 73 (3), 221–242. https://doi.org/10.1007/bf00381442.
Kirschner, D.L., Sharp, Z.D., Masson, H., 1995. Oxygen isotope thermometry of quartz-calcite veins: unraveling the thermal-tectonic history of the subgreenschist facies Morcles nappe (Swiss Alps). Geol. Soc. Am. Bull. 107 (10), 1145–1156. https://doi.org/10.1130/0016-7606(1995)107⟨1145:OITOQC⟩2.3.CO;2.
Kirschner, D.L., Cosca, M.A., Masson, H., Hunziker, J.C., 1996, August. Staircase $^{40}Ar/^{39}Ar$ spectra of fine-grained white mica: timing and duration of deformation and empirical constraints on argon diffusion. Geology 24 (8), 747–750. https://doi.org/10.1130/0091-13(1996)024⟨0747:SAASOF⟩2.3.CO;2.
Kirschner, D.L., Masson, H., Cosca, M.A., 2003, July. An $^{40}Ar/^{39}Ar$, and stable isotope study of micas in low-grade fold-and-thrust belt: an example from the Swiss Helvetic Alps. Contrib. Mineral. Petrol. 145 (4), 460–480. https://doi.org/10.1007/s00410-003-0461-2.
Kiss, D., Duretz, T., Schmalholz, S.M., 2020. Tectonic inheritance controls nappe detachment, transport and stacking in the Helvetic nappe system, Switzerland: insights from thermomechanical simulations. Solid Earth 11 (2), 287–305. https://doi.org/10.5194/se-11-287-2020.
Konstantinovskaya, E., Malavieille, J., 2005. Accretionary orogens: erosion and exhumation. Geotectonics 39 (1), 69–86.
Lacassin, R., 1988. Large-scale foliation boudinage in gneisses. J. Struct. Geol. 10 (6), 643–647. https://doi.org/10.1016/0191-8141(88)90030-2.
Lacassin, R., Mattauer, M., 1985. Kilometre-scale sheath fold at Mattmark and implications for transport direction in the Alps. Nature 315 (6022), 739–742. https://doi.org/10.1038/315739a0.
Lacassin, R., Tapponnier, R., Bourjot, L., 1990. Culminations anticlinales d'échelle crustale et imbrication de la lithosphère dans les Alpes, apports du profil ECORSCROP. Comptes rendus de l'Académie des sciences. Série 2, Mécanique, Physique, Chimie, Sciences de l'univers, Sciences de la Terre 310 (6), 807–814.
Lajaunie, C., Courrioux, G., Manuel, L., 1997. Foliation fields and 3D cartography in geology: principles of a method based on potential interpolation. Math. Geol. 29 (4), 571–584. https://doi.org/10.1007/bf02775087.
Leloup, P.H., Arnaud, N., Sobel, E.R., Lacassin, R., 2005. Alpine thermal and structural evolution of the highest external crystalline massif: the Mont Blanc. Tectonics 24 (4). https://doi.org/10.1029/2004tc001676.
Lemoine, M., Tricart, P., 1986. Les Schistes lustrés piémontais des Alpes occidentales: approche stratigraphique, structurale et sédimentologique. Eclogae Geol. Helv. 79 (2), 271–294.
Marshall, D., Meisser, N., Taylor, R.P., 1998. Fluid inclusion, stable isotope and Ar-Ar evidence for the age and origin of gold-bearing quartz veins at Mont Chemin, Switzerland. Mineral. Petrol. 62 (3), 147–165.
Menard, G., Thouvenot, F., 1987. Coupes équilibrées crustales: méthodologie et application aux Alpes occidentales. Geodin. Acta 1 (1), 35–45. https://doi.org/10.1080/09853111.1987.11105123.
Mennessier, G., Carme, F., Belliere, J., Dhellemes, R., Antoine, P., Dabrowski, H., Bordet, C., 1977. Carte géologique de la France, feuille de Saint-Gervais-les-Bains (Sheet 703, scale 1:50,000). French geological survey: Bureau de Recherches Géologiques et Minières.
Mosar, J., 1989. Deformation interne dans les Prealpes medianes (Suisse). Eclogae Geol. Helv. 82 (3), 765–793.
Pairis, B., Pairis, J.L., Porthault, B., 1973. Présence de Crétacé supérieur reposant sur le socle dans le massif des Aiguilles Rouges, Alpes de Haute Savoie. Compt. Rend. Acad. Sci. Paris 276, 1131–1134.
Pairis, J.L., Pairis, B., Bellière, J., Rosset, J., Détraz, H., Muller, A., Uselle, J.P., 1992. Carte géologique de la france, feuille de Cluses, (sheet 679, scale 1:50,000). French geological survey: Bureau de Recherches Géologiques et Minières.
Paréjas, E., 1922. Géologie de la zone de Chamonix comprise entre le Mont-Blanc et les Aiguilles rouges. Mém. Soc. Phys. Hist. Nat. Genève 39 (7), 374–442.
Paréjas, E., 1925. La tectonique du Mont Joly (Haute-Savoie). Eclogae Geol. Helv. 19 (2), 420–503. https://doi.org/10.5169/SEALS-158423.
Passchier, C., Trouw, R., 2005. Foliations, lineation and lattice preferred orientation. In: Microtectonics. Springer Berlin Heidelberg, pp. 67–109.
Pfiffner, O.A., 1993. The structure of the Helvetic nappes and its relation to the mechanical stratigraphy. J. Struct. Geol. 15 (3–5), 511–521. https://doi.org/10.1016/0191-8141(93)90145-z.
Pfiffner, O.A., 2014. Geology of the Alps (2nd edition, translated from German). Wiley-Blackwell.
Pfiffner, O.A., 2017. Thick-skinned and thin-skinned tectonics: a global perspective. Geosciences 7 (3), 71. https://doi.org/10.3390/geosciences7030071.
Pfiffner, O.A., Lehner, P., Heitzmann, P., Mueller, S., Steck, A., 1997. Deep Structure of the Swiss Alps: Results of NRP 20. Birkhäuser.
Pfiffner, O.A., Schlunegger, F., Buiter, S.J.H., 2002. The Swiss Alps and their peripheral foreland basin: Stratigraphic response to deep crustal processes. Tectonics 21 (2), 3–16. https://doi.org/10.1029/2000tc900039.
Pfiffner, O.A., Burkhard, M., Hänni, R., Kammer, A., Kligfield, R., Mancktelow, N.S., Menkveld, J.W., Ramsay, J.G., Schmid, S.M., Zurbriggen, R., 2010. Structural Map of the Helvetic Zone of the Swiss Alps, including Vorarlberg (Austria) and Haute Savoie (France), 1: 100 000. Geological Special Map 128.
Plancherel, R., Broquet, P., Caron, C., 1998. Carte géol France (1/50 000) feuille de Samoëns-Pas-de-Morgins (655), Orléans.
Platt, J., 1984. Balanced cross-sections and their implications for the deep structure of the northwest Alps: discussion. J. Struct. Geol. 6 (5), 603–606. https://doi.org/10.1016/0191-8141(84)90072-5.
Poty, B., Cathelineau, M., 1974. La formation des cristaux dans les fentes alpines du massif du Mont-Blanc. Le Règne Minéral 5, 19–21.
Poty, B., Stadler, H.A., Weisbord, A.M., 1974. Fluid inclusions studies in quartz from fissures of western and central Alps. Schweiz. Mineral. Petrogr. Mitt. 54, 717–752.
Quinquis, H., Audren, C., Brun, J.P., Cobbold, P.R., 1978. Intense progressive shear in Ile de Groix blueschists and compatibility with subduction or obduction. Nature 273 (5657), 43–45. https://doi.org/10.1038/273043a0.
Ramsay, J.G., 1981. Tectonics of the Helvetic Nappes. Geol. Soc. Lond., Spec. Publ. 9 (1), 293–309. https://doi.org/10.1144/gsl.sp.1981.009.01.26.
Reinhard, M., Preiswerk, H., 1927. Über Granitmylonite im Aiguilles-Rouges-Massiv (westliches Wallis). Buchdruckerei Emil Birkhäuser.
Ribes, C., Ghienne, J.-F., Manatschal, G., Dall'Asta, N., Stockli, D.F., Galster, F., Karner, G.D., 2020. The Grès Singuliers of the Mont Blanc region (France and Switzerland):s tratigraphic response to rifting and crustal necking in the Alpine Tethys. Int. J. Earth Sci. 109 (7), 2325–2352. https://doi.org/10.1007/s00531-020-01902-z.
Rolland, Y., Cox, S., Boullier, A.M., Pennacchioni, G., Mancktelow, N., 2003. Rare earth and trace element mobility in mid-crustal shear zones: insights from the mont blanc massif (western alps). Earth Planet. Sci. Lett. 214 (1–2), 203–219. https://doi.org/10.1016/s0012-821x(03)00372-8.
Rolland, Y., Rossi, M., Cox, S.F., Corsini, M., Mancktelow, N., Pennacchioni, G., Boullier, A.M., 2008. $^{40}Ar/^{39}Ar$ dating of synkinematic white mica: insights from fluid-rock reaction in low-grade shear zones (mont blanc massif) and constraints on timing of deformation in the NW external alps. Geol. Soc. Lond., Spec. Publ. 299 (1), 293–315. https://doi.org/10.1144/sp299.18.
Rossi, M., Rolland, Y., 2014. Stable isotope and Ar/Ar evidence of prolonged multiscale fluid flow during exhumation of orogenic crust: example from the Mont Blanc and Aar Massifs (NW Alps). Tectonics 33 (9), 1681–1709. https://doi.org/10.1002/2013TC003438.
Rossi, M., Rolland, Y., Vidal, O., Cox, S.F., 2005. Geochemical variations and element transfer during shear-zone development and related episyenites at middle crust depths: insights from the Mont Blanc granite (French - Italian Alps). Geological Society of London, Special Publications 245 (1), 373–396. https://doi.org/10.1144/GSL.SP.2005.245.01.18.
Ruffini, R., Polino, R., Callegari, E., Hunziker, J., Pfeifer, H., 1997. Volcanic clast-rich turbidites of the Taveyanne sandstones from the Thônes syncline (Savoie, France): records for a Tertiary postcollisional volcanism. Schweiz. Mineral. Petrogr. Mitt. 77 (2), 161–174.
Seward, D., Mancktelow, N.S., 1994. Neogene kinematics of the central and western Alps: evidence from fission-track dating. Geology 22 (9), 803–806. https://doi.org/10.1130/0091-7613(1994)022⟨0803:NKOTCA⟩2.3.CO;2.

Simonetti, M., Carosi, R., Montomoli, C., Cottle, J.M., Law, R.D., 2020. Transpressive deformation in the southern european variscan belt: new insights from the aiguilles rouges massif (western alps). Tectonics 39 (6). https://doi.org/10.1029/2020tc006153.

Simon-Labric, T., Rolland, Y., Dumont, T., Heymes, T., Authemayou, C., Corsini, M., Fornari, M., 2009. $^{40}Ar/^{39}Ar$ dating of Penninic Front tectonic displacement (Western Alps) during the Lower Oligocene (31–34 Ma). Terra Nova 21 (2), 127–136. https://doi.org/10.1111/j.1365-3121.2009.00865.x.

Spitz, R., Bauville, A., Epard, J.L., Kaus, B.J., Popov, A.A., Schmalholz, S.M., 2020. Control of 3-D tectonic inheritance on fold-and-thrust belts: insights from 3-D numerical models and application to the Helvetic nappe system. Solid Earth 11 (3), 999–1026. https://doi.org/10.5194/se-11-999-2020.

Steck, A., Vocat, D., 1973. Zur mineralogie der granitmylonite von miéville, aiguilles rouges massiv. Schweiz. Mineral. Petrogr. Mitt. 54, 474–477.

Steyrer, H.P., Sturm, R., 2002. Stability of zircon in a low-grade ultramylonite and its utility for chemical mass balancing: the shear zone at miéville, Switzerland. Chem. Geol. 187 (1–2), 1–19. https://doi.org/10.1016/s0009-2541(02)00010-4.

Triboulet, S., 1980. Etude geologique entre Belledonne et Mont Blanc: la terminaison septentrionale du massif de Belledonne et les terrains de son enveloppe Alpes françaises (Doctoral dissertation, Université Pierre et Marie Curie Paris VI). Retrieved from. https://tel.archives-ouvertes.fr/tel-00616709.

Trumpy, R., 1971. Sur le jurassique de la zone helvétique en suisse. Ann. Geol. Inst. Hungary 54 (2), 370–382.

Vanardois, J., Roger, F., Trap, P., Goncalves, P., Lanari, P., Paquette, J.-L., Barou, F., 2022. Exhumation of deep continental crust in a transpressive regime: the example of variscan eclogites from the Aiguilles-Rouges Massif (western alps). J. Metamorph. Geol. https://doi.org/10.1111/jmg.12659.

Von Raumer, J., Bussy, F., 2004. Mont blanc and aiguilles rouges geology of their polymetamorphic basement (external massifs, Westerns Alps, France-Switzerland). Mém. Géol. (Lausanne) 42, 1–210.

Supporting Information

Contents of this file

- Tables S1 to S4.
- Figures S1 to S10.

Introduction

The supplements provide the location of the outcrops discussed in the publication (Table S1), the average measures reported in the stereographic plots from the figure 3a (Table S2), technical information about the EBSD analysis (Table S3), details about the datations from the bibliography cited in the publication (Table S4), the figure 3a without stereo-plots and surcharge (Figure S1), stereo plots from figure 3a with all the data used for calculating average plane and lineation (Figure S2), complementary field pictures (Figure S3 to S8), the image at microscale of the sample ARe096 from the Gietroz normal fault (Figure S9) and the sections used for the estimation of exhumation (Figure S10).

Table S1. Locations of outcrops used in the study.

Location ID	Studied Sites	Decimal Longitude	Decimal Latitude	Elevation in Meters	Verbatim Locality
AR0025	FF1	6.950569	46.02661	1965	Col des Posettes, Vallorcine, France
AR0027	FF1	6.953102	46.02507	2008	Col des Posettes, Chamonix-Mont-Blanc, France
AR0139	HGT6	6.874016	45.98791	2955	Aiguilles Rouges, Aiguille du Belvedere, Chamonix-Mont-Blanc, France
AR0141	HGT6	6.873149	45.987858	2966	Aiguilles Rouges, Aiguille du Belvedere, Chamonix-Mont-Blanc, France
AR0152	TB1	6.883872	45.94979	1287	Aiguilles Rouges, Les Praz, Chamonix-Mont-Blanc, France
AR0162		6.87577	46.019135	2630	Mont-Oreb, Aiguilles Rouges, Vallon de Berard, Vallorcine, France
AR0178	HGT2	6.861869	46.01774	2532	Mont-Buet, Aiguilles Rouges, Vallon de Berard, Vallorcine, France
AR0184		6.857506	46.01343	2454	Mont-Buet, Aiguilles Rouges, Vallon de Berard, Vallorcine, France
AR0184b		6.857152	46.013	2450	Mont-Buet, Aiguilles Rouges, Vallon de Berard, Vallorcine, France
AR0190	FF3	6.999964	46.05488	1490	Forclaz pass, Valais, Switzerland
AR0271	FF2	6.97485	46.04682	2040	Carraye, Les Tseppes, Valais, Switzerland
AR0358	FB1	6.973778	46.08449	1360	Aiguilles Rouges, Finhaut, Valais, Switzerland
AR0359	FB1	6.976246	46.085842	1332	Aiguilles Rouges, Finhaut, Valais, Switzerland
AR0370b		6.96539	46.06789	1070	Aiguilles Rouges, Finhaut, Valais, Switzerland
AR0391	TB2	6.93418	46.000328	1517	Montroc, Chamonix-Mont-Blanc, France
AR0392	TB2	6.934502	46.000233	1509	Montroc, Chamonix-Mont-Blanc, France
AR0393	TB2	6.935156	46.000435	1488	Montroc, Chamonix-Mont-Blanc, France
AR0394	TB2	6.934862	46.000626	1488	Montroc, Chamonix-Mont-Blanc, France
AR0395	TB2	6.935742	46.000843	1500	Montroc, Chamonix-Mont-Blanc, France
AR0396	TB2	6.936321	46.001965	1525	Montroc, Chamonix-Mont-Blanc, France
AR0411	TB1	6.889766	45.95017	1153	Aiguilles Rouges, Les Praz, Chamonix-Mont-Blanc, France
AR0447	PMsz2	6.791885	45.95824	2059	Crete Blanche, Pormenaz, Servoz, France
AR0453	PMsz2	6.79339	45.95871	2076	Crete Blanche, Pormenaz, Servoz, France
AR0454	PMsz2	6.793369	45.958714	2082	Crete Blanche, Pormenaz, Servoz, France
AR0455	PMsz2	6.793432	45.958782	2082	Crete Blanche, Pormenaz, Servoz, France
AR0482	PMsz1	6.806119	45.90461	1365	Le Coupeau, Les Houches, France
AR0483	PMsz1	6.80579	45.904827	1346	Le Coupeau, Les Houches, France
AR0484	PMsz1	6.805527	45.9048	1347	Le Coupeau, Les Houches, France
AR0485	PMsz1	6.805086	45.90484	1337	Le Coupeau, Les Houches, France
AR0486	PMsz1	6.804257	45.90493	1326	Le Coupeau, Les Houches, France
AR0765	FB2	6.917144	45.9997	1733	Les Cheserys, Aiguilles Rouges, Chamonix-Mont-Blanc, France
AR0779	FB2	6.918403	46.00137	1688	Les Cheserys, Aiguilles Rouges, Chamonix-Mont-Blanc, France
AR0874	FB3	6.922863	46.07913	1986	Eastern side of Emosson lake, Valais, Switzerland
AR0875	FB3	6.9227004	46.08043	1976	Eastern side of Emosson lake, Valais, Switzerland
AR0892	HBT4	6.906337	46.09824	1986	North of Emosson lake, Valais, Switzerland
AR0894	FB3	6.922009	46.083485	1971	Aiguilles Rouges, Eastern side of Emosson lake, Valais, Switerland
AR0895	FB3	6.924889	46.07647	1996	Aiguilles Rouges, Eastern side of Emosson lake, Valais, Switerland
AR0896	FB3	6.924889	46.07618	1994	Aiguilles Rouges, Eastern side of Emosson lake, Valais, Switerland
AR0897	FB3	6.916172	46.075157	1997	Aiguilles Rouges, Eastern side of Emosson lake, Valais, Switerland
AR0903		6.928097	46.099403	2269	Col de Barberine, Valais, Switzerland
AR0909		6.92832	46.09988	2283	Col de Barberine, Valais, Switzerland
AR0905	HBT1	6.928226	46.09963	2280	Col de Barberine, Valais, Switzerland
AR0906	HBT1	6.928317	46.099693	2279	Col de Barberine, Valais, Switzerland
AR0907	HBT1	6.928324	46.099777	2280	Col de Barberine, Valais, Switzerland
AR0912	HBT1	6.928404	46.100166	2298	Col de Barberine, Valais, Switzerland
AR0914	HBT1	6.928567	46.100517	2314	Col de Barberine, Valais, Switzerland
AR0915	HBT1	6.92848	46.10068	2342	Col de Barberine, Valais, Switzerland
AR0916	HBT1	6.928534	46.1008	2346	Col de Barberine, Valais, Switzerland
AR0917	HBT1	6.928748	46.100895	2355	Col de Barberine, Valais, Switzerland
AR0919	PMsz3	6.796878	45.95758	2189	Pointe Noire de Pormenaz, Servoz, France
AR1451		6.837431	46.0711	1003	Haut-Giffre, Nant des Pères, Sixt-Fer-a-Cheval, France
AR1470		6.8435555	46.072613	1056	Haut-Giffre, Nant des Pères, Sixt-Fer-a-Cheval, France
AR1472	HGT5	6.813543	45.977247	2159	Moede d'Anterne, Passy, France
AR1925	HGT3	6.813335	45.977212	2170	Moede d'Anterne, Passy, France
AR1926	HGT3	6.81643	45.979589	2179	Moede d'Anterne, Passy, France

Table S2. Measures plotted in the stereographic diagrams in figure 3. HGT: Haut-Giffre Thrust; TB: Tour Back Thrust; PMsz: Pormenaz-Merlet shear zone; FB: Finhaut back thrust; FF: Forclaz fault.

Site	Mean Fault Plane Strike ; Dip ; Quadrant	Mean Lineation Trend/Plunge
HGT1	N019 ; 23°W	285/25
HGT2	N020 ; 33°W	280/32
HGT3	N045 ; 13°W	288/05
HGT5	N038 ; 32°E	-
HGT6	N058 ; 09°NW	288/05
TB1	N179 ; 50°W	309/39
TB2	N003 ; 39°W	303/31
PMsz1	N157 ; 34°E	96/55
PMsz2	N006 ; 72° SE	105/80
PMsz3	N055 ; 22° SE	96/55
FB1	N013 ; 43°W	297/42
FB2	N019 ; 75°W	285/75
FB3	N015 ;67°W	304/62
FF1	N031 ; 62°E	95/60
FF2	N008 ; 28°E	133/24
FF3	N030 ; 77°E	186/61

Table S3. Summarizing measurement conditions, details of used instruments, and sample preparation during Electron BackScattered Diffraction (EBSD) analysis.

Instrument	FIB Zeiss NVision 40
Location	INSA Lyon
Working conditions	Acceleration voltage 340 kV Acquisition speed 10 Hz Exposure time 20 ms
Acquisition software	Oxford Instruments Channel 5.0
Sample ID	ARe42
Sample preparation	Polished carbon-coated (5 microns) thin section (30 um)
Image resolution	385x292 px
Mean indexing	72.5%
Optical step size	6um
Field width	2
Field height	1.74 um
Number of data points	111 650

Table S4. Details on datations samples from figure 15.

Sample	Latitude Decimal (EPSG:4326)	Longitude	Location	Tectonic Unit	Mineral	Plateaux Ages (Ma, 2σ)	Inv. Isochrone Age (Ma, 2σ)	Age Range (Ma)
C6[1]	45.89639	6.87835	Plan de l'Aiguille	MBsz	Biotite	19.75 ± 0.21	21.8 ± 3	
S68[1]	46.05072	6.94603	Vallorcine	VMsz	Phengite	14.3 ± 0.2 & 22.9 ± 0.9	14.5 ± 0.3 & 23.4 ± 0.4	
ME27[2]	45.89951	6.88742	Plan de l'Aiguille	MBsz	K-Feldspar	10.61 ± 0.15 (min age)		
C8[2]	45.89534	6.89365	Plan de l'Aiguille	MBsz	Biotite	16.6 ± 0.7		
C8[2]	45.89534	6.89365	Plan de l'Aiguille	MBsz	K-Feldspar	10.98 ± 0.2 (min age)		
DE65[3]	46.06699	7.07607	Angle Fault	MBsz	White mica			14.30 - 20.41
DE79[3]	46.10759	7.06844	La Bâtiaz	HBT	White mica	20.28 ± 0.21	20.18 ± 0.49	
S02[3]	46.10666	7.06827	Sur le Sex	HBT	White mica	15.09 ± 0.15	15.07± 0.23	
93-29-A[4]	46.17236	7.12788	Morcles	HBT	2-6 µm mica	~19 & 21		
92-29-J[4]	46.10615	7.06903	Morcles	HBT	2-6 µm mica			13.6 - 22.7

[1] Rolland et al., 2008
[2] Leloup et al., 2005
[3] Egli et al., 2017
[4] Kirschner et al., 2003

MBsz : Mont-Blanc shear zone
VMsz : Vallorcine Miéville shear zone
HBT : Helvetic Basal Thrust

Figure S1. Same as figure 3a without stereo plots and surcharge.

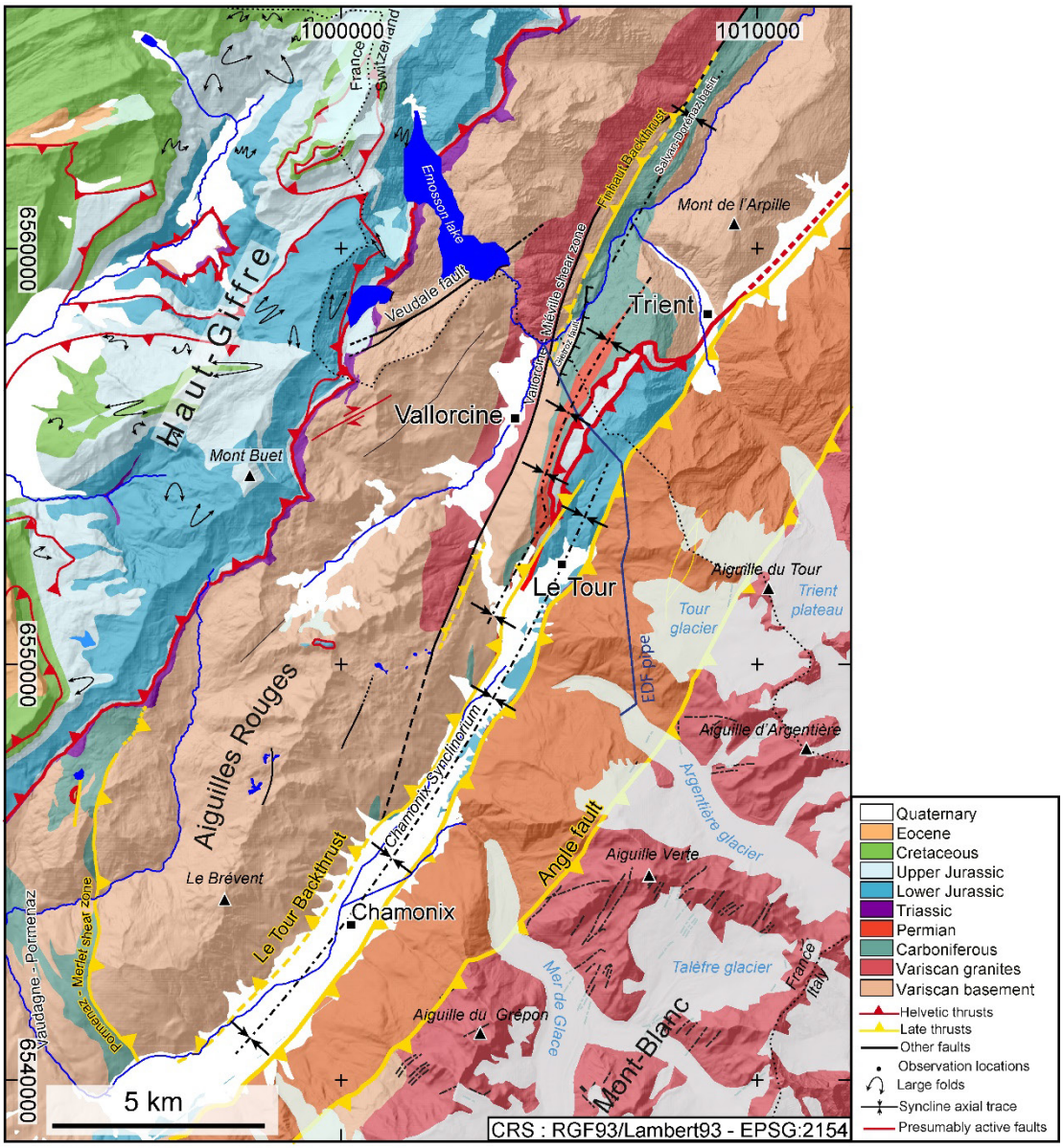

Figure S2. All data used for the calculation of the mean plane and mean lineation in the stereo plots used in figure 3a. Stereoplots are in lower hemisphere, equal area, north up.

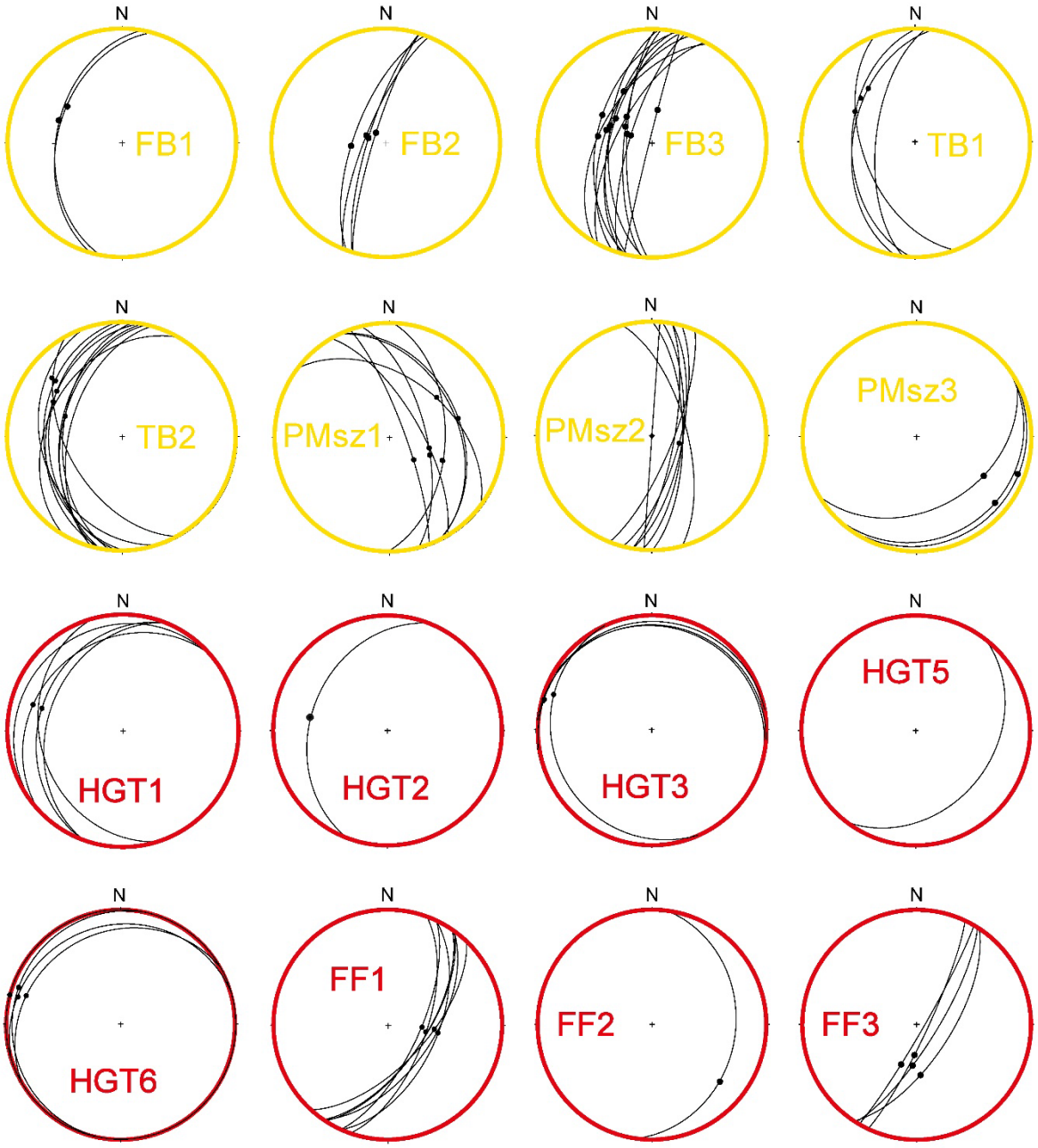

FB : Finhaut back thrust
HGT : Haut-Giffre Thrust
FF : Forclaz fault
PMsz : Pormenaz-Merlet shear zone

: Shear or fault plane
• : Lineation

Figure S3. Undeformed Triassic: a) Basal Triassic unconformity with stratigraphic and angular unconformity above Variscan gneiss that show a steep foliation (bottom of the Haut-Giffre); b) red and green siltites showing ripple marks (Barberine pass area).

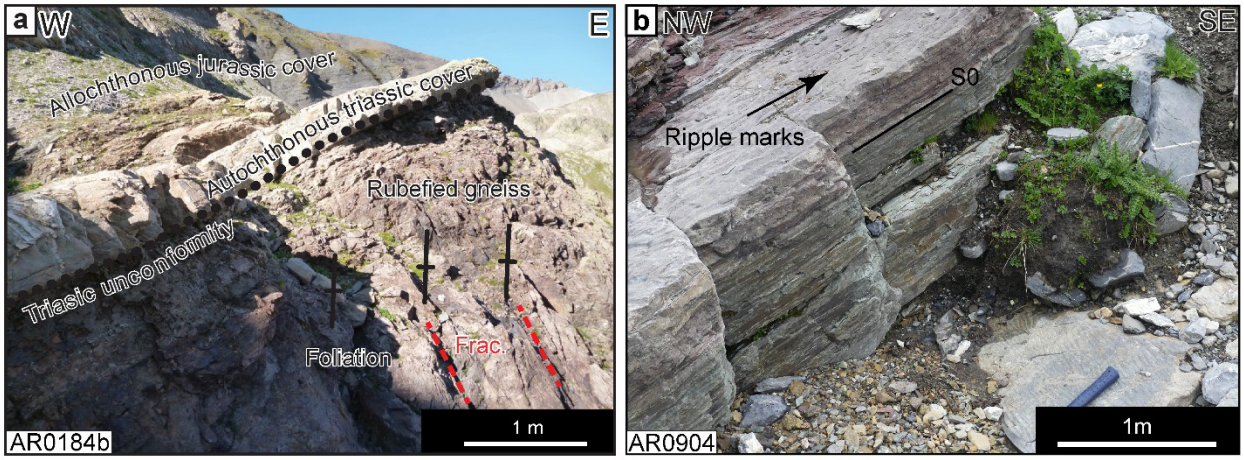

Figure S4. (a) Site HGT2 Stretching lineation trending N280°, compatible with a displacement towards the WNW inside the shear zone at the bottom of the Mesozoic sedimentary serie. (b) Triassic sandstone layer affected by an isoclinal fold with the fold axis trending N279°. This fold is a sheath fold that has highly curvilinear axes, with the axis parallel to the direction of transport. Such folds occur in shear zones with a high simple shear rate ($\gamma \geq 10$) (Cobbold and Quinquis, 1980; Quinquis et al., 1978, Lacassin & Mattaeuer, 1985).

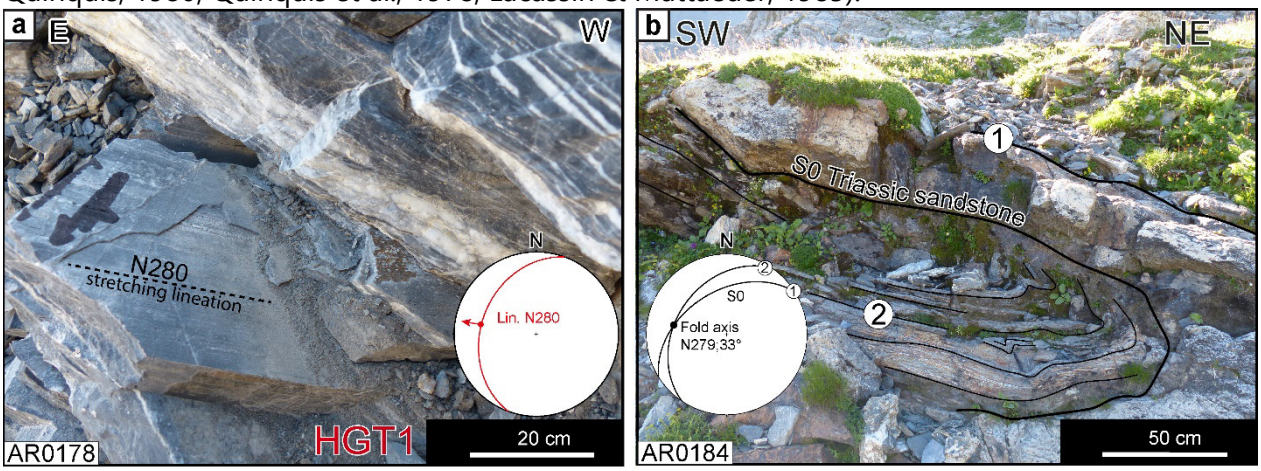

Figure S5. Site HGT3 (Souay area): a) white limestones that are mylonitized and metamorphosed into marbles. They bear a well-visible stretching lineation, trending N288°. The limestones are also asymmetrically folded with axis trending N032° and shear planes cross cutting the axial plane. The lineation, shear plane, and asymmetry of the fold suggest a direction of shear towards the WNW.

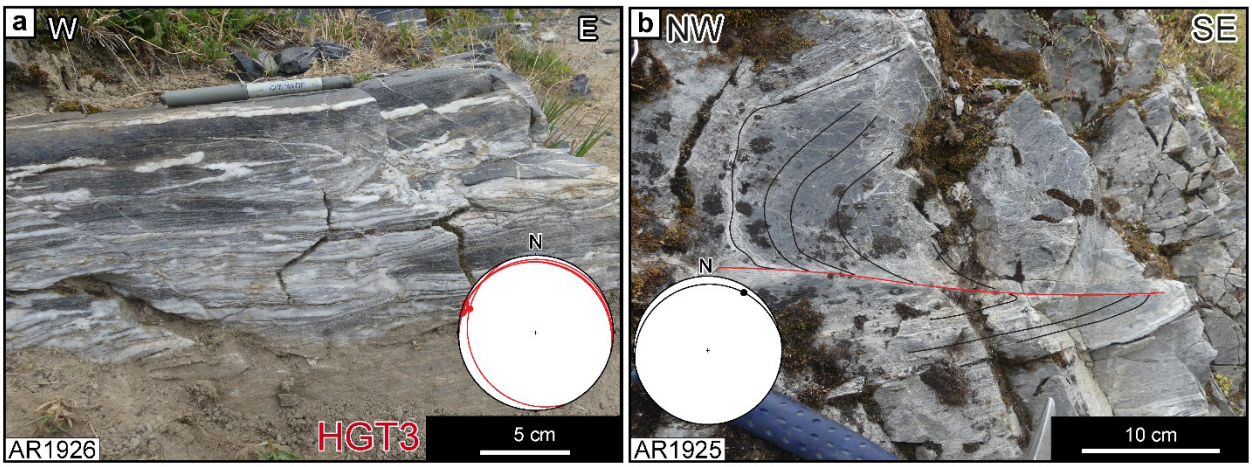

Figure S6. Site HGT5 (Sixt window): a) Horizontal basal Triassic unconformity above chloritoschist basement.; b) Thrust fault into the Jurassic limestones above the Triassic serie. The shear sense is towards the NW.

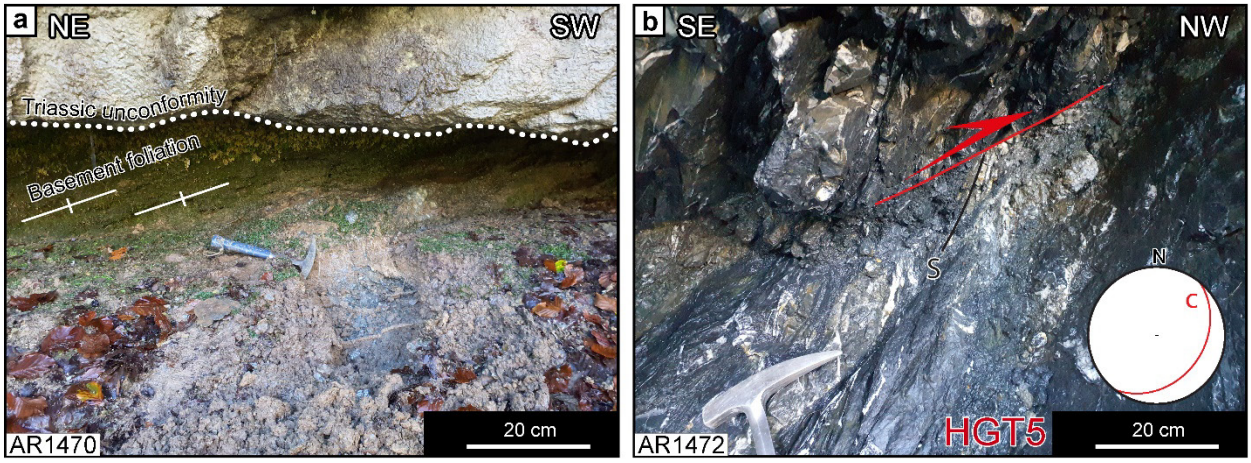

Figure S7. Site HGT6 (Aiguille du Belvedère): a) Stretching lineation trending N285°, affecting the black slates atop the summit; b) Sheared and stretched dolomites above the Triassic unconformity. The stretching lineation trends N130°.

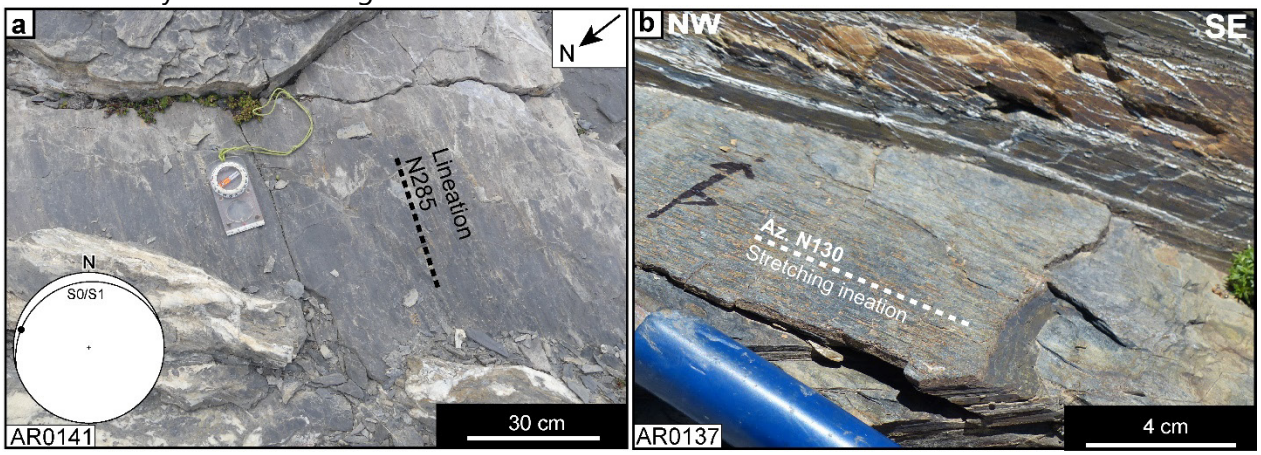

Figure S8. a) Steep thrust affects the limestones, and initial foliation is cross cut by steep faults (station AR453). b) Flat reverse fault associated with the Pormenaz-Merlet shear zone with a striation trending N120°, indicating top to the northwest.

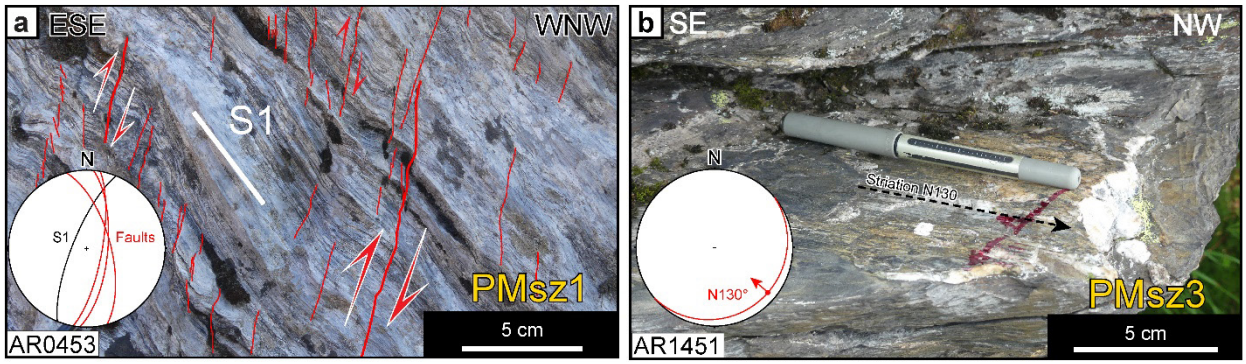

Figure S9. Thin section of sample ARe096, (station AR0370b) from the Gietroz fault (Cf. Figure 10 and 3a). The sample is a pseudotachylite with quartz and micas, the C/S relation is interpreted as normal sens of shear (SE down).

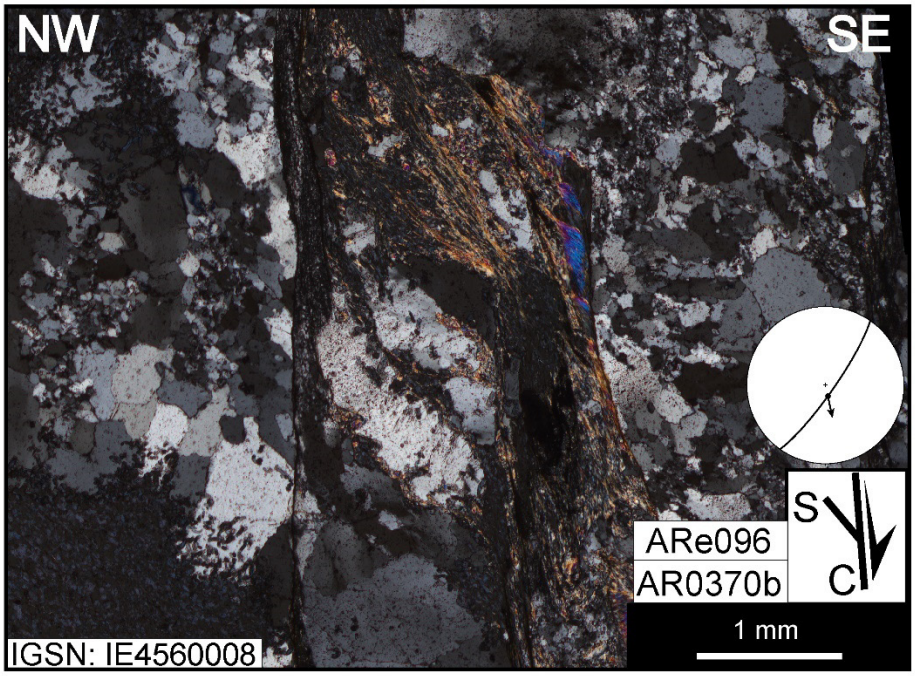

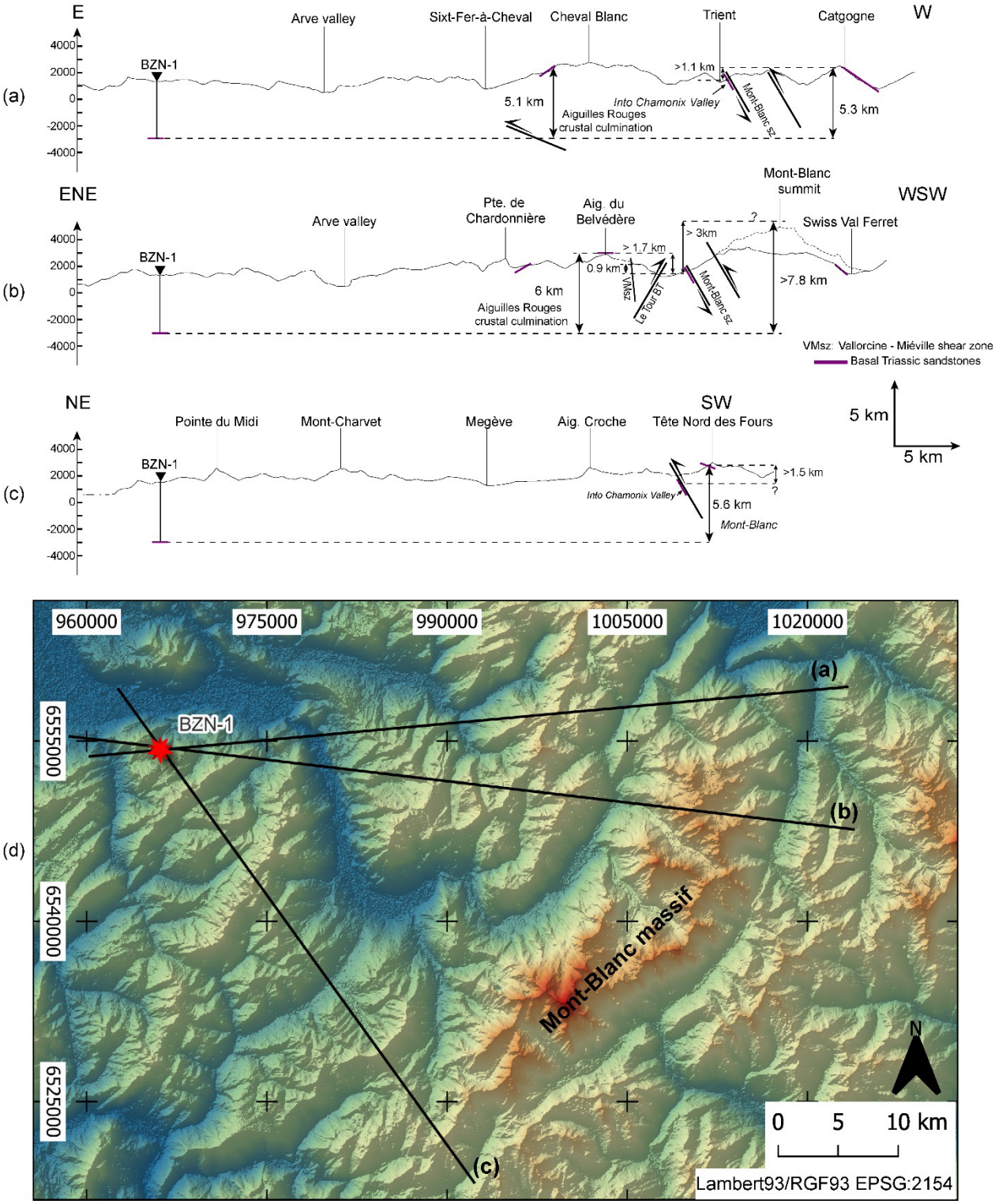

Figure S10. Sections highlighting the Triassic unconformity in order to estimate the amount of exhumation between the massifs: (a) Section through Chablais, Haut-Giffre, Aiguiles Rouges and northern Mont-Blanc massif (Catogne); (b) Section through Désert de Platé, Aiguille du

Belvédère and Mont-Blanc massif (Âmone); (c) Section through Aravis, Mont-Joly, Col du Bonhomme and southern Mont-Blanc massif (Tête Nord des Fours).